Transactions of the ASME®

Transactions of the ASME, Journal of Engineering for Gas Turbines and Power (ISSN 0742-4795) is published quarterly (Jan., April, July, Oct.) for $175.00 per year by The American Society of Mechanical Engineers, 345 East 47th Street, New York, NY 10017. Second class postage paid at New York, NY and additional mailing offices. POSTMASTER: Send address changes to Transactions of the ASME, Journal of Engineering for Gas Turbines and Power, c/o THE AMERICAN SOCIETY OF MECHANICAL ENGINEERS, 22 Law Drive, Box 2300, Fairfield, NJ 07007-2300.
CHANGES OF ADDRESS must be received at Society headquarters seven weeks before they are to be effective. Please send old label and new address.
PRICES: To members, $40.00, annually: to nonmembers, $175.00. Add $30.00 for postage to countries outside the United States and Canada.
STATEMENT from By-Laws. The Society shall not be responsible for statements or opinions advanced in papers or . . . printed in its publications (B7.1, par. 3).

INDEXED by Applied Mechanics Reviews and Engineering Information, Inc. Canadian Goods & Services Tax Registration #126148048

Journal of Engineering for Gas Turbines and Power

Published Quarterly by The American Society of Mechanical Engineers

VOLUME 118 • NUMBER 1 • JANUARY 1996

TECHNICAL PAPERS

Advanced Energy Systems

1 **A General Simulation Model for Stirling Cycles**
S. Schulz and F. Schwendig

8 **Nondimensional Schmidt Analysis for Optimal Design of Stirling Engines**
R. Impero Abenavoli, M. Carlini, H. Kormanski, K. Rudzinska, and A. Sciaboni

15 **High-Enthalpy Extraction Demonstration With Closed-Cycle Disk MHD Generators**
N. Harada, T. Suekane, K. Tsunoda, H. Yamasaki, and S. Shioda

Gas Turbines: Coal Utilization

22 **A Coal-Fired Heat Exchanger for an Externally Fired Gas Turbine**
P. R. Solomon, M. A. Serio, J. E. Cosgrove, D. S. Pines, Y. Zhao, R. C. Buggeln, and S. J. Shamroth

Gas Turbines: Cogeneration

32 **Coadunation of Technologies: Cogeneration and Thermal Energy Storage**
S. Somasundaram, M. K. Drost, D. R. Brown, and Z. I. Antoniak

Gas Turbines: Combustion and Fuels

38 **Emission and Performance of a Lean-Premixed Gas Fuel Injection System for Aeroderivative Gas Turbine Engines** (94-GT-234)
T. S. Snyder, T. J. Rosfjord, J. B. McVey, A. S. Hu, and B. C. Schlein

46 **Low-NO_x Premixed Combustion of MBtu Fuels Using the ABB Double Cone Burner (EV Burner)** (94-GT-394)
K. Döbbeling, H. P. Knöpfel, W. Polifke, D. Winkler, C. Steinbach, and T. Sattelmayer

54 **Residual Reactivity of Burned Gases in the Early Expansion Process of Future Gas Turbines**
B. Leide and P. Stouffs

61 **A Catalytic Combustor for High-Temperature Gas Turbines** (94-GT-211)
N. Vortmeyer, M. Valk, and G. Kappler

65 **Flow Behavior With an Oscillating Motion of the Impinging Jet in a Dump Diffuser Combustor** (94-GT-233)
S. Honami, T. Shizawa, A. Sato, and H. Ogata

72 **Studies of Lean Blowout in a Step Swirl Combustor** (94-GT-216)
M. D. Durbin and D. R. Ballal

78 **Reducing Gas Turbine Emissions Through Hydrogen-Enhanced, Steam-Injected Combustion**
J. R. Maughan, J. H. Bowen, D. H. Cooke, and J. J. Tuzson

86 **A Spinning Finite Beam Element of General Orientation Analyzed With Rayleigh/Timoshenko/Saint-Venant Theory** (94-GT-77)
T. J. S. Abrahamsson and J. H. Sällström

95 **Improving Traditional Balancing Methods for High-Speed Rotors**
J. Ling and Y. Cao

100 **Coupled Shaft-Torsion and Blade-Bending Vibrations of a Rotating Shaft–Disk–Blade Unit**
S. C. Huang and K. B. Ho

107 **Effects of Bearing and Shaft Asymmetries on the Resonant Oscillations of a Rotor-Dynamic System**
R. Ganesan

115 **Instability Threshold and Stability Boundaries of Rotor-Bearing Systems**
W. J. Chen

122 **Nonlinear Analysis of Rotordynamic Instabilities in High-Speed Turbomachinery** (94-GT-78)
D. S. H. Chan

130 **Forced Harmonic Response of Grouped Blade Systems: Part I—Discrete Theory** (94-GT-203)
L. F. Wagner and J. H. Griffin

(Contents continued on page 45)

(Contents continued)

137 Forced Harmonic Response of Grouped Blade Systems: Part II—Application (94-GT-204)
L. F. Wagner and J. H. Griffin

146 Aircraft Crash Caused by Stress Corrosion Cracking (94-GT-298)
H. J. Kolkman, G. A. Kool, and R. J. H. Wanhill

Gas Turbines: Vehicular

150 Durability Evaluation of Ceramic Components Using CARES/LIFE (94-GT-362)
N. N. Nemeth, L. M. Powers, L. A. Janosik, and J. P. Gyekenyesi

159 Plasticity Considerations in Probabilistic Ceramic-to-Metal Joint Design (94-GT-229)
D. A. ONeil, J. H. Selverian, and K. S. Kim

167 Development of a Low-Emission Combustor for a 100-kW Automotive Ceramic Gas Turbine (II) (94-GT-33)
H. Kumakura, M. Sasaki, D. Suzuki, and H. Ichikawa

173 Hybrid Bearing Technology for Advanced Turbomachinery: Rolling Contact Fatigue Testing (94-GT-386)
J. F. Dill

179 SPSLIFE: A User-Friendly Approach to the Structural Design and Life Assessment of Ceramic Components (94-GT-486)
T. Bornemisza and A. Saith

184 Ceramic Hybrid Bearings in Air-Cycle Machines (94-GT-393)
L. Burgmeier and M. Poursaba

Gas Turbines: Vibrations

191 Evaluation of Ceramic Rotor Strength by Cold and Hot Spin Tests (94-GT-460)
M. Watanabe and H. Ogita

Power: Feedwater Systems

198 Early Detection of Feedwater-Heater Leaks
E. Hansen, R. Godwin, D. Wood, and L. Turner

Power: Fluidized Beds

204 Control of a Fluidized Bed Combustor Using Fuzzy Logic
S. J. Koffman, R. C. Brown, and R. R. Fullmer

Power

210 Functional Forms to Describe Thermodynamic Properties of Gases for Fast Calculations
J. Pátek

214 Computational Fluid Dynamics Analysis of a Steam Power Plant Low-Pressure Turbine Downward Exhaust Hood
R. H. Tindell, T. M. Alston, C. A. Sarro, G. C. Stegmann, L. Gray, and J. Davids

TECHNICAL BRIEF

225 Magnetism and Stray Currents in Rotating Machinery
P. I. Nippes

ANNOUNCEMENTS

31 Change of address form for subscribers

Inside back cover Information for authors

S. Schulz
Professor.

F. Schwendig
Research Assistant.

Department of Chemical Engineering,
University of Dortmund,
Dortmund, Federal Republic of Germany

A General Simulation Model for Stirling Cycles

A mathematical model for the calculation of the Stirling cycle and of similar processes is presented. The model comprises a method to reproduce schematically any kind of process configuration, including free piston engines. The differential balance equations describing the process are solved by a stable integration algorithm. Heat transfer and pressure loss are calculated by using new correlations, which consider the special conditions of the periodic compression/expansion respectively of the oscillating flow. A comparison between experimental data achieved by means of a test apparatus and calculated data shows a good agreement.

Introduction

Based on the original Stirling engine, several process configurations have been developed. Such configurations are, e.g., the Ringbom engine, containing an overdriven free displacer, or systems with both a free piston and a free displacer. With regard to the computer simulation of the various processes, it is advantageous to describe the different configurations in an appropriate systematic way. The configurations can be integrated into the calculation algorithm in the form of a data file by means of this systematic description without changing the calculation algorithm itself. In the following, a method for describing any kind of process configuration is presented before the calculation model itself is developed.

Systematic Description of Different Process Configurations

The principle of this method, which considers not only the ordinary kinematic engines, but also the compact free piston systems, as well as systems with more than one single process volume, is demonstrated in the case of a free piston Stirling engine. Figure 1 indicates the sketch of this engine. At first, only those process units of the machine are considered that hold the process volume (cylinders, heat exchangers, regenerator). These units are filled with working gas and, thus, have to be mathematically treated in the same way. Each of these units has one or more outlets, with which it is connected to another component of the engine. Exactly two outlets of different units are coupled at any connecting point. The configuration is completely specified, if for all connecting points it can definitely be stated which two units are linked with which of their outlets.

First of all, the engine must be schematically decomposed in its components (Fig. 2), and the units and the connecting points are numbered. Next, all necessary information about the configuration is recorded by means of two lists. The first list comprises the information on the type of unit (e.g., unit No. 2 is a heat exchanger). The second list states how the units are linked (e.g., connecting point No. 3 links outlet 2 of unit 3 to outlet 1 of unit 4).

With regard to the mathematical treatment of the whole system at the connecting points, "information" is exchanged between the two linked units. In case of the gas volumes, which have been handled up to now, this "information" is the mass flow and the enthalpy flow. When other types of unit are also added to the configuration, the exchange of information contains other quantities as well. Consequently, the principle of units and connecting points can also be transferred to free piston components (free pistons, gas springs, mechanical springs). Figure 3 shows the schematic linkage of these parts. In this layout the "outlets" of the free piston components are either the frontal areas of a free piston or the end of a mechanical spring. They are formally treated in the same way as the outlets of the gas volumes. The information being exchanged between the components in order to calculate the movement of the free pistons are pressure forces, spring forces, positions of the free pistons, and velocities of the free pistons. The presented method permits the reproduction of all possible process configurations within a simulation model, including free piston engines and duplex Stirling machines.

General Calculation of the Process

The calculation of the state of the working gas is based on differential balance equations for mass, momentum, and energy. These equations have to be transformed in order to enable mathematical treatment within a simulation model. A suitable method for this mathematical treatment is the method of finite volume elements, where the whole process volume is divided into small balance volumes. Each of these finite volumes is described by separate balance equations:

Mass balance for the ith volume element

$$\frac{dm_i}{dt} = \sum \dot{m}_{i,\text{in}} - \sum \dot{m}_{i,\text{out}} \tag{1}$$

Energy balance for the ith volume element

$$\frac{dU_i}{dt} = \dot{Q}_i - P_i + \sum \dot{H}_{i,\text{in}} - \sum \dot{H}_{i,\text{out}}. \tag{2}$$

The mass flows passing the boundaries $i - \frac{1}{2}$ between adjacent volume elements i and $i - 1$ are calculated by means of the instationary Bernoulli equation considering pressure losses

$$\left(\rho \cdot \frac{du}{dt}\right)_{i-1/2} \cdot \Delta x = \left(\frac{\rho}{2} \cdot u^2\right)_{i-1} - \left(\frac{\rho}{2} \cdot u^2\right)_i + p_{i-1} - p_i - \Delta p_{\text{loss}}. \tag{3}$$

As a whole, these equations represent an ordinary differential equation system. The only independent variable is the time t. The dependent variables are the masses m_i, the temperatures T_i, and the flow velocities $u_{i-1/2}$. However, the integration of this differential equation system with time does not give stable results. This is due to the fact that the calculation of the mass flow is based on pressure differences. Therefore, very small

Contributed by the Advanced Energy Systems Division for publication in the JOURNAL OF ENGINEERING FOR GAS TURBINES AND POWER. Manuscript received by the Advanced Energy Systems Division February 14, 1992; revision received September 16, 1992. Associate Technical Editor: M. J. Moran.

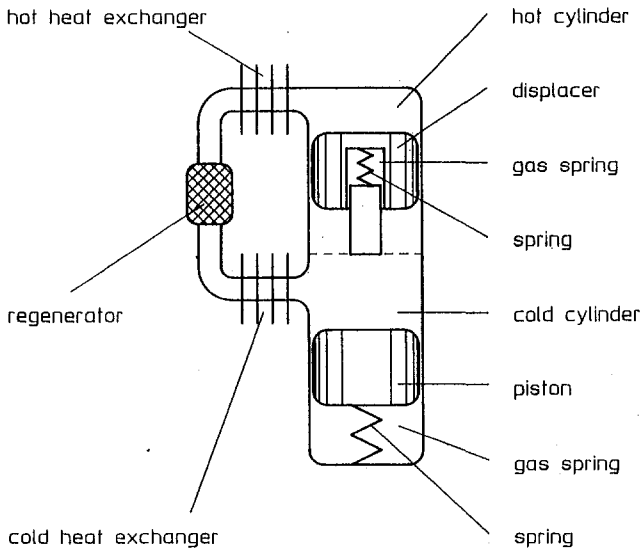

Fig. 1 Sketch of the free piston Stirling engine

integration intervals must be used, which lead to long computing times. In order to avoid such long-lasting calculations, the mass flows are determined in a different way. It is assumed that any local pressure differences are compensated for all times throughout the process volume. Based on this idea, several authors derived different equations for the determination of the mass flow rates (e.g., Urieli and Berchowitz, 1984). In this paper another algorithm is outlined.

The assumption of pressure compensation is only introduced in order to calculate the mass flows. The determination of the mechanical power, however, requires the consideration of pressure gradients, which are obtained using the known mass flow rates calculated previously. The friction forces and acceleration forces appearing in the Bernoulli equation can be determined by means of the mass flows. Finally, the Bernoulli equation is inverted, i.e., the pressure difference between neighboring volume elements $p_{i-1} - p_i$ is obtained.

The calculation of the mass flow rates, neglecting pressure gradients, does not lead to noticeable inaccuracies. This is demonstrated in Fig. 4. The diagram shows the calculated mass flow rates for the same process plotted against the angle for one cycle. The dotted curve is calculated according to the assumption of a total pressure compensation while the solid curve is calculated in the conventional way, i.e., accounting for pressure differences. The curves are almost equal. Therefore, the corresponding pressure gradients, which in one case result from the predetermined mass flows and in the other case lead to the calculated mass flows, coincide also.

First, the calculation procedure for the mass flow rates assuming a pressure compensation is derived for an ideal gas with constant heat capacities. The internal energy of a volume element i is given by:

$$U_i = m_i \cdot c_v \cdot T_i \tag{4}$$

$$U_i = p_i \cdot c_v \cdot V_i / R \tag{5}$$

According to the assumption that the pressure is equal in all the volume elements, the internal energy U_i is proportional to the magnitude of the corresponding volume V_i:

$$U_i \sim V_i \tag{6}$$

Consequently U_i can be obtained from the internal energy U_{tot} of the total working gas by multiplying U_{tot} by the volume ratio V_i/V_{tot}:

$$U_i = U_{\text{tot}} \cdot V_i / V_{\text{tot}} \tag{7}$$

The change of the total internal energy with time is equal to the sum of mechanical power and all the heat flows of the process.

$$\frac{dU_{\text{tot}}}{dt} = \sum \dot{Q}_j - \sum P_j \tag{8}$$

Referring to Eq. (7), the derivative of U_i with time is then given by:

$$\frac{dU_i}{dt} = \frac{V_i}{V_{\text{tot}}} \cdot \frac{dU_{\text{tot}}}{dt} + \frac{U_{\text{tot}}}{V_{\text{tot}}} \cdot \frac{dV_i}{dt} - \frac{U_{\text{tot}} \cdot V_i}{V_{\text{tot}}^2} \cdot \frac{dV_{\text{tot}}}{dt} \tag{9}$$

Applying the above-mentioned equation, the derivative of U_i is obtained without a special energy balance for volume element i. Next, the known value of dU_i/dt can be used to solve Eq.

Nomenclature

A = area
a = thermal conductivity
c_p = mean specific heat capacity at constant pressure
c_v = mean specific heat capacity at constant volume
d = diameter
F = factor of the amplitude in Eq. (31)
f = frequency
$\dot{H}$ = enthalpy flow
m = mass
$\dot{m}$ = mass flow
Nu = Nusselt number = $\alpha \cdot d/\lambda$
n = number of volume elements
P = mechanical power
Pe_ω = kinematic Péclet number = $\omega \cdot d^2/a$
p = pressure
$\dot{Q}$ = heat flow
R = specific gas constant
Re = Reynolds number = $u_m \cdot d/\nu$
Re_ω = kinematic Reynolds number = $\omega \cdot d^2/\nu$
r = radial coordinate
T = temperature
t = time
U = internal energy
u = axial flow velocity
V = volume
v = radial flow velocity respectively ratio of amplitudes
w = velocity of a piston
x = axial coordinate
z = compressibility factor
α = heat transfer coefficient
β = phase shift
γ = phase shift
η = dynamic viscosity
λ = heat conductivity
ν = kinematic viscosity
ξ = friction factor
φ = phase shift
ρ = density
ω = angular velocity

Subscripts

C = cold part of the engine
c = complex
eff = effective
H = hot part of the engine
i = ith volume element
im = imaginary part
in = flowing in
j = jth volume element
loss = loss
M = regenerator matrix
m = cross-sectional mean value
max = maximum value
out = flowing out
qu.st. = quasi-steady
re = real part
st = stationary conditions
t = turbulent
tot = total
W = warm part of the engine
w = wall

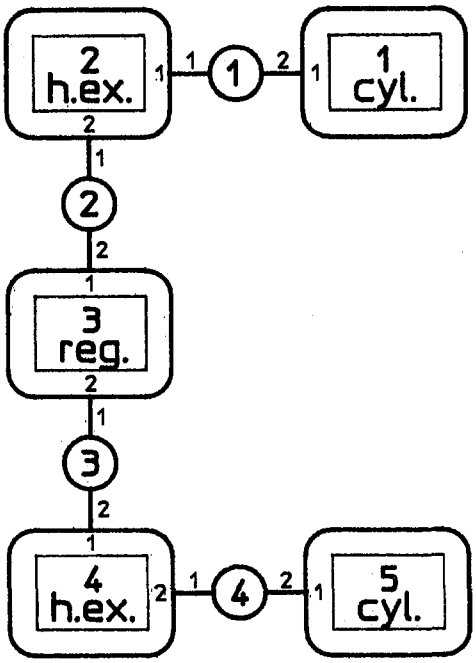

Fig. 2 Schematic decomposition of the Stirling engine: process volume

2. The heat flow $\dot{Q}_i$ and the mechanical power P_i of the volume element i result from the current state of the process (temperatures, flow velocities, volume changes, etc.). As a matter of fact, only the enthalpy flows between adjacent volume elements are still unknown quantities in Eq. (2).

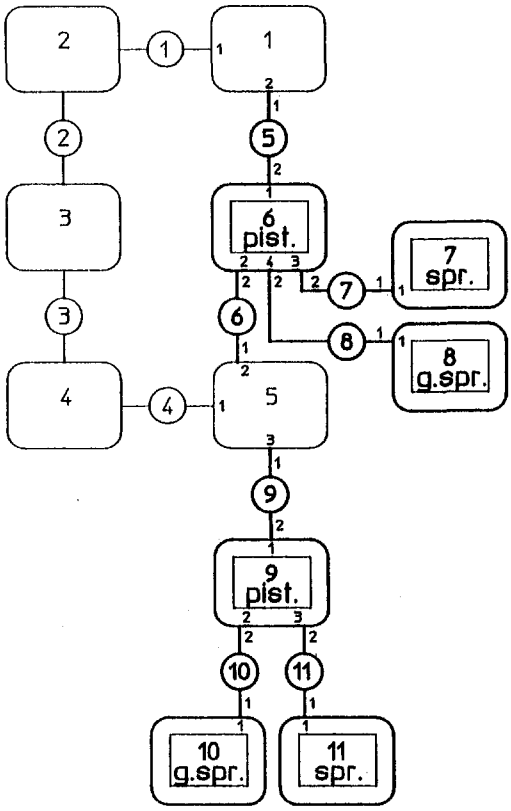

Fig. 3 Schematic decomposition of the Stirling engine: free piston components

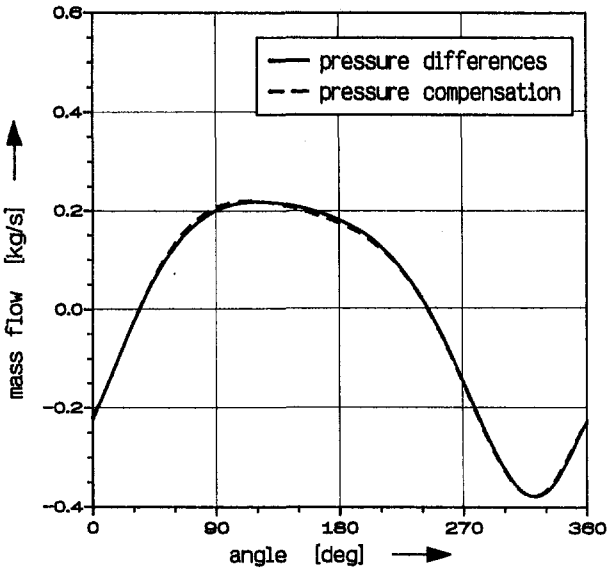

Fig. 4 Comparison between mass flow rates, calculated considering and neglecting local pressure differences

$$\dot{H}_{i,\text{in}} - \dot{H}_{i,\text{out}} = \frac{dU_i}{dt} - \dot{Q}_i + P_i \tag{10}$$

Equation (10) is valid for all n volume elements. Thus, a system of linear equations for the unknown enthalpy flows is obtained, which can easily be solved. Finally, the mass flow rates result from the enthalpy flows due to:

$$\dot{m} = \dot{H}/(c_p \cdot T) \tag{11}$$

T is the temperature of the mass flow between the adjacent volume elements. According to the procedure presented, it is possible to calculate the mass flows in a stable manner and above all accurately.

Up to now the equations have been derived assuming ideal gas behavior. In order to consider real gas behavior the correlations have to be extended by the compressibility factor z. The factor z can be expressed as a function of temperature and pressure:

$$z = (p \cdot V)/(m \cdot R \cdot T) \tag{12}$$

In case of a real gas the heat capacities c_p and c_v also change in temperature and pressure. Instead of Eq. (7) the relation between the internal energy of volume element i and the internal energy of the whole process volume reads as follows:

$$U_i = U_{\text{tot}} \cdot \frac{c_{v,i} \cdot V_i/z_i}{\sum (c_{v,j} \cdot V_j/z_j)} \tag{13}$$

The derivative of U_i with time depends not only on the derivatives of U_{tot} and the volumes V_i, but also on the derivatives of the compressibility factors z_i and the heat capacities $c_{v,i}$. However, the effect of dz_i/dt and $dc_{v,i}/dt$ on dU_i/dt is relatively small:

$$\frac{1}{c_v} \cdot \frac{dc_v}{dt} \quad \text{and} \quad \frac{1}{z} \cdot \frac{dz}{dt} \ll \frac{1}{U} \cdot \frac{dU}{dt} \quad \text{and} \quad \frac{1}{V} \cdot \frac{dV}{dt} \tag{14}$$

Therefore, the derivative of U_i can be easily determined by neglecting dz_i/dt and $dc_{v,i}/dt$ in order to avoid an iterative calculation:

$$\frac{dU_i}{dt} = \frac{c_{v,i} \cdot V_i/z_i}{\sum (c_{v,j} \cdot V_j/z_j)} \cdot \frac{dU_{\text{tot}}}{dt} + U_{\text{tot}} \cdot \frac{c_{v,i}/z_i}{\sum (c_{v,j} \cdot V_j/z_j)} \cdot \frac{dV_i}{dt} - U_{\text{tot}} \cdot \frac{c_{v,i} \cdot V_i/z_i}{[\sum (c_{v,j} \cdot V_j/z_j)]^2} \cdot \sum \left(\frac{c_{v,j}}{z_j} \cdot \frac{dV_j}{dt} \right) \tag{15}$$

Consideration of real gas behavior only influences the determination of dU_i/dt. The calculation of the mass flows is effected by means of Eqs. (10) and (11).

So far pressure differences due to friction and inertia forces have been neglected. However, they have an important influence on the mechanical power output of the process. The pressure differences are determined by using the known mass flow rates between adjacent volume elements. Therefore, the Bernoulli Eq. (3) is evaluated. The equation is inverted; thus, the pressure difference between adjacent volume elements $p_{i-1} - p_i$ can be calculated:

$$p_{i-1} - p_i = \Delta p_{\text{loss}} - \left(\rho \cdot \frac{du}{dt}\right)_{i-1/2} \cdot \Delta x - \left(\frac{\rho}{2} \cdot u^2\right)_{i-1} + \left(\frac{\rho}{2} \cdot u^2\right)_i \quad (16)$$

The quantities on the right-hand side of the equation are obtained from the known mass flow rates. This equation, suitable for all boundaries between volume elements, leads to a system of linear equations with $n - 1$ equations and n unknown pressures (n = number of volume elements). The missing equation results from the requirement that the gas mass is constant within the entire process volume.

$$\sum m_j = \sum \frac{V_j \cdot p_j}{R \cdot T_j \cdot z_j} = m_{\text{tot}} = \text{const.} \quad (17)$$

$$\frac{V_1}{T_1 \cdot z_1} \cdot p_1 + \frac{V_2}{T_2 \cdot z_2} \cdot p_2 + \cdots = R \cdot m_{\text{tot}} \quad (18)$$

The compressibility factors z_i are easily calculated by using the pressures p_i of the last integration step. As a consequence, the linear equation system consists of n equations and can be solved in order to obtain the pressure distribution in the process volume.

After the analytical determination of the mass flow rates and the mass distribution (resulting from the pressure distribution), the energy balance (Eq. (2)) has to be integrated. For this purpose this equation is transformed in such a way that temperature T_i is the variable to be integrated:

$$m_i \cdot c_{v,i} \cdot \frac{dT_i}{dt} = \dot{Q}_i - P_i + \dot{m}_{i,\text{in}} \cdot c_{p,\text{in}} \cdot T_{\text{in}} - \dot{m}_{i,\text{out}} \cdot c_{p,\text{out}} \cdot T_{\text{out}} - (\dot{m}_{i,\text{in}} - \dot{m}_{i,\text{out}}) \cdot c_{v,i} \cdot T_i - (\dot{m}_{i,\text{in}} - \dot{m}_{i,\text{out}}) \cdot T_i \cdot \frac{dc_{v,i}}{dt} \quad (19)$$

The derivative of c_v is again neglected. T_{in} and T_{out} represent the temperatures of the mass flows between adjacent volume elements. They have to be determined by interpolating or extrapolating the known temperatures of the volume elements. For this reason a linear temperature profile is assumed within a volume element. The temperature T_i is assumed to be the temperature in the center of the volume element i.

The gradient of the temperature profile results from the temperatures of the two adjacent volumes, as shown in Fig. 5. The temperature of the mass flow leaving a volume element depends on the direction of the mass flow. This is illustrated by means of the arrows in Fig. 5.

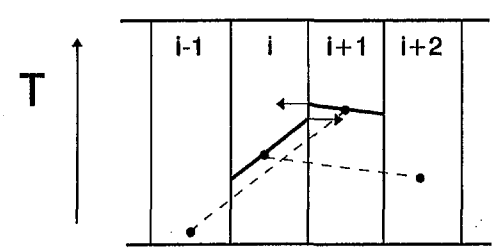

Fig. 5 Axial temperature profile within a volume element

$\dot{m}_{i+1/2}$ from i to $i + 1$:

$$\rightarrow T_{i+1/2} = T_i + (T_{i+1} - T_{i-1})/4 \quad (20)$$

$\dot{m}_{i+1/2}$ from $i + 1$ to i:

$$\rightarrow T_{i+1/2} = T_{i+1} - (T_{i+2} - T_i)/4 \quad (21)$$

The heat flow $\dot{Q}_i$ exchanged between the wall and the gas is calculated by using a heat transfer coefficient:

$$\dot{Q}_i = (\alpha \cdot A)_i \cdot (T_{w,i} - T_i) \quad (22)$$

The mechanical power P_i results from the current pressure and the volume change. The mass flows $\dot{m}_{i,\text{in}}$ and $\dot{m}_{i,\text{out}}$ were analytically calculated in advance. Thus, Eq. (19) can be transformed as follows:

$$\frac{dT_i}{dt} = [\{(\alpha \cdot A)_i \cdot T_{w,i} - P_i + (\dot{m} \cdot c_p \cdot T)_{i,\text{in}} \pm (\dot{m} \cdot c_p)_{i,\text{out}} \cdot (T_{i+1} - T_{i-1})/4\}/(m \cdot c_{v,i})] - [\{(\alpha \cdot A)_i + (\dot{m} \cdot c_p)_{i,\text{out}} + (\dot{m}_{i,\text{in}} - \dot{m}_{i,\text{out}}) \cdot c_{v,i}\}/(m \cdot c_{v,i})] \cdot T_i \quad (23)$$

Because of the very large heat transfer rates in the regenerators, the numerical integration of Eq. (23) is difficult due to problems of stability. In order to avoid such problems, the following calculation procedure is derived. Each volume element is decoupled from the process and treated separately for one integration step. Except for the temperatures T_i, all quantities are assumed to be constant during this integration step. They represent constant boundary conditions for the calculation of the temporal change of T_i. Therefore, the differential Eq. (23) can be schematically written as follows:

$$\frac{dT_i}{dt} = A_i - B_i \cdot T_i \quad (24)$$

A_i and B_i are constant for one integration step due to the abovementioned assumption. Thus, Eq. 24 can be solved analytically

$$T_i^1 = \frac{A_i}{B_i} + \left(T_i^0 - \frac{A_i}{B_i}\right) \cdot e^{-B_i} \cdot \Delta t \quad (25)$$

T_i^0 = temperature at time t^0
T_i^1 = temperature at time $t^1 = t^0 + \Delta t$

In order to effect the next integration step, the new values of A_i and B_i must be determined.

The integration procedure presented is stable for any integration step width. However, the accuracy of the results decreases with larger step width. The main reason for this fact is the nonuniform treatment of the temperature of the fluid flowing between volume elements. If the fluid leaves a volume element, its temperature changes according to the temperature of this volume element. On the contrary, the temperature of the fluid entering a volume element is assumed to be constant for one integration step. This leads to an error regarding the energy balance and affects the results, being dependent on the chosen step width. When the step width is zero, this error disappears. However, as Fig. 6 demonstrates, the results obtained by using large step width (-> short calculation time) are often sufficiently accurate. The diagram indicates the calculated mechanical power and heat flows for a Stirling engine depending on the chosen integration step width.

So far the method for the determination of the working fluid's state has been presented. Two further aspects have to be taken into account in order to calculate the entire process. First, the temperature distribution of the regenerator matrix affects the

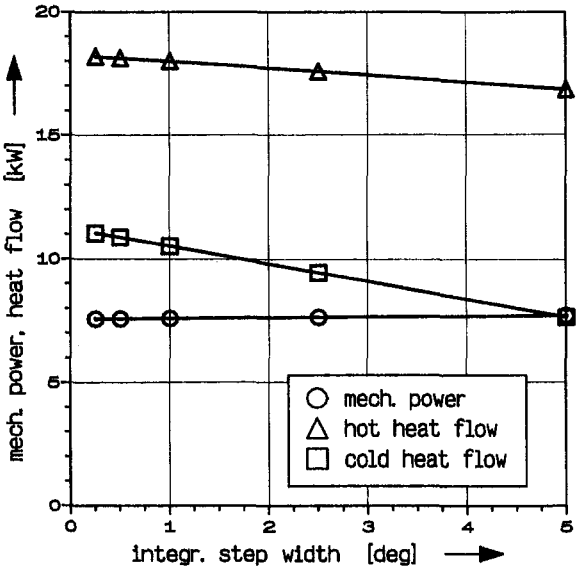

Fig. 6 Calculated mechanical power and heat flows versus integration step width

heat flows in the connected heat exchangers and is obtained by an energy balance:

$$\frac{\partial(\rho \cdot A \cdot c_v \cdot T)}{\partial t} = \frac{\partial}{\partial x}\left(\lambda \cdot A \cdot \frac{\partial T}{\partial x}\right) + \frac{\partial \dot{Q}}{\partial x} \tag{26}$$

Second, the motion of the free pistons results from a force balance:

$$\frac{dx}{dt} = w \tag{27}$$

$$m \cdot \frac{dw}{dt} = \sum C_i \cdot x + \sum A_i \cdot p_i - m \cdot g - D \cdot w - \text{sign}(w) \cdot K \tag{28}$$

$\Sigma\, C_i \cdot x$ = forces of mechanical springs
$\Sigma\, A_i \cdot p_i$ = pressure forces
$m \cdot g$ = gravitational force
$D \cdot w$ = damping force
$\text{sign}(w) \cdot K$ = friction force between piston and wall

Mathematical Description of the Pressure Losses

Referring to the general description of the calculation procedure, the pressure loss up to now has only been treated as a formal quantity (e.g., Eq. (3)). However, simulation of a process requires a special mathematical description of the pressure losses in order to obtain their appropriate values. The correlations should consider the special flow characteristics within the Stirling processes, since the pressure losses considerably affect the mechanical power. The flow periodically changes its direction. This results in a deformation of the velocity profile compared to stationary flow conditions. Uchida (1956) investigated the fully developed incompressible oscillating flow for laminar conditions. He solved the momentum balance

$$\frac{\partial u}{\partial t} = -\frac{1}{\rho} \cdot \frac{\partial p}{\partial x} + \nu \cdot \left(\frac{\partial^2 u}{\partial r^2} + \frac{1}{r} \cdot \frac{\partial u}{\partial r}\right) \tag{29}$$

analytically assuming a sinusoidally changing pressure gradient:

$$\frac{\partial p}{\partial x} = \left(\frac{dp}{dx}\right)_{\max} \cdot \cos(\omega t) \tag{30}$$

The resulting cross-sectional mean velocity u_m is also described by a sine function, but with a phase shift φ compared to the pressure gradient:

$$u_m(t) = -\left(\frac{dp}{dx}\right)_{\max} \cdot \frac{F}{\rho \cdot \omega} \cdot \cos(\omega t + \varphi)$$

$$F = F(\text{Re}_\omega), \quad \varphi = \varphi(\text{Re}_\omega) \tag{31}$$

The factor F of the amplitude and the phase shift φ depend only on the dimensionless frequency Re_ω. In order to obtain an applicable correlation for the pressure losses, in case of the simulation model, the pressure gradient dp/dx has to be described as a function of the mean velocity u_m. First, it is useful to analyze the quasi-steady equation where the friction forces are calculated subject to the Hagen–Poisseuille law being valid for steady flow.

$$\left(\frac{dp}{dx}\right)_{qu.st.} = \xi \cdot \frac{\rho}{2} \cdot u_m \cdot |u_m| \cdot \frac{1}{d} + \rho \cdot \frac{du_m}{dt} \tag{32}$$

$\xi = 64/\text{Re}$, u_m according to Eq. (31)

$$\left(\frac{dp}{dx}\right)_{qu.st.} = \left(\frac{dp}{dx}\right)_{\max} \cdot F \cdot (1024/\text{Re}_\omega^2 + 1)^{1/2} \times \cos(\omega t + \varphi + \gamma) \tag{33}$$

$$\gamma = \arctan\left(\frac{\text{Re}_\omega}{32}\right)$$

The difference between the real pressure gradient dp/dt (Eq. (30)) and the quasi-steady pressure gradient $(dp/dx)_{\text{qu.st.}}$ (Eq. (33) is expressed by the relation of the amplitudes v and the phase shift β (Figs. 7 and 8):

$$v = \frac{1}{F \cdot (1024/\text{Re}_\omega^2 + 1)^{1/2}} \tag{34}$$

$$\beta = \varphi + \gamma \tag{35}$$

The phase shift β is less than 7.5° and can be neglected. It is sufficient to correct the quasi-steady pressure gradient by the amplitude ratio v in order to reproduce the exact pressure gradient more accurately. One can determine v more easily by using Eq. 36 instead of Eq. 34 as the factor F includes the Bessel function:

$$v = \left[(1 + 0.00565 \cdot \text{Re}_\omega)^{-20} + \left(\frac{1.7}{\text{Re}_\omega^{0.06467}}\right)^{-20}\right]^{-1/20} \quad (\text{Re}_\omega < 1000) \tag{36}$$

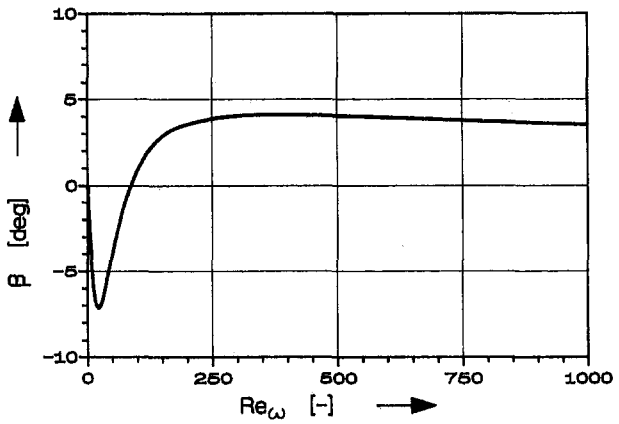

Fig. 7 Phase shift between the exact pressure gradient and the quasi-stationary pressure gradient

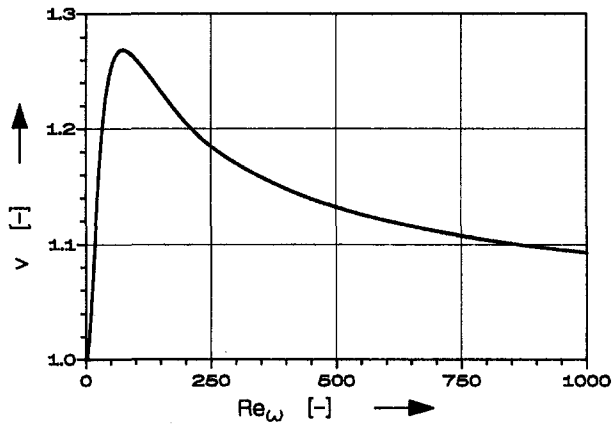

Fig. 8 Ratio between the amplitude of the exact pressure gradient and the amplitude of the quasi-stationary pressure gradient

In order to consider turbulent flow conditions for oscillating flow, differential Eq. (29) has to be solved by using a turbulence model to describe the eddy viscosity. Another method that simplifies the problem is to apply the correlations that were derived for laminar flow and to replace the viscosity η appearing in the dimensionless frequency by an effective viscosity η_{eff}. This effective viscosity represents the degree of turbulence:

$$\mathrm{Re}_{\omega,\mathrm{eff}} = \omega \cdot d^2 \cdot \rho / \eta_{\mathrm{eff}} \tag{37}$$

η_{eff} is obtained from the known pressure drop laws of the steady flow. It is defined as the seeming viscosity, which results in the turbulent pressure drop while being integrated into the pressure drop law of laminar flow.

$$\xi = \frac{64}{\mathrm{Re}_{\mathrm{eff}}} = \frac{64 \cdot \eta_{\mathrm{eff}}}{|u_m| \cdot d \cdot \rho} \tag{38}$$

The pressure drop for turbulent flow is also given by the law of Blasius:

$$\xi = \left(\frac{1}{100 \cdot \mathrm{Re}}\right)^{1/4} = \left(\frac{\eta}{100 \cdot |u_m| \cdot d \cdot \rho}\right)^{1/4} \tag{39}$$

According to the above-mentioned law, the effective viscosity can be determined as follows:

$$\frac{\eta_{\mathrm{eff}}}{\eta} = \frac{1}{64} \cdot \frac{1}{100^{1/4}} \cdot \mathrm{Re}^{3/4} \tag{40}$$

Using η_{eff} to calculate $\mathrm{Re}_{\omega,\mathrm{eff}}$, Eq. 36 can be applied in order to correct the quasi-steady pressure loss of a turbulent oscillating flow.

Heat Transfer

The heat transfer in the heat exchangers of Stirling engines is especially influenced by the periodic compression and expansion. The compensation of temperature differences between wall and fluid is permanently disturbed. By analyzing a simple model process, it is investigated how the above-mentioned conditions change the heat transfer compared to steady-state conditions. A tubular balance volume is confined by movable pistons, which produce a sinusoidal volume change (Fig. 9). The heat transport process is described according to the following partial differential equation:

$$c_v \cdot \frac{\partial(\rho \cdot T)}{\partial t} = \frac{1}{r} \cdot \frac{\partial}{\partial r}\left(r \cdot \lambda_{\mathrm{eff}} \cdot \frac{\partial T}{\partial r}\right) - c_p \cdot \frac{1}{r} \cdot \frac{\partial}{\partial r}[r \cdot (\rho \cdot v \cdot T)] - c_p \cdot \frac{\partial(\rho \cdot u \cdot T)}{\partial x} \tag{41}$$

This equation considers the convective energy transport in axial and radial direction. In case of turbulent flow conditions, λ_{eff} is determined by applying a turbulence model (Nagano and Hishida, 1987; Cebeci, 1973), while in case of laminar conditions λ_{eff} conforms to the fluid property λ.

The periodic volume change results in periodic changes of the transferred heat q and the mean fluid temperature T_m. In order to reproduce the relation between q and $T_w - T_m$ for such oscillating conditions, Pfriem (1940) developed the concept of the complex Nusselt number:

$$q_c = \mathrm{Nu}_c \cdot \frac{\lambda}{d} \cdot (T_w - T_m)_c \tag{42}$$

with

$$\mathrm{Nu}_c = \mathrm{Nu}_{re} + i \cdot \mathrm{Nu}_{im} = |\mathrm{Nu}| \cdot e^{i\varphi} \tag{43}$$

Assuming sinusoidal changes of q and $T_w - T_m$, the real part of q_c is determined as follows:

$$q = \frac{\lambda}{d} \cdot \mathrm{Nu}_{re} \cdot (T_w - T_m) + \frac{\lambda}{d} \cdot \frac{\mathrm{Nu}_{im}}{\omega} \cdot \frac{d(T_w - T_m)}{dt} \tag{44}$$

The absolute value $|\mathrm{Nu}|$ represents the ratio between the amplitudes of q and $T_w - T_m$; the argument φ is equal to the phase shift between the periodic changes of q and $T_w - T_m$. The complex Nusselt number is constant, although it is an instationary process. In order to obtain an applicable correlation for Nu_c, the differential Eq. (41) is solved by means of varying process parameters. The results are used to fit the absolute value as well as the argument of Nu_c.

Laminar flow conditions:

$$\frac{|\mathrm{Nu}|}{\mathrm{Nu}_{st}} = 1.385 + 0.00482 \cdot [\ln(\mathrm{Pe}_\omega + 1)]^{3.65} \tag{45}$$

$$\varphi = 45° \cdot (1 - 1.0275^{-\mathrm{Pe}_\omega^{0.83}}) \tag{46}$$

$$(\mathrm{Pe}_\omega < 1000)$$

Turbulent flow conditions:

$$\frac{|\mathrm{Nu}|}{\mathrm{Nu}_{st}} = 1 + a + b \cdot [\ln(\mathrm{Pe}_\omega + 1)]^c \tag{47}$$

$$\varphi = 45° \cdot (1 - d^{-\mathrm{Pe}_\omega^{0.54}}) \tag{48}$$

$$a = \frac{0.385}{1 + \left(\frac{\mathrm{Re}}{3380}\right)^{0.686}} \tag{49}$$

$$b = \frac{0.00482}{1 + \left(\frac{\mathrm{Re}}{1730}\right)^{1.65}} \tag{50}$$

$$c = 0.0536 \cdot \mathrm{Re}^{0.231} + 3.65 \tag{51}$$

$$d = 1 + \frac{21.5}{\mathrm{Re}^{0.726}} \tag{52}$$

$$(\mathrm{Pe}_\omega < 1000,\ \mathrm{Re} < 50{,}000)$$

Fig. 9 Model process for the investigation of the heat transfer under periodic compression and expansion

Pe_ω = dimensionless frequency of the volume change
Nu_{st} = Nusselt number of a comparison process without volume changes

Regenerator

As mentioned above, the modeling of the regenerator has an important influence on the calculated heat flows of the heat exchangers. In order to obtain realistic values for the heat flows, several loss mechanisms of the regenerator have to be taken into account. The energy balance Eq. (26) comprises the losses caused by axial heat conduction and incomplete heat transfer.

The additional loss mechanism of back mixing of the gas in axial direction is introduced. Back mixing affects the process similar to axial heat conduction. It is described by a dispersion coefficient. The coefficient can be calculated with correlations mentioned by, e.g., Wen and Fan (1975).

Comparison With Experimental Results

Table 1 shows a comparison between experimental and calculated data. The experimental data were obtained with a Vuilleumier machine, which is described in detail by Richter (1988) and Kühl (1990). The Vuilleumier cycle is a heat pump process deduced from the Stirling cycle. It consists of three temperature levels for the heat input and output. Kühl carried out a large number of test runs measuring the three heat flows by varying the following process parameters:

(*a*) mean pressure
(*b*) frequency
(*c*) temperature in the hot heat exchanger
(*d*) temperature in the warm heat exchanger
(*e*) temperature in the cold heat exchanger

Ten of the measuring points were selected. The calculated and measured heat flows are compared in Table 1. The values show a good agreement. In relation to the sum of the three heat flows, as a scale for the size of the process, the deviations are less than five percent.

Conclusions

The simulation model presented comprises new aspects concerning the general organization of the calculation algorithm and the determination of heat transfer and pressure losses. The correlations for the heat transfer and the pressure losses consider the characteristic conditions of the periodic compression/expansion relating to the oscillating flow. They were derived in a theoretical way.

A comparison shows that the results obtained with the simulation model are in good agreement with experimental data of a Vuilleumier cycle.

Table 1 Comparison between experimental data and calculated data

p [MPa]	f [Hz]	T_H [°C]	T_W [°C]	T_C [°C]	$\dot{Q}_H$ [W]	$\dot{Q}_W$ [W]	$\dot{Q}_C$ [W]
10	6,67	500	40	0	exp.: 3800 calc.: 4080	exp.: 5010 calc.: 5210	exp.: 980 calc.: 1230
10	5	500	40	0	exp.: 3060 calc.: 3260	exp.: 3880 calc.: 4110	exp.: 720 calc.: 960
10	3,33	500	40	0	exp.: 2330 calc.: 2470	exp.: 2850 calc.: 2990	exp.: 400 calc.: 630
10	6,67	400	40	0	exp.: 3270 calc.: 3560	exp.: 4190 calc.: 4440	exp.: 690 calc.: 930
10	6,67	500	50	0	exp.: 3780 calc.: 4180	exp.: 4600 calc.: 4940	exp.: 650 calc.: 890
10	6,67	500	40	10	exp.: 3650 calc.: 3890	exp.: 5160 calc.: 5340	exp.: 1300 calc.: 1520
10	6,67	500	40	−10	exp.: 3950 calc.: 4270	exp.: 4810 calc.: 5080	exp.: 690 calc.: 920
9	6,67	500	40	0	exp.: 3580 calc.: 3780	exp.: 4640 calc.: 4790	exp.: 890 calc.: 1100
7	6,67	500	40	0	exp.: 2980 calc.: 3140	exp.: 3830 calc.: 3960	exp.: 660 calc.: 870
5	6,67	500	40	0	exp.: 2330 calc.: 2500	exp.: 2950 calc.: 3100	exp.: 420 calc.: 590

References

Cebeci, T., 1973, "A Model for Eddy Conductivity and Turbulent Prandtl Number," ASME *Journal of Heat Transfer,* Vol. 95, pp. 227–234.

Kühl, H.-D., 1990, "Verallgemeinerte thermodynamische Beschreibung regenerativer Gaskreisprozesse," *VDI-Fortschrittsbericht,* Vol. 19, No. 42, Düsseldorf.

Nagano, Y., and Hishida, M., 1987, "Improved Form of the $k-\epsilon$-Model for Wall Turbulent Shear Flows," ASME *Journal of Fluids Engineering,* Vol. 109, pp. 156–160.

Pfriem, H., 1940, "Der periodische Wärmeübergang bei kleinen Druckschwankungen," *Forschung auf dem Gebiete des Ingenieurwesens,* Vol. 11, No. 2, pp. 67–75.

Richter, N., 1988, "Theoretische Untersuchungen und konstruktive Vorschläge für die Realisierung einer Vuilleumier-Wärmepumpe," *VDI-Fortschrittsbericht,* Vol. 19, No. 29, Düsseldorf.

Uchida, S., 1956, "The Pulsating Viscous Flow Superposed on the Steady Laminar Motion of Incompressible Fluid in a Circular Pipe," *Zeitschrift für angewandte Mathematik und Physik,* Vol. 7, pp. 403–421.

Urieli, J., and Berchowitz, D. M., 1984, *Stirling Cycle Engine Analysis,* Adam Hilger Ltd., Bristol.

Wen, C. Y., and Fan, L. T., 1975, *Models for Flow Systems and Chemical Reactors,* Marcel Dekker Inc., New York.

R. Impero Abenavoli
Università de Roma "La Sapienza," Rome, Italy

M. Carlini
Università della "Tuscia" di Viterbo, Viterbo, Italy

H. Kormanski

K. Rudzinska
Technical University of Gdansk, Gdansk, Poland

A. Sciaboni
Università de Roma "La Sapienza," Rome, Italy

Nondimensional Schmidt Analysis for Optimal Design of Stirling Engines

General directions for rough optimal calibration of Stirling machines can be given by a non-dimensional Schmidt model (nDSM). Since different relative parameters and performance indices have been analyzed by nDSM models, there is lack of uniform conclusions in the literature. This paper describes a new nDSM of six parameters and compares four performance indices as functions of relative parameters. Two optimization tasks of two and five parameters are formulated and solved using the nDSM. Maximized criterion is cycle work per unit of mean pressure and total swept volume. An optimization code based on the algorithm of conjugate gradients with projection on linear constraints is described. The optimal values of volume phase angle, nondimensional swept volume, and dead volume are presented for different constraints imposed on temperature ratio and relative dead volumes.

Introduction

A number of analytical and computerized models for Stirling engine thermodynamic analysis have been elaborated (Carlini et al., 1985; Heams et al., 1982; Martini, 1983; Schock, 1978; Urieli and Berchowitz, 1984). Some models have been applied to optimal design of Stirling machines. However, these complex computer codes are too slow for optimization purposes; they are more suitable for sophisticated analysis of systems design.

Simpler and faster codes, based on idealized analysis, used during optimization, provide general conclusions for a wide class of engine configuration, rather than precise instructions for a particular project design. One of the simplest approaches is the Schmidt analysis, still applied successfully in preliminary design. A reasonable determination of the optimal engine parameters requires the imposition of appropriate constraints; otherwise one comes to fairly obvious conclusions such as:

- swept volumes should be as large as possible
- dead volumes should be as small as possible
- temperature difference should be as large as possible
- pressure or total mass of gas should be as high as possible.

In actual design, the optimal values of these parameters attain lower and upper limits. Only the optimal value of volume phase angle α is not precisely known before computing.

One arrives at more interesting and pragmatic conclusions while taking into account constraints imposed on variables referring to more than one of engine cells (for instance: total swept volume, total dead volume, mean gas pressure, etc.). An indirect approach to respect constraints is considering nondimensional performance indices in the Schmidt model, such as

$$\frac{W}{p_{\text{mean}}V_C}, \frac{W}{MRT_K}, \text{ or } \frac{W}{p_{\max}V_T}.$$

Maximization of a nondimensional index, for instance, the Schmidt number (work per cycle, per mean pressure unit, per compression (or expansion) swept volume unit) is equivalent to the imposition of limits on the variables in the denominator of the index.

Several four-parameter nondimensional Schmidt models were presented by Berchowitz and Wyatt-Mair (1979), Walker (1980), and Naso (1991). However, conclusions were not definite because various indices were not compared to one another and only one-parameter analysis was carried out.

In this paper, using a six-parameter nondimensional Schmidt model, the four most interesting indices are compared in a multiparameter analysis to obtain directions for an optimal multivariable engine calibration.

Nondimensional Schmidt Model (nDSM)

A nondimensional version of the six-parameter Schmidt model presented in this paper has been developed for multiparameter analysis.

The nondimensional Schmidt models considered previously (Walker, 1980; Naso, 1991), are characterized by only one dead volume V_D, whose temperature is constant and equal to $T_D = (T_H + T_K)/2$. They deal with four nondimensional parameters: α, $\tau = T_K/T_H$, $\varphi_C = V_C/V_E$, and $\varphi_D = V_D/V_E$.

Another Schmidt model (Urieli and Berchowitz, 1984) discriminates three separate dead volumes, namely:

- heater and hot clearance volume, V_H
- regenerator volume, V_R
- cooler and cold clearance volume, V_K.

The temperatures corresponding to these spaces are the following:

$$T_H,\ T_R = (T_H - T_K)/\ln\,(T_H/T_K) \text{ and } T_K.$$

According to this formulation, in the nondimensional version of the six-parameter Schmidt model discussed in this paper, three nondimensional parameters

$$\varphi_H = V_H/V_E,\ \varphi_R = V_R/V_E, \text{ and } \varphi_K = V_K/V_E$$

have been introduced instead of φ_D.

Such a form of the Schmidt model is not only more appropriate to the analysis of actual Stirling engines, but it also enables one to divide the optimal dead volume into three spaces V_H, V_R and V_K, which is not possible by using a four-parameter model.

Contributed by the Advanced Energy Systems Division for publication in the JOURNAL OF ENGINEERING FOR GAS TURBINES AND POWER. Manuscript received by the Advanced Energy Systems Division March 3, 1992; revision received October 13, 1992. Associate Technical Editor: M. J. Moran.

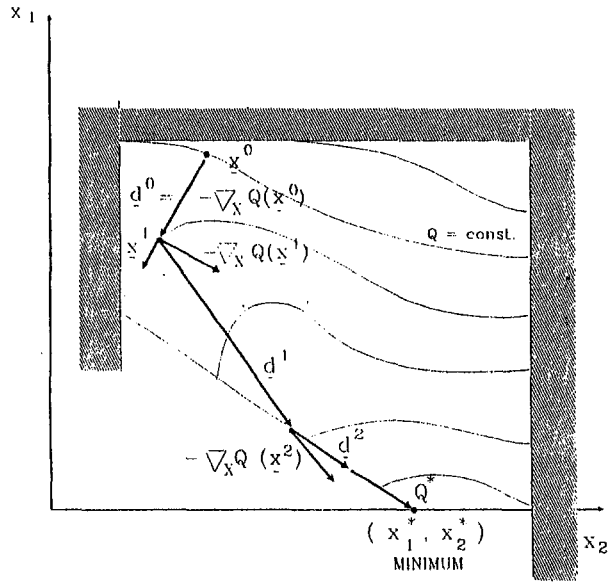

Fig. 1 Conjugate gradient algorithm with projection on linear constraints

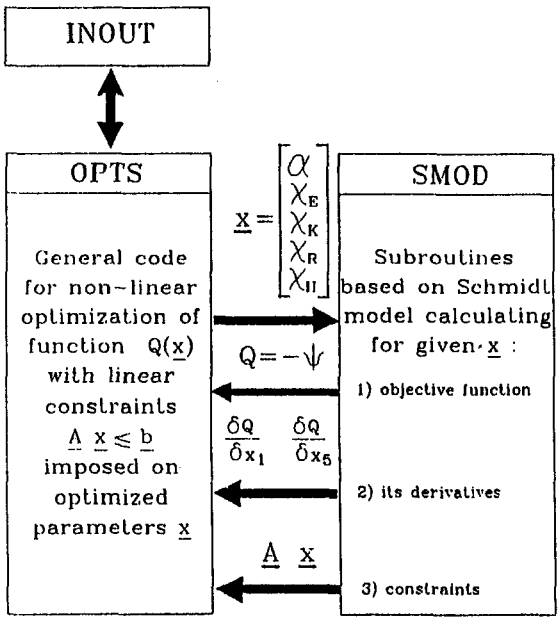

Fig. 2 Modules of computer program

The optimal vectors of parameters, denoted by asterisks (α^*, φ_C^*, φ_H^*, φ_K^*, φ_R^*, τ^*), correspond to the point in six-dimensional space where the maximum of a chosen performance index exists. The following indices have been analyzed and compared to one another:

$$\psi_1 = W/(p_{\text{mean}} V_E) \tag{1}$$

$$\psi_2 = W/(p_{\max} V_T) \tag{2}$$

$$\psi_3 = W/(MRT_K) \tag{3}$$

$$\psi_4 = W/(p_{\text{mean}} V_T) \tag{4}$$

Note that the indices ψ_2, ψ_3, ψ_4 are correctly formulated for optimization purposes because they limit the mass of working gas and total working volume to finite values. The index ψ_1, i.e., the *Schmidt number,* is not in an appropriate form for optimization, because V_C may reach an infinite value. Nevertheless, the index ψ_1 has been included into the comparative analysis. Other criteria of this type, such as $W/(p_{\max} V_E)$, $W/(p_{\max} V_C)$ and $W/(p_{\text{mean}} V_C)$, have been omitted in the further discussion, since their properties are similar to ψ_1.

The indices ψ_1, ψ_2, ψ_3, ψ_4 are calculated as follows:

$$\psi_1 = \pi \frac{\sqrt{1-b^2}-1}{b} [\varphi_C \sin\beta + \sin(\beta-\alpha)] \tag{5}$$

$$\psi_2 = \pi \sqrt{\frac{1-b}{1+b}} \frac{\sqrt{1-b^2}-1}{b(1+\varphi_C)} [\varphi_C \sin\beta + \sin(\beta-\alpha)] \tag{6}$$

$$\psi_3 = \frac{2\pi}{s} \frac{\sqrt{1-b^2}-1}{b\sqrt{1-b^2}} [\varphi_C \sin\beta + \sin(\beta-\alpha)] \tag{7}$$

$$\psi_4 = \frac{\pi}{\varphi_C+1} \frac{\sqrt{1-b^2}-1}{b} [\varphi_C \sin\beta + \sin(\beta-\alpha)] \tag{8}$$

where

$$b = c/s \tag{9}$$

$$c = (\tau^2 + 2\tau\varphi_C \cos\alpha + \varphi_C^2)^{1/2} \tag{10}$$

$$s = \varphi_C + 2\varphi_K + \varphi_R \frac{2\tau \ln(1/\tau)}{1-\tau} + 2\varphi_H\tau + \tau \tag{11}$$

$$\beta = \arccos[(\tau\cos\alpha + \varphi_C)/c] \tag{12}$$

The formulae for calculation ψ_2 or ψ_3 given by Naso (1991) and Walker (1980) are particular cases of formulas (5)–(12). It is readily evident that φ_H and φ_K may be replaced by zero, φ_R by φ_D, T_R by $(T_H + T_K)/2$. Therefore, all the conclusions presented in this paper look suitable for these four-parameter models.

The parameters of the six-parameter nDSM discussed are limited as follows:

$$\alpha \in (0; \pi) \quad \varphi_K \in <0; \infty)$$

$$\varphi_C \in (0; \infty) \quad \varphi_R \in <0; \infty)$$

Nomenclature

A = fixed matrix of linear constraints
b = fixed vector of linear constraints
d = search direction vector
p = pressure of gas
Q = minimized function
T = temperature
V = volume
W = work per cycle
x = vector of design variables
α = volume phase angle
λ = step in one-dimensional optimization
τ = cooler to heater temperature ratio
φ = volume related to V_E
χ = volume related to V_T
ψ = nondimensional work per cycle

Subscripts

C = swept compression space
E = swept expansion space
D = total dead space
H = heater and hot clearance space
K = cooler and cold clearance space
mean = mean value
max = maximal value
min = minimal value
R = regenerator space
T = total working space = $C + E$

Superscripts

* = optimal value
(k) = kth iteration during optimization process

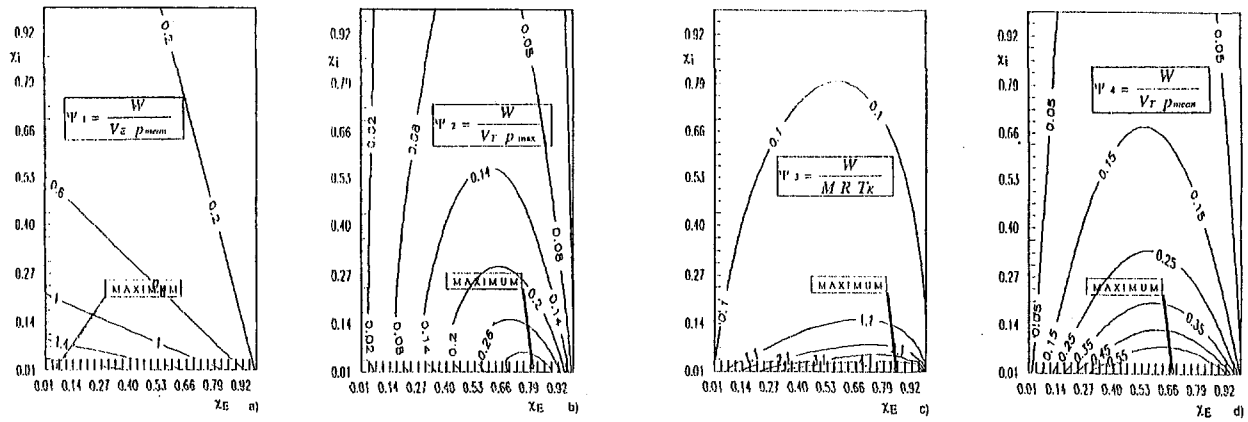

Fig. 3 Performance indices ψ_1, ψ_2, ψ_3, ψ_4 as functions of $\chi_E = (V_E/V_T)$ and $\chi_i = (V_i/V_T) = (\frac{1}{3})(V_D/V_T)$, where $i = H, R, K$ ($\alpha = \frac{1}{2}\pi$, $\tau = 0.1$)

$$\varphi_H \in <0; \infty) \quad \tau \in (0; 1)$$

The most crucial parameters for an optimal calibration are α and φ_C, because the others always converge to bottom feasible limits during optimization. For this reason the infinite interval for the parameter φ_C is not convenient, whereas omission of upper limits on φ_H, φ_K, φ_R does not disturb at all. To avoid these difficulties the relative parameters defined by formulae (13), (14), (15) and (16) are suggested. They refer all the volumes to the total working volume:

$$\chi_E = V_E/V_T \quad \chi_E \in (0; 1) \tag{13}$$

$$\chi_H = V_H/V_T \quad \chi_H \in <0; \infty) \tag{14}$$

$$\chi_K = V_K/V_T \quad \chi_K \in <0; \infty) \tag{15}$$

$$\chi_R = V_R/V_T \quad \chi_R \in <0; \infty) \tag{16}$$

These parameters have been introduced into Eqs. (5)–(12) using the following relationships:

$$\varphi_C = 1/\chi_E - 1 \quad \varphi_K = \chi_K/\chi_E$$

$$\varphi_H = \chi_H/\chi_E \quad \varphi_R = \chi_R/\chi_E \tag{17}$$

The least values of bottom limits imposed on the parameters χ_H, χ_K, χ_R, and τ are 0, 0, 0, 0.1, respectively.

A computer code, written in FORTRAN, has been elaborated to analyze the model and to draw maps of the functions (5), (6), (7), and (8).

Optimization Problems

The analysis of the nDSM has shown that the following problems should be solved maximizing $\psi \in (\psi_1, \psi_2, \psi_3, \psi_4)$:

- determination of the optimal division of total swept and dead volumes among engine cells at different temperatures
- determination of the optimal volume phase angle.

Two tasks for *two-* and *five-parameter* optimization have been formulated as follows:

Task 1 (two-parameter optimization):

$$\max_{(\alpha,\chi_E)} \psi(\alpha, \chi_E) = \psi(\alpha^*, \chi_E^*) = \psi^* \tag{18}$$

subject to:

$$0.01 \le \alpha \le 3.13 \tag{19}$$

$$0.01 \le \chi_E \le 0.99 \tag{20}$$

$$\chi_K = \chi_R = \chi_H = \tfrac{1}{3}\chi_{D\min} \tag{21}$$

while τ and $\chi_{D\min}$ have fixed values.

Task 2 (five-parameter optimization with bottom limit on total dead volume):

$$\max_{(\alpha,\chi_E,\chi_K,\chi_R,\chi_H)} \psi(\alpha, \chi_E, \chi_K, \chi_R, \chi_H)$$

$$= \psi(\alpha^*, \chi_E^*, \chi_K^*, \chi_R^*, \chi_H^*) = \psi^* \tag{22}$$

subject to:

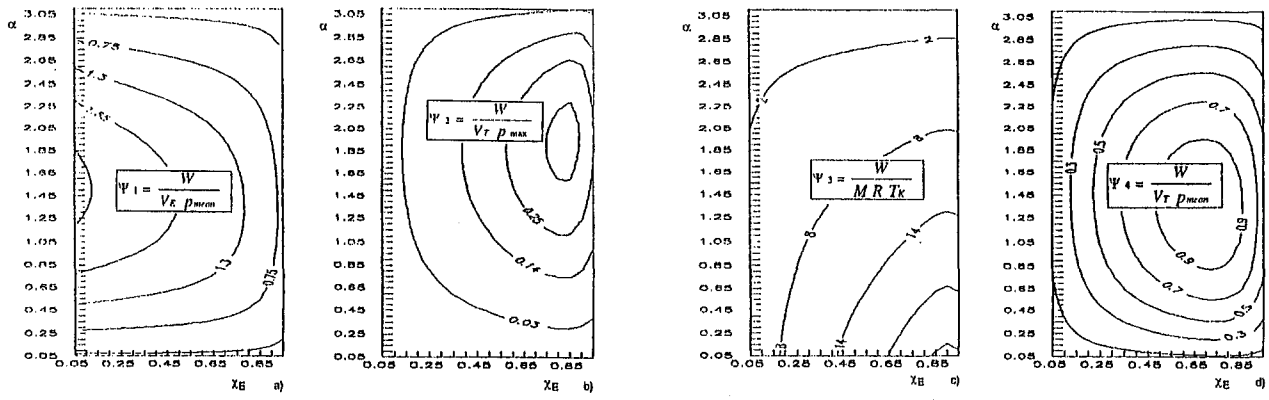

Fig. 4 Optimal (α^*, χ_E^*) calibration for small values of $\tau = (T_K/T_H)$ and $\chi_i = (V_i/V_T)$, $i = H, R, K$ ($\chi_i = 0$, $\tau = 0.1$): comparison among indices ψ_1, ψ_2, ψ_3, ψ_4

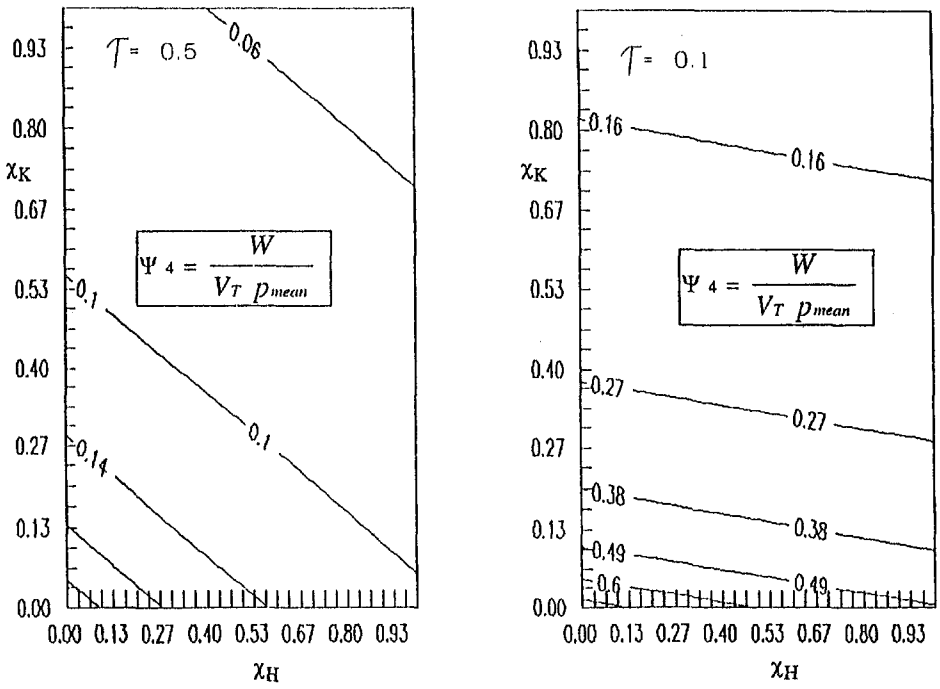

Fig. 5 Influence of relative heater volume χ_H and relative cooler volume χ_K on the index ψ_4 ($\chi_R = 0.1$, $\chi_E = 0.5$, $\alpha = \frac{1}{2}\pi$): comparison for two values of τ

$$0.01 \leq \alpha \leq 3.13 \tag{23}$$

$$0.01 \leq \chi_E \leq 0.99 \tag{24}$$

$$\chi_K \geq 0.0 \tag{25}$$

$$\chi_R \geq 0.0 \tag{26}$$

$$\chi_H \geq 0.0 \tag{27}$$

$$\chi_K + \chi_R + \chi_H \geq \chi_{D\min} \tag{28}$$

while τ and $\chi_{D\min}$ are fixed parameters.

In both tasks $\chi_{D\min}$ is the lowest value of total relative dead volume. It is worth noticing that Task 1 is equivalent to the five-parameter optimization task (22), (23), and (24) with the following additional constraints:

$$\chi_K \geq \chi_{D\min}/3 \tag{29}$$

$$\chi_R \geq \chi_{D\min}/3 \tag{30}$$

$$\chi_H \geq \chi_{D\min}/3 \tag{31}$$

while τ and $\chi_{D\min}$ are fixed parameters.

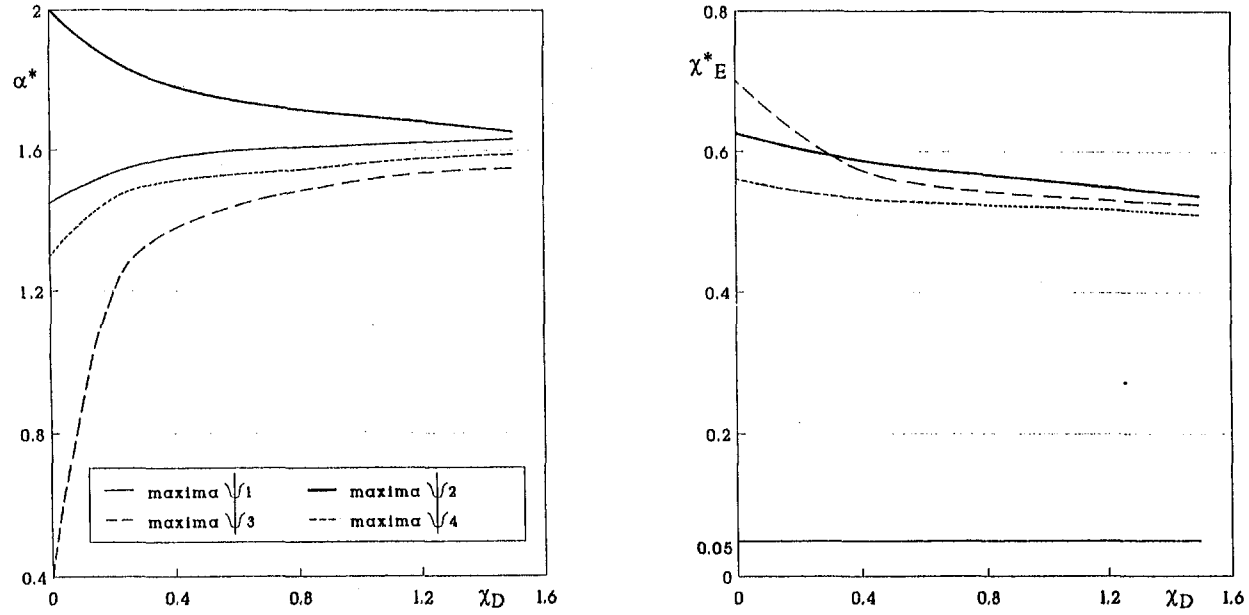

Fig. 6 Optimal values of parameters (α^*, χ_E^*) maximizing particular indices ψ_1, ψ_2, ψ_3, ψ_4: comparison for various values of relative dead volume χ_D and temperature ratio $\tau = 0.5$ (first task)

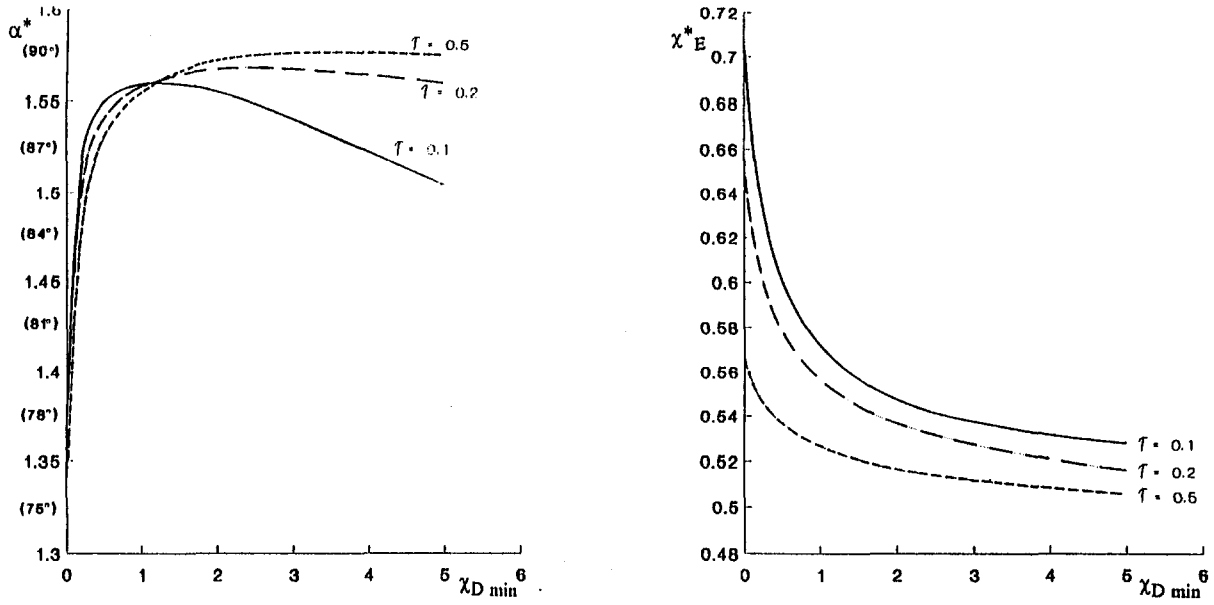

Fig. 7 Optimal values (α^*, χ_E^*) that maximize ψ_4 presented in terms of χ_D and τ, when three dead volumes are equal (first task)

To solve the tasks above formulated a *nonlinear programming* algorithm has been used. It has been elaborated for the following general mathematical problem:

$$\min_{\mathbf{x}} Q(\mathbf{x}) = Q(\mathbf{x}^*) = Q^* \tag{32}$$

subject to:

$$\mathbf{Ax} \leq \mathbf{b} \tag{33}$$

where $\mathbf{x}_{n*1}$ and $\mathbf{b}_{m*1}$ are vectors and $\mathbf{A}_{m*n}$ is a matrix.

Figure 1 illustrates how the algorithm works. The algorithm approaches the minimum $\mathbf{x}^*$ in a sequential way, starting from any point $\mathbf{x}^\circ$ satisfying conditions (33). The search direction vector $\mathbf{d}$ is determined in each iteration. The minimum of Q is found along the line defined by $\mathbf{d}$ using polynomial approximation of function $Q(\mathbf{x} + \lambda\mathbf{d})$, $\lambda \geq 0$. A conjugate gradient method (Gill et al., 1981) is used for calculating $\mathbf{d}$ in successive steps. The vector $\mathbf{d}$ is projected on active boundaries when $\mathbf{x}$ belongs to a bordering hyperplane.

Figure 2 presents modules of the computer program coded in FORTRAN:

(1) INOUT—subroutines reading input parameters and printing optimal values;
(2) OPTS—subroutines minimizing $Q(\mathbf{x})$ subject to linear constraints;
(3) SMOD—subroutines calculating values of Q,

$$\frac{\vartheta Q}{\vartheta x_t}, \ldots \frac{\vartheta Q}{\vartheta x_n}$$

and $\mathbf{Ax} - \mathbf{b}$ for given $\mathbf{x}$.

For the optimization tasks, formulated in this paper, the following notation is used:

Task 1:

$$Q = -\psi, \quad \mathbf{A} = \begin{bmatrix} -1 & 0 \\ 1 & 0 \\ 0 & -1 \\ 0 & 1 \end{bmatrix},$$

$$\mathbf{x} = \begin{bmatrix} \alpha \\ \chi_E \end{bmatrix}, \quad \mathbf{b} = \begin{bmatrix} -0.01 \\ 3.13 \\ -0.01 \\ 0.99 \end{bmatrix}$$

Task 2: $Q = -\psi$

$$\mathbf{A} = \begin{bmatrix} -1 & 0 & 0 & 0 & 0 \\ 1 & 0 & 0 & 0 & 0 \\ 0 & -1 & 0 & 0 & 0 \\ 0 & 1 & 0 & 0 & 0 \\ 0 & 0 & -1 & 0 & 0 \\ 0 & 0 & 0 & -1 & 0 \\ 0 & 0 & 0 & 0 & -1 \\ 0 & 0 & -1 & -1 & -1 \end{bmatrix},$$

$$\mathbf{x} = \begin{bmatrix} \alpha \\ \chi_E \\ \chi_K \\ \chi_R \\ \chi_H \end{bmatrix}, \quad \mathbf{b} = \begin{bmatrix} -0.01 \\ 3.13 \\ -0.01 \\ 0.99 \\ 0.0 \\ 0.0 \\ 0.0 \\ -\chi_{D\min} \end{bmatrix}$$

Discussion and Conclusions

Two-dimensional selected maps of the indices ψ_1, ψ_2, ψ_3, ψ_4 are presented and compared in Figs. 3, 4, and 5. Solutions of the optimization task for various pairs of fixed parameters (τ, $\chi_{D\min}$) are shown in Figs. 6 to 10. Solutions of Task 1 for four indices are presented in Fig. 6, while solutions of Task 1 and Task 2 corresponding to the optimization of ψ_4 are compared in Figs. 7 to 10.

On the basis of the results obtained some conclusions can be formulated.

1 Differences Among the Performance Criteria. The criteria ψ_1, ψ_2, ψ_3, ψ_4 as functions of (χ_i, χ_E), $i = H, K, R$ or as functions of (α, χ_E) are not equivalent and reach their maximal values in different points of the maps. This effect is particularly strong for small values of χ_D and τ (Figs. 3, 4, 6). However, for all the indices, the maxima exist at the minimal considered values of the dead volumes and the temperature ratio

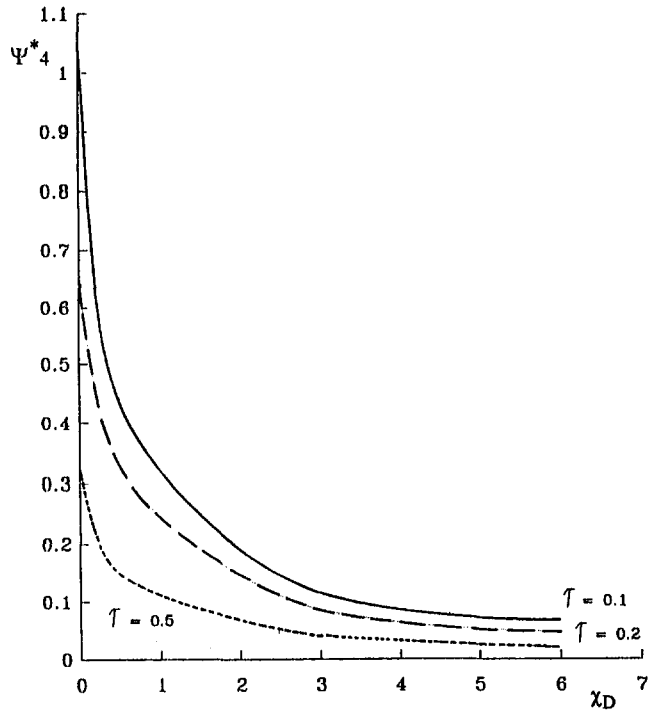

Fig. 8 The index ψ_4, calculated for optimal values (α^*, χ_E^*) and equal dead volumes, as a function of χ_D and τ (first task)

τ (Figs. 3, 5, 8, 10). The optimal values of the volume phase angle α^* and the expansion volume to the working volume ratio χ_E^* strongly depend on a kind of criterion, constraints, and fixed input parameters (Figs. 4, 6, 7, 9). Four indices ψ as functions of (α, χ_E), computed at the best fixed input parameters (i.e., $\tau = 0.1$, and χ_H, χ_R, $\chi_K = 0$), are presented in Fig. 4. It is seen that for this ideal case maxima of the considered functions exist in quite different points of the (α, χ_E) plane. However, as τ or χ_i, $i = K, H, R$ increases, the functions ψ_2, ψ_3, ψ_4 become more similar to one another and their maxima approach the central area around the point $\alpha = \pi/2$ and $\chi_E = \frac{1}{2}$, (Figs. 6, 7).

2 Choice of the Performance Criterion. The maps of the index ψ_1 in Figs. 3(a), 4(a), and the graph of χ_E in Fig. 6 confirm, as previously mentioned, that the use of a nondimensional criterion with only one working volume in the denominator leads to useless conclusions for the engine design. The figures show that the value of χ_E^* always equals the minimal simulated value of χ_E while maximizing ψ_1. It means that the compression swept volume V_C should be infinitely larger than the expansion swept volume V_E. In fact, according to its definition, the index ψ_1 limits the value V_E to one unit but does not limit the volume V_C at all. Therefore, to maximize ψ_4, the model tries to increase the total swept volume V_T as much as possible. The problem of optimizing nDSM parameters consists of a proper choice of a criterion among ψ_2, ψ_3, ψ_4, that bounds both working spaces. The index ψ_4 seems to be the best one, because it gives the most reasonable solutions in a wide range of χ_D.

3 Optimal Division of Dead Volume Among the Three Heat Exchangers. The optimal partition depends on the constraints imposed on the variables χ_i. In both the optimization tasks a bottom limit $\chi_{D\min}$ has been imposed on relative dead volume χ_D. In the first task all the parameters χ_i have their own bottom limits, each equal to $\chi_{D\min}/3$. In the second task only the sum of χ_i, $i = K, H, R$, should be greater than $\chi_{D\min}$. Since the constraints imposed on each variable χ_i separately are stronger than the limit imposed on their sum, the maximal relative work ψ_4^* corresponding to the former task is meaningfully less than the one corresponding to the latter task (Figs. 7 to 10). This is observed because of different distributions of $\chi_{D\min}$ among three heat exchangers. In Task 2 the final values of χ_K^*, χ_R^* reach their bottom limits (zero in our extreme example) and $\chi_H^* = \chi_{D\min} - \chi_K^* - \chi_R^*$. Such results indicate that the lower the heat exchanger temperature, the greater attention should be paid in diminishing its dead volume. This conclusion is confirmed on the map $\psi_4(\chi_H, \chi_K)$ in Fig. 5.

4 Optimal Division of Total Swept Volume. The optimal share of V_E in V_T (parameter χ_E) strongly depends on a kind of criterion, constraints, and values of the fixed parameters τ, χ_H, χ_R, χ_K (Figs. 6, 7, 9). According to the discussion given in paragraph (2), only the indices ψ_2, ψ_3 and ψ_4 have been taken under consideration. For these criteria the optimal values of χ_E^* are always greater than 0.5; this means that V_E should

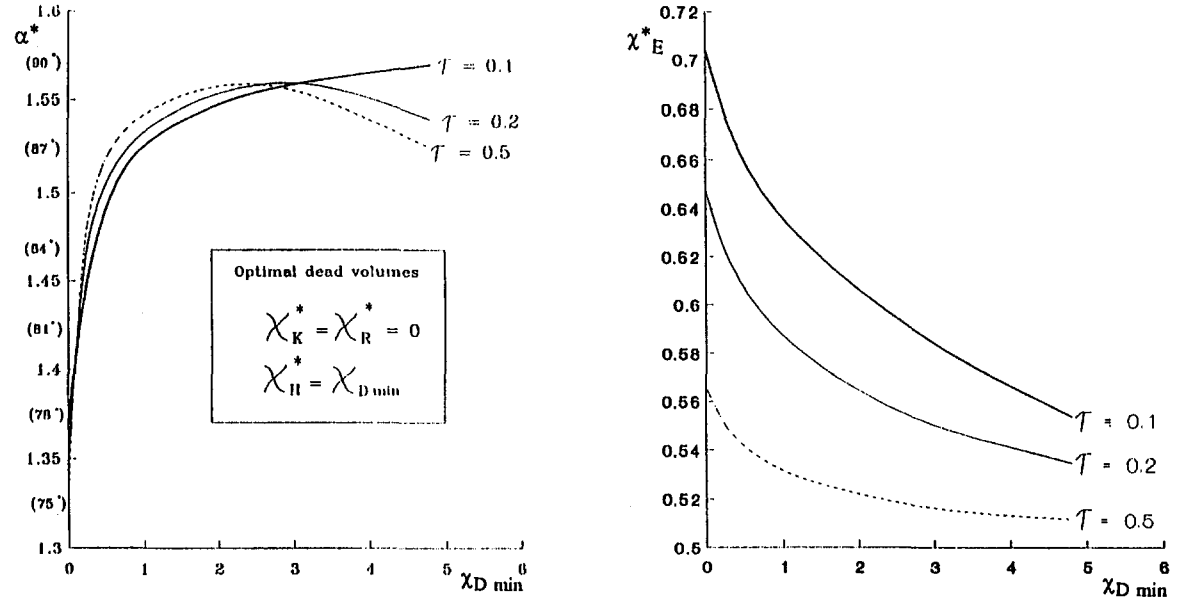

Fig. 9 Optimal values (α^*, χ_E^*, χ_K^*, χ_R^*, χ_H^*), that maximize ψ_4, presented in terms of $\chi_{D\min}$ and τ, where $\chi_{D\min}$ is the bottom limit for the joint dead volume (second task)

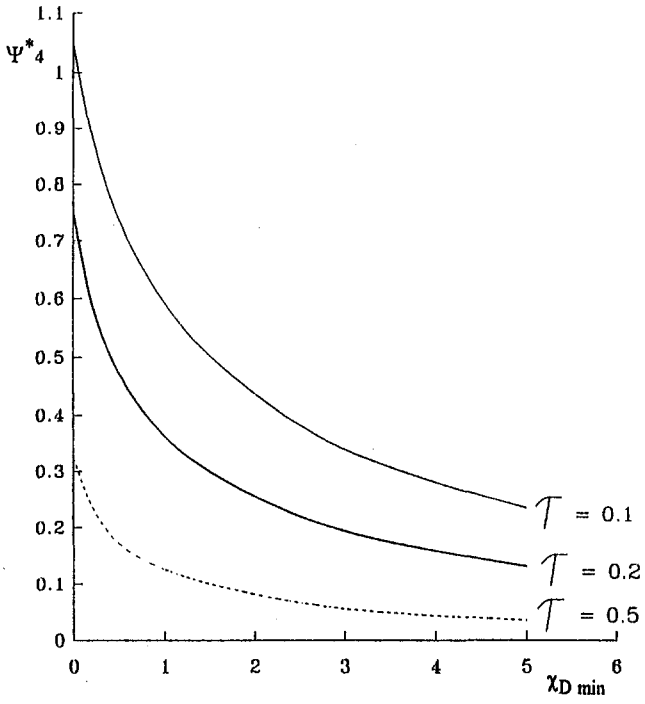

Fig. 10 The index ψ_4 calculated for optimal five parameters and fixed values of τ and $\chi_{D\min}$ (second task)

be greater than V_C. In all the cases the parameter χ_E^* increases while the parameters τ or χ_i, $i = H, K, R$ are getting smaller. The least values of χ_E^* are obtained when the index ψ_4 is maximized.

5 Optimal Volume Phase Angle. For all the indices the optimal volume phase angle, α^*, is around $\pi/2$ for great values of dead volumes. However, graphs of α^* diverge as $\chi_H = \chi_R = \chi_K = (\frac{1}{3})\chi_D$ approach zero (Fig. 5). According to the index ψ_2, the values α^* are greater than $\pi/2$. According to other criteria the parameter α^* decreases below $\pi/2$. A particularly strong effect occurs while considering the index ψ_3, when α^* tends toward its minimal value as χ_D tends to zero (Fig. 6). For the index ψ_4 (Figs. 7 and 9) the optimal volume phase angle α^* is less than $\pi/2$ for small values of χ_D. While χ_D is increasing, α^* increases too and reaches the maximum of $\alpha^*(\chi_D)$ near $\pi/2$. After that point the function $\alpha^*(\chi_D)$ decreases.

The six-parameter nondimensional Schmidt analysis is a suitable tool for preliminary design. The maximization of the index $\psi_4 = W/(V_T p_{\text{mean}})$ should be preferred to determine the optimal division of total dead and swept volumes, as well as optimal volume phase angle. The obtained results show that volumes of hot cells of engines should be greater than cold parts. The angle α^* approaches $\pi/2$ as dead volume increases.

These results will be used to modify the design of the Stirling cycle hot air engine MAC-02 being tested in the Laboratory of the "Dipartimento di Meccanica e Aeronautica dell'Università di Roma, La Sapienza."

The main purpose of the optimization process is to increase the power.

Acknowledgments

The authors are grateful to Prof. Vincenzo Naso and Prof. Emilio Spedicato for their support during the research.

References

Berchowitz, D. M., and Wyatt-Mair, G. F., 1979, "Closed-Form Solutions for a Coupled Ideal Analysis of Free-Piston Stirling Engines," *Proceedings of the 14th Intersociety Energy Conversion Engineering Conference,* Boston, MA.

Carlini, M., Cichy, M., and Mancini, M., 1985, "Validation of Thermodynamic and Mechanical Models of Free Piston Stirling Engines," *Proceedings of the 20th Intersociety Energy Conversion Engineering Conference,* Miami Beach, FL.

Gill, P. E., Murray, W., and Wright, M., 1981, *Practical Optimization,* Academic Press, New York.

Heams, T. J., et al., 1982, "Stirling Engine Thermodynamic Analysis: A Users Guide to SEAM1," ANL-82-59.

Martini, W. R., 1983, "Stirling Engine Design Manual," DOE/NASA/3194-1, NASA CR-168088, 2nd ed.

Naso, V., 1991, "La macchína dí Stirling," Editoriale ESA, Masson, Milano.

Schock, A., 1978, "Nodal Analysis of Stirling Cycle Devices," *Proceedings, 13th Intersociety Energy Conversion Engineering Conference,* San Diego, CA.

Urieli, I., and Berchovitz, D. M., 1984, *Stirling Cycle Engine Analysis,* Adam Higler Ltd., Bristol.

Walker, G., 1980, *Stirling Engines,* Oxford University Press, Oxford.

High-Enthalpy Extraction Demonstration With Closed-Cycle Disk MHD Generators

N. Harada[1]

T. Suekane

K. Tsunoda

H. Yamasaki

S. Shioda

Dept. of Energy Sciences,
Tokyo Institute of Technology,
4259 Nagatsuta, Midori-ku,
Yokohama 227, Japan

Recent results of high-enthalpy extraction experiments with closed-cycle MHD disk generators are described. Power generation experiments were carried out with two types of facility: the shock tube facility with the Disk-IV generator and the FUJI-1 blow-down facility. In the shock tube experiments, the effect of channel shape on generator performance was studied using helium seeded with cesium as working fluid. A more divergent channel shape was effective in sustaining a high Hall field throughout the channel and achieving high generator performance even under the strong MHD interaction. High-enthalpy extraction of 27.3 percent was achieved. Furthermore, these experimental results agree well with the results of one-dimensional calculations. In the FUJI-1 blow-down experiments, the effect of stagnation gas pressure on performance was studied with a working gas of seeded argon. The highest enthalpy extraction ratio of 15.7 percent was achieved with the lower stagnation pressure of 0.46 MPa, whereas the largest output power of 516.7 kW and power density of 70 MW/m^3 were extracted with the nominal stagnation pressure of 0.6 MPa. This suggested the possibility of a part-load operation without significant degradation of generator performance by reducing stagnation pressure.

Introduction

Recently, an increase of conversion efficiency from thermal energy to electricity has become very important, not only for saving resources and creating a stable supply of electricity, but also for environmental requirements. From this point of view, combined cycle power plants with a magnetohydrodynamic (MHD) generation system as a topping cycle have great advantages for high conversion efficiency and less environmental pollution. In particular, a closed-cycle MHD (CCMHD) power generation system, where seeded inert gas is used as a working medium, has inherent advantages of higher output power density, higher enthalpy extraction, and resultant higher efficiency compared with those of an open-cycle system.

For a CCMHD system, however, because of using nonequilibrium plasma, it is well known that ionization instability (or electrothermal instability) reduces electrical conductivity, the Hall parameter, and therefore, output performance, if instability develops in the generator channel [1, 2]. A lot of effort had been made to suppress ionization instability. It was found that operating in the regime of fully ionized seed (F.I.S.) was very attractive to eliminate this instability and that the recovery of plasma parameters almost to their laminar values was obtained in the regime of F.I.S. [3, 4]. So far power generation experiments using shock tube facility have been conducted to demonstrate high-enthalpy extraction. Using seeded argon as a working gas, enthalpy extractions higher than 15 percent were achieved only for a higher stagnation temperature of 4000 K [5]. At the Massachusetts Institute of Technology, disk generator experiments with inlet swirl showed a substantial increase in generator performance [6] and at the moderate temperature range of 2100~3500 K, high-enthalpy extractions of 17~20 percent were obtained at the Eindhoven University of Technology [7]. Since unstable conditions of plasma was utilized in these experiments, strong inhomogeneous discharge structure with large fluctuations was observed, and consequently both gas-dynamic and output performance were reduced, particularly under these high-MHD interactions.

At the Tokyo Institute of Technology, performance of a disk-type CCMHD generator has been studied using both the shock tube facility [8, 9] and the FUJI-1 blow-down facility [10, 11]. The main purpose of these experimental studies is to achieve sufficient high-enthalpy extraction for required high conversion efficiency in a commercial power plant with uniform plasma under the condition of fully ionized seed.

In the shock tube experiments, a high-enthalpy extraction ratio of over 20 percent was achieved for the stagnation temperature of around 2000 K using helium seeded with cesium as a working gas [8]. The experimental results showed good agreement with the results of one-dimensional calculations. This indicates that the strong deceleration by Lorentz force resulted in the decrease of Hall field in the downstream part of the channel [9]. Furthermore, it was suggested by numerical prediction that a more divergent channel geometry would reduce the bad effects of flow deceleration. In this paper, the effect of channel geometry on generator performance is studied experimentally using the new disk generator with a more divergent channel shape than the previous Disk-III generator.

A series of power generation experiments have been conducted with the disk generators, Disk-F2 and Disk-F3, in the FUJI-1 blow-down experiments. Output power of the Disk-F2 generator was increased up to 240 kW and the enthalpy extraction ratio reached up to 7.3 percent using cesium seeded argon as a working gas [10]. However the results suggested that the performance of the Disk-F2 generator was limited by insufficient channel geometry. In order to improve generator performance, the new Disk-F3 generator with a large area ratio of the exit cross section to the inlet was installed, and then a series of power extraction experiments were carried out. A remarkable increase in both output power and power density was obtained and the enthalpy extraction ratio was improved up to 15 percent with the reduced stagnation pressure [11, 12].

The new generator Disk-F3a, which has a higher area ratio than the Disk-F3, has been installed in the FUJI-1 facility and

[1] Current address: Dept. of Electrical Engineering, Nagaoka University of Technology, 1603-1 Kamitomioka, Nagaoka 940-21, Japan.

Contributed by the Advanced Energy Systems Division for publication in the JOURNAL OF ENGINEERING FOR GAS TURBINES AND POWER. Manuscript received by the Advanced Energy Systems Division December 6, 1991; revision received November 23, 1992. Associate Technical Editor: M. J. Moran.

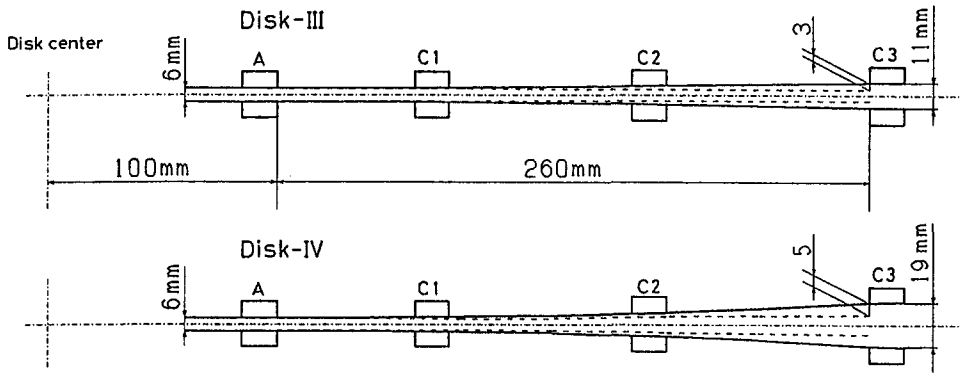

Fig. 1 Schematic cross-sectional view of the Disk-III and Disk-IV generator

power generation experiments were performed to study the effect of stagnation gas pressure on the performance. Results are described in the present paper.

Shock Tube Experiments

Experimental Setup and Conditions. In a series of shock tube experiments, the effect of channel geometry on generator performance have been studied in detail. The new disk generator channel "Disk-IV" was installed in the shock tube facility. Cross-sectional views of the Disk-III and Disk-IV channels are shown in Fig. 1, where the actual channel shape is shown by a solid line and the effective one, which is used in the numerical calculations, is shown by a dashed line. The effective channel height is calculated by subtracting the displacement thickness of the boundary layer from the actual channel height. This displacement thickness is assumed to be 0.5 mm at the inlet of both channels, 3 mm at the exit of the Disk-III, and 5 mm at the exit of the Disk-IV channel according to the measured static pressure distribution and to the results of the r–z plane two-dimensional calculation [13]. The shape of the new Disk-IV channel is more divergent than the previous Disk-III channel, especially in the downstream part, so that the effect of gas flow deceleration due to an MHD interaction is expected to be reduced.

Figure 2 shows the output power and the enthalpy extraction ratio predicted by a one-dimensional calculation using the effective channel shape. The procedures and the basic equations are presented in [9, 14]. It can be seen clearly from this figure that, for the case of the Disk-IV channel with the more divergent channel shape, the output power and the enthalpy extraction ratio increase significantly, with the latter predicted to be over 30 percent. The value of load resistance, which gives the peak output power, shifts to a larger value. These results are ascribed to the increase of Hall electromotive force owing to both the reduction of flow deceleration effect and the increase of Hall parameter because of the low static gas pressure.

Experimental conditions are shown in Table 1. Helium seeded with cesium was used as the working medium. The stagnation temperature was in the neighborhood of 2000 K, which is expected for a closed-cycle MHD commercial plant. Seed fraction was kept on the order of 10^{-4}.

Experimental Results. Power generation experiments were carried out by changing the external load resistance in the range of 1 Ω ~ 15 Ω, and results compared with the results obtained by the Disk-III generator. The Hall voltage–Hall current characteristics are shown in Fig. 3. The electrical output power and enthalpy extraction ratio are plotted in Fig. 4 against the external load resistance. In these figures, open circles show the results with the Disk-IV channel. A substantial increase of output power and enthalpy extraction ratio is seen in the range of load resistance 2.5 Ω ~ 7.0 Ω for the case of the Disk-IV channel. Especially for the load resistance of 3.5 Ω, the highest output power of 510 kW and the corresponding enthalpy extraction ratio of 27.3 percent were achieved. The more divergent channel shape of Disk-IV results in these substantially higher

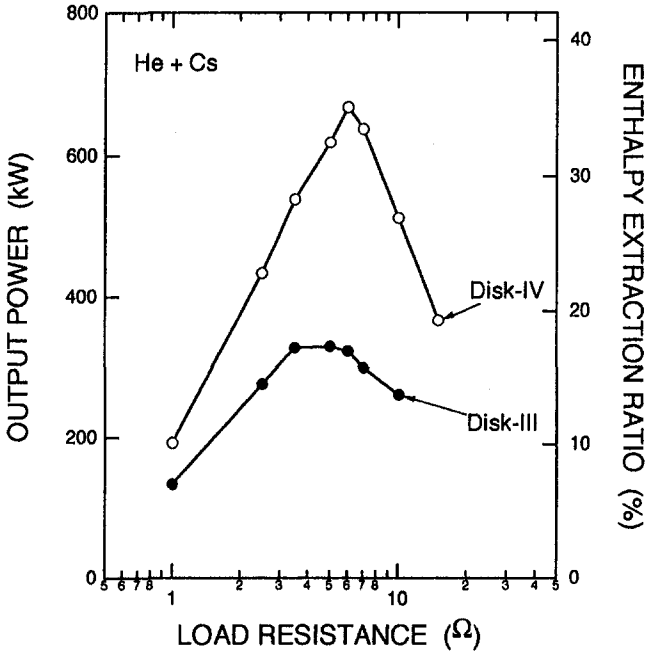

Fig. 2 Calculated output power and enthalpy extraction ratio versus load resistance

Table 1 Experimental conditions for the shock tube experiments

Channel	Disk-III, Disk-IV
Working gas	He + Cs
Stagnation gas temperature (K)	1950 ~ 2100
Stagnation gas pressure (MPa)	0.25 ~ 0.28
Thermal input (MW)	1.9 ~ 2.1
Seed fraction	1×10^{-4}
Magnetic field strength (T)	2.6 (r=0) 1.8 (r=0.36m)
Load resistance (Ω)	1.0 ~ 15.0

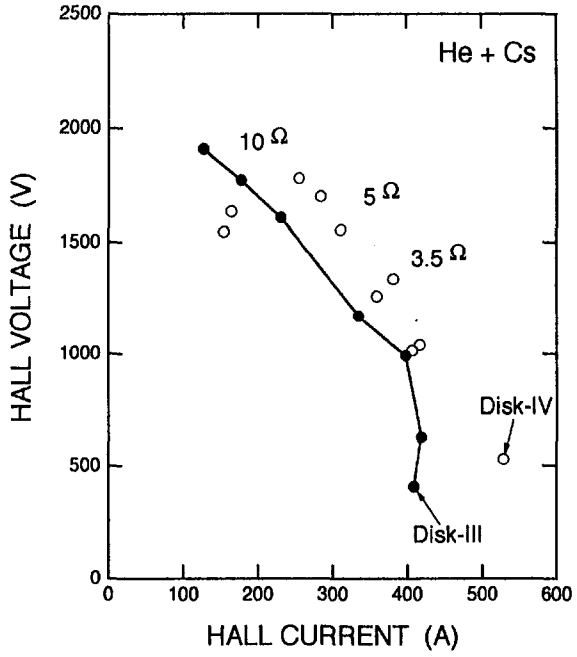

Fig. 3 Hall voltage–Hall current characteristic of the Disk-IV generator

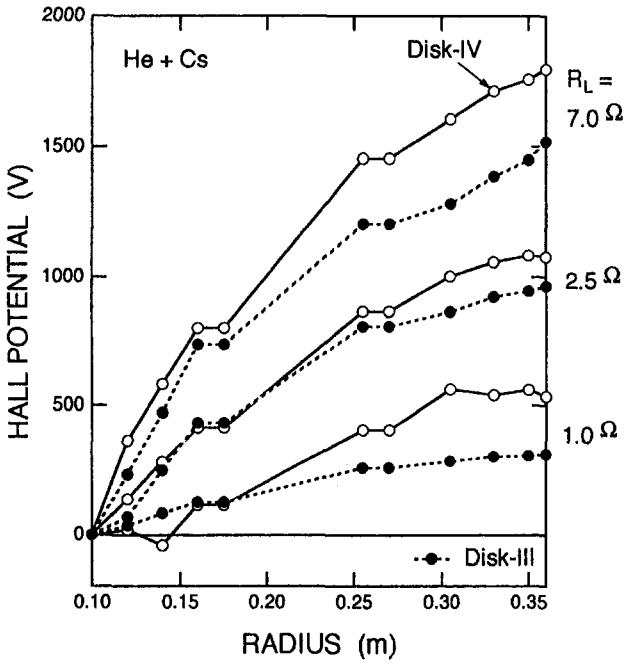

Fig. 5 Hall potential distributions for load resistances of 1 Ω, 2.5 Ω, and 7 Ω

values of output performance than the case of Disk-III channel. It can also be seen that the value of load resistance that yields the peak output power shifts to larger values 3.5 Ω~5Ω compared to 2.5 Ω in the case of Disk-III. These results agree qualitatively well with the calculated ones shown in Fig. 2. A quantitative discrepancy, however, still exists between them. The main cause for this discrepancy is considered to be insufficient prediction of the boundary layer thickness.

Hall Potential Distribution. Typical Hall potential distribution along the radial direction for the load resistances of 1.0 Ω, 2.5 Ω, and 7.0 Ω are shown in Fig. 5, where the results with the Disk-III channel are also shown by dashed lines. It is evident on comparing those two cases that a high Hall field can be sustained even in the downstream part of a channel for the case of Disk-IV generator. For the case of smaller load resistance of 1.0 Ω, the negative Hall potential region appears near the anode because of the lower electrical conductivity, owing to the small Joule heating of electrons.

Comparison of the experimental results with calculated ones of a Hall potential distribution are shown in Fig. 6. The experimental results agree quite well with the calculated ones for all load resistances. When the load resistance is 1.0 Ω, the calculated result looks wavelike in distribution. This can be understood if ionization instability prevails in the channel. The plasma becomes separated into two phases: a power-generating plasma with a positive gradient of Hall potential, and a power-consum-

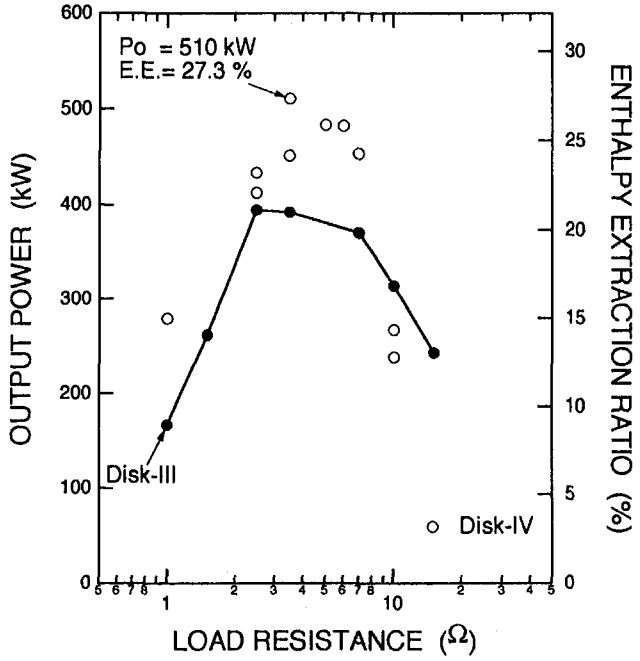

Fig. 4 Output power and enthalpy extraction ratio versus load resistance

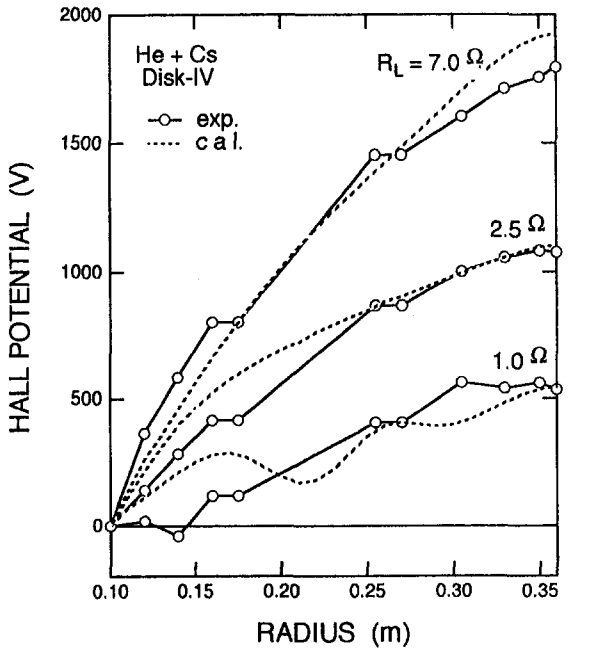

Fig. 6 Comparison of measured Hall potential distributions with calculated ones

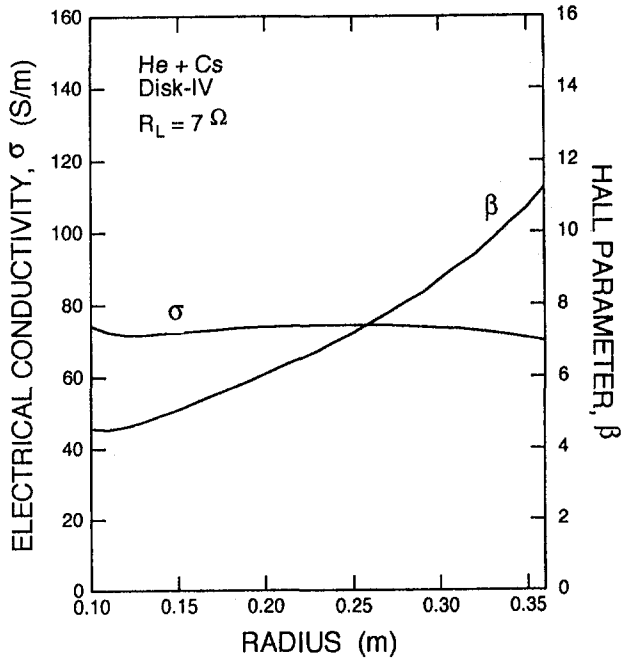

Fig. 7 Calculated distributions of electrical conductivity and Hall parameter

ing plasma with a negative gradient. In the experiment, such a negative gradient part can be seen near the anode. The Hall field in the disk generator can be expressed as

$$E_r = -(\beta U_r B + U_\theta B) + \frac{1+\beta^2}{\sigma} j_r \qquad (1)$$

where the first two terms are Hall electromotive force. In the present case, the Hall electromotive force associated with the radial gas velocity is dominant because an inlet swirl is not employed. The last term denotes the voltage drop due to internal resistance. Therefore, the negative gradient of Hall potential distribution in the experiment with the load resistance of 1.0 Ω suggests that the electrical conductivity is still low at the inlet of the disk channel due to the effect of inlet relaxation. Typical calculated distributions of electrical conductivity and Hall parameter with the external load of 7 Ω are shown in Fig. 7. We can see that Hall parameter is about 4.5 at the inlet and it increases to 11 at the exit because static pressure decreases downstream. An almost constant value of electrical conductivity of about 70 S/m and no significant decrease at the inlet region can be seen. This fact corresponds to calculated Hall potential distribution with no significant voltage drop due to ionization relaxation as shown in Fig. 6. The main cause of the discrepancy in the Hall potential distribution at the inlet region may be ascribed to the uncertainty of electron temperature assumed in the calculations and of using ionization rate. If both the two-dimensional effect and the inlet relaxation can be properly taken into account, the agreement is expected to be improved.

Gas Velocity. Figure 8 shows the variation of gas velocity in the radial direction for external loads of 2.5 Ω and 10 Ω, together with the calculated ones, which are shown by dashed lines. The radial component of gas velocity is estimated by the so-called correlation method: the distance between two different positions of measurement divided by the delay time, which gives the maximum value of correlation function between these two signals. The larger load resistance results in the stronger effect of flow deceleration because of the stronger interaction between the flow and the electromagnetic field. The present results are quantitatively explained by one-dimensional calculations.

FUJI-1 Blow-Down Experiments

Experimental Setup and Conditions. Experimental studies on the performance of a closed-cycle MHD disk generator have been conducted not only with the shock tube facility but also the FUJI-1 blow-down facility. The last series of power generation experiments, Runs 6208, 6209, and 6210, were carried out with the new generator, Disk-F3a. The FUJI-1 facility is described in earlier papers [15, 16]. Figure 9 shows a schematic diagram of the Disk-F3a generator. It has four pairs of water-cooled ring electrodes, A1, A2, C1, and C2. The first (A1) and the second (A2) anodes are externally short circuited, and the external load resistance is connected between the second anode (A2) and the second cathode (C2). The insulating walls are made of silicon nitride. The channel also has optical windows, static pressure ports, and electrical probes along the radial direction.

The dimensions and the designed inlet Mach number of the Disk-F3 and Disk-F3a channels are summarized in Table 2. The previous experimental results with the Disk-F3 channel showed a strong increase in static pressure, which suggested the remarkable decrease of gas velocity owing to the strong MHD interaction [10, 12]. We have to reduce the effect of flow deceleration in order to achieve higher performance. For the new Disk-F3a channel, the ratio of an exit cross-sectional area to an inlet one is increased from 3.5 of the Disk-F3 channel to 4.2. It is noted that the designed inlet Mach number is also increased from 2.3 to 2.6.

The experimental conditions are shown in Table 3. Argon seeded with cesium was used as the working medium. In this series of experiments, the stagnation pressure was changed to 0.46, 0.60, and 0.69 MPa in order to study the effect of stagnation pressure on generator performance for a given channel geometry. It must be noted that the thermal input is also changed from 2.57 MW to 3.84 MW, corresponding to the change in stagnation pressure. Seed fractions were kept low, on the order of 10^{-4} for all runs.

A typical time history of the upstream stagnation pressure, the seed fraction, the load resistance, and the output Hall voltage

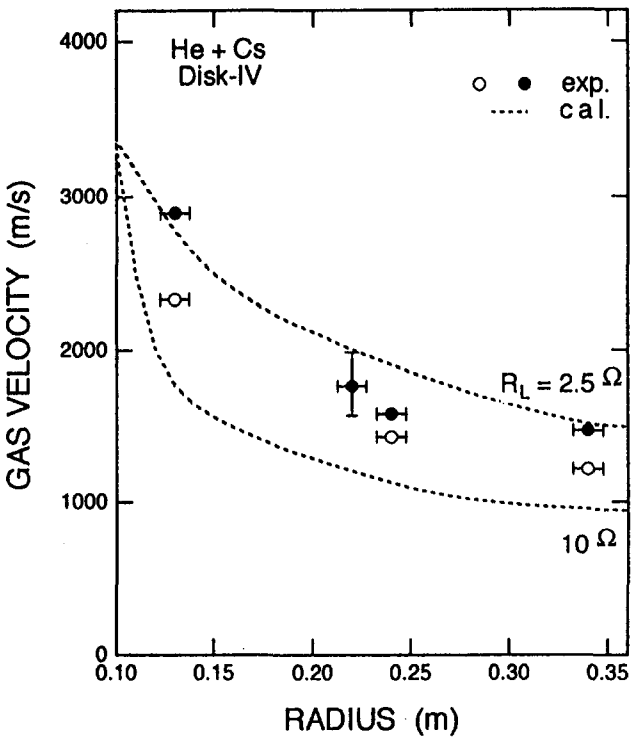

Fig. 8 Variation of gas velocity along the radial direction

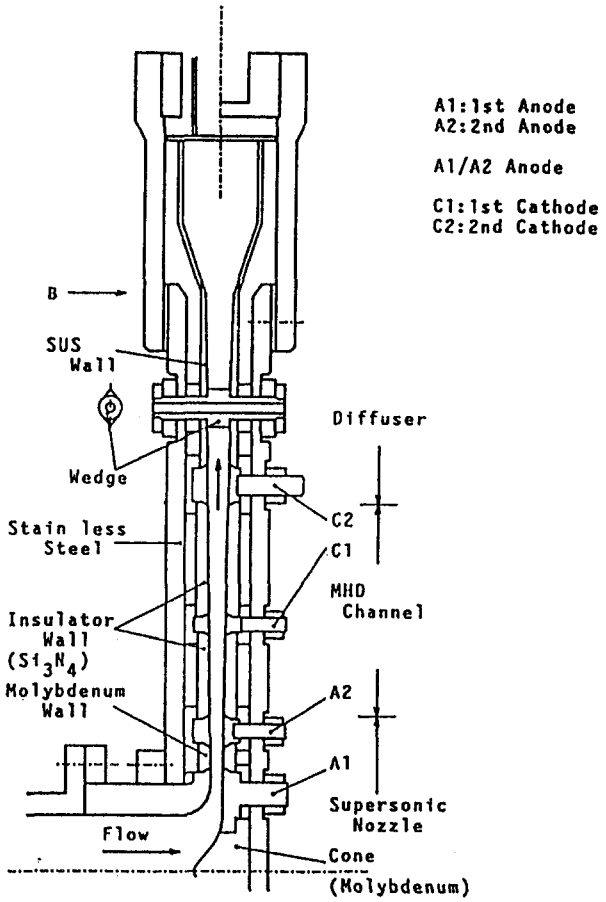

Fig. 9 Schematic cross-sectional view of the Disk-F3a generator

in Run 6208 are shown in Fig. 10. In this run, two values of seed fraction about 2×10^{-4} (50~65 s) and 3×10^{-4} (70~95 s) are examined. We can see a noticeable fluctuation in measured seed fraction. It is reported that this fluctuation is the main cause of the fluctuation of output power [11]. In each period, the load resistance is changed stepwise in the range of 0.07 Ω~2.5 Ω. We can see that the output Hall voltage shows also steplike change with the change of load resistance. This output voltage reaches up to 700 V, which corresponds to the averaged Hall field of 3.5 kV/m for the case of 2.5 Ω.

Table 2 Dimensions and designed inlet Mach number of disk generators

Channel	Disk-F3	Disk-F3a
Anode		
radius (mm)	160	160
height (mm)	14.7	16.0
2nd Cathode		
radius (mm)	380	380
height (mm)	22.0	28.0
Inlet Mach number	2.3	2.6
Area ratio (exit/inlet)	3.5	4.2

Table 3 Experimental conditions for the FUJI-1 blow-down experiments

Run number	6208	6209	6210
Working gas	Ar + Cs	Ar + Cs	Ar + Cs
Stagnation gas temperature (K)	1850	1850	1890
Stagnation gas pressure (MPa)	0.46	0.60	0.69
Thermal input (MW)	2.57	3.40	3.84
Seed fraction	$2.0 \sim 3.0 \times 10^{-4}$	$1.7 \sim 1.8 \times 10^{-4}$	$1.6 \sim 1.7 \times 10^{-4}$
Magnetic field strength (T)	4.4	(inlet) ~ 2.7	(exit)

Hall Voltage–Hall Current Characteristics. Hall voltage–Hall current characteristics for various stagnation pressures are shown in Fig. 11. It can be seen that Hall current increases in the near short circuit regime and Hall voltage decreases in the near open circuit when stagnation pressure is increased. This decrease in Hall voltage is ascribed to the decrease of Hall parameter as the pressure increases. It is known that the gradient of a voltage-current characteristic corresponds to an internal resistance of a plasma. We can see from Fig. 11 that the internal resistance becomes large with the decrease of gas pressure.

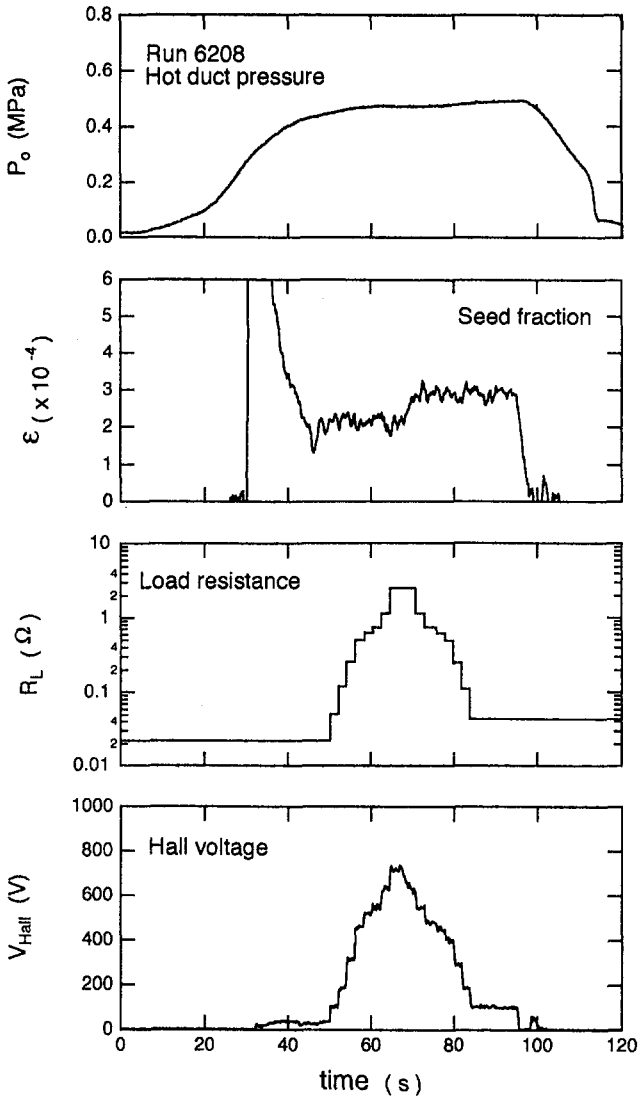

Fig. 10 Typical traces of stagnation pressure, seed fraction, load resistance, and output Hall voltage

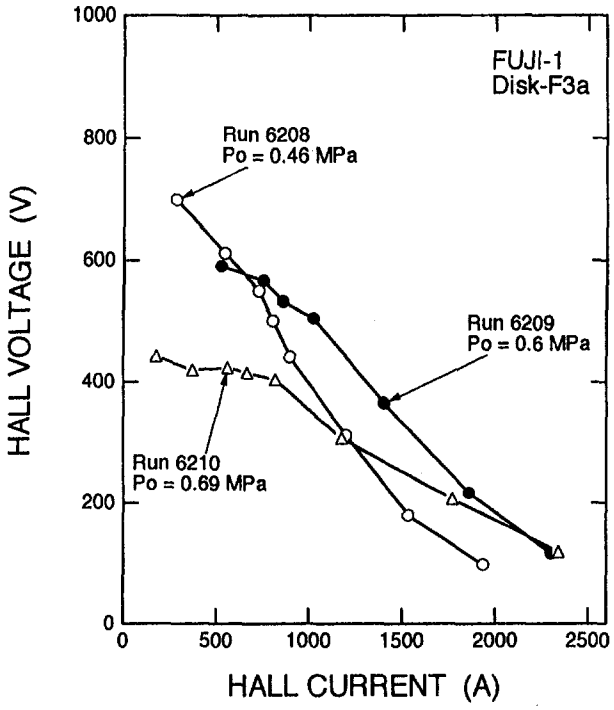

Fig. 11 Hall voltage–Hall current characteristics for various stagnation pressures

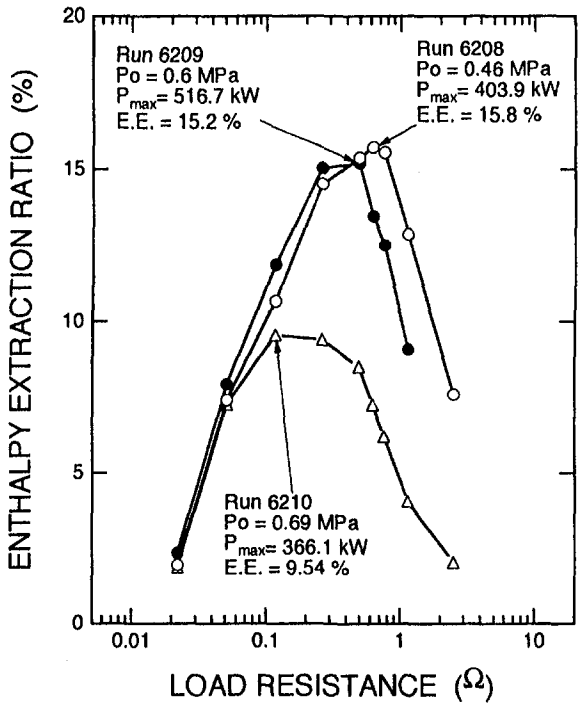

Fig. 13 Enthalpy extraction ratio versus load resistance for various stagnation pressures

Figures 12 and 13 show the output power and enthalpy extraction ratio against the load resistance for various stagnation pressures. The highest enthalpy extraction ratio of 15.7 percent is achieved with the stagnation pressure of 0.46 MPa, whereas the largest output power of 516.7 kW and corresponding high output power density of 70 MW/m^3 are extracted with the stagnation pressure of 0.6 MPa. It is important that for the case of 0.46 MPa, which corresponds to a part-load condition by about 25 percent reduction of thermal input from the nominal condition of 0.6 MPa, the obtained enthalpy extraction ratio keeps the same level of over 15 percent as the nominal value. This result suggests the possibility of a part-load operation without significant degradation in enthalpic efficiency by means of reducing stagnation pressure.

The value of load resistance that provides the peak output power shifts to higher values as the pressure decreases. This can be ascribed to the increase of an internal impedance of a plasma due to the decrease of gas pressure.

Hall Potential Distribution and Swirl. Measured Hall potential distributions along the radial direction are shown in Fig. 14, when the output power reaches its maximum for each stagnation pressure. We can see that a high Hall field can be mea-

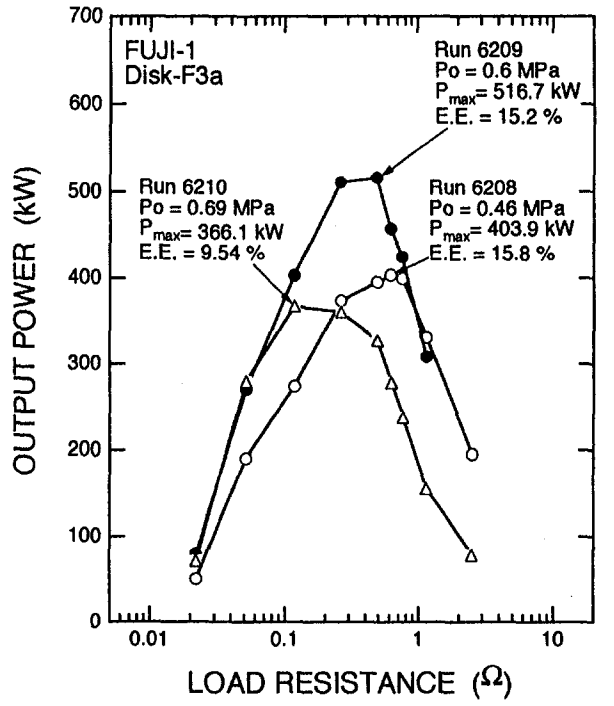

Fig. 12 Output power versus load resistance for various stagnation pressures

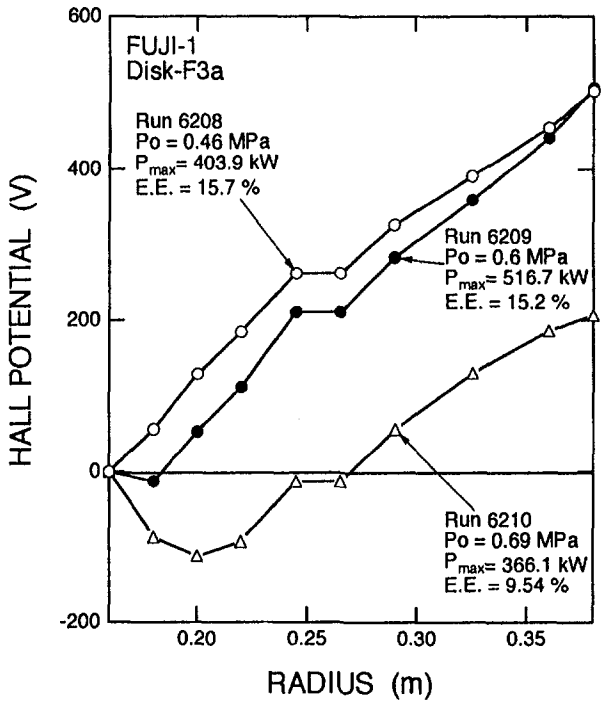

Fig. 14 Hall potential distributions along the radial direction

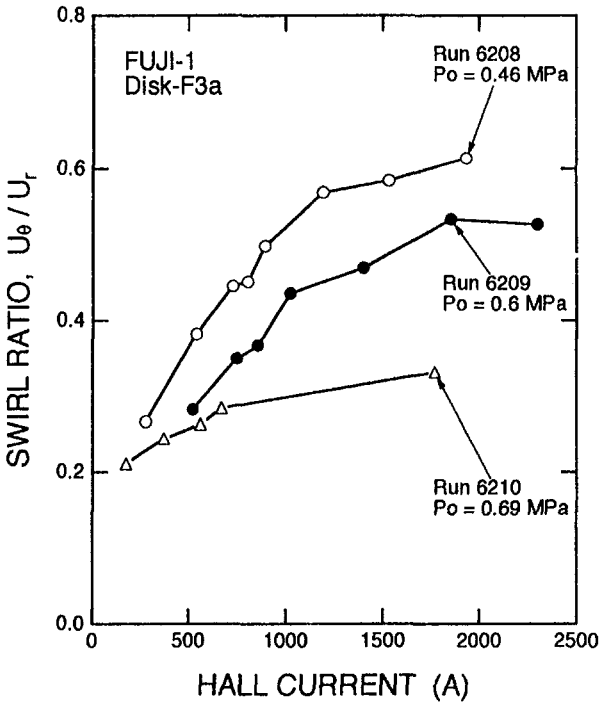

Fig. 15 Swirl ratio at the exit of disk channel against Hall current

sured even at the entrance of a channel for the lower stagnation pressure of 0.46 MPa, whereas the negative Hall potential region appears near the anode in Run 6209 with the stagnation pressure of 0.6 MPa. A low gas pressure and corresponding high Hall parameter results in the enhancement of Joule heating even in the supersonic nozzle, and therefore, the negative Hall potential disappears in Run 6208. On the other hand, for the case of the higher stagnation pressure of 0.69 MPa, the negative Hall potential at the entrance of the channel becomes much more significant. This voltage drop reduces the output voltage very much and results in the reduction of output power.

The swirl is defined as the ratio of an azimuthal component of gas velocity U_θ to a radial component U_r. In the FUJI-1 experiments, this swirl is measured at the wedge, which is located just downstream of channel exit as shown in Fig. 9. Results are plotted in Fig. 15 against the Hall current for various stagnation pressures. It can be seen that the negative swirl becomes large with the increase of Hall current. This is quite reasonable because this is induced by the Lorentz force $J_r \times B$. The swirl is enhanced with the decrease of stagnation pressure. For lower gas pressures, the effect of this Lorentz force becomes relatively significant due to the decrease of the inertial force.

Experiments With He/Cs Working Gas. Results of the shock tube experiments showed the advantages of using helium, which include high induced voltage, high output power density, and also high-enthalpy extraction ratio [8, 17]. In the FUJI-1 facility, the experiments with helium working gas are left to be studied. After the last power generation runs with an argon working gas, modification of the facility and preparation for helium experiments have been carried out. Special attention was paid to the electrical isolation because the output voltage is predicted to be above 3 kV owing to high velocity of helium.

Conclusions

Power generation experiments with closed-cycle disk MHD generators were carried out to demonstrate high-enthalpy extraction. Concluding remarks are as follows.

In the shock tube disk experiments, the effect of channel shape on generator performance was studied using helium seeded with cesium as the working medium. More divergent channel geometry was effective to sustain high Hall field throughout the channel, and resulted in a remarkable increase in both output power and enthalpy extraction ratio. The highest enthalpy extraction ratio of 27.3 percent was achieved with the new Disk-IV generator. Present experimental results of the effect of channel shape on the generator performance, the Hall potential, and the gas velocity distributions agreed quantitatively well with the results of one-dimensional calculations.

In the FUJI-1 blow-down experiments, the new disk generator Disk-F3a with a large area ratio of the exit cross section to the inlet was installed, and performance was studied for various stagnation pressures. A high output power of 516.7 kW and corresponding power density of over 70 MW/m^3 were obtained with the nominal condition of stagnation pressure 0.6 MPa. On the other hand, the highest enthalpy extraction ratio of 15.7 percent was achieved with the lower pressure of 0.46 MPa, which corresponded to the 25 percent reduction of thermal input from the nominal case. This result suggests the possibility of a part-load operation without significant degradation in enthalpic efficiency by means of reducing stagnation pressure. For the case of higher stagnation pressure, the inlet negative Hall potential became much more pronounced owing to small Joule heating, and reduced the output power. The swirl at the exit of the channel was measured and was enhanced with the increase of Hall current and with the decrease of stagnation pressure.

References

1 Solbes, A., "Quasilinear Plasma Wave Study of Electrothermal Instabiliies," *Proc. 4th Int. Conf. on MHD,* Vol. 1, 1968, pp. 499–518.

2 Brederlow, G., and Witte, K. J., "Effective Electrical Conductivity and Related Properties of a Nonequilibrium High Pressure MHD Plasma," *AIAA J.,* Vol. 12, No. 1, 1974, pp. 83–90.

3 Nakamura, T., and Riedmüller, W., "Stability of Nonequilibrium MHD Plasma in the Regime of Fully Ionized Seed," *AIAA J.,* Vol. 12, No. 5, 1974, pp. 661–668.

4 Yamasaki, H., and Shioda, S., "MHD Power Generation With Fully Ionized Seed," *J. of Energy,* Vol. 1, No. 5, 1977, pp. 301–305.

5 Klepeis, J., and Hruby, V., "MHD Power Generation Experiments With a Large Disk Channel: Verification of Disk Scaling Laws," *Proc. 15th Symp. on Eng. Aspects of MHD,* 1976, pp. VI.3.1–VI.3.6.

6 Loubsky, W. J., Hruby, V., and Louis, J. F., "Detailed Studies in a Disk Generator With Inlet Swirl Driven by Argon," *Proc. 15th Symp. on Eng. Aspects of MHD,* 1976, pp. VI.4.1–VI.4.5.

7 Veefkind, A., "High Enthalpy Extraction From a Shock Tunnel Driven Noble Gas MHD Disk Generator," Informal paper presented at the I.L.G. Closed Cycle Specialist Meeting, 1985.

8 Harada, N., et al., "High Enthalpy Extraction From a Helium Driven Disk MHD Generator," *J. of Propulsion and Power,* Vol. 5, No. 3, 1989, pp. 353–357.

9 Harada, N., et al., "High Performance of a Nonequilibrium Disk MHD Generator," *Proc. 10th Int. Conf. on MHD,* Vol. III, 1989, pp. XII.7–XII.14.

10 Yamasaki, H., et al., "High Interaction Disk Experiments in the FUJI-1 Facility," *Proc. 26th Symp. on Eng. Aspects of MHD,* 1988, pp. 7.1.1–7.1.7.

11 Yamasaki, H., et al., "High Enthalpy Extraction in the FUJI-1 Disk Generator Experiments," *Proc. of 10th Int. Conf. on MHD,* Vol. III, 1989, pp. XII.30–XII.37.

12 Yamasaki, H., et al., "High Enthalpy Extraction Experiments With the FUJI-1 Disk Generator," *Proc. of 27th Symp. on Eng. Aspects of MHD,* 1989, pp. 6.1.1–6.1.7.

13 Biswas, D., et al., "Boundary Layer Effects in He and Ar Driven Disk MHD Generators," *Energy Convs. and Mgmt.,* Vol. 28, No. 1, 1988, pp. 105–115.

14 Harada, N., et al., "Performance of an Inert Gas Driven Disk MHD Generator," *Proc. 27th Symp. on Eng. Aspects of MHD,* 1989, pp. 8.13.1–8.13.8.

15 Yamasaki, H., et al., "Closed Cycle MHD Disk Experiments at T.I.T.," *Proc. of 23rd Symp. on Eng. Aspects of MHD,* 1985, pp. 430–438.

16 Harada, N., et al., "Results of High Interaction Experiments in Closed Cycle MHD Facilities at Tokyo Institute of Technology," *Proc. of 24th Symp. on Eng. Aspects of MHD,* 1986, pp. 42–53.

17 Harada, N., et al., "High Enthalpy Experiments With a Closed Cycle Disk MHD Generator," *Proc. of 9th Int. Conf. on MHD,* Vol. II, 1986, pp. 374–383.

P. R. Solomon

M. A. Serio

J. E. Cosgrove

D. S. Pines

Y. Zhao

Advanced Fuel Research, Inc.,
87 Church Street,
East Hartford, CT 06108

R. C. Buggeln

S. J. Shamroth

Scientific Research Associates, Inc.,
50 Nye Road,
Glastonbury, CT 06033

A Coal-Fired Heat Exchanger for an Externally Fired Gas Turbine

Significant improvements in efficiency for electricity generation from coal can be achieved by cycles that employ a high-temperature, highly recuperative gas turbine topping cycle. The principal difficulty of employing a gas turbine in a coal-fired power generation system is the possible erosion and corrosion of the high-temperature rotating gas turbine components caused by the coal's inorganic and organically bound constituents (ash, sulfur, and alkali metals). One route to overcome this problem is the development of an externally fired gas turbine system employing a coal fired heat exchanger. The solution discussed in this paper is the design of a Radiatively Enhanced, Aerodynamically Cleaned Heat-Exchanger (REACH-Exchanger). The REACH-Exchanger is fired by radiative and convective heat transfer from a moderately clean fuel stream and radiative heat transfer from the flame of a much larger uncleaned fuel stream, which supplies most of the heat. The approach is to utilize the best ceramic technology available for high-temperature parts of the REACH-Exchanger and to shield the high-temperature surfaces from interaction with coal minerals by employing clean combustion gases that sweep the tube surface exposed to the coal flame. This paper presents a combined experimental/computational study to assess the viability of the REACH-Exchanger concept. Experimental results indicated that the REACH-Exchanger can be effectively fired using radiation from the coal flame. Both computation and experiments indicate that the ceramic heat exchanger can be aerodynamically protected by a tertiary stream with an acceptably low flow rate.

1 Introduction

The combined pressures to establish energy security, improve pollution control, and reduce global warming are encouraging the development of cleaner, more efficient technologies to convert coal into electricity. Significant improvements in efficiency can be achieved by cycles that employ a high-temperature, highly recuperative gas turbine topping cycle. The principal difficulty of employing a gas turbine in a coal-fired power generation system is the possible erosion and corrosion of the high-temperature rotating gas turbine components caused by the coal's inorganic and organically bound constituents (ash, sulfur, and alkali metals). One route to overcome this problem is the development of an externally fired gas turbine system employing a coal-fired heat-exchanger. The chief advantage of this route is that the problems caused by the coal's inorganic constituents are switched from the high-temperature rotating parts of the gas turbine to the high-temperature stationary parts of a heat exchanger. The technology barrier is that ceramics are required because of the high temperature, but state-of-the-art materials are either mechanically and thermally deficient (Al_2O_3), or mechanically durable (SiC), but susceptible to oxidation or to corrosion from the coal's ash, sulfur, or alkali. The key issue is, then, the development of methods to fire a high-temperature heat exchanger with coal in such a way that the potential damage from the inorganic constituents is minimized. Several such systems are currently under development [1–4].

The present paper addresses a combined experimental/computational study of an innovative technique for firing high-temperature heat exchangers in which heat exchangers placed near the furnace outer diameter are fired by radiant energy from a central coal flame and convective energy from a clean burning stream introduced at the burner outer diameter. This clean burning stream also provides flow management to shield the ceramic heat exchangers from the coal's inorganic and organically bound constituents.

2 REACH-Exchanger Concept

The solution discussed in this paper is the design of a Radiatively Enhanced, Aerodynamically Cleaned Heat-Exchanger (REACH-Exchanger) [5]. The REACH-Exchanger is fired by radiative and convective heat transfer from a moderately clean fuel stream and radiative heat transfer from the flame of a much larger uncleaned fuel stream, which supplies most of the heat. The approach is to utilize the best ceramic technology available for high-temperature parts of the REACH-Exchanger and to shield the high-temperature surfaces from interaction with coal minerals by employing clean combustion gases that sweep the tube surface exposed to the coal flame.

The proposed REACH-Exchanger and coal burner configuration are shown schematically in Fig. 1. Several such units are integrated into a High-Temperature Advanced Furnace (HITAF) shown in Fig. 2. In the base case system considered, the REACH-Exchanger receives air preheated to 1280°F (693°C) elsewhere in the furnace using a metal heat exchanger. The temperature is raised to 2111°F (1155°C) in the REACH-Exchanger and further heated in an in-duct burner to 2530°F (1388°C) before introduction to the gas turbine. In this system, 80 percent of the energy to the REACH-Exchanger is supplied by radiation. The clean stream can be natural gas or volatile products of pyrolysis, low Btu gas from coal carbonization, or products of coal gasification. The uncleaned stream can be coal or char.

There are several questions that must be answered to determine the technical feasibility of a power generating cycle employing the REACH-Exchanger/HITAF concept.

1 Can the REACH-Exchanger be effectively fired using radiation from the coal flame?

Contributed by the International Gas Turbine Institute for publication in the ASME JOURNAL OF ENGINEERING FOR GAS TURBINES AND POWER. Manuscript received by the International Gas Turbine Institute July 1, 1993. Associated Technical Editor: H. L. Julien.

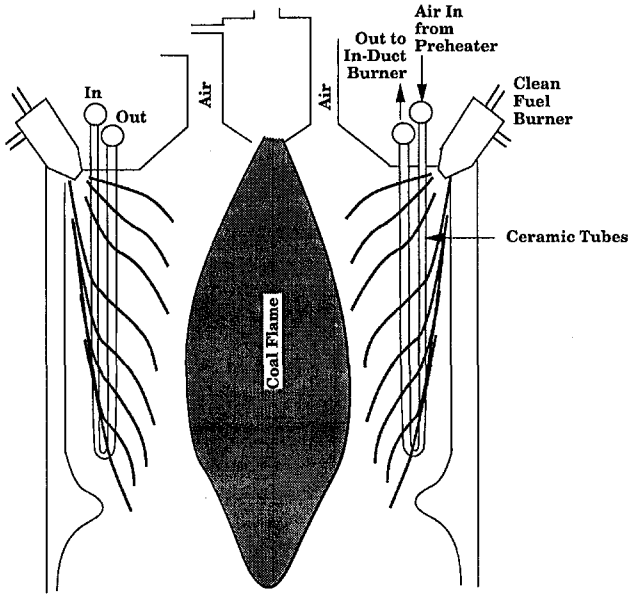

Fig. 1 HITAF/REACH-Exchanger burner

2 Can it be aerodynamically protected using a practical mass flow rate of gas?
3 Does the REACH-Exchanger/HITAF concept lead to a high efficiency practical power generation cycle?
4 Can a ceramic heat exchanger be economically and reliably fabricated?

Two projects were funded by DoE to provide answers to the first two questions. An experimental project [6] was pursued under the Small Business Innovation Research (SBIR) program. A theoretical project [7] was pursued to examine the aerodynamic cleaning using two-phase computational fluid dynamic methods.

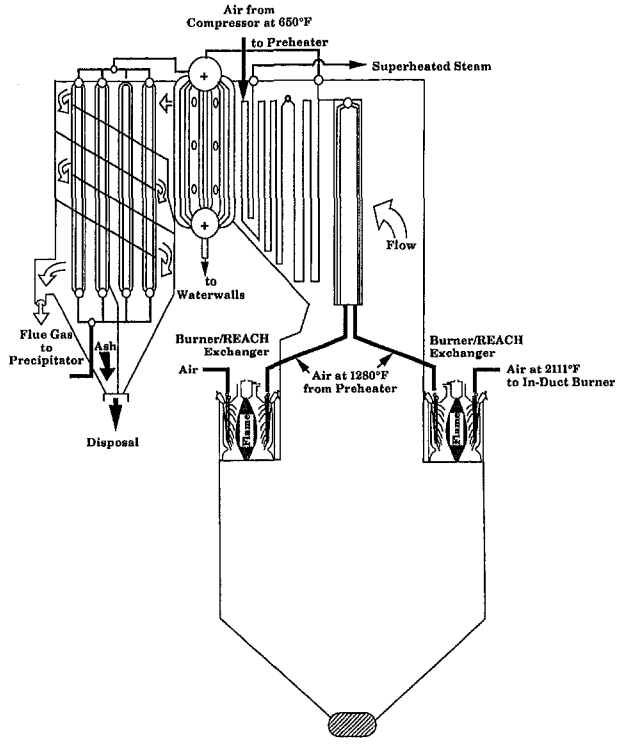

Fig. 2 HITAF showing two REACH-Exchanger burner units

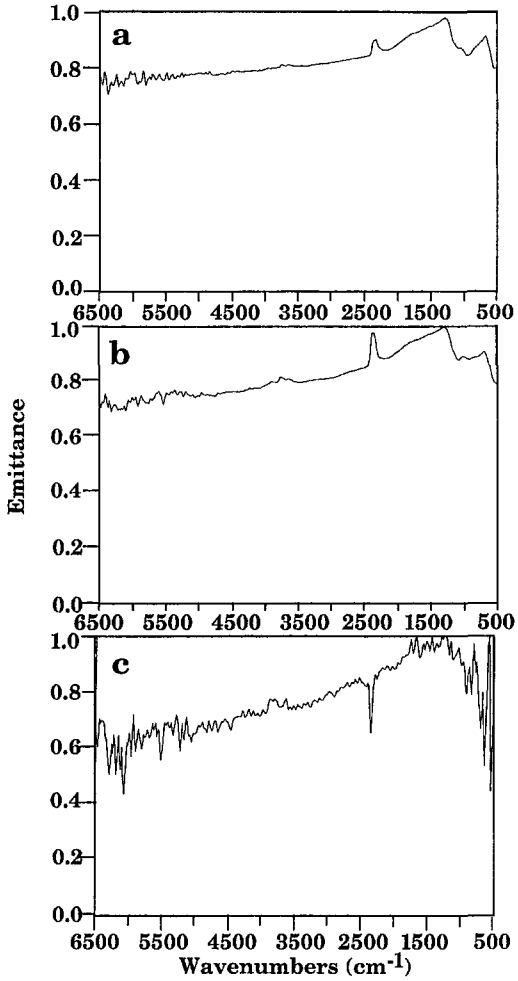

Fig. 3 Emittance spectra at elevated temperatures for Dupont Lanxide material number 91-X-1096: (a) (1033°F) 556°C; (b) (1881°F) 1027°C; (c) (2653°F) 1456°C

3 Experimental

The objective of the experimental program was to test the proposed REACH-Exchanger in a well-instrumented laboratory facility and assess its advantages in a power generating system. The work was performed in a 0.5 million Btu/hr (0.15 MW) coal combustion facility previously described [8, 9]. The facility was modified to allow firing of dry coal and to include a heat exchanger and in-situ FT-IR diagnostics to measure flame radiation and flame constituent concentrations. The facility was then employed in a series of tests to determine the heat-exchanger efficiency. A second series of tests examined the efficiency of aerodynamically protecting the heat exchanger surface.

Ceramics. The spectral emittances of three ceramic heat-exchanger materials were determined at elevated temperatures using an FT-IR based emissometer developed by AFR [10–12]. The samples were provided by DuPont Lanxide Composites, Inc., and are fabricated from SiC particulate reinforced alumina. Figure 3 displays the emittance spectra of material designation number 91-X-1096 at 1033°F (556°C), 1881°F (1027°C), and 2653°F (1456°C). Heat-exchanger tubes (length, 2 ft (0.61 m), o.d. = 2 in. (0.05 m) of material number 91-X-1096 were supplied for the REACH-Exchanger tests.

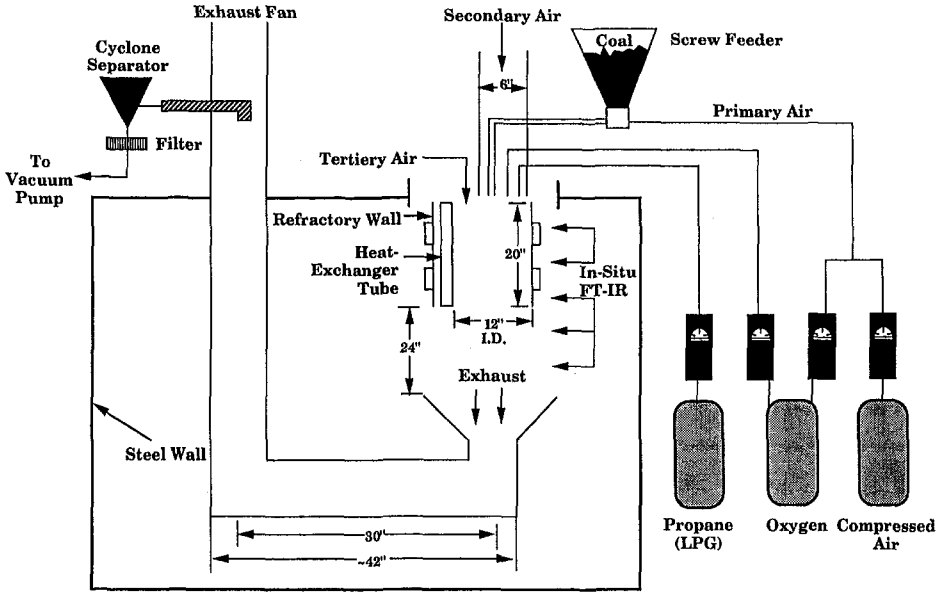

Fig. 4 Schematic diagram of pulverized coal combustion facility with incorporated heat exchanger tube

Combustion Facility. The facility consisted of a fire-proof room approximately 8 ft × 10 ft × 8 ft (2.4 m × 3.0 m × 2.4 m) high, allowing a flame region of about 5 ft (1.5 m) between the nozzle and exhaust stack. The CWF is burned in a down-fired geometry. The facility included a specially designed flame gun containing refractory walls for flame stability, a water/gas cooled isokinetic gas and particle collector for material balance, thermocouples, pitot tubes, and an optical bench with three-dimensional movement capability for FT-IR E/T in-situ measurements. The facility employs large diameter (i.d. = 12 in. (0.3 m)), thin (1 in. 0.025 m)) refractory walls, which greatly reduce radiation and convective losses from the flame. The thinness of the refractory walls allows steady state to be achieved quickly. Self-sustaining steady-state CWF flames using air as the atomizing gas have been achieved within 5 minutes and maintained for periods of up to ninety minutes. The refractory has holes for optical access. The heat release rate in this facility is up to 0.5×10^6 Btu/hr (0.15 MW).

The facility was modified to allow firing of dry coal and to incorporate a ceramic heat exchanger. Figure 4 shows a schematic of the system for a case where dry coal is fired and combustion products of propane gas are used to heat and purge the heat exchange area. The facility also incorporated a Bomem Michelson 110 FT-IR spectrometer for emission/transmission line-of-sight measurements as a function of height within the flame. Figure 5 depicts the FT-IR optical configuration coupled to the coal flame.

Facility Shakedown. The modified facility was run to determine its operating characteristics. The facility was operated with Upper Freeport Coal supplied by ABB Combustion Engineering, Inc. with the following dry basis analyses: V.M. = 34.9 percent; FC = 58.5 percent; Ash = 6.3 percent; C = 80.8 percent; H = 5.5 percent; O = 4.7 percent; N = 1.6 percent; S = 1.1 percent. Initial FT-IR measurements indicated low temperatures in the flame and particles collected in the stack showed low carbon burnout (<66 percent) even though the volume of combustion air being supplied exceeded theoretical requirements. Most likely, inadequate mixing of the secondary air and the fuel jet was occurring due to an oversized secondary air duct. To compensate for this, oxygen was injected (~12.5 percent of necessary fuel requirements) into the flame at the nozzle exit. This improved the carbon burnout to 73 percent and particle/soot temperatures as high as 2781°F (1527°C) were observed in the flame. A constant LPG (propane) pilot was required to maintain ignition of the coal. The extra oxygen and propane pilot were required because of the small size of the pilot facility and would not be required in a commercial size reactor. The use of these additives allowed the studies of temperatures that would be achieved in a larger flame.

4 Experimental Results

Test Case 1. Figure 6 depicts the conditions and measured temperatures in the first test (test case 1*a*) of the REACH-Exchanger. The heat-exchanger temperatures were measured

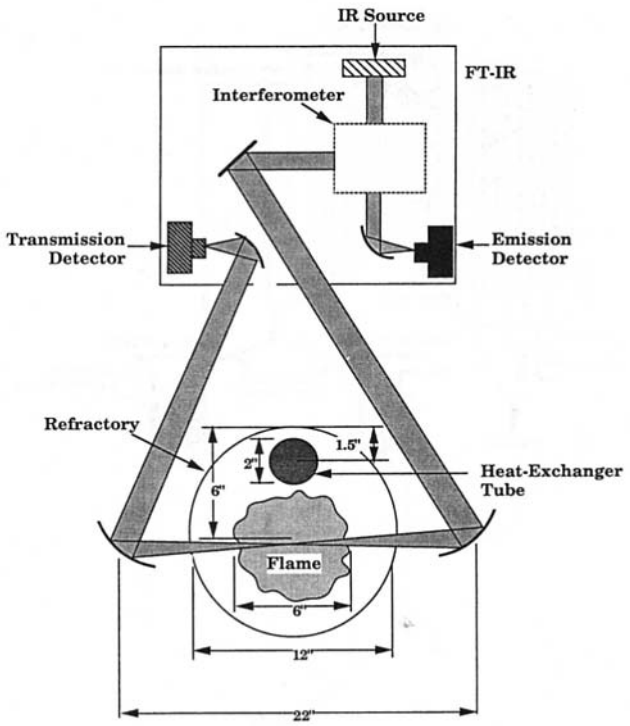

Fig. 5 Configuration of the modified Bomem Michelson 110 FT-IR for in-situ measurements of the REACH-Exchanger flame

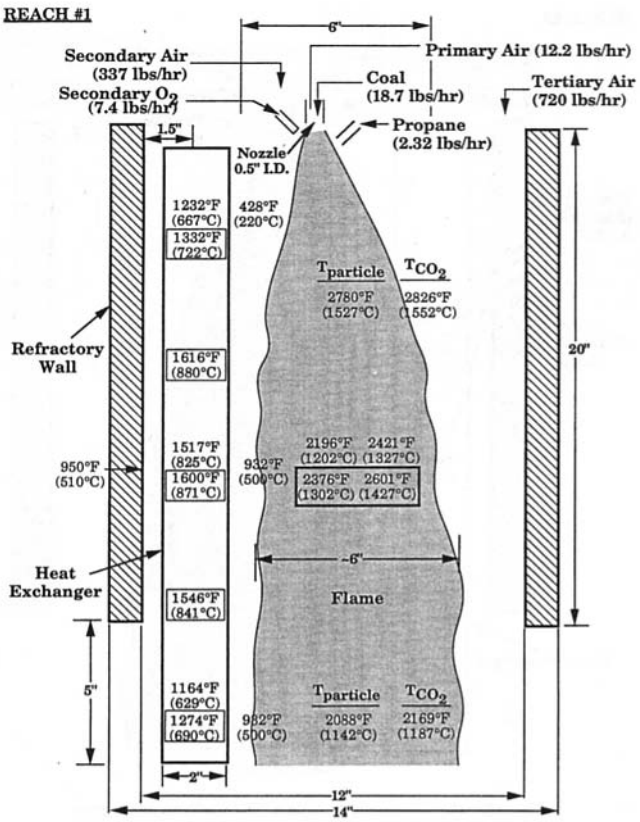

Fig. 6 Measured temperatures of the heat-exchanger tube and its surrounding environment (case 1*a*). Temperatures in boxes were obtained by enriching the primary air with oxygen (case 1b).

with thermocouples mounted inside the heat exchanger. Tests were done with a static working fluid. This was the simplest experiment to perform and is a reasonable test because the radiative heat transfer to the ceramic is so efficient and convective heat transfer to the working fluid is so inefficient that the temperature for the flow case is calculated to be only 50°F (28°C) lower. A suction pyrometer measured the gas temperatures between the heat exchanger and the flame. The tertiary air at 720 lb/hr (0.09 kg/sec) provided a vertical shielding sweep of the heat exchanger. For this flow, the excess air maintained a clean zone $\frac{3}{4}$ in. (1.9 cm) thick in front of the heat exchanger. The heat exchanger reached a maximum measured temperature of 1517°F (825°C) even though the flame was 38 percent transmissive and the cleaning air between the tube and the flame was ~932°F (500°C). The data suggest that when extrapolated to an optically thick flame at higher temperature and with a hot cleaning flow, the required heat transfer to the ceramic can be achieved. After 143 minutes of total exposure time to the flame under these conditions, visual inspection and mechanical abrasion of the heat-exchanger surface with a Q-tip revealed no observable evidence of slagging or fouling.

The flame temperature was increased by ~180°F (100°C) by enriching the primary air/coal feed with oxygen (test case 1*b*). This resulted in an average increase of ~90°F (50°C) of the heat exchanger and an improved carbon burnout of 79 percent. Additional thermocouples were mounted in the heat-exchanger tube and a maximum temperature of 1616°F (880°C) was obtained (see Fig. 6 data in boxes). Again, no visual evidence of slagging on the heat exchanger was observed.

Test Case 2. The second set of experiments concentrated on the aerodynamic shielding effect of the tertiary air on the heat-exchanger surface. In test case 2, the tertiary air was held at 326 lb/hr (0.04 kg/s) compared to 720 lb/h (0.09 kg/s) for case 1. The injection geometry was the same. For this case, there was no clean zone of tertiary air flow between the flame and the front surface of the ceramic. A photograph of the heat-exchanger tube after only 6 minutes of exposure to the flame shows significantly more slagging (as shown by the removal of slag by the Q-tip) of the tube surface than in case 1, where no slagging was observed.

FT-IR transmittance measurements were made between the flame and the heat-exchanger surface at a level just below the refractory. Figure 7(*b*) presents the transmittance spectrum as 100 minus percent transmittance. The FT-IR analysis of flames has been described previously [13–15]. The presence of soot, char, and ash is indicated by the uniform loss of transmitted radiation across the whole spectrum. The presence of gaseous combustion products (H_2O, CO_2) is indicated by specific absorption bands. An FT-IR transmittance measurement was also obtained in case 1 (Fig. 7*a*). Clearly, the 100 minus percent transmittance spectra of case 2 show increased attenuation of the IR beam due to the presence of particles and combustion products (CO_2 and H_2O).

Test Case 3. A third set of experiments concentrated on providing localized cleaning of the heat-exchanger surface under conditions of "low" tertiary air flow (326 lb/hr). In test case 3, 8.35 lb/hr (3.79 kg/h) of compressed air was blown behind the heat-exchanger tube from a 0.5 in. (1.3 cm) i.d. pipe nozzle. The nozzle was positioned at an angle 40 deg to the

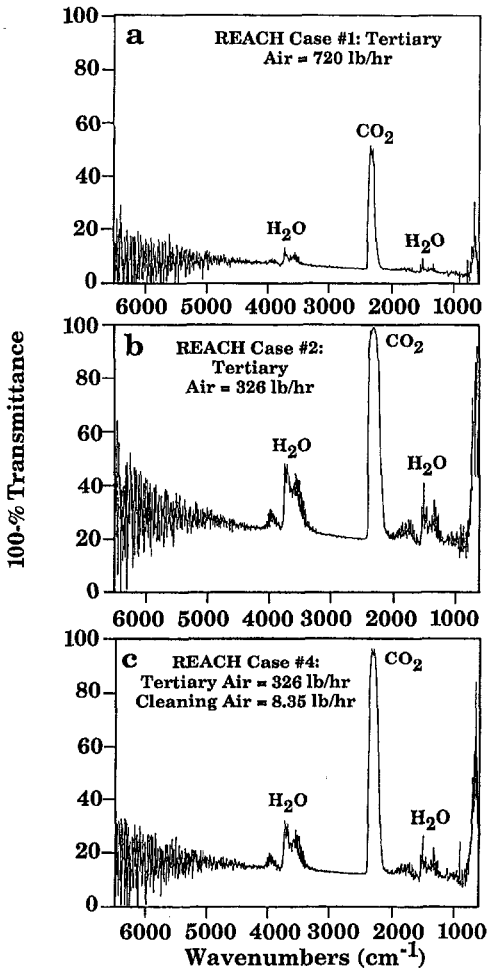

Fig. 7 FT-IR 100 minus percent transmittance spectra taken between the heat exchanger and the flame (1 in. below refractory) for (*a*) test case #1: tertiary air = 720 lb/hr; (*b*) test case #2: tertiary air = 326 lb/hr; (*c*) test case #4: tertiary air = 326 lb/hr, localized cleaning air = 8.35 lb/hr

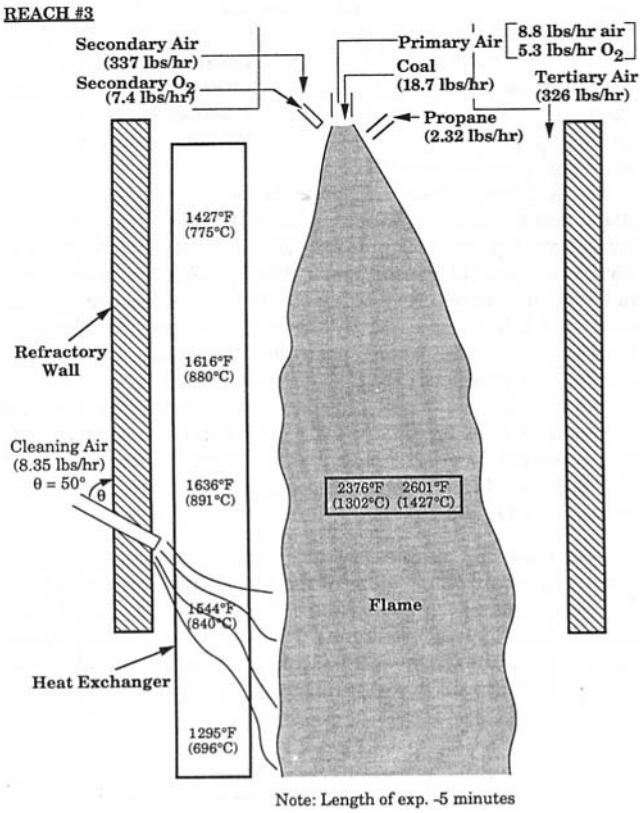

Fig. 8 Configuration of case #3 localized cleaning

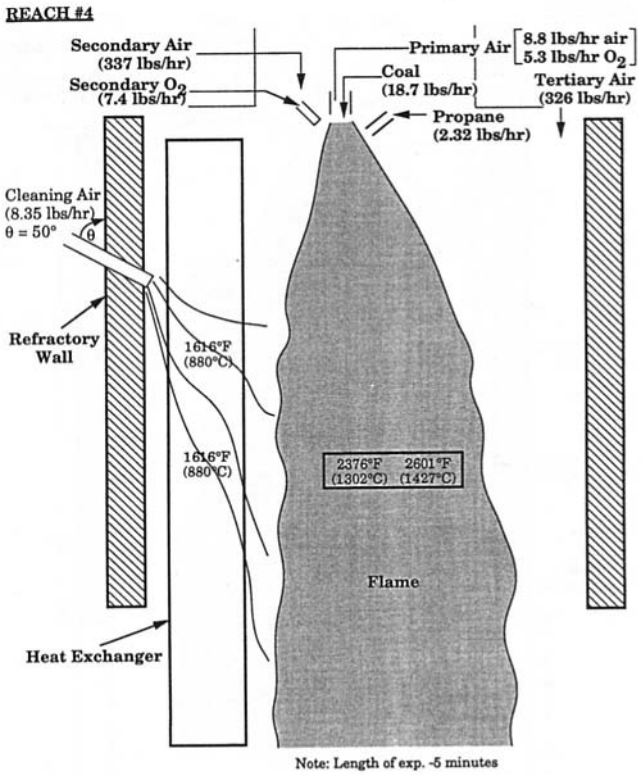

Fig. 10 Configuration of case #4 localized cleaning

tube normal, 7 in. (17.8 cm) above tube bottom as shown in Fig. 8. A sharp contrast between the fouled section of the tube and the clean section is observed in Fig. 9. The figure shows that the heat-exchanger remains clean only where the nozzle air sweeps the back and side of the tube in the lower left corner.

Test Case 4. The results of test case 3 warranted relocating the localized cleaning air to a higher position along the heat-exchanger tube. In test case 4 (Fig. 10), the nozzle was mounted 16 in. (40.6 cm) above the tube bottom. Blowing 8.35 lb/hr (3.79 kg/h) at this higher position allowed the shielding sweep to surround the heat-exchanger and resulted in a much cleaner heat-exchanger surface, comparable to the cleaning results achieved using a "high" tertiary air flow (test case 1). FT-IR transmission measurements (Fig. 7*c*) showed a decrease in IR attenuation due to particles, CO_2, and H_2O. The combustion product concentrations were lower than that of case 2 (Fig. 7*b*), but higher than in case 1 (Fig. 7*a*).

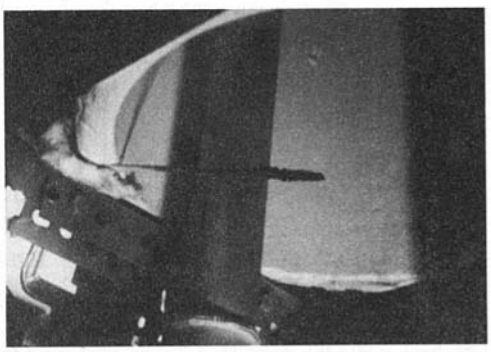

Fig. 9 Photograph of heat exchanger tube after ~6 minutes exposure of case #3 conditions. Note the clean region of the tube in the lower left corner where the nozzle air sweeps the tube.

Test Case 5. In test case 5, the air nozzle from case 4 was replaced by a propane torch with a 1 in. (2.5 cm) i.d. nozzle in order to reduce some of the convective heat losses associated with the "cool" tertiary air. The flame was positioned so as to maximize the distribution of its heat along the length of the tube which resulted in the flame impinging on the tube at a very high angle (65 deg) to the normal of the tube. The propane flow rate was 0.74 lb/hr (0.34 kg/h) along with an undetermined flow of air induced by the venturi action of the torch. Under low tertiary air conditions (test case 5*a*), the heat-exchanger tube reached a maximum temperature of 1967°F (1075°C); however, a layer of slag was deposited on the tube. Under high tertiary air conditions (test case 5*b*) the tube reached a maximum temperature of 1742°F (950°C) and no slagging was observed.

FT-IR Characterization of the Flame. FT-IR measurements of temperatures for particles and CO_2 for concentrations for particles, soot, and CO_2, for the fraction of ignited particles and for the radiance intensity in the flame were obtained. The method is described in [13–15]. The transmittance data indicated that the flame was not opaque (average transmittance ~40 percent). The normalized radiance data, which are compared to Planck functions, show flame temperatures in the range 2012°F (1100°C) to 2822°F (1550°C). The maximum particle temperature observed was 2781°F (1527°C) in test case 1*a*. Figure 11 depicts the transmittance (expressed as 100 minus percent transmittance), radiance, and normalized radiance spectra calculated to obtain these measurements 13 in. (33 cm) from the burner/nozzle for test case 1*b*.

5 CFD Modeling of Aerodynamic Cleaning

Two-phase computational fluid dynamics (CFD) was employed to investigate potential strategies for injecting a cleansing stream into the HITAF/REACH-Exchanger to protect the heat-exchanger elements from coal particles and corrosive coal combustion products. The CFD study was done for a candidate

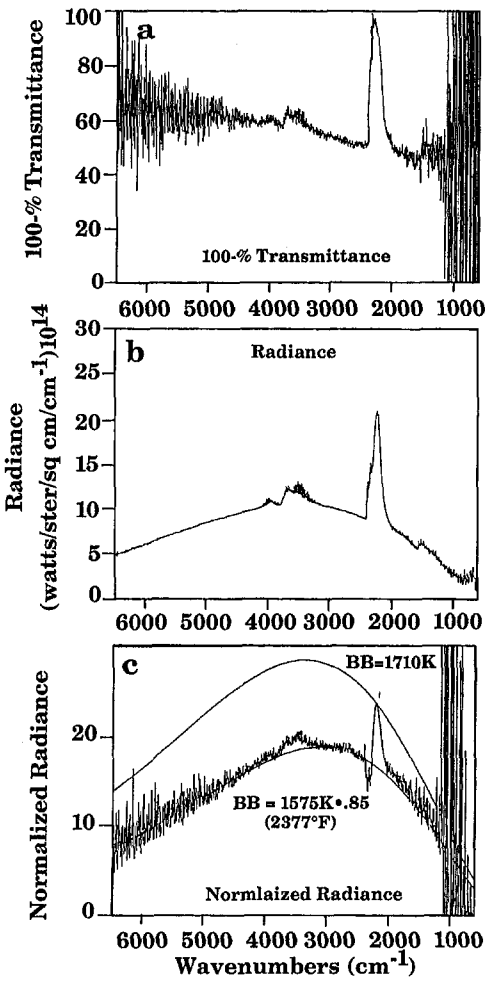

Fig. 11 FT-IR E/T spectra of oxygen-enhanced flame taken at position #2 (13 in. from nozzle): (*a*) 100 minus percent transmittance; (*b*) radiance; (*c*) normalized radiance

full-scale burner. A complete CFD study was not performed on the experimental apparatus because of its complicated nonsymmetric geometry.

At present there is no single code that contains the appropriate coal chemistry package and particle dispersion model to provide a complete solution. Therefore, a combination of two codes was used. The first code was PCGC-2 [13, 16], which has been developed for pulverized coal combustion. This code contains the required coal combustion models as well as radiative heat transfer. The major problem of PCGC-2 in regard to the present effort is dispersion of particles by the background turbulent flow. The second code used was CELMINT [17, 18], which has been developed for two-phase rocket flows. CELMINT does not have coal chemistry and does not include radiative energy transfer. However, it does have a verified model for particle dispersion by turbulence (e.g., [18, 19]).

In the present study a combusting gaseous flow calculation was first run with PCGC-2 to obtain the energy field including heat transfer effects. The resulting temperature was then used as input for CELMINT, which solved the momentum and continuity equations for the gaseous flow under the PCGC temperature solution. For the present study, the flow was assumed to be lightly loaded. Under lightly loaded conditions, the gaseous continuous phase is not affected by the discrete particulate phase. Therefore, the Lagrangian portion of CELMINT was then used to track particles under the influence of the background gaseous flow and gravity. Three major mechanisms are present that would cause particle and trace species dispersion. The first is convective transport by the background flow, the second is the ballistic trajectory dictated by the particle flow angle on inflow, and the third is dispersion of particles by the turbulent component of the background flow. The CELMINT analysis used here to track the particles includes all three. Although thermophoresis is an additional mechanism for the deposition of fine particles, it has not been included. In the present study the region between the coal flame and the heat exchanger contains gas colder than the heat exchanger. Thus, thermophoresis would tend to drive particles away from the heater, and neglect of this effect provides a conservative estimate.

For the present study, particles are tracked from the inflow port, which is the central coal/air stream along the axis (Fig. 12). For the purpose of the present study, it is assumed that upon inflow the axial velocity is equal to the axial velocity of the background flow. In addition, a particle radial velocity is assumed such that the flow angle relative to the axis of symmetry is 6 deg. The turbulence of the continuum background flow was obtained from a solution of the two-equation $k-\epsilon$ turbulence model. This provided a local turbulence intensity, which is input into a statistical algorithm to provide the instantaneous flow leading to particle dispersion by background turbulence. This algorithm adds a fluctuating component to the local background mean flow, allowing the particle to be influenced by the background flow turbulence. The procedure is based upon a random number generator; however, for each run the generator is always started at the same place, thus making the results deterministic in the sense that for (*i*) a given background flow and (*ii*) a given number of inflow particles with prescribed velocity and position, the particle paths generated are repeat-

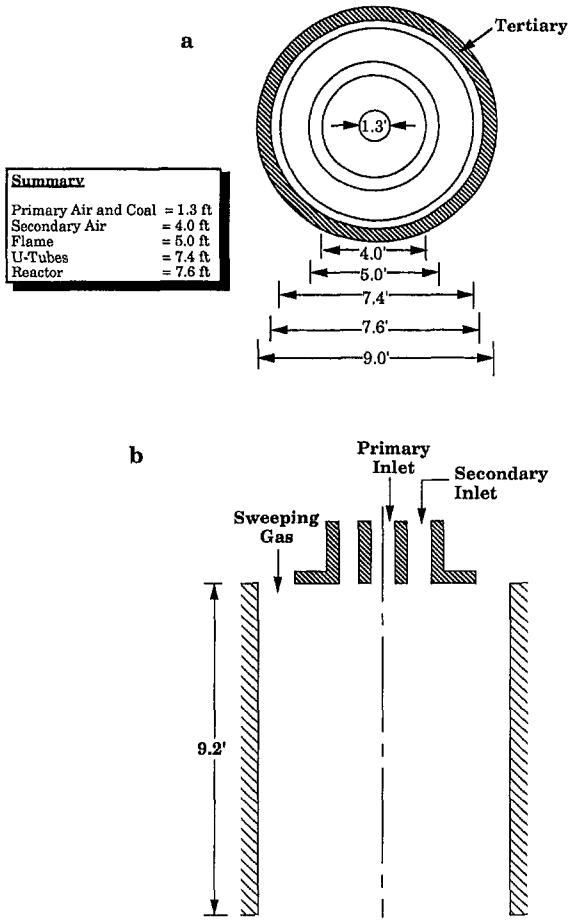

Fig. 12 The REACH-Exchanger reactor geometry used for the CFD model: (*a*) top view; (*b*) side view. The positions of the heat-exchanger tubes are not shown.

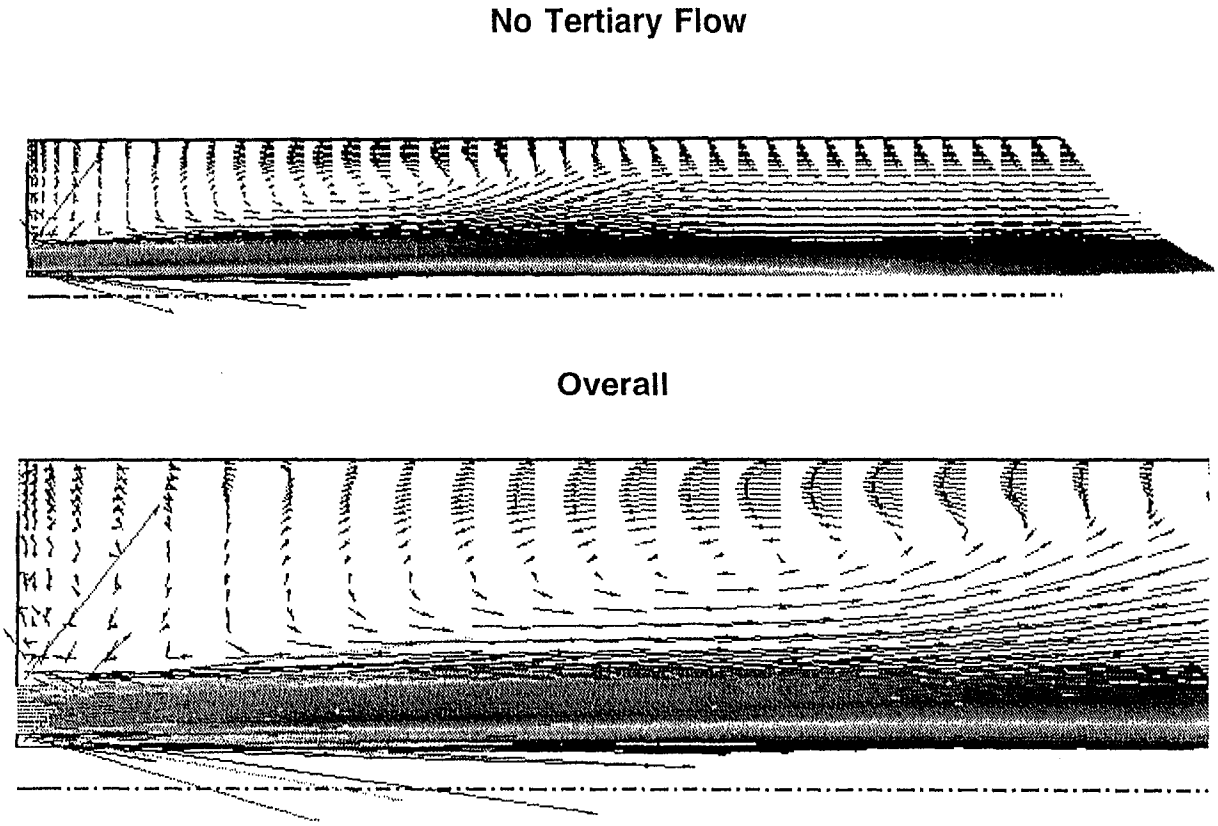

Fig. 13 Velocity vector plots case #1 (no tertiary flow)

able. However, if a new particle is added between two existing particles, the new particle path, in general, will not be confined to the region between the two original particle paths. This is important in interpreting the plots. In addition, due to the random nature of the process, there is always a chance that any single particle may follow an unexpected path.

The initial radial velocity is most important for the large particles, as it provides the initial particle momentum, which is modified with time by the background flow drag force and turbulence. It is less important for small particles since their low mass (i.e., low momentum) makes them come to equilibrium with the background flow more quickly. In contrast, the background turbulence has more influence on the smaller particles. This provides a random, instantaneous flow field, which influences the particles via a random drag force and those particles having lower momentum, i.e., the smaller particles, are more subject to these turbulent fluctuations.

The calculations were carried out for a single burner with the geometry shown in Fig. 12. The calculation assumes a primary stream mass flux of 10.9×10^3 lb/hr (1.37 kg/s), a secondary mass flux of 39.3×10^3 lb/hr (4.96 kg/s), and a tertiary stream mass flux of 11.1×10^3 lb/hr (1.40 kg/s) for the second and third cases considered. Five sets of calculations were performed. The first had no tertiary injection; the second had tertiary injection from an annulus located at the top of the furnace near the outer edge; the third had flow injected from a slit at the outer diameter wall located approximately one-half way along the length of the furnace. The fourth had tertiary flow injected from both top and outer walls. The fifth had injection from the top and two places on the outer walls. Both the forth and fifth cases had twice the total tertiary injection of cases 2 and 3. Gravity was included in the calculation. The furnace radius was approximately 4.5 ft (1.4 m) and the length 30 ft (9.2 m).

Velocity vector plots for two of the five cases are shown in Figs. 13 and 14, both for the overall flow field and a "closeup" of the recirculation zone. The direction of flow is shown by the direction of arrows plotted on the figure and the amplitude is represented by the length of the arrows. Particle paths were run for particles originating in the primary stream. Particle path results for Case 1 are shown in Fig. 15. In Figs. 13–15, the inflow at the top of the furnace is at the left, the axis of symmetry at the bottom, the outer wall at the top and outflow at the right. The plots have been rotated by 90 deg from their physical orientation for ease of viewing. Gravity is in the left-to-right direction. Particle paths were calculated for particle radii of 10 μm, 30 μm, and 100 μm and each result is shown separately. For each case, particles were injected at twenty-four separate inlet locations. Many thousands of particles were injected at each inlet location and the trajectory of each particle was determined by its interaction with the background flow. The interaction had both a mean and a random component and each trajectory shown represents the statistical average of all particles entering the flow from the specific injection location.

Figures 13 and 15 show the base case; no tertiary injection. The development of the flow field shows the primary and secondary jets mixing with the quiescent flow and the resulting recirculation region are evident in Fig. 13. In these plots, velocity vectors near the centerline are omitted, as they were large and obscured the rest of the plot. Figure 15 shows particle trajectories for the base case. In assessing the results, note that the heat exchanger is to be placed at 80 percent of the furnace radius. For no tertiary flow, it is clear that the entire range of particles considered presents a problem. The particles would be dangerously close to the heat exchanger at approximately 40 percent of the length (for 10 μm), 60 percent (for 30 μm), and 40 percent (for 100 μm), respectively.

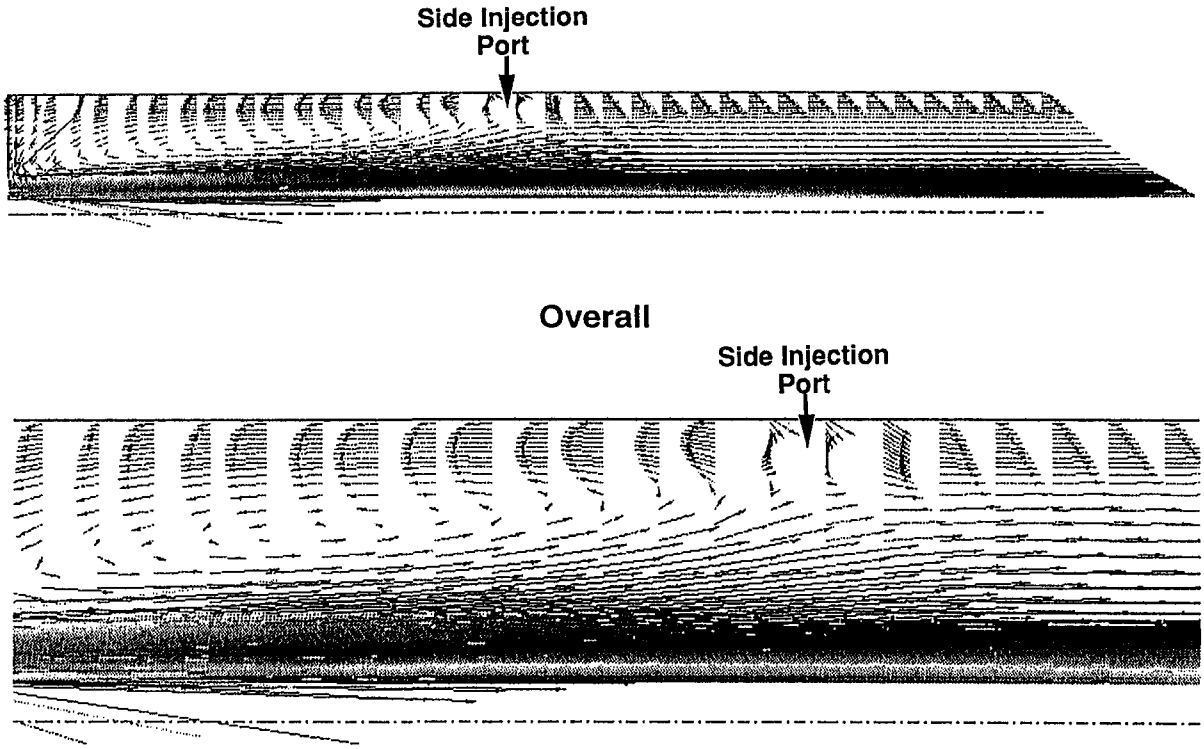

Fig. 14 Velocity vector plots case #3 (tertiary flow: side injection)

For tertiary air injected at the top of the reactor, Case 2 (not shown), the tertiary air is very quickly turned toward the centerline after injection and adds an additional buffer to the original secondary stream buffer around the primary coal/air stream. This should add protection to the flow. The particle trajectories now become dangerously close at 60 percent of the length (for 10 μm), 70 percent of the length (for 30 μm), and 50 percent of the length (for 100 μm), respectively. Clearly, even this modest amount of tertiary injection is very beneficial. Figure 14 shows the flow for side injection, which energizes the flow downstream of the injection hole. This provides protection in the downstream region for 75, 83, and 60 percent of the length, for the 10, 30, and 100 μm particles, respectively. For the two combined injection cases, where gas was injected at the top of the furnace and along the side wall, further improvement is noted. These results are summarized in Table 1.

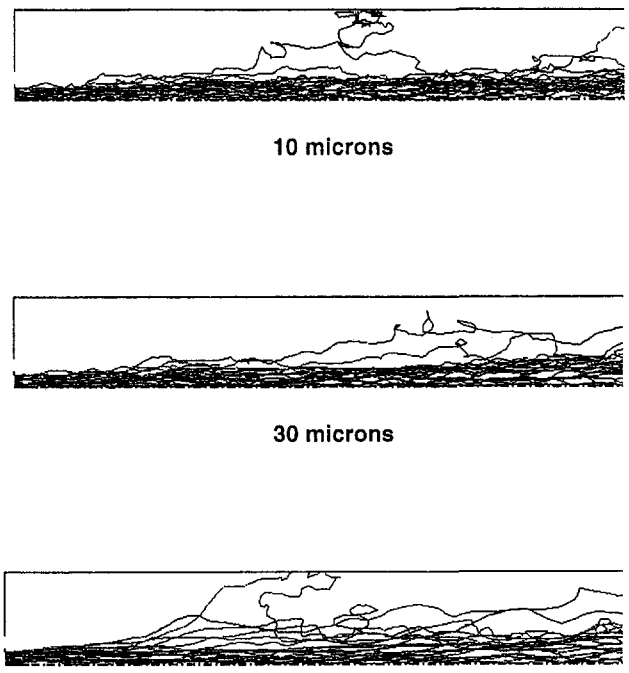

Fig. 15 Particle paths case #1 (no tertiary flow)

These preliminary calculations indicate that even with a modest amount of cleansing air, heat exchange elements can be protected for 60 percent of the furnace length. Other strategies combining top and side injection, changing the side injection angle, and/or changing the side injection number of ports are likely to further improve these results.

From the above results, it appears that additional optimization of the cleaning effect could be achieved by adjusting the relative amounts of secondary and tertiary air buffers. Based on this understanding, one more calculation (case 6) was carried out. In case 6, the original secondary air flow was split into two equal parts. One half of it was fed from the secondary inlet I with a reduced diameter of 1.04 m. The other half was injected from the secondary II inlet, which is an annulus located at 0.872

Table 1 Lengths protected

Particle Size	Case 1 No Inj	Case 2 Top Inj	Case 3 Side Inj	Case 4 Comb. Inj	Case 5 Comb. Inj.	Case 6
10 μm	40%	60%	75%	90%	90%	30%
30 μm	60%	70%	83%	100%	95%	95%
100 μm	40%	50%	60%	70%	80%	95%

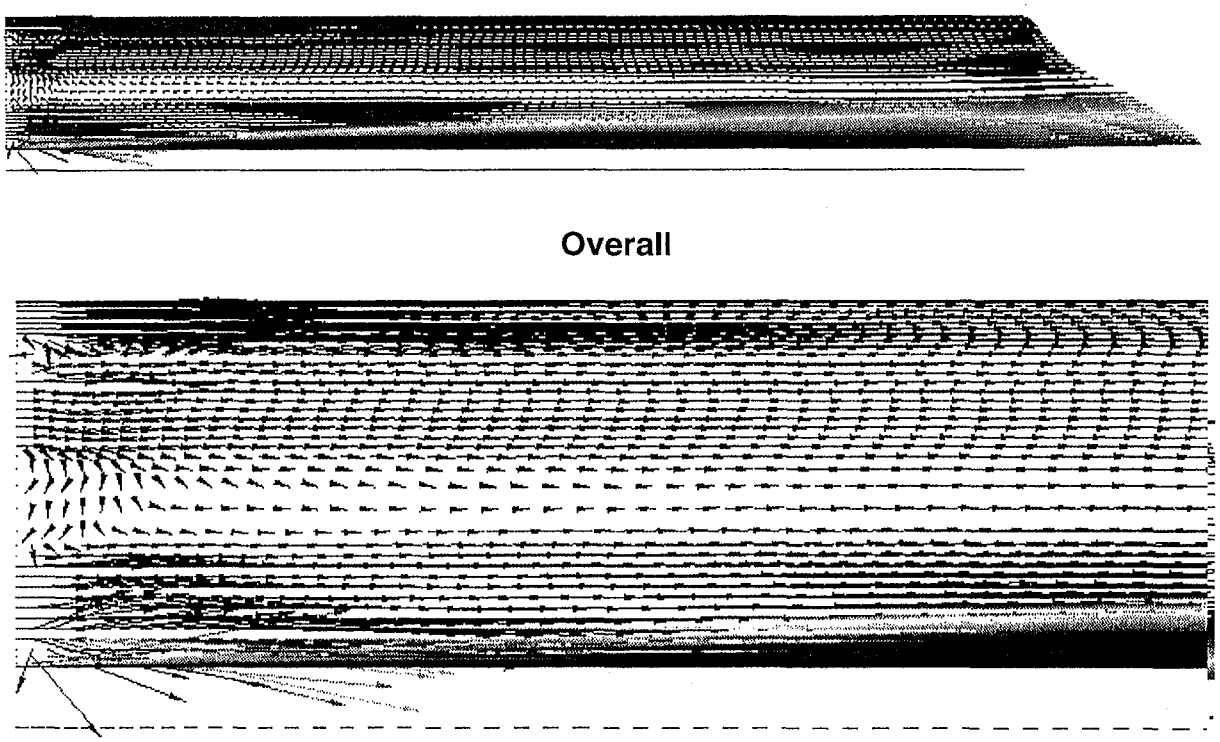

Fig. 16 Velocity vector plots case #6 (two secondary injections)

meters from the center line of the reactor cylinder. There is no side injection.

The velocity vector plots are given in Fig. 16. The flow patterns obtained were considerably different from those obtained in the previously run cases. The large recirculation normally obtained on the outer wall was not observed. As expected, two small recirculation zones were formed in the base regions, but these zones are small and have little effect on the flow pattern. As indicated in Table 1, the results for Case 6 are the most promising for larger particles. For the 10 μm case one particle does penetrate the region of the heat exchanger. This design controls particle transport mechanism No. 1 very well, but the small particles that are mostly affected by the turbulence can still cause fouling problem. Better turbulence control could be achieved by design modifications in both geometry and firing schemes.

In addition, although not shown here, results have been obtained to show the sensitivity of the calculations to inlet primary stream flow angle and turbulence level. As expected, in general, although anomalies do appear due to the statistical nature, reducing the inlet primary stream flow angle reduces particle spread and increasing turbulence increases primary stream spread.

6 Conclusions

A combined experimental/computational study has been performed to assess the viability of a coal-fired heat exchanger for an externally fired gas turbine. Experimental results indicated that the REACH-Exchanger can be effectively fired using radiation from the coal flame. Both computation and experiments indicate that the ceramic heat exchanger can be aerodynamically protected by a tertiary stream with an acceptably low flow rate. This work provides affirmative answers to two of the major questions regarding REACH-Exchanger efficiency and viability.

- The program results demonstrate that the radiative heat exchange is extremely effective. Heat-exchanger temperatures up to 1967°F (1075°C) were achieved in a coal flame whose temperature was boosted using propane addition, even though the flame was not optically thick (~60 percent) at a lower temperature than would be achieved in the HITAF. The data suggest that when extrapolated to an optically thick flame at the higher temperature expected in the HITAF, the required heat transfer to the ceramic can be achieved.
- Both experiments and modeling show that aerodynamic shielding can be accomplished with a practical amount of clean gas (less than 20 percent of the total flow) to sweep the surface of the heat exchanger.

Acknowledgments

This work was supported under Contract Nos. DE-AC22-92PC92196 and DE-FG05-92ER81323 from the U.S. Department of Energy. Dr. Clifford Smith is the Contract Monitor.

We wish to thank DuPont Lanxide Composites, Inc., for supplying the test ceramics.

References

1 Zabolotny, E. R., Vivenzio, T. A., and LeHaye, P., *Proceedings of the American Power Conference,* 52nd Annual Meeting, Chicago, IL, Apr. 23–25, 1990.

2 LeHaye, P. G., and Zabolotny, E., *Proc. IGTI,* Vol. 4, 1989, p. 263.

3 Foster Wheeler Development Corporation, "Development of a High-Performance Coal-Fired Power Generating System With Pyrolysis Gas and Char-Fired High Temperature Furnace (HITAF)," Quarterly Progress Report (3), for U.S. DoE/PETC Contract No. DE-AC22-91PC1154, 1992.

4 United Technologies Research Center, "Coal-Fired High Performance Power Generating System," Quarterly Progress Report, for U.S. DoE/PETC Contract No. DE-AC22-92PC91155, July 1–Sept. 30, 1992.

5 Solomon, P. R., Bates, S. C., Carangelo, R. M., and Hamblen, D. G., "Coal Fired Heating Apparatus and Method," patent application, 1991.

6 Solomon, P. R., Serio, M. A., Cosgrove, J. E., Pines, D. S., and Zhang, Y., "An Advanced Coal Fired Heat Exchanger/Gas Turbine Topping Cycle for a High Efficiency Power Plan," Final Report for U.S. Department of Energy, Contract No. DE-FG05-92ER81323, May, 1993.

7 Advanced Fuel Research, Inc., "Feasibility Study for an Advanced Coal Fired Heat-Exchanger/Gas Turbine Topping Cycle for a High Efficiency Power Plant," DoE Contract #DE-AC22-92PC92196.

8 Solomon, P. R., Best, P. E., Chien, P. L., and Goodman, R. M., "A Laboratory Combustion Facility for Evaluation of CWF," 6th International Workshop on Coal-Liquid and Alternate Fuels Technology, Halifax, Canada, 1986.

9 Solomon, P. R., Chien, P. L., and Best, P. E., "Measurement and Optimization of Combustion Performance of Coal Water Fuels," US DOE Contract No. DE-AC01-85ER80320 Final Report, 1986.

10 Markham, J. R., Solomon, P. R., and Best, P. E., "A FT-IR Based Instrument for Measuring Spectral Emittance of Material at High Temperature," *Review of Scientific Instruments,* Vol. 61, 1991, p. 3700.

11 Markham, J. R., Best, P. E., Solomon, P. R., and Yu, Z. Z., "Measurement of Radiative Properties of Ash and Slag by FT-IR Emission and Reflection Spectroscopy," ASME *Journal of Heat Transfer,* Vol. 114, 1992, p. 458.

12 Markham, J. R., Kinsella, K., Carangelo, R. M., Brouillette, C. R., Carangelo, M. D., Best, P. E., and Solomon, P. R., "A Bench Top FT-IR Instrument for Simultaneously Measuring Surface Spectral Emittance and Temperature," *Review of Scientific Instrument,* in press, 1993.

13 Solomon, P. R., Markham, J. R., Zhang, Y. P., Carangelo, R. M., Brewster, B. S., and Smoot, L. D., "The Study of a Coal Flame by FT-IR Emission/Transmission Tomography and Comprehensive Modeling," Sci-Mix Poster Session, ACS Meeting, Washington, DC, 1990.

14 Solomon, P. R., Chien, P. L., Carangelo, R. M., Best, P. E., and Markham, J. R., *Proc. The 22nd Symposium (Int.) on Combustion,* The Combustion Institute, Pittsburgh, PA, 1988, p. 211.

15 Markham, J. R., Zhang, Y. P., Carangelo, R. M., and Solomon, P. R., *FT-IR Emission/Transmission Tomography of a Coal Flame,* The 23rd Symposium (Int) on Combustion, The Combustion Institute, 1990, pp. 1869–1875.

16 Smith, P. J., Smoot, L. D., and Fletcher, T. H., "User's Manual for a Computer Program for 2-Dimensional Coal Gasification of Combustion (PCGC-2)," Interim Report Vol. II prepared for U.S. DoE/METC Contract No. DE-AC21-81MC16518, Combustion Laboratory, Brigham Young University, Oct. 1983; see also Smoot, L. D., and Brewster, B. S., "User's Manual for 1990 Version of Pulverized Coal Gasification and Combustion 2-Dimensional (87-PCGC-2)," rev., ACERC, Brigham Young University, July 1991.

17 Sabnis, J. S., de Jong, F. J., and Gibeling, H. J., "Calculation of Particle Trajectories in Solid-Rocket Motors With Arbitrary Acceleration," *J. Prop. Power,* Vol. 8, Sept.–Oct., 1992.

18 Sabnis, J. S., Choi, S. K., Buggeln, R. C., and Gibeling, H. J., "Computation of Two-Phase Shear Layer Flow Using an Eulerian–Lagrangian Analysis," AIAA Paper No. 88-3202, 1988.

19 Sabnis, J. S., and de Jong, F. J., "Calculation of the Two-Phase Flow in an Evaporating Spray Using an Eulerian–Lagrangian Analysis," AIAA Paper No. 90-0447, 1990.

S. Somasundaram
Energy Sciences Department.

M. K. Drost
Energy Sciences Department.

D. R. Brown
Technology Systems Analysis Department.

Z. I. Antoniak
Analytical Sciences Department.

Pacific Northwest Laboratory,
Richland, WA 99352

Coadunation of Technologies: Cogeneration and Thermal Energy Storage

Thermal energy storage can help cogeneration meet the energy generation challenges of the 21st century by increasing the flexibility and performance of cogeneration facilities. Thermal energy storage (TES) allows a cogeneration facility to: (1) provide dispatchable electric power while providing a constant thermal load, and (2) increase peak capacity by providing economical cooling of the combustion turbine inlet air. The particular systems that are considered in this paper are high-temperature diurnal TES, and TES for cooling the combustion turbine inlet air. The paper provides a complete assessment of the design, engineering, and economic benefits of combining TES technology with new or existing cogeneration systems, while also addressing some of the issues involved.

Introduction

Cogeneration is playing an increasingly important role in providing an independent and on-site high-efficiency source of power generation and thermal energy for space heating and cooling, as well as industrial process heat applications. However, the range of applications of cogeneration technology could be further extended if the generation of electricity could be decoupled from the generation of thermal energy for process use or space conditioning. The technology of thermal energy storage (TES) provides just such a decoupling that allows for the production of dispatchable power while fully utilizing the thermal energy available from the prime mover of the cogeneration system. The thermal energy from the prime mover exhaust can be stored either as sensible heat or as latent heat and used during peak demand periods to produce electric power or process steam/hot water. However, the additional materials and equipment necessary for a TES system will add to the capital as well as to the maintenance costs. Therefore, the economic benefits of adding TES to a conventional cogeneration system would have to outweigh the increased costs of the combined system.

The Pacific Northwest Laboratory (PNL)[1] leads the U.S. Department of Energy's Thermal Energy Storage Program. The program focuses on developing TES for daily cycling (diurnal storage), annual cycling (seasonal storage), and utility-scale applications [utility thermal energy storage (UTES)]. Several of these technologies can be used in a new or an existing cogeneration facility to increase its efficiency further and promote the use of the technology within the utility and the industrial sectors.

This paper will address some of the TES systems that are readily applicable to be combined with cogeneration systems, as well as provide an update on the current status of these TES systems. TES allows a cogeneration facility to (1) provide dispatchable electric power while providing a constant thermal load, and (2) increase peak capacity by providing economical cooling of the combustion turbine inlet air. The particular systems that will be addressed are high-temperature diurnal TES, and TES for cooling the combustion turbine inlet air. Several of the engineering and economic feasibility studies involving the integration of the technologies are in various stages of completion at PNL.

Issues. A number of emerging issues may limit the number of useful applications of the cogeneration technology. Some of these include:

- Mismatch between the demand for electricity and thermal energy on a daily basis: Increasingly, utilities are requiring cogenerators to provide dispatchable power while most industrial thermal loads are relatively constant during the day. A high-temperature diurnal TES system can decouple the generation of electricity from the production of thermal energy, allowing the cogeneration facility to supply dispatchable power during the peak periods of the day.
- Mismatch between the demand for electricity and thermal energy on a seasonal basis: In many cases, the demand for electric power peaks during the hot summer months because of the air-conditioning loads, while the demand for thermal energy is either constant or peaks during the cold winter months because of the space heating loads. A seasonal TES system enables a facility to produce electricity to meet the summer peak demands while storing the thermal energy output for use during the winter season.
- Ambient temperature effects on combustion turbine capacity: Being a constant-volume machine, the capacity of a combustion turbine prime mover can be significantly reduced during periods of high ambient temperature. In many regions of the country, periods of high ambient temperature also coincide with the peak demand periods for electric power. A suitable TES system can reduce capacity losses by allowing economic cooling of combustion turbine inlet air.

It is clear, therefore, that TES can be combined with a wide range of cogeneration system applications. The rest of the paper will provide a more complete assessment of the design, engineering, and economic benefits of combining the TES technology with new or existing cogeneration systems and adequately address some of the issues discussed above.

Diurnal TES For Heat Storage Applications

A number of emerging issues may limit the number of useful applications of cogeneration. One of these is a mismatch between the demand for electricity and thermal energy on a daily basis. Increasingly, utilities are requiring cogenerators to pro-

[1] Operated for the U.S. Department of Energy by Battelle Memorial Institute under Contract DE-AC06-76RLO 1830.

Contributed by the International Gas Turbine Institute and presented at the International Cogen-Turbo Power Congress and Exhibition, Bournemouth, United Kingdom, September 21–23, 1993. Manuscript received at ASME Headquarters March 3, 1994. Associate Technical Editor: H. Lukas.

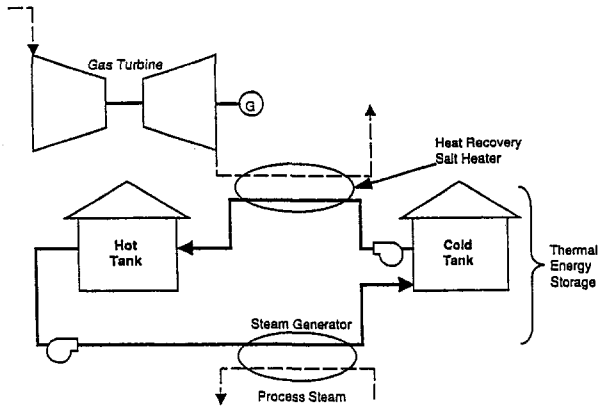

Fig. 1 Integrating TES in a natural-gas-fired cogeneration facility

vide dispatchable power, while most industrial thermal loads are relatively constant during the day. Diurnal TES can decouple the generation of electricity from the production of thermal energy, allowing a cogeneration facility to supply dispatchable power. Diurnal TES stores thermal energy recovered from the exhaust of the prime mover (gas turbine) to meet daily variations in the demand for electric power and thermal loads.

Concept. The concept for integrating TES in a natural-gas-fired cogeneration facility is shown in Fig. 1. The facility consists of (1) a gas turbine prime mover, (2) a heat recovery salt heater, (3) a thermal energy storage system, and (4) a salt-heated steam generator. The gas turbine is operated during peak demand time periods and the exhaust heat is used to heat molten salt in a heat recovery salt heater. Cold salt [288°C (550°F)] is pumped from the cold salt tank, through the heat recovery salt heater, where it is heated to between 510°C (950°F) and 538°C (1000°F) before being pumped to the hot salt storage tank. Hot salt is continuously removed from the hot salt tank and used as a heat source to meet the constant thermal load. A cogeneration plant with a TES system sized for an 8-h peak demand period would provide a 30 MWe peaking capacity compared to a similar conventional cogeneration facility that would provide a 10 MWe base load.

TES System Description

Depending on the characteristics of the thermal load, a variety of thermal storage systems can be used. Options for thermal storage include:

- Molten Nitrate Salt TES: Molten salt is an excellent thermal energy storage medium for high-temperature TES applications. Current molten salt TES concepts use a mixture of sodium nitrate (60 wt%) and potassium nitrate (40 wt%) that can operate at temperatures up to 566°C (1050°F). However, the mixture freezes at 240°C (464°F). To help prevent freezing, molten salt systems are usually operated at temperatures above approximately 288°C (550°F). The minimum operating temperature limits the amount of waste heat that can be recovered from a combustion turbine's exhaust because the exhaust can only be cooled to approximately 315°C (600°F). Typically molten salt TES uses separate hot and cold salt tanks. A more complete discussion of molten salt TES is presented by Drost et al. (1989).
- Oil/Rock TES: Oil/rock TES is an attractive alternative for lower temperature applications. Low-cost heat transfer oils such as Caloria HT-43[2] can operate at temperatures up to 304°C (580°F). The TES system consists of a single large tank that is filled with a mixture of oil and a low-cost filler, such as river rock. The tank is operated to maintain hot oil at the top of the tank and cold oil at the bottom of the tank. This arrangement stratifies the fluid in the tank, resulting in minimal mixing between the hot and cold regions of the tank. During normal operation, cold oil is removed from the bottom of the tank, heated in the heat recovery oil heater, and returned to the top of the storage tank. Thermal energy is stored in the mixture of oil and rock. Oil/rock TES is less expensive than molten salt TES, but it is limited to low-temperature applications. Oil/rock TES is described in more detail by Drost et al. (1990).
- Combined Molten Salt and Oil/Rock TES: The advantages of both storage concepts can be retained by using a combination of molten salt TES for high-temperature (>288°C) and an oil/rock TES for lower temperature (<288°C) thermal energy storage. This allows the combustion turbine exhaust to be cooled to near ambient conditions.
- Hitec[3] Salt TES: Hitec salt is another molten salt that operates between 454°C (850°F) and 177°C (350°F). It is a mixture of sodium nitrate (7 wt%), potassium nitrate (53 wt%), and sodium nitrite (40 wt%). Hitec salt would allow greater heat recovery from turbine exhaust than molten salt, but would not be as applicable as the molten salt at higher temperatures (as in combined-cycle power production applications). In addition, the Hitec salt is a little more expensive than the molten salt.

Selection of the storage concept will depend on characteristics of the thermal load. If high-temperature thermal energy is required to meet the thermal load, a choice of the molten salt TES, Hitec salt TES, or a combined molten salt and oil/rock TES can be used. Alternatively, if the thermal load uses thermal energy at a temperature below 288°C (550°F), oil/rock TES may be the preferred option.

Benefits. The use of high-temperature TES in cogeneration applications has the following benefits:

- High-temperature TES will allow a natural-gas-fired cogeneration facility to produce dispatchable power while meeting constant thermal loads.
- High-temperature TES integrated in a natural-gas-fired cogeneration facility allows all power generation to occur during periods of peak demand; the installed capacity of the prime mover will be substantially larger than for a conventional cogeneration facility. A cogeneration plant with a TES system sized for an 8-h peak demand period would provide 30 MWe of peaking capacity compared to a similar conventional cogeneration facility that would provide 10 MWe of base-load capacity.
- All natural gas is used to fire the combustion turbine (compared to direct natural gas firing of the waste heat steam generator). This results in high-efficiency operation by ensuring that all natural gas is used to produce both electric power and thermal energy.

Technical Status. Molten nitrate salt TES has been extensively investigated for solar thermal power generation applications. Investigations have included bench-scale testing, detailed design studies, and field demonstrations. Based on the results of these investigations, the Department of Energy and a group of electric utilities are sufficiently confident of the technical feasibility of the concept to embark on the $40 million Solar II demonstration of molten salt central receiver technology. This suggests that molten nitrate salt TES is technically ready for a large-scale cogeneration demonstration. The technical status of

[2] Trademark of the Exxon Corporation, Houston, TX.

[3] Trademark of the DuPont Corporation, Wilmington, DE.

molten salt TES is discussed in more detail by Drost et al. (1989). Oil/rock storage has been successfully demonstrated for solar thermal applications and is commercially available. Hitec salt has been used in several industries.

Alternative salts that can operate between 566°C (1050°F) and 121°C (250°F) have been identified, but additional research is necessary before large-scale demonstration is justified. Successful development of a TES system using alternative salts could avoid the need for a combined molten salt and oil/rock TES system to cover the entire temperature range.

Plant Concept Details

The conceptual design of a cogeneration plant with TES was developed in sufficient detail to determine a meaningful cost estimate. The relevant features of a conventional cogeneration plant are discussed first, followed by a discussion of the selected arrangements of the cogeneration plant with TES. The essential features of the oil/salt heater design is followed by a discussion of the oil/salt storage system design and the steam generator design.

Conventional Cogeneration Plant. One of the primary goals of this study was to develop concept arrangements that minimize the impact of including TES on the design and the layout of the cogeneration plant. Therefore, there is substantial similarity between the conventional cogeneration plant and the cogeneration/TES design. The conventional cogeneration plant consists of a prime mover (a gas turbine, in this case) that is fired by a natural gas combustor. In addition to producing power through the generator, the turbine exhaust at 531°C (988°F) is used in a heat recovery steam generator (HRSG) to produce process steam loads. The net efficiency of the gas turbine is assumed to be 31 percent (a heat rate of 11,000 Btu/kWh) for larger gas turbines ($\geq$180 MWe rating) and 29.6 percent (a heat rate of 11,500 Btu/kWh) for smaller turbines ($<$180 MWe rating).

Cogeneration Plant with TES for Peaking. An oil/rock or salt TES system interposed between the gas turbine and the steam generator in a conventional cogeneration plant can provide a cycling capability. Instead of generating steam directly, the heat from the gas turbine exhaust is used to heat the oil or molten salt, which is then stored. The gas turbine is operated whenever peaking power capacity is needed by the utilities. The TES serves to decouple the steam generator and the turbine from the rest of the plant, allowing process steam production to continue for the entire day. The oil/rock storage system has been developed extensively for solar thermal power generation, while the molten nitrate salt system has been discussed in an earlier study (Drost et al., 1989). In the case of the heat recovery salt heater, it may be possible to use direct heat exchange between the exhaust gas and the salt. If feasible, direct-contact heat exchange would dramatically decrease the cost of the heat recovery salt heater and would improve performance. There was no attempt made to optimize the sizes of the components of the different systems evaluated in the study. Hence, more advantageous versions of each TES/cogeneration system or other system configurations including combined-cycle systems with molten salt storage could have been designed and analyzed.

Oil/Salt Heater Design. The turbine exhaust oil (or molten salt) heater replaces the HRSG in the conventional cogeneration plant. The overall convective heat transfer coefficient was assumed to be 150 $W/m^2 \cdot °C$ (26.6 $Btu/h \cdot ft^2 \cdot °F$) for all the heater designs because the dominant resistance to heat transfer is on the gas side. However, the clean turbine exhaust (from combusting natural gas) permits extensive use of fins to improve heat transfer on the gas side. The log mean temperature difference was calculated to be about 111°C (200°F), 17°C (31°F), and 48°C (87°F) for the oil heater, molten salt heater, and the Hitec salt heater, respectively.

Oil/Salt Storage System Design. The oil storage system consists of a heat transfer oil and river rock storage medium. The oil and rock are contained in one or more carbon steel tanks, depending on the size of the TES system. The tank or tanks are insulated to reduce heat loss, and appropriate foundations and miscellaneous equipment are included. A substantial fraction of the tank volume is filled with the inexpensive rock; the remaining volume is filled with the more costly oil. The oil, which is about a quarter of the storage volume, stores about 20 percent of the thermal energy as sensible heat, while the rest of it is stored in the rock. Hot oil is added or removed from the top of the tank, while cool oil is added or removed from the bottom of the tank. This arrangement maintains a density-driven segregation (thermocline) between the hot oil in the top of the tank and the cool, denser oil in the bottom of the tank. The thermal storage capacity of the tank is determined by the temperature range achievable in the heat transfer medium (oil, in this case). The typical range has been from 288°C (550°F) at the high end to about 121°C (250°F) at the low end. This would give rise to a ΔT of 300°F unless pinch-point considerations in the steam generator dictated a higher exit temperature for the oil, which would typically increase the size of the storage system.

The salt storage system could also use a single storage tank (with a thermocline) or separate hot and cold molten salt tanks. Recent studies suggest that the cost savings associated with a thermocline system are small because the cost of the cold tank in the two-tank system is a small fraction of the total cost. In addition, it may be difficult to maintain the thermocline because of the radiation heat transfer between the hot and cold regions of the tank. The design temperatures were assumed to range from 288°C (550°F) to 510°C (950°F), and 177°C (350°F) to 454°C (850°F) for the molten salt and the Hitec salt systems, respectively.

Steam Generator Design. The steam generator is used to supply the constant 24-hr steam load from the hot oil or salt. The steam generator system consists of two separate heat exchangers: (1) a preheater where the temperature of the feedwater is raised to the saturation temperature, and (2) an evaporator where saturated steam is generated. The heat exchangers are of single-pass tubular design with water/steam contained in the tubes. A single-pass design was selected because of the desire to have counterflow heat exchange in the preheater, whereas the evaporator uses a parallel-flow arrangement.

There are certain issues that are as yet unresolved with respect to the molten salt applications in heat recovery steam generators. These include hydride buildup due to tube wall hydrogen migration, tube sheet thermal gradient limits, and materials longevity. Liquid sodium systems have resolved these issues; however, liquid sodium is not as good for storage.

Results

The results of the evaluation of thermal energy storage (TES) systems integrated with simple gas turbine cogeneration systems are described below. The TES system captures and stores thermal energy from the gas turbine exhaust for immediate or future generation of process heat. Integrating thermal energy storage with conventional cogeneration equipment increases the initial cost of the combined system, but offers the following two significant advantages by decoupling electric power and process heat production: (1) Electric power can be generated on demand, irrespective of the process heat load profile, thus increasing the value of the power produced. (2) Although supplementary firing could be employed to serve independently varying electric and process heat loads, this approach is inefficient com-

Table 1 Break-even electric rates for boiler steam costs (levelized)

Steam pressures	690 kPa (100 psi)	3448 kPa (500 psi)
Levelized cost of steam from conventional boiler	$9.03/klb	$9.13klb
System configuration	Breakeven electric rates (cents per kwh)	
Conventional cogeneration (base-load power)	3.5	3.8
Cogeneration with TES (12-hr peak power)		
Oil-rock	4.5	5.4
Molten salt	7.9	7.9
Hitec salt	5.9	6.0
Cogeneration with TES (8-hr peak power)		
Oil-rock	5.0	6.0
Molten salt	9.5	9.6
Hitec salt	7.0	7.1
Simple gas turbine	7.5 to 8.0	7.5 to 8.0

pared to integrating TES with cogeneration, which can serve the two independent loads while firing all fuel in the gas turbine.

The results of the engineering and economic analyses for two different steam pressures and for the different system configurations considered in this study are given in Tables 1 and 2. The break-even electric rates at which the levelized steam cost is the same as that of the conventional boiler is given in Table 1. The breakeven rate for the conventional cogeneration system is 3.5¢/kWh, while that for the combined system varies depending on the storage medium for the TES system. There is

Table 2 Cost breakdown for the different system configurations and steam loads (millions of dollars)

Steam Conditions	Generating hrs/per day	System Configuration	Capital Cost	Fuel Cost	O&M Cost	Electric Revenue[a]
690 kPa (164°C)	24	Conventional boiler	22.9	12.3	2.3	--
100 psi (328°F)	24	Conventional cogeneration	42.9	22.8	5.8	23.9
		Cogeneration with TES				
	12	Oil/rock	91.7	24.0	6.5	33.7
	12	Molten salt	255.1	34.0	19.2	83.9
	12	Hitec salt	150.5	24.0	10.4	44.3
	8	Oil/rock	123.0	24.0	6.6	37.5
	8	Molten salt	355.9	34.0	24.7	101.0
	8	Hitec salt	205.3	24.0	12.2	52.5
3448 kPa (242°C)	24	Conventional boiler	23.7	12.4	2.4	--
500 psi (467°F)	24	Conventional cogeneration	44.9	23.2	6.0	26.2
		Cogeneration with TES				
	12	Oil/rock	124.4	29.4	8.4	49.1
	12	Molten salt	259.3	34.6	19.5	85.4
	12	Hitec salt	152.7	24.4	10.5	45.2
	8	Oil/rock	166.6	29.4	8.9	54.4
	8	Molten salt	361.1	34.6	25.0	103.0
	8	Hitec salt	208.5	24.4	12.4	53.5

[a]Electric revenue required to provide 690 kPa steam at $9.03/klb or 3448 kPa steam at $9.13/klb

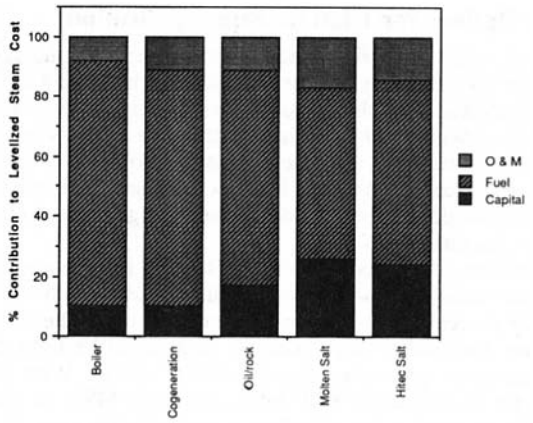

Fig. 2 Cost of producing steam by different system configurations

very little variation of the rate between the two steam pressure conditions assumed. The corresponding rate for a gas turbine plant is given for comparison. It can be seen that the oil/rock TES system can provide on-peak power at a cost of 4.5 to 6.0¢/kWh, which is less expensive than the simple gas turbine case. The Hitec and molten salt cases are less attractive for these two steam pressure conditions. The Hitec salt can provide peak power at a slightly less expensive rate than the molten salt, primarily because of the wider temperature range of the storage system. Alternative system configurations such as combined-cycle systems and higher temperature storage conditions may prove more attractive for systems with molten salt as the storage media. In general, lower temperature storage reduces the size and cost of the storage media heater, while higher temperature storage reduces the size and cost of the media-heated steam generator. Poor heat transfer in the gas turbine exhaust heater (on the gas side) puts a premium on the lower approach temperatures required of high-temperature storage systems. Thus, the oil-rock system has a heat exchanger sizing and cost advantage over the two salt systems. The oil-rock system is also the least expensive (on a $/MWht basis) when each storage system is allowed to cycle through its maximum temperature range. Pinch-point design restrictions in the steam generator reduce, but do not eliminate the advantage of oil-rock storage at 3448 kPa (500 psi) steam pressure compared to the 690 kPa (100 psi) case. It should also be noted that the systems evaluated have not be optimized; more advantageous versions of each TES/cogeneration system could be identified by considering other combinations of storage media temperature range and heat exchanger approach temperatures. Varying these design factors trades off heat exchanger and storage system costs. Also, future research and development efforts focused on the salt storage media may further reduce the costs of such storage media and make them more attractive for wider range of temperature conditions.

The cost breakdown, as well as the required total revenue from the sale of electricity (corresponding to the break-even electric rates) for the different system configurations, is given in Table 2. The combination of TES with a base cogeneration system does add to the capital equipment costs and the total O&M costs, but the increase in the electric power revenue (resulting from sales during intermediate and peak periods of the day at higher rates compared to the sale of base-load power) may offset the increased costs. It can also be seen (Fig. 2) that the predominant portion of the total cost of producing steam by the different system configurations is associated with fuel, which, in turn, essentially dictates the overall economic feasibility of the system. The combined system is assumed to operate 12 hours a day (peak period) to maximize the value of the electric power.

TES Options for Chill Storage Applications

Most utilities in the United States experience the greatest demand for electricity during periods of high ambient temperature. Unfortunately, the performance of many power plants decreases with increasing ambient temperature. This is especially true of gas turbines that use a constant volume of incoming ambient air as the working fluid. As ambient temperature increases, the density of the inlet air and the generating capacity of the gas turbine decreases.

A review of data on existing gas turbine installations shows that the summer capacity of a typical gas turbine is between 15 and 25 percent lower than the winter capacity of the same gas turbine. Nationally, this represents an 8000 MWe reduction in summer peak generating capacity (DOE 1991). With projections for an additional 5000 MWe to 10,000 MWe of new gas turbine capacity to be added each year for the next 10 years (Anon., 1990), the corresponding deficit in gas turbine summer generating capacity could be as large as 20,000 MWe.

Diurnal Ice Storage System. Traditionally, evaporative cooling has been used to cool the gas turbine inlet air. Water is evaporated by the air entering the compressor, lowering the air temperature. However, evaporative cooling can only reduce the temperature of the inlet air to the wet bulb temperature. Actual cooling will be determined by the wet bulb and dry bulb temperatures of the incoming air and the efficiency of the evaporative cooler. As an example, evaporative coolers will reduce the temperature of inlet air at 37.8°C (100°F) and a relative humidity of 45 percent to between 23.8°C and 26.6°C (75°F and 80°F). Further reductions in inlet air temperature will require additional cooling (Ondryas, 1991).

Absorption cycle chillers, driven by the thermal energy in the exhaust of the gas turbine and electrically driven mechanical chillers, have been considered for gas turbine inlet air cooling but both approaches have significant shortcomings (Ondryas, 1991). The most successful approach to providing gas turbine inlet cooling uses off-peak electric power to drive a vapor compression cycle ice maker, producing ice that is then stored. During the next peak in electricity demand, the stored ice is used to cool the gas turbine inlet air to approximately 4.4°C (40°F). A diurnal ice thermal energy storage (TES) system has been installed at Lincoln Electric System's Rokeby Station and has increased the summer peaking capacity of a gas turbine from 53MWe to 64 MWe. The capital cost to increase the capacity of the gas turbine was approximately $165/kWe (Anon., 1992).

Aquifer Thermal Energy Storage System. While the diurnal ice TES system installed at the Rokeby Station is very attractive, other thermal energy storage options may also be of interest. Seasonal thermal energy storage (STES) technology includes a number of techniques that can efficiently and economically store thermal energy for long periods of time. Current research suggests that aquifer thermal energy storage (ATES) is the most economical concept and is nearest to commercialization. Therefore, this study focuses on evaluating ATES as a representative STES system; however, other systems are available and may be attractive for specific applications. An ATES system can collect and store winter chill, available during cold winter months, for gas turbine inlet air cooling when required.

Aquifer thermal energy storage is a technology that allows relatively low-grade thermal energy to be stored and retrieved for future use on either a seasonal or diurnal basis. Water pumped from a set of supply wells is either heated or cooled and then injected into a set of storage wells. Later, the storage wells are pumped and the warm or cool water can be used to meet a thermal load (see Fig. 3). The principal advantages of ATES are the use of an existing aquifer formation as both the media and physical containment component of the storage system, the use of water as the heat transfer medium, and the concept's ability to store energy on either a seasonal or diurnal basis. The concept is limited, however, to locations where the energy source, energy application, and a suitable aquifer are in close proximity to each other.

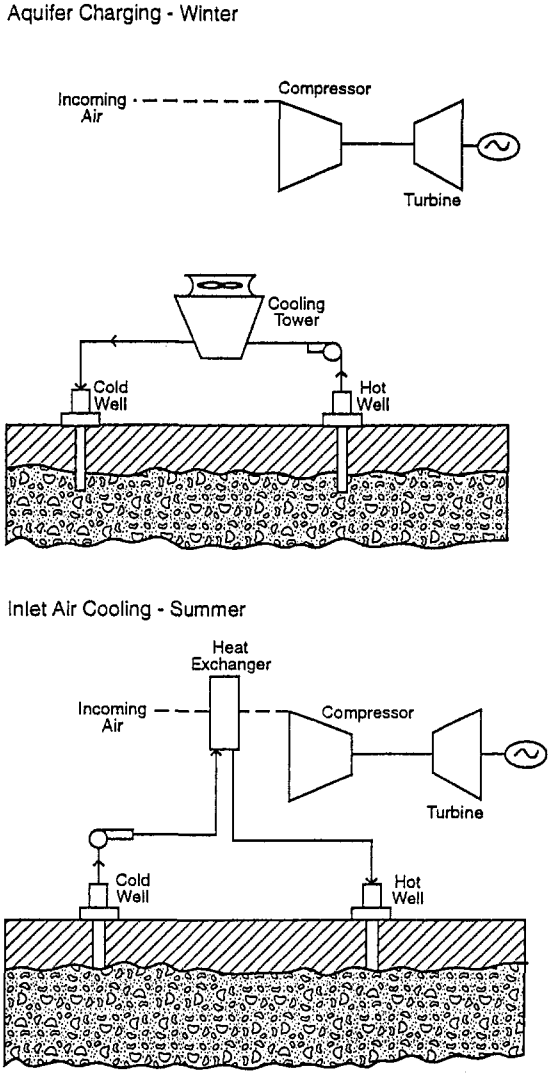

Fig. 3 Gas turbine inlet air cooling using aquifer thermal energy storage

For gas turbine inlet air cooling applications, water withdrawn from supply wells is chilled by cold winter air in a conventional cooling tower prior to injection into storage wells. The chilled water is stored until periods with high ambient temperature occur, when chilled water is withdrawn from the aquifer and used in a heat exchanger to cool the gas turbine inlet air. The heated water is then returned to the aquifer and stored until the next winter, when it is again cooled using winter chill. ATES eliminates the need to use off-peak electric power for charging storage, and reduces the cost of charging storage while minimizing fuel consumption and environmental impacts associated with the generation of off-peak electric power.

The objective of this study was to compare the performance and economics of seasonal thermal energy storage in aquifers (aquifer thermal energy storage) with diurnal ice thermal energy storage for gas turbine inlet air cooling. The investigation consisted of developing computer codes to model the performance of a gas turbine, energy storage system, heat exchangers, and ancillary equipment. The performance models were combined with cost models to calculate unit capital costs and levelized energy costs for each concept. The levelized energy cost was calculated for three technologies (an oversized gas turbine, a

diurnal ice thermal energy storage system, and an aquifer seasonal thermal energy storage system) operating at two annual capacity factors (0.05 and 0.2) in two locations (Minneapolis, Minnesota, and Birmingham, Alabama). System designs were based on precooling the inlet air from the summer design temperature (37.8°C or 100°F at both locations) to 4.4°C (40°F) with ice storage, 7.2°C (45°F) with ATES in Minneapolis, and 11.1°C (52°F) with ATES in Birmingham. These temperatures were selected based on previous experience (Ebeling et al., 1992; Spurr, 1986; Midkiff and Brett, 1991). As a result, each of the inlet air precooling systems results in a different amount of incremental power relative to operating without precooling. The size of the larger gas turbines was arbitrarily set to provide the same incremental generating capacity at the summer design temperature (37.8°C or 100°F) as the two ATES precooled systems.

Precooling gas turbine inlet air with cold water supplied by an aquifer thermal energy storage system provided lower cost electricity than simply increasing the size of the turbine for meteorological and geological conditions existing in the Minneapolis vicinity. A 15 to 20 percent cost reduction resulted for both 0.05 and 0.2 annual operating factors. In contrast, ice storage precooling was found to be between 5 and 20 percent more expensive than larger gas turbines for the Minneapolis location.

In Birmingham, aquifer thermal energy storage precooling was preferred at the higher capacity factor and ice storage precooling was the best option at the lower capacity factor. In both cases, the levelized cost was reduced by approximately 5 percent when compared to larger gas turbines.

These preliminary results indicate that aquifer thermal energy storage systems should be given serious consideration as an option for increasing peak generating capacity with combustion turbines. Like all aquifer thermal energy storage applications, the concept's cost effectiveness will vary significantly with site-specific geological conditions.

Conclusions

Thermal energy storage can help cogeneration meet the challenges of the 1990s by increasing the flexibility and performance of cogeneration facilities. Thermal energy storage also allows a cogeneration facility to provide dispatchable electric power while providing a constant thermal load. The results for the assumed steam load show that the conventional cogeneration system and the cogeneration plant combined with the oil/rock TES system do have lower levelized costs of producing steam compared to the conventional boiler plant operation as long as the selling price of electricity remains above $0.06/kWh. The break-even price for the sale of electricity (at which the steam costs are the same for the three plant options) is in the range of $0.045 to 0.06/kWh for the cogeneration system using oil/rock TES. This represents a 25 percent to 40 percent reduction in the cost of peak power when compared to $0.08/kWh for a gas turbine plant; and a 14 percent to 35 percent reduction compared to a peak power cost of approximately $0.07/kWh for a combined cycle plant.

The oil/rock storage system for TES remains the most attractive option for the assumed thermal load quality. A higher quality of the assumed thermal load (e.g., at higher pressures and temperatures) will favor the molten salt TES system because of the higher temperature range that is achievable in such a system. The economies of scale with respect to the costs of the gas turbine, the oil/salt heater, oil/rock or salt storage system, and the heat recovery steam generator, as well as magnitude of energy loss from the storage system, also favor the larger-sized system components. Further cost reductions may result from optimization of individual components in the combined plant configurations and research and development induced TES system improvements.

With regard to precooling the gas turbine inlet air with cold water supplied by an ATES system, the preliminary results indicate that ATES and ice storage precooling systems should be considered as options for increasing peak generating capacity of combustion turbines. The preferred system will depend on site-specific conditions and operating requirements. Like all ATES applications, its cost effectiveness will vary significantly with site-specific geologic conditions. Generally, ice storage systems will look most attractive in low capacity factor applications, while ATES systems will look best at higher capacity factors.

Further experience with ATES and ice storage precooling systems will be needed to reduce the cost uncertainty associated with these systems and allow more conclusive comparative assessments. In addition, other inlet air precooling options should be considered, such as surface-engineered seasonal chill storage systems using ice or artificial snow.

References

Anon., 1990, "Can Manufacturing Capacity Keep Up With New Orders for CTs," *Power Engineering*, Vol. 94, p. 45.

Anon., 1992, "Ice Maker Adds Low-Cost Kilowatts to Peaking Unit," *Power*, Vol. 136, No 1. McGraw-Hill, New York.

Drost, M. K., Antoniak, Z. I., Brown, D. R., and Sathyanarayana, K., 1989, "Thermal Energy Storage for Power Generation," PNL-7107, Pacific Northwest Laboratory, Richland, WA.

Drost, M. K., Antoniak, Z. I., Brown, D. R., and Somasundaram, S., 1990, "Thermal Energy Storage for Integrated Gasification Combined-Cycle Power Plants," PNL-7403, Pacific Northwest Laboratory, Richland, WA.

Ebeling, J. A., Halil, R., Bantam, D., Bakenhus, B., Schreiber, H., and Wendlend, R., 1992, "Peak Gas Turbine Capacity Enhancement Using Ice Storage for Compressor Inlet Air Cooling," ASME Paper No. 92-GT-265.

Midkiff, K. C., and Brett, C. E., 1991, "1990 Annual Report, Monitoring of Aquifer Chill Energy System," University of Alabama, Tuscaloosa, AL.

Ondryas, I. S., 1991, "Go Beyond Evaporative Coolers to Stretch Gas Turbine Output," *Power*, Vol. 135, No. 7, McGraw-Hill, New York.

Smith, S. S., Undated, "GE Aeroderived Gas Turbine Performance," GER-3572B, General Electric Company, Schenectady, NY.

Spurr, M., 1986, "Aquifer Thermal Energy Storage District Cooling in Downtown St. Paul," DE-FG01-85CE26520, District Heating Development Company, St. Paul, MN.

U.S. Department of Energy, 1991, "Inventory of Power Plants in the United States 1990," DOE/EIA-0095(90), United States Department of Energy, Washington, DC.

Emission and Performance of a Lean-Premixed Gas Fuel Injection System for Aeroderivative Gas Turbine Engines

T. S. Snyder

T. J. Rosfjord

J. B. McVey

United Technologies Research Center,
East Hartford, CT 06108

A. S. Hu

B. C. Schlein

Pratt & Whitney,
Division of UTC,
East Hartford, CT 06108

A dry-low-NO_x, high-airflow-capacity fuel injection system for a lean-premixed combustor has been developed for a moderate pressure ratio (20:1) aeroderivative gas turbine engine. Engine requirements for combustor pressure drop, emissions, and operability have been met. Combustion performance was evaluated at high power conditions in a high-pressure, single-nozzle test facility, which operates at full baseload conditions. Single digit NO_x levels and high combustion efficiency were achieved. A wide operability range with no signs of flashback, autoignition, or thermal problems was demonstrated. NO_x sensitivities to pressure and residence time were found to be small at flame temperatures below 1850 K (2870°F). Above 1850 K some NO_x sensitivity to pressure and residence time was observed and was associated with the increased role of the thermal NO_x production mechanism at elevated flame temperatures.

Introduction

The achievement of low-NO_x emissions is essential to the viability of any gas turbine to be used in large-scale industrial applications such as electrical power generation. Governmental regulations and increasing environmental awareness can be expected to continue to drive acceptable emission levels downward. For these reasons, most turbine manufacturers have undertaken efforts (Solt and Tuzson, 1993) to develop combustion systems having the potential for achieving the lowest possible NO_x levels while not significantly increasing the cost of the combustion system. Although the injection of water or steam and catalytic exhaust gas treatment are two NO_x control strategies that have been put into use, the cost associated with these systems is significant. An industry goal is to develop approaches not requiring such treatment. Two approaches that have received high levels of development attention to attain this goal are the rich-quench, lean-burn (RQL) and lean-premixed NO_x control strategies.

The RQL low-NO_x control strategy, in which first fuel-rich then fuel-lean combustion is employed, has excellent operability and is the subject of ongoing development efforts (Rizk and Mongia, 1991). Although this approach does not have the possible flashback/autoignition problem of premixed systems for very high inlet temperature applications, the NO_x control potential is limited by the ability of the quench process to dilute the fuel-rich mixture rapidly and uniformly. Improper execution of the quench process will result in the generation of local high temperatures and thus thermal NO_x production. Efforts therefore continue to be focused on premixing systems.

Adoption of the lean-premixed approach for natural-gas-fired aeroderivative engines, which have relatively small combustor volumes available to perform both the fuel–air premixing task and the post-flame zone CO oxidation task, are expected to produce less than 25 ppm NO_x (@ 15 percent O_2) (Leonard and Stegmaier, 1994). Large, low-pressure heavy machines are expected to approach "single-digit" NO_x levels (Aigner and Muller, 1993; Becker et al., 1986). These levels are significantly lower than those envisioned only a few years ago (Angello and Lowe, 1989).

Prior combustion studies were conducted by United Technologies to investigate lean-premixed and direct injection dry-low-NO_x concepts applicable to moderate-pressure-ratio aeroderivative engines (McVey et al., 1993). Results indicated that although the lean direct injection approach had excellent operability characteristics, the NO_x control potential was inferior to that for the lean-premixed system. Several lean premixed concepts were evaluated for the ability to control NO_x while maintaining adequate stability. Two of the lean-premixing concepts, the aero-vane injector and the perforated plate injector, achieved excellent NO_x control; however, a large number of injection sites was required. (The aero-vane injector incorporated hundreds of fuel injection orifices; the perforated plate injector consisted of premixing tubes each with several injection sites.) Subsequent to that reported work, a premixing concept, featuring design simplicity, and fewer injection sites produced even lower NO_x levels and exhibited excellent stability margin. The swirl-stabilized combustion zone produced by this device featured a large recirculation region. As reported for the aero-vane device, the large recirculation zone produced in swirl stabilized combustion systems does not produce adverse effects on NO_x, even when long residence times exist. Other studies (Nicol et al., 1995) have since theoretically confirmed that thermally generated NO_x, which is residence time dependent, is only a small contributor to NO_x emissions in a properly designed premixing combustion system for moderate pressure ratio engines. This simplified-design concept, hereafter referred to as the tangential entry (TE) concept, is the subject of this paper.

One of the challenges to the development of a practical lean premixed system is to assure that sufficient flame stability margin and robust operation is achieved at high power (baseload operation) while maintaining excellent NO_x control. Robust operation at baseload implies the absence of flashback/autoigni-

Contributed by the International Gas Turbine Institute and presented at the 39th International Gas Turbine and Aeroengine Congress and Exposition, The Hague, The Netherlands, June 13–16, 1994. Manuscript received by the International Gas Turbine Institute February 18, 1994. Paper No. 94-GT-234. Associate Technical Editor: E. M. Greitzer.

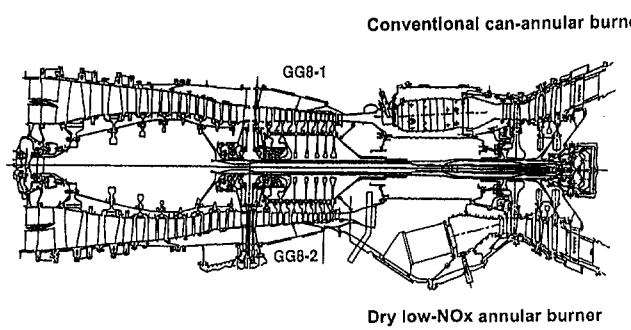

Fig. 1 Large flow capacity dry low NO_x TE nozzle combustion system incorporated in FT8 engine

tion and thermal distress as the airflow and fuel flow are deviated from normal operating conditions. The premixing system must also demonstrate the ability to maintain high combustion efficiencies over the entire engine operating envelope.

This paper summarizes efforts undertaken to develop the TE concept for application in the United Technologies Turbo Power FT8 engine. A diagram showing how the concept is implemented in the engine is shown in Fig. 1. When contrasted with the conventional burner (shown above the centerline in the figure), the most notable design impact is the bulging of the diffuser case and the canting of the burner. This flow path change provides sufficient flow area for the diffuser discharge air to pass between the fuel feed lines and injector support struts and reach the fuel injector inlet air slots located on the outboard section of the nozzle. For engine design simplicity, the number of fuel injectors is minimized. The initial engine design called for 18 nozzles to be circumferentially distributed about an annular burner. Each nozzle was required to pass a high level of airflow with an acceptable airside pressure drop level. The nozzle designed and evaluated to meet this flow requirement was designated the TE92 nozzle. As the engine design progressed, further pressures to reduce the number of nozzles and the individual nozzle pressure drop resulted in a decrease in the number from 18 to 16. This even more aggressive nozzle design was designated as TE93C in this paper.

Approach

The combustor development effort is planned as a three-phase effort: (1) single-nozzle tests to develop the fuel premixing system; (2) sector tests to develop the combustor cooling scheme and piloting system required for low-power operation; (3) engine tests to develop control strategies and document engine emission performance. This paper describes that portion of the first phase that dealt with the experimental evaluation of the behavior of the TE nozzle under combusting flow conditions. The following three sections describe the TE nozzle, test apparatus, and the test conditions.

Tangential Entry Nozzle. The terminology "tangential entry" was adopted to reflect the air scroll orientation that imparts the maximum tangential momentum to the air as it enters the combustion chamber. The high-flow capacity TE nozzle consists of two main components: a scroll swirler and a conical centerbody, Fig. 2. Two cylindrical arc scrolls with radius R, are offset a distance S from the plane of symmetry (Fig. 2(b)), and mounted between two baseplates (Fig. 2(a)). The dimensions shown are for the 18-nozzle engine design (TE92). The inner edges of the scrolls are diametrically opposed to one another and tangent to a circle having a diameter D. The burner airflow enters the swirler through the two rectangular inlet slots, with length L, formed by the scroll offset, and exits through a circular hole (of a diameter equal to that of the tangent circle). Main gas fuel is supplied to two manifolds and injected into the inlet air from an array of orifices located on the outer scroll surface opposite the trailing edge of the opposing scroll. The orifice array specifications are detailed below. The conical centerbody, which could allow for the incorporation of liquid fuel hardware, has a base diameter equal to the swirler exit diameter and is tapered at an angle that places its apex at the end of the inlet slot.

The geometry as described above formed the framework for the TE nozzle baseline design. During development, modifications were made to accommodate:

1 Piloting: low-emission operation over the entire power range required some form of staging.
2 Airflow capacity: a reduction in air pressure loss, lower than the pressure loss achieved by the original concept demonstration, was necessary to improve engine heat rate and overall cycle efficiencies.
3 Fuel–air premixing: higher levels of the fuel and air premixing by the TE nozzle was desired to obtain single-digit NO_x control at baseload conditions.

During the initial screening tests, it was determined that operation down to 40 percent power could be achieved through the use of a pilot located at the centerbody tip. For this injector development program, a "bulkhead pilot" was incorporated into the baseline design which extended stable, efficient operation down to idle conditions, Fig. 2(a). This allowed the cone to be dedicated for liquid fuel in a separate development effort. The pilot consisted of an array of orifices located at the nozzle exit plane such that fuel was directed into the recirculation region formed as the nozzle flow expanded into the combustion chamber.

Airflow capacity evaluations were conducted using cold-flow plexiglass models of the TE nozzle. An exit diameter of 7.8 cm (3.1 in.) and a slot length of 15.8 cm (6.2 in.) were selected

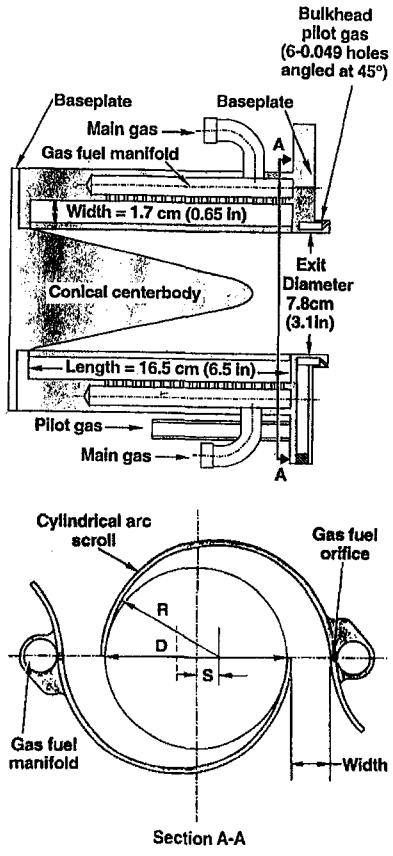

Fig. 2 Schematic diagram of TE92 fuel nozzle geometry and dimensions

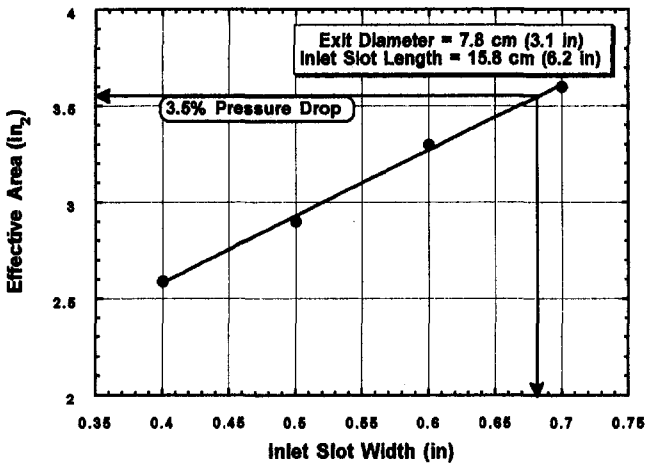

Fig. 3 TE nozzle effective area dependence on inlet slot width

based upon the available space in the engine. Parametric variations of the inlet slot width were made to determine the influence of slot width on the nozzle effective area, Fig. 3. These results, in addition to analytical predictions, were used to specify the TE92 dimensions shown in Fig. 2.

A 4 percent airflow pressure drop was achieved for the TE92 nozzle. However, it was desired to further decrease the airflow pressure loss from 4 to 3 percent and decrease the number of nozzles per engine from 18 to 16. Furthermore, cone tip thermal distress problems during off-design operation (discussed later) led to the incorporation of an airflow passage on the axis of the cone. The airflow admitted to this passage was counter swirled relative to the main flow by installing a 45-deg simple swirler in the passage. Air flow rates constituting 12 percent of the total primary zone airflow produced favorable performance (Fig. 4). The geometric characteristics of this more aggressive design (TE93C) are compared with the TE92 in Table 1.

Gas jet penetration calculations, using a correlation for a gas jet injected normal to a crossflow (Hautman et al., 1991), were used to specify the number and diameter of the fuel orifices. The fuel pressure drop calculated for baseload fuel flows, orifice spacing, and the inlet slot geometry were combined into a parameter (Holdeman, 1991) for optimizing the mixing of penetrating jets. This configuration was referred to as medium penetration.

Variations in the main gas fuel orifice array were made to improve the level of fuel–air premixing produced by the medium penetration configuration. Five different orifice arrays

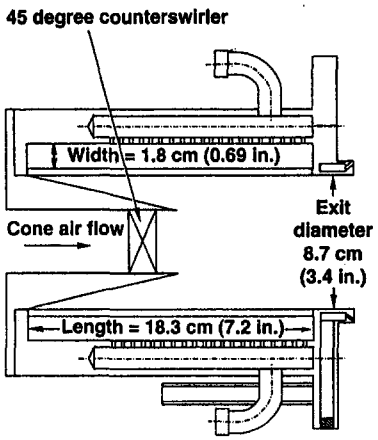

Fig. 4 Schematic diagram of TE93C fuel nozzle geometry and dimensions

Table 1 TE nozzle dimensions and airflow capacity

	TE92	TE93C
Length (L)	16.5 cm (6.5 in)	18.3 cm (7.2 in)
Width (W)	1.7 cm (0.65 in)	1.8 cm (0.69 in)
Diameter (D)	7.8 cm (3.1 in)	8.7 cm (3.4 in)
Combustor Airflow	65%	67.5%
Airflow Capacity	2.6 kg/s (5.7 pps)	2.9 kg/s (6.3 pps)
Pressure Drop	4%	3%
Nozzles per Engine	18	16

having three different penetration levels were evaluated for the ability to control NO_x at baseload conditions, Fig. 5. The calculated penetrations were approximately 25, 50, and 90 percent of the slot width and were identified as low, medium, and high penetration, respectively. Two variations of the high-penetration case were tested. The first (10 holes per inlet) achieved high penetration, but with a fuel pressure drop greater than practical for an engine fuel system. The second (5 holes per inlet) achieved high penetration with a fuel pressure drop that met the engine limitations. Configurations that produced low penetration were comprised of a large number of small orifices while high-penetration configurations were comprised of a smaller number of large-diameter orifices. The span over which fuel was injected into the inlet slot was maintained approximately the same for the low, medium, and high-penetration cases. A fourth configuration maintained high penetration and biased the fuel toward the downstream end of the inlet slot.

Single Nozzle Rig (SNR) Test Facility. The SNR test facility (Fig. 6) and related systems permitted independent control of airflow, gas fuel flows, inlet temperature, inlet pressure and combustor pressure. The SNR consisted of a series of circular cross-sectional components flanged together. Facility air was metered by a venturi before being heated by a nonvitiating heater. The inlet static pressure (P_{inlet}) and inlet stagnation temperature (T_{inlet}) of the air were measured inside the fuel prep section before entering the TE nozzle. The fuel prep section also allowed access for nozzle modifications, fuel line connections, and TE nozzle surface thermocouple attachments. The nozzle was secured to a 2.54-cm-thick water-cooled bulkhead flange. Gaseous fuel was delivered to the main fuel manifolds and bulkhead pilot manifold using independently regulated and metered supplies. Commercial grade methane, having the characteristics of natural gas, was supplied by tube trailers.

Two test sections formed the combustion chamber. The chamber length is defined by the distance from the bulkhead to the gas sampling probes. The assembly of these sections could be varied to achieve combustor lengths of 12.7 cm, 25.4 cm,

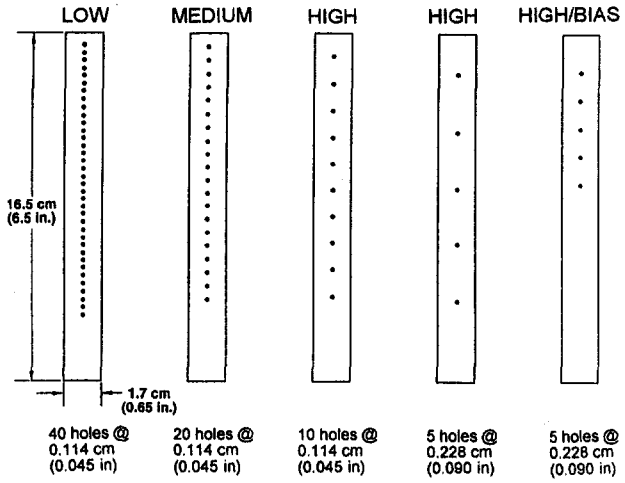

Fig. 5 TE92 main gas fuel orifice configurations

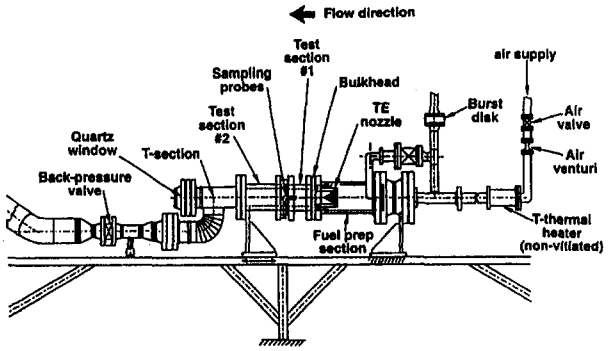

Fig. 6 Schematic diagram of SNR test facility

or 45.7 cm. The 25.4 cm combustor length was commonly used. This provided a 6 ms (combusting) residence time, which is characteristic of the engine combustor. Each test section consisted of a cylindrical section of jacketed steel pipe containing a 2.54 cm thick castable ceramic liner, which provided a 15.2 cm ID chamber. The insulating liner was cast from a commercially available ceramic consisting mostly of alumina. The outer jacket was fed with water coolant at a nominal coolant flow rate of 38 liters/min; this provided a usable test apparatus pressure rating of 20 atm. Each test section contained a passage in which a 20-joule spark ignitor was located. Note that no provisions were made to investigate the effect of bulkhead cooling air or liner cooling air on the combustor performance; these activities are conducted in sector rig tests.

A water-cooled instrumentation section containing six emission probes and a static pressure tap was located immediately downstream of the combustion chamber. A second static pressure tap was located on the bulkhead faceplate. (These combustor pressure measurements were nearly identical during all tests.) The probes were positioned at different radii based on equal area segments. The probe inlets were designed (Chiappetta and Colket, 1984) to provide a combination of aerodynamic and thermodynamic quenching in order to freeze the chemical reactions of CO and NO rapidly. Flows through the probes were controlled such that gas samples could be gathered from any combination of probes. Generally, either individual samples or "ganged" samples from all six were acquired.

A transition section (T-section) diverted the flow through two 90 deg turns prior to encountering exhaust coolant water sprays and the back-pressure valve. A window was located in the T-section along the combustion centerline in order to permit observation and recording of the flame patterns. Determinations of blowout limits were made on the basis of total and permanent disappearance of flame as the fuel flow was slowly decreased. A remotely controlled back-pressure valve controlled the combustion pressure.

Temperatures, pressures, airflow rates, and fuel flows were measured by conventional transducers, scanners, and flow meters; data were processed by an automatic data acquisition and recording system. Standard gas analysis instruments were used to determine the molar concentrations of CO_2, CO, O_2, UHC, and NO_x in the collected sample. The emission data presented herein have been corrected to 15 percent O_2 in a dry sample by using a correction factor (CF):

$$X_i(\text{corrected}) = CF * X_i(\text{measured})$$

where

$$CF = (0.21 - 0.15)/(0.21 - X_{O_2})$$

$$i = \text{CO, UHC, } NO_x$$

X_{O_2} = mole fraction of oxygen in dried sample

Table 2 FT8 baseload operating conditions

Inlet Pressure (Pinlet)	19 atm
Inlet Temperature (Tinlet)	740 K
Primary Zone Equivalence Ratio(Phi)	0.51
Primary Zone Flame Temperature (Tflame)	1820 K (2820 F)
Engine Combustion Residence Time	6 ms
Percent Combustor Airflow (TE92)	65%
(TE93C)	67.5%
No Pilot Required	

Test Conditions. As noted earlier, the testing reported here was conducted primarily at conditions corresponding to the baseload operating point of the FT8 engine. The test configurations do not account for the combustor liner cooling air or temperature profiling air that may be required for the engine. Therefore, the emissions measured and the flows delivered correspond to those of the primary zone of the combustor. The flows correspond to the total fuel flow and either 65 percent (TE92 nozzle) or 67.5 percent (TE93C nozzle) of the combustor airflow. (Our experience has been that secondary air addition has no effect on the measured level of emissions. The dilution effect is accounted for by converting the emission measurements to a fixed percentage of O_2 (15 percent) in the sample.) Baseload conditions are defined in Table 2:

Combustion Test Results

The test results reported herein are separated into two sections; the first section reports baseload performance for the TE92 nozzle; the second section for the TE93C nozzle. Pressure, residence time, inlet fuel/air maldistribution effects on NO_x and measured airflow capacity are also presented. While not documented in this paper, tests using various combinations of pilot fuel injection and premixing main gas fuel were conducted in the SNR facility to demonstrate that the designs provide sufficient flame stability and robustness throughout the entire engine operating envelope while maintaining high combustion efficiencies. Documentation of part-power operation is being conducted in a sector rig.

TE92 Nozzle Emission and Performance. Measured NO_x levels for the four different injection schemes are shown in Fig. 7. NO_x levels were very sensitive to changes in the penetration both higher and lower than the baseline, medium penetration case and exhibited an exponential dependence with flame temperature. In particular, higher gas fuel penetration with a smaller number of orifices reduced NO_x levels to 8 ppm at baseload. This experience was not consistent with the Holdeman criterion

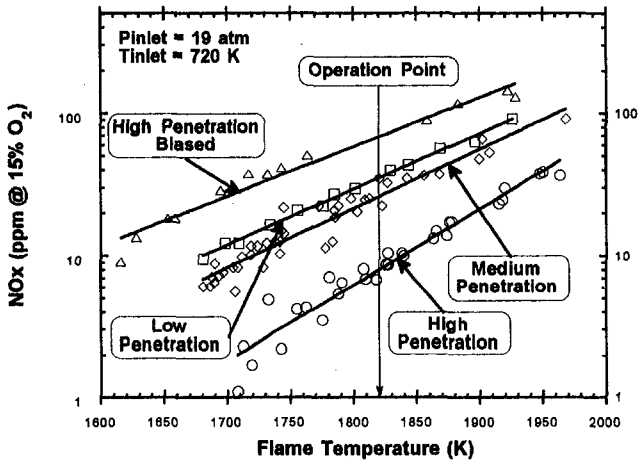

Fig. 7 TE92 NO_x emission dependence on flame temperature for four different orifice configurations

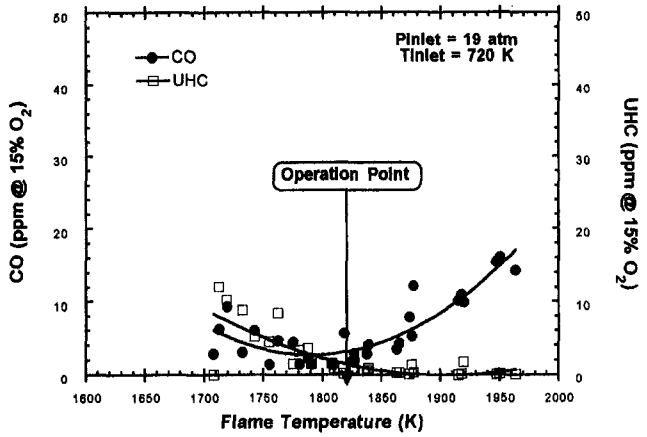

Fig. 8 CO and UHC emissions for TE92 high-penetration configuration

probably because the vigorous mixing within the TE nozzle was the dominant mixing process. Lower gas fuel penetration increased NO_x levels to 36 ppm. The effect of the eightfold larger number of orifice sites (40 versus 5) of the low-penetration configuration was far outweighed by the radial high penetration effect.

Extensive CFD, water flow visualization, airflow velocity measurements, cold flow mixing studies and analytical calculations were made to help understand the effect of injecting gas fuel into a highly swirled airflow generated by the TE geometry. Results indicated that the highest velocity gradients inside the nozzle existed close to the centerbody surface. Injection of fuel into these regions, no matter how coarse, promoted extremely rapid and uniform mixing of the fuel and air by the time the mixture reached the exit plane.

Cone tip temperature measurements acquired during combustion tests indicated temperatures comparable to Tinlet levels for the low and medium penetration cases. However, when the penetration was increased to high levels, cone tip temperatures in excess of 1000 K were experienced as the test conditions were increased from part-power to baseload conditions.

The results of the cold flow studies were examined to ascertain possible causes of high cone tip temperatures. In general, fuel injected at the upstream end of the inlet slot is transported to the axis of the flow path while fuel injected toward the downstream end of the inlet slot remains at the outer periphery of the exiting flow. Velocity measurements verified the anticipated presence of a depressed axial velocity on the flow axis. It was postulated that if even a small fuel flow was supplied to this region, a flame would be stabilized and cause high cone temperatures. The high/bias orifice configuration, designed to prevent fueling of the flow on the axis, did yield low cone tip temperatures at all conditions. However, the NO_x levels increased to 70 ppm. Additional testing determined that the cone tip temperature problem was created by the upstream-most orifice in the high penetration orifice configuration. By decreasing the penetration associated with that orifice in the TE92 nozzle, successful robust operation could be achieved.

At baseload conditions, carbon monoxide (CO) and unburned hydrocarbon (UHC) levels for the high penetration configuration were well below 25 ppm over the entire flame temperature range tested, Fig. 8. CO levels increased as the flame temperature was increased above 1800 K, in agreement with calculated CO equilibrium behavior. Efficiencies based upon emission measurements for all four configurations were above 99.99 percent and remained high until lean blowout (LBO) occurred. LBO for the high penetration configuration occurred at a flame temperature of approximately 1700 K, corresponding to an equivalence ratio of 0.45 (Figs. 7 and 8). This provided a large margin relative to the baseload operation point of 1820 K.

Part-power tests were conducted to determine the TE nozzle's range of operation. At baseload, the nozzle operated over a wide flame temperature range on either side of the operation point, providing adequate stability without the need for pilot. At inlet temperatures, pressures, and fuel flows corresponding to reduced engine power, small amounts of bulkhead pilot provided adequate combustion stability while maintaining high efficiencies and producing only a small impact on NO_x production. Efficiencies of 99.9 percent were achieved down to 20 percent power. Reducing the power level to Idle conditions caused the efficiency to fall to 93 percent. These results were sufficient to demonstrate the ability to sustain efficient operation over the entire FT8 operating range. (Additional developments of the bulkhead pilot are taking place in a sector rig test program.)

The sensitivity of NO_x to pressure and residence time were found to be a function of both the level of premixing and the flame temperature, Fig. 9. Both the low and high-penetration cases showed a divergence in the NO_x levels, for the two pressure levels tested, as the flame temperature was increased. For a high level of premixing (via increasing fuel penetration), the NO_x fell below 10 ppm for flame temperatures below approximately 1850 K and was insensitive to pressure changes from 14 atm to 19 atm. However, the lower level of premixing (via low fuel penetration) exhibited sensitivities to pressure even at 1800 K. The negligible NO_x sensitivity to pressure over this flame temperature range has been observed in other well-premixed systems (Leonard and Stegmaier, 1994) and has been explained by the decreased importance of thermal NO_x production at these low flame temperatures (Nicol et al., 1995). As the flame temperature was increased, for the high-penetration configuration, above 1850 K, NO_x production became a stronger function of pressure, which can be explained by the increased role of the thermal NO_x production mechanism.

Similarly, the NO_x sensitivity to residence time also increased as the flame temperature increased above 1850 K for the low penetration configuration, Fig. 10. At a flame temperature of 1820 K, NO_x sensitivities to residence time were small, $NO_x \sim 0.6$*TAU. However, increasing the flame temperature to 1900 K, resulted in a much greater NO_x sensitivity to residence time, $NO_x \sim 4.3$*TAU. Again, thermal NO_x, which is resident time dependent, plays a strong role at high flame temperatures but only a small role at low flame temperatures.

NO_x sensitivity (using the TE92 high penetration configuration) to the local fuel – air ratio in each inlet was evaluated during a test where the fuel supply to each manifold was controlled separately. This allowed changing the fuel – air ratio in each of the inlets while maintaining the same overall fuel – air ratio (flame temperature). Figure 11 shows the NO_x sensitivity to fuel – air ratio changes in inlet slot #1 expressed in terms of

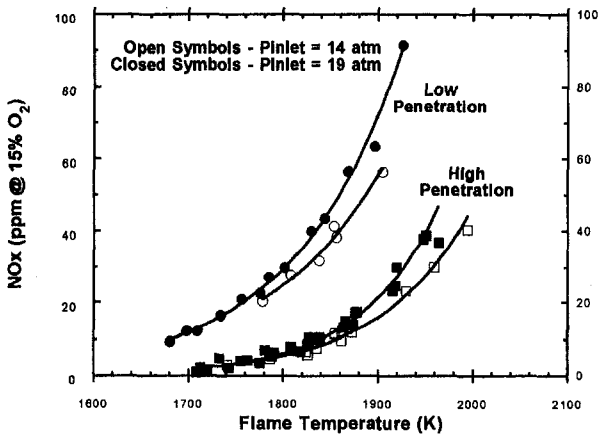

Fig. 9 TE92 NO_x emission dependence on pressure for two different levels of premixing

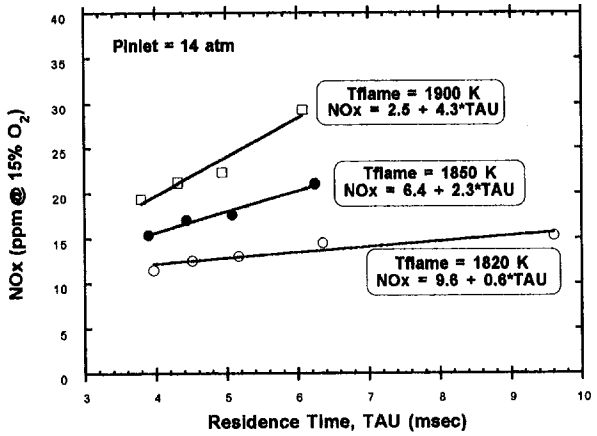

Fig. 10 NO_x dependence on combusting residence time (TAU) for the TE92 medium-penetration orifice configuration

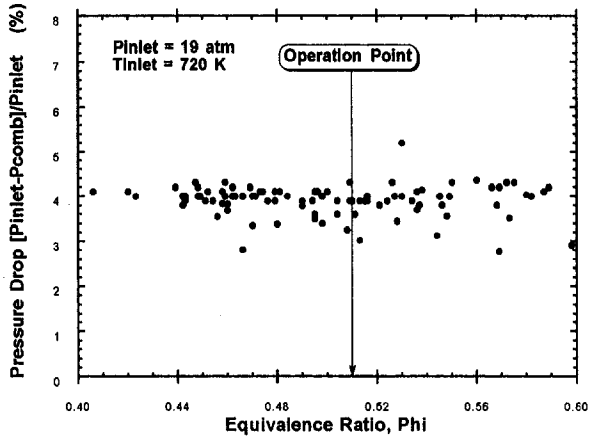

Fig. 12 TE92 nozzle pressure drop during combustion for four different orifice configurations tested

the flame temperature that would be achieved upon complete mixing. Large variations in the slot inlet fuel – air ratio, which corresponded to a flame temperature range from 1700 K to 1950 K, produced a negligible influence on NO_x. This desired tolerance was consistent with the cold flow results, which identified the very high velocity gradients near the cone surface, which uniformly mix the fuel and air in the high penetration case. These results suggested that if nonuniform feeding of the inlet slots existed in the engine, as a result of imperfect diffuser performance or unequal fuel-feed, neither flame stability nor NO_x production should be affected.

Figure 12 shows the (hot flow) nozzle airflow pressure drop measured during combustion tests for the four different orifice configurations. The average pressure drop was 4 percent, which was higher than the 3.5 percent drop predicted using cold flow results. A goal of the TE93C design was to reduce this loss by one percentage point.

TE93C Nozzle Emissions and Performance. The TE93C nozzle was first evaluated at baseload conditions using a high-penetration orifice array scaled from the TE92 experience. NO_x, CO, and UHC emission levels were all similar to those obtained by the TE92 nozzle. Temperatures measured on the cone surface remained low for all operating conditions. During baseload tests, the amount of airflow supplied to the cone was held constant at the design point of 12 percent.

Reductions in the amount of airflow supplied to the cone were made to determine the robustness of the TE93C's operation at baseload. Suitable valving was installed such that the pressure drop across the cone air flow passage could be reduced relative to the pressure drop across the main air passage. The cone airflow variation achieved as a function of this difference in pressure drop ranged from 12 percent (no reduction from design) to 8.5 percent of the total flow, Fig. 13. Over this range, no change in NO_x level was observed. This indicated that the cone airflow mixed thoroughly with the main flow prior to the occurrence of combustion. Cone surface temperatures remained low as the cone flow rate was varied. These results indicated that nozzle performance would be quite tolerant to unanticipated cone flow rate excursions.

Airflow capacity obtained from pressure drop measurements during hot testing indicated the TE93C design reduced the air pressure drop to the desired 3 percent level. Nozzle pressure drop excursions above and below the design operation point of 3 percent were made to determine possible operational problems while maintaining the design 12 percent cone flow rate. These excursions were accomplished by modulating the backpressure valve position and the total air flowrate while maintaining the same inlet pressure and inlet temperature. (The inlet pressure was reduced to 13.5 atm for this test series.) The insensitivity of NO_x to nozzle pressure drop is shown in Fig. 14. The slightly lower NO_x levels at the higher pressure drops are associated with reduced residence times. No flashback or elevated cone temperature problems were experienced over this nozzle pressure drop range. Taken together, the avoidance of operability problems for low nozzle airflow pressure drop and cone flow rates indicated that the TE93C design was a robust, low-NO_x producing device meeting the FT8 engine requirements.

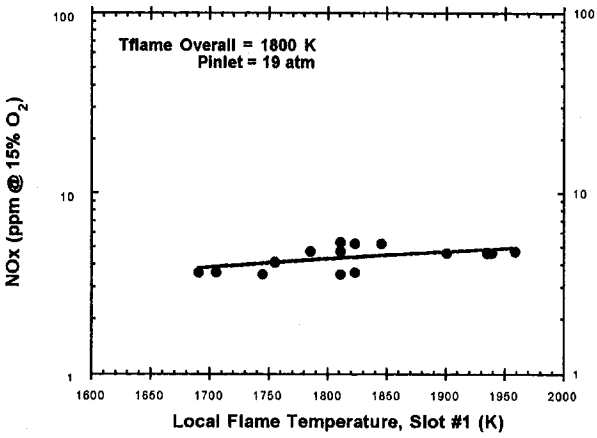

Fig. 11 TE92 NO_x emission dependence on inlet fuel/air maldistribution between inlet slots for high-penetration configuration

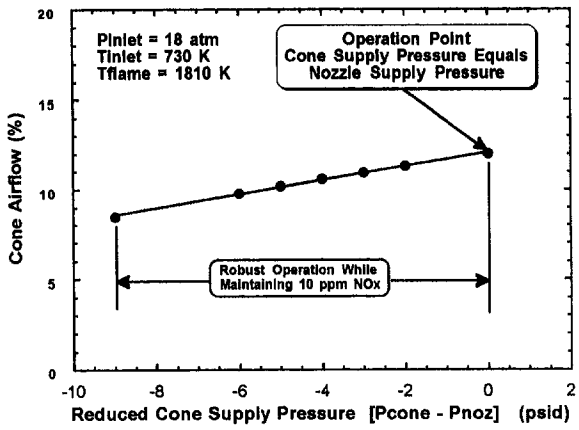

Fig. 13 TE93C operability and NO_x control maintained for reduced cone airflow

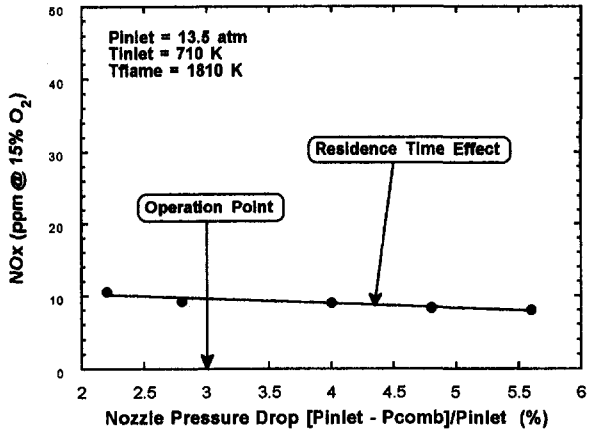

Fig. 14 TE93C robust, low-NO_x operation preserved over wide nozzle pressure drop range

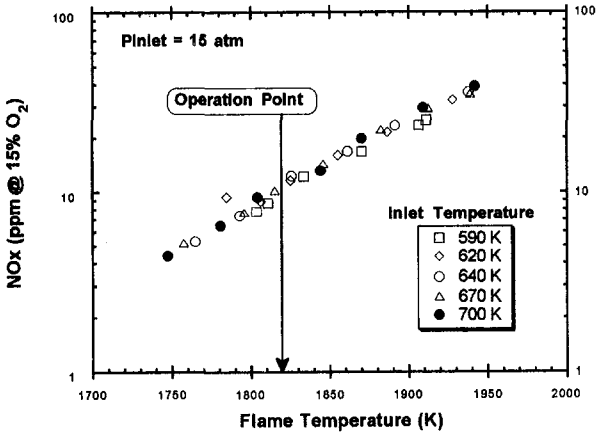

Fig. 16 TE93C NO_x emission dependence on flame temperature for five different inlet temperatures

The effect of inlet pressure on NO_x emissions was also evaluated for this design. Figure 15 shows the NO_x dependence on flame temperature for four different inlet pressures ranging from 5 to 18 atm at a constant inlet temperature and the same residence times. These results indicate some NO_x pressure dependence—a generally greater dependence for temperatures higher than 1800 K. The curves converge as the flame temperature is reduced. These results are consistent with the TE92 pressure sensitivity results (Fig. 9).

The independence of NO_x level to inlet temperature over the range from 590 to 700 K is shown in Fig. 16. A significant dependence on inlet temperature had previously been observed for different TE92 configurations, which exhibited elevated cone tip temperatures; this suggested combustion was taking place in the cone tip wake where high fuel concentrations were present. The NO_x insensitivity to inlet temperature for the TE93C design is consistent with the elimination of any combustion inside the nozzle or diffusion flame combustion. Both cone tip temperature measurements and surface temperature measurements at the nozzle exit have indicated no signs of flame propagation into the nozzle, even when the TE93C is operated at off-design conditions.

Conclusions

1 NO_x levels well below 25 ppm are achievable in moderate pressure ratio aeroderivative engines using a reasonable number of simple, rugged, high-air-flow capacity, high-swirl, tangential entry fuel injectors.

2 NO_x performance is sensitive to the extent to which the fuel jets penetrate into the scroll flow. A large number of injection sites is not required; five high-penetration sites per inlet produced the desired NO_x control. Penetration of fuel to the centerbody surface can lead to high NO_x levels and operability problems. Use of a counterswirling centerbody air flow and a reduced fuel penetration of the upstream-most orifice effectively eliminates operability problems.

3 NO_x performance should be insensitive to diffuser flow nonuniformities.

4 NO_x performance and operability for these nozzles is insensitive to nozzle pressure drop down to 2 percent and inlet air temperatures ranging from 590 to 700 K.

5 The NO_x performance signature for a given design can be confidently expressed as an exponential function of the flame temperature derived from the primary zone fuel–air ratio. Careful control of primary zone stoichiometry in the engine is a prerequisite for low-NO_x engine performance.

6 NO_x sensitivities to pressure and residence time were found to be small at flame temperatures below 1850 K. Above 1850 K some NO_x sensitivity to pressure and residence time was observed and was associated with the increased role of the thermal NO_x production mechanism at elevated flame temperatures.

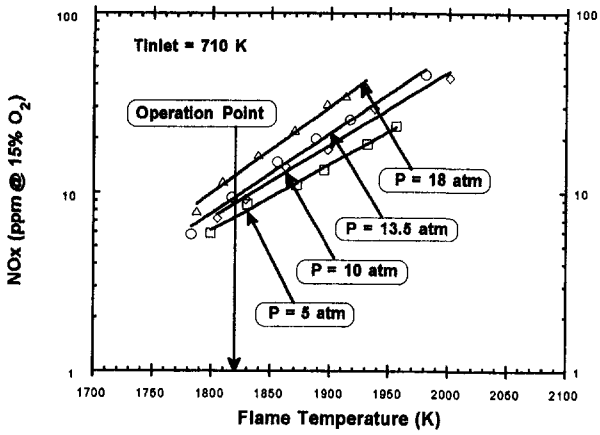

Fig. 15 TE93C NO_x emission dependence on flame temperature for four different inlet pressures

Recommendation

The slight dependence of NO_x levels on pressure and residence time suggest that the fuel–air mixture produced by these devices is well mixed, but not perfectly mixed. Further reductions in NO_x levels are probably achievable through refinement of the injector orifice array. Cold flow studies should be conducted to evaluate the extent of mixture uniformity improvement that can be achieved.

References

Aigner, M., and Muller, G., 1993, "Second-Generation Low-Emission Combustors for ABB Gas Turbines: Field Measurements With GT11N-EV," ASME JOURNAL OF ENGINEERING FOR GAS TURBINES AND POWER, Vol. 115, pp. 533–536.

Angello, L., and Lowe, P., 1989, "Dry Low NO_x Combustion Development for Electric Utility Gas Turbine Applications—A Status Report," ASME Paper 89-GT-254, Toronto, Ontario, Canada.

Becker, B., Berenbrink, P., and Brandner, H., 1986, "Premixing Gas and Air to Reduce NO_x Emissions With Existing Proven Gas Turbine Combustion Chambers," ASME Paper No. 86-GT-157.

Chiappetta, L. M., and Colket, M. B., III, 1984, "Design Considerations for Aerodynamically Quenching Gas Sampling Probes," ASME *Journal of Heat Transfer*, Vol. 106, pp. 460–466.

Hautman, D. J., Haas, R. J., and Chiappetta, L., 1991, "Transverse Gaseous Injection Into Subsonic Air Flows," AIAA Paper No. 91-0576.

Holdeman, J. D., 1991, "Mixing of Multiple Jets With a Confined Subsonic Crossflow," AIAA Paper No. 91-2458.

Leonard, G., and Stegmaier, J., 1994, "Development of an Aeroderivative Gas Turbine Dry Low Emissions Combustion System," ASME JOURNAL OF ENGINEERING FOR GAS TURBINES AND POWER, Vol. 116, pp. 542–546.

McVey, J. B., Padget, F. C., Rosfjord, T. J., Hu, A. S., Peracchio, A. A., Schlein, B., and Tegel, D. R., 1993, "Evaluation of Low-NO_x Combustor Concepts for Aeroderivative Gas Turbine Engines," ASME JOURNAL OF ENGINEERING FOR GAS TURBINES AND POWER, Vol. 115, pp. 581–587.

Nicol, D. G., Steele, R. C., Marinov, N. M., and Malte, P. C., 1995, "The Importance of the Nitrous Oxide Pathway to NO_x in Lean-Premixed Combustion," ASME JOURNAL OF ENGINEERING FOR GAS TURBINES AND POWER, Vol. 117, pp. 100–111.

Rizk, N. K., and Mongia, H. C., 1991, "Low NO_x Rich-Lean Combustion Concept Application," AIAA Paper No. 91-1962.

Solt, J. C., and Tuzson, J., 1993, "Status of Low NO_x Combustor Development," ASME Paper No. 93-GT-270.

Low-NO_x Premixed Combustion of MBtu Fuels Using the ABB Double Cone Burner (EV Burner)

K. Döbbeling

H. P. Knöpfel

W. Polifke

D. Winkler

C. Steinbach

T. Sattelmayer

Department of Aerodynamics,
ABB Corporate Research Center,
Dättwil, Switzerland

A novel combustion technique, based on the Double Cone Burner, has been developed and tested. NO_x emissions down to very low levels are reached without the usual strong dilution of the fuel for MBtu syngases from oxygen-blown gasification of coal or residual oil. A limited amount of dilution is necessary in order to prevent ignition during the mixing of fuel and combustion air. The relevant properties of the fuel are reviewed in relation to the goal of achieving premixed combustion. The basic considerations lead to a fuel injection strategy completely different from that for natural gas. A high-speed premixing system is necessary due to the very short chemical reaction times of MBtu fuel. Fuel must be prevented from forming ignitable mixtures inside the burner for reliability reasons. A suitable fuel injection method, which can be easily added to the ABB double cone burner, is described. In common with the design of the standard EV burner, the MBtu EV burner with this fuel injection method is inherently safe against flashback. Three-dimensional flow field and combustion modeling is used to investigate the mixing patterns and the location of the reaction front. Two burner test facilities, one operating at ambient and the other at full gas turbine pressure, have been used for the evaluation of different burner designs. The full-pressure tests were carried out with the original gas turbine burner size and geometry. Combining the presented numerical predictive capabilities and the experimental test facilities, burner performance can be reliably assessed for a wide range of MBtu and LBtu fuels (residue oil gasification, waste gasification, coal gasification, etc.). The atmospheric tests of the burner show NO_x values below 2 ppm at an equivalence ratio equal to full-load gas turbine operation. The NO_x increase with pressure was found to be very high. Nevertheless, NO_x levels of 25 vppmd (@ 15 percent O_2) have been measured at full gas turbine pressure. Implemented into ABB's recently introduced gas turbine GT13E2, the new combustion technique will allow a more straightforward IGCC plant configuration without air extraction from the gas turbine to be used.

Introduction

The significant increase in gas turbine efficiency in the last decade has contributed to the economic feasibility of integrated gasification combined cycle processes. A further incentive has been provided by the very low emissions of gas turbine combustors running on clean fuels (i.e., no fuel-bound nitrogen or sulfur components). The hydrocarbons used for the gasification can be residual oils, coal, or industrial waste. In particular, the oxygen-blown gasification of refinery residues in combination with a CC plant is expected to be widely introduced on a commercial scale. The processes deliver syngases with a heating value approximately one third of that of natural gas, whereas syngases from air-blown processes have even lower heating values. The higher heating value (smaller fuel mass flow) facilitates the syngas desulfurization and HCN removal processes. If the problem of excessive NO_x production during combustion of syngas fuels can be solved without resorting to the common technique of heavy dilution, the surge margins of some standard gas turbines (e.g., ABB's GT13E2 or GT8C) are sufficient for direct MBtu operation.

Contributed by the International Gas Turbine Institute and presented at the 39th International Gas Turbine and Aeroengine Congress and Exposition, The Hague, The Netherlands, June 13–16, 1994. Manuscript received by the International Gas Turbine Institute March 4, 1994. Paper No. 94-GT-394. Associate Technical Editor: E. M. Greitzer.

Specification of MBtu Fuel Properties

Oxygen-blown gasification delivers syngases with heating values of the order of 10 to 16 MJ/kg (≈210–300 Btu/scf), compared to heating values of less than 5 MJ/kg (≈100 Btu/scf) for air blown processes. Different feed stock compositions and gasification processes lead to a variety of syngas compositions and heating values. As shown below, residual oil gasification syngas is the most challenging syngas composition as far as premix burner technology is concerned. Consequently, the burner tests were carried out with this fuel type.

A typical residual oil gasification fuel from oxygen-blown processes can be represented by a typical volumetric composition of 45 percent H_2, 48 percent CO, and 7 percent N_2 and a lower heating value of 15 MJ/kg (277 Btu/scf). The H_2/CO ratio is about 1.

Coal gasification syngas has a volumetric composition of typically 30 percent H_2, 60 percent CO, and 10 percent N_2 and a lower heating value of approximately 12 MJ/kg (234 Btu/scf). The H_2/CO ratio is only 0.5. Compared to residual oil gasification syngas, the hydrogen content and consequently the flame velocity is lower.

Reliable premixed combustion systems for gas turbines have only been developed for natural gas to date. The main reason for this situation is the unique properties of natural gas under lean premixed conditions. Long ignition delay times and high self-ignition temperatures make it possible to control pre-igni-

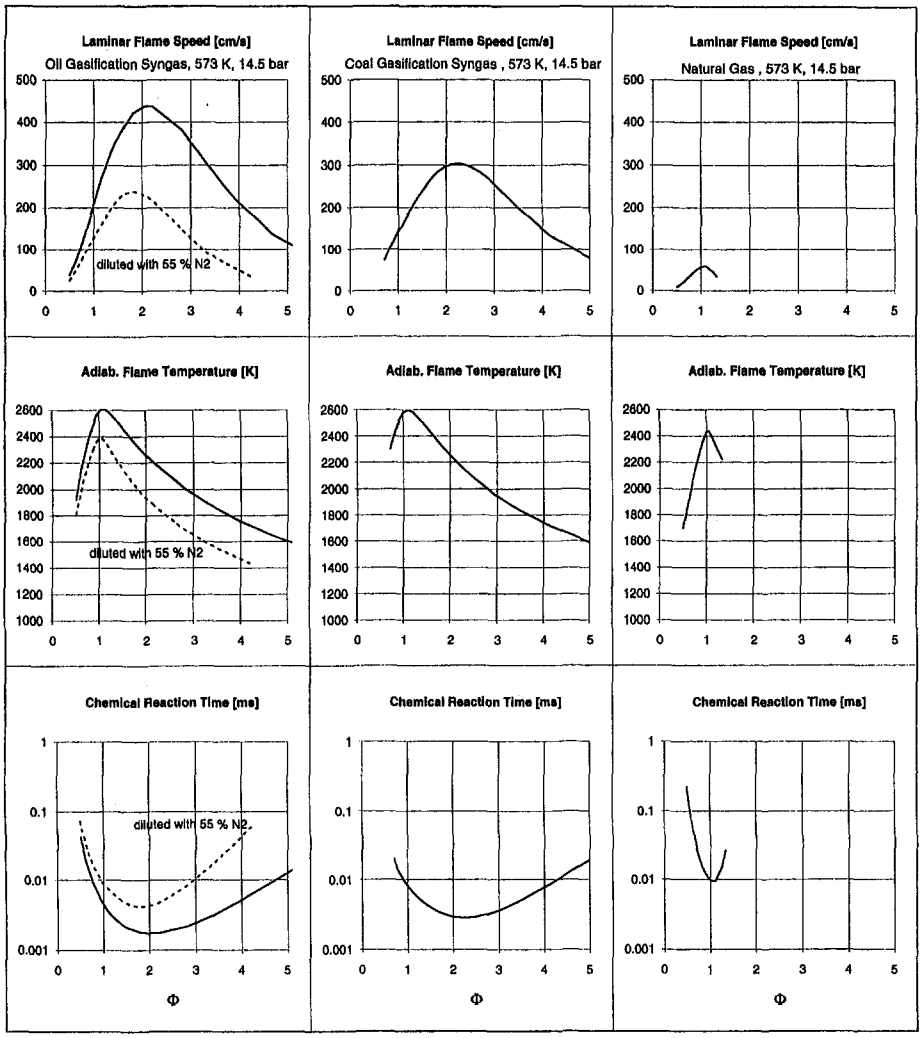

Fig. 1 Flame speed, flame temperature, and chemical reaction time for different syngas compositions and for natural gas

tion and the aerodynamic and thermoacoustic behavior of such combustors with well-designed burners (e.g., the Double Cone Burner). Conversion for other fuels is much more critical, since now combustion chemistry introduces constraints in addition to those for a natural gas combustor. The problem of ignition of oil No. 2 during the evaporation phase is well known. In order to highlight the fact that MBtu fuels behave even worse, their basic combustion properties are briefly summarized below and compared to those of natural gas.

The laminar flame speed, the adiabatic flame temperature, and the chemical reaction time of syngases with the above-mentioned compositions and of natural gas are plotted in Fig. 1. Properties of residual oil syngas with a 55 percent (Vol.) dilution of N_2 are given by the dotted lines in the left column in Fig. 1. All values have been calculated with a one-dimensional laminar flame code (Kee et al., 1992) for a pressure of 14.5 bar and a preheat temperature of 300°C. The chemical kinetics data base was that of Miller and Bowmann (1989) with 52 species and 251 elementary reaction equations.

The peak laminar flame velocity of the syngases is about an order of magnitude higher than the laminar flame velocity of methane. Since intense turbulence will increase the flame speeds significantly above the respective laminar values shown in Fig. 1 (Liu et al., 1989), it is obvious that the effective flame speed reaches the order of the flow speed in the burner. As a consequence, flashback into the premixing section can hardly be avoided. Wall boundary layers, wakes, or local zones of low velocity (e.g., downstream of fuel jets mixing with air) are particularly critical. The highest flame velocity of the syngas/air mixture occurs at fuel-rich conditions (fuel equivalence ratio approximately 2). Hence, during the mixing of a fuel jet with the air, fuel-rich zones in the jet mixing layer can act as flame holders and prevent the fuel from fully mixing with the air prior to ignition.

The maximum flame temperature for both oil and coal syngas is 2600 K (4200°F), which is about 200 K higher than that of methane. This is not a problem if full premixing is achieved, since the (mixed) flame temperature can be selected via the overall equivalence ratio. However, if flame stabilization occurs in regions where the mixing is not yet perfect, the stoichiometry in the flame front will vary. The fuel, which burns richer than average, will produce very high peak temperatures with NO_x formation rates far higher than in the natural gas case.

The time scale of the chemical reaction in a premixed laminar flame is plotted in the lower row of Fig. 1. This time scale is the integrated time of a fluid element passing the flame's reaction zone. The reaction times for both syngases are one fifth of that of natural gas. These very small time scales emphasize the high flashback risk of burners operated on syngases. The time scale of the premixing process must be faster than the chemical time scale. The constraints resulting from Damköhler number considerations are very similar to those mentioned above: Flashback can only be avoided if no low-speed flow regions exist within the mixing zone. The flame can travel upstream wherever

partially premixed fluid elements have residence times longer than the chemical times, for instance in wall boundary layers or wakes.

The effect of diluting syngases with an inert gas (nitrogen in this case) is seen in the left column of Fig. 1 (dotted lines). With only 55 percent (Vol.) N_2 dilution, the flame speed can be approximately halved, while the maximum flame temperature drops to values comparable to natural gas. This effect can be exploited to delay ignition until further downstream. In practice, the effect of moderate dilution is very strong, since rich combusting zones, which are most critical for flame stabilization and NO_x production, are no longer present if the shift of the ignition point downstream is sufficient.

In comparing residual oil and coal syngases, the flame speed is considerably lower for the latter. It is expected from the calculations that premixing can be achieved for coal-derived gas with much less dilution. In contrast, the maximum flame temperature is only slightly lower for coal gasification syngas.

Influence of the Combustion Technique on the Integrated Gasification Combined Cycle

Much higher fuel flows must be handled due to the lower heating value of MBtu gases. The fuel–air ratio at the combustor inlet will increase from 3 percent (for NG) to more than 12 percent for diluted syngases. The maximum dilution allowed is governed by the required surge margin of the compressor. The main goal of the burner development described was to provide a combustion technique with a sufficiently low degree of dilution for NO_x control, in order to avoid undesired air extraction from the compressor, which is commonly used to match the compressor to the turbine in MBtu operation.

Table 1 shows the combustor outlet volume flow with respect to the combustor inlet air flow for different fuels. The combustor outlet temperatures and pressure are constant for all cases under consideration, and the volume flows are normalized to standard conditions. A simple rule can be deduced:

From the viewpoint of compressor operation, undiluted combustion of syngas is not very different from the combustion of natural gas with a water to fuel ratio of unity. If dilution of the syngas is required (e.g., 55 percent N_2 dilution), operation is similar to that with natural gas and a water to fuel ratio of 2. As a consequence, standard gas turbines with high surge margins (like the GT13E2) are a good base for moderately diluted syngas combustion.

A major constraint for using a standard gas turbine without modifications for syngas is that the NO_x emission may not exceed the values achieved for natural gas (i.e., for ABB gas turbines considerably lower than 25 vppmd (@ 15 percent O_2) without water injection). For the NO_x control in syngas applications, two different approaches can be followed: the commonly applied diffusion burner technique and the new premix burner technique. They differ significantly in their complexity and their influence on plant layout and operating characteristics.

The approach of the conventional diffusion burner technique is to lower the heating value, and thus the maximum flame temperature, to very low levels by strong dilution of the syngas with nitrogen or water, if the NO_x limitations are more stringent.

Table 1 Combustor outlet volume flow

fuel	natural gas	coal syngas	oil syngas	natural gas	oil syngas 55% N_2 dilution	natural gas
water to fuel ratio	0	0.0	0.0	1.0	0.0	2.0
V_{out}/V_{air} $[m^3_n/m^3_n]$ [scf/scf]	1.047	1.091	1.087	1.101	1.193	1.172

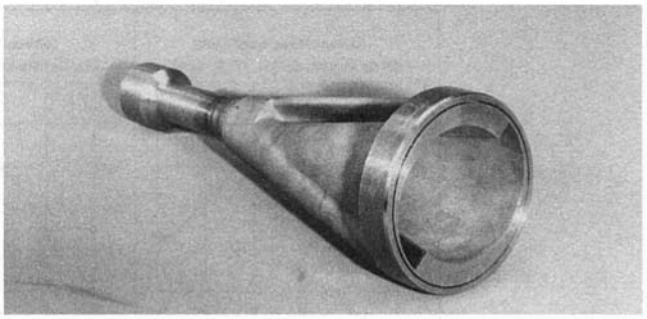

Fig. 2 ABB's EV burner for natural gas operation

This technique requires air extraction from the compressor and a high degree of integration between the air separation/gasification plant and the gas turbine. Very large volume flows of the low-grade fuel have to be controlled. A considerable amount of high-quality water is consumed by the gas turbine with this technique.

The premix combustion technique described below needs only moderate nitrogen dilution for NO_x control. Air extraction can be avoided for standard gas turbines if the surge margin is sufficient (see Table 1). The air separation/gasification unit is operated independently of the gas turbine. Compared to the diffusion burner technique, much smaller volume flows have to be handled and no water is used for NO_x control.

It can be shown that the total plant efficiency (Döbbeling et al., 1993) of the nonintegrated concept with premix burners exceeds that of fully or partly integrated concepts using the conventional diffusion burner technique.

Description of the EV Burner and the MBtu Fuel Premixing System

Basic Operation Principle of the EV Burner. ABB's EV burner is also known as the Double Cone Burner, because it consists of two half-cones moved apart perpendicular to their centerlines. Two inlet slots of constant slot width (see Fig. 2) are formed. Air entering through these slots is mixed with gaseous fuel emerging from a large number of holes along each of the slots. Since the slot width is constant and the diameter of the burner cross section increases from the cone tip (upstream end of the burner) to the end of the cone (downstream end of the burner), the swirl number (defined by the ratio of axial to circumferential momentum flux) of the air entering the burner increases continuously. If the swirl number exceeds a certain threshold, vortex breakdown occurs on the axis of the swirling flow. With a suitably adjusted slot width, cone angle, and burner length, this central recirculation zone is formed on the centerline at the end of the burner and serves as an aerodynamic flame holder. The burner flow field and the vortex breakdown can be predicted by an analytic calculation described in detail by Keller et al. (1991). Stable combustion is possible due to the central recirculation zone even at conditions close to extinction with flame temperatures well below 1500°C, without the need for pilot flames (Sattelmayer et al., 1992; Aigner et al., 1990). It can be shown by reaction kinetics that if high combustor outlet temperatures are required (as is the case for modern high-efficiency gas turbines), a system without the need for piloting flames is the best solution for minimum NO_x emissions. The burner is inherently safe against flashback, since the fuel is injected and mixed in the inlet slots where flow velocities are very high. No fuel is present upstream of the burner.

EV Premix Burner Operation in Gas Turbines. A large amount of operating experience has been accumulated for ABB's Double Cone Burner operating on natural gas with NO_x emissions of less than 15 ppmvd (@ 15 percent O_2). ABB's

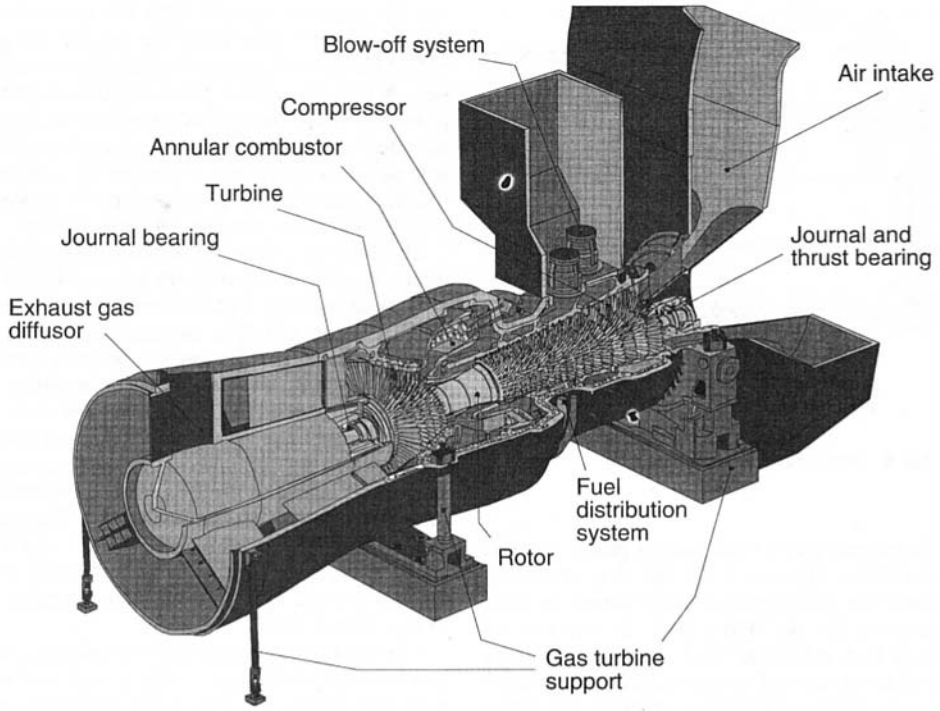

Fig. 3 ABB's GT13E2 thermal block

GT8, GT9, GT10, GT11, and GT13 type machines use this burner in multiburner assemblies either in silo combustors or in annular combustors. Details on the operation experience with silo EV combustors are given by Aigner and Müller (1993); annular combustor operation experience is described by Strand (1993). Figure 3 shows the thermal block of the GT13E2 with its annular combustor, which is well suited for syngas applications. A detailed description of the combustion technology for natural gas and oil No. 2 for this machine is given by Senior et al. (1993). Excellent temperature pattern factors are achieved due to the relatively small size of the burner. ABB's strategy is to use one burner geometry for all of ABB's gas turbines.

Modification of the EV Burner for MBtu Fuels. An appropriate injection method for MBtu gases has to take the critical properties of these fuels into account. An attempt to apply mixing principles suitable for natural gas to more critical fuels will not provide the necessary performance. Injection of the fuel along the inlet slots is no longer appropriate due to the high flame velocities of hydrogen-containing fuels and the higher volume flux, which distorts the incoming airflow profile. At high hydrogen content, flames stabilize at the gas injection holes and premixing cannot be achieved. This does not compromise the reliability of the EV burner but does increase the NO_x emissions.

The specialized flow field of the Double Cone Burner provides an excellent basis for the implementation of a very rapid injection method, since the vortex breakdown blocks most of the cross sectional area near the outlet. The desired high air velocities are found in a layer close to the cone halves. As a consequence, the fuel can be injected into this layer of maximum axial velocity. In order to prevent ignition in unmixed regions, injection of fuel into the inner and outer recirculation zones is avoided. A number of plain holes facing radially inward close to the burner end serve as fuel injectors as shown in Fig. 4. Since no fuel is found inside the burner and care has been taken to keep the outer recirculation zone free from unmixed fuel, safe and reliable operation of the burner even with high-hydrogen-content fuels is achieved. Due to the high velocity of the gas injection, the flame stabilizes downstream of the burner, where the fuel jets reach the hot recirculation zone (see Fig. 5). The air leaving the burner is quickly entrained into the fuel jets. The injector can easily be combined with the standard EV

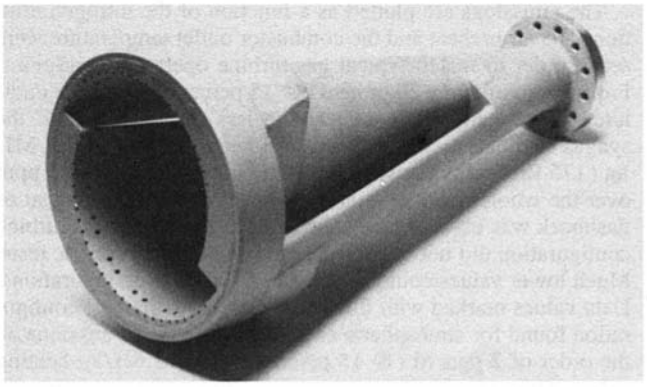

Fig. 4 ABB's MBtu EV burner

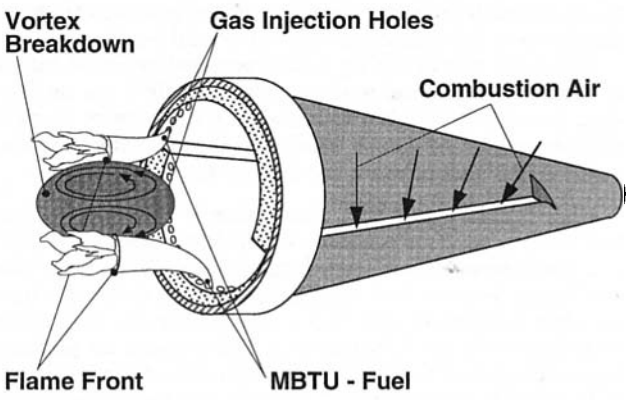

Fig. 5 Sketch of the radial jet mixing system for the MBtu EV burner

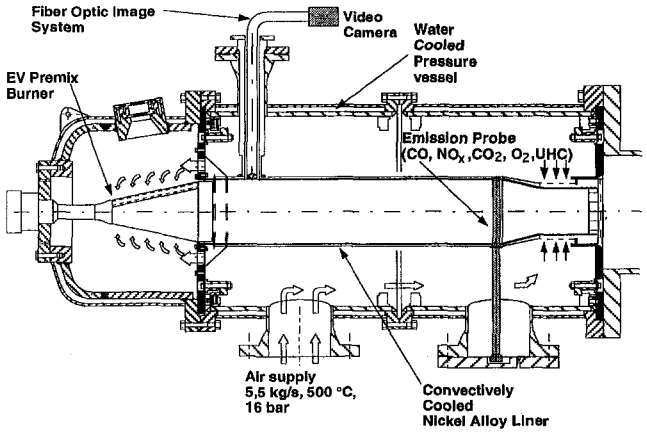

Fig. 6 High-pressure test rig

burner. Operation in premix mode with natural gas is possible independently of the MBtu injector. If oil No. 2 is chosen as backup fuel, the natural gas fuel channels in the burner are used with slight modifications for the MBtu fuel. In the case of natural gas as backup fuel, additional fuel channels to supply the MBtu injection holes at the end of the burner are provided. Despite the completely different injection methods for MBtu gases and natural gas, the flame shape and the location of the reaction front are essentially the same in both cases.

Description of the Test Facilities

Two full-scale test rigs are used for a systematic testing program for EV burners, one operating at ambient pressure, the other at gas turbine pressure. A wide range of measurements are possible, and some of the techniques that have been used for the development of the MBtu EV burner are described here. The major components of the metrology for both test rigs are temperature measurements with thermocouple probes and the exhaust analysis for CO, CO_2, O_2, NO, NO_2, and UHC with infrared absorption, paramagnetic, chemiluminescence, and flame ionization detectors. These instruments are controlled by a microcomputer. An automatic calibration can be requested. The probe technique is a suction, water quenched, heated line system.

Atmospheric Test Rig. The atmospheric test rig provides excellent optical access through the exhaust duct and via large windows in the air plenum chamber upstream of the burner. A full range of fluid supply services are metered, automatically monitored, and logged by a microcomputer. These include full-temperature, nonvitiated combustion air up to 3000 kg/h and two separate combustor cooling air supplies. Apart from the standard fuel supply of natural gas and light oil, CO, H_2, and N_2 are available from pressurized cylinders in sufficient quantities to run at full-load conditions for several hours.

The single burner test rig was constructed to permit the use of EV burners identical to those found in ABB's gas turbines. Care has also been taken to ensure that the burners tested in the atmospheric rig can be transferred directly without modification to the high-pressure test facility described below.

High-Pressure Test Rig. In October 1991, a high-pressure test facility was commissioned, which allows quick, cost-effective, and therefore extensive testing of single EV machine burners. Figure 6 shows the test rig along with the combustor liner. An axial compressor and then a two-stage radial compressor with intercooler are followed by a high-pressure air preheater to provide up to 5.5 kg/s (12 lb/s) nonvitiated combustion air at 16 bar (232 psi) and 500°C (932°F). The test rig consists of a plenum chamber upstream of the burner, two water-cooled tubular pressure vessels with 0.6 m inner diameter, and the rectangular chamber liner. The hot exhaust gases are quenched before the pressure reduction throttle and discharge to the chimney. A process control unit is used to operate the test rig independently from the microcomputer data logging system. Measurements relevant for the safe operation of the rig, such as fuel and air mass flows and a number of temperature and pressure readings, are directly connected to the process control unit and then passed on to the data logging system.

The liner is a nickel-base alloy construction, cooled convectively in order not to obscure genuine burner emissions by film cooling air effects. Optical access is provided by a fiber optical video system, which is mounted downstream of the burner in the flame tube. In addition, the plenum upstream of the burner is equipped with several windows, enabling direct observation of the mixing zone through the burner slots. Four water-cooled suction probes are mounted at different axial stations and are connected to the computer-controlled gas analysis system. Pressure fluctuations as well as static pressures are monitored at different positions in the flame tube. Temperature is measured at 40 different locations in the burner and the liner walls. Due to the easy accessibility of the burner and the water cooling of the test section, two separate burner studies can be carried out in less than 8 hours.

CO and H_2 are supplied in pressurized cylinders; liquid nitrogen is evaporated from a supply tank and subsequently mixed with the CO and H_2. The three mass flows are separately controlled and metered. The fuel supply system allows the syngas composition and dilution to be changed during a test run, which makes the testing very flexible and cost effective. About 30 minutes of full-load operation on syngas is possible with the amount of CO and H_2 stored in the pressurized cylinders.

Results of Ambient and High-Pressure Burner Tests

Burner tests have been carried out with a fuel composition equal to the oil gasification syngas (45 percent H_2, 48 percent CO, and 7 percent N_2). Oil gasification syngas is more difficult to burn in a premix flame (higher flame velocities) and will also give higher NO_x emissions (higher maximum flame temperature) than coal gasification syngas. NO_x emission values measured with this syngas composition in the full-scale high-pressure experiments can therefore be regarded as conservative estimate for coal gasification fuel in the gas turbine combustor. A burner capable of burning residual oil gasification syngas in a premix flame can also be operated on coal gasification syngas and will produce even lower NO_x emissions.

Ambient Pressure Tests. A large number of different injection geometries have been screened in atmospheric tests. Filled circles in Fig. 7 represent the NO_x emissions at atmospheric conditions for the injection geometry that yielded the lowest emissions at high pressure.

The emissions are plotted as a function of the nitrogen dilution. The air preheat and the combustor outlet temperature were set in order to match typical gas turbine operation conditions. From approximately 20 ppmvd (@ 15 percent O_2) for the undiluted syngas, emissions decrease to less than 2 ppmvd if the syngas is diluted with nitrogen to a heating value of 7.5 MJ/kg (175 Btu/scf). Measured CO emissions are less than 8 ppm over the whole range of heating values. No burner overheat or flashback was observed. Interestingly, the optimum gas turbine configuration did not deliver the best data in atmospheric tests. Much lower values could be measured for other configurations: Data values marked with filled triangles show the best configuration found for atmospheric conditions with NO_x emissions on the order of 2 ppmvd (@ 15 percent O_2) at 12 MJ/kg heating value. Atmospheric testing proved not to be of great value for defining the best injector.

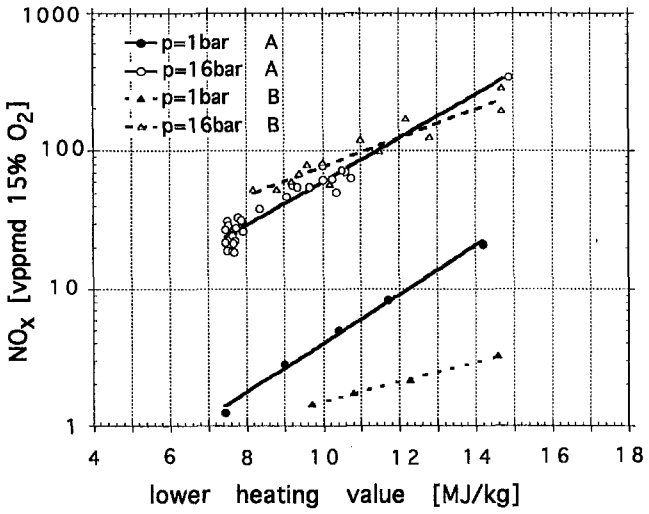

Fig. 7 NO_x emissions as a function of the lower heating value for MBtu fuels

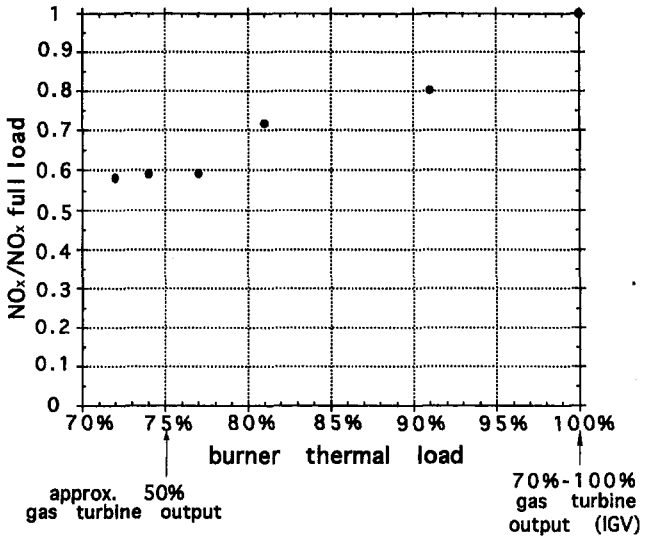

Fig. 8 NO_x emissions at part load

High-Pressure Tests. Data values marked with open circles in Fig. 7 show the results of the high-pressure tests at 16 bar (232 psi). The air preheat and the combustor outlet temperature were set in order to match typical gas turbine operation conditions. It is seen that the NO_x emissions are on the order of 350 ppmvd (@ 15 percent O_2) for undiluted syngas and decrease to less than 25 ppmvd (@ 15 percent O_2) if the syngas is diluted to 7.5 MJ/kg (175 Btu/scf). At a heating value comparable to coal gasification syngas (12 MJ/kg) the NO_x emissions are 120 ppmvd (@ 15 percent O_2), but one has to keep in mind that oil gasification syngas diluted to 12 MJ/kg (234 Btu/scf) has a higher hydrogen content than coal derived gas.

During the tests, burner temperatures were always close to the inlet air temperature, even if undiluted syngas was used. This ensures that safe operation (with higher NO_x emissions) is possible if the nitrogen dilution supply fails or if large heating value fluctuations occur during load changes of the gas turbine or the gasifier/ASU plant. The MBtu EV burner is of the same inherently safe design as the standard EV burner for natural gas operation. Burner noise was observed to be even lower than for natural gas operation. Due to the very compact reaction zone and the rapid mixing, perfect CO burnout was achieved. The strong decrease in NO_x emissions with falling heating value is caused by a more complete premixing of fuel and air. With increasing dilution the flame stabilizes downstream of the fuel injection nozzles, whereas in the undiluted case only partial premixing is possible upstream of the stabilization zone.

The NO_x emissions scale with pressure to the power of 0.8 to 0.9. This indicates that perfect premixing is not achieved with this type of fuel injection. It should be noted that other injection geometries gave lower emissions at atmospheric conditions, but had pressure scaling with exponents of more than 1.2, i.e., emissions at high pressure were 40 times higher than at ambient pressure. An example for this is given by the open and filled triangles in Fig. 7. For case A (triangles) the cross-sectional area of the injection holes was decreased by 40 percent compared to case B (circles). It must be concluded that low emissions at ambient pressure tests are a necessary but not sufficient condition for low emissions at high pressure. The reason for this is the strong nonlinear interaction of flame temperature, fuel/air mixing, and NO_x formation. Additionally, burners of smaller size produce considerably lower emissions in comparison to full-scale burners. However, this effect is not found for natural gas operation, since the characteristic mixing time of the injector (which is linearly coupled to the burner size) is only of major importance for MBtu combustion. In summary, it was found that only full-scale full-pressure burner experiments give reliable data concerning safe burner operation and emission values.

Part Load. The part-load performance was investigated in ambient pressure tests for injection geometry A. Figure 8 shows the NO_x emissions for burner thermal loads from 70 to 100 percent. As expected, NO_x emissions decrease with lower load (higher air equivalence ratio). In this load range, CO emissions were well below 8 ppmvd (@ 15 percent O_2) even at atmospheric conditions, which usually produce CO emissions substantially higher than high-pressure tests. Furthermore, if the compressor mass flow can be reduced by approximately 30 percent with a variable inlet guide vane system, these very low emissions can be sustained down to less than 50 percent gas turbine power output without the need for fuel staging. The high hydrogen content in the moderately diluted fuel and the rapid mixing in the near field of the burner are very advantageous in this context.

Steam Dilution. The effect of steam dilution was also investigated in the atmospheric test rig and compared to nitrogen dilution of a mixture with approximately equal volumetric content of hydrogen and carbon monoxide. Figure 9 shows that

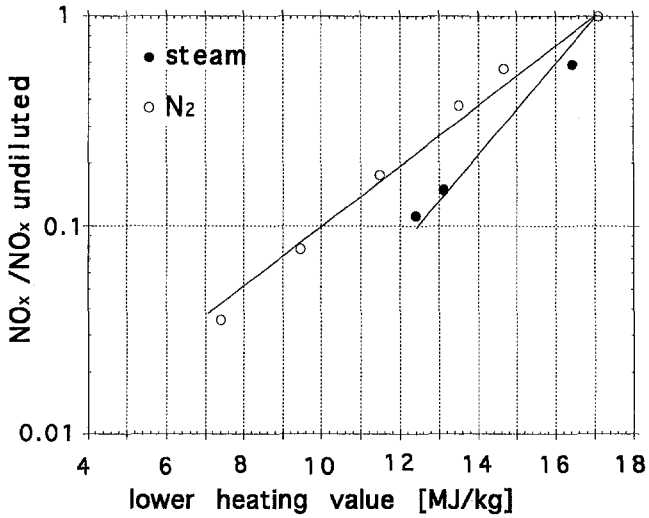

Fig. 9 NO_x emissions with steam injection compared to N_2 dilution

steam is more effective than nitrogen when a comparison is made on the basis of the lower heating value of the mixture. On the other hand, the nitrogen dilution technique is often economically superior to steam, due to the unfavorable costs of high-quality water. Additionally, a higher total plant efficiency can be reached with N_2 (Döbbeling et al., 1993). Steam dilution is an alternative if no nitrogen is available.

Numerical Flow Field Simulation

The optimization of the hole geometry and distribution requires appropriate numerical tools. A three-dimensional flow field simulation was used to study different injection geometries. A finite volume code with the $k-\epsilon$ turbulence model and a species transport equation for the fuel was used. With the knowledge of the local equivalence ratio and the temperature in the fuel air mixing zone, local laminar flame velocities and chemical time scales could be determined. Additional information on the turbulent properties of the flow field allows application of empirical correlations for the local turbulent flame velocity (Liu et al., 1989). A comparison of this turbulent flame velocity with the local convective velocity yields the zones where flame stabilization is most likely to occur. It is obvious that only those flames that stabilize far enough downstream of the fuel injection will allow the fuel to premix with sufficient quantities of air. For the numerical simulation, the flow field in the burner was assumed to be cyclically repetitive within the sector between two MBtu injection holes. With this simplification, a large number of grid cells can be used to discretize the fuel injection and premixing region. A total number of 50,000 computational cells was used.

Figure 10 shows a surface where the calculated turbulent flame velocity is 5 m/s in the burner flow field. A sector of the burner containing three MBtu injection holes is shown. The rapid decrease of the concentration on the axis of the fuel jets restricts high turbulent flame velocities to the near field of the injection nozzles and the interaction region of adjacent fuel jets, where turbulence levels are high.

Two principal modes of flame stabilization are shown in Fig. 11(a, b) for two different injection geometries. In Fig. 11(a) the flame front is seen to stabilize immediately downstream of the injection locations of each individual fuel jet, whereas in Fig. 11(b) flame stabilization is found far downstream of the fuel injection holes in a region where the jets reach the hot recirculation zone. A fuel injection geometry that stabilizes in regions of high fuel concentration (Fig. 11(a)) is certainly producing very high NO_x values. The very low NO_x values that can be achieved with premixed combustion of MBtu fuels need suitable fuel injection geometries, which delay flame stabilization until the fuel and air are mixed (see Fig. 11(b)).

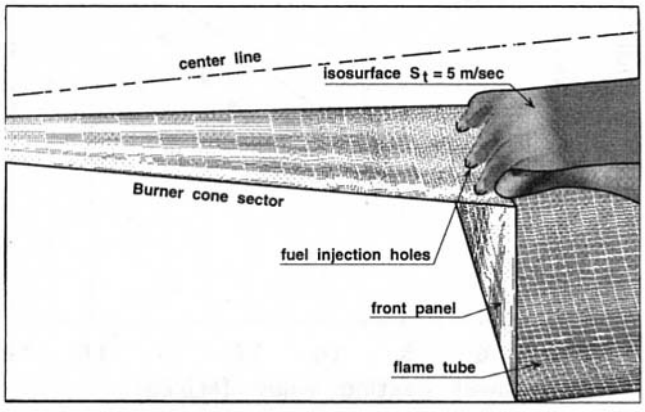

Fig. 10 Calculated turbulent flame velocity in the MBtu EV burner

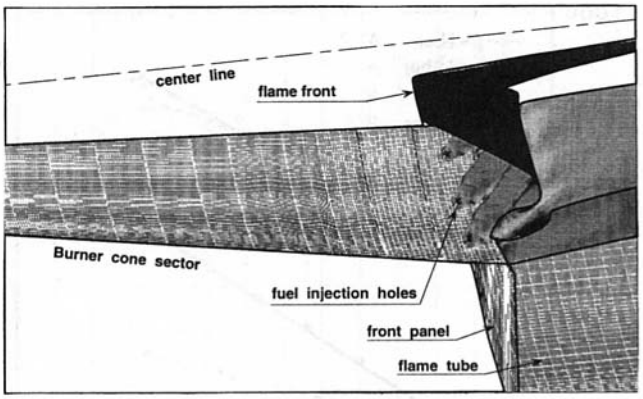

Fig. 11(a) Flame stabilization at the injection holes

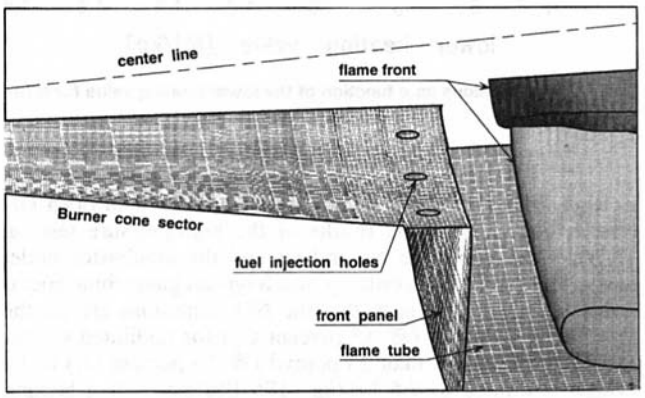

Fig. 11(b) Flame stabilization downstream of the burner (premix mode)

Fig. 11 Calculated flame front location in the MBtu EV burner for two different injection geometries

Conclusions

The ABB Double Cone Burner can be used for the premixed combustion of MBtu fuels, if a suitable fuel injection system is used. A full-scale burner has been tested at 1 and 16 bar pressure. It was found that with moderate nitrogen dilution of the syngas, NO_x emission levels less than 25 vppmd (@ 15 percent O_2) can be achieved at full gas turbine conditions. Since the properties of syngas fuels differ strongly from natural gas, and since the NO_x emissions exhibited a complicated, geometry-specific pressure dependency, only full-scale full-pressure tests give reliable results with respect to emissions and safe operation of a burner. The use of premix burners allows easy adaptation of standard gas turbines to MBtu fuels. Air extraction and water saturation or steam injection can be avoided. Numerical methods can be employed to predict the flame front location and to optimize the injection geometry of MBtu burners for minimum emissions. These numerical predictions will be used to extrapolate the experimental findings to different syngas compositions and gas turbine operating conditions.

References

Aigner, M., Mayer, A., Schiessel, P., and Strittmatter, W., 1990, "Second Generation Low-Emission Combustors for ABB Gas Turbines: Tests Under Full-Engine Conditions," ASME Paper No. 90-GT-308.

Aigner, M., and Müller, G., 1993, "Second-Generation Low-Emission Combustors for ABB Gas Turbines: Field Measurements With GT11N-EV," ASME JOURNAL OF ENGINEERING FOR GAS TURBINES AND POWER, Vol. 115, pp. 533–536.

Döbbeling, K., Knöpfel, H. P., Sattelmayer, T., Müller, P., and Reyser, K., 1993, "ABB's Medium Btu EV Burner for Syngas Applications—Test Results and GCC Integration Concept," presented at the Twelfth EPRI Conference on Coal Gasification Power Plants, San Francisco, CA.

Jury, W., Müller, P., and Reyser, K., 1992, "Gas Turbine (GT) Air Separation Unit (ASU) Integration for GCC: A Study based on ABB EV Burner Technology for Gas Turbines," presented at the EPRI Conference on Clean Coal Combustion Technology, San Francisco, CA.

Kee, R. J., Grcar, J. F., Smooke, M. D., and Miller, J. A., 1992, "A Fortran Program for Modeling Steady Laminar One-Dimensional Premixed Flames," Sandia Report Sand85-8240. UC-401.

Keller, J. J., Sattelmayer, T., and Thüringer, F., 1991, "Double Cone Burners for Gas Turbine Type 9 Retrofit Application," Paper No. G01, presented at the 19th International Congress on Combustion Engines (CIMAC), Florence, Italy.

Liu, Y., Lenze, B., and Leuckel, W., 1989, "Investigation on the Laminar and Turbulent Burning Velocity of Premixed Lean and Rich Flames of CH_4–H_2 Mixtures," presented at the 12 Int. Coll. on the Dynamics of Explosions and Reactive Systems (ICDERS), Ann Arbor, MI.

Miller, J. A., and Bowmann, C. T., 1989, *Prog. Energy Combustion Sci.*, Vol. 15, p. 287.

Sattelmayer, T., Felchlin, M. P., Haumann, J., Hellat, J., and Styner, D., 1992, "Second-Generation Low-Emission Combustors for ABB Gas Turbines: Burner Development and Tests at Atmospheric Pressure," ASME JOURNAL OF ENGINEERING FOR GAS TURBINES AND POWER, Vol. 114, pp. 118–125.

Senior, P., Lutum, E., Polifke, W., and Sattelmayer, T., 1993, "Combustion Technology of the ABB GT13E2 Annular Combustor," Paper No. G22, presented at the 20th International Congress on Combustion Engines (CIMAC), London, United Kingdom.

Strand, T., 1993, "Retrofitting a Low Emission Combustor to a Twin Shaft Gas Turbine," Paper No. G13, presented at the 20th International Congress on Combustion Engines (CIMAC), London, United Kingdom.

Residual Reactivity of Burned Gases in the Early Expansion Process of Future Gas Turbines

B. Leide

P. Stouffs

Laboratoire Artemis,
Ecole des Mines de Nantes-Isitem,
La Chantrerie C.P. 3023,
44087 Nantes, France

The present study investigates the chemical evolution of the burned gases in a first-stage nozzle operated under high inlet temperature and pressure conditions as they are foreseen for next-generation high-efficiency gas turbine machinery. Coupled aero-thermochemical simulations are performed up to the extreme case of stoichiometric combustion without ulterior dilution. The intent is to provide an estimation of possible consequences arising from the residual reactivity of gases downstream from the combustor. These consequences might affect the future design of the expansion path in order to render nonstationary chemistry compatible with aerodynamics, energetics, and environmental aspects.

1 Introduction

In order to improve thermal efficiency, gas turbines have been considerably developed in recent years with respect to their maximum working fluid temperatures and pressures. This evolution has been made possible by the progress in the fields of materials research (e.g., use of intermetallics, thermal barrier coating) and advanced cooling techniques (e.g., impingement, film, and evaporative cooling) as well as the aerodynamic research allowing higher pressure delivery by the compressor (e.g., transonic blade geometry). Ambitious research programs, like the Integrated High Performance Turbine Engine Technology (IHPTET), examine gas turbine operation at the highest available gas temperature, the one of stoichiometric firing near 2600 K. Reference [1] reviews actual US governmental and industrial initiatives. Reference [2] presents a survey of recent advances in the field of hot-path gas turbine material research.

The analysis of the *chemical evolution* of the working fluid in gas turbines is usually applied and limited to the combustion system sections (primary, intermediate, and dilution zones). However, the current trend toward higher turbine inlet temperature (TIT) could invalidate the assumption of frozen chemical composition of the gases downstream from the combustion system, that is in the first stages of the expansion turbine. As TIT gets higher than 1800 K, it becomes necessary to account for molecular *dissociation* and *recombination mechanisms* involving supplementary heat release. Given the extremely fast changing aerothermodynamic conditions (temperature, pressure, velocity) during expansion, the above-mentioned chemical mechanisms are assumed to be governed by kinetics. A coupled analysis with respect to both aerodynamics and chemistry becomes necessary when one aims to understand the impact of a chemically reactive working fluid on the flow evolution in this part of the engine. However, the literature review indicated only one existing work in the field of reactive expansion nozzle flow of gas turbines [3].

2 Chemistry in the Nozzle

Working Fluid Composition. The thermodynamic state and molecular composition of the mixture of burned gases entering into the first-stage guide nozzle of the expansion turbine is dependent on the type and actual operating conditions of the upstream combustion system. The future trend of gas turbine combustion systems that perform at high exit temperature levels will generally accelerate chemical kinetics of the fuel oxidation process. Thus, the mixture of burned gases that leaves the combustion system of these future engines can be characterized by putting forward the following two hypotheses:

Hypothesis 1: The gas mixture entering the nozzle is free of hydrocarbon molecules. The absence of hydrocarbon molecules marks an important difference with traditional reactive fluid modeling in the domain of gas turbines. The early-combustion *oxidative pyrolysis* is no longer to be included in the kinetic model.

For the present study, a second hypothesis is introduced:

Hypothesis 2: At the expansion turbine nozzle inlet, the equilibrium concentration for any considered species is attained, except for NO species. This assumption translates the acceleration effect for any kinetics in future combustion systems due to increased temperature levels. The NO species is excluded from this consideration because of the well-known significantly lower reaction velocities (for more detailed explanation see Section 4).

In order to respect the main dissociation/recombination mechanisms of the combustion products, the following species are retained for the present study: CO_2, CO, H_2O, H_2, H, OH, O_2, O, N_2, N, and NO.

The Kinetic Mechanism. The fluid undergoes rapidly changing temperature and pressure conditions while expanding through the nozzle. The temperature decrease enhances the chemical recombination of dissociated products, whereas the pressure decrease favors dissociation. Thus, the application of a kinetic mechanism composed of exclusively elementary bidirectional reactions becomes obligatory. Only the competition between the forward and backward progressing reactions can correctly describe the actual local fluid composition.

The adaption of the *Quasi-Global Approach,* originally reported by [5], to the actually considered situation is straightforward: the suppression of the global-step submodel for the hydrocarbon oxidation leads to an exclusively kinetic reaction mechanism.

The retained reactions are listed below:

Contributed by the International Gas Turbine Institute and presented at ASME Cogen Turbo Power '94, Portland, Oregon, October 25–27, 1994. Manuscript received by the International Gas Turbine Institute July 11, 1994; revision received April 24, 1995. Associate Technical Editor: E. M. Greitzer.

Elementary Kinetic Mechanism	
No.	Reaction
1	$CO + OH \rightleftharpoons CO_2 + H$
2	$OH + H_2 \rightleftharpoons H + H_2O$
3	$OH + OH \rightleftharpoons H_2O + O$
4	$O + H_2 \rightleftharpoons OH + H$
5	$H + O_2 \rightleftharpoons OH + O$
6	$O + H + M \rightleftharpoons OH + M$
7	$O + O + M \rightleftharpoons O_2 + M$
8	$H + H + M \rightleftharpoons H_2 + M$
9	$H + OH + M \rightleftharpoons H_2O + M$

In order to analyze pollutant formation history throughout the nozzle, it was decided to extend the above-cited reaction mechanism by incorporating the following *Zeldovich* mechanism for nitrogen oxide formation:

10	$O + N_2 \rightleftharpoons N + NO$
11	$N + O_2 \rightleftharpoons NO + O$
12	$N + OH \rightleftharpoons NO + H$

The resulting mechanism of 12 reactions/11 species satisfies the major requirement of studying the high-temperature dissociation/recombination phenomena and allows the survey of important pollutant formation such as CO and NO.

The Reactive-Fluid Equations. Each individual chemical species S_i is assumed to obey the *ideal gas law,* that is, Dalton's law is applicable. The equation of state for the gas mixture is then written as follows:

$$p = \sum_i \left(\frac{\rho_i}{M_i}\right) \Re T = \frac{\rho}{M} \Re T \tag{1}$$

When thermochemical calculations in reactive media are performed, the *absolute enthalpy*[1] has to be employed. It is constituted of the sensible enthalpy plus the chemical energy required for forming the chemical species from its naturally occurring elements at the same reference temperature.

$$h^* = \sum_i x_i (h_i(T) + \Delta h^o_{fi}) \tag{2}$$

[1] Not to be confused with *stagnation enthalpy.*

Note that the absolute enthalpy of the reactive ideal gas mixture is additionally pressure dependent via the molar fraction terms x_i. Considering an arbitrary reaction j and species i,

$$\sum_i \nu'_{ij} S_i \underset{k_{bj}}{\overset{k_{fj}}{\rightleftharpoons}} \sum_i \nu''_{ij} S_i \tag{3}$$

the rate-of-progress variable R_j is written as follows:

$$R_j = k_{f_j} \prod_i [S_i]^{\nu'_{ij}} - k_{b_j} \prod_i [S_i]^{\nu''_{ij}} \tag{4}$$

The forward reaction rates k_{fj} are computed by use of *Arrhenius* expressions in function of $\mathbf{A}_j$, $\mathbf{E}_j$, and $\mathbf{N}_j$ for the reactions 1 . . . 9 [5] and for the reactions 10 . . . 12 [6]:

$$k_{fj} = \mathbf{A}_j T^{\mathbf{N}_j} \exp\left(\frac{-\mathbf{E}_j}{\Re T}\right) \tag{5}$$

The backward reaction rates k_{bj} have been obtained by use of the tabulated equilibrium data K_{pj}, [7], the equilibrium relation (6), and Eq. (7) between K_{cj}, k_{fj} and k_{bj}:

$$K_{pj} = K_{cj} \left(\frac{p^o}{\Re T}\right)^{-\sum_i \Delta\nu_{ij}} \tag{6}$$

$$K_{cj} = \frac{\prod_i [S_i]^{\nu''_{ij}}}{\prod_i [S_i]^{\nu'_{ij}}} = \frac{k_{fj}}{k_{bj}} \tag{7}$$

With, by definition, the stoichiometric change of number of moles for species i in reaction j

$$\Delta\nu_{ij} = \nu''_{ij} - \nu'_{ij} \tag{8}$$

the net rate-of-generation ω_i of species i is obtained by summing over any reaction j where the ith species is involved:

$$\omega_i = \sum_j \Delta\nu_{ij} R_j \tag{9}$$

3 Nozzle Flow Model

Real flow fields in turbomachinery application present nonuniformities provoked by clearance effects, wake phenomena, and secondary flows and thus these flow fields are three dimensional. Unsteady pressure fluctuations, due to compressor operation and flame oscillations, occur in real operation at the expansion turbine intake.

Nomenclature

A = nozzle section, m^2
$\mathbf{A}$ = frequency factor
$\mathbf{E}$ = activation energy, J/mol
h^* = absolute enthalpy, J/kg, J/mol
Δh^o_{fi} = species formation enthalpy, J/mol
$\Delta H^o_{r,CH_4}$ = reaction heat of methane, J/mol
$k_{f,b}$ = forward/backward rates
$K_{p,c}$ = pressure/concentration based equilibrium constants
L = nozzle length, m
$\dot{m}$ = mass flux, kg/s
M = molar mass, kg/mol
n = volumetric products/dry air ratio
$\mathbf{N}$ = pre-exponential temperature exponent
p = pressure, Pa
p^o = reference pressure, 10^5 Pa
q = heat, J/mol
R = rate-of-progress variable, mol/m^3 s
$\Re$ = universal gas constant, J/mol K
S = atomic, molecular species
$[S]$ = species concentration, mol/m^3
t = time, s
T = temperature, K
T^0 = reference temperature, 298 K
v = velocity, m/s
x = molar fraction, mol/mol
z = nozzle axis, m
α = volumetric fuel/products ratio
ϵ = stoichiometric fuel/air ratio
η_{comb} = combustion efficiency
ν = stoichiometric number of moles
ρ = density, kg/m^3
ϕ = fuel richness
ω = species rate-of-generation, mol/m^3 s

Subscripts

diss = relative to molecular dissociation
i = summation index species
in = relative to nozzle inlet section
j = summation index reaction
noz = relative to location in the nozzle
out = relative to nozzle outlet section

Superscripts

$'$ = reactants
$''$ = products

Table 1 Simulation inlet conditions

	TIT	P	ϕ
case	K	*bar*	[–]
"1600"	1600	25.0	0.38
"1800"	1800	30.0	0.47
"2000"	2000	35.0	0.57
"2200"	2200	39.0	0.69
"2400"	2400	42.0	0.87
"2600"	2600	45.0	0.98

As the intent of the present work is to provide basic information about the interferences of the reactivity of the working fluid and its fluid-mechanical evolution throughout the nozzle flow, it was decided, in a first phase, to elaborate a stationary model with one spatial dimension only, here the nozzle axis z. Hence, the flow field is described by its cross-averaged characteristics. This approach offers the substantial advantage of a comparative study between reactive flow simulations over a wide range of nozzle input operational conditions: by imposing total flow uniformity for all cases, observed deviations on flow and fluid characteristics are exclusively due to chemistry and one can be sure that observations are free of masked fluid-dynamic side effects, which could be specific for individual simulation cases. Finally, the application of a frictionless and adiabatic flow model renders the simulation observations more comparative, as well.

The Flow Equations. The one-dimensional and stationary nozzle flow is then described by the mass Eq. (10), the momentum Eq. (11), and the energy Eq. (12):

$$d\dot{m} = d(\rho A v) = 0 \tag{10}$$

$$0 = v\frac{dv}{dz} + \frac{1}{\rho}\frac{dp}{dz} \tag{11}$$

$$0 = \frac{dh^*}{dz} + v\frac{dv}{dz} \tag{12}$$

The Nozzle Geometry. The one-dimensional nozzle geometry has been determined by approximating the given dimensions of the hot-core test turbine [8, 9]. The inlet section of a single nozzle $A_{in} = 1.544\ 10^{-3}$ m^2, the ratio of inlet to outlet sections $A_{in}/A_{out} = 2.8554$, and the chord length $L = 0.055$ m have been respected.

The geometry has been kept unchanged throughout the present study for each simulation case. The mass flow is recalculated in order always to correspond to Mach = 0.2 at the nozzle inlet. The nozzle outlet velocity during simulations is close to Mach = 0.8, which meets the cross-averaged exit Mach number [9].

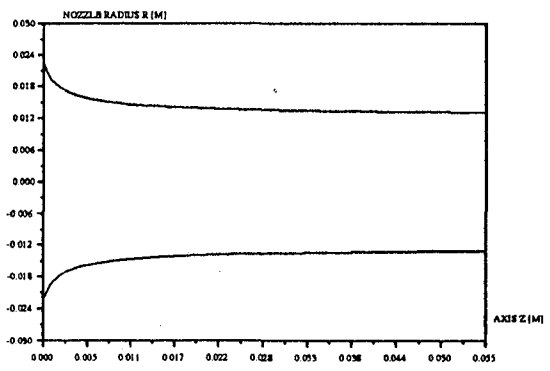

Fig. 1 The retained nozzle geometry

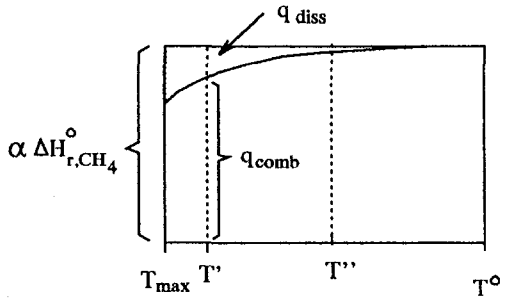

Fig. 2 Combustion efficiency as it is affected by dissociation (qualitative illustration)

4 Combustor Exit—Nozzle Inlet

Generic Combustion Model. A combustion model has been developed with respect to Hypotheses 1 and 2, which have been introduced in Section 2. The zero-dimensional model generates a burned-gas mixture as it is discharged from a methane/air gas turbine combustion system. As input data two operating conditions are required: the turbine inlet pressure and the combustion chamber exit temperature (TIT).

As oxidizer dry air with 21 percent oxygen and 79 percent nitrogen is employed. The corresponding combustion equation is written as follows:

$$\alpha CH_4 + \frac{1}{n}(0.21O_2 + 0.79N_2) \rightarrow x_{CO_2}CO_2 + x_{CO}CO + x_{O_2}O_2 + x_OO + x_{H_2O}H_2O + x_{OH}OH + x_{H_2}H_2 + x_HH + x_{N_2}N_2 + x_NN + x_{NO}NO \tag{13}$$

with the volumetric *fuel/products ratio* $\alpha = \phi\epsilon/n$, the fuel richness ϕ, the stoichiometric *fuel/air* ratio $\epsilon = 0.105$, the volumetric *products/dry air* ratio $n = 1.58/(2x_{N_2} + x_{NO} + x_N)$.

The molar composition is based on equilibrium data from the Janaf tables [7].

Table 1 lists the combustor outlet conditions that have been chosen for the present study. Case "1600" represents actual advanced gas turbine machinery. Case "2600" may be considered as the maximum amount of available turbine inlet temperature of real machinery with respect to *methane* fuel. This operational point was taken from data of a test turbine (cf., [8, 9]) with which stoichiometric combustion without ulterior dilution air supply has been experimented. Cases "1800" . . . "2400" have been aligned in between and are supposed to represent future evolution of combustion chamber exit conditions.

The Particular Case of NO. Particular remarks have to be given concerning the nitrogen chemistry because of slower reaction velocities than those reported for the hydrocarbon chemistry. Except for very fuel-rich conditions, the main NO contributions arise over a large range of combustion conditions (T, P, ϕ and residence time) from the *thermal–NO Zeldovich*

Table 2 Effect of dissociation heat

	$\lvert q_{diss}\rvert$	$\lvert q_{comb}\rvert$	η_{comb}
case	*J/mol*	*J/mol*	%
"1600"	13	31016	99.95
"1800"	46	37880	99.88
"2000"	143	45215	99.68
"2200"	405	53213	99.24
"2400"	1115	61834	98.23
"2600"	4454	70895	94.09

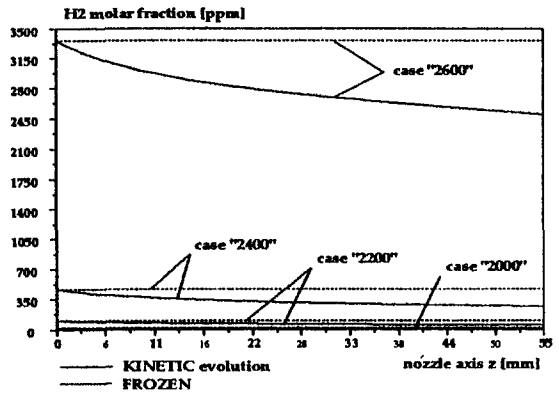

Fig. 3 H_2 evolution throughout the nozzle

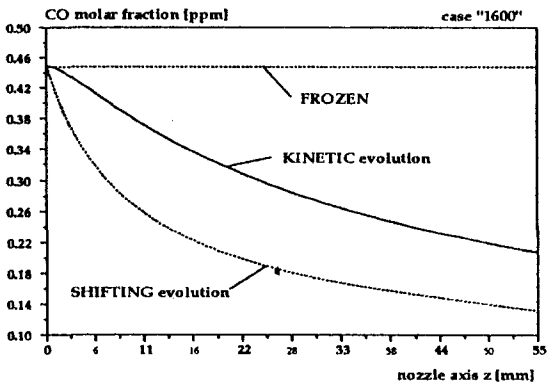

Fig. 6 CO evolution, case "1600"

formation mechanism. In actual gas turbine applications, the high-temperature primary combustion zone is mainly responsible for thermal NO formation. Especially when vortex-type recirculation zones increase the residence time in the primary zone, even the relative slow progressing rate of these reactions may deliver substantial concentrations of NO. Nevertheless, actually reported NO concentrations at the combustion chamber outlet lie largely below the ones that would be obtained by an equilibrium calculation at the corresponding local temperature.

With respect to the leading observations, the following assumption is made: The combustion model, used in order to reproduce the molar fluid composition at the combustion chamber outlet, sets the NO concentration to a tolerated-by-the-law emission level, that is 25 ppm.

As it is not the primary purpose of the present study, the present combustion model credits and anticipates this way the actual research programs for very low-NO producing gas turbine combustion systems.

Combustion Efficiency Affected by Lack of Molecular Recombination. The combustion efficiency η_{comb} can be defined as the ratio of released heat during combustion to the available heat in the fuel. Denoting q_{comb} the heat released by creation of one mole of products, this yields:

Table 3 Maximum deviation "kinetic-shifting" of molar fraction x_{CO}

	$\Delta x_{CO,max}$	$x_{CO,in}$	$\Delta x_{CO,max}/x_{CO,in}$
case	*ppm*	*ppm*	%
"1600"	0.11	0.45	24.4
"1800"	0.45	5.6	8.0
"2000"	1.13	45	2.5
"2200"	2.65	264	0.98
"2400"	6.72	1356	0.50
"2600"	48.60	9795	0.50

Table 4 Ratio of released heat over drop of absolute enthalpy

	$\lvert q_{noz}(L)\rvert$	$\lvert\Delta h^*_{noz}\rvert$	$q_{noz}(L)/\Delta h^*_{noz}$
case	J/mol	J/mol	%
"1600"	5	3649	0.1
"1800"	21	4165	0.5
"2000"	63	4702	1.3
"2200"	170	5275	3.2
"2400"	444	5914	7.5
"2600"	1254	6786	18.5

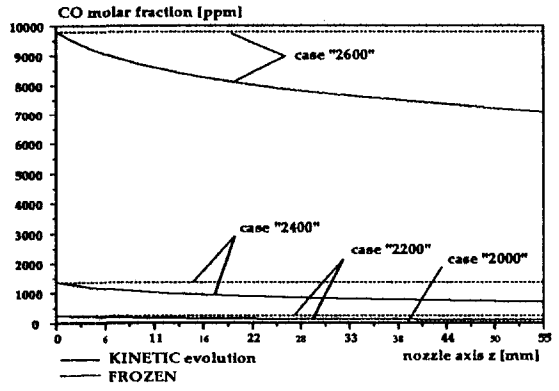

Fig. 4 CO evolution throughout the nozzle

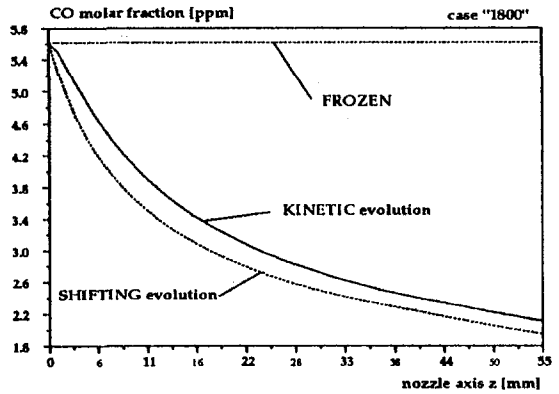

Fig. 5 CO evolution, case "1800"

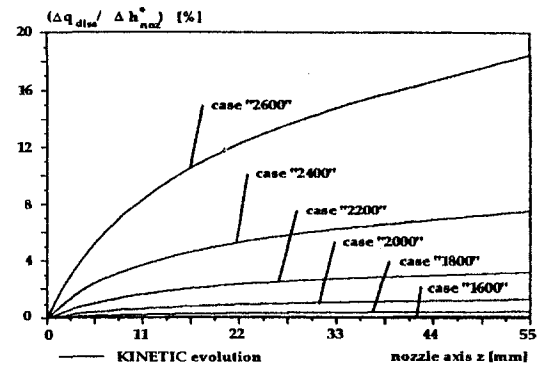

Fig. 7 Local ratio: $q_{noz}(z)/\Delta h^*_{noz}$

$$\eta_{\text{comb}} = \frac{q_{\text{comb}}}{\alpha \Delta H^o_{r,\text{CH}_4}} \tag{14}$$

with the heat of reaction (LHV) of methane:

$$\Delta H^o_{r,\text{CH}_4} = 2\Delta h^o_{f,\text{H}_2\text{O}} + \Delta h^o_{f,\text{CO}_2} - \Delta h^o_{f,\text{CH}_4} \tag{15}$$

While the combustion products are maintained at temperatures higher than $\simeq$1800 K, a significant part of species appear in their nonrecombined forms. As molecular recombination reactions are of exothermal nature, their noncompletion means that some chemical heat remains unreleased. Following our assumptions, the combustion products at the exit of the combustor are free of unburned hydrocarbon molecules. So, the difference between the maximum available heat release and the actual one is the chemical heat that the nonrecombined products retain, q_{diss}, which leads to the combustion efficiency with dissociated products only:

$$\eta_{\text{comb}} = \frac{q_{\text{comb}}}{\alpha \Delta H^o_{r,\text{CH}_4}} = 1 - \frac{q_{\text{diss}}}{\alpha \Delta H^o_{r,\text{CH}_4}} \tag{16}$$

Assuming equilibrium, Fig. 2 illustrates qualitatively how the heat release during combustion depends on the temperature of the products. It can be seen that only the temperature below T''', which is $\simeq$1600 K, could attain combustion efficiencies of $\eta_{\text{comb}} \simeq 1.0$, whereas all intermediate levels, T', up to the extreme case of stoichiometric combustion, $T_{\max}$, present growing amounts of q_{diss}. Thus, the combustion efficiency is affected. An estimation of this influence can be given easily. The heat released by reaction (13) is given by:

$$q_{\text{comb}} = \sum_i (x_i \Delta h^o_{fi}) - \alpha \Delta h^o_{f,\text{CH}_4} \tag{17}$$

Thus, the unreleased heat due to dissociation is given by:

$$q_{\text{diss}} = \alpha \Delta H^o_{r,\text{CH}_4} - \sum_i (x_i \Delta h^o_{fi}) + \alpha \Delta h^o_{f,\text{CH}_4} \tag{18}$$

q_{comb} and q_{diss} depend on temperature, pressure and richness via x_i and α. Table 2 shows the results obtained for the series of operational points introduced in Table 1.

The initiation of significant dissociation occurs at around 1800 K. Further temperature increase enhances the dissociation mechanisms and more heat is unreleased. Case "2600" shows that dissociation of the burned gases retains up to 5.9 percent of the available combustion heat.

At this point an important statement can be given: From the energetic point of view, the component downstream of the combustor should be able to recuperate this chemical heat by favoring molecular re-combination.

Model Coupling. After the input of the operating conditions at the combustion chamber outlet, (TIT, P), during a first phase, the generic combustion submodel reproduces the burned gas mixture composition. Because the molar composition of the gas mixture satisfies the equilibrium state, any chemical kinetic velocity vanishes in the nozzle inlet section, except for the reactions (10) . . . (12) involving NO (see Section 4). As soon as the fluid enters the nozzle, aerodynamics starts to modify fluid velocity, temperature, and pressure. The chemistry reacts and modifies the local molar gas mixture composition. The resulting chemical heat release is implicitly taken into account by employing the absolute enthalpy h^* (see Eqs. (2) and (12)).

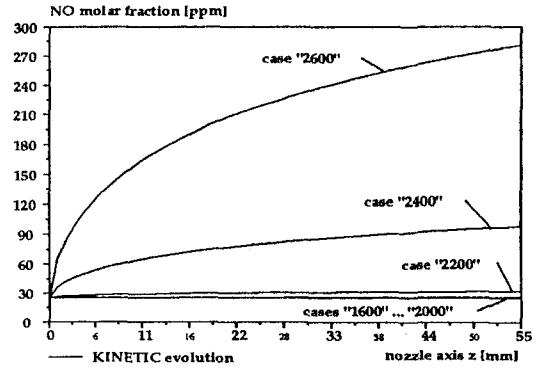

Fig. 8 NO evolution throughout nozzle from initial value 25 ppm

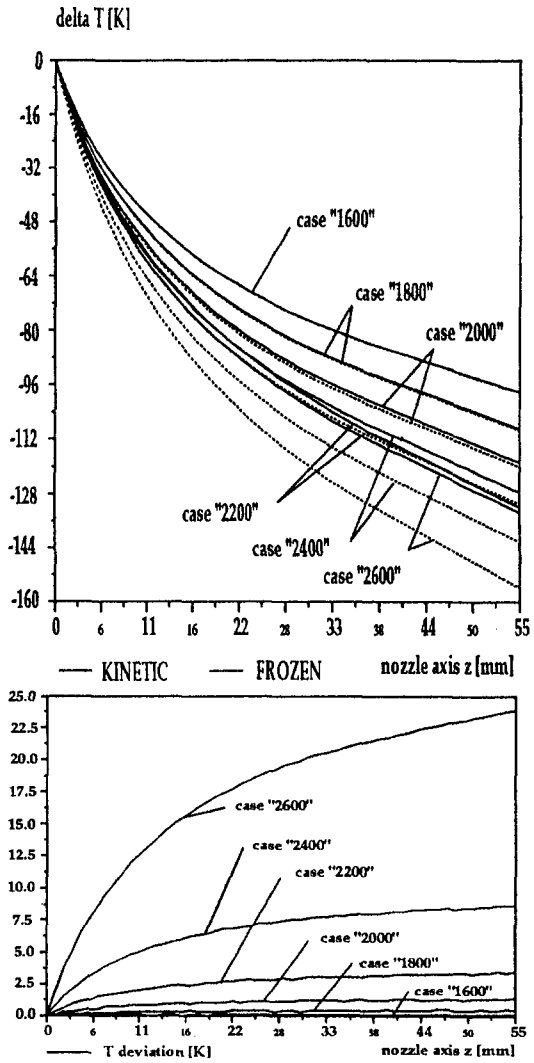

Fig. 9 $\Delta T = TIT - T(z)$ and temperature deviation: $T_{\text{kinetic}} - T_{\text{frozen}}$

The definition of q_{diss}, which has been introduced to describe the state of the fluid at the exit of the combustor, that is at the inlet of the nozzle, can be extended to describe the local state of the fluid in the nozzle. The chemical heat release from the nozzle inlet up to the location z can thus be written:

$$q_{\text{noz}}(z) = q_{\text{diss,in}} - q_{\text{diss}}(z) \tag{19}$$

so that $q_{\text{noz}}(L)$ represents the part of $q_{\text{diss,in}}$, which has been recovered via molecular recombination in the nozzle. (Refer to Fig. 7 and Table 4 in the following section.)

The code used in this study was the NEPTUNIX O.D.E. solver [10]. The independent variable is the nozzle axis z. As the nozzle geometry together with the chosen simulation intake conditions produces subsonic flows only, the stationary resolutions are performed as initial-value problems.

Simulation Scenarios. The reactive flow simulations have been performed for the nozzle intake conditions "1600" . . . "2600" (see Section 4) under the following three simulation

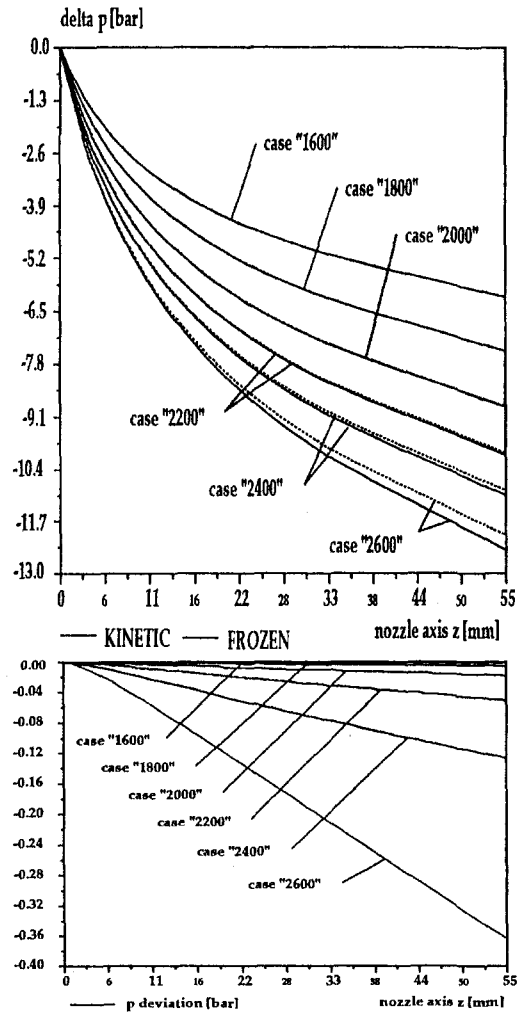

Fig. 10 $\Delta p = p_{in} - p(z)$ *and pressure deviation:* $p_{kinetic} - p_{frozen}$

scenarios, which differ substantially from the chemical point of view:

Scenario F: *frozen* molar fluid composition: any species is fixed at its equilibrium amount corresponding to the actual nozzle inlet conditions TIT, p, and ϕ; (except x_{NO} fixed at 25 ppm)

Scenario K: *kinetically* progressing fluid composition of the expanding gas mixture

Scenario S: temperature and pressure-dependent *shifting equilibrium* composition of the expanding gas mixture (except x_{NO} fixed at 25 ppm)

The first scenario (F) represents the traditional approach in the field of expansion-turbine flow modeling. The second one, (K), allows the fluid composition to progress according to local chemical reactivity by means of the kinetic species formation or consumption rates. The actual residence time intervenes and possibly *quenches*[2] the kinetic progression. The third scenario (S) assumes infinitely rapid kinetics. Everywhere in the nozzle, the molar fluid composition attains its equilibrium state. Henceforth, the maximum local chemical heat recuperation via molecular recombination is supposed in this third scenario.

5 Results

Molar Fluid Composition. Except for the evolution of carbon monoxide CO at low temperatures and nitrogen oxide NO in general, the following statement can be given as a significant result of the present study:

The kinetic flow simulations indicate insignificant deviations from shifting equilibrium fluid compositions.

Characteristic time scales of the molecular recombination chemistry here analyzed are smaller than those produced by the expanding nozzle flow. In other words, the local residence time throughout the nozzle flows allows chemical kinetics to progress toward equilibrium without being hindered by aerodynamic variation of temperature and pressure.

Figures 3 and 4 illustrate the situation for the simulation cases "2000" ... "2600" and the species H_2 and CO. In fact, the molar fraction evolutions corresponding to the kinetic and shifting scenarios are invisibly confined in the continued lines. The dashed lines trace the frozen molar fractions from the nozzle inlet section.

However, in cases "1600" ... "1800", that is at the low temperature end of the analyzed range, the CO oxidation is somewhat retarded. This effect is shown in Figs. 5 and 6. Relative to the inlet amount, the maximum deviation, located at z = 16 mm, peaks up to 24 percent in the lowest temperature case. As soon as the temperature level rises over 2000 K, the maximum deviations drop down to under 2.5 percent while being observed continuously closer to the nozzle front end. Table 3 indicates the maximum deviations $\Delta x_{CO,max}$ between the kinetic and shifting scenarios of CO species for all simulation cases.

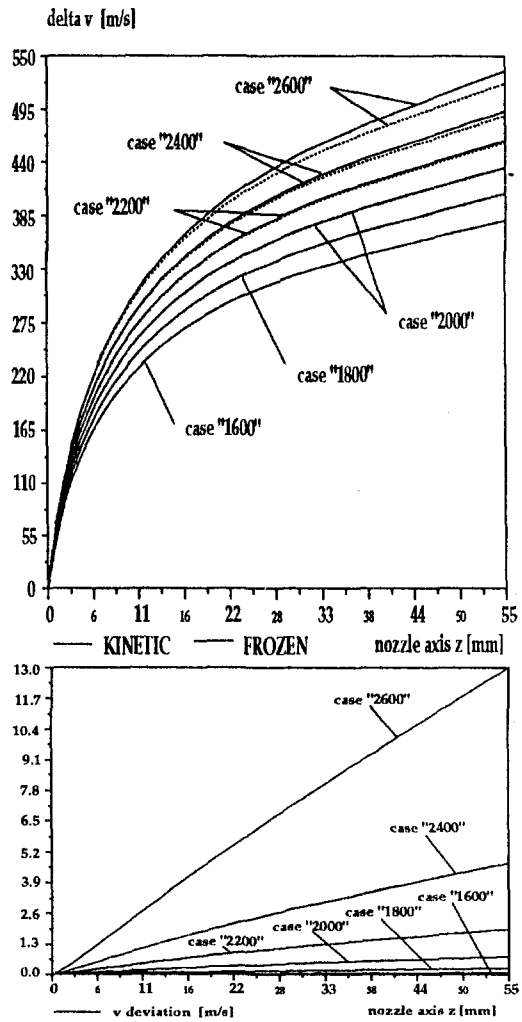

Fig. 11 $\Delta v = v_{in} - v(z)$ *and velocity deviation:* $v_{kinetic} - v_{frozen}$

[2] A well-known phenomenon in air-breathing trans- and supersonic combustion applications such as Ramjet engines (cf. [4, 5]).

Energetics. The local chemical heat release due to molecular recombination during the nozzle flow is presented in Table 4 and Fig. 7. It is compared to the drop of absolute enthalpy over the actual nozzle flow, $\Delta h^*_{noz} = h^*_{in} - h^*_{out}$. In the cases "1600" and "1800" the part of released chemical heat remains negligible, indicating the nearly complete recombination of combustion products that leave the upstream combustion system at these temperature levels. This proportion rises steadily as the temperature level increases. In the case of stoichiometric TIT, the chemical heat release amounts up to 18 percent of the drop of absolute enthalpy over the nozzle flow.

Environmental Aspects. From the environmental point of view, the behaviors of CO and NO species are of interest. The reader may refer to Figs. 4–6 for the results concerning CO. The NO formation mechanism (reactions 10 . . . 12) reacts in a significantly slower way than the recombination mechanism (reactions 1 . . . 9). However, the rising temperature level has an accelerating effect on NO formation. Figure 8 traces the evolution of the NO molar fraction and the latter effect can be seen starting from simulation case "2200" through "2600."

Aerodynamics. For the flow characteristics T, p, and v, only negligible deviations between kinetic and shifting scenarios are observed. Hence, their graphic representation is identical in Figs. 9 . . . 11 (continued lines). The dashed lines indicate the frozen scenarios, that is, the evolution of the expanding flow as it would be predicted without accounting for progressing chemistry. It can be seen that the difference between these two scenarios is not negligible as soon as TIT $\geq$ 2200 K.

6 Conclusions

1 For TIT $\geq$ 2000 K, the combustion efficiency is limited in the range of 99.7 . . . 94.1 percent due to lack of molecular recombination of the combustion products.

2 For TIT $\geq$ 2000 K, the local fluid composition in the nozzle attains equilibrium (except NO). Hence, the part of chemical heat contained in the dissociated products, that could be released according to local thermodynamic conditions, is fully recovered. Only the low temperature cases ("1600", "1800") indicate retarded recombination of CO. As CO equilibrium concentrations are extremely low for these temperature levels, the above-mentioned phenomenon has negligible energetic influence. However, it should be noted that the assumption of equilibrium composition at nozzle inlet tends to underestimate actually encountered CO concentrations for these combustion system exit temperatures.

3 For TIT $\geq$ 2200 K, the deviation in flow characteristics T and v, revealed by means of frozen-kinetic simulation comparisons, lie above actual aerodynamic precision ranges of prediction. Hence, future nozzle design calculations will have to abandon the traditional assumption of frozen fluid composition.

4 For TIT $\geq$ 2200 K, the nitrogen-oxide chemistry reacts within the nozzle residence time. Downstream NO-abatement methods will become necessary in order to guarantee low-emission gas turbine operation.

These results are based on a monodimensional flow modelization. Further work is necessary to take account of bi- or tridimensional effects, especially temperature field and fluid composition inhomogeneities.

Acknowledgments

This study is a result of a recently started research project at the Artemis laboratory (Prof. R. Gicquel, Ecole des Mines de Paris) in collaboration with the Catholic University of Louvain (Prof. P. Wauters and Prof. J. Martin) at Louvain-La-Neuve/Belgium and the University of Florence/Italy (late Prof. S. Stecco). The authors acknowledge the continuous interest and support of these institutes. As well they would express their special thanks toward Mr. F. Hirsinger at O.N.E.R.A./Châtillon for helpful discussions.

References

1 de Piolenc, M., Sept. 1992, "Latest Jet Engine Technology Could Radically Change Industrial Designs," *Gas Turbine World.*

2 Gras, J. M., 1992, "Matériaux de Turbines à Combustion—Evolution des Tendances," EDF-DER, Service IPN, Dép. SID, F-92141 Clamart.

3 Mencherini, A., 1993, "Alcuni Aspetti nella Simulazione della Combustione/Espansione nelle Turbine a Gas," Tesi di Laurea, Università di Firenze.

4 Schuetz, H., and Muehleck, P., 1991, "Influence of the Flight Trajectory on the Exhaust Gas Composition of a H_2-Fueled Air-Breathing Ramjet Engine," *Orbital Transports* Meteorological, Technical and Chemical Aspects. Springer Verlag, H. Oertl and H. Körner, eds., Braunschweig, 3rd Aerospace Symposium. Aug. 26–28.

5 Edelman, R. B., and Fortune, O. F., 1969, "A Quasi-Global Chemical Kinetic Model for the Finite Rate Combustion of Hydrocarbon Fuels With Application to Turbulent Burning and Mixing in Hyper-sonic Engines and Nozzles," presented at the AIAA 7th Aerospace Sciences Meeting, New York.

6 Miller, J. A., and Bowman, C. T., 1989, "Mechanism and Modelling of Nitrogen Chemistry in Combustion," *Prog. Energy Combust. Sci.,* Vol. 15, pp. 287–338.

7 Chase, M. W., Davies, C. A., Downey, J. R., Frurip, D. J., McDonald, R. A., and Syverud, A. N., 1985, *Janaf Thermo-chemical Tables,* 3rd ed., American Chemical Society, American Inst. of Physics, Nat. Bureau of Standards.

8 Szanca, E. M., Schum, H. J., and Hotz, G. M., 1974, "Research Turbine for High-Temperature Core Engine Application," NASA Technical Note D-7557, Washington, DC.

9 Goldman, L. J., and Seasholtz, R. G., 1982, "Laser Anemometer Measurements in an Annular Cascade of Core Turbine Vanes and Comparison With Theory," NASA Technical Paper 2018.

10 C. I. S. I.-Ingenierie. "NEPTUNIX-O.D.E. Solver and Model Description," Division Génie Logiciel et Application," 3 rue Lecorbusier, SILIC 232, F-94528 Rungis.

A Catalytic Combustor for High-Temperature Gas Turbines

N. Vortmeyer

M. Valk

G. Kappler

Lehrstuhl für Flugantriebe,
Technische Universität München,
München, Federal Republic of Germany

Catalytic combustion has been the subject of thorough research work for over two decades, mainly in the U.S. and Japan. However, severe material problems in the ceramic or metallic monolith prevented regular operation in most cases. Still, during these two decades, turbine inlet temperatures were raised remarkably, and lean premix combustors have become standard in stationary gas turbines. In view of these facts, a simple "monolith-in-tube" concept of a catalytic combustor was adapted for the use in high-temperature gas turbines. Its essential feature is the fact that a considerable portion of the homogeneous gas phase reaction is shifted to the thermal reactor, thus lowering the catalyst temperature. This is achieved by the employment of very short catalyst segments. The viability of this concept has been demonstrated for a variety of pure hydrocarbons, alcohols as well as common liquid fuels. Extensive experimental investigations of the atmospheric combustor led to the assessment of parameters such as reference velocity, fuel-to-air ratio, and fuel properties. The maximum combustor exit temperature was 1673 K with a corresponding catalyst temperature of less than 1300 K for diesel fuel. Boundary conditions were in all cases combustion efficiency (over 99.9 percent) and pressure loss (less than 6 percent). Additionally, a model has been developed to predict the characteristic values of the catalytic combustor such as necessary catalyst length, combustor volume, and emission characteristics. The homogeneous reaction in the thermal reactor can be calculated by a one-dimensional reacting flow model.

Introduction

Catalytic combustion has been the subject of thorough research work for over two decades because of their often proven low emission capabilities. But up to now no commercial application to engine combustors have appeared. Most of the designers of catalytic combustors consider the very short life expectation of the catalyst under typical gas turbine temperature conditions as reason for this fact. Figure 1, showing two catalytic combustors of North American (Ekstedt et al., 1982) and Japanese (Kitajima and Kajita, 1989) origin, represents the advanced design of this combustor type, nevertheless exhibiting overly high catalyst temperatures.

The upper allowable temperature for actual catalytic material for oxidation of hydrocarbons and carbon monoxide is about 1273 K (1,000°C) (Wolsing et al., 1990; Öser and Brandstetter, 1984; Kawakami et al., 1989). It cannot be supposed that catalyst manufacturers will place at our disposal in the near future materials that can withstand the maximum flame temperatures in the premix burners of modern high-temperature gas turbines.

One concept to overcome this problem is shown on the left-hand side of Fig. 2. The catalytic combustor for fuel gas uses a triple-staged fuel injection system with one injection device behind the catalyst in the thermal reactor, thus limiting the catalyst temperature to approximately 1073 K (800°C) (Furuya et al., 1987).

Similarly, the catalytic combustor presented in this paper was developed with the aim of keeping the catalyst temperature well below the maximum flame temperature without tertiary fuel injection into the thermal reactor. As can be seen on the right-hand side of Fig. 2, this is achieved by employing very short catalyst segments and/or high flow velocities. Thus a considerable portion of the homogeneous gas phase reaction is shifted to the thermal reactor behind the catalyst, in turn lowering catalyst temperature.

Apparatus and Instrumentation

The atmospheric test combustor is shown in Fig. 3. The inner diameter of 11 cm was chosen in accordance with the air flow capacity of the combustor test rig to simulate reference velocities of 10 to 30 m/s at a maximum combustor inlet temperature of 700 K. To avoid imperfections in fuel–air mixing, static mixers were integrated into the premixing/prevaporizing section. This part of the combustor is followed by the catalytic reactor and the thermal reactor with a length of 2 m. The catalytic reactor is shown additionally in enlargement in the lower right part of Fig. 3.

The instrumentation of the test rig focused mainly on two tasks: observation of the gas phase reaction in the thermal reactor initiated by the catalyst and registration of catalyst temperature. The latter was attained by inserting very thin thermocouples into the structure of the catalyst. A bend with an observation window (OW) in the test rig allowed a (qualitative) visual assessment of the radial uniformity of combustion in the monolith via color tone. After leaving the catalyst, gas samples (X) were taken from the reacting gas at fixed axial distances, as illustrated in Fig. 4. These samples were analyzed on their content of unburned hydrocarbons (UHC), carbon monoxide (CO), nitrogen oxides (NO_x), and carbon dioxide (CO_2). Together with data from thermocouple measurements (T) this makes it possible to follow the progress of the reaction in the thermal reactor from the catalyst exit plane to complete combustion. UHC data specify the summation of all hydrocarbon species because of the use of a flame ionization detector (FID).

The test combustor was fueled with three different groups of fuels: paraffins, alcohols, and commercial liquid fuels. Range of operation was limited by the requirements of at least 99.9 percent combustion efficiency at the end of the thermal reactor (CO $<$ 20 ppm, HC $<$ 2 ppm). The maximum of pressure loss was 6 percent. Additionally, catalyst temperature never exceeded 1300 K up to a maximum flame temperature (equals combustor exit temperature) of 1673 K.

Contributed by the International Gas Turbine Institute and presented at the 39th International Gas Turbine and Aeroengine Congress and Exposition, The Hague, The Netherlands, June 13–16, 1994. Manuscript received by the International Gas Turbine Institute February 19, 1994. Paper No. 94-GT-211. Associate Technical Editor: E. M. Greitzer.

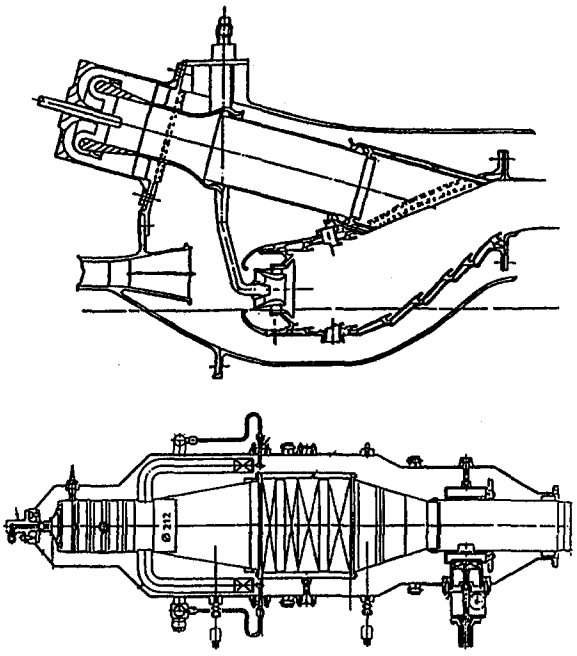

Fig. 1 Catalytic combustors of North American (Ekstedt et al., 1982) and Japanese (Kitajima and Kajita, 1989) origin

Results

Figure 5 shows a typical thermal reactor flame, resulting from combustion of propane. The catalyst of 40 mm length caused a pressure loss of 2.35 percent. The figure reports the mole fraction of CO and UHC and measured temperature in the thermal reactor flow plotted against the axial distance from catalyst exit plane. It reveals a typical profile of combustion of hydrocarbons: The fast decomposition of hydrocarbons is accompanied by production of the intermediate CO, which is burned after autoignition of the mixture, characterized by a steep increase of gas temperature. The relatively slow oxidation of CO determines the required length of the thermal reactor for complete combustion. In this case complete combustion with less than 10 ppm CO and less than 1 ppm UHC was attained after a reactor length of 0.80 cm; maximum temperature of catalyst was about 70 K below combustor exit temperature. No NO_x emissions were found for the catalytic combustion of propane, with an attained maximum flame temperature of 1600 K.

The measured data of Fig. 5 were compared to calculated values of the mole fractions of CO and UHC and gas temperature. To model homogeneous gas phase combustion in the thermal reactor, the stationary one-dimensional conservation equations of a chemical reacting multicomponent flow were used (Kee et al., 1980), written as

$$\dot{m}\cdot\frac{dT}{dx}-\frac{A}{c_p}\cdot\frac{d}{dx}\left(\lambda\cdot\frac{dT}{dx}\right)+\frac{A}{c_p}\sum_{i=1}^{I}\rho Y_i V_i c_{p,i}\frac{dT}{dx}+\frac{A}{c_p}\sum_{i=1}^{I}M_i\dot{\omega}_i'''h_i=0$$

$$\dot{m}\cdot\frac{dY_i}{dx}+\frac{d}{dx}(\rho A Y_i V_i)-A\dot{\omega}_i'''M_i=0$$

$$\dot{m}=\rho w A$$

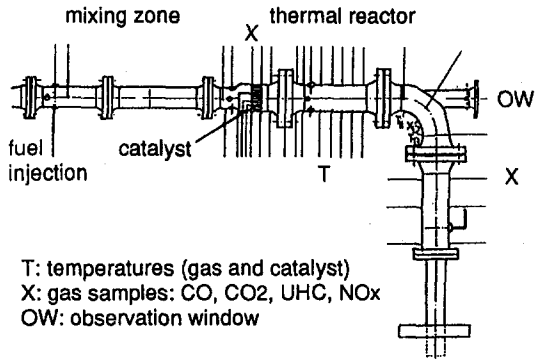

Fig. 4 Probe location

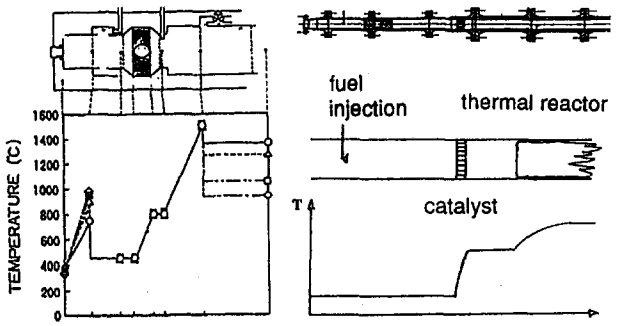

Fig. 2 Catalytic combustors with catalyst temperatures below flame temperature. Left: combustor with triple-staged fuel injection (Furuya et al., 1987); right: concept presented in this paper: the homogeneous flame induced by the short catalyst is shifted to the thermal reactor.

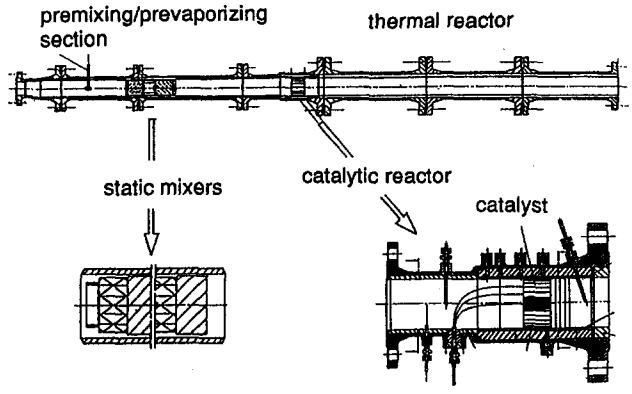

Fig. 3 Catalytic test combustor

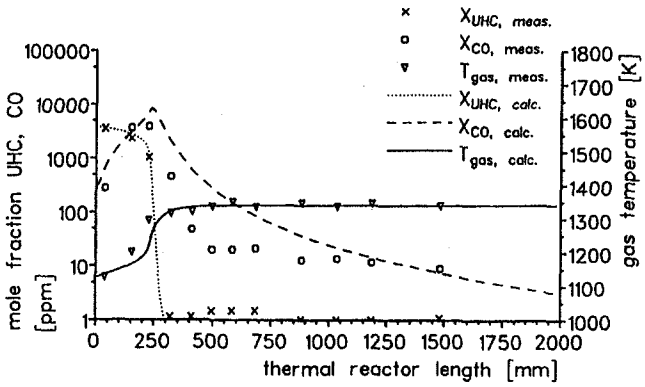

Fig. 5 Comparison of measured and calculated profiles of CO and UHC content and gas temperature in the thermal reactor (fuel: propane; catalyst length: 40 mm; equivalence ratio: 0.28; reference velocity: 15.6 m/s; thermal reactor inlet temperature: 1125 K; flame temperature: 1341 K; maximum catalyst temperature: 1274 K)

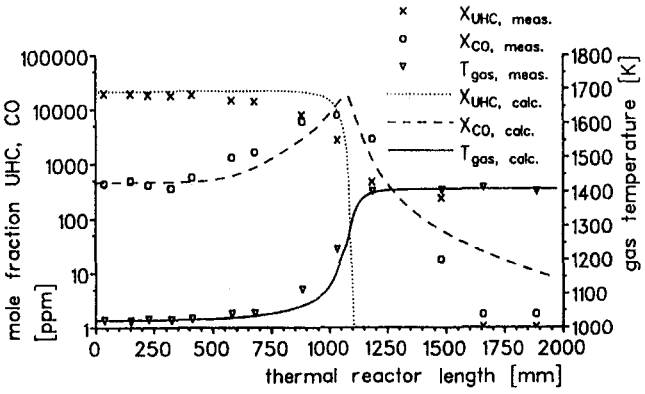

Fig. 6 Comparison of measured and calculated profiles of CO and UHC content and gas temperature in the thermal reactor (fuel: methanol; catalyst length: 20 mm; equivalence ratio: 0.32; reference velocity: 17.6 m/s; thermal reactor inlet temperature: 1023 K; flame temperature: 1406 K; maximum catalyst temperature: 1300 K)

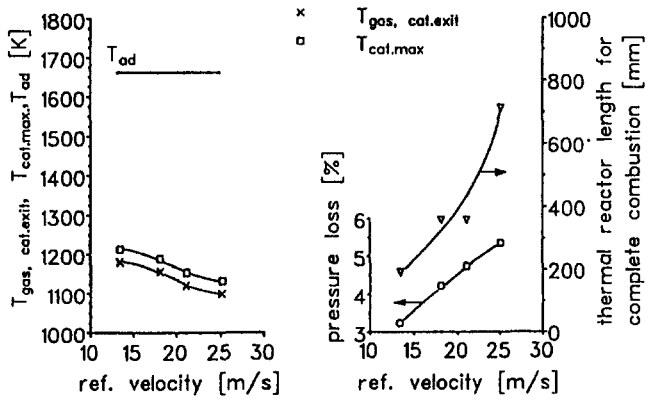

Fig. 7 Influence of reference velocity on characteristic combustor parameters at constant equivalence ratio (diesel fuel; catalyst length: 60 mm; catalyst inlet temperature: 596 K)

To calculate chemical reaction, the reaction mechanism developed by Westbrook and Pitz (1984) for combustion of propane and propene (WP84) with 163 elementary reactions and 41 species was integrated. The measured data of gas composition and gas temperature at the catalyst exit were used as inlet conditions for the calculation with the above-mentioned equations:

$$Y_{i,x=0} = Y_{i,\text{cat.exit}}$$

$$T_{x=0} = T_{\text{gas,cat.exit}}$$

Numerical solution was executed with the program PREMIX (Kee et al., 1980) of the program package CHEMKIN (Kee et al., 1985).

Figure 5 shows a good agreement between calculated and measured data of CO, UHC, and gas temperature; no modifications of reaction constants of the WP84 mechanism were done.

Figure 6 gives a comparison of calculated and measured profiles of CO, UHC, and gas temperature for a thermal reactor flame behind a catalyst of merely 20 mm length, here from the combustion of methanol. The pressure loss of the catalytic combustor was about 2.2 percent. Complete combustion was attained after a thermal reactor length of 1.5 m. Catalyst temperature was more than 100 K below maximum flame temperature. Again, as in the case of propane combustion no NO_x could be found. This circumstance was stated for all nitrogen-free fuels.

Calculated profiles of Fig. 6 were obtained by inserting into the above-mentioned equations a reaction mechanism for methanol oxidation introduced by Norton and Dryer (1989). Again agreement of calculated and measured data is satisfactory.

The information presented in Figs. 5 and 6 allows a convincing explanation of the principle of the presented catalytic combustor. The catalyst's task is to raise the gas temperature via heterogeneous catalyzed surface reactions up to a level allowing autoignition and following complete combustion of the partially oxidized mixture entering the thermal reactor. The initiated thermal oxidation is sustained solely by mechanisms of homogeneous high-temperature combustion. The catalyst forms no chemical species that noticeably enhance or retard the progress of thermal combustion.

The combustion of commercial diesel fuel is illustrated in Fig. 7. An increase of combustor heat release is attained by raising reference velocity, keeping the equivalence ratio of mixture constant. The increase of reference velocity causes reduced residence time of the gas in the catalyst, thereby decreasing the amount of fuel oxidized inside. The smaller the amount of fuel burned in the catalyst, the lower the temperature of the gas entering the thermal reactor and the maximum catalyst temperature. Subsequently, the lower gas temperature leads to a prolongation of ignition delay time. Thus, the increase of reference velocity causes a disproportional extension of required thermal reactor length for sufficient combustion efficiency (less than 20 ppm CO and 2 ppm UHC). It should be mentioned that the combustion of the diesel fuel containing a small amount of nitrogen yielded NO_x emissions of 2 ppm maximum.

The influence of increasing combustor heat release rate by raising equivalence ratio on combustor operation is illustrated in Fig. 8. Holding reference velocity constant, the percentage of fuel burned inside the catalyst remains approximately constant, thus raising the temperature level of the catalyst. Hence, higher flame temperatures and thermal reactor inlet temperatures cause a considerable reduction of required thermal reactor length for increasing equivalence ratio.

Additionally, combustor operation depends on the length of the catalyst. The comparison of the results of catalysts of 40 and 60 mm length shown in Fig. 8 reveals that the shorter one oxidizes less fuel under same operating conditions, thus showing a lower exit gas temperature and a lower catalyst temperature. The consequence is a substantial increase in required thermal reactor volume for the shorter catalyst, with the beneficial effect of lower catalyst temperatures under the same operating conditions.

Summary and Conclusions

A main drawback to the application of catalytic combustors in modern high-temperature gas turbines is the limited life ex-

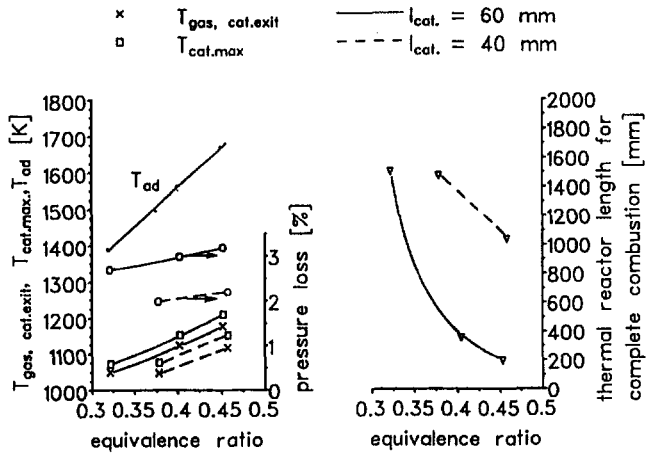

Fig. 8 Influence of equivalence ratio and catalyst length on characteristic combustor parameters at constant reference velocity (diesel fuel; reference velocity: 13.5 m/s; catalyst inlet temperature: 580 K)

pectancy of a catalyst under typical combustor temperature conditions. As a possible solution to this problem, a combination of a catalyst and a following thermal reactor was tested. This configuration proved its ability to attain complete combustion with acceptable pressure losses over a broad range of operation, keeping catalyst temperatures well below maximum flame temperature. Data were presented for the combustion of propane, methanol, and diesel fuel. The homogeneous gas phase combustion in the thermal reactor can be calculated by a one-dimensional model, using current reaction mechanisms.

This catalytic premix combustor has to be compared now to swirl-stabilized combustors, which are already being used successfully in stationary gas turbines. Burning very lean mixtures, catalytic combustors exhibit a flame stability superior to that of a swirl-stabilized premix burner. This fact is illustrated by Fig. 5, showing a clean and stable combustion of propane with a maximum flame temperature of 1341 K.

Considering the actual combustor temperature level of modern high-temperature gas turbines, it can be recognized that even a swirl-stabilized burner provides sufficient flame stability for operation. Future work should therefore focus on the question of whether a catalytic combustor keeps its well-known advantages such as low NO_x emissions compared to the introduced swirl-stabilized burner even in the high-temperature region.

References

Ekstedt, E. E., Lyon, T. F., Sabla, P. E., and Dodds, W. J., 1982, "NASA Clean Catalytic Combustor Program," ASME Paper No. 82-JPGC-GT-11.

Furuya, T., Hayata, T., Yamanaka, S., Koezuka, J., Yoshine, T., and Ohkoshi, A., 1987, "Hybrid Catalytic Combustion for Stationary Gas Turbine—Concepts and Small Scale Test Results," ASME Paper No. 87-GT-99.

Glassman, I., 1987, *Combustion,* 2nd ed., Academic Press, Orlando, FL.

Kawakami, T., Furuya, T., Sasaki, Y., Yoshine, T., Furuse, Y., and Hoshino, M., 1989, "Feasibility Study on Honeycomb Ceramics for Catalytic Combustor," ASME Paper No. 89-GT-41.

Kee, R. J., Miller, J. A., and Jefferson, T. H., 1980, "CHEMKIN: A General-Purpose, Problem-Independent, Transportable, Fortran Chemical Kinetics Code Package," SAND80-8003, Sandia National Laboratories, Albuquerque, NM.

Kee, R. J., Grcar, J. F., Smooke, M. D., and Miller, J. A., 1985, "A Fortran Program for Modeling Steady Laminar One-Dimensional Premixed Flames," SAND85-8240, Sandia National Laboratories, Albuquerque, NM.

Kitajima, J., and Kajita, S., 1989, "Catalytic Combustor for Small Gas Turbine: Combustor Development," ASME Paper No. 89-GT-265.

Norton, T. S., and Dryer, F. L., 1989, "Some New Observations on Methanol Oxidation Chemistry," *Combustion Science and Technology,* Vol. 63, pp. 107–129.

Öser, P., and Brandstetter, W., 1984, "Grundlagen zur Abgasreinigung von Ottomotoren mit der Katalysatortechnik," *Motortechnische Zeitschrift,* Vol. 45, p. 201ff.

Westbrook, C. K., and Pitz, W. J., 1984, "A Comprehensive Chemical Kinetic Reaction Mechanism for Oxidation and Pyrolysis of Propane and Propene," *Combustion Science and Technology,* Vol. 37, pp. 117–152.

Wolsing, W. F., Kruse, W., Punke, A., and Rickert, G., 1990, "Tendenzen der Katalysatorentwicklung für moderne Ottomotoren," Bericht Fa. Engelhard Kali-Chemie.

S. Honami

T. Shizawa

Department of Mechanical Engineering,
Science University of Tokyo,
Tokyo, 162, Japan

A. Sato

Aero-Engine and Space Operations,
Ishikawajima-Harima,
Heavy Industries Co., Ltd.,
Tokyo, Japan

H. Ogata

Jet Engine Division,
Kawasaki Heavy Industries Ltd.,
Kobe, Japan

Flow Behavior With an Oscillating Motion of the Impinging Jet in a Dump Diffuser Combustor

This paper presents flow behavior with an oscillating motion of an impinging jet upon a flame dome head and its reattachment to the casing wall, when a distorted flow is provided at the inlet of the dump diffuser combustor. A Laser-Doppler Velocimeter was used for the measurements of the time-averaged flow within a sudden expansion region. A surface pressure fluctuation survey on the flame dome head and flow visualization by a smoke wire technique with a high-speed video camera were conducted from the viewpoint of the unsteady flow features of the impinging jet. There exists a high-vorticity region at the jet boundary, resulting in the production of turbulence kinetic energy. In particular, higher vorticity is observed in the higher velocity side of the jet. The jet near the dome head has favorable characteristics about the flow rate distribution into the branched channel. Reynolds shear stress and turbulence energy are produced near the reattachment region. The jet has an oscillating motion near the dome head with asymmetric vortex formation at the jet boundary.

Introduction

It is important to obtain the uniform temperature profile at the exit of the combustor of the gas turbine engine, regardless of flow conditions such as the distorted velocity profiles due to the operating condition of the compressor and the misassembling in the maintenance process. In order to protect the thermal fatigue of the blade material and to reduce NO_x formation, the favorable characteristics of the flow rate distribution into the branched annular channels have been requried. The dump diffuser combustor, which has a blunt shape at the flame dome head and a sudden expansion region at the diffuser section, has been developed to obtain better characteristics compared with the conventional shape with the gradual changes in the area ratio.

Recent aeroengine combustors have been of the dump diffuser type because of the reason mentioned above. However, the flow behavior within the dump diffuser in the combustor has been less understood, although the performance of the pressure loss and the geometric parameter affecting the diffuser performance have been investigated by many authors. The aerodynamic performance of the annular type diffuser, the prediffuser geometry, and the influence of the inlet flow condition on the diffuser performance have been discussed by Biaglow (1971), Fishenden and Stevens (1974), Stevens et al. (1976), Klein et al. (1974, 1980), and Honami and Morioka (1990).

In the present paper the flow has an inlet distortion due to the installation of the distortion bar upstream of the diffuser. The detailed flow behavior is discussed from the viewpoints of the time-averaged and fluctuated flow fields. In particular, the mean velocity and Reynolds stress profiles with two components in the sudden expansion region were measured by a Laser-Doppler Velocimetry (LDV) system with a frequency shifter. The survey of surface pressure fluctuation on the flame dome clarifies the unsteady behavior of the branched flow oscillation. The flow visualization by a smoke wire technique associated with a high-speed video camera gives a better understanding of the dynamic behavior of the jet oscillation issuing from the prediffuser. The oscillating motion due to the vortex formation at the edges of the shear layer of the jet introduces the favorable characteristics of the flow rate distribution.

Experimental Apparatus and Procedures

Figure 1 shows the experimental test apparatus. The detailed description on the test rig was provided by Honami and Morioka (1990). A two-dimensional channel configuration is used in the present experiment instead of the annular one used in the actual combustor. The height in the inlet and test sections of the channel is 20 mm. The branched section of the channel consists of parallel walls. The branched channels are commonly connected with a large reservoir. The area expansion ratio of the diffuser exit to the inlet section is 2.0. The aspect ratio of the width of the inlet and branched sections to the height is 15 to obtain a two-dimensional flow at the midspan. The flame dome has a semicircular shape 50 mm in radius. The prediffuser geometry with an opening angle of 10 deg is used. The dump gap of 3.0 between the prediffuser exit and the flame dome head is employed as the reference configuration, which is discussed in detail in the following section. Station 1 upstream of the prediffuser inlet, which is defined as the reference station, station 2 at the prediffuser exit, and station 3 at the branched channel exit are selected as representative stations in the streamwise direction. A coordinate system where the Z coordinate is taken in the spanwise direction is also illustrated in Fig. 1. A two-dimensional distortion bar with a rectangular cross section having a blockage area of 20 percent of the channel height is installed near the nozzle exit, in order to obtain the distorted velocity profile at the reference station. The nondimensional vorticity of 0.3 was obtained at the channel center of the reference station.

Figure 2 shows the optical arrangement and the data acquisition system of LDV, which is employed for the measurements of velocity components, U and V, in X and Y directions in the sudden expansion region. LDV is of the forward scattering type with a 15 mW He–Ne light source. A frequency shifter of

Contributed by the International Gas Turbine Institute and presented at the 39th International Gas Turbine and Aeroengine Congress and Exposition, The Hague, The Netherlands, June 13–16, 1994. Manuscript received by the International Gas Turbine Institute February 19, 1994, Paper No. 94-GT-233. Associate Technical Editor: E. M. Greitzer.

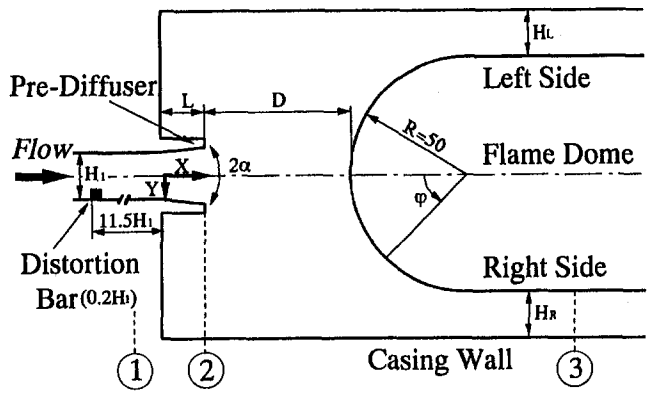

Fig. 1 Experimental test apparatus

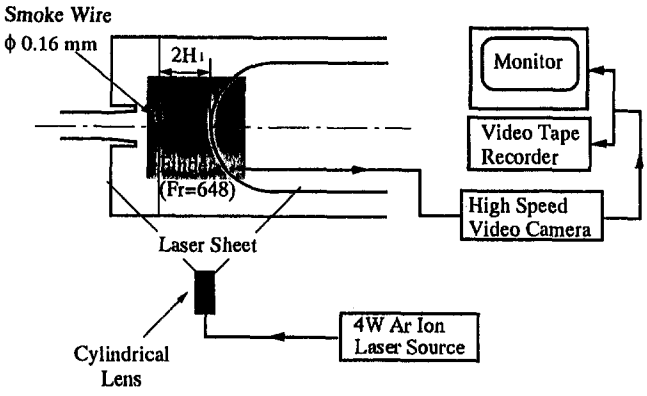

Fig. 3 Flow visualization system

40 MHz is used to detect the flow reversal. Four mirrors are utilized for traversing the measuring volume of 0.22 mm in diameter and 5.3 mm in length in the X–Y plane. An edible oil as a tracer particle is supplied through the atomizer installed at the nozzle inlet. A signal from the photomultiplier is processed by a tracker signal processor and converted by 12 bit A/D convertor. 1024 samples are stored in the memory of a 16 bit microprocessor, since the samples of 1024 to 6144 points show no explicit difference of convergence according to the preliminary survey about the appropriate number of samples. Velocity data are also processed by the 3σ method where the data out of range of three times the standard deviation are discarded as statistically undesirable.

The mean velocity vector is determined by rotating the laser light sheet by ±45 deg. Only the tangential velocity to the dome is obtained near the dome surface, since no possible rotation of laser light sheet is obtained because of the interference of the surface. The experiments were made under the condition of Reynolds number of 4.0×10^4 at station 1 where the reference length, H_1, was 20 mm and the reference velocity, U_{ref}, was 30 m/s.

Figure 3 shows the flow visualization system. It consists of a thin smoke wire placed two channel heights upstream of the dome head and 4 W Ar ion laser as a sheet of light source and a high-speed video camera. The smoke tracer is provided for a longer duration time of a couple of seconds than the conventional wire, as the mixture of titanium dioxide and plaster powder in addition to liquid paraffin is coated on the wire surface. The experiment for the visualization was conducted under the condition of Reynolds number of 2.0×10^3 to obtain the clear picture of the smoke. The frame rate of the video camera is selected at 648 frames per second, since the frequency of the oscillating jet is on the order of 20 Hz at the Reynolds number conducted.

Figure 4 depicts a block diagram of the frequency analyzer system of the pressure fluctuation. Samples of 100 K points

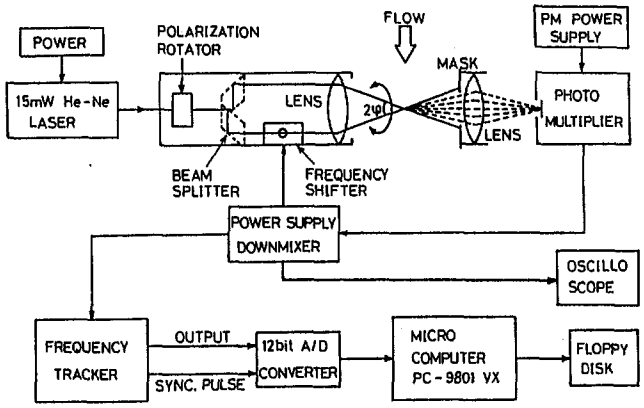

Fig. 2 Optical arrangement and data acquisition system

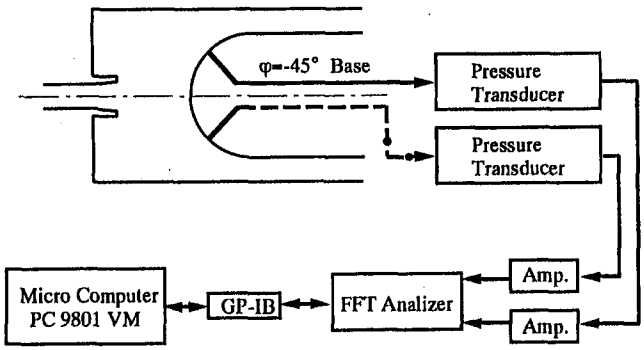

Fig. 4 Frequency analyzer system of pressure fluctuation

Nomenclature

C_{pw} = surface pressure coefficient
D = dump gap
f = frequency of the oscillating jet
H_1 = channel height
k = turbulence kinetic energy
L = prediffuser length
Q = volume flow rate
R = radius of flame dome
Re = Reynolds number at reference point = $U_{ref} \times H_1/\nu$
St = Strouhal number = $f \times H_1/U_1$
t = time
T = period of jet oscillation
U, V, W = mean-velocity components in X, Y, and Z directions
u, v, w = fluctuation velocity components in X, Y, and Z directions
X, Y, Z = streamwise, transverse, and spanwise coordinates (see Fig. 1)
α = half of prediffuser opening angle
λ_{1-3} = total pressure loss between stations 1 and 3
φ = angle from flame dome head
Ω = nondimensional vorticity

Subscripts

1, ref = reference point
2 = prediffuser exit
3 = branched channel exit
L = left side of channel
R = right side of channel

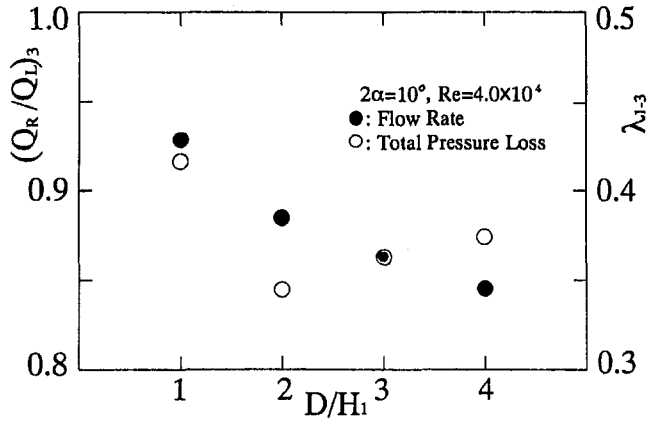

Fig. 5 Flow rate distribution and total pressure loss

were taken through the pressure transducer. The pressure fluctuation at $\varphi = \pm 45$ deg on the flame dome were measured simultaneously by the two pressure transducers at the different Reynolds numbers in order to survey the unsteadiness of the oscillating jet.

Results and Discussion

Diffuser Performance. Figure 5 shows the dependence of the dump gap upon the characteristics of flow rate distribution into the branched channels and the total pressure loss between stations 1 and 3. Q_L and Q_R are the flow rate at the left and right side in the branched channel, when looking downstream. The right side corresponds to the lower velocity region at the inlet, as the distortion bar is placed at the right side.

The characteristics of the flow rate distribution become worse with increasing dump gap. The total pressure loss has an optimum performance at the dump gap of 2. However, the dump gap of 3 was selected as the reference configuration, because an easy procedure was attained from the instrumentation viewpoint, and the fundamental flow feature for the gap of 3 was almost similar to that for the gap of 2. The results mentioned hereafter corresponds to the case of dump gap of 3.

Time-Averaged Flow Characteristics. Figure 6(*a*) shows the surface pressure on the casing walls with and without the inlet distortion. The term *asymmetric* in the figure is used for the case with the inlet distortion. The reattachment process occurs at $X/H_1 = 5.5$. The pressure rises in the reattachment region and the reattachment length in the recirculating region on the right

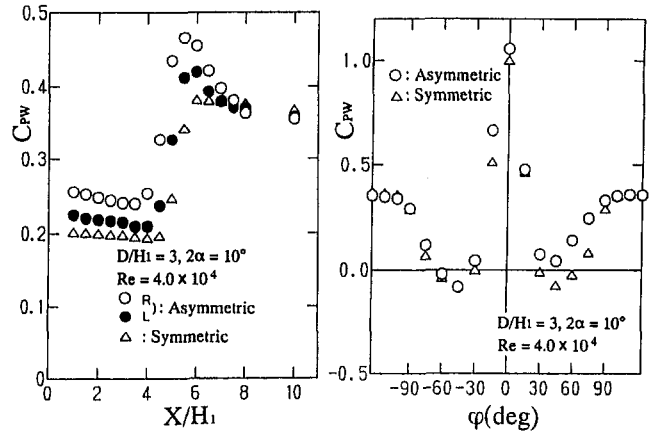

(*a*) on the casing walls (*b*) on the flame dome

Fig. 6 Surface pressure

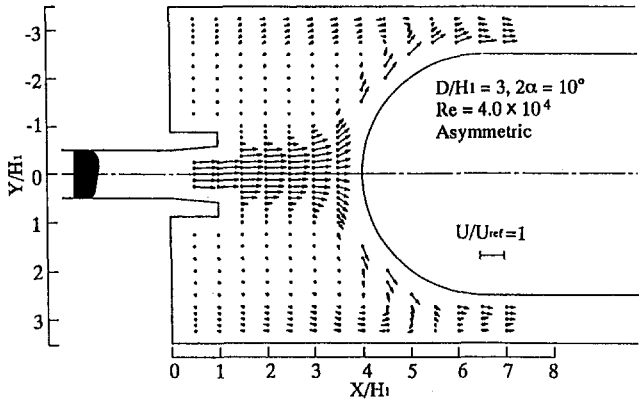

(*a*) Overall plot

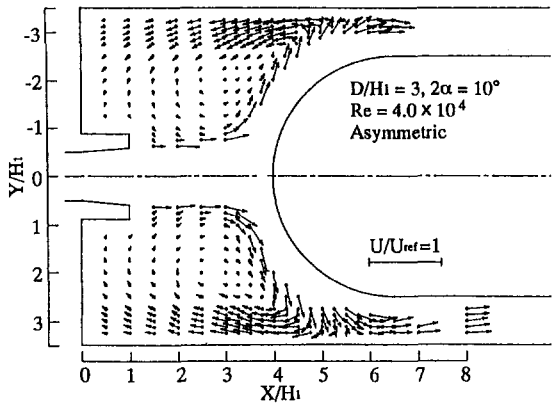

(*b*) In the recirculating region

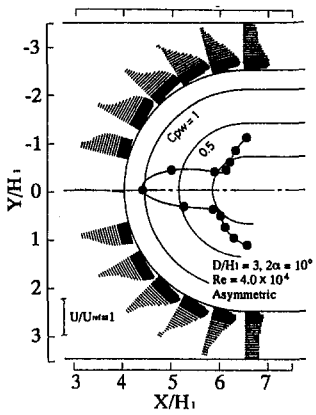

(*c*) Tangential velocity to the dome

Fig. 7 Velocity vector

side is shorter than that on the left side. The overshooting of the pressure is clearly observed on both sides near $X/H_1 = 6$, i.e., downstream of the reattachment point. It is worth denoting that the reattachment and the recovery processes with the inlet distortion have somewhat complicated feature compared with the condition without the inlet distortion.

Figure 6(*b*) shows the surface pressure on the flame dome. In case of the inlet distortion, the stagnation point shifts toward the left side (a higher velocity side, and a negative region of φ) by 1.5 deg. Downstream of the stagnation point, the acceleration occurs up to $\varphi = \pm 45$ deg. The dip of the pressure on the left side is larger than that on the right one. Then, the acceleration rate at the left side is more rapid. Downstream of the dip position, the flow is forced to decelerate and the boundary layer develops on the dome surface under the adverse pressure gradient.

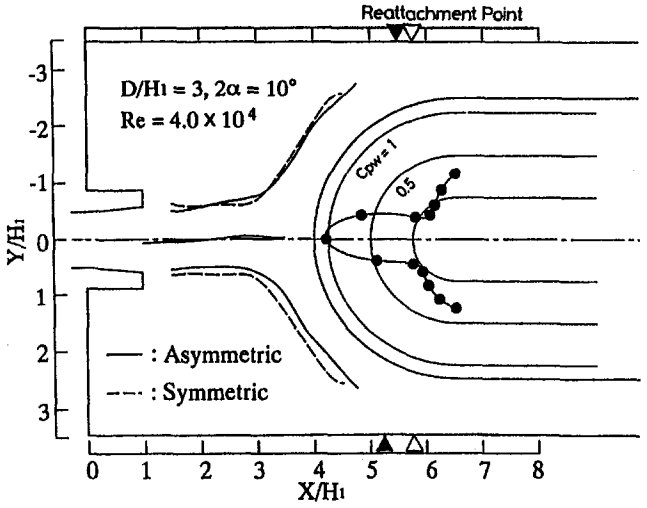

Fig. 8 Separating streamline with and without inlet distortion

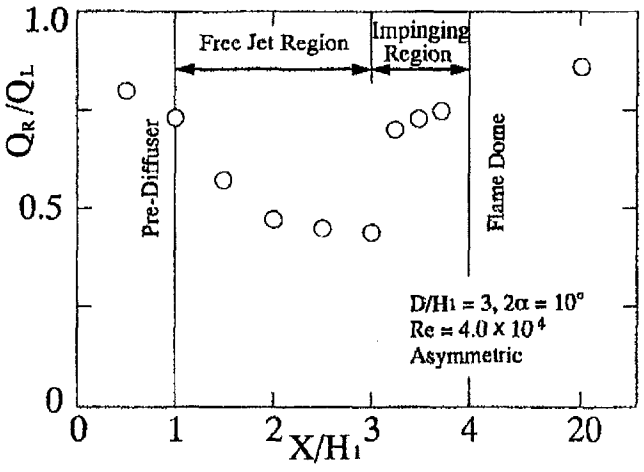

Fig. 9 Ratio of flow rate in the jet

Figure 7(a) shows an overall vector plot of the time averaged velocity with inlet distortion. Although a similar plot was obtained by Honami and Morioka (1990), the old LDV system without the frequency shifter could not detect the flow reversal.

Figure 7(b) shows the same vector plot to magnify the recirculating motion in the recirculating region by changing a vector scale.

Figure 7(c) also shows the tangential velocity to the dome in order to accentuate the near-wall flow on the dome. We observe that the jet from the prediffuser impinges on the dome head, deviates along the dome, and reattaches on the casing wall. After reattachment, the flow is divided into the recirculating flow and the flow entering into the branched channels. There are severe pressure gradients both normal to the casing wall and in the streamwise direction. Then, the flow accelerates rapidly near the casing wall as shown in Fig. 7(c). However, the flow acceleration does not occur in the case without inlet distortion.

Figure 8 illustrates the separating streamline, which is obtained from the stream function reduced by integrating the velocity data as shown in Fig. 7. The reattachment points on the casing wall are also shown in Fig. 8, which are determined by a wall flow sensor based on a heat tracer principle.

Figure 9 shows the ratio of the flow rate in the right side of the jet, Q_R, to that in the left one, Q_L. The border of both sides was distinguished by the transverse position, which showed the zero value in the profile of the transverse velocity V. The ratio, Q_R/Q_L, decreases downstream of the prediffuser due to an increase of the flow rate of the left side. It goes up near the dome because the flow rate in the right side increases rapidly. The deviation of the streamline and the shift of the stagnation point near the dome head introduce favorable flow rate characteristics. Then, the jet has the two regions in the streamwise direction. One is a free jet region and the other is an impinging one, as shown in Fig. 9. After all, the jet near the dome head has the favorable characteristics about the flow rate distribution into the branched channels.

Figure 10 depicts the contour plot of vorticity with an axis in the spanwise direction reduced from the mean velocity gradients. The vorticity is normalized by the reference velocity and the channel height at the inlet. The jet has the higher vorticity at the edge of the shear layer. The shear layer in the left side provides higher vorticity than that in the right side in the region along the separating streamline in Fig. 8.

Figures. 11(a, b) show the profiles of Reynolds shear stress, $\overline{uv}$, and the turbulence kinetic energy, k, in the sudden expansion region and the branched channels measured by the LDV system. Turbulence kinetic energy is estimated by the measured $\overline{u^2}$ and $\overline{v^2}$, since the spanwise component, $\overline{w^2}$, is assumed to be an arithmetic mean of $\overline{u^2}$ and $\overline{v^2}$.

The jet has higher turbulence energy at the shear layer edge and in the reattachment region. The high strain rate of the mean velocity in the jet boundary corresponds to the high vorticity region in Fig. 10. This process is explained by examining the Reynolds stress transport equations. The high strain rate introduces the production of the Reynolds shear stress and turbulence energy.

In the reattachment process, however, the turbulence energy production has a somewhat complicated mechanism. The separating streamline as shown in Fig. 8 has streamline curvature. The flow has *stable* curvature in the free jet region and *unstable* curvature downstream of it. Stable curvature suppresses the turbulence energy production in the shear layer such as in the boundary layer on the convex surface. As the shear layer along the dome reattaches on the casing wall, the reattaching shear layer has a complicated structure of vortex evolution due to stable and unstable curvature effects. In particular, the unstable effect just upstream of reattachment prompts the shear layer to produce the Reynolds stress. Therefore, the reattachment introduces enormously large turbulence energy.

Unsteady Flow Structure. From the viewpoint of the time-averaged flow mechanism, the favorable characteristics of the flow rate distribution were found to be closely related to the

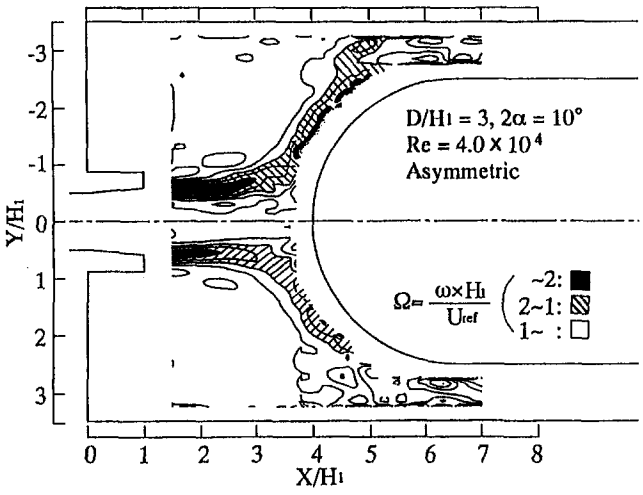

Fig. 10 Contour plot of vorticity

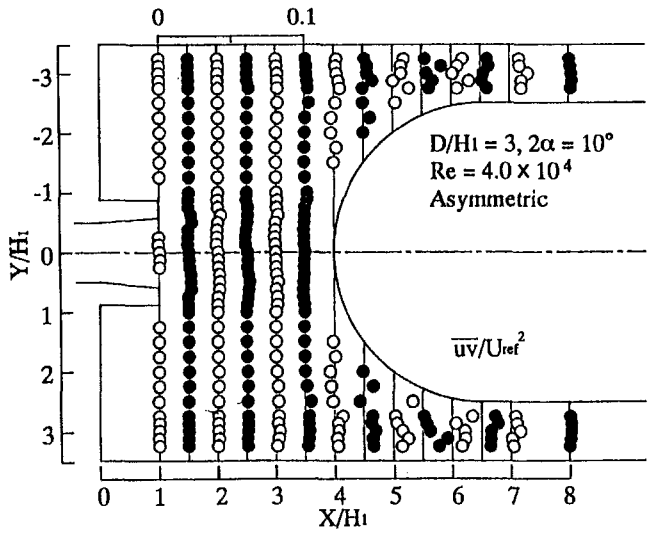

Fig. 11(*a*) Reynolds shear stress

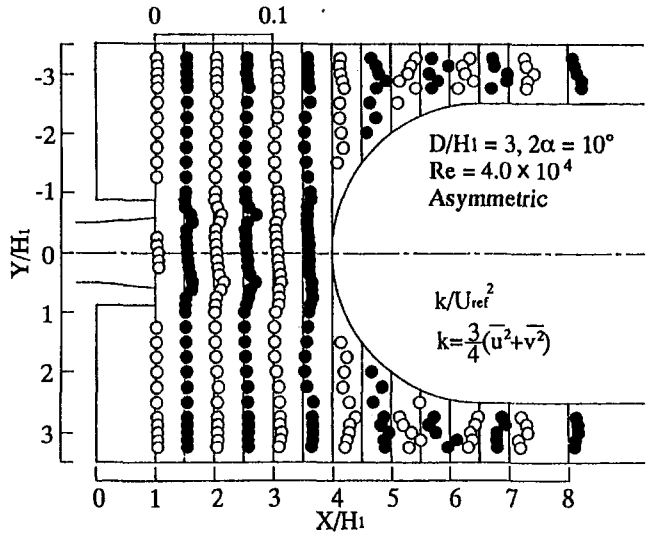

Fig. 11(*b*) Turbulence kinetic energy

behavior of the impinging jet upon the dome head. The dynamic behavior of the jet oscillation will be discussed in detail from the unsteady viewpoint in the following sections.

Flow Visualization. Figure 12 shows the smoke photos of the oscillating motion of the impinging jet taken by the high-speed video camera at Re = 2×10^3. The upper side (left side of the jet) has the higher velocity at the inlet. The oscillation frequency is estimated to be about 18 to 20 Hz from the reduction of the frame rate. At $t = 0$, which is temporarily decided as the start of oscillation, a large scale of vortex formation is found at the shear layer edge near the dome at the upper side. The jet deviates toward the right side and generates a smaller vortex at the right side than that in the left side at $t = T/3$. In such an oscillating motion, the impinging jet shows asymmetric vortex formation near the dome head.

The flow visualization was also conducted under the condition without inlet distortion. Although the photo is not shown in the paper, the oscillation of the jet itself also occurs, but the oscillation mode is different in the range of low Reynolds number. The jet shows almost the same dominant frequency, but a common phase in contrast to a counterphase in case of the distorted flow at the inlet. The impinging jet with the common phase generates a large scale of vortices at the shear layer edges at the same time, and does not deviate in the transverse direction. The phase mode becomes a counterphase with increasing Reynolds number in the symmetric case.

Pressure Fluctuation. Figure 13 shows the cross spectrum and phase between surface pressure fluctuations on the dome at two points 45 deg apart from the dome center. The spectrum has a dominant frequency at 18 Hz with a phase angle of π. This means that the flow oscillates at 18 Hz with a counterphase. The whipping motion of the jet observed from the flow visualization at low Reynolds number was confirmed by the pressure fluctuation survey. It is required to know how the dominant frequency depends on the Reynolds number in the higher Reynolds number range.

Figure 14 shows the nondimensional dominant frequency, which corresponds to Strouhal number versus Reynolds number in the cases with and without the inlet distortion. The size of a circle or square symbol is proportional to strength of the cross spectra of the pressure fluctuations. The datum obtained by the flow visualization is also included. Most of the data are the case

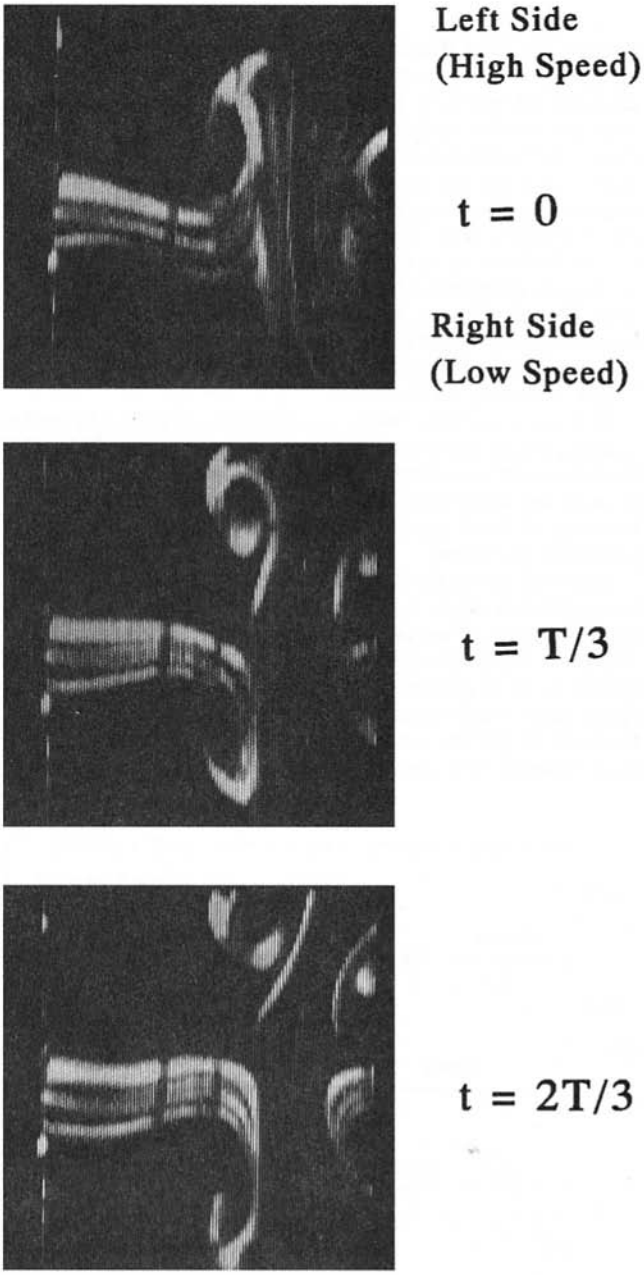

Fig. 12 Flow visualization by smoke-wire method, Re = 2×10^3

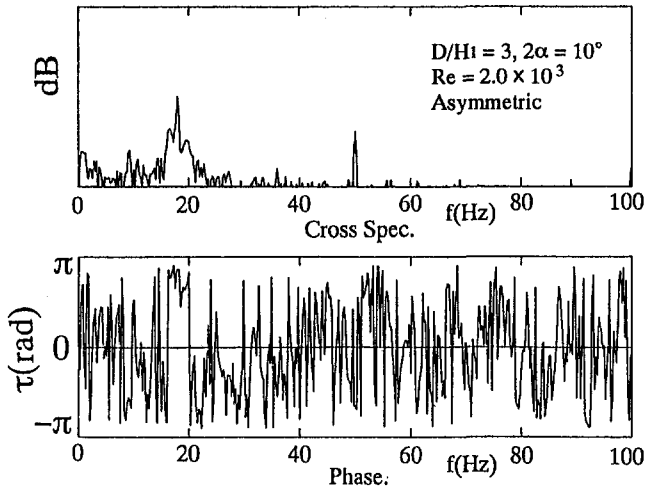

Fig. 13 Cross spectrum and phase of pressure fluctuations

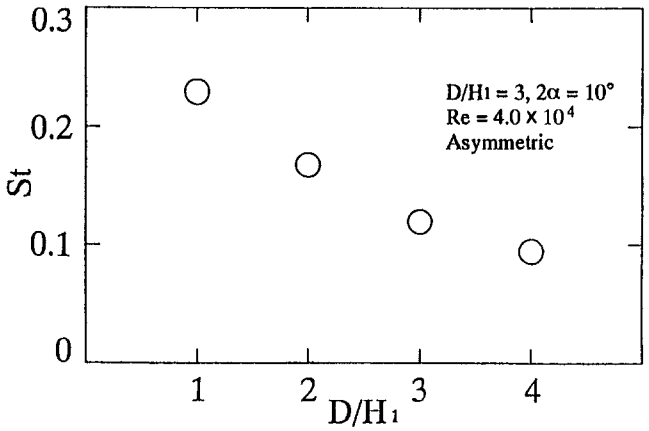

Fig. 15 Effect of dump gap on Strouhal number (stage 2)

without the inlet distortion. The oscillation has three stages including the fundamental Strouhal number of 0.03 and higher ones of 0.12 and 0.24. Then, the fundamental stage and higher ones are defined as stages 1, 2, and 3, respectively. The step change in Strouhal number is observed in such a manner from stage 3 to stage 2 with increasing Reynolds number. Thus, the impinging jet has also a whipping motion in higher Reynolds number range, as the dominant frequency in the pressure fluctuation is observed in the higher range. In particular, the counterphase is frequently observed under the condition without the inlet distortion in the range of high Reynolds number. This means in the symmetric case that the oscillation mode with the common phase is unstable in high Reynolds number, but stable in low Reynolds number.

In a real combustor under the condition of higher Reynolds number, the jet instability and Strouhal number are affected by the complicated channel configuration and a mass extraction through the dome head and so on. A survey on the dynamic behavior of these types of oscillation in the actual engine is needed in the future.

Figure 15 shows the dependence of a dump gap on the Strouhal number of stage 2. The unsteady motion is dominated by the multistages of the oscillation frequency and the dump gap. Therefore, the oscillation mechanism of the impinging jet seems similar to an edge tone phenomenon in an impinging jet on a sharp edge. Furthermore, the branched flows mix inside the reservoir in the present experiment. The feedback path might exist through the reservoir, although its volume was large enough. Future works are requried to confirm the pressure propagation as in a feedback mechanism in the edge tone or in the feedback path in the real combustor.

Figure 16 illustrates the unsteady flow behavior near the dome. A solid line is a time-averaged streamline dividing the left and right sides of the jet. The shaded portion corresponds to the region with the high Reynolds shear stress and vorticity. The thick lines indicate the streamline and vortex formation at each stage of a period. Thus, the impinging jet at the low Reynolds number range has an oscillating motion with asymmetric behavior of the vortex formation at the jet boundary near the dome head.

Conclusions

The present study is focused on understanding of flow behavior within the dump diffuser with the inlet distortion, particu-

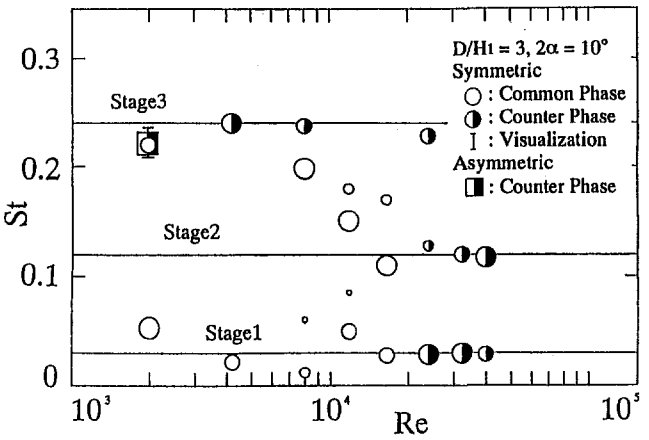

Fig. 14 Effect of Reynolds number on Strouhal number

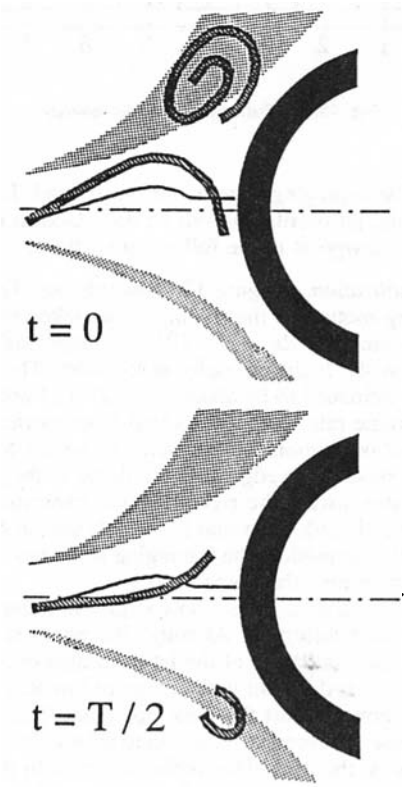

Fig. 16 Jet behavior near the dome at low Reynolds number

larly from the viewpoints of the time-averaged and fluctuated flow of the impinging jet upon the dome. The following conclusions are obtained:

1 There exists a high-vorticity region at the jet boundary resulting in the production of the turbulence kinetic energy. In particular, higher vorticity is observed in the higher velocity side of the jet.

2 The jet near the dome head has favorable characteristics about the flow rate distribution into the branched channels.

3 Reynolds shear stress and turbulence kinetic energy are produced near the reattachment region on the casing wall.

4 The impinging jet has an oscillating motion near the dome head with asymmetric vortex formation at the jet boundary.

Acknowledgments

This work was supported by Tanikawa Fund Promotion of Thermal Technology, whose support is gratefully acknowledged. The authors would like to thank Ms. Tomoko Morozumi and Mr. Kiyoshi Wada, who assisted in the data acquisition.

References

Biaglow, J. A., 1971, "Effect of Various Diffuser Designs of the Performance on an Experimental Turbojet Combustor Insensitive to Radial Distortion of Inlet Airflow," NASA TM X-2216.

Fishenden, C. R., and Stevens, S. J., 1974, "The Performance of Annular Combustor-Dump Diffusers," AIAA Paper No. 74-1097.

Honami, S., and Morioka, T., 1990, "Flow Behavior in a Dump Diffuser With Distorted Flow at the Inlet," ASME Paper No. 90-GT-90.

Klein, A., et al., 1974, "Experimental Investigation of the Performance of Short Annular Combustor-Dump Diffusers," *Proceedings, 2nd International Symposium on Air Breathing Engines,* pp. 1–13.

Klein, A., et al., 1980, "The Effect of Blade-Wakes on the Performance of Short Dump-Diffuser Type Combustor Inlet," ASME *Journal of Fluids Engineering,* Vol. 102, pp. 236–241.

Stevens, S. J., et al., 1976, "The Influence of Compressor Exit Conditions on the Performance of Combustor-Dump Diffuser," AIAA Paper No. 76-726.

Studies of Lean Blowout in a Step Swirl Combustor

M. D. Durbin

D. R. Ballal
Fellow ASME

Department of Mechanical and Aerospace Engineering, University of Dayton, Dayton, OH 45469

The design requirements of a modern gas turbine combustor are increasingly dictated by wide stability limits, short flame length, and uniform mixing. To achieve the best trade-off between these three factors, flame characteristics (length, shape, mixedness), lean blowout (LBO), and optimum combustor configuration should be investigated over a wide range of inner and outer air velocities, inner and outer vane angles, and co- versus counterswirl arrangements. Such an investigation was performed in a step swirl combustor (SSC) designed to simulate the fuel–air mixing pattern in a gas turbine combustor dome fitted with an airblast atomizer. It was found that an increase in the outer vane angle and a decrease in inner air velocity decreased the flame length. LBO was improved when outer flow swirl intensity was increased. An optimum hardware and velocity configuration for the SSC was found for inner swirl = 45 deg, outer swirl = 60 deg, coswirl direction, and inner air velocity = outer air velocity = 16 m/s. This optimum SSC configuration yielded: (i) low values of LBO, (ii) short flame length, (iii) uniformly mixed stable flame, and (iv) little or no variation in these characteristics over the range of operation of SSC. Finally, the co- versus counterswirl arrangements and the operation of the optimized combustor configuration are discussed.

Introduction

An important design requirement of a modern gas turbine combustor is good combustion stability; that is, the combustor should sustain burning over a wide range of fuel–air ratios encompassing the entire range of engine operating conditions, including rapid acceleration and deceleration. Also, short flame length and uniform mixing are equally important. To achieve the best trade-off between wide stability limits, short flame length, and uniform mixing, the characteristics of the flame, lean blowout (LBO), optimum combustor geometry, and their influence on LBO should be investigated. This provides the necessary impetus for our research.

In this paper, experimental studies in a step swirl combustor (SSC) burning gaseous propane fuel were performed. The fuel was injected in the form of an annular jet coaxially sandwiched between two swirling airstreams. This configuration simulates the fuel–air mixing pattern just downstream of an airblast atomizer located in the dome region of a modern annular gas turbine combustor. The SSC was also intended to be a marriage between the two combustor configurations extensively studied earlier in our laboratory: a step combustor (Sturgess et al., 1990, 1991) and a swirl combustor (Takahashi et al., 1990). Specifically, we have investigated, over a wide range of inlet conditions of velocity, swirl vane angles, and swirl directions (coswirl versus counterswirl): (*i*) flame characteristics such as length, shape, and mixedness; (*ii*) LBO; and (*iii*) combustor flow field patterns. Special emphasis was given to assess the flame characteristics of coswirl versus counterswirl arrangements. For example, counterswirl may generate a strong shear layer but the opposed airstreams tend to nullify the swirling motion in the flow field. On the other hand, coswirl generates a high tangential momentum but produces a weaker shear layer. The combustion process in the SSC was also optimized in terms of a short flame length, high level of mixedness, and low LBO. Such results are presented and their implications to practical combustor design are discussed.

Contributed by the International Gas Turbine Institute and presented at the 39th International Gas Turbine and Aeroengine Congress and Exposition, The Hague, The Netherlands, June 13–16, 1994. Manuscript received by the International Gas Turbine Institute February 19, 1994. Paper No. 94-GT-216. Associate Technical Editor: E. M. Greitzer.

Experimental Work

The SSC. Figure 1 shows a schematic diagram of the SSC, which has 150 × 150-mm cross section with rounded corners, length of 754 mm, and a step height of 55 mm. The SSC provides a geometrically simple, optically accessible research combustor capable of reproducing the fuel–air mixing pattern downstream of the airblast atomizer located in the dome region of a modern annular combustor. The SSC also offers independent control over inner and outer airstreams so that velocities can be easily optimized. In a practical airblast atomizer, effective areas would have to be changed to perform similar optimization; this is time consuming and expensive. The SSC was mounted on a vertical combustion tunnel with a three-axis traversing mechanism described by Sturgess et al. (1990). Measurements of various flame and flow parameters were performed using different instruments, the principal one being a three-component Laser-Doppler Anemometer (LDA).

Fuel was supplied to the combustor by the annular fuel tube (20 mm i.d. and 29 mm o.d.), which is coaxially sandwiched between two swirling airstreams; the inner air jet (20 mm dia) and the outer annular air jet (29 mm i.d. and 40 mm o.d.). The combustor exit has a 45 percent blockage orifice plate on top, which simulates the back pressure exerted by the dilution jets in a practical gas turbine combustor (see Sturgess et al., 1990). The SSC has quartz windows on all four sides to permit visual observations and laser diagnostics measurements. Optical access in the axial direction was about 250 mm from the burner tube exit; in the radial direction, it was about 30 mm (3-D LDA) and 70 mm (2-D LDA) from the centerline.

Stationary helical vane swirlers were located 25 mm upstream from the burner tube exit in each of the air passages. The inner swirler had six vanes with a central 1.4-mm-dia hole to prevent the flame from anchoring to the swirler. The outer swirler had 12 vanes. Inner swirler lengths are 25, 19, and 19 mm, respectively, for 30, 45, and 60 deg swirlers; outer swirler lengths are 32, 25, and 19 mm, respectively, for the 30, 45, and 60 deg swirlers. The lengths and number of vanes were designed to insure that there was no straight-through airflow into the combustor. Practical combustors usually employ axial-flow-type swirler vanes. The swirler vanes are usually flat for ease of manufacturing. However, the flow does not follow the angle of

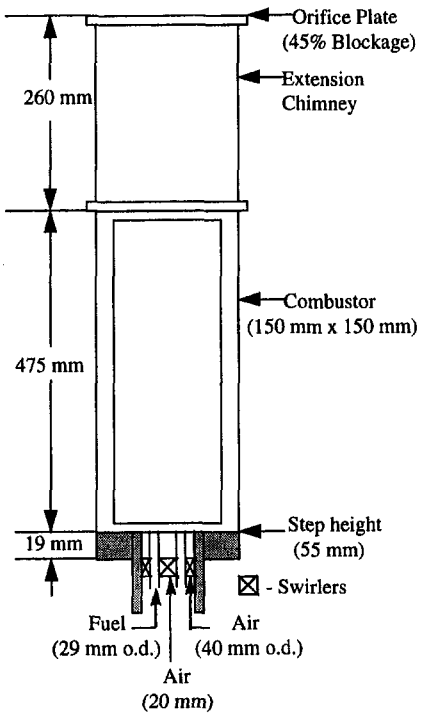

Fig. 1 Schematic diagram of a step swirl combustor

the flat vane as accurately as it does the angle of the helical vane. The swirlers were precision-fabricated in a rapid prototype manufacturing process known as stereolithography. These swirlers performed satisfactorily at high temperatures in our combustor.

Instrumentation. Figure 2 shows a custom-made three-component LDA system used for velocity measurements. This is a three-beam two-component (axial and radial) set using a 514.5 nm line of an 18 W argon-ion laser with a component separation based on polarization. A two-beam third component (tangential) set uses a 488.0 nm line with separation by color. Since the third component is normal to the first and second components, the measurement volume had a quasi-spherical shape of 100 μm diameter and the calculated fringe spacing was 3.6 μm. The LDA system has Bragg cell frequency shifting (10 MHz for the first and second channels, and 30 MHz for the third channel) for measurements in recirculatory flows, 4-σ filtering software for spurious signals (e.g., due to seed agglomeration), and a correction subroutine to account for the LDA signal-biasing effects in combusting flows. A fluidized-bed seeder was used to inject submicron-sized (<1 μm) ZrO_2 particles into each passage. Counter-type (TSI 1990C) signal processors and tailor-made coincidence circuit ensured valid data rate acquisition. All the LDA signals were processed using our custom-designed software, which calculates intensity, shear stresses, higher moments (skewness and kurtosis), and pdfs. Typical LDA sampling rates exceeded 1 kHz for both isothermal and combusting flow measurements.

Error Analysis. Both the fuel flow and airflow were monitored by separate electronic flow control units to within 1 and 3 percent, respectively. The combined error produced an uncertainty of 1.5 percent in equivalence ratio. The primary source of error in LDA measurement is the statistical bias of the final measured velocity toward higher mass flux (velocity $\times$ density) when number-weighted averages are used to calculate stationary statistics. Chen and Lightman (1985) and Glass and Bilger (1978) have discussed bias correction schemes. After allowing for this bias, we estimated that for the single-stream seeding and relatively high-sampling rates of our experiments, the uncertainty in the measurement of mean velocity was 1 percent and for rms velocity 5 percent. Near the flame front, where intermittency would be much higher, the uncertainty in rms velocity could be as high as 7 percent. The long-term repeatability of measurements was found to be within 5 percent for turbulence quantities.

Test Conditions. Table 1 lists the test matrix for the SSC experiments. All tests were performed at room temperature and atmospheric pressure using gaseous propane fuel to establish a baseline. It should be noted that advanced, near-stoichiometric combustors of the future will admit fuel into the primary zone in a prevaporized state, and therefore, may not require high air velocities (>100 m/s) for liquid fuel atomization employed in conventional combustors. The SSC was operated to study flame characteristics, flow field, and LBO. Five variables were extensively tested: (*i*) inner air velocity, (*ii*) outer air velocity, (*iii*) inner vane angle, (*iv*) outer vane angle, and (*v*) coswirl versus counterswirl. The SSC was operated over a wide range of equivalence ratios. LBO data were collected by maintaining a constant airflow rate, heating the combustor to a near-steady-state temperature at stoichiometric fuel–air ratio, and then gradually decreasing the fuel flow rate until blowout occurred. This is a procedure similar to that adopted by Sturgess et al. (1991). The flame length was defined as the distance from the nozzle exit to the flame tip and measured by taking individual color snapshots of the combustion process, enlarging these photographs, and then carefully plotting the luminous boundary of the flame front. These photographs also provided data for visually assessing the quality of mixing (mixedness) within the combustion zone, e.g., for a constant fuel and airflow rate, a yellow or sooty flame indicates locally rich zones, which suggests poor mixing.

Results

Flame Characteristics. Flame length measurements were performed because the length directly governs the length of the combustor dome. The measurements were taken at stoichiometric equivalence ratios to establish a baseline. Long-exposure photographs of the flame were taken with a 35-mm camera. Typical photographs are presented in Figs. 3(*a*)–(*c*) to illustrate how flame configuration (length, width, and shape) changes for no-swirl, inner swirl, and outer swirl conditions. As seen in Fig. 3(*a*), for the no-swirl case, the flame is lifted and the combustion zone is located closer to the combustor exit. Introducing a mild swirl in the inner airflow (Fig. 3(*b*)) not only shortens the flame, but also causes it to bulge out and fill the combustor cross section. Finally, as shown in Fig. 3(*c*),

Nomenclature

D = inner air nozzle diameter
LBO = lean blowout
P = pressure
Re = Reynolds number
U = axial mean velocity
Y, Z = radial and axial distance, respectively
θ = swirl vane angle
ϕ = equivalence ratio

Subscripts

i = inner
o = outer

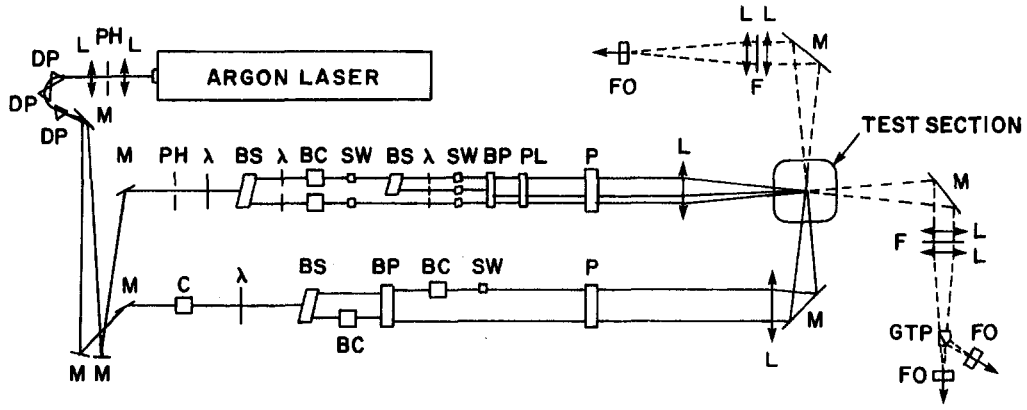

BC	Bragg Cell	FO	Fiber Optic Positioner	P	Periscope
BP	Beam Positioning Prism	GTP	Glan-Thompson Prism	PH	Pinhole
BS	Beam Splitter	L	Lens	SW	Steering Wedge
DP	Dispersion Prism	M	Mirror	λ	Half-Wave Plate
F	Filter				

Fig. 2 Schematic of a custom-made three-component LDA system used for velocity measurements

swirling the outer *instead* of the inner airflow produces an attached flame with a *not-so-beneficial* elongated combustion zone downstream.

Flame lengths were measured for many different SSC operating conditions; these are shown plotted in Figs. 4–6. It should be noted that for all cases except the no-swirl conditions, the flame was nearly attached to the nozzle exit (at stoichiometric values). Figure 4 shows a substantial increase in flame length with a threefold increase in inner air velocity (for a constant value of outer air velocity and constant $\phi = 1.0$) for all combinations of swirler angles. Clearly, this appears to be due to a direct decrease in the mixture residence time. Figure 5 compares flame length with changes in outer airflow for a constant value of inner airflow. It is found that the flame length decreases, but only when the outer vane angle is 60 deg or higher, i.e., only when the outer swirl intensity (both velocity and vane angle) is sufficiently high. Finally, Fig. 6 illustrates the variation of flame length with co- and counterswirl conditions for a velocity combination $U_i = 48$ m/s and $U_o = 16$ m/s. For all combinations of inner and outer vane angles, the coswirl direction produced shorter flames. It was also found that for equal velocities of inner and outer airstreams, the flame was very short and there was no noticeable difference in flame length between co- and counterswirl conditions.

To further assess the influence of swirl direction on the combustion process, Figs. 7(*a*) and 7(*b*) show the photographs of co- and counterswirl flame structures, respectively. Both flames rapidly spread outward. However, the coswirl flame (Fig. 7(*a*)) has a dimple shape at the center and shows some yellowish streaks downstream (evidence of nonuniform mixing and diffusion-controlled combustion), whereas the counterswirl flame (Fig. 7(*b*)) has a bulb shape, which fully confines the bluish (evidence of uniform, premixed) combustion process.

Since the co- versus counterswirl effects are of great interest in practical combustor design, LDA velocity measurements were made to confirm the findings given above. Figures 8(*a*)–(*c*) show the radial variation of mean axial velocity at three different axial locations downstream of the fuel nozzle. These LDA measurements were made by seeding the fuel flow. A comparison between Figs. 8(*a*) and 8(*b*) demonstrates the changes in flowfield due to combustion, while Figs. 8(*b*) and 8(*c*) illustrate the co- versus counterswirl effects.

Figure 8(*a*) shows the inner recirculation zone, which grows from a width of 0.25D (at Z/D = 0.35) to 0.45D (at Z/D = 2.25) in the cold flow. In the annular fuel tube region, which is sandwiched between the inner and outer airflow, the axial velocity component is positive and decreases rapidly from its inner mean value of 16 m/s to the outer mean value of 8 m/s.

Table 1 Test matrix for the step swirl combustor experiments (all tests at room temperature and atmospheric pressure with gaseous propane fuel)

Variable	Range
Inner vane angle, θ_i, degrees	30, 45, and 60
Outer vane angle, θ_o, degrees	30, 45, and 60
Vane configuration	co and counter-swirl
Inner air velocity, U_i, m/s	16, 32, and 48
Re	20, 40, and 60 x 10^3
Outer air velocity, U_o, m/s	8 and 16
Re	14 and 28 x 10^3

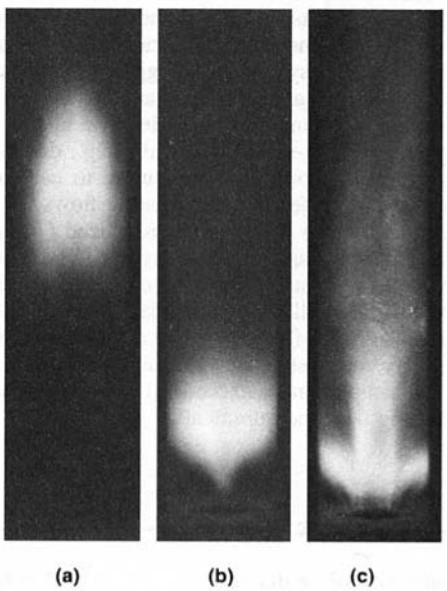

Fig. 3 Photographs illustrating the flame structure for different swirl configurations: (*a*) no-swirl, $\theta_i = \theta_o = 0$, (*b*) inner swirl, $\theta_i = 45$ deg, $\theta_o = 0$, and (*c*) outer swirl, $\theta_o = 30$ deg, $\theta_i = 0$. Test conditions were at $\phi = 1.0$, $U_i = 16$ m/s, and $U_o = 8$ m/s.

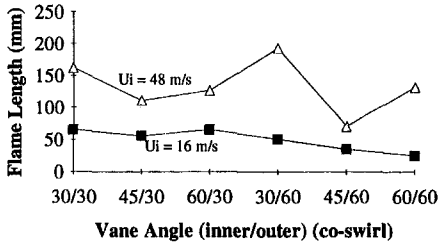

Fig. 4 Variation of flame length with vane angle at two different values of inner air velocity (U_o = 8 m/s)

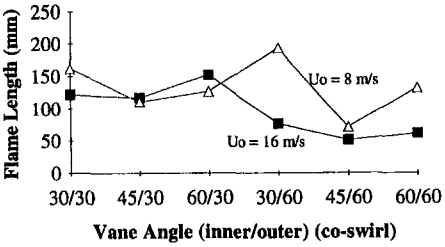

Fig. 5 Flame length as a function of vane angle and outer air velocity (U_o = 8 m/s)

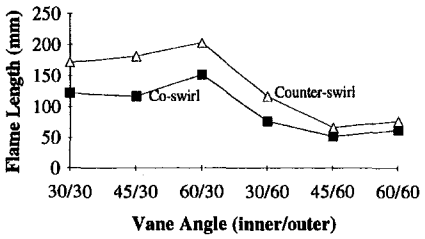

Fig. 6 A comparison of flame lengths with co- and counterswirl arrangements (U_i = 48 m/s, U_o = 16 m/s)

Finally, the velocity decays to a low, but still positive value (i.e., no outer recirculation zone at least for Y/D up to 1.5) as one moves radially outward from the edge of the outer air tube to the combustor wall.

As seen in Fig. 8(b), the heat release of combustion produces the acceleration of the axial velocity component and elongation

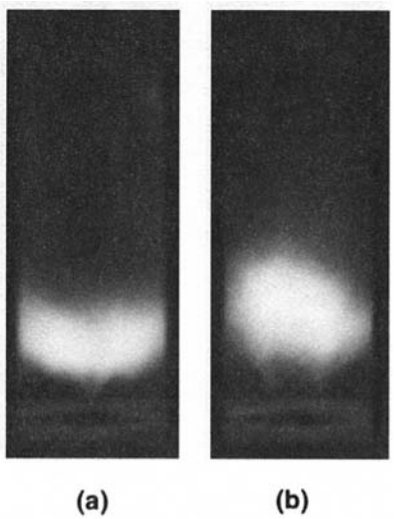

Fig. 7 Photographs illustrating the flame structure for (a) coswirl and (b) counterswirl arrangements. Test conditions were ϕ = 1.0, U_i = 16 m/s, U_o = 8 m/s, $\theta_i = \theta_o$ = 30 deg.

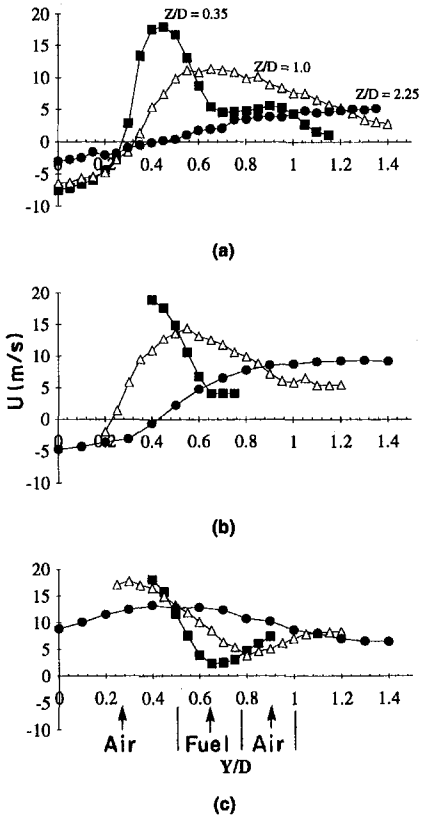

Fig. 8 Radial variation of mean axial velocity at three different locations downstream of the fuel nozzle: (a) cold flow coswirl, (b) hot flow coswirl, (c) hot flow counterswirl, test conditions were ϕ = 1.0, U_i = 16 m/s, U_o = 8 m/s, $\theta_i = \theta_o$ = 30 deg

of inner recirculation zone in the axial (downstream) direction. For example, at Z/D = 1, combustion has elongated (and hence decreased) the recirculation zone width by 30 percent; and downstream of this location, it has increased the maximum mean axial velocity by 50 percent in this Y/D range. This means that throughout the inner recirculation zone, velocity gradients have increased significantly, contributing to intense mixing and uniformity. These results are consistent with the dimple-shaped central flame structure observed in the photograph in Fig. 7(a).

Figure 8(c) illustrates the axial mean velocity profiles for counterswirl direction. These results show no evidence of any inner recirculation zone. Moreover, in the annular gap corresponding to the fuel tube location, the velocity profile has a minimum. Presumably, this arises due to the flow velocity cancellation effect produced by the counterrotating swirl. Also, the annular fuel jet is subjected to strong shearing action of counterrotating braids along its inner and outer boundaries. As is evident in Fig. 7(b), this shearing action produces a very thin annular film near the nozzle exit (Z/D up to 1), which supports an attached flame structure in the combustor.

It should be noted that, in our experiments, the co- and counterswirl arrangement had identical overall pressure drop. Yet there is a difference in their mixing characteristics and, hence, in the flame structures. Thus, expressing the mixing quality only in terms of the overall pressure drop can be deceptive.

LBO Observations. LBO equivalence ratios were recorded for all the test conditions documented in Table 1. Rich blowout data were also collected to verify combustion stability of SSC for various parametric combinations. However, in Figs. 9 and 10, only LBO data are presented (repeatability to ±0.01) because of their great practical importance. These data may be put into proper perspective by noting that, for a perfectly mixed

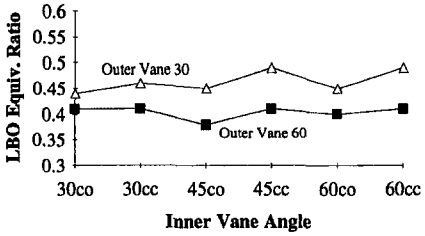

Fig. 9 Effect of outer vane angle on LBO at U_i = 32 m/s, U_o = 16 m/s (co represents coswirl, cc represents counterswirl)

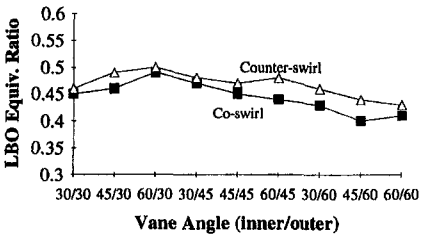

Fig. 10 A comparison of LBO data for co- and counterswirl arrangements (U_i = 32 m/s, U_o = 16 m/s)

propane–air flame, the value of equivalence ratio at the lean flammability limit is 0.55.

Figure 9 shows that an increase in outer swirl vane angle improves the stability of lean mixtures (i.e., LBO values decrease). An outer vane angle of 60 deg produces strong outer recirculation zones, which keep the flame attached to the exit nozzles and stabilize the combustion process. Strong outer swirl produces locally fuel-rich zones by directing the outer airflow away from the fuel jet, thereby further assisting flame stability.

Figure 10 shows LBO data for co- and counterswirl. When inner air velocity is significantly higher than the outer air velocity, coswirl provides more stable combustion and always yields *slightly* lower LBO values than the counterswirl condition. This presumably occurs because, as shown in Fig. 7(*a*), the coswirl flow direction produces less-uniform mixing in the combustor than the counterswirl flow direction. An imperfectly mixed diffusion flame blows out at a lower overall equivalence ratio because combustion is sustained in the locally rich mixture regions. This is good for stability but it should be recognized that the reactants are not uniformly mixed. Thus, there is an important *trade-off* to be considered when assessing burning characteristics of co- and counterswirl flows. No detectable differences in LBO values were found for co- and counterswirl flow conditions when inner and outer air velocities were equal.

Optimum Configuration. The preceding results on flame length and LBO suggest an optimum configuration of inner and outer velocities, inner and outer swirl vane angles, and co- versus counterswirl, which yields: (*i*) low LBO values, (*ii*) short flame length, (*iii*) uniformly mixed stable flame, and (*iv*) little or no variation in these characteristics over the SSC range of operation. Figure 11 shows that the optimum vane angle (θ_i = 45 deg, θ_o = 60 deg) provides low LBO values (average equivalence ratio = 0.38 ± 0.04) and short flame lengths (average 55 mm ± 10 mm) over the range of air velocities tested. For all other inner and outer vane angle combinations, the average LBO values were greater, average flames were longer, or more data variability was present. Likewise, in Fig. 12, the optimum inner and outer velocity split (U_i = U_o = 16 m/s) provides low values of LBO (average equivalence ratio = 0.41 ± 0.03) and short flame length (average 52 mm ± 8 mm) over the range of vane angles tested.

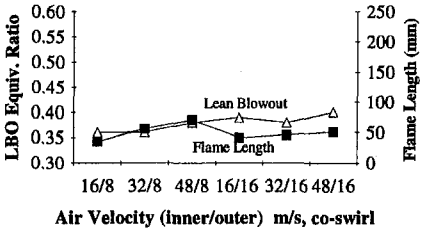

Fig. 11 Variation of LBO and flame length with airflow for an optimum vane angle configuration (θ_i = 45 deg, θ_o = 60 deg)

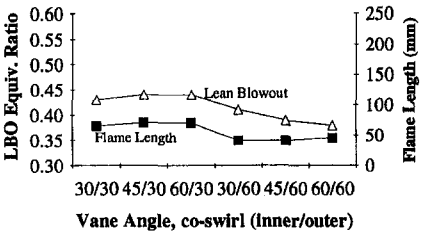

Fig. 12 Variation of LBO and flame length with vane angle for an optimum air velocity split (U_i = U_o = 16 m/s)

Figures 13(*a*) and 13(*b*) show the flame structure at the optimum condition (inner swirl = 45 deg, outer swirl = 60 deg, coswirl direction, inner air velocity = outer air velocity = 16 m/s) for equivalence ratios ϕ = 1 and 0.5, respectively. It is observed that the flame structure remains confined to the combustor dome region over this range of equivalence ratio. At the overall stoichiometric mixture ratio (Fig. 13(*a*), the flame is evenly dispersed throughout the combustor and the same observation holds true at the LBO operating condition (Fig. 13(*b*)). While this may be aerodynamically desirable, other factors such as combustor dome cooling, high-altitude ignition, and emissions requirements can dictate the optimum flame structure in a practical combustor. Finally, no noticeable change was observed in flame size and shape when the inner swirl angle was increased from 45 to 60 deg.

Discussion

In these experiments it was observed that, compared to the counterswirling arrangement, the coswirling flow spread the fuel–air mixture to the combustor walls and produced a slightly shorter flame, a lower LBO value, and less variability of the

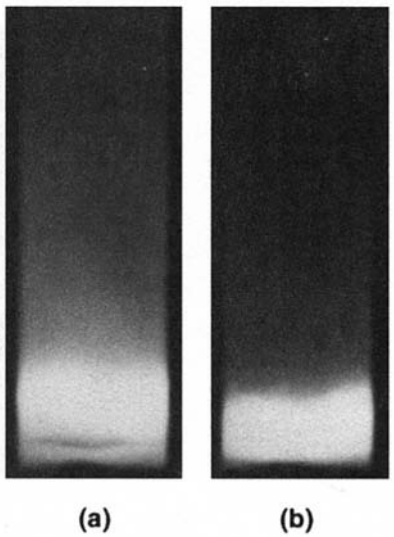

Fig. 13 Photographs illustrating the flame structure at the optimum conditions (θ_i = 45 deg, θ_o = 60 deg, U_i = U_o = 16 m/s), (*a*) ϕ = 1.0, (*b*) ϕ = 0.5

combustion characteristics with changes in hardware and flow conditions. For a coswirl arrangement, Brady and Samuelsen (1991), Brady et al. (1991), and Sowa et al. (1993) have observed an excessive transport of *liquid* fuel to the combustor walls, resulting in unstable operation. Since the momentum of their liquid fuel sheet was likely to be higher than that of our gaseous propane annular jet, their observations on combustor wall heating and combustion instability were absent in our tests. Also, as Sowa et al. (1993) have pointed out, the shorter combustor dome length required to confine this type of flame may suppress the formation and strength of large-scale turbulent eddies, which trigger combustion instabilities. As shown in Fig. 7(*a*), we did observe some yellow streaks downstream; these streaks indicate nonuniform mixing and diffusion-controlled combustion. However, combustion instability for the co-swirl arrangement at the LBO operating point was no worse than with the counterswirl flow arrangement.

Finally, detailed velocity and temperature mappings of the SSC using LDA and CARS diagnostics are currently being performed to ascertain the role of inner and outer recirculation zones on the combustion stability near lean blowout.

Summary and Conclusions

A unique SSC was designed to simulate the fuel–air mixing pattern produced by an airblast atomizer located in the combustor dome of a modern annular gas turbine combustor. Experiments were performed to study flame characteristics (length, shape, and mixedness), LBO, and flow patterns in this combustor over a wide range of inner and outer velocities, inner and outer vane angles, and co- versus counterswirl arrangements. This research resulted in the following findings:

1 The two most significant parameters that contributed to decreasing the flame length are; an increase in the outer vane angle and a decrease in inner air velocity. Visual flame sooting decreased when the inner vane angle or air velocity was increased.

2 LBO improved when outer swirl intensity was increased. When inner air velocity was higher than outer air velocity, coswirl yielded slightly lower values of LBO than the counterswirl arrangement. However, LBO values remained unchanged for equal inner and outer velocities.

3 An optimum hardware and flow configuration for the SSC was found for inner vane angle = 45°, outer vane angle = 60°, co-swirl direction, and inner air velocity = outer air velocity = 16 m/s. This configuration yielded: (*i*) low LBO values, (*ii*) short flame length, (*iii*) uniformly mixed stable flame, and (*iv*) little or no variation in these characteristics over the SSC range of operation.

4 Photographs indicated and LDA velocity measurements confirmed that the co-swirl flame has a dimple-shape, produces a slightly shorter flame stabilized by the inner recirculation zone, a lower value of LBO, and less variability of the combustion characteristics with changes in hardware and flow conditions. In contrast, the counter-swirl flame has a bulb-shape which fully confined the bluish, partially premixed combustion process to the center of the combustor dome, requires a slightly higher value of LBO, and needs a longer combustor dome length to confine it. These important differences between the two swirling arrangements can influence the off-design performance of the combustor.

5 Finally, no noticeable change was observed in the flame size and shape over a range of test conditions when the combustor was operated with the optimum configuration. This knowledge should be of value to the combustor designer.

Acknowledgments

This work was supported by the U.S. Air Force, Wright Laboratory, Fuels and Lubrications Division, Aero-Propulsion and Power Directorate, Wright-Patterson Air Force Base, Dayton, OH, under contract No. F33615-92-C-2207, with Mr. Charles W. Frayne serving as the Air Force Technical Monitor. The authors wish to thank Drs. G. J. Sturgess and W. M. Roquemore for valuable discussions, and Mr. M. D. Vangsness for his help with the LDA measurements.

References

Brady, R. A., and Samuelsen, G. S., 1991, "Visualization of Dome Region Mixing in a Quartz Combustor," ASME Paper No. 91-GT-360.

Brady, R. A., Sowa, W. A., and Samuelsen, G. S., 1991, "A Study of Dome Region Fuel-Air Mixing in a Model Rich Burn-Quick Mix Lean Burn Combustor," NASA TM189112.

Chen, T. H., and Lightman, A. J., 1985, "Effects of Particle Arrival Statistics on Laser Anemometer Measurements," ASME FED-Vol. 33, pp. 172–176.

Glass, M., and Bilger, R. W., 1978, "The Turbulent Jet Diffusion Flame in Coflowing Stream-Some Velocity Measurements," *Combustion Science and Technology,* Vol. 18, pp. 165–177.

Sowa, W. A., Brady, R. A., and Samuelsen, G. S., 1993, "Mixing in the Dome Region of a Staged Gas Turbine Combustor," *AIAA Journal of Propulsion and Power,* Vol. 9, pp. 702–707.

Sturgess, G. J., Lesmerises, A. L., Heneghan, S. P., and Ballal, D. R., 1990, "Design and Development of a Research Combustor for Lean Blowout Research," ASME JOURNAL OF ENGINEERING FOR GAS TURBINES AND POWER, Vol. 114, pp. 13–19.

Sturgess, G. J., Sloan, D. G., Roquemore, W. M., Shouse, D., Lesmerises, A. L., Ballal, D. R., Heneghan, S. P., Vangsness, M. D., and Hedman, P. O., 1991, "Flame Stability and Lean Blowout—A Research Program Progress Report," Paper No. 91-7037, *Proceedings of Tenth ISABE,* Nottingham, England, pp. 372–384.

Takahashi, F., Schmoll, W. J., and Vangsness, M. D., 1990, "Effects of Swirl on the Stability and Turbulent Structure of Jet Diffusion Flames," AIAA Paper No. 90-0036.

Reducing Gas Turbine Emissions Through Hydrogen-Enhanced, Steam-Injected Combustion

J. R. Maughan

J. H. Bowen

GE Corporate R&D,
General Electric Company,
Schenectady, NY 12301

D. H. Cooke
M. W. Kellogg Company,
Houston, TX 77210

J. J. Tuzson
Gas Research Institute,
Chicago, IL 60202

The potential for reducing emissions from gas turbines by injecting steam for NO_x control and hydrogen for CO control is evaluated through laboratory-scale combustion experiments. Results showed that hydrogen addition into a steam-injected diffusion combustor at hydrogen/fuel molar ratios of approximately 20 percent was associated with somewhat increased NO_x production and reduced CO emissions. Both effects are attributed to an increase in the local stoichiometric flame temperature. However, the decrease in CO was greater than the increase in NO_x, resulting in a net emissions benefit, or a shifting of the NO_x–CO curve toward the origin. Consequently, a greater range of NO_x/CO emissions targets could be achieved when hydrogen was available. Additional experiments on premixed systems with hydrogen injection showed a significant increase in operability. Cost estimates for producing hydrogen with a conventional fired steam reformer suggested high capital costs unless ample steam is already available. Hence, the technology is particularly well suited for turbines that use steam for power augmentation. Alternate reforming technology, such as catalytic partial oxidation, offers the potential for reduced capital costs.

Introduction

Of the several routes to lower emissions from natural gas-fueled gas turbines, steam or water injection was the first approach to be widely applied and is still the most prevalent NO_x abatement technique in use. Steam injection achieves significant levels of NO_x reduction without major modifications to the combustion hardware or gas turbine operating characteristics, and can augment power output as well. In addition, steam injection is readily controllable and can be varied from site to site to meet local regulations as required without other modifications to the combustion system [1].

The accompanying schematic of the aerodynamic zones within a typical gas turbine combustor (Fig. 1) will help clarify how steam injection affects emissions. Air entering the head end through the primary air swirler creates a swirling flow and recirculation zone into which the fuel nozzle injects gaseous fuel. Combustion occurs as the fuel mixes into the surrounding airflow. Aerothermal conditions in this region are best characterized by the overall head end temperature. This calculated value is the bulk, average temperature of the primary flame zone, based on complete combustion and mixing of the air, fuel, and steam (if present) entering this region. Although the bulk head end temperature is generally in the 2800–3000°F range, temperatures locally where fuel is mixing into the air and burning at a stoichiometric fuel/air ratio are significantly hotter, resulting in thermal NO_x formation. Head end conditions dominate the amount of NO_x produced by the combustor.

The recirculating flame zone is followed by a plug flow region where CO is rapidly consumed. Any additional dilution air entering further downstream reduces the head end temperature to the bulk, average combustor exit temperature, which is typically 2100–2500°F.

CO emissions are largely determined by the time–temperature history of the products after they leave the recirculating reaction zone. If the head end temperature is high, there will be ample concentrations of OH to react with the CO, and ample time for CO burnout. At lower temperatures, however, there may be insufficient time for the CO to be consumed prior to the quenching action of the dilution jets and the turbomachinery.

By injecting steam into the combustor with the fuel, the peak temperature in the local, stoichiometric flamelets is reduced, thereby limiting NO_x production sharply. The addition of steam reduces both the head end and combustor exit temperature unless additional fuel is injected to maintain constant temperature conditions and increase power.

CO emissions are also strongly affected by steam injection. The cooling of the flame that reduces NO_x production also inhibits CO burnout and increases the extent of the flame zone. At high levels of steam injection, the burning zone can become long enough to interact with the dilution jets, drawing in large amounts of air, which quench reaction rates and elevate CO emissions sharply.

Accordingly, the reduction of NO_x by steam injection is generally limited by the accompanying increase in CO emissions. In most applications, current steam injection technology does not allow emissions targets lower than 25 ppm NO_x, and in some instances 42 ppm, to be met without exceeding CO standards.

Regulated emissions levels, however, are rapidly dropping below 25 ppm NO_x, placing considerable pressure on the development of lower emissions combustors for both new and existing machines. One option now under aggressive development is the engineering of entirely new systems, which achieve low NO_x through lean, premixed combustion. While these designs promise to achieve low NO_x without steam or water injection, they are also associated with a number of disadvantages that make a dry low NO_x retrofit unattractive. Entirely new combustion hardware is needed as well as new control systems and piping. Operating and maintenance procedures are significantly affected. Furthermore, most dry low NO_x systems are still associated with considerable technical risk, including operability range and CO levels as NO_x emissions drop toward single digits. Because of the technical challenges, it is likely to be several years before DLN systems are available across all of the manufacturers' product lines, including machines that are now steam-injected.

An alternative technology and the subject of this research is to improve the performance of existing steam-injected systems.

Contributed by the International Gas Turbine Institute and presented at ASME Cogen Turbo Power '94, Portland, Oregon, October 25–27, 1994. Manuscript received by the International Gas Turbine Institute July 11, 1994. Associate Technical Editor: E. M. Greitzer.

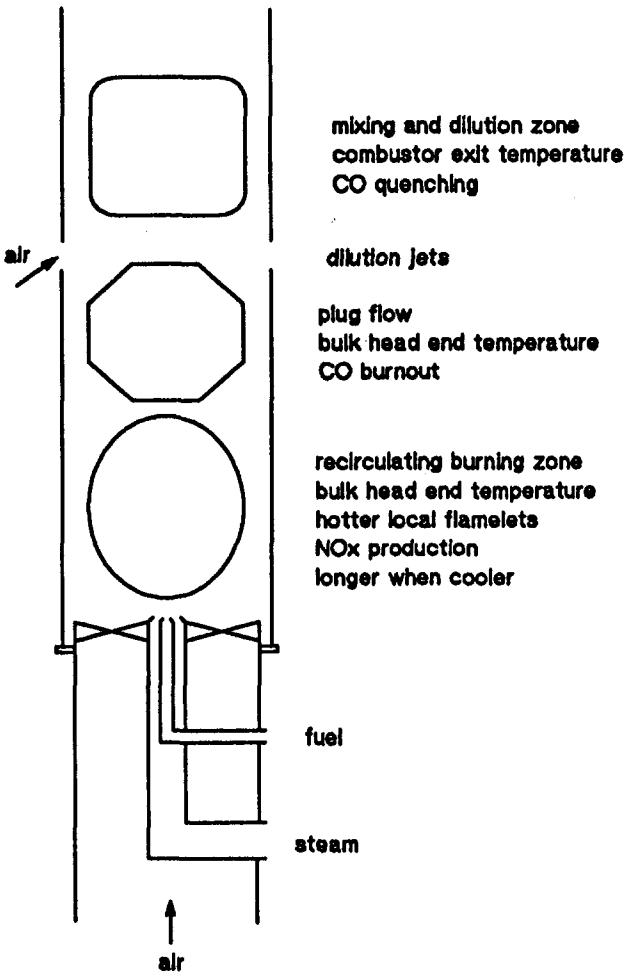

Fig. 1 Schematic of gas turbine combustion zones

One proposal for reducing CO from steam-injected combustors is to inject hydrogen as well. Hydrogen is expected to have several benefits in the combustor. Hydrogen will result in higher local flame temperatures, increased reaction rates in the recirculation zone, and greater OH concentrations and CO burnout rates. In addition, hydrogen will lower the lean flammability limit and draw the flame toward the head end of the combustor, allowing greater residence time for CO burnout. All of these characteristics should help reduce CO emissions. Consequently, it is expected that hydrogen injection will enable lower overall emissions targets to be met with steam injection.

The proposed source of hydrogen is partial reforming of the natural gas fuel in a separate, stand-alone reformer. When methane in the fuel and steam from a steam generator are heated together to a temperature of approximately 1400°F, the CH_4 begins to decompose and react with the steam to form hydrogen. In addition, carbon monoxide and carbon dioxide are formed, with the H_2/CO and H_2/CO_2 ratios increasing with temperature. Typical mole percents of the composition exiting a reformer at 1400°F would be 42 percent H_2, 41 percent H_2O, 6 percent CH_4, 6 percent CO_2, and 5 percent CO. In practice, only a portion of the available fuel supply would be reformed and blended back into the feedstock to result in the required hydrogen concentrations.

Combustion of reformed fuels containing hydrogen is also a key element of the proposed Chemically Recuperated Gas Turbine Cycle, a concept where the endothermic methane reforming reactions are used to recover gas turbine exhaust energy [2, 3]. Similar fuels are also derived from the gasification of coal [4, 5].

The primary objective of the current research was to evaluate the technical potential of adding hydrogen to natural gas in order to achieve reduced NO_x and CO levels in steam-injected gas turbines. This objective was achieved through laboratory-scale experiments in a pressurized combustor with thermodynamic and aerodynamic conditions representative of a variety of gas turbines, including aeroderivatives, smaller mechanical drive machines, and heavy duty industrial gas turbines. Additional details are available in [6].

Although some effort was placed on identifying the chemical and aerothermal effects of hydrogen and steam injection, testing was principally directed at assessing the impact of hydrogen injection on NO_x emissions, CO emissions, flame stability, and combustor turndown, and on determining the amount of hydrogen required for a significant positive effect.

Experimental Facility

The experimental facility used for these experiments is shown as a schematic in Fig. 2. The pressure vessel is a 10 in. schedule 40 pipe rated to 300 psig at 1000°F. Four 4 in. quartz windows rated at 300 psig at 700°F are mounted on the vessel and provide optical access on three levels.

Air is supplied from a multistage, intercooled centrifugal compressor. Maximum air flow in the facility is 10 lbm/s at 550 psia, although these experiments used only a fraction of that capacity. Preheating of the supplied air to a maximum temperature of 1000°F can be achieved with a natural gas-fired, nonvitiating, process gas heater.

Air is supplied to the vessel through two independent lines. One line is used as vessel cooling air and operates with a maximum capacity of 1 lbm/s at 500°F, although typically unheated air is passed through this line. A second air line provides combustion air for the test and has a maximum airflow capacity of 0.3 lbm/s. This air passes through an independently controlled, 26 kW electric circulation heater, which allows for local control of the combustion air inlet temperature. Air flow through both air lines is metered with venturi flow meters and controlled with pneumatically actuated control valves. Vessel back pressure is controlled with a 1 in., water-cooled control valve at the vessel exhaust.

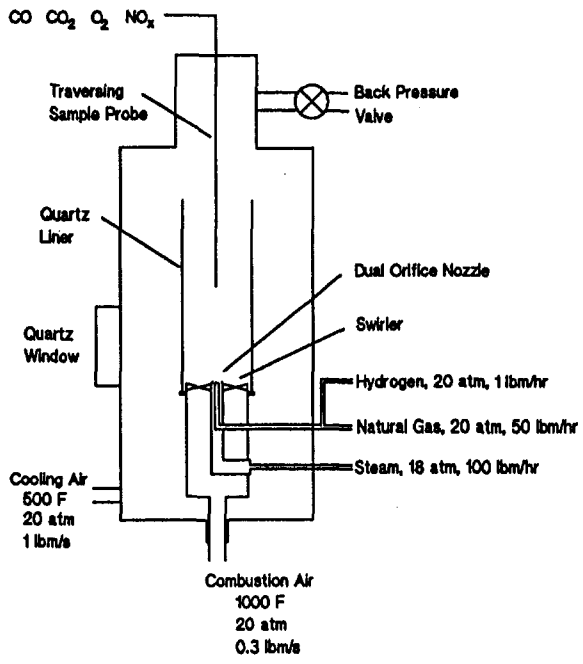

Fig. 2 Schematic of test facility used for initial screening tests

Natural gas fuel is supplied from a reciprocating gas compressor with a maximum capacity of 500 psig and 0.3 lbm/s, although again only a fraction of that capacity is needed here. Fuel is metered with a venturi flow meter and controlled with an electrically actuated control valve. The electric actuator provides extremely fine control of the flow rate.

Steam is supplied from an electric steam generator located inside the test cell, which produces saturated steam at 250 psig and a rate of 86 lbm/hr. Heat tracing of the steam line between the generator and the vessel prevents condensation and provides some superheating. The steam flow rate is also metered with a venturi flow meter and controlled with an electrically actuated control valve. The pressure taps and measurement lines leading to the steam venturi flow meter are continuously purged with a small amount of nitrogen to prevent condensation. The purge flow is controlled with flow restrictors to less than 60 sccm, which is less than 0.2 percent of the steam flow in these tests and introduces an error of less than 0.05 in. water column in the flow venturi differential pressure measurements.

Hydrogen is supplied from a manifold of three size A gas cylinders, and is also controlled with an electrically actuated control valve. Because of the low flow rates involved in these tests, the hydrogen flow rate was determined by the measured pressure drop across a 3 ft length of 0.063 in. tubing, which served as essentially a laminar flow element flow meter. The measured flow rate over the expected range of Reynolds numbers was calibrated with a positive displacement bellows meter.

Gas sampling was performed with a single point, axial traversing, water-cooled probe and standard combustion gas analysis techniques. An uncooled gas sample was analyzed for NO and NO_x concentrations in a heated chemiluminescent analyzer. An additional portion of the gas sample was cooled, dried, and analyzed for CO and CO_2 in an infrared gas analyzer and for O_2 in a paramagnetic analyzer. All emissions data were standardized to dry conditions at 15 percent O_2. The probe was designed to provide some degree of thermal and pressure quenching to minimize CO burnout. A type B thermocouple was also installed at the tip of the gas sampling probe, allowing for axial traverses of centerline temperature.

All pressure, temperature, and emissions measurements are connected to a data acquisition controller for measurement and analog to digital conversion, and are subsequently fed into a personal computer running real-time data reduction and display software programmed in BASIC.

The combustor operating condition was defined in terms of the bulk, adiabatic, head end temperature, which is calculated from the measured flows of combustion air, natural gas, steam, and hydrogen. In the special case of natural gas and air only, the calculated bulk temperature and accuracy of the measured flow rates can be checked by comparison to the measured CO_2 and O_2 concentrations. In such instances, data consistently agreed to within 2 percent after careful calibration of the gas analyzers. This confirms the accuracy of the measured flow rates. During testing, the four critical flow rates were controlled to maintain the desired calculated temperature, steam/fuel mass ratio, and H_2/fuel mole ratio.

Initial Screening Tests

A schematic of the combustor used in the initial screening tests is also included in Fig. 2. Note that the initial tests were simplified by the absence of dilution jets. Consequently, the average head end and combustor exit temperatures are the same (neglecting heat losses). The primary swirler was taken from a GE LM1600 gas turbine, and has a diameter of approximately 1.5 in. The fuel nozzle used in all testing was scaled for reduced pressure from a steam-injected fuel nozzle for the LM1600. It consists of a central fuel passage, and a surrounding annular passage for steam flow. Hydrogen is premixed with the fuel well upstream of the fuel nozzle.

The swirler and fuel nozzle exit into a quartz tube with an inner diameter of 2.06 in. There are no dilution jets in this combustor and no air enters the combustor except through the swirler. The quartz liner is held in place with a graphite packing assembly at the base of the liner. Although quartz is a somewhat fragile material, there is little pressure drop across the liner in this configuration and the liner durability was generally good. However, the quartz can lose its clarity in a relatively short time, particularly with large amounts of steam injection.

The effects of steam and hydrogen injection on emissions from this flame are shown in Figs. 3 and 4. In these figures, the combustor head end, bulk adiabatic temperature, as calculated from the measured flow rates, was held at 2800°F while the steam/fuel mass ratio was increased to 2.0, resulting in approximately 8 ppm NO_x and 43 ppm CO without hydrogen injection. Adding hydrogen up to a hydrogen/fuel molar ratio of approximately 0.32 (while adjusting fuel and steam flows for a constant bulk head end temperature) increased NO_x to 12 ppm while CO decreased significantly to less than 10 ppm. This is consistent with the premise that hydrogen is increasing the local flame temperature, accelerating both CO burnout and NO_x production.

The NO_x–CO curve compiled from Figs. 3 and 4 is shown in Fig. 5, along with the NO_x–CO curve associated with steam injection alone at a head end temperature of 2800°F. These data show that the increase in CO associated with steam injection can be partially offset with hydrogen injection. For comparable levels of NO_x, the hydrogen-injected combustor produces less CO. The movement of the NO_x–CO curve toward the origin is significant. Clearly hydrogen injection would be of no benefit if the improvement in CO were not greater than the degradation in NO_x emissions.

Figure 6 contains similar data for a head end bulk temperature of 2500°F. The hydrogen fuel ratio is increased from 0 to 0.2 molar for steam fuel ratios of 0.5, 1.0, 1.5, and 2.0. Note that NO_x increases in all cases as hydrogen is added, but that flames with less steam and higher NO_x exhibit the greatest increase in NO_x. This is consistent with the exponential nature of NO_x production. The hotter flame interface shows the greatest increase in NO production rate when the temperature is increased by roughly a fixed amount. For a steam/fuel ratio of 2.0, the local flame temperature and NO_x emissions are lower. Conse-

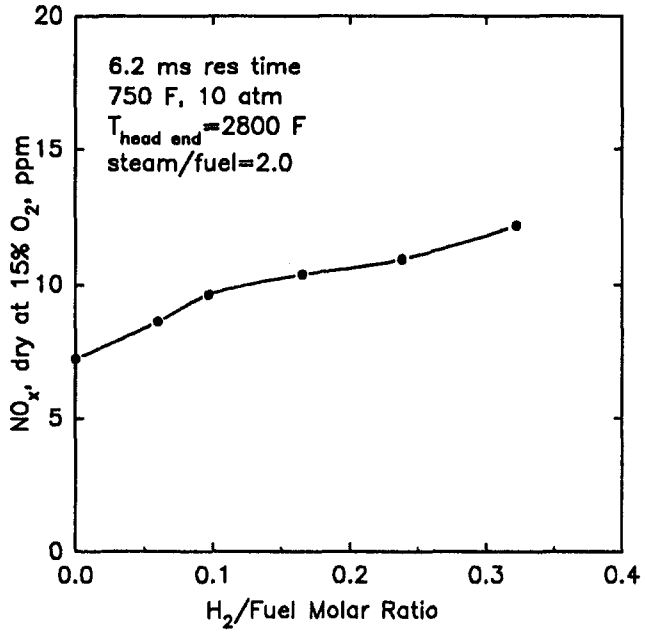

Fig. 3 Effect of H_2 injection on NO_x emissions from a steam-injected diffusion flame

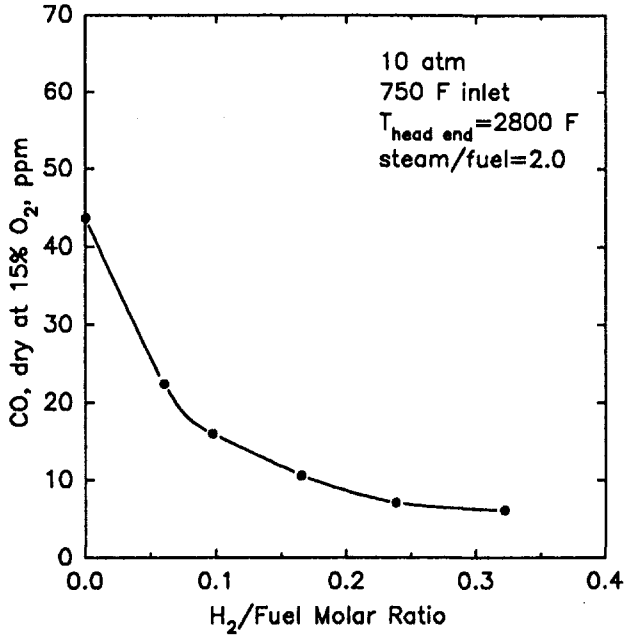

Fig. 4 Effect of H_2 injection on CO emissions from a steam-injected diffusion flame

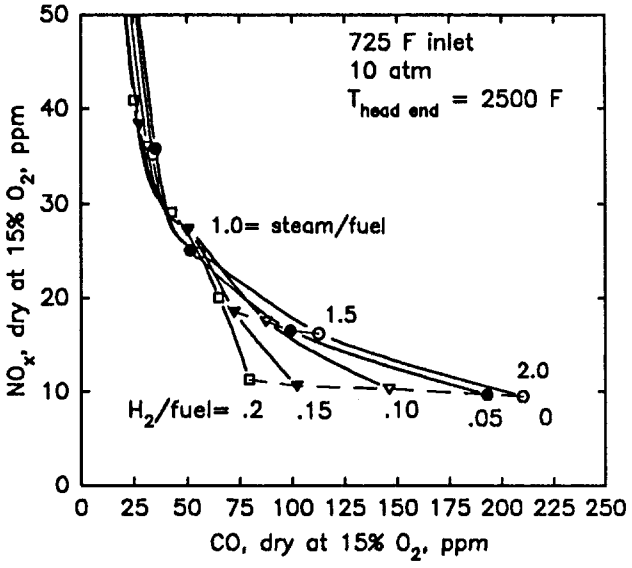

Fig. 6 Effect of both hydrogen and steam injection on NO_x–CO curve for a diffusion flame held at constant head end bulk temperature

quently, the effect of increasing the local temperature with hydrogen is less pronounced, although some increase can be seen.

At this temperature of 2500°F, steam injection results in considerable quantities of CO, approximately 225 ppm at steam/fuel = 2.0. Injecting hydrogen results in a significant increase in the CO burnout rate, and lower emissions. As with the NO_x emissions data, the impact of hydrogen injection varies with the steam fuel ratio. For low steam injection rates, local flame temperatures are high, and the CO burnout rate is already sufficiently rapid for complete oxidation. A further increase caused by hydrogen injection can have no significant impact. The opposite, of course, is true when steam injection rates are high.

Hydrogen generation from a portion of the fuel feedstock would also result in the formation of CO, CO_2 and H_2O as byproducts. Additional testing with H_2/CO/CO_2 mixtures instead of pure hydrogen, however, confirmed that these diluents do not significantly affect results, as long as the bulk, head end temperature is held constant. The H_2/CO and H_2/CO_2 molar ratios chosen for testing were 7.8 and 6.5, respectively, which correspond to conditions exiting a typical steam reformer at 1400°F. The corresponding bottled gas mixture, as delivered, was 10 percent CO, 12 percent CO_2, and 78 percent H_2, by volume. In practice, water vapor would also be generated by the reformer, with a H_2/H_2O molar ratio of 1.01. Although this water vapor would be premixed into the fuel, unlike the steam used for NO_x suppression, it was nevertheless neglected in the current testing because of its relatively small quantity (compared to the surrounding steam). This testing showed no significant change in NO_x or CO emissions, suggesting that the presence of the other minor diluents associated with reforming natural gas does not negate the noted emissions advantages of the hydrogen.

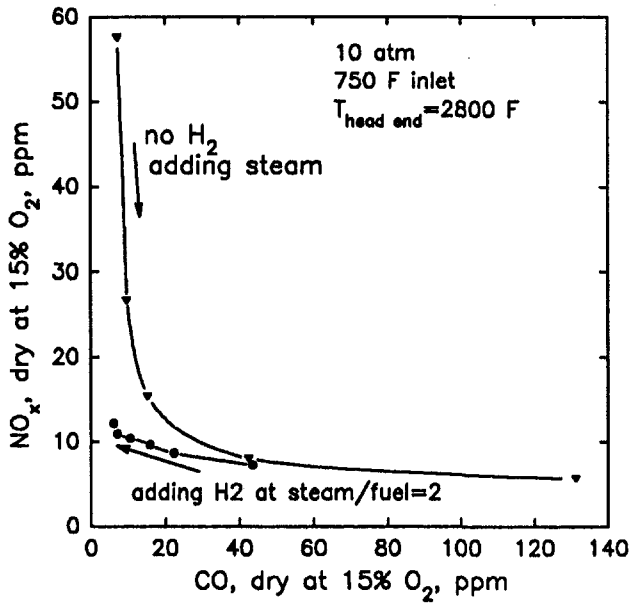

Fig. 5 NO_x–CO curve for steam injection and steam and hydrogen injection in a diffusion flame held at constant bulk temperature

Axial centerline emissions profile data for the NO_x concentration (corrected to 15 percent O_2) are shown in Fig. 7 for a combustor temperature of 2500°F. Profiles of a dry, baseline flame are shown along with data for steam/fuel = 2.0 (mass) and for steam/fuel = 2.0 and H_2/fuel = 0.2 (molar). In general, the NO_x profiles are fairly flat, reflecting the observation that NO is produced in the initial, hottest regions of the flame where local reaction temperatures rise well above the bulk average due to the non-premixed flame. NO_x is neither created nor destroyed further in the cooler regions downstream, although mixing of the different flame regions can affect the centerline concentration. Consistent with the earlier data, steam injection reduces NO_x formation while hydrogen injection causes a slight increase.

The corresponding CO profiles in Fig. 8 show the rapid oxidation of CO to low equilibrium levels within the combustor when steam is not injected. The effect of steam injection, however, is to delay the oxidation of CO, causing it to plateau at levels of several hundred ppm before eventually decaying to lower concentrations. The primary cause of this increase is that mixing of the steam into the flame results in localized regions that are too cool for complete oxidation of the fuel. Consequently, greater amounts of partially burned fuel (and therefore CO) recirculate back toward the swirler, increasing CO concentrations along the centerline.

Although the data show that these elevated CO emissions will eventually burn out if given sufficient residence time, the

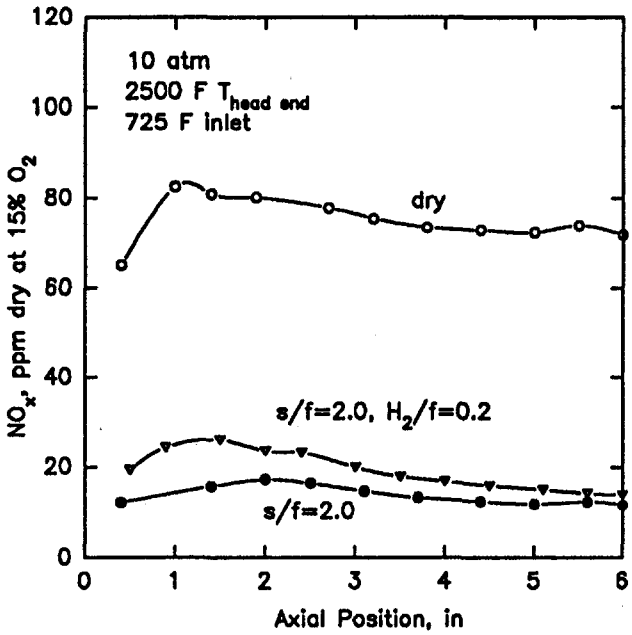

Fig. 7 Centerline axial profiles of NO_x concentration in a dry diffusion flame, a flame with steam injection, and a flame with steam and hydrogen injection

distance from the flame zone to the quenching action of the dilution jets is generally not sufficient for complete burnout if the CO plateau stretches too long. In a gas turbine combustor, interaction of the CO plateau with the dilution jets and the rapid expansion of the turbine itself results in greater CO emissions with steam injection. Whether and how much CO results depends not only on the amount of CO in the products before quenching but also on the temperature of the products, as that will determine the CO burnout rate.

Hydrogen injection significantly reduces the magnitude of the CO concentration on the plateau. Again, the improved CO burnout is attributed to elevated local flamelet temperatures and increased reactivity of the products. Note, however, that the extent of the plateau is not significantly affected. Additional work, beyond the objectives of the current study, is required to understand fully the aerodynamics and chemical kinetics responsible for these profiles.

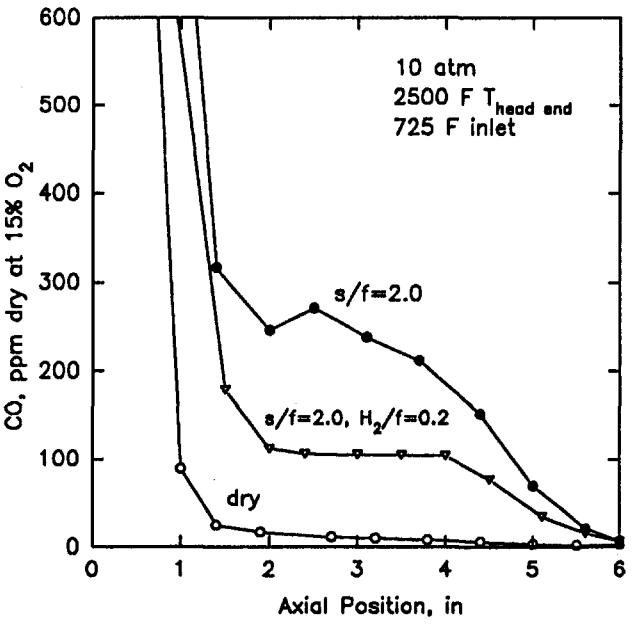

Fig. 8 Centerline axial profiles of CO concentration in a dry diffusion flame, a flame with steam injection, and a flame with steam and hydrogen injection

Results for Combustor With Dilution Jets

The results just described demonstrated the potential for hydrogen injection to reduce CO emissions from steam-injected gas turbines. The next test objective was to characterize combustor performance over a larger range of conditions. Accordingly, the combustor was modified somewhat to be more representative of a gas turbine combustor.

The configuration for the earlier tests (shown in Fig. 2) was not wholly representative of a gas turbine combustor because it had no dilution or primary jets, which can significantly affect CO burnout, flame length, and turndown. To better represent these aspects of performance, and the effects of steam and hydrogen on them, the combustor was modified by adding dilution jets, as shown in Fig. 9. The combustion liner was lengthened to the vessel exit and six dilution holes were added, targeting a dilution mass flow of approximately 20 percent of combustion air flow. The axial length between the swirler exit and dilution plane was 5.0 in. Because extending the liner to the exit of the vessel creates a pressure drop across the liner, quartz is no longer suitable for a liner material, and stainless steel liners were used.

These jets drop the bulk head end or burning zone temperature from approximately 2800°F to a combustor exit temperature of 2400°F, and tend to quench the flame at that axial location, giving rise to increased CO at lower temperatures. In addition, the jets mix the flow and result in an averaged emissions sample further downstream in the liner. The sample probe during testing was located 6 in. above the dilution jets. While this configuration does not exactly match the time–temperature history of a gas turbine because there is no turbine downstream for a further drop in temperature and aerodynamic quenching, it is a closer representation. The calculated, adiabatic, bulk head end temperature is still used as the principal indicator of combustor operating condition.

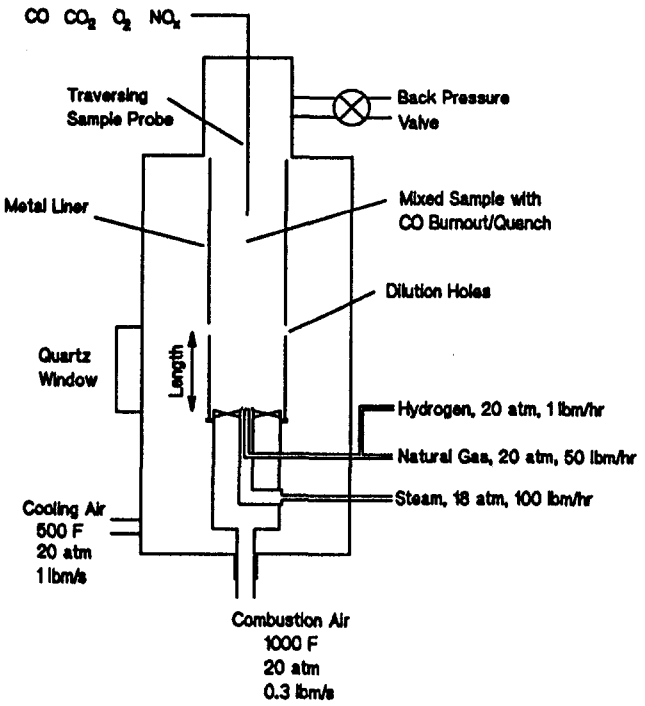

Fig. 9 Schematic of modified test facility and combustor with dilution jets

Typical emissions data for the modified combustor are shown in Figs. 10 and 11. Four curves are shown, including a dry diffusion baseline, hydrogen injection alone at H_2/fuel = 0.2 molar, steam injection alone at steam/fuel = 2.0 mass, and for both steam and hydrogen injection (at rates of 0.2 and 2.0, respectively). Each curve extends to the minimum operating temperature, below which lean blowout occurs.

Trends are consistent with the earlier data. NO_x emissions are a concern at high temperatures, while CO emissions are a concern at lower temperatures. Steam injection decreases NO_x and increases CO, while H_2 injection has the opposite effect. The effect of hydrogen injection under elevated CO conditions is evident from the figure for both dry and steam-injected conditions, and illustrates another potential benefit of hydrogen injection in a gas turbine combustor. The increased reactivity of the hydrogen not only improves CO burnout at low combustor exit temperatures, but also can be used to extend combustor turndown. The data show how H_2 injection improves stability and turndown because of its wide flammability limit and high stoichiometric flame temperature.

Testing was further expanded to account for the additional CO and CO_2 that would be associated with the hydrogen formation. Accordingly, a bottled mixture of H_2, CO, and CO_2 was blended into the fuel instead of pure hydrogen. For the massively steam-injected flame, the additional diluents (including steam from the reforming process) had no discernible effect, as is perhaps expected because the amount of CO, CO_2, and steam is insignificant compared to the NO_x suppression steam.

For the dry diffusion flame, however, significant effects were seen when the steam associated with reforming was considered. When steam at a steam/fuel ratio of 0.3 (mass) was mixed into the natural gas along with the H_2/CO/CO_2 blend, a significant fraction of the performance improvement offered by H_2/CO/CO_2 injection alone was eroded.

Although that test condition represents a steam/H_2 ratio about twice what would be expected from a reformer (lower steam flow rates could not be metered), the data nevertheless suggest significant benefit to condensing water vapor out of the reformed fuel prior to combustion if lean blowout (LBO) enhancement for a non-steam-injected diffusion flame is the objective.

The ability to meet low NO_x and CO targets is enhanced by the capability to inject hydrogen with the fuel gas. To illustrate this, the amount of steam and hydrogen injection required to meet hypothetical NO_x and CO emissions goals in the combustor sketched in Fig. 9 was determined over a range of combustor head end temperatures. These data are tabulated in Table 1.

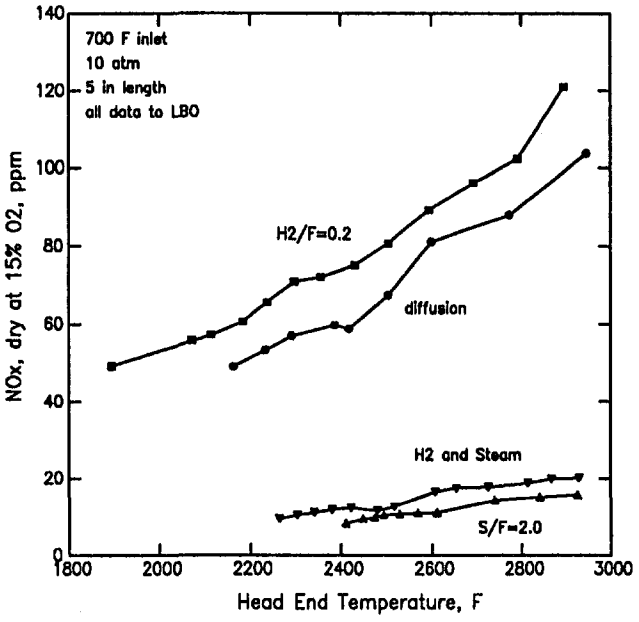

Fig. 10 Effect of steam and hydrogen injection on NO_x emissions and lean blowout limit for the modified combustor with dilution jets

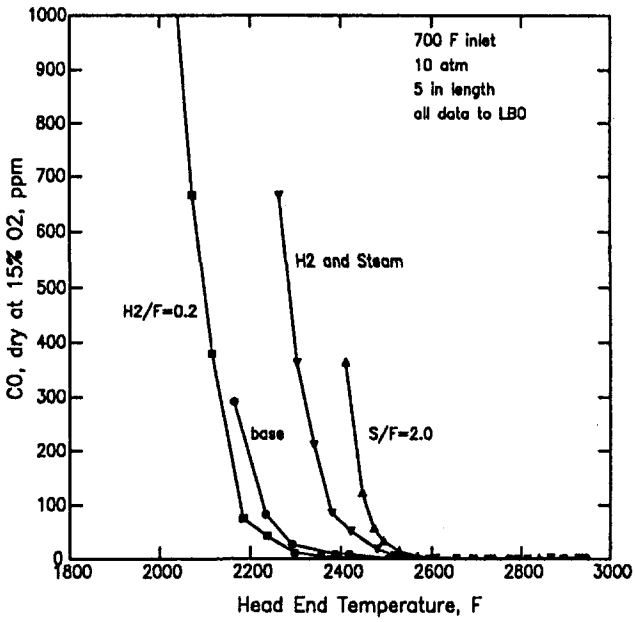

Fig. 11 Effect of steam and hydrogen injection on CO and lean blowout for the modified combustor with dilution jets

In this idealized combustor, NO_x and CO levels are considerably lower than in actual gas turbines, and NO_x targets of 42 and 25 ppm can be met through steam injection without excessive CO production or hydrogen injection. Hydrogen is needed only when CO levels begin to rise sharply as the steam injection drives NO_x to single digits. Also, note that, because of the rapid increase in CO burnout rates with temperature, overall lower emissions targets are actually easier to achieve in a hotter combustor. An increase in the combustor head end and exit temperature allows greater steam injection and NO_x suppression without CO quenching.

The range of emissions goals that can be met in this laboratory combustor, however, is clearly expanded through the use of hydrogen injection to include 9/25 and 9/9 at 2450°F and 25/50 and 25/25 at 2400°F, although additional steam must be

Table 1 Steam and hydrogen flowrates required to meet hypothetical emissions targets in a simplified, laboratory combustor

Steam-to-Fuel / H_2-to-Fuel Ratios Required to Meet NO_x/CO Targets of:

Head End	NO_x/CO Target					
Temp.	42/25	25/50	25/25	9/50	9/25	9/9
3000	0.88/0	1.4/0	1.4/0	2.7/0	2.7/0	2.7/0
2900	0.5/0	1.2/0	1.2/0	2.5/0	2.5/0	2.5/0
2800	0.3/0	0.9/0	0.9/0	2.5/0	2.5/0	2.5/0
2600	0.2/0	0.3/0	0.3/0	2.3/0	2.3/0	2.2/0
2500	0.2/0	0.2/0	0.2/0	2.2/0	2.2/0	2.2/0
2450	0.2/0	0.2/0	0.2/0	2.1/0	2.2/0.1	2.5/0.15
2400	0.2/0	0.2/0	0.2/0.1	2.3/0.25	LBO	LBO
2300	0.2/0	LBO				
2200	0/0	LBO				
2100	LBO					

added with the hydrogen to keep NO_x below target levels. In effect, hydrogen injection is the equivalent of operating the combustor with a hotter head end temperature.

Although CO emissions in operating machines are inherently higher, similar effects will be seen. Hydrogen injection is effective over a relatively narrow temperature range in this combustor as a consequence of the steep increase in CO with a drop in temperature near blowout (Fig. 11). These CO curves appear considerably steeper than most engine data taken over the same range, and are probably affected by inadequate quenching after dilution, CO burnout between the dilution jets and the probe, lack of film cooling, and the relatively weak recirculation drawing dilution air back into the primary flame zone. Hydrogen injection may have a wider range of application in an actual machine.

Steam and Hydrogen Injection in a Premixed Combustor

Similar testing of the effects of hydrogen injection was performed for fully premixed combustion, where the air, H_2, CO, CO_2, and steam are all fully premixed before entering the combustor. Data in Fig. 12 show NO_x production and the lean blowout temperature for baseline premixed flames and for a premixed flame with H_2 injection. Hydrogen injection lowers the lean blowout temperature without affecting NO_x significantly.

In a diffusion flame, hydrogen injection increases local temperatures in the reaction zone. In a premixed flame, however, the reaction temperature is essentially uniform throughout the combustor. Consequently, NO_x production, which is governed by temperature, is less affected by hydrogen injection, as long as the bulk head end temperature is held constant, as is the case here. Reaction rates and flammability limits, however, are enhanced by hydrogen injection, allowing the flame to be stabilized at an overall lower temperature. CO data show a similar improvement.

In a premixed flame the effect of steam is expected to be less pronounced than in a diffusion flame, as the steam/fuel ratio is uniform (and lower) throughout the combustion zone. Steam injection to a steam/fuel mass ratio of 0.3 did not affect these results. That level exceeds the amount of steam expected from reforming natural gas for hydrogen production.

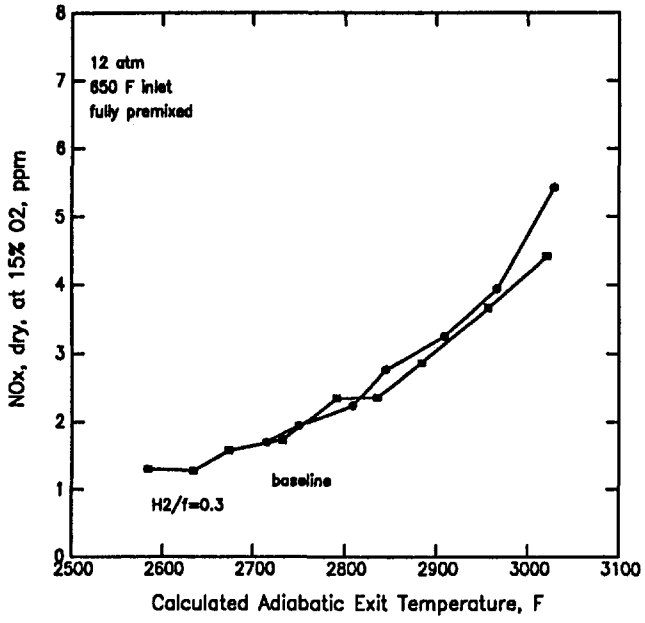

Fig. 12 Effect of hydrogen injection on NO_x emissions and stability in a premixed flame

Discussion of Potential Application

A companion study by the M. W. Kellogg Co. [6] was used to determine the expected concentrations exiting a natural gas reformer, and to assess the most promising reformer technologies and applications. Two reformer processes were investigated. The first was fired steam partial reforming, where a mixture of steam and methane is heated and then passed through catalyst filled tubes contained in a fired furnace, whereby CO and H_2 are produced. This is the proven, economical, state-of-the-art method in many syngas processes. The $H_2/CO/CO_2$ concentrations used in this testing were determined from this type of reformer.

The capital costs of the fired reformer system were found to be rather high for small applications, however, unless ample steam is already available. Consequently, current steam-injected applications appear to be the best candidates for this technology. Gas turbines such as the GE LM5000 and LM1600 generate steam in exhaust duct heat recovery systems, which is used for power augmentation, efficiency enhancement, and NO_x control. The available steam could also be used for reforming natural gas and generating hydrogen.

Another hydrogen production process that appears rather promising was also investigated. This is a newly developed, low-temperature, steam-free, catalytic partial oxidation (POX) process [7]. Installed capital costs for the new process appear to be much lower, but the process is unproven and there are uncertainties involved. Integration of a simplified hydrogen-reforming process with existing steam generation equipment offers the potential for a low-cost, effective route to lower emissions.

An additional application that bears consideration is the possibility of including a hydrogen source with some dry low NO_x installations. Achieving acceptable part-load CO emissions on dry low NO_x combustors tuned for extremely low NO_x appears to be a major technical challenge. That technology is now under development. Maintaining premixed operation over an acceptable portion of the load range is also a concern. The availability of hydrogen at such sites could result in a significant improvement in performance. Data shown earlier demonstrated how hydrogen injection in a premixed combustor can reduce CO and improve turndown. The cost of the hydrogen generation would have to be compared to the costs of a CO catalyst, or significant further combustor development.

Conclusions

This testing in a laboratory-scale, swirl-stabilized combustor has demonstrated the potential of hydrogen-enhanced, steam-injected combustion. Premixing hydrogen into natural gas prior to combustion in a steam-injected flame raised NO_x emissions and lowered CO emissions. In general, however, when sufficient steam was injected for significant NO_x suppression, CO emissions were lowered more than NO_x was increased, moving the NO_x–CO curve toward the origin. This allowed greater steam to be injected without CO production, and allowed lower emissions targets to be achieved. Hydrogen/fuel molar ratios of approximately 15 to 20 percent were required for CO reductions of 50 percent. Additional minor diluents such as CO and CO_2 in the fuel did not significantly affect results. Testing was performed under aerodynamic and thermodynamic conditions sufficiently similar to gas turbine combustors that comparable results can be reliably predicted for actual engine testing.

In addition, under all conditions tested, the sharp increase in CO associated with operating the combustor at lower temperatures was diminished with hydrogen injection and the lean blow out limit was extended to lower temperatures. This was characteristic of both dry and steam-injected flames, and of diffusion and premixed combustion. Hydrogen/fuel ratios of approximately 20 percent reduced CO by a factor of two and extended operability by over 100°F.

The possibility of integrating a natural gas reformer with the waste heat boiler at a STIG site, or an alternate technology such as the POX reformer, offers the potential for a relatively low-cost system for very low emissions. A complete plant study, targeting a specific steam-injected machine, is needed before the costs can be more reliably estimated.

Although conditions in gas turbines and aircraft engines are significantly more complex than those tested here, these screening tests show the potential for improving combustor emissions and performance with hydrogen injection. Future research and sector testing with an integrated reformer will allow the emissions benefit to be more directly quantified for a target machine, and will determine the development effort needed to apply the most suitable reformer technology.

Acknowledgments

Funding for this work from the Gas Research Institute under contract No. 5091-293-2188 and the direction of J. J. Tuzson is gratefully acknowledged. The support of J. F. Dalpe at GE-CRD and of GE Power Generation and GE Aircraft Engines is also greatly appreciated.

References

1 Tuzson, J., "Status of Steam-Injected Gas Turbines," ASME JOURNAL OF ENGINEERING FOR GAS TURBINES AND POWER, Vol. 114, 1992, pp. 682–686.

2 Janes, J., "Chemically Recuperated Gas Turbine," California Energy Commission Draft Staff Report P500-90-001, 1990.

3 Lutz, A. E., "Kinetic Computations of NO_x Emissions From Reformed Fuel Mixtures in Lean-Premixed Gas Turbines," presented at the Combustion Institute Western States Section Fall Meeting, Paper No. 92-96, 1992.

4 Sabla, P. E., and Kutzko, G. G., "Combustion Characteristics of the GE LM2500 Combustor With Hydrogen-Carbon Monoxide-Based Low Btu Fuels," ASME Paper No. 85-GT-179, 1985.

5 Allen, R. P., Battista, R. A., and Ekstrom, T. E., "Characteristics of an Advanced Gas Turbine With Coal-Derived Fuel Gases," ASME Paper No. 91-JPGC-GT-5, 1991.

6 Maughan, J. R., Bowen, J. H., Kimura, S. G., Cooke, D. H., and Joshi, G., "Evaluation of Reducing Gas Turbine Emissions Through Hydrogen-Enhanced Steam-Injected Combustion," Gas Research Institute Final Report, GRI-93/0272, 1993.

7 Green, M. L. H., Cheetham, A. K., and Vernon, P. D. F., "Catalytic Gas Conversion Method," U.S. Patent No. 5149464, 1992.

A Spinning Finite Beam Element of General Orientation Analyzed With Rayleigh/Timoshenko/Saint-Venant Theory

T. J. S. Abrahamsson
Saab Military Aircraft,
Linköping, Sweden

J. H. Sällström
Division of Solid Mechanics,
Chalmers University of Technology,
Göteborg, Sweden

Linear vibrations are studied for a straight uniform finite beam element of general orientation spinning at a constant angular speed about a fixed axis in the inertial space. The gyroscopic and circulatory matrices and also the geometric stiffness matrix of the beam element are presented. The effect of the centrifugal static axial load on the bending and torsional dynamic stiffnesses is thereby accounted for. The Rayleigh/Timoshenko/Saint-Venant theory is applied, and polynomial shape functions are used in the construction of the deformation fields. Nonzero off-diagonal elements in the gyroscopic and circulatory matrices indicate coupled bending/shearing/torsional/tensional free and forced modes of a generally oriented spinning beam. Two numerical examples demonstrate the use and performance of the beam element.

1 Introduction

Spinning finite beam elements in structural vibration analysis have been treated by several researchers since the early 1970s. Practical applications are found for turbines, combustion engines, space structures, etc. An early investigation of spinning flexible rotors modeled by use of finite shaft elements was made by Ruhl [1] in 1970. He employed the Euler/Bernoulli beam theory but neglected gyroscopic moments for the finite shaft elements. In 1980 Nelson [2] presented a study of flexible rotors, which utilized a finite Rayleigh/Timoshenko spinning shaft element. He considered rotatory inertia, bending/shearing deformation and gyroscopic forces, and also second-order effects of a large static axial load. Asymmetric rotors were studied by Kang et al. [3]. They developed a finite beam element for modeling asymmetric shafts. A method for calculating matrices for a generally oriented finite beam element was given by Likins [4] in 1972.

A set of governing linear differential equations of motion, in body-fixed coordinates, for a generally oriented spinning Euler/Bernoulli/Saint-Venant finite beam element, with distributed parameters, was established by Wittrick and Williams [5] in 1982. They derived the dynamic stiffness matrix in stationary harmonic vibration for the spinning beam element. In order to obtain simplified differential equations with constant coefficients, they assumed that the static axial sectional force along the beam (from the centrifugal field) did not vary irrespective of the orientation of the element. They also assumed that the torsional motion of the beam element did not couple with the bending/tensional motion. In 1988, Leung and Fung [6] established, by use of an analytical mechanics approach and assumed shape functions, the governing constant-coefficient matrices of a spinning Euler/Bernoulli/Saint-Venant finite beam element, also neglecting the coupling between the torsional and bending/tensional motions.

In 1991, Lundblad [7] advanced an exact (without spatial discretization errors) harmonic dynamic stiffness matrix of a generally oriented spinning Rayleigh/Timoshenko/Saint-Venant beam element considering stiffness, inertia, gyroscopic, and circulatory effects. He also included internal and external viscous damping effects. Lundblad showed that couplings exist between the torsional motion and the bending/shearing/tensional motion. Like Wittrick and Williams [5], he approximated the static axial sectional force in the generally oriented element as being constant. Lundblad's method involves extensive numerical work when establishing the dynamic stiffness matrix.

The present work adopts Lundblad's classical mechanics approach using d'Alembert forces in the derivation of the constant-coefficient spinning-speed-dependent gyroscopic, circulatory, and geometric stiffness matrices $\mathbf{G} = \mathbf{G}(\Omega)$, $\mathbf{H} = \mathbf{H}(\Omega)$, and $\mathbf{K}^g = \mathbf{K}^g(\Omega)$. These matrices appear in the equations of motion of a discretized damped beam element. In matrix form one has

$$\mathbf{M}\ddot{\mathbf{n}}(t) + [\mathbf{C} + \mathbf{G}(\Omega)]\dot{\mathbf{n}}(t) + [\mathbf{K} + \mathbf{K}^g(\Omega) + \mathbf{H}(\Omega)]\mathbf{n}(t) = \mathbf{N}(t) \quad (1)$$

Here $\mathbf{n}$ is the nodal displacement vector containing the six beam end translations and the six beam end rotations taken in a corotating coordinate system. The load vector $\mathbf{N}$ contains the vectorially associated end forces and end moments. The constant spinning speed is denoted by Ω.

In the derivation of the geometric stiffness matrix, the spatial variation of the axial load (due to centrifugal forces) is accounted for. Rayleigh/Timoshenko/Saint-Venant theory and polynomial shape functions are used throughout. The elastic stiffness matrix $\mathbf{K}$, the damping matrix $\mathbf{C}$ and the mass matrix $\mathbf{M}$ in Eq. (1) are independent of the spinning speed and can be found elsewhere, e.g., in Archer [8] or Przemieniecki [9], and are not reproduced here. The effect of a corotating ambient medium of Winkler type along each beam member (as included in the work by Lundblad [7]) can be taken into account in the same manner as used by Sällström [10] for a nonrotating beam element. The case with a rotating beam element in a nonrotating damped ambient medium will not be treated here.

The present work is an extension of that by Leung and Fung [6] in the sense that it also considers rotatory inertia and shear deformation in a manner consistent with the assumptions used by Rayleigh and Timoshenko. The matrices derived here can, therefore, be compared to the results by Leung and Fung [6] only in some special cases.

Contributed by the International Gas Turbine Institute and presented at the 39th International Gas Turbine and Aeroengine Congress and Exposition, The Hague, The Netherlands, June 13–16, 1994. Manuscript received by the International Gas Turbine Institute February 4, 1994. Paper No. 94-GT-77. Associate Technical Editor: E. M. Greitzer.

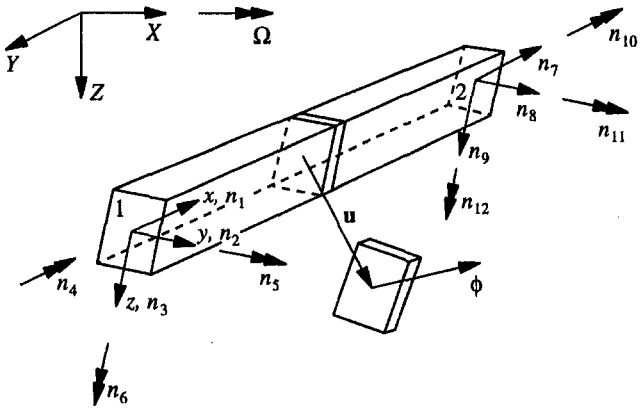

Fig. 1 Perspective view of straight uniform beam element 12 in corotating global coordinate system *XYZ*. Beam spins at constant angular rate Ω about global *X* axis, the direction of which is fixed in inertial space. Beam end translations and rotations n_1 to n_{12} and vectorially associated end loads N_1 to N_{12} are indicated. Local coordinate system *xyz* (with nondimensional length coordinate $\xi = x/L$). A beam lamina *dx* translated u and rotated ϕ from nondisplaced position is shown (different scales for geometry and deformation have been used). Beam properties are: mass distribution *m*, lamina radii of inertia r_x, r_y, and r_z, tensional stiffness *EA*, torsional stiffness GI_t, bending stiffnesses EI_y and EI_z, and shearing stiffnesses k_zGA and k_yGA.

2 Coordinates and Inertia Loading

A typical finite spinning beam element is shown in Fig. 1. The beam element is uniform and initially straight (in the nonspinning state) with its undeformed geometric centerline coinciding with the local coordinate axis x. The shear center and the mass center are assumed to coincide with the geometric center of the beam cross section. The nondimensional coordinate $\xi = x/L$, varying between zero at beam end number 1 and unity at beam end number 2, will be used in the assumed polynomial shape functions. No external loads act on the element except at its ends 1 and 2. The distributed inertia forces $\mathbf{U}$ and moments $\mathbf{\Phi}$ acting on a beam lamina of unit length and with cross-sectional area A are

$$\mathbf{U}(\xi) = -\int_A \mathbf{a}(\xi)\rho dA \tag{2a}$$

$$\mathbf{\Phi}(\xi) = -\int_A \mathbf{p} \times \mathbf{a}(\xi)\rho dA \tag{2b}$$

with

$$\mathbf{U}^T = \{U_x\ U_y\ U_z\} \tag{3a}$$

$$\mathbf{\Phi}^T = \{\Phi_x\ \Phi_y\ \Phi_z\} \tag{3b}$$

The forces per unit length in the local directions x, y, z are denoted by U_x, U_y, and U_z, and the corresponding moments about the axes x, y, z by Φ_x, Φ_y, and Φ_z. The acceleration vector $\mathbf{a}$ of the lamina element dA is determined by its position and by its relative motion in the corotating global coordinate system XYZ, and also by the spinning speed Ω of that coordinate system. The position of the lamina element dA is given by the coordinates $Y(\xi)$ and $Z(\xi)$ of the undeformed beam axis in the global coordinate system XYZ and by the translation $\mathbf{u}(\xi)$ and rotation $\boldsymbol{\phi}(\xi)$ of the beam cross section in the local coordinate system xyz, and, finally, by the position vector $\mathbf{p}_0$ of the element dA within the nonrotated beam cross section A. By evaluating the integrals in Eqs. (2a, b), with the proper acceleration vector $\mathbf{a}$ and position vector $\mathbf{p} = \mathbf{p}_0 + \boldsymbol{\phi} \times \mathbf{p}_0$ inserted, one obtains the inertia loading as

$$\mathbf{U} = \mathbf{U}_m + \mathbf{U}_g + \mathbf{U}_c + \mathbf{B}_u \tag{4a}$$

$$\mathbf{U}_m = -\mathbf{A}_u^{(2)}\ddot{\mathbf{u}} \tag{4b}$$

$$\mathbf{U}_g = -\mathbf{A}_u^{(1)}\dot{\mathbf{u}} \tag{4c}$$

$$\mathbf{U}_c = -\mathbf{A}_u^{(0)}\mathbf{u} \tag{4d}$$

$$\mathbf{\Phi} = \mathbf{\Phi}_m + \mathbf{\Phi}_g + \mathbf{\Phi}_c + \mathbf{B}_\phi \tag{4e}$$

$$\mathbf{\Phi}_m = -\mathbf{A}_\phi^{(2)}\ddot{\boldsymbol{\phi}} \tag{4f}$$

$$\mathbf{\Phi}_g = -\mathbf{A}_\phi^{(1)}\dot{\boldsymbol{\phi}} \tag{4g}$$

$$\mathbf{\Phi}_c = -\mathbf{A}_\phi^{(0)}\boldsymbol{\phi} \tag{4h}$$

The distributed loads $\mathbf{U}_m$ and $\mathbf{\Phi}_m$ are the usual inertia loads of a vibrating nonspinning beam in a fixed coordinate system. The gyroscopic parts, $\mathbf{U}_g$ and $\mathbf{\Phi}_g$, and the circulatory parts, $\mathbf{U}_c$ and $\mathbf{\Phi}_c$, of the inertia loading are used in the following for the derivations of the gyroscopic and circulatory matrices, respectively. State-independent static centrifugal loads $\mathbf{B}_u$ and $\mathbf{B}_\phi$ act on the beam element. These loads will cause an axial sectional force in the beam element. The influence of the axial loading on the vibratory motion will be taken into account by considering the geometric stiffness effect in the analysis.

The matrix $\mathbf{A}_u^{(2)}$ of mass per unit length and the matrix $\mathbf{A}_\phi^{(2)}$ of mass moments of inertia per unit length are used in a mass matrix derivation,

$$\mathbf{A}_u^{(2)} = m\begin{bmatrix} 1 & 0 & 0 \\ 0 & 1 & 0 \\ 0 & 0 & 1 \end{bmatrix} \tag{5a}$$

$$\mathbf{A}_\phi^{(2)} = m\begin{bmatrix} r_x^2 & 0 & 0 \\ 0 & r_y^2 & 0 \\ 0 & 0 & r_z^2 \end{bmatrix} \tag{5b}$$

They are given here for completeness but will not be further used in this work. The matrices $\mathbf{A}_u^{(1)}$ and $\mathbf{A}_\phi^{(1)}$, with elements $a_{u,ij}^{(1)}$ and $a_{\phi,ij}^{(1)}$, are associated with Coriolis forces and moments. They can be obtained by use of the projections Ω_x, Ω_y and Ω_z on the local xyz directions of the spin vector $\mathbf{\Omega}$. These skew-symmetric matrices are

$$\mathbf{A}_u^{(1)} = m\begin{bmatrix} 0 & -2\Omega_z & 2\Omega_y \\ 2\Omega_z & 0 & -2\Omega_x \\ -2\Omega_y & 2\Omega_x & 0 \end{bmatrix} \tag{6a}$$

$$\mathbf{A}_\phi^{(1)} = m\begin{bmatrix} 0 & -\Omega_z(r_x^2 + r_y^2 - r_z^2) & \Omega_y(r_x^2 + r_z^2 - r_y^2) \\ \Omega_z(r_x^2 + r_y^2 - r_z^2) & 0 & -\Omega_x(r_y^2 + r_z^2 - r_x^2) \\ -\Omega_y(r_x^2 + r_z^2 - r_y^2) & \Omega_x(r_y^2 + r_z^2 - r_x^2) & 0 \end{bmatrix} \tag{6b}$$

For a normal beam the matrix elements $a_{\phi,23}^{(1)}$ and $a_{\phi,32}^{(1)}$ are zero and they will be omitted in the further presentation of this work. The displacement-dependent centrifugal forces and moments are represented by the two matrices, $\mathbf{A}_u^{(0)}$ and $\mathbf{A}_\phi^{(0)}$

$$\mathbf{A}_u^{(0)} = m\begin{bmatrix} -(\Omega_y^2 + \Omega_z^2) & \Omega_x\Omega_y & \Omega_z\Omega_x \\ \Omega_y\Omega_x & -(\Omega_z^2 + \Omega_x^2) & \Omega_y\Omega_z \\ \Omega_x\Omega_z & \Omega_z\Omega_y & -(\Omega_x^2 + \Omega_y^2) \end{bmatrix} \tag{7a}$$

$$\mathbf{A}_{\phi}^{(0)} = m\begin{bmatrix} (\Omega_y^2 - \Omega_z^2) & \Omega_x\Omega_y & -\Omega_z\Omega_x \\ -\Omega_y\Omega_x & (\Omega_z^2 - \Omega_x^2) & \Omega_y\Omega_z \\ \Omega_x\Omega_z & -\Omega_z\Omega_y & (\Omega_x^2 - \Omega_y^2) \end{bmatrix} \times \begin{bmatrix} (r_y^2 - r_z^2) & 0 & 0 \\ 0 & (r_z^2 - r_x^2) & 0 \\ 0 & 0 & (r_x^2 - r_y^2) \end{bmatrix} \quad (7b)$$

The elements of these two matrices are denoted by $a_{u,ij}^{(0)}$ and $a_{\phi,ij}^{(0)}$ in the following. It can be noted that the matrix $\mathbf{A}_{\phi}^{(0)}$ is generally neither symmetric nor skew-symmetric, which results in a circulatory matrix of a general form. The static loads due to centrifugal forces and moments acting on the beam element are here represented by the column vectors $\mathbf{B}_u$ and $\mathbf{B}_\phi$,

$$\mathbf{B}_u = \begin{Bmatrix} \beta_{u1} \\ \beta_{u2} \\ \beta_{u3} \end{Bmatrix} = m\Omega^2\mathbf{L}\begin{Bmatrix} 0 \\ Y(\xi) \\ Z(\xi) \end{Bmatrix} \quad (8a)$$

$$\mathbf{B}_\phi = \begin{Bmatrix} \beta_{\phi 1} \\ \beta_{\phi 2} \\ \beta_{\phi 3} \end{Bmatrix} = -m\begin{Bmatrix} \Omega_y\Omega_z(r_z^2 - r_y^2) \\ \Omega_z\Omega_x(r_x^2 - r_z^2) \\ \Omega_x\Omega_y(r_y^2 - r_x^2) \end{Bmatrix} \quad (8b)$$

In Eq. (8a) the matrix $\mathbf{L}$ (not to be confused with the beam length L) is the rotation matrix from the global XYZ to local xyz coordinates.

3 Shape Functions and Assumed Deformations

The gyroscopic, circulatory, and geometric stiffness matrices will all be derived in consistency with an assumed deformation field of the beam element. The static deformation functions of a Rayleigh/Timoshenko/Saint-Venant beam element loaded at its ends in bending/shearing, torsion, and tension will be used. The linear and angular displacements of the beam element at a position ξ can be calculated as functions of the nodal translations and rotations (see Fig. 1), together with the assumed shape functions,

$$\begin{Bmatrix} \mathbf{u}(\xi) \\ \boldsymbol{\phi}(\xi) \end{Bmatrix} = \boldsymbol{\Psi}(\xi)\mathbf{n} \quad (9)$$

Here the shape function matrix $\boldsymbol{\psi}(\xi)$ is

$$\boldsymbol{\Psi}^T(\xi) = \begin{bmatrix} \psi_{1,1} & 0 & 0 & 0 & 0 & 0 \\ 0 & \psi_{3,3}(\theta_z) & 0 & 0 & 0 & -\psi_{5,3}(\theta_z) \\ 0 & 0 & \psi_{3,3}(\theta_y) & 0 & \psi_{5,3}(\theta_y) & 0 \\ 0 & 0 & 0 & \psi_{1,1} & 0 & 0 \\ 0 & 0 & \psi_{3,5}(\theta_y) & 0 & \psi_{5,5}(\theta_y) & 0 \\ 0 & -\psi_{3,5}(\theta_z) & 0 & 0 & 0 & \psi_{5,5}(\theta_z) \\ \psi_{1,7} & 0 & 0 & 0 & 0 & 0 \\ 0 & \psi_{3,9}(\theta_z) & 0 & 0 & 0 & -\psi_{5,9}(\theta_z) \\ 0 & 0 & \psi_{3,9}(\theta_y) & 0 & \psi_{5,9}(\theta_y) & 0 \\ 0 & 0 & 0 & \psi_{1,7} & 0 & 0 \\ 0 & 0 & \psi_{3,11}(\theta_y) & 0 & \psi_{5,11}(\theta_y) & 0 \\ 0 & -\psi_{3,11}(\theta_z) & 0 & 0 & 0 & \psi_{5,11}(\theta_z) \end{bmatrix} \quad (10)$$

The shape functions $\psi_{i,j}$ of the beam element used here can be found in the textbook by Przemieniecki [9]. They are repeated for completeness:

$$\psi_{1,1} = 1 - \xi \quad (11a)$$

$$\psi_{1,7} = \xi \quad (11b)$$

$$\psi_{3,3}(\theta_y) = [(1 - 3\xi^2 + 2\xi^3) + \theta_y(1 - \xi)]/(1 + \theta_y) \quad (11c)$$

$$\psi_{3,5}(\theta_y) = [(-\xi + 2\xi^2 - \xi^3)L + \theta_y(-\xi + \xi^2)L/2]/(1 + \theta_y) \quad (11d)$$

$$\psi_{3,9}(\theta_y) = [(3\xi^2 - 2\xi^3) + \theta_y\xi]/(1 + \theta_y) \quad (11e)$$

$$\psi_{3,11}(\theta_y) = [(\xi^2 - \xi^3)L + \theta_y(\xi - \xi^2)L/2]/(1 + \theta_y) \quad (11f)$$

$$\psi_{5,3}(\theta_y) = [(6\xi - 6\xi^2)/L]/(1 + \theta_y) \quad (11g)$$

$$\psi_{5,5}(\theta_y) = [(1 - 4\xi + 3\xi^2) + \theta_y(1 - \xi)]/(1 + \theta_y) \quad (11h)$$

$$\psi_{5,9}(\theta_y) = [(-6\xi + 6\xi^2)/L]/(1 + \theta_y) \quad (11i)$$

$$\psi_{5,11}(\theta_y) = [(-2\xi + 3\xi^2) + \theta_y\xi]/(1 + \theta_y) \quad (11j)$$

The bending/shearing ratio parameters are defined as

$$\theta_y = \frac{12EI_y}{k_zGAL^2} \quad (12a)$$

$$\theta_z = \frac{12EI_z}{k_yGAL^2} \quad (12b)$$

The shape functions of an Euler/Bernoulli beam element can be obtained as the special case for which both θ_y and θ_z are zero. The gyroscopic, circulatory, and geometric stiffness matrices of a spinning Euler/Bernoulli beam element can thus easily be recovered, if required, from the matrices presented below.

4 Gyroscopic and Circulatory Matrices

The consistent nodal load vector $\mathbf{N}_g$ due to the gyroscopic parts of the distributed inertia loading is given by the relation (see Cook et al. [11]):

$$\mathbf{N}_g = \int_0^1 \boldsymbol{\Psi}^T\begin{Bmatrix} \mathbf{U}_g \\ \boldsymbol{\Phi}_g \end{Bmatrix} L d\xi \quad (13)$$

Using Eqs. (4c) and (4g) for the gyroscopic part of the inertia load, together with the assumed linear and angular velocities $\{\dot{\mathbf{u}}^T\dot{\boldsymbol{\phi}}^T\}^T = \boldsymbol{\Psi}\dot{\mathbf{n}}$, one obtains

$$\mathbf{N}_g = -\mathbf{G}\dot{\mathbf{n}} \quad (14a)$$

$$\mathbf{G} = \int_0^1 \boldsymbol{\Psi}^T\begin{bmatrix} \mathbf{A}_u^{(1)} & \mathbf{0} \\ \mathbf{0} & \mathbf{A}_\phi^{(1)} \end{bmatrix}\boldsymbol{\Psi} L d\xi \quad (14b)$$

Equation (14b) gives the 12 × 12 gyroscopic matrix of the beam element. The 96 nonzero elements of this skew-symmetric matrix are given in the appendix.

The consistent nodal load vector $\mathbf{N}_c$ due to the circulatory parts of the distributed inertia loading is

$$\mathbf{N}_c = \int_0^1 \boldsymbol{\Psi}^T\begin{Bmatrix} \mathbf{U}_c \\ \boldsymbol{\Phi}_c \end{Bmatrix} L d\xi \quad (15)$$

Using Eqs. (4d) and (4h) for the circulatory part of the inertia load, together with the assumed linear and angular displacements in Eq. (9), one obtains

$$\mathbf{N}_c = -\mathbf{H}\mathbf{n} \quad (16a)$$

$$\mathbf{H} = \int_0^1 \boldsymbol{\Psi}^T\begin{bmatrix} \mathbf{A}_u^{(0)} & \mathbf{0} \\ \mathbf{0} & \mathbf{A}_\phi^{(0)} \end{bmatrix}\boldsymbol{\Psi} L d\xi \quad (16b)$$

Equation (16b) gives the nonsymmetric circulatory 12 × 12 matrix $\mathbf{H}$. This matrix generally holds 136 nonzero elements as given in the appendix. This implies that couplings exist in all possible combinations of bending/shearing, tensional, and torsional vibrations.

5 Axial Load Distribution

When a large static axial compressive/tensional force acts on a beam element of a frame structure, the stiffnesses in bending and torsion of that element are decreased/increased. Since the static distributed centrifugal loads $\mathbf{B}_u$ and $\mathbf{B}_\phi$ make the axial loads dependent on the spinning speed Ω of the structure, large spinning speeds may cause buckling instability of the structure. The calculation of the axial sectional forces must be treated as

a nonlinear problem calling for an iterative solution method for spinning speeds causing large deformations.

However, for small deformations, a linear analysis can be made and the compressive axial loads can be obtained by superimposing the solutions of two complementary static problems. In the first problem the consistent loads $\mathbf{N}^{cent}$ pertaining to the distributed inertia loads $\mathbf{B}_u$ and $\mathbf{B}_\phi$ are calculated for each beam element. These loads are applied to the joints of the structure. The corresponding static displacements $\mathbf{p}^{st}$ can then easily be calculated by use of the assembled global static stiffness matrix $\mathbf{K}$ of the structure. In the second problem the distributed inertia loads $\mathbf{B}_u$ and $\mathbf{B}_\phi$ are applied together with fictitious so-called fixed-loads, i.e., the loads that should be applied to the joints of the structure to prevent them from moving. These nodal loads are equal to the reversed consistent nodal loads, $-\mathbf{N}^{cent}$. This means that each beam element can be studied separately. Superposition of the solutions of these two complementary problems gives the solution of the actual problem and the total actual static axial force distribution $H(\xi)$.

In the first problem a constant static compressive axial force H_0 for each beam element is easily determined since the axial deformation of each beam element is implicitly known through the vector $\mathbf{p}^{st}$. Here both the displacement vector $\mathbf{p}^{st}$ and the axial force H_0 in each beam element are proportional to the square of the spinning speed Ω.

The consistent nodal loads due to the static centrifugal loading can be calculated as

$$\mathbf{N}^{cent} = \int_0^1 \mathbf{\Psi}^T \begin{Bmatrix} \mathbf{B}_u \\ \mathbf{B}_\phi \end{Bmatrix} L d\xi \tag{17}$$

The force and moment elements of the consistent nodal load vector $\mathbf{N}^{cent}$ can be calculated using Eqs. (8*a*, *b*) for static centrifugal load. One finds

$$N_1^{cent} = \frac{L}{6}(2\beta'_{u1} + \beta''_{u1}) \tag{18a}$$

$$N_2^{cent} = \frac{L}{60}(21\beta'_{u2}\theta_{z1} + 20\beta'_{u2}\theta_{z2} + 9\beta''_{u2}\theta_{z1} + 10\beta''_{u2}\theta_{z2}) - \beta_{\phi 3}\theta_{z1} \tag{18b}$$

$$N_3^{cent} = \frac{L}{60}(21\beta'_{u3}\theta_{y1} + 20\beta'_{u3}\theta_{y2} + 9\beta''_{u3}\theta_{y1} + 10\beta''_{u3}\theta_{y2}) + \beta_{\phi 2}\theta_{y1} \tag{18c}$$

$$N_4^{cent} = N_{10}^{cent} = \frac{L}{2}\beta_{\phi 1} \tag{18d, e}$$

$$N_5^{cent} = -\frac{L^2}{120}(6\beta'_{u3}\theta_{y1} + 5\beta'_{u3}\theta_{y2} + 4\beta''_{u3}\theta_{y1} + 5\beta''_{u3}\theta_{y2}) + \frac{L}{2}\beta_{\phi 2}\theta_{y2} \tag{18f}$$

$$N_6^{cent} = \frac{L^2}{120}(6\beta'_{u2}\theta_{z1} + 5\beta'_{u2}\theta_{z2} + 4\beta''_{u2}\theta_{z1} + 5\beta''_{u2}\theta_{z2}) + \frac{L}{2}\beta_{\phi 3}\theta_{z2} \tag{18g}$$

$$N_7^{cent} = \frac{L}{6}(\beta'_{u1} + 2\beta''_{u1}) \tag{18h}$$

$$N_8^{cent} = \frac{L}{60}(9\beta'_{u2}\theta_{z1} + 10\beta'_{u2}\theta_{z2} + 21\beta''_{u2}\theta_{z1} + 20\beta''_{u2}\theta_{z2}) + \beta_{\phi 3}\theta_{z1} \tag{18i}$$

$$N_9^{cent} = \frac{L}{60}(9\beta'_{u3}\theta_{y1} + 10\beta'_{u3}\theta_{y2} + 21\beta''_{u3}\theta_{y1} + 20\beta''_{u3}\theta_{y2}) - \beta_{\phi 2}\theta_{y1} \tag{18j}$$

$$N_{11}^{cent} = \frac{L^2}{120}(4\beta'_{u3}\theta_{y1} + 5\beta'_{u3}\theta_{y2} + 6\beta''_{u3}\theta_{y1} + 5\beta''_{u3}\theta_{y2}) + \frac{L}{2}\beta_{\phi 2}\theta_{y2} \tag{18k}$$

$$N_{12}^{cent} = -\frac{L^2}{120}(4\beta'_{u2}\theta_{z1} + 5\beta'_{u2}\theta_{z2} + 6\beta''_{u2}\theta_{z1} + 5\beta''_{u2}\theta_{z2}) + \frac{L}{2}\beta_{\phi 3}\theta_{z2} \tag{18l}$$

Here the β'_{ui} and β''_{ui} are the static centrifugal loads in the direction i at the beam ends 1 and 2, respectively; see Eq. (8). The additional bending/shearing parameters θ_{y1}, θ_{y2}, θ_{z1}, and θ_{z2} are defined in Eq. (A.2) in Appendix.

In the second problem the axial force variation $H^{fix}(\xi)$ within each beam element depending on the distributed inertia loads $\mathbf{B}_u$ and $\mathbf{B}_\phi$ will be determined. The centrifugal force distributions are given by Eqns. (8*a*, *b*). Their dependence on the beam element orientation is given by the 3×3 rotation matrix $\mathbf{L}$ with elements l_{ij}. The force distribution along the beam axis can be extracted as

$$U_x = m\Omega^2[l_{12}Y(\xi) + l_{13}Z(\xi)] \tag{19}$$

As the beam lamina position $(Y(\xi), Z(\xi))$ varies linearly with the beam coordinate ξ, one has

$$Y(\xi) = Y_1 + \Delta Y \xi \tag{20a}$$

$$\Delta Y = Y_2 - Y_1 \tag{20b}$$

$$Z(\xi) = Z_1 + \Delta Z \xi \tag{20c}$$

$$\Delta Z = Z_2 - Z_1 \tag{20d}$$

Here (Y_1, Z_1) and (Y_2, Z_2) are the YZ-coordinates of the beam ends 1 and 2. The axial load distribution $H^{fix}(\xi)$ of a beam with both ends fixed and with the applied external load given by Eq. (19) can now be calculated with basically an axial equilibrium consideration as

$$H^{fix} = H_1^{fix}(2\xi - 1) + H_2^{fix}(3\xi^2 - 1) \tag{21a}$$

$$H_1^{fix} = \tfrac{1}{2}mL\Omega^2(l_{12}Y_1 + l_{13}Z_1) \tag{21b}$$

$$H_2^{fix} = \tfrac{1}{3}mL\Omega^2(l_{12}\Delta Y + l_{13}\Delta Z) \tag{21c}$$

The total compressive axial force distribution is thus given by

$$H(\xi) = H_0 + H_1^{fix}(2\xi - 1) + H_2^{fix}(3\xi^2 - 1) \tag{22}$$

6 Geometric Stiffness Matrix

The geometric stiffness matrix for a beam studied in the xz-plane can be derived (see Cook et al. [11]) as

$$\mathbf{K}^g = -\int_0^1 \mathbf{\Psi}'^T_{3,\cdot} H(\xi) \mathbf{\Psi}'_{3,\cdot} d\xi / L \tag{23}$$

The row vector $\mathbf{\Psi}'_{3,\cdot}$ is the derivative of the third row of the matrix $\mathbf{\Psi}$ in Eq. (10). The elements of the geometric stiffness matrix pertaining to the displacement in the xz-plane are given in the appendix. The stiffness in torsion is also affected by the axial force in a beam element developed for a spinning structure. The torsional stiffness GI_t of an element is reduced with the factor $H_0 i_x^2$. Here, the parameter i_x is the radius of area inertia and H_0 is the constant axial force calculated when the consistent loads of Eq. (18) are applied.

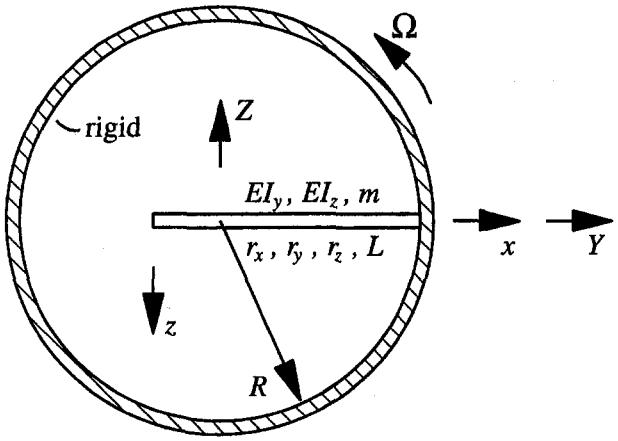

Fig. 2 Spinning rigid ring of radius R with a radially oriented cantilever beam of length L = 1.0 m. Beam has circular cross section with diameter $2r$ = 10.0 mm. Young's modulus is E = 200 GPa. Density is ρ = 8000 kg/m^3. Relevant beam properties are: bending stiffnesses $EI_y = EI_z$ = 98.2 Nm^2, mass per unit length m = 0.628 kg/m, radii of inertia r_x = 3.54 mm, and $r_y = r_z$ = 2.5 mm. Fundamental frequency for zero spinning speed is ω_{10} = 43.9 rad/s.

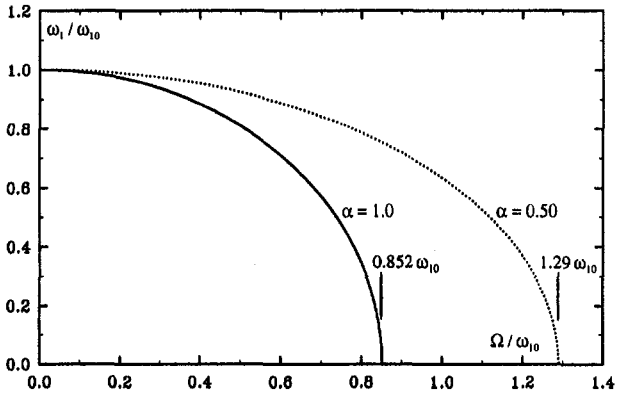

Fig. 4 Calculated dimensionless fundamental frequency ω_1/ω_{10} plotted versus dimensionless spinning speed Ω/ω_{10} of cantilever beam in Fig. 2 for ratios $\alpha = R/L$ equal to 1.0 and 0.50. Beam is modeled with four finite elements of equal length. Axial compressive force varies parabolically within each beam element.

7 Numerical Examples

Two sample problems have been studied, and the numerical results are presented below. The first example has been chosen to verify the stiffness reduction represented by the geometric stiffness matrix $\mathbf{K}^g = \mathbf{K}^g(\Omega)$. In the second example, the bending/torsional coupling effect for a straight beam is studied. Only beams having a doubly symmetric cross section will be considered here.

Example A: Cantilever Beam on a Rotating Rigid Ring

The fundamental eigenfrequency and the stability of a spinning cantilever beam are studied. The Euler/Bernoulli beam theory is employed. The cantilever beam is clamped to a rigid ring and directed along a radius toward the center; see Fig. 2. The ring spins in its plane around the center. In Fig. 3 the beam is studied for the large ratio $\alpha = R/L = 100$ of radius to beam length. The beam is then subjected to a nearly uniformly distributed axial external load, resulting in a linearly varying axial sectional force, and the classical Greenhill [12] buckling load should be recovered. Instability by divergence occurs when the fundamental eigenfrequency has decreased to zero. The calculated fundamental eigenfrequency is plotted versus the spinning speed for four cases in Fig. 3. Subdivisions of the beam into one and four finite elements of equal length are made. The finite elements used have a geometric stiffness matrix either taking into account a linearly varying compressive axial force or assuming an average constant axial force in each beam element. The Greenhill buckling load $q_c = 7.837EI/L^3$ corresponds to the critical spinning speed $\Omega_c = 0.0798\omega_{10}$ with $\omega_{10} = 0.3562\pi^2(EI_y/mL^4)^{1/2} = 43.9$ rad/s. Figure 3 shows the significance of allowing a linearly varying compressive axial force. One finite element with a linear axial force gives better results than four finite elements with an average constant axial force in each beam element. In Fig. 4 the beam is studied for the ratio $\alpha = R/L$ equal to 1.0 and 0.5. Also here the fundamental eigenfrequency is plotted versus the spinning speed. The beam is modeled with four elements taking into account a parabolically varying compressive tensional axial force. The calculated speeds, which give instability by divergence for the two cases, are indicated in Fig. 4. The numerical results presented in Fig. 4 coincide with those given by Gürgöze [13]. Various similar structures for other parameter values have also been studied by Bauer and Eidel [14].

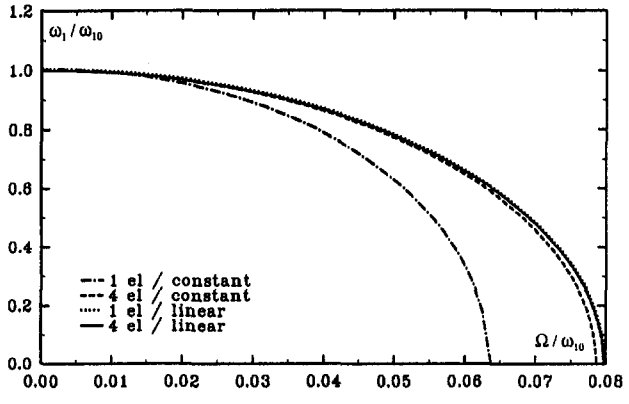

Fig. 3 Calculated dimensionless fundamental frequency ω_1/ω_{10} plotted versus dimensionless spinning speed Ω_1/ω_{10} of cantilever beam in Fig. 2 for ratio $\alpha = R/L$ = 100. Beam is modeled with one and four finite elements, respectively, of equal length. Axial compressive force is taken as constant within each element or as linearly varying within each element.

Example B: Cantilever Beam Spinning as a Blade

Free and forced vibration of a spinning cantilever beam system is studied. The beam is oriented perpendicularly to the spin axis, which passes through the clamped end of the beam; see Fig. 5. The beam has a cruciform cross section with a low torsional stiffness GI_t as compared to the bending stiffnesses EI_y and EI_z. A similar beam was studied by Leung and Fung [6], but their beam was much stiffer in torsion. Here, the beam is modeled with four elements of equal length. Figure 6 shows the calculated lowest six natural frequencies of the beam plotted versus the spinning speed. The four natural frequencies ω_1, ω_2, ω_5, and ω_6 pertaining to bending coincide with the results presented by Leung and Fung [6]. For zero spinning speed Ω, the eigenfrequencies pertaining to eigenmodes describing a bending motion in the XY-plane coincide with the corresponding eigenfrequencies for the YZ-plane. The two distinct eigenfrequencies ω_3 and ω_4 for zero spinning speed Ω in Fig. 6 pertain to torsional motion. When the spinning speed Ω increases, the system becomes stiffer mainly because of the increasing tensional axial force depending on the centrifugal acceleration. For a nonzero spinning speed Ω, separate eigenmodes in bending and torsion no longer exist, i.e., the eigenmodes describe a coupled motion in both bending in the XY-plane and torsion about the Y direction, or bending in the YZ-plane and tension in the Y direction. Note that the eigenmodes discussed here are described in a corotating coordinate system. In Fig. 7 the

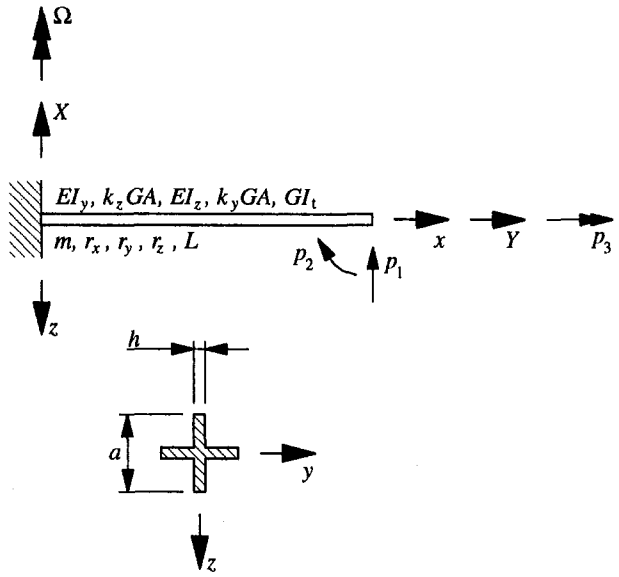

Fig. 5 Spinning cantilever beam of length L = 8.0 m oriented perpendicularly to spin axis passing through clamped end. Beam has doubly-symmetric cruciform cross-section with dimensions a = 0.20 m and h = 3.0 mm. Young's modulus is E = 200 GPa, density ρ = 8000 kg/m^3, and Poisson's ratio ν = 0.30. Beam properties are: bending stiffnesses EI_y = EI_z = 0.40 MNm^2, shearing stiffnesses k_zGA = k_yGA = 38.8 MN, torsional stiffness GI_t = 0.277 kNm^2, mass per unit length m = 9.6 kg/m, radii of inertia r_x = 57.7 mm and r_y = r_z = 40.8 mm. Displacements p_1, p_2 and p_3 of beam end are shown.

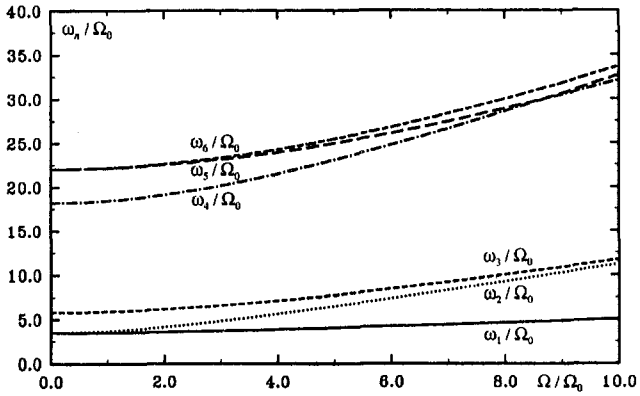

Fig. 6 Calculated lowest six dimensionless eigenfrequencies ω_n/Ω_0 of beam in Fig. 5 plotted versus dimensionless spinning speed Ω/Ω_0 with $\Omega_0 = (EI_y/mL^4)^{1/2}$ = 3.19 rad/s

magnitudes and phases of three displacements are plotted versus the frequency of a harmonic load applied to the beam in Fig. 5 in the p_1 direction. Note that both the load and the displacements are taken in a corotating coordinate system. The coupling between bending in the XY plane and torsion about the Y direction shown in Fig. 7 is not included in the paper by Leung and Fung [6]. It should be observed that the Rayleigh/Timoshenko beam theory has been used in the present study.

8 Concluding Remarks

The gyroscopic, circulatory, and geometric stiffness matrices of a spinning finite Rayleigh/Timoshenko/Saint-Venant beam element have been derived. In combination with the classical stiffness, damping, and mass matrices of such a beam element, these matrices constitute the discrete counterpart to the exact dynamic stiffness matrices presented by Wittrick and Williams [5] (Euler/Bernoulli beam theory) and Lundblad [7] (Rayleigh/Timoshenko beam theory). The ability to represent a spatially varying axial force distinguishes the present discretized approach from the "exact" approach presented by these authors. Another advantage of using the discrete parameter element over the exact distributed parameter element is that the dynamic stiffness can be computed with a drastically reduced effort and time. The matrices are also well suited for a transient vibration analysis with time-marching algorithms.

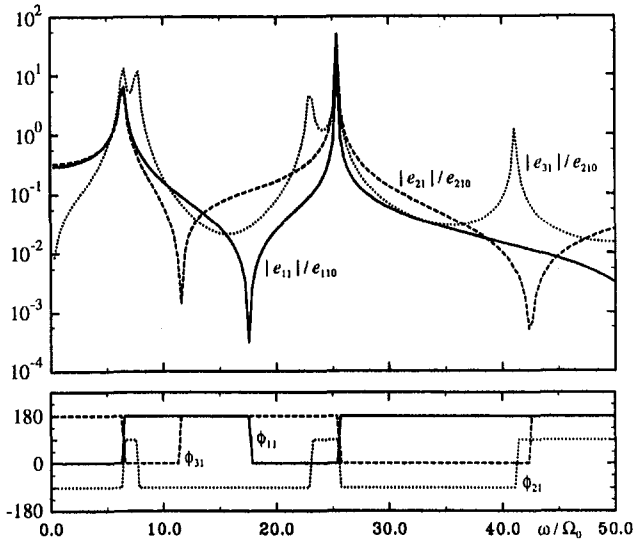

Fig. 7 Calculated magnitudes and phases of three complex dimensionless flexibilities are plotted versus dimensionless load frequency ω/Ω_0. Spinning speed is $\Omega = 5\Omega_0$. Normalizing flexibilities are $e_{110} = L^3/3EI_y$ and $e_{210} = L^2/2EI_y$.

The coupling elements of the gyroscopic and circulatory matrices predict a coupled bending/shearing/tensional/torsional vibration of the generally oriented spinning beam. Some of the coupling elements are, to the authors' knowledge, presented here for the first time for a discretized element. The coupled free vibration of a spinning beam system with the influence on the bending/shearing motion by the torsional coupling has been demonstrated in a numerical example.

Acknowledgments

The work reported in this paper was partly sponsored by the Volvo Car Corporation. Fruitful discussions with Professor Bengt Å. Åkesson at the Division of Solid Mechanics, Chalmers University of Technology, are gratefully acknowledged.

References

1 Ruhl, R. L., "Dynamics of Distributed Parameter Rotor Systems: Transfer Matrix and Finite Element Techniques," PhD Dissertation, Cornell University, 1970.

2 Nelson, H. D., "A Finite Rotating Shaft Element Using Timoshenko Beam Theory," ASME *Journal of Mechanical Design,* Vol. 102, 1980, pp. 793–803.

3 Kang, Y., Shih, Y.-P., and Lee, A.-C., "Investigation on the Steady-State Responses of Asymmetric Rotors," ASME *Journal of Vibration and Acoustics,* Vol. 144(2), 1992, pp. 194–208.

4 Likins, P. W., "Finite Element Appendage Equations for Hybrid Coordinate Dynamic Analysis," *International Journal of Solids and Structures,* Vol. 8(5), 1972, pp. 709–731.

5 Wittrick, W. H., and Williams, F. W., "On the Free Vibration Analysis of Spinning Structures by Using Discrete or Distributed Mass Models," *Journal of Sound and Vibration,* Vol. 82(1), 1982, pp. 1–15.

6 Leung, A. Y. T., and Fung, T. C., "Spinning Finite Elements," *Journal of Sound and Vibration,* Vol. 125(3), 1988, pp. 523–537.

7 Lundblad, H. M., "Forced Harmonic Vibration of Rotating Beam Systems in Space Analysed by Use of Exact Finite Elements," *International Journal for Numerical Methods in Engineering,* Vol. 32(3), 1991, pp. 571–594.

8 Archer, J. S., "Consistent Matrix Formulations for Structural Analysis Using Finite-Element Techniques," *AIAA Journal,* Vol. 3(10), 1965, pp. 1910–1918.

9 Przemieniecki, J. S., *Theory of Matrix Structural Analysis,* McGraw-Hill, New York, 1968.

10 Sällström, J. H., "Fluid-Conveying Damped Rayleigh-Timoshenko Beams in Transverse Vibration Analyzed by Use of an Exact Finite Element, Part II: Applications," *Journal of Fluids and Structures,* Vol. 4(6), 1990, pp. 573–582.
11 Cook, R. D., Malkus, D. S., and Plesha, M. E., *Concepts and Applications of Finite Element Analysis,* 3rd ed., Wiley, New York, 1989.
12 Timoshenko, S. P., and Gere, J. M., *Theory of Elastic Stability,* 2nd ed., McGraw-Hill, Singapore, 1963.
13 Gürgöze, M., "On the Dynamical Behaviour of a Rotating Beam," *Journal of Sound and Vibration,* Vol. 143(2), 1990, pp. 356–363.
14 Bauer, H. F., and Eidel, W., "Vibration of a Rotating Uniform Beam, Part II: Orientation Perpendicular to the Axis of Rotation," *Journal of Sound and Vibration,* Vol. 112(2), 1988, pp. 357–375.

APPENDIX

The 96 nonzero elements of the skew-symmetric gyroscopic matrix **G** of the beam element defined by Eq. (14*b*) are, except for the common divisor 840,

$$g_{1,2} = g_{7,8} = -g_{2,1} = -g_{8,7} = a^{(1)}_{u,12}(294\theta_{z1} + 280\theta_{z2})L \quad (A.1a)$$

$$g_{1,3} = g_{7,9} = -g_{3,1} = -g_{9,7} = a^{(1)}_{u,13}(294\theta_{y1} + 280\theta_{y2})L \quad (A.1b)$$

$$g_{1,5} = -g_{7,11} = -g_{5,1} = g_{11,7} = -a^{(1)}_{u,13}(42\theta_{y1} + 35\theta_{y2})L^2 \quad (A.1c)$$

$$g_{1,6} = -g_{7,12} = -g_{6,1} = g_{12,7} = a^{(1)}_{u,12}(42\theta_{z1} + 35\theta_{z2})L^2 \quad (A.1d)$$

$$g_{1,8} = -g_{2,7} = -g_{8,1} = g_{7,2} = a^{(1)}_{u,12}(126\theta_{z1} + 140\theta_{z2})L \quad (A.1e)$$

$$g_{1,9} = -g_{3,7} = -g_{9,1} = g_{7,3} = a^{(1)}_{u,13}(126\theta_{y1} + 140\theta_{y2})L \quad (A.1f)$$

$$g_{1,11} = g_{5,7} = -g_{11,1} = -g_{7,5} = a^{(1)}_{u,13}(28\theta_{y1} + 35\theta_{y2})L^2 \quad (A.1g)$$

$$g_{1,12} = g_{6,7} = -g_{12,1} = -g_{7,6} = -a^{(1)}_{u,12}(28\theta_{z1} + 35\theta_{z2})L^2 \quad (A.1h)$$

$$g_{2,4} = g_{2,10} = g_{4,8} = -g_{8,10} = -g_{4,2} = -g_{10,2} = -g_{8,4} = g_{10,8} = 420a^{(1)}_{\phi,13}\theta_{z1} \quad (A.1i)$$

$$g_{3,4} = g_{3,10} = g_{4,9} = -g_{9,10} = -g_{4,3} = -g_{10,3} = -g_{9,4} = g_{10,9} = -420a^{(1)}_{\phi,12}\theta_{y1} \quad (A.1j)$$

$$g_{4,5} = g_{10,11} = -g_{5,4} = -g_{11,10} = 70a^{(1)}_{\phi,12}(\theta_{y1} + 4\theta_{y2})L \quad (A.1k)$$

$$g_{4,6} = g_{10,12} = -g_{6,4} = -g_{12,10} = 70a^{(1)}_{\phi,13}(\theta_{z1} + 4\theta_{z2})L \quad (A.1l)$$

$$g_{4,11} = -g_{5,10} = -g_{11,4} = g_{10,5} = -70a^{(1)}_{\phi,12}(\theta_{y1} - 2\theta_{y2})L \quad (A.1m)$$

$$g_{4,12} = -g_{6,10} = -g_{12,4} = g_{10,6} = -70a^{(1)}_{\phi,13}(\theta_{z1} - 2\theta_{z2})L \quad (A.1n)$$

$$g_{2,3} = g_{8,9} = -g_{3,2} = -g_{9,8} = a^{(1)}_{u,23}(312\theta_{y1}\theta_{z1} + 294\theta_{y1}\theta_{z2} + 294\theta_{y2}\theta_{z1} + 280\theta_{z2}\theta_{y2})L \quad (A.1o)$$

$$g_{2,5} = -g_{8,11} = -g_{5,2} = g_{11,8} = -a^{(1)}_{u,23}(44\theta_{y1}\theta_{z1} + 42\theta_{y1}\theta_{z2} + 35\theta_{y2}\theta_{z1} + 35\theta_{y2}\theta_{z2})L^2 \quad (A.1p)$$

$$g_{2,9} = -g_{3,8} = -g_{9,2} = g_{8,3} = a^{(1)}_{u,23}(108\theta_{y1}\theta_{z1} + 126\theta_{y1}\theta_{z2} + 126\theta_{y2}\theta_{z1} + 140\theta_{y2}\theta_{z2})L \quad (A.1q)$$

$$g_{2,11} = g_{5,8} = -g_{11,2} = -g_{8,5} = a^{(1)}_{u,23}(26\theta_{y1}\theta_{z1} + 28\theta_{y1}\theta_{z2} + 35\theta_{y2}\theta_{z1} + 35\theta_{y2}\theta_{z2})L^2 \quad (A.1r)$$

$$g_{3,6} = -g_{9,12} = -g_{6,3} = g_{12,9} = -a^{(1)}_{u,23}(44\theta_{y1}\theta_{z1} + 35\theta_{y1}\theta_{z2} + 42\theta_{y2}\theta_{z1} + 35\theta_{y2}\theta_{z2})L^2 \quad (A.1s)$$

$$g_{3,12} = g_{6,9} = -g_{12,3} = -g_{9,6} = a^{(1)}_{u,23}(26\theta_{y1}\theta_{z1} + 35\theta_{y1}\theta_{z2} + 28\theta_{y2}\theta_{z1} + 35\theta_{y2}\theta_{z2})L^2 \quad (A.1t)$$

$$g_{5,6} = g_{11,12} = -g_{6,5} = -g_{12,11} = a^{(1)}_{u,23}(8\theta_{y1}\theta_{z1} + 7\theta_{y1}\theta_{z2} + 7\theta_{y2}\theta_{z1} + 7\theta_{y2}\theta_{z2})L^3 \quad (A.1u)$$

$$g_{5,12} = -g_{6,11} = -g_{12,5} = g_{11,6} = -a^{(1)}_{u,23}(6\theta_{y1}\theta_{z1} + 7\theta_{y1}\theta_{z2} + 7\theta_{y2}\theta_{z1} + 7\theta_{y2}\theta_{z2})L^3 \quad (A.1v)$$

The additional bending/shearing parameters are defined as

$$\theta_{y1} = 1/(1 + \theta_y) \quad (A.2a)$$

$$\theta_{y2} = \theta_y/(1 + \theta_y) \quad (A.2b)$$

$$\theta_{z1} = 1/(1 + \theta_z) \quad (A.2c)$$

$$\theta_{z2} = \theta_z/(1 + \theta_z) \quad (A.2d)$$

It should be noted that none of these 96 elements vanishes when the Euler/Bernoulli theory ($\theta_{y2} = \theta_{z2} = 0$) is employed.

The 136 nonzero elements of the nonsymmetric circulatory 12×12 matrix **H** in Eq. (16*b*) are, except for the common divisor $2520L$,

$$h_{1,1} = h_{7,7} = 840a^{(0)}_{u,11}L^2 \quad (A.3a)$$

$$h_{1,2} = h_{7,8} = h_{2,1} = h_{8,7} = a^{(0)}_{u,12}(882\theta_{z1} + 840\theta_{z2})L^2 \quad (A.3b)$$

$$h_{1,3} = h_{7,9} = h_{3,1} = h_{9,7} = a^{(0)}_{u,13}(882\theta_{y1} + 840\theta_{y2})L^2 \quad (A.3c)$$

$$h_{1,5} = -h_{7,11} = h_{5,1} = -h_{11,7} = -a^{(0)}_{u,13}(126\theta_{y1} + 105\theta_{y2})L^3 \quad (A.3d)$$

$$h_{1,6} = -h_{7,12} = h_{6,1} = -h_{12,7} = a^{(0)}_{u,12}(126\theta_{z1} + 105\theta_{z2})L^3 \quad (A.3e)$$

$$h_{1,7} = h_{7,1} = 420a^{(0)}_{u,11}L^2 \quad (A.3f)$$

$$h_{1,8} = h_{2,7} = h_{8,1} = h_{7,2} = a^{(0)}_{u,12}(378\theta_{z1} + 420\theta_{z2})L^2 \quad (A.3g)$$

$$h_{1,9} = h_{3,7} = h_{9,1} = h_{7,3} = a^{(0)}_{u,13}(378\theta_{y1} + 420\theta_{y2})L^2 \quad (A.3h)$$

$$h_{1,11} = -h_{5,7} = h_{11,1} = -h_{7,5} = a^{(0)}_{u,13}(84\theta_{y1} + 105\theta_{y2})L^3 \quad (A.3i)$$

$$h_{1,12} = -h_{6,7} = h_{12,1} = -h_{7,6} = -a^{(0)}_{u,12}(84\theta_{z1} + 105\theta_{z2})L^3 \quad (A.3j)$$

$$h_{2,2} = h_{8,8} = a^{(0)}_{u,22}(936\theta^2_{z1} + 1764\theta_{z1}\theta_{z2} + 840\theta^2_{z2})L^2 + 3024a^{(0)}_{\phi,33}\theta^2_{z1} \quad (A.3k)$$

$$h_{2,3} = h_{8,9} = a^{(0)}_{u,23}(936\theta_{y1}\theta_{z1} + 882\theta_{y1}\theta_{z2} + 882\theta_{y2}\theta_{z1} + 840\theta_{y2}\theta_{z2})L^2 - 3024a^{(0)}_{\phi,32}\theta_{y1}\theta_{z1} \quad (A.3l)$$

$$h_{3,2} = h_{9,8} = a^{(0)}_{u,23}(936\theta_{y1}\theta_{z1} + 882\theta_{y1}\theta_{z2} + 882\theta_{y2}\theta_{z1} + 840\theta_{y2}\theta_{z2})L^2 - 3024a^{(0)}_{\phi,23}\theta_{y1}\theta_{z1} \quad (A.3m)$$

$$h_{2,4} = h_{2,10} = -h_{8,10} = -h_{8,4} = -1260a^{(0)}_{\phi,31}\theta_{z1}L \quad (A.3n)$$

$$h_{4,2} = h_{10,2} = -h_{10,8} = -h_{4,8} = -1260a^{(0)}_{\phi,13}\theta_{z1}L \quad (A.3o)$$

$$h_{2,5} = -h_{8,11} = -a^{(0)}_{u,23}(132\theta_{y1}\theta_{z1} + 126\theta_{y1}\theta_{z2} + 105\theta_{y2}\theta_{z1} + 105\theta_{y2}\theta_{z2})L^3 + 252a^{(0)}_{\phi,32}\theta_{z1}(\theta_{y1} - 5\theta_{y2})L \quad (A.3p)$$

$$h_{5,2} = -h_{11,8} = -a^{(0)}_{u,23}(132\theta_{y1}\theta_{z1} + 126\theta_{y1}\theta_{z2} + 105\theta_{y2}\theta_{z1} + 105\theta_{y2}\theta_{z2})L^3 + 252a^{(0)}_{\phi,23}\theta_{z1}(\theta_{y1} - 5\theta_{y2})L \quad (A.3q)$$

$$h_{2,6} = -h_{8,12} = h_{6,2} = -h_{12,8} = a^{(0)}_{u,22}(132\theta^2_{z1} + 231\theta_{z1}\theta_{z2} + 105\theta^2_{z2})L^3 + 252a^{(0)}_{\phi,33}\theta_{z1}(\theta_{z1} - 5\theta_{z2})L \quad (A.3r)$$

$$h_{2,8} = h_{8,2} = a^{(0)}_{u,22}(324\theta^2_{z1} + 756\theta_{z1}\theta_{z2} + 420\theta^2_{z2})L^2 - 3024a^{(0)}_{\phi,33}\theta^2_{z1} \quad (A.3s)$$

$$h_{2,9} = h_{8,3} = a^{(0)}_{u,23}(324\theta_{y1}\theta_{z1} + 378\theta_{y1}\theta_{z2} + 378\theta_{y2}\theta_{z1} + 420\theta_{y2}\theta_{z2})L^2 + 3024a^{(0)}_{\phi,32}\theta_{y1}\theta_{z1} \quad (A.3t)$$

$$h_{2,11} = -h_{8,5} = a^{(0)}_{u,23}(78\theta_{y1}\theta_{z1} + 84\theta_{y1}\theta_{z2} + 105\theta_{y2}\theta_{z1} + 105\theta_{y2}\theta_{z2})L^3 + 252a^{(0)}_{\phi,32}\theta_{z1}(\theta_{y1} - 5\theta_{y2})L \quad (A.3u)$$

$$h_{5,8} = -h_{11,2} = -a^{(0)}_{u,23}(78\theta_{y1}\theta_{z1} + 84\theta_{y1}\theta_{z2} + 105\theta_{y2}\theta_{z1} + 105\theta_{y2}\theta_{z2})L^3 - 252a^{(0)}_{\phi,23}\theta_{z1}(\theta_{y1} - 5\theta_{y2})L \quad (A.3v)$$

$$h_{2,12} = -h_{6,8} = h_{12,2} = -h_{8,6} = -a^{(0)}_{u,22}(78\theta^2_{z1} + 189\theta_{z1}\theta_{z2} + 105\theta^2_{z2})L^3 + 252a^{(0)}_{\phi,33}\theta_{z1}(\theta_{z1} - 5\theta_{z2})L \quad (A.3w)$$

$$h_{3,3} = h_{9,9} = a^{(0)}_{u,33}(936\theta^2_{y1} + 1764\theta_{y1}\theta_{y2} + 840\theta^2_{y2})L^2 + 3024a^{(0)}_{\phi,22}\theta^2_{y1} \quad (A.3x)$$

$$h_{3,4} = h_{3,10} = -h_{9,10} = -h_{9,4} = 1260a^{(0)}_{\phi,21}\theta_{y1}L \quad (A.3y)$$

$$h_{4,3} = h_{10,3} = -h_{10,9} = -h_{4,9} = 1260a^{(0)}_{\phi,12}\theta_{y1}L \quad (A.3z)$$

$$h_{3,5} = -h_{9,11} = h_{5,3} = -h_{11,9} = -a^{(0)}_{u,33}(132\theta^2_{y1} + 231\theta_{y1}\theta_{y2} + 105\theta^2_{y2})L^3 - 252a^{(0)}_{\phi,22}\theta_{y1}(\theta_{y1} - 5\theta_{y2})L \quad (A.3A)$$

$$h_{3,6} = -h_{9,12} = a^{(0)}_{u,23}(132\theta_{y1}\theta_{z1} + 105\theta_{y1}\theta_{z2} + 126\theta_{y2}\theta_{z1} + 105\theta_{y2}\theta_{z2})L^3 - 252a^{(0)}_{\phi,23}\theta_{y1}(\theta_{z1} - 5\theta_{z2})L \quad (A.3B)$$

$$h_{6,3} = -h_{12,9} = a^{(0)}_{u,23}(132\theta_{y1}\theta_{z1} + 105\theta_{y1}\theta_{z2} + 126\theta_{y2}\theta_{z1} + 105\theta_{y2}\theta_{z2})L^3 - 252a^{(0)}_{\phi,32}\theta_{y1}(\theta_{z1} - 5\theta_{z2})L \quad (A.3C)$$

$$h_{3,8} = h_{9,2} = a^{(0)}_{u,23}(324\theta_{y1}\theta_{z1} + 378\theta_{y1}\theta_{z2} + 378\theta_{y2}\theta_{z1} + 420\theta_{y2}\theta_{z2})L^2 + 3024a^{(0)}_{\phi,23}\theta_{y1}\theta_{z1} \quad (A.3D)$$

$$h_{3,9} = h_{9,3} = a^{(0)}_{u,33}(324\theta^2_{y1} + 756\theta_{y1}\theta_{y2} + 420\theta^2_{y2})L^2 - 3024a^{(0)}_{\phi,22}\theta^2_{y1} \quad (A.3E)$$

$$h_{3,11} = -h_{5,9} = h_{11,3} = -h_{9,5} = a^{(0)}_{u,33}(78\theta^2_{y1} + 189\theta_{y1}\theta_{y2} + 105\theta^2_{y2})L^3 - 252a^{(0)}_{\phi,22}\theta_{y1}(\theta_{y1} - 5\theta_{y2})L \quad (A.3F)$$

$$h_{3,12} = -h_{9,6} = -a^{(0)}_{u,23}(78\theta_{y1}\theta_{z1} + 105\theta_{y1}\theta_{z2} + 84\theta_{y2}\theta_{z1} + 105\theta_{y2}\theta_{z2})L^3 - 252a^{(0)}_{\phi,23}\theta_{y1}(\theta_{z1} - 5\theta_{z2})L \quad (A.3G)$$

$$h_{4,4} = h_{10,10} = 840a^{(0)}_{\phi,11}L^2 \quad (A.3H)$$

$$h_{4,5} = h_{10,11} = 210a^{(0)}_{\phi,12}(\theta_{y1} + 4\theta_{y2})L^2 \quad (A.3I)$$

$$h_{5,4} = h_{11,10} = 210a^{(0)}_{\phi,21}(\theta_{y1} + 4\theta_{y2})L^2 \quad (A.3J)$$

$$h_{4,6} = h_{10,12} = 210a^{(0)}_{\phi,13}(\theta_{z1} + 4\theta_{z2})L^2 \quad (A.3K)$$

$$h_{6,4} = h_{12,10} = 210a^{(0)}_{\phi,31}(\theta_{z1} + 4\theta_{z2})L^2 \quad (A.3L)$$

$$h_{4,10} = h_{10,4} = 420a^{(0)}_{\phi,11}L^2 \quad (A.3M)$$

$$h_{4,11} = h_{10,5} = -210a^{(0)}_{\phi,12}(\theta_{y1} - 2\theta_{y2})L^2 \quad (A.3N)$$

$$h_{5,10} = h_{11,4} = -210a^{(0)}_{\phi,21}(\theta_{y1} - 2\theta_{y2})L^2 \quad (A.3O)$$

$$h_{4,12} = h_{10,6} = -210a^{(0)}_{\phi,13}(\theta_{z1} - 2\theta_{z2})L^2 \quad (A.3P)$$

$$h_{6,10} = h_{12,4} = -210a^{(0)}_{\phi,31}(\theta_{z1} - 2\theta_{z2})L^2 \quad (A.3Q)$$

$$h_{5,5} = h_{11,11} = a^{(0)}_{u,33}(24\theta^2_{y1} + 42\theta_{y1}\theta_{y2} + 21\theta^2_{y2})L^4 + 84a^{(0)}_{\phi,22}(4\theta^2_{y1} + 5\theta_{y1}\theta_{y2} + 10\theta^2_{y2})L^2 \quad (A.3R)$$

$$h_{5,6} = h_{11,12} = -a^{(0)}_{u,23}(24\theta_{y1}\theta_{z1} + 21\theta_{y1}\theta_{z2} + 21\theta_{y2}\theta_{z1} + 21\theta_{y2}\theta_{z2})L^4 + 42a^{(0)}_{\phi,23}(8\theta_{y1}\theta_{z1} + 5\theta_{y2}\theta_{z1} + 5\theta_{y1}\theta_{z2} + 20\theta_{y2}\theta_{z2})L^2 \quad (A.3S)$$

$$h_{6,5} = h_{12,11} = -a^{(0)}_{u,23}(24\theta_{y1}\theta_{z1} + 21\theta_{y1}\theta_{z2} + 21\theta_{y2}\theta_{z1} + 21\theta_{y2}\theta_{z2})L^4 + 42a^{(0)}_{\phi,32}(8\theta_{y1}\theta_{z1} + 5\theta_{y2}\theta_{z1} + 5\theta_{y1}\theta_{z2} + 20\theta_{y2}\theta_{z2})L^2 \quad (A.3T)$$

$$h_{5,11} = h_{11,5} = -a^{(0)}_{u,33}(18\theta^2_{y1} + 42\theta_{y1}\theta_{y2} + 21\theta^2_{y2})L^4 - 84a^{(0)}_{\phi,22}(\theta^2_{y1} + 5\theta_{y1}\theta_{y2} - 5\theta^2_{y2})L^2 \quad (A.3U)$$

$$h_{5,12} = h_{11,6} = a^{(0)}_{u,23}(18\theta_{y1}\theta_{z1} + 21\theta_{y1}\theta_{z2} + 21\theta_{y2}\theta_{z1} + 21\theta_{y2}\theta_{z2})L^4 - 42a^{(0)}_{\phi,23}(2\theta_{y1}\theta_{z1} + 5\theta_{y2}\theta_{z1} + 5\theta_{y1}\theta_{z2} - 10\theta_{y2}\theta_{z2})L^2 \quad (A.3V)$$

$$h_{6,11} = h_{12,5} = a^{(0)}_{u,23}(18\theta_{y1}\theta_{z1} + 21\theta_{y1}\theta_{z2} + 21\theta_{y2}\theta_{z1} + 21\theta_{y2}\theta_{z2})L^4 - 42a^{(0)}_{\phi,32}(2\theta_{y1}\theta_{z1} + 5\theta_{y2}\theta_{z1} + 5\theta_{y1}\theta_{z2} - 10\theta_{y2}\theta_{z2})L^2 \quad (A.3W)$$

$$h_{6,6} = h_{12,12} = a^{(0)}_{u,22}(24\theta^2_{z1} + 42\theta_{z1}\theta_{z2} + 21\theta^2_{z2})L^4 + 84a^{(0)}_{\phi,33}(4\theta^2_{z1} + 5\theta_{z1}\theta_{z2} + 10\theta^2_{z2})L^2 \quad (A.3X)$$

$$h_{6,9} = -h_{12,3} = a^{(0)}_{u,23}(78\theta_{y1}\theta_{z1} + 105\theta_{y1}\theta_{z2} + 84\theta_{y2}\theta_{z1} + 105\theta_{y2}\theta_{z2})L^3 + 252a^{(0)}_{\phi,32}\theta_{y1}(\theta_{z1} - 5\theta_{z2})L \quad (A.3Y)$$

$$h_{6,12} = h_{12,6} = -a^{(0)}_{u,22}(18\theta^2_{z1} + 42\theta_{z1}\theta_{z2} + 21\theta^2_{z2})L^4 - 84a^{(0)}_{\phi,33}(\theta^2_{z1} + 5\theta_{z1}\theta_{z2} - 5\theta^2_{z2})L^2 \quad (A.3Z)$$

It should be noted that several elements representing a coupling between motions in tension, torsion, and bending/shearing in the two planes xy and xz, will vanish in the case that the spin axis X is parallel to any of the principal axes x, y and z.

The symmetric geometric stiffness matrix for displacement in the xz-plane has been derived from Equation (23). The contribution to the geometric stiffness matrix from the constant part of the axial loading is, except for the common divisor $60L$,

$$k^{ga}_{3,3} = -k^{ga}_{3,9} = k^{ga}_{9,9} = -H_a(72\theta^2_{y1} + 120\theta_{y1}\theta_{y2} + 60\theta^2_{y2}) \quad (A.4a)$$

$$k^{ga}_{3,5} = k^{ga}_{3,11} = -k^{ga}_{5,9} = -k^{ga}_{9,11} = 6H_a\theta^2_{y1}L \quad (A.4b)$$

$$k^{ga}_{5,5} = k^{ga}_{11,11} = -H_a(8\theta^2_{y1} + 10\theta_{y1}\theta_{y2} + 5\theta^2_{y2})L^2 \quad (A.4c)$$

$$k^{ga}_{5,11} = H_a(2\theta^2_{y1} + 10\theta_{y1}\theta_{y2} + 5\theta^2_{y2})L^2 \quad (A.4d)$$

Here, the constant axial force is $H_a = H_0 - H_1^{\text{fix}} - H_2^{\text{fix}}$. The linear variation of the axial loading $H_b = 2H_1^{\text{fix}}$ contributes to the geometric stiffness with, except for the common divisor $840L$,

$$k^{gb}_{3,3} = -k^{gb}_{3,9} = k^{gb}_{9,9}$$
$$= -H_b(504\theta^2_{y1} + 840\theta_{y1}\theta_{y2} + 420\theta^2_{y2}) \quad (A.5a)$$
$$k^{gb}_{3,5} = -k^{gb}_{5,9} = H_b(84\theta^2_{y1} + 112\theta_{y1}\theta_{y2} + 70\theta^2_{y2})L \quad (A.5b)$$
$$k^{gb}_{3,11} = -k^{gb}_{9,11} = -H_b(112\theta_{y1}\theta_{y2} + 70\theta^2_{y2})L \quad (A.5c)$$
$$k^{gb}_{5,5} = -H_b(28\theta^2_{y1} + 42\theta_{y1}\theta_{y2} + 35\theta^2_{y2})L^2 \quad (A.5d)$$
$$k^{gb}_{5,11} = H_b(14\theta^2_{y1} + 70\theta_{y1}\theta_{y2} + 35\theta^2_{y2})L^2 \quad (A.5e)$$
$$k^{gb}_{11,11} = -H_b(84\theta^2_{y1} + 98\theta_{y1}\theta_{y2} + 35\theta^2_{y2})L^2 \quad (A.5f)$$

The contribution from the quadratic variation $H_c = 3H_2^{\text{fix}}$ of the axial loading is, except for the common divisor $420L$,

$$k^{gc}_{3,3} = -k^{gc}_{3,9} = k^{gc}_{9,9}$$
$$= -H_c(144\theta^2_{y1} + 252\theta_{y1}\theta_{y2} + 140\theta^2_{y2}) \quad (A.6a)$$
$$k^{gc}_{3,5} = -k^{gc}_{5,9} = H_c(30\theta^2_{y1} + 49\theta_{y1}\theta_{y2} + 35\theta^2_{y2})L \quad (A.6b)$$
$$k^{gc}_{3,11} = -k^{gc}_{9,11} = -H_c(12\theta^2_{y1} + 63\theta_{y1}\theta_{y2} + 35\theta^2_{y2})L \quad (A.6c)$$
$$k^{gc}_{5,5} = -H_c(8\theta^2_{y1} + 14\theta_{y1}\theta_{y2} + 14\theta^2_{y2})L^2 \quad (A.6d)$$
$$k^{gc}_{5,11} = H_c(6\theta^2_{y1} + 28\theta_{y1}\theta_{y2} + 14\theta^2_{y2})L^2 \quad (A.6e)$$
$$k^{gc}_{11,11} = -H_c(36\theta^2_{y1} + 42\theta_{y1}\theta_{y2} + 14\theta^2_{y2})L^2 \quad (A.6f)$$

Improving Traditional Balancing Methods for High-Speed Rotors

J. Ling

Y. Cao

Department of Mechanical Engineering,
Florida International University,
Miami, FL 33199

This paper introduces frequency response functions, analyzes the relationships between the frequency response functions and influence coefficients theoretically, and derives corresponding mathematical equations for high-speed rotor balancing. The relationships between the imbalance masses on the rotor and frequency response functions are also analyzed based upon the modal balancing method, and the equations related to the static and dynamic imbalance masses and the frequency response function are obtained. Experiments on a high-speed rotor balancing rig were performed to verify the theory, and the experimental data agree satisfactorily with the analytical solutions. The improvement on the traditional balancing method proposed in this paper will substantially reduce the number of rotor startups required during the balancing process of rotating machinery.

Introduction

Influence coefficients and modal balancing methods are two major balancing methods that are used extensively today. The essence of the influence coefficient method is to apply m times trial masses for m rotor balance planes existing in the rotor machinery to obtain all influence coefficients between the rotor and the bearings (Larsson, 1976; Little and Pilkey, 1976).

The principle of the modal balancing method is to balance rotors by their modal shapes. The minimum number of balance planes required is equal to the number of vibration modes to be balanced (Rao, 1983). But both balancing methods have serious shortcomings. When they are applied in the rotor balancing procedure, rotating machinery is required to start up many times. The procedure is very time-consuming and expensive, especially for steam turbines. In order to reduce the number of rotating machinery startups, the frequency response functions in the mechanical vibration and some improvements on these traditional balancing methods are introduced in this paper.

Theoretical Analyses

Frequency Response Function. In a linear, constant coefficient system of the rotor bearing, an impulsive excitation is applied on a rotor at an arbitrary location, and the displacement of the rotor-bearing system at another arbitrary location is measured. After the Fourier transform, the ratio of the impulsive excitation to the displacement is the frequency response function between the two arbitrary locations of the rotor-bearing system, which is given by:

$$H(f) = \frac{X(f)}{F(f)}. \tag{1}$$

Since the frequency response function given by Eq. (1) is a complex function, it can be written as:

$$H(f) = |H(f)| \exp[-j\varphi(f)], \tag{2}$$

where $\varphi(f)$ is the phase factor of the system, which denotes the phase angle that the output signal lags behind the input signal, and $|H(f)|$ is the gain factor of the system, which denotes the augmented level of the ratio of the output to the input (Newland, 1975; Beauchamp, 1973). Therefore, for a given frequency, the denominator of the frequency response function is the force applied to a point in the rotor-bearing system. If the force applied to the point is a resonated concentrated force, it can be interpreted as an eccentric force caused by an imbalance mass that exists at the point and rotates in the same frequency. Similarly, the phase of the frequency response function can be interpreted as the phase angle that the vibration amplitude on the bearing lags behind the eccentric force. From this analysis, it is evident that the magnitude and phase factor of the frequency response function are related to the vibration results caused by the imbalance rotor when it rotates. Since the frequency response function reflects the intrinsic dynamic characteristics of the system, and has nothing to do with the nature of the excitations and responses (Marple, 1987), the frequency response functions can be found through a shock excitation on the rotor-bearing system. Thus, the number of startups of the rotating machinery can be reduced during the mass balance procedure for rotating machinery.

Relation Between the Frequency Response Function and the Influence Coefficient. Considering the simple rotor-bearing system shown in Fig. 1 with the two bearings fixed on the ground and negligible gyroscopic effects, if a trial mass $\bar{P}_i$ is applied on the balance plane i (i = I, II) of a rotor, according to the theory of rotor dynamics, the eccentric force caused by $\bar{P}_i$ is $\bar{F}_i$ when the rotor rotates at an angular velocity, ω. The projection of the eccentric force on a vertical plane passing through the rotor axis is $F_i \sin \omega t$. Therefore, the bearing k (k = 1, 2) in the same direction presents the corresponding resonance vibration. The projection of the eccentric force and the resonance vibration can be written in terms of complex functions as:

$$f(t) = F_i \exp[j(\omega t + \varphi)], \tag{3}$$

and

$$x(t) = X_{ik} \exp(j\omega t), \tag{4}$$

where i and k are the indexes for the rotor balance planes and the rotor bearings, respectively. If we take a Fourier transform for both $f(t)$ and $x(t)$, the frequency response function between the balance plane, i, and bearing, k, can be obtained:

$$H_{ik}(f) = \frac{X_{ik}}{F_i} \exp[-j\varphi_{ik}(f)]. \tag{5}$$

On the other hand, according to the definition of influence coefficient, K, we have:

Contributed by the International Gas Turbine Institute for publication in the JOURNAL OF ENGINEERING FOR GAS TURBINES AND POWER. Manuscript received by the International Gas Turbine Institute October 19, 1994. Associate Technical Editor: R. E. Kielb.

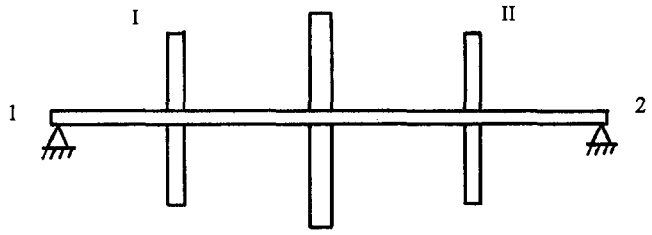

Fig. 1 Rotor-bearing system modal

$$\bar{K} = \frac{\bar{M}}{\bar{P}} = \frac{M \text{ at } \alpha}{P \text{ at } \theta}, \tag{6}$$

where $\bar{K}$, $\bar{M}$, and $\bar{P}$ are vectors, $\bar{M}$ is the bearing vibration caused by trial mass $\bar{P}$ itself, α is the phase angle of bearing vibration, θ is the angle between the location of trial mass $\bar{P}$ and the white line on the end face of the rotor. In order to simplify the analysis, the trial mass $\bar{P}$ was applied in the direction of the white line on the end face of the rotor. Thus, since $\theta = 0$, Eq. (6) reduces to:

$$\bar{K} = \frac{M \text{ at } \alpha}{P}. \tag{7}$$

The complex formulation for $\bar{K}$ can be expressed as:

$$K = \frac{M}{P} \exp(j\alpha). \tag{8}$$

For the system shown in Fig. 1, if we apply the trial mass, $\bar{P}_i$, on the balance plane i, and measure the vibration on the bearing, k, the influence coefficient of the system becomes:

$$K_{ik} = \frac{M_{ik}}{P_i} \exp(j\alpha_{ik}). \tag{9}$$

Comparing the frequency response function, Eq. (5), with the influence coefficient, Eq. (9), under the same system and angular velocity, it is clear that X_{ik} has a meaning similar to M_{ik}. However, the magnitude of M_{ik} is twice that of X_{ik}, since M_{ik} is the overall vibration amplitude (peak to peak) of the bearing, i.e.,

$$M_{ik} = 2X_{ik}. \tag{10}$$

The functions of F_i and P_i are similar, and both of them can cause bearing vibration. The two parameters are related through the following equation:

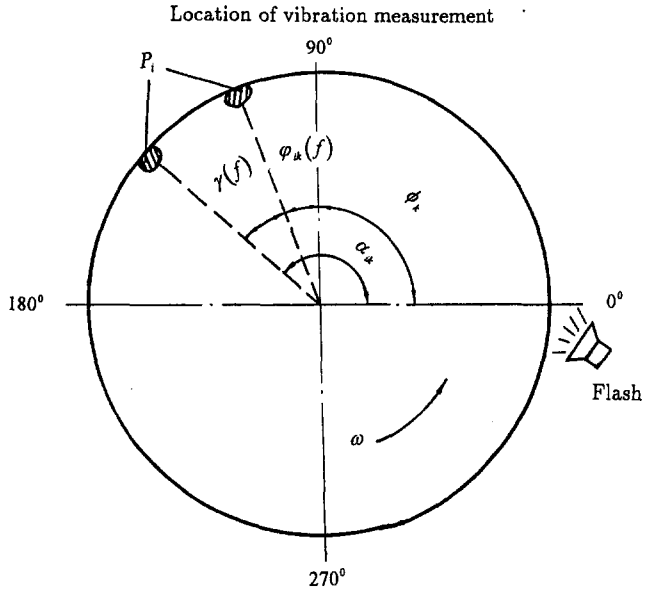

Fig. 2 Phase angle analysis of influence coefficient

$$F_i = |r_i - y_i|\omega^2 P_i, \tag{11}$$

where r_i is the radius of the location where the trial mass is applied on the balance plane i, and y_i is the deflection of rotor at the balance plane, i.

The phase angle, $\varphi_{ik}(f)$, of the frequency response function denotes the phase angle that the maximum vibration amplitude on the bearing, k, lags the excitation (or imbalance mass). The phase angle, α_{ik}, of the influence coefficient is an angle between the white line on the end face of rotor and the reference point (zero point) on the machinery housing. According to the method of flash phase angle measurement in balancing the rotating machinery, when the trial mass, P_i ($\theta = 0$), rotates through an angle, $\varphi_{ik}(f)$, relative to the measuring point for bearing vibration, the maximum vibration amplitude of the rotor reaches that point at the bearing, k. As shown in Fig. 2, since the instrument flash frequency is the same as the bearing vibration frequency, the white line is seen at the same location when the instrument flashes every time. At the same time, there is a phase lag angle, $\gamma(f)$, in vibration measuring instruments. The angle between the white line and zero point of the machinery housing equals the vibration phase angle on bearing, k. Therefore, we know from Fig. 2 that the phase angle, α_{ik}, on bearing, k, which is caused by the trial mass, P_i, on balance plane, i, is:

Nomenclature

F = eccentric force, N
f = frequency, Hz
$f(t)$ = projection of eccentric force on a vertical plane, N
$H(f)$ = frequency response function, m/N
K = influence coefficient, μm/g-deg
M = vibration amplitude, μm
m = balance mass, g
P = trial mass, g
r = radius of location where trial mass is applied, m
t = time, s
X = vibration amplitude, μm
X' = asymmetrical vibration amplitude, μm
$x(t)$ = displacement, μm
y = deflection of rotor at the balance plane, m
α = phase angle of the bearing vibration, deg
$\gamma(f)$ = phase lag angle of the measuring instrument, deg
θ = angle between the imbalance mass and the white line on the end face of the rotor, deg
ϕ = phase angle between measuring location and white line on the end face of rotor, deg
ϕ_k = phase angle between the measuring location and the reference (zero) point, deg
$\varphi(f)$ = phase factor of the system, deg
ω = angular velocity, rad/s

Superscripts

$\bar{}$ = vector

Subscripts

A = asymmetry
i = balance plane
k = bearing
s = symmetry

$$\alpha_{ik} = \phi_k + \varphi_{ik}(f) + \gamma(f), \tag{12}$$

where ϕ_k is the angle between the vibration measuring location on the bearing, k, and the zero point of the machinery housing, and $\gamma(f)$ is the phase lag angle of the measuring instrument. Through the foregoing analyses, we know that the phase angle of the frequency response function is a part of the phase angle of the influence coefficient, i.e., the phase angle of the influence coefficient includes the phase angle of the frequency response function. Substituting Eqs. (9), (10), and (11) into Eq. (8), we obtain:

$$\begin{aligned} K_{ik} &= \frac{M_{ik}}{P_i}\exp[j\alpha_{ik}] = \frac{M_{ik}}{P_i}\exp[j(\phi_k + \varphi_{ik}(f) + \gamma(f)] \\ &= 2|r_i + y_i|\omega^2 \frac{X_{ik}}{F_i}\exp[-j\varphi_{ik}(f)] \\ &\quad \times \exp[j(\phi_k + 2\varphi_{ik}(f) + \gamma(f)] \\ &= 2|r_i + y_i|\omega^2 \exp[j(\phi_k + 2\varphi_{ik}(f) \\ &\qquad + \gamma(f)]H_{ik}(f). \end{aligned} \tag{13}$$

The corresponding vectorial form is:

$$\bar{K}_{ik} = 2|r_i + y_i|\omega^2|H_{ik}(f)| \quad \text{at} \quad \phi_k + \varphi_{ik}(f) + \gamma(f). \tag{14}$$

Since r_i is much greater than y_i,

$$\bar{K}_{ik} \approx 2r_i\omega^2|H_{ik}(f)| \quad \text{at} \quad \phi_k + \varphi_{ik}(f) + \gamma(f)\ (i, k = 1, 2, 3, \ldots). \tag{15}$$

Equation (15) represents the relationship between the frequency response function and the influence coefficient. If the frequency response function of the rotor-bearing system is found through measurements, the influence coefficients of the rotor-bearing system can be calculated, and the magnitude and location of the imbalance masses on the rotor can be obtained by the influence coefficient method. Thus, the number of startups of rotating machinery can be reduced since the influence coefficients need not be obtained by experiments on site.

Improving the Method of Modal Balancing

Based on our experience in rotor balancing of steam turbines, the imbalance masses on the rotor can be divided into symmetric imbalance masses and asymmetric imbalance masses. The symmetric imbalance masses force the "first mode" of vibration, i.e., the type of vibration where both ends of the shaft tend to throw out in the same direction. The asymmetric imbalance masses force the "second mode" of vibration where the shaft ends tend to throw out in opposite directions to each other (Goodwin, 1989). Therefore, the symmetric and asymmetric imbalance masses must be balanced, respectively.

Determining the Phase Angle of the Imbalance Mass. When imbalance mass, $\bar{m}$, exists on the balance plane, i, of the rotor and rotates in angular velocity, ω, as shown in Fig. 3, if we measure the vibration on the bearing, k, the angle between the imbalance mass, $\bar{m}$, and the white line on the end face of rotor, based upon the aforementioned flash phase angle measurement method, is:

$$\theta = \phi + \varphi_{ik}(f) + \gamma(f), \tag{16}$$

where ϕ is the angle between the location of the vibration measured and the white line on the end face of the rotor, and $\gamma(f)$ is the phase lag angle of the measuring instrument. When rotating machinery is being run near its first critical speed, the rotor-bearing system mainly presents the first mode caused by the symmetric imbalance mass:

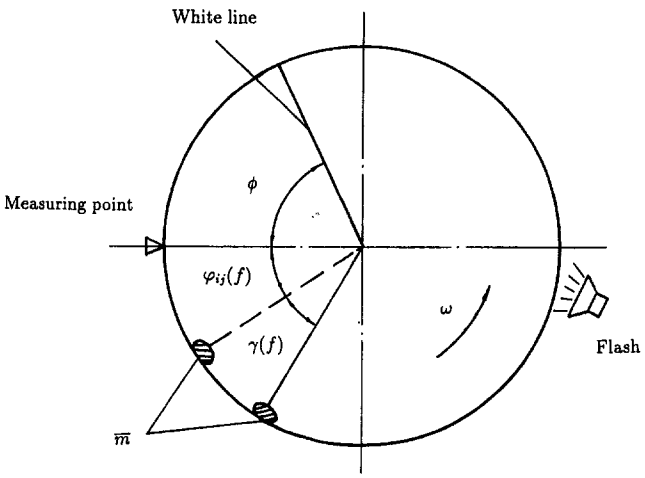

Fig. 3 Phase angle analysis of modal balance

$$\varphi_{ik}(f) = \varphi_1 \quad (i, k = 1, 2, 3, \ldots), \tag{17}$$

where φ_1 is a phase lag angle of the displacement behind the symmetric imbalance mass in the first mode. Since the phase angles of all frequency response functions of this system near the first critical speed are approximately the same, the phase angle, θ_s, between the symmetric imbalance mass $\bar{M}_s$ and the white line on the end face of the rotor can be calculated as long as the angle, ϕ, and the arbitrary, $\varphi_{ik}(f)$, of the rotor-bearing system near the first critical speed are obtained, i.e.,

$$\theta_s = \phi + \varphi_{ik}(f) + \gamma(f) \quad (i, k = 1, 2, 3, \ldots). \tag{18}$$

Similarly, when the rotating velocity is near the second critical speed, the rotor-bearing system mainly presents the "second mode" caused by the asymmetric imbalance masses. As shown in Fig. 1, the difference of the phase angles of the vibrations between bearing 1 and bearing 2 is 180 deg. The asymmetric imbalance masses distributed on the rotor have the same magnitudes, but opposite directions. The corresponding phase angles are:

$$\theta_{1A} = \phi + \varphi_{11}(f) + \gamma(f), \tag{19}$$

and

$$\theta_{2A} = \theta_{1A} + \pi, \tag{20}$$

where the subscripts 1 and 2, denote the balance planes 1 and 2, of the rotor.

Determining the Magnitudes of the Imbalance Masses. From the definition of the frequency response function, we know that its vector expression is:

$$\bar{H}(f) = \frac{\bar{X}(f)}{\bar{F}(f)}, \quad \text{or} \quad \bar{F}(f)\bar{H}(f) = \bar{X}(f). \tag{21}$$

Assuming that the balance masses, $\bar{m}_1$ and $\bar{m}_2$, are applied on the balance planes 1 and 2, and that the eccentric forces caused by $\bar{m}_1$ and $\bar{m}_2$ are $\bar{F}_1(f)$ and $\bar{F}_2(f)$, if the input is eccentric force, $\bar{F}_i(f)$, on the balance plane, $i(i = 1, 2)$, and the output is the displacement, $X_{ik}(f)$, of bearing, k, the frequency response function of the rotor-bearing system is:

$$\bar{H}_{ik}(f) = \frac{\bar{X}_{ik}(f)}{\bar{F}_i(f)} \quad (i, k = 1, 2), \tag{22}$$

since both $\bar{F}_1(f)$ and $\bar{F}_2(f)$ on balance planes 1 and 2, affect every bearing of the rotor-bearing system. So, for bearing 1, by the principle of linear superposition, we obtain:

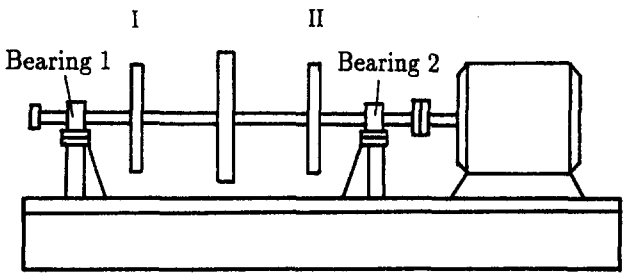

Fig. 4 High-speed rotating testing rig

$$\bar{F}_1(f)\bar{H}_{11}(f) + \bar{F}_2(f)\bar{H}_{21}(f) = \bar{X}_{11}(f) + \bar{X}_{21}(f) = \bar{X}_1(f), \quad (23)$$

where $\bar{X}_1(f)$ is the general vibration amplitude on bearing 1 under the common action of $\bar{F}_1(f)$ and $\bar{F}_2(f)$. The rotor-bearing system mainly presents the first mode by symmetric forces, $\bar{F}_{1s}(f)$ and $\bar{F}_{2s}(f)$, on the balance planes, 1 and 2, when it is near the first critical speed. Therefore, for the symmetric rotor:

$$\bar{F}_s(f) = \bar{F}_{1s}(f) = \bar{F}_{2s}(f), \quad (24)$$

and

$$\bar{X}_s(f) = \bar{X}_{1s}(f) = \bar{X}_{2s}(f), \quad (25)$$

where $\bar{X}_{1s}(f)$ and $\bar{X}_{2s}(f)$ are vibration amplitudes in the same direction of bearings 1 and 2. Substitution of Eqs. (25) and (24) into Eq. (23) gives:

$$\bar{F}_s(f)[\bar{H}_{11}(f) + \bar{H}_{21}(f)] = \bar{X}_s(f). \quad (26)$$

Near the first critical speed, $\varphi_{11}(f)$ is approximately equal to $\varphi_{21}(f)$. Therefore, the amplitude of Eq. (26) becomes:

$$F_s(f)[|H_{11}(f)| + |H_{21}(f)|] = X_s(f). \quad (27)$$

Since the distribution of imbalance masses along the length of the rotor is arbitrary, the balance condition can be established by the principle that the vibration amplitudes on the bearing are equal. Assuming that the vibration amplitude of the same direction caused by the symmetric imbalance masses on the rotor is X_0, i.e., $X_0 = 2X_s(f)$, since the vibration amplitudes measured in practice are the overall vibration amplitudes, the balance condition is:

$$F_s(f)[|H_{11}(f)| + |H_{21}(f)|] = \tfrac{1}{2}X_0. \quad (28)$$

Also, since

$$F_s(f) = m_s|r_1 + y_1|\omega^2 \approx m_s r_1\omega^2, \quad (29)$$

substituting Eq. (29) into Eq. (28) yields:

$$m_s r_1\omega^2[|H_{11}(f) + |H_{21}(f)|] = \tfrac{1}{2}X_0, \quad (30)$$

or

$$m_s = \frac{X_0}{2\omega^2 r_1[|H_{11}(f)| + |H_{21}(f)|]}. \quad (31)$$

Similarly, near the second critical speed, the asymmetric forces, $F_{1A}(f)$ and $F_{2A}(f)$, on the rotor have the same magnitudes and opposite directions. From Eq. (23), we get:

$$\bar{F}_{1A}(f)\bar{H}_{11}(f) + \bar{F}_{2A}(f)\bar{H}_{21}(f) = \bar{X}_A(f). \quad (32)$$

Since $\varphi_{11}(f) = -\varphi_{21}(f)$, and $F_A(f) = F_{1A}(f) = F_{2A}(f)$, the amplitude of Eq. (32) is:

$$F_A(f)[|H_{11}(f)| - |H_{21}(f)|] = X_A(f). \quad (33)$$

The balance condition is:

$$F_A(f)[|H_{11}(f) - |H_{21}(f)|] = \tfrac{1}{2}X'_0, \quad (34)$$

where X'_0 is the asymmetric vibration amplitude on the bearing ($X'_0 = 2X_A(f)$). Therefore, the equation for the asymmetric imbalance mass is:

$$m_A = \frac{X'_0}{2\omega^2 r_1[|H_{11}(f) - |H_{21}(f)|]}. \quad (35)$$

Experimental Verification

In order to verify the theoretical relation derived, experiments were carried out using the high-speed rotating testing rig shown in Fig. 4. In the experiments, $r_i = 0.13$ m, and the first critical speed is 2130 rpm. The system used to measure the frequency response function in the rotor-bearing system is shown in Fig. 5. When the rotating velocity is 120 rpm, the balance plane, 1, was struck in the horizontal direction with a calibrated hammer, whose striking force can be measured, and the displacement responses of bearings 1 and 2, in the horizontal direction were measured. The force signals of the calibrated hammer and the displacement response signals of the bearings were all amplified and transmitted to a magnetic tape recorder. Similarly, the balance plane, 2, was struck in the same manner and all signals were stored in the magnetic tape recorder. All signals were then sent into the Fourier analyzer to be processed, and all frequency response functions of the rotor-bearing system were obtained. At $f_0 = 30$ Hz, the corresponding frequency response functions are shown as follows:

$$H_{11}(f_0) = 0.333 \times 10^{-7}\exp(-j2).$$

$$H_{12}(f_0) = 0.265 \times 10^{-7}\exp(-j1.5).$$

$$H_{21}(f_0) = 0.256 \times 10^{-7}\exp(-j7.9).$$

$$H_{11}(f_0) = 0.413 \times 10^{-7}\exp(-j1.5).$$

Having measured that $\gamma(f_0) = 335$ deg, and $\phi_k = 180$ deg, all influence coefficients of the rotor-bearing system were calculated using above-derived frequency response functions. The values of the calculated influence coefficients were very close to the measured values, and both of them were used in the rotor balance with very satisfactory results. After the balance, the residual vibrations of the rotor-bearing system were reduced to a much lower level. These results are shown in Table 1.

For the improved method of modal balancing, the symmetric imbalance masses, $\bar{m}_s$, were balanced near the first critical speed because the rotating speed of the experimental equipment could not reach the second critical speed. The methods used for the frequency response function were the same as the ones pre-

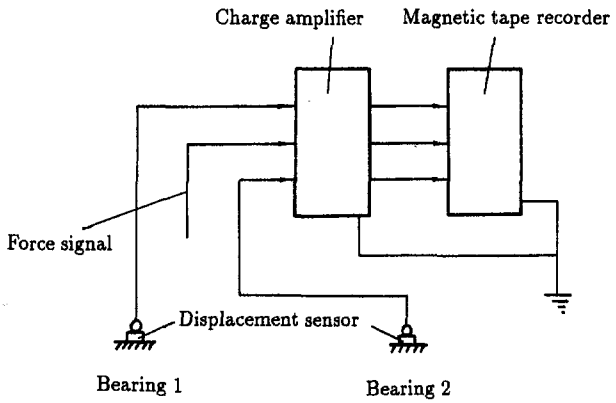

Fig. 5 Signal measuring system

Table 1

Item / Method	K11 $\frac{\mu m}{g}$ ·degrees	K12 $\frac{\mu m}{g}$ ·degrees	K21 $\frac{\mu m}{g}$ ·degrees	K22 $\frac{\mu m}{g}$ ·degrees	Original vibration data in horizontal direction μm·degrees		Residual vibration in horizontal direction μm·degrees	
					Bearing 1	Bearing 2	Bearing 1	Bearing 2
Measuring Value (I)	0.320 at 153.5°	0.256 at 159°	0.225 at 159°	0.363 at 168.1°	21.7 at -97°	22.7 at -97°	2.3 at -125°	1.6 at -135°
Calculation Value	0.307 at 157°	0.245 at 156.5°	0.237 at 162.5°	0.382 at 156.5°	21.7 at -97°	22.7 at -97°	2.3 at -168°	4.1 at -175°
Measuring Value (II)	0.321 at 161.7°	0.261 at 163.5°	0.227 at 161.4°	0.396 at 170.1°	15.5 at 82°	21.3 at 81°	1.9 at 97°	4.4 at 155°
Calculation Value	0.307 at 157°	0.245 at 156.5°	0.237 at 162.5°	0.382 at 156.5°	15.5 at 82°	21.3 at 81°	3.0 at 101°	4.5 at 42°

Table 2

Item / No	Symmetrical imbalance applied on balance plane g·degrees	Bearing vibration in horizontal direction g·degrees		Symmetrical vibration amplitude, X_0, and phase angle, ϕ μ·degrees	Symmetrical imbalance calculated g·degrees	Fractional error	
		Bearing 1	Bearing 2			$\frac{\Delta M}{Ms}$ %	$\frac{\Delta\alpha}{360}$ %
1	18.15 at 135°	14.5 at 8°	19 at 35°	16.3 at 156.7°	18.0 at 134.7°	-0.83	-0.08
2	9.75 at 50°	8.7 at 113°	16.5 at 116°	12.6 at 65°	13.92 at 43°	29.67	-1.94
3	16.77 at 22.5°	13.7 at 129°	23.4 at 135°	18.52 at 47.3°	20.45 at 25.3°	18.00	0.8
4	16.50 at 90°	12.7 at 46°	20 at 58°	16.26 at 126.7°	17.96 at 104.7°	8.13	4.1
5	10.59 at 28°	7 at 130°	17 at 137°	11.98 at 55°	13.23 at 23°	19.96	-1.4

viously used. When $f_1 = 31.5$ Hz, the amplitudes of the frequency response functions, through the Fourier analyzer, are:

$$|H_{11}(f_1)| + |H_{21}(f_1)| = 0.889 \times 10^{-7},$$

and

$$\varphi(f_1) = 3 \text{ deg.}$$

During the experiment, various imbalance masses were first added on the balance planes, 1 and 2, of the rotor, and then M_s was calculated by the improved method of modal balancing. Comparing the added symmetric imbalance masses with the calculated symmetric imbalance masses, the phase angles and the magnitudes are very close. Therefore, the agreement between the theoretical results and the experimental results is acceptable. The detailed results are shown in Table 2.

Conclusions

The method of finding the influence coefficients of a rotor-bearing system and the imbalance masses on the balance planes directly through the frequency response function is a very important improvement on traditional balancing methods. The proposed theory has been verified by experiments, and has proven to be feasible and effective. The new method can eliminate the imbalance masses of rotors effectively, and reduce the number of startups of rotating machinery during the balancing procedure. The improvement is especially important for steam turbines, where much man-power and money can be saved. On-site testing are needed for further verification of the proposed theory.

Acknowledgments

The authors would like to thank Mrs. Helen Rooney at Florida International University for her help in preparing this manuscript.

References

Beauchamp, K. G., 1973, *Signal Processing Using Analog and Digital Techniques,* Unwin Hyman, London, United Kingdom.

Goodwin, M. J., 1989, *Dynamics of Rotor-Bearing Systems,* Unwin Hyman, London, United Kingdom.

Larsson, L. O., 1976, "On the Determination of the Influence Coefficients in Rotor Balancing, Using Linear Regression Analysis," *Proc. IMechE Conf. Vibrations in Rotating Machinery,* Cambridge, United Kingdom.

Little, R. M., and W. D. Pilkey, 1976, "A Linear Programming Approach for Balancing Flexible Rotors," ASME *Journal of Engineering for Industry,* Vol. 98, pp. 1030–1035.

Marple, S. L., 1987, *Digital Spectral Analysis With Applications,* Prentice-Hall, Inc., Englewood Cliffs, NJ.

Newland, D. E., 1975, *An Introduction to Random Vibrations and Spectral Analysis,* Longman, London–New York.

Rao, J. S., 1983, *Rotor Dynamics,* Wiley Eastern, New Delhi.

Coupled Shaft-Torsion and Blade-Bending Vibrations of a Rotating Shaft–Disk–Blade Unit

S. C. Huang[1]
Professor.

K. B. Ho
Graduate student.

Department of Mechanical Engineering,
National Taiwan Institute of Technology,
43, Keelung Road, Sec. 4,
Taipei, 106 Taiwan

A new approach to analyzing the dynamic coupling between shaft torsion and blade bending of a rotating shaft–disk–blade unit is introduced. The approach allows the shaft to vibrate freely around its rotation axis instead of assuming a periodic perturbation of the shaft speed that may accommodate the shaft flexibility only to a limited extent. A weighted residual method is applied, and the receptances at the connections of blades and shaft–disk are formulated. Numerical examples are given for cases with between two and six symmetrically arranged blades. The results show not only coupling between the shaft, disk, and blades, but also coupling between individual blades where the shaft acts as a rigid support and experiences no torsional vibration. The blade-coupling modes occurred only in repeated frequencies. Finally, the effect of shaft speed on the modal frequencies was investigated. Plots illustrating the occurrence of critical speeds and flutter instabilities are presented.

1 Introduction

Shaft–disk–blade units, shown schematically in Fig. 1, are widespread in engineering applications that include turbine-generator systems, turbine engines, and rotor compressors. Thus, the vibration characteristics of such units are of great importance and have been investigated for years. As the unit operates, power is transmitted either from the blades to the shaft (turbine generator) or from the shaft to the blades (compressor). In either case, shaft torsional modes always couple with blade bending modes. The purpose of this paper is to develop a simple approach for analyzing this coupling and to explore interactions between the shaft and blades.

Much research related to such units rotating at a constant speed has been published, e.g., Bauer and Eidel (1988), Subrahmanyam et al. (1982), Sisto et al. (1983), Subrahmanyam and Kaza (1986), Ansari (1986), and Yigit et al. (1988). The blades were typically modeled as a rotating beams, uniform or pretwisted, and the approaches ranged from analytic methods for simple geometries to finite difference and finite element methods for more complicated geometries. There have been many papers published since the 1970s on blade–disk assemblies where the flexibility of the disk is included, e.g., Ewins (1973), Ewins and Srinivasan (1983), Kielb and Rieger (1985), etc. However, the authors were unable to find work that also addressed the flexibility of the shaft. The closest relevant research that addressed shaft-torsion effects at all focused on instability phenomena due to speed perturbations and nonlinear effects. The present research seeks to determine the natural frequencies of the shaft–disk–blade unit as a whole.

The present research assumes that the shaft vibrates around a constant rotating axis and the blades to be clamped to a rigid disk. Any interactions between shaft torsion and blade bending are transmitted through the rigid disk. The analytical approach utilizes the concept of structure combination. The vibration characteristics of shaft–disk (torsion) and the blades (bending) are first solved separately using a mixed weighted residuals method. Then the receptance method is used to combine the components and yield the characteristic equation of the shaft–disk–blade unit, from which the natural frequencies and mode shapes of the unit follow directly.

Examples of units with two to six blades were analyzed. The results show coupling not only between the shaft, disk, and blades, but also between individual blades. When excited at one of the blade-coupling frequencies, the blades "balance" themselves such that the shaft experiences no torsional vibration. It was also discovered that the blade-coupling modes usually occur in repeated frequencies, and the degree of repetition increases with the number of blades. There are hence multiple modes associated with each blade-coupling frequency. The authors divide these modes into classes and give them physical interpretations. Finally, the variation of natural frequencies of the unit with the rotation speed is discussed. Frequency diagrams are used to show occurrences of critical speeds and flutter instabilities.

2 Equations of Motion

2.1 Shaft–Disk Subsystem. The energy expressions associated with the shaft–disk subsystem are

$$T_s = \frac{1}{2}\int_0^l I_s\left(\frac{\partial\theta}{\partial t}+\Omega\right)^2 dz + \frac{1}{2} I_d\left(\frac{\partial\theta}{\partial t}+\Omega\right)^2\Big|_{z=\xi} \tag{1}$$

$$U_s = \frac{1}{2}\int_0^l GJ_s\left(\frac{\partial\theta}{\partial x}\right)^2 dz \tag{2}$$

$$W_s = [F(t)r_d + M_T(t)](\theta + \Omega t)|_{z=\xi} \tag{3}$$

where l is the shaft length, ξ denotes the disk location on shaft, and $\theta(z, t)$ is the torsional displacement of the shaft as viewed from a frame rotating at constant angular velocity Ω. Symbols are defined further in the nomenclature. Note that (F, M_T) represents a force/moment combination acting on the outer circumference of the disk due to the interaction between the disk and each blade. There are as many force sets as blades connected. Since the blade's receptances are identical, only one force set needs to be considered.

Next, we employ the modal expansion method, i.e.,

$$\theta(z, t) = \sum_{s=1}^{\infty} \eta_s(t)\Phi_s(z) \tag{4}$$

where the sth mode shape, $\Phi_s(z)$, was derived to be of the form

[1] Current address: Visiting Scholar, Engineering Science and Mechanics, Virginia Polytechnic Institute and State University, Blacksburg, VA 24061-0219.

Contributed by the International Gas Turbine Institute for publication in the JOURNAL OF ENGINEERING FOR GAS TURBINES AND POWER. Manuscript received by the International Gas Turbine Institute November 16, 1995. Associate Technical Editor: R. E. Kielb.

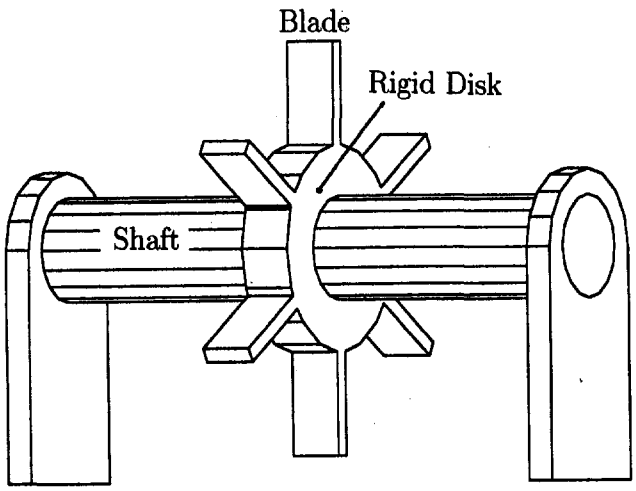

Fig. 1 A shaft–disk–blade unit

$$\Phi_s(z) = \sin(c\omega_s z)[h(z) - h(z-\xi)] + \frac{\sin(c\omega_s\xi)}{\sin[c\omega_s(l-\xi)]}\sin[c\omega_s(l-z)h(z-\xi)] \quad (5)$$

where $c = (I_s/GJ_s)^{1/2}$ and $h(z)$ is the unit step function. Subsequently, the equations of motion can be written

$$\ddot{\eta}_s + \omega_s^2\eta_s = g_s \quad (6)$$

where

$$\omega_s^2 = \frac{S_{ss}}{N_{ss}}$$

$$g_s = \frac{f_s}{N_{ss}} \quad (7)$$

and

$$S_{ss} = \int_0^l GJ_s(\partial\Phi_s/\partial z)^2 dz$$

$$f_s = (F(t)r_d + M_T(t))\Phi_s(\xi)$$

$$N_{ss} = \int_0^l I_s\Phi_s^2 dz + I_d\Phi_s^2(\xi) \quad (8)$$

2.2 Rotating Blades. Figure 2 shows a single rotating blade cantilevered off a rigid, spinning disk. This figure also illustrates the coordinate systems being used in the paper. The XYZ coordinate system is inertial, and the xyz frame rotates at constant speed Ω. The angle between these two sets is Ωt, and the torsional flexibility of the shaft is represented by displacements around the z axis. This torsional vibration of the shaft-disk is affected by the blade bending vibrations, and vice versa.

With the coordinates established, the bending vibration of the blade is now addressed. The total displacement of the blade relative to the rotating frame, denoted by $v(x, t)$, is composed of rotation of the disk, $\theta(\xi, t)$, and the blade transverse displacement. The energies associated with the blade are the strain energy, U_b^s, the strain energy due to initial stress (from rotation), U_b^i, the kinetic energy, T_b, and the work done by the boundary forces, W_b. Omitting the intermediate steps, these energies are expressed as

$$T_b = \frac{1}{2}\int_{r_d}^{r_a}\left\{\rho A[\dot{v}^2 + (x^2 + v^2)\Omega^2 + 2x\dot{v}\Omega] + I_b\left(\frac{\partial\dot{v}}{\partial x} + \Omega\right)^2\right\}dx \quad (9)$$

$$U_b = U_b^s + U_b^i = \int_{r_d}^{r_a}\left[\frac{EI_A}{2}\left(\frac{\partial^2 v}{\partial x^2}\right)^2 + \frac{1}{4}\Omega^2\rho A(r_a^2 - x^2)\left(\frac{\partial v}{\partial x}\right)^2\right]dx \quad (10)$$

$$W_b = \left\{-M_T(t)\left(\Omega t + \frac{\partial v}{\partial x}\right) - F(t)(r_d\Omega t + v)\right\}_{x=r_d} \quad (11)$$

The isotropic Euler beam model has been assumed for the blade throughout the derivation. While more detailed models for the blade may provide more precise results, the purpose of the paper is to introduce the approach and to look into the coupling effects, and the Euler beam model serves well for this purpose. Note that $F(t)$ and $M_T(t)$ appeared here with minus signs.

The extended Hamilton's principle yields the equation of motion and the appropriate boundary conditions for the blade:

EOM:

$$\rho A[-\ddot{v} + \Omega^2 v] + I_b\frac{\partial^2\ddot{v}}{\partial x^2} - EI_A\frac{\partial^4 v}{\partial x^4} + \frac{\rho A\Omega^2}{2}\times\left[-2x\frac{\partial v}{\partial x} + (r_a^2 - x^2)\frac{\partial^2 v}{\partial x^2}\right] = 0 \quad (12)$$

BC's

$$\left\{-I_b\frac{\partial\ddot{v}}{\partial x} + EI_A\frac{\partial^3 v}{\partial x^3} - \frac{\rho A\Omega^2}{2}(r_a^2 - x^2)\frac{\partial v}{\partial x} - F(t)\right\}\delta v|_{x=r_d} = 0 \quad (13)$$

Nomenclature

E = Young's modulus
F = interactive force of blade and disk
GJ_s = shaft torsional rigidity
I = polar/lateral moment of inertia
I_A = area moment of inertia
l = shaft length
M_T = interactive moment of blade and disk
r_a = blade outer position
r_d = blade inner position (disk radius)
R_B = blade boundary residual
R_I = blade interior residual
T = kinetic energy
U = potential energy
u_m = the mth mode of a free–free, nonrotating beam
v = blade displacement relative to the rotating frame
W = applied work
α_{ij} = blade receptance
β_{ij} = shaft-disk receptance
η_s = shaft-disk modal participation factor
θ = shaft torsional displacement relative to rotating frame
ξ = disk location
ξ_{ij} = matrix entry of the receptance matrix
ρ = blade density
Φ_s = the sth mode shape of the shaft disk
ψ = weighting functions
Ω = rotation speed
ω = synchronous frequency
ω_m = the mth bending natural frequency of a free beam
ω_s = the sth torsional natural frequency of the shaft disk

Subscripts

b = for blade
d = for disk
s = for shaft

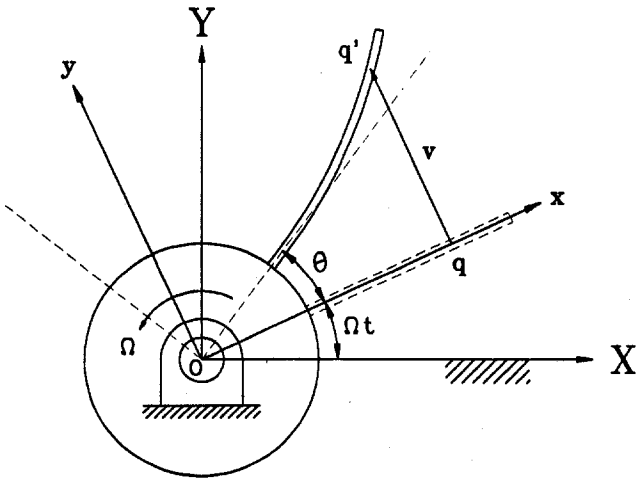

Fig. 2 A rotating blade and the referenced frames

$$\left\{-I_b \frac{\partial \ddot{v}}{\partial x} + EI_A \frac{\partial^3 v}{\partial x^3}\right\}\delta v|_{x=r_a} = 0 \tag{14}$$

$$\left\{-EI_A \frac{\partial^2 v}{\partial x^2} - M_T(t)\right\}\delta\left(\frac{\partial v}{\partial x}\right)\Big|_{x=r_d} = 0 \tag{15}$$

$$-EI_A \frac{\partial^2 v}{\partial x^2}\,\delta\left(\frac{\partial v}{\partial x}\right)\Big|_{x=r_a} = 0 \tag{16}$$

3 Eigenvalue Problem

When the shaft–disk–blade system is in synchronous vibration, the interactions between the blade and the shaft–disk are harmonic, i.e.,

$$\begin{aligned} F(t) &= Fe^{i\omega t} \\ M_T(t) &= M_T e^{i\omega t} \\ \theta(z, t) &= \Theta(z)e^{i\omega t} \\ v(x, t) &= V(x)e^{i\omega t} \end{aligned} \tag{17}$$

Substitution of these equations into the shaft–disk equation for torsional response yields

$$\Theta(z) = \sum_{s=1}^{\infty} \frac{Fr_d + M_T}{N_s(\omega_s^2 - \omega^2)}\Phi_s(\xi)\Phi_s(z) \tag{18}$$

Similarly, the blade response can be obtained from

$$\rho A(\omega^2 + \Omega^2)V - I_b\omega^2 V'' - EI_A V'''' + \frac{\rho A\Omega^2}{2} \times [-2xV' + (r_a^2 - x^2)V''] = 0 \tag{19}$$

$$\left\{I_b\omega^2 V' + EI_A V''' - \frac{\rho A\Omega^2}{2}(r_a^2 - x^2)V' - F\right\}\Big|_{x=r_d} = 0 \tag{20}$$

$$\{I_b\omega^2 V' + EI_A V'''\}|_{x=r_a} = 0 \tag{21}$$

$$(-EI_A V'' - M_T)|_{x=r_d} = 0 \tag{22}$$

$$-EI_A V''|_{x=r_a} = 0 \tag{23}$$

where the primes denote the differentiations with respect to x. The ω's that satisfy these equations are the natural frequencies of the combined system. Unfortunately, the equations cannot be solved at this moment since F and M_T remain unknown. Subsequent analysis will, however, show that F and M_T are internal reactions of the combined system and thus need not be known to solve for the eigenfrequencies.

Direct solutions of the continuous eigenvalue problem given in Eqs. (19)–(23) is inefficient and impractical. Thus, a mixed weighted residual method was applied using the following mode shapes of a free–free, nonrotating beam as the trial functions for the rotating blade.

$$u_1(x) = 1 \tag{24}$$

$$u_2(x) = \left(x - \frac{r_a + r_d}{2}\right) \tag{25}$$

$$\begin{aligned} u_n(x) = {} & (\cos \alpha_n(r_a - r_d) - \cosh \alpha_n(r_a - r_d)) \\ & \times (\sin \alpha_n(x - r_d) + \sinh \alpha_n(x - r_d)) \\ & - (\sin \alpha_n(r_a - r_d) - \sinh \alpha_n(r_a - r_d)) \\ & \times (\cos \alpha_n(x - r_d) + \cosh \alpha_n(x - r_d)) \end{aligned}$$

$$n = 3, 4, 5, \ldots \tag{26}$$

where $\cos \alpha_n(r_a - r_d)\cdot\cosh \alpha_n(r_a - r_d) = 1$. Note that u_1 and u_2 are the translational and rotational rigid-body modes, respectively.

The blade displacement is now approximated as

$$V(x) = \sum_{m=1}^{N} c_m u_m(x) = \{c\}^T\{u\} \tag{27}$$

where N is the number of functions deemed necessary to yield satisfactory convergence. The interior and boundary residuals of the blade are

$$\begin{cases} R_I = L\{V\} - \lambda M\{V\} \\ R_B = \sum_{k=1}^{4} B_k[V] \end{cases} \tag{28}$$

where L, M, and B_k are linear differential operators as given in Eqs. (19)–(23). Next, we enforce the weighted residuals to be zero, i.e.,

$$\int_D u_r R_I dD + \sum_{k=1}^{4}\int_S \psi_{rk}R_k dS = 0, \quad r = 1, 2, \ldots, N \tag{29}$$

where D and S denote the domain and the boundary of the system. The test functions ψ_{rk} are chosen so that all the boundary residuals yield consistent units, e.g., u_r for force boundary and u_r' for moment boundary. After re-arrangement, Eq. (29) yields

$$\sum_{m=1}^{N} [\Phi_{rm} - (\omega_m^2 + \Omega^2)\Gamma_{rm}]\{c\} = 0, \quad r = 1, 2, \ldots, N \tag{30}$$

in which

$$\begin{aligned} \Phi_{rm} = {} & \int_{r_d}^{r_a} u_r L[u_m]dx + B_1[u_m]u_r|_{x=r_d} \\ & + B_2[u_m]u_r|_{x=r_a} + B_3[u_m]u_r'|_{x=r_d} + B_4[u_m]u_r'|_{x=r_a} \end{aligned} \tag{31}$$

$$\Gamma_{rm} = \rho A \int_{r_d}^{r_a} u_r u_m dx \tag{32}$$

Note that ω_m is the mth natural frequency of the nonrotating, free–free blade and that the trial functions satisfy the eigenvalue problem

$$\begin{aligned} EI_A u_m'''' - \rho A\omega_m^2 u_m &= 0 \\ EI_A u_m'''|_{r_d}^{r_a} &= 0 \\ EI_A u_m''|_{r_d}^{r_a} &= 0 \end{aligned} \tag{33}$$

Substituting these results into Eqs. (31)–(32) and neglecting

some secondary terms, e.g., rotary inertia (Ho, 1994), we arrive at

$$\sum_{m=1}^{N}\left\{c_m\int_{r_d}^{r_a}[\tfrac{1}{2}\rho A\Omega^2(r_a^2-x^2)u_r'u_m'-\rho A(\omega^2-\omega_m^2+\Omega^2)u_ru_m]dx+(u_mF+u_m'M_T)|_{x=r_d}\right\}=0\quad r=1,2,\ldots,N \tag{34}$$

or in a matrix notation

$$[A(\omega)]\{c\}=-F\{u\}-M_T\{u'\} \tag{35}$$

where the matrix $[A(\omega)]$ has the synchronous frequency ω embedded and $\{u\}$ is the column vector of the assumed modes.

4 Receptance Method for Eigenfrequencies

The receptance α_{ij} is defined as the ratio of displacement response at point i to a unit harmonic force input at point j (Bishop and Johnson, 1960), with α_{ii} and α_{ij} called the direct and cross receptances, respectively. In the present analysis, the connection between the blade and disk is accomplished by enforcing *displacement* and *slope* continuity at the interface. For convenience the junction 1 is assigned for displacement connection and the junction 2 for slope connection.

By alternatively setting $F=1$, $M_T=0$ and $F=0$, $M_T=1$, one will obtain the corresponding receptances. First, for the shaft–disk, denoted β,

$$\beta_{12}=\beta_{21}=\sum_{s=1}^{N}\frac{r_d\Phi_s^2(\xi)}{N_s(\omega_s^2-\omega^2)} \tag{36}$$

$$\beta_{11}=r_d^2\beta_{22},\quad \beta_{22}=\sum_{s=1}^{N}\frac{\Phi_s^2(\xi)}{N_s(\omega_s^2-\omega^2)} \tag{37}$$

Consequently, a receptance equation for the shaft–disk due to one blade connection is

$$\begin{Bmatrix}v\\ \theta\end{Bmatrix}=\begin{bmatrix}\beta_{11}&\beta_{12}\\ \beta_{21}&\beta_{22}\end{bmatrix}\begin{Bmatrix}F\\ M_T\end{Bmatrix} \tag{38}$$

Note that since the disk is rigid and only the torsional vibration is considered, each blade imposes the same effect and yields the same equation.

The derivation of the receptances of the blades, denoted by α, starts from Eq. (35). In the same manner as above, i.e., alternately setting either $-F$ or $-M_T$ equal to unity, the receptances of the blade are obtained as

$$\alpha_{11}=\{u\}^T\{A(\omega)\}^{-T}\{u\}|_{x=r_d} \tag{39}$$

$$\alpha_{12}=\{u\}^T\{A(\omega)\}^{-T}\left\{\frac{\partial u}{\partial x}\right\}\Big|_{x=r_d} \tag{40}$$

$$\alpha_{21}=\left\{\frac{\partial u}{\partial x}\right\}^T\{A(\omega)\}^{-T}\{u\}|_{x=r_d} \tag{41}$$

$$\alpha_{22}=\left\{\frac{\partial u}{\partial x}\right\}^T\{A(\omega)\}^{-T}\left\{\frac{\partial u}{\partial x}\right\}\Big|_{x=r_d} \tag{42}$$

Similarly, the receptance equation for each blade is

$$\begin{Bmatrix}v\\ \theta\end{Bmatrix}=\begin{bmatrix}\alpha_{11}&\alpha_{12}\\ \alpha_{21}&\alpha_{22}\end{bmatrix}\begin{Bmatrix}-F\\ -M_T\end{Bmatrix} \tag{43}$$

Recall that all the receptances are functions of the synchronous frequency ω.

Enforcing the equilibrium and compatibility equations, the receptance equation for a shaft–disk with n blades is derived as

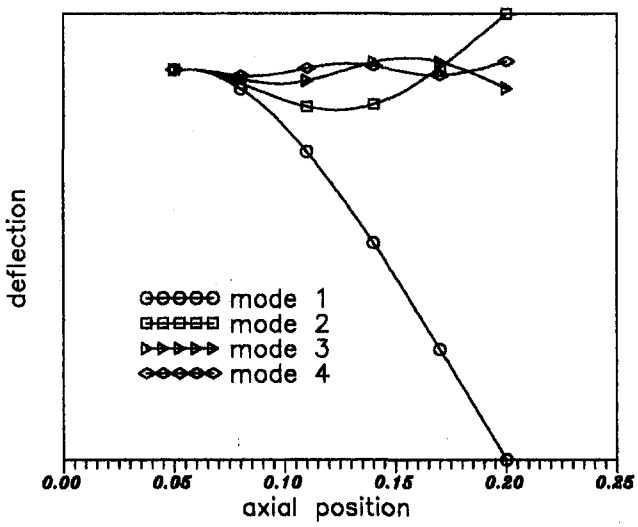

Fig. 3 Mode shapes of a clamped blade solved by the method

$$\begin{bmatrix}\xi_{11}&\xi_{12}&\cdots&\xi_{1n}\\ \xi_{21}&\xi_{22}&\cdots&\xi_{2n}\\ \vdots&\vdots&\ddots&\vdots\\ \xi_{n1}&\xi_{n2}&\cdots&\xi_{nn}\end{bmatrix}\begin{bmatrix}\begin{Bmatrix}F\\ M_T\end{Bmatrix}_1\\ \vdots\\ \begin{Bmatrix}F\\ M_T\end{Bmatrix}_n\end{bmatrix}=0 \tag{44}$$

where

$$\xi_{ii}=\begin{bmatrix}\alpha_{11}+\beta_{11}&\alpha_{12}+\beta_{12}\\ \alpha_{21}+\beta_{21}&\alpha_{22}+\beta_{22}\end{bmatrix} \tag{45}$$

$$\xi_{ij}=\begin{bmatrix}\beta_{11}&\beta_{12}\\ \beta_{21}&\beta_{22}\end{bmatrix} \tag{46}$$

The characteristic equation of the shaft-disk-blades unit is then obtained by letting the determinant of Eq. (44) vanish, i.e.,

$$\begin{vmatrix}\xi_{11}&\xi_{12}&\cdots&\xi_{1n}\\ \xi_{21}&\xi_{22}&\cdots&\xi_{2n}\\ \vdots&\vdots&\ddots&\vdots\\ \xi_{n1}&\xi_{n2}&\cdots&\xi_{nn}\end{vmatrix}=0 \tag{47}$$

In this equation, ξ_{ii} physically represents the direct correlation of blade and disk, and ξ_{ij} represents the cross correlation of the jth blade and the disk's ith location.

5 Numerical Results

It is first of interest to look at the simple case of a nonrotating, rigid-shaft unit. This corresponds to a cantilevered blade, so it provides a chance to check the validity of the approach. A rigid shaft is approximated by making its torsional rigidity very large ($G=8.274\times10^{15}$). The first four calculated mode shapes appear to be identical to those of a true cantilever blade, as shown in Fig. 3. The authors terminated the series of trial functions when an additional term changed the results by less than 0.5 percent. With this convergence criterion, the four natural frequencies obtained each showed about 1.6 percent difference from the perfectly clamped free blade. If the series of trial functions was allowed to be very long, the results would converge to the cantilever blade solution.

In the following, numerical examples simulating between two and six blades are illustrated. Table 1 shows the geometric and material properties selected for the system. Note that the length of the blade has been exaggerated to clarify the coupling effects.

Table 2 lists the first three torsional frequencies of the shaft–disk and the first three bending frequencies of the cantilever blade for reference in further discussions. The reason the natural frequencies of the cantilever blade are shown instead of the

Table 1 Geometric and material properties of the illustrated examples

disk radius	r_d	0.05 m
blade outer end	r_a	0.2 m
Young's modulus	E	$2.0685(10)^2$ GPa
Shaft shear modulus	G	8.274(10) GPa
density	ρ	$7.83(10)^3$ Kg/m^3
blade's area moment of inertia	I_A	$5.777(10)^{-10}$ m^4
blade's cross-section	A	$8.258 \times (10)^{-5}$ m^2
disk's polar area moment of inertia	J_d	$7.590(10)^{-3}$ m^4
shaft length	l	0.3 m
rotation speed	Ω	$(0 \sim 3200)$ Hz

free–free blade is that these frequencies represent the extreme cases of the shaft–disk–blade unit and can thus be used as an upper bound on the frequencies. For instance, it is at once realized that the first natural frequency of the unit should fall below 343.62 Hz when any shaft torsional flexibility is introduced.

Figure 4 shows the mode shapes of two-blade system. The first mode occurs at 321.90 Hz. As expected, this is lower than the first natural frequency of the single cantilever blade. From the shape one can tell that the first blade mode dominates, yet the shaft flexibility pulls the frequency slightly down. This is a torsion-bending coupled mode. The second mode occurs at 343.62 Hz, equal to the first natural frequency of the single cantilever blade (Table 2). In this mode, the two blades always vibrate exactly out of phase with equal amplitude so that the resultant moment exerted on the disk by the blades is zero. In this mode, classified by the authors as a blade-coupling mode, the shaft acts as a rigid support and experiences no torsional vibration. This means the blades' influence on each other is transmitted through the shaft–disk without causing any shaft vibration. The blade-coupling modes will be seen in repeated frequencies for even numbers of blades exceeding two. The third mode, with the frequency 1211.06 Hz, exhibits a degree of blade bending somewhere between the cantilever blade's first and second modes, but it is also strongly influenced by the first torsional mode (1303.27 Hz) of the shaft–disk. As seen in the figure, the shaft experiences much larger angular displacements. This is another torsion-bending coupled mode. The fourth and the sixth modes are blade-coupling modes.

Figure 5 shows the modes of four-blade case. It is seen that the odd-numbered modes exhibit coupling between the shaft and blades (torsion-bending) and the even modes are blade-coupling only. The blade-coupling modes were found at repeated frequencies. There exist hence multiple modes at any one of these frequencies. Thomas (1979) investigated axisymmetric structures and divided the repeated modes into classes. The authors here interpret these repeated modes in the same manner from a physical point of view. Let us take the fourth frequency as an example, where there exist three linearly independent modes, as illustrated in Fig. 6. In mode (A), the moment exerted on the shaft by any blade is balanced by its opposite blade. The number adjacent to each blade denotes its relative vibration amplitude. In mode (B), a blade is balanced by its adjacent blade, and there is again no net moment on the shaft. The two modes described above both belong to the classification "balanced-in-pair." It means that for every vibrating blade there is always a blade of equal amplitude and opposite phase to balance it. These balanced-in-pair modes become more and more complicated with the increasing number of blades. Mode (C) is an extreme case of blade-coupling in which the three blades vibrate in phase with equal amplitude and the fourth blade vibrates out of phase and with three times the vibration amplitude. Note that the modes shown are linearly independent, but not orthogonal to one another. These modes can be transformed into normal modes via an orthogonalization process for mathematical convenience. For example, three normal modes corresponding to Fig. 6 can be obtained as: $\frac{1}{2}\{1, -1, 1, -1\}^T$, $(1/\sqrt{10})\{1, -2, -1, 2\}^T$, and $(1/\sqrt{10})\{2, 1, -2, 1\}^T$.

The second interesting feature the authors would like to address is how the frequencies of the torsion-bending coupled modes changes with the number of blades. Figure 7 illustrates the first three torsion-bending coupled modes of the five- and six-blade cases. Let us furthermore compose a table (Table 3) containing these three frequencies for systems with two to six blades. The + and − signs inside the parentheses indicate whether the frequency was increased or decreased due to the addition of one blade. The frequencies of the first and the second modes decreased, so one would conclude that the effect of mass loading from the added blades was greater than any stiffness added. The third mode showed the opposite effect. The trend on the frequency increase/decrease due to the addition of a blade can be predicted as follows. We write down the torsional natural frequencies of the isolated shaft-disk in an ascending order (in the examples 1303.3, 10835.7, 10997.8, 21671.3, etc.). Frequencies of modes located in the first region (0. − 1303.3)

Table 2 Natural frequencies of shaft disk and clamped blade (Hz)

system n. f.	ω_1	ω_2	ω_3
blade	343.62	2153.74	6031.32
shaft-disk	1303.27	10835.67	10997.79

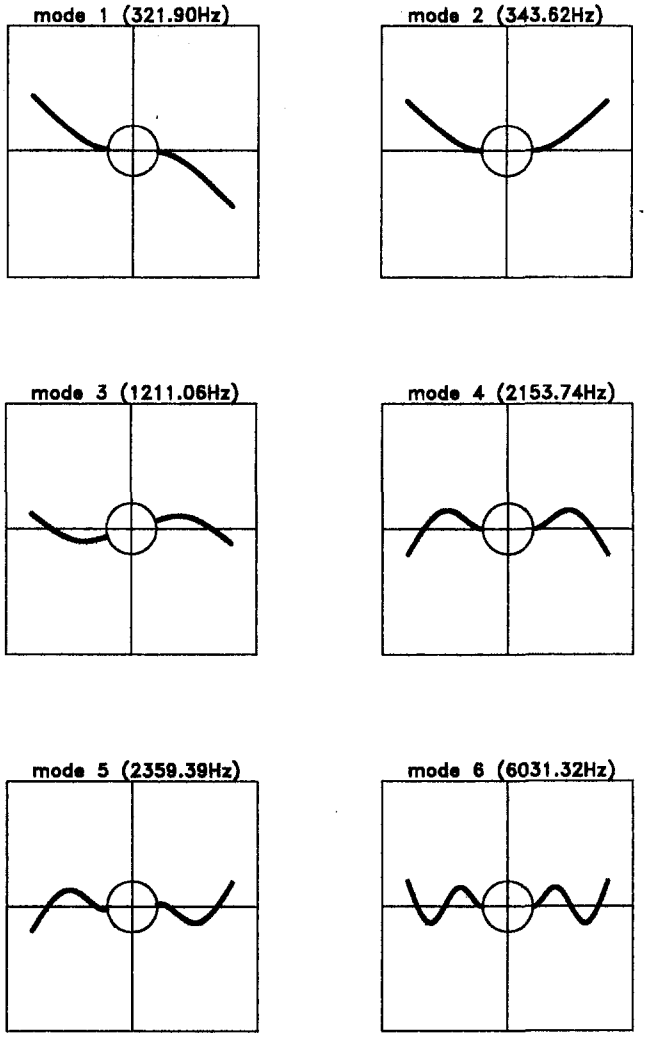

Fig. 4 The first six modes of the two-blade unit at $\Omega = 0$

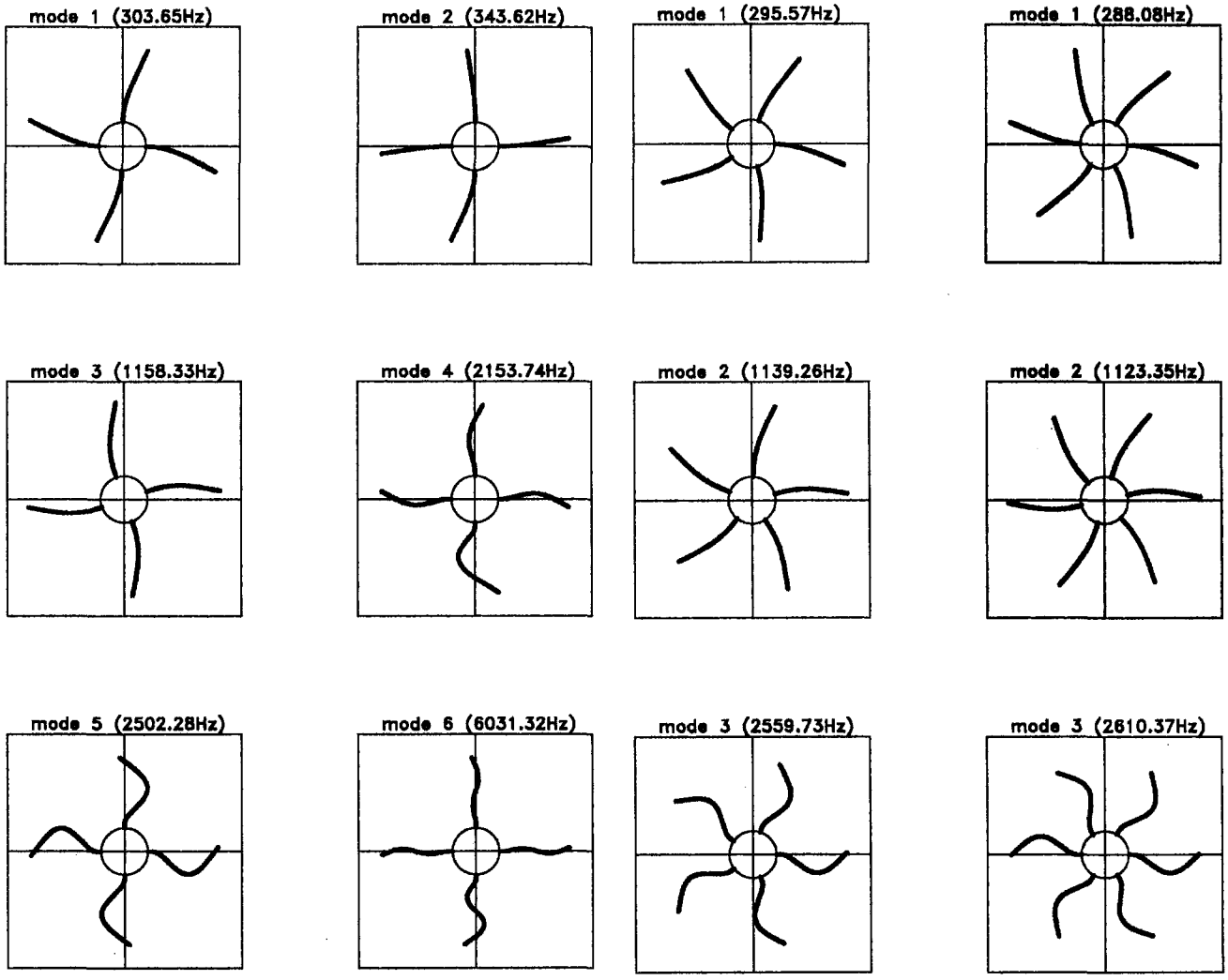

Fig. 5 The first six modes of the four-blade unit at $\Omega = 0$

Fig. 7 The first three torsion-bending coupled modes for five- and six-blade units at $\Omega = 0$

of the combined shaft–disk–blade system will be lowered by the addition of blades, whereas the frequencies of modes that lie between 1303.3 and 10835.7 will increase. The effect repeats itself alternatively in the subsequent frequency regions. This phenomenon is better understood if one draws the receptance graphs illustrated by Sodel (1981).

Another point of interest to the authors is how the shaft's rotation speed affects the natural frequencies of the unit. Figures 8 and 9 show the variation of the first few system frequencies with the rotation speed for two- and three-blade cases. These curves are similar to those often seen in rotor systems; each natural frequency splits into two branches, one increasing and one decreasing, as the rotation speed increases from zero. The lower branches eventually intersect the abscissa at what are customarily referred to as critical speeds of the system, which belong to the divergent type of instability. After the critical speeds, the lower curves "reflect" and ultimately merge with the upper branch. In the vicinity of the merging point, the sensitivity of ω to Ω approaches infinity, so it is very difficult to get the numerical solutions. That is why the curves showed scattering in these regions. After this "merged" speed, the system will experience instability from flutter, i.e., it will have eigenvalues in the right-half plane. The flutter phenomena were not shown in these figures, since the system has been assumed to be in synchronous motion ($e^{i\omega t}$) to determine the natural frequencies. If the flutter is of concern, one may assume the form $e^{\lambda t}$ and re-solve the problem.

6 Conclusions

The authors investigated the coupling between shaft-torsion and blade-bending vibration modes of shaft–disk–blade units.

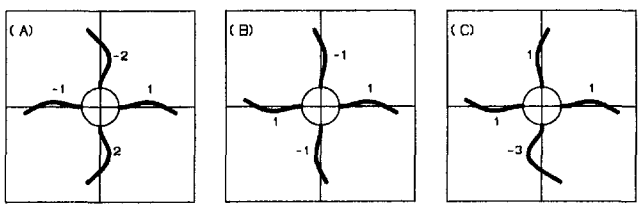

Fig. 6 Examples of the repeated blade-coupling modes

Table 3 Shaft–disk–blade unit coupled natural frequencies (Hz)

no. of blades	ω_1	ω_2	ω_3
2	321.90	1211.06	2359.39
3	312.40(−)	1181.67(−)	2436.32(+)
4	303.65(−)	1158.33(−)	2502.28(+)
5	295.57(−)	1139.26(−)	2559.73(+)
6	288.08(−)	1123.35(−)	2610.37(+)

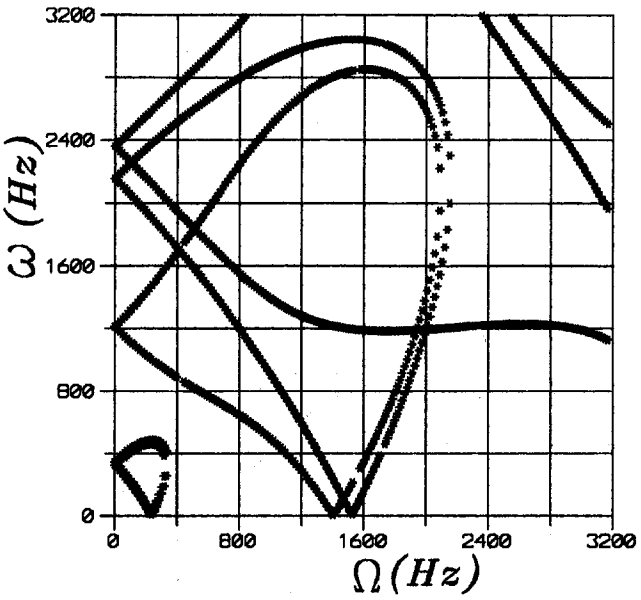

Fig. 8 Variation of natural frequencies with rotation speed (two blades)

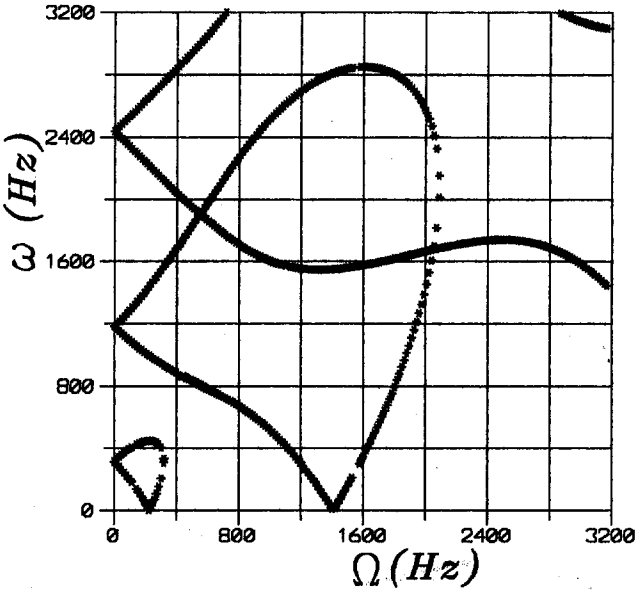

Fig. 9 Variation of natural frequencies with rotation speed (three blades)

The approach employed a mixed weighted residual method in conjunction with the receptance method to yield the coupled frequencies and mode shapes. Numerical results followed and verified the validity of this approach. This approach proved valuable in physical comprehension, in calculation of interaction forces, and in determining the sensitivity of the system's frequencies to variations in some parameters. However, the approach also identified some drawbacks in numerical root finding. The determinant of the receptance matrix drops by orders of magnitude as the number of blades is increased. The search for natural frequencies became more sensitive to the data precision, especially when repeated frequency occurred as in blade-coupling modes. Although caution has to be taken always, authors had no difficulties getting the results presented.

The blade used here was modeled as a simple Euler beam, but the approach works as well for more complicated blade models. The keys are the receptances at the roots of the blades. As long as these receptances can be obtained, more likely by experiments for pretwisted blade, the approach can be applied and yields good results.

The authors have drawn some conclusions from the numerical results. In addition to the coupled torsion-bending modes, the unit exhibits some pure blade-coupling modes, and these modes usually occur in repeated frequencies. When the system vibrates at one of the blade-coupling modes, the shaft experiences no vibration, acting like a rigid base, and the frequency is the same as that of a simple cantilever blade. Among the blade-coupling modes, the extreme case occurs when all except one blade vibrate in phase of equal amplitude and the odd blade vibrates exactly out of phase with much larger amplitude. The addition of a blade to the unit results in frequency increase or decrease, and a method for predicting the direction was presented.

Finally, the authors studied the effects on the shaft–disk–blade system of the shaft rotation speed. As is usually seen in rotor systems, each frequency at rest splits into two with increasing rotation speed. The lower curve eventually intersects the abscissa and reaches the so-called critical speed. After the critical speed, the curve flaps over and finally merges with the upper curve. After the merged speed, the system is experiencing the flutter type instability.

Acknowledgments

The authors are very grateful to Mr. Eric Austin at Virginia Tech. for his help in improving the quality of the paper, especially the English.

References

Ansari, K. A., 1986, "On the Importance of Shear Deflection, Rotatory Inertia, and Coriolis Forces in Turbines Blade Vibrations," ASME JOURNAL OF ENGINEERING FOR GAS TURBINES AND POWER, Vol. 108, pp. 319–324.

Bauer, H. F., and Eidel, W., 1988, "Vibration of a Rotating Uniform Beam. Part II: Orientation Perpendicular to the Axis of Rotation," *Journal of Sound and Vibration,* Vol. 122, pp. 357–375.

Bishop, R. E. D., and Johnson, D. C., 1960, *The Mechanics of Vibration,* Cambridge University Press, London.

Ewins, D. J., 1973, "Vibration Characteristics of Bladed Disc Assemblies," *Journal of Mechanical Engineering Science,* Vol. 15, No. 3, pp. 165–185.

Ewins, D. J., and Srinivasan, A. V., eds., 1983, *Vibrations of Bladed Disk Assemblies,* ASME, New York.

Ho, K. B., 1994, "A Simple Approach to Coupled Vibration of a Shaft-Disk-Blades System," M.S. thesis [in Chinese], National Taiwan Institute of Technology.

Kielb, R. E., and Rieger, N. F., eds., 1985, *Vibrations of Blades and Bladed Disk Assemblies,* ASME, New York.

Sisto, F., Chang, A., and Sutcu, M., 1983, "The Influence of Coriolis Forces on Gyroscopic Motion of Spinning Blades," ASME JOURNAL OF ENGINEERING FOR POWER, Vol. 105, pp. 342–347.

Sodel, W., 1981, *Vibration of Shells and Plates,* Marcel Dekker, New York.

Subrahmanyam, K. B., Kulkarni, S. V., and Rao, J. S., 1982, "Analysis of Lateral Vibration of Rotating Cantilever Blades Allowing for Shear Deflection and Rotary Inertia by Ressiner and Potential Energy Methods," *Mechanism and Machine Theory,* Vol. 17, No. 4, pp. 235–241.

Subrahmanyam, K. B., and Kaza, K. R. V., 1986, "Vibration and Buckling of Rotating Pretwisted, Preconed Beams Including Coriolis Effects," ASME *Journal of Vibration, Acoustics, Stress, and Reliability in Design,* Vol. 108, pp. 140–149.

Thomas, D. L., 1979, "Dynamics of Rotationally Periodic Structures," *Int. Journal for Numerical Methods in Engineering,* Vol. 14, pp. 81–102.

Yigit, A., Scott, R. A., and Galip Ulsoy, A., 1988, "Flexural Motion of a Radially Rotating Beam Attached to a Rigid Body," *Journal of Sound and Vibration,* Vol. 121, pp. 201–210.

Effects of Bearing and Shaft Asymmetries on the Resonant Oscillations of a Rotor-Dynamic System

R. Ganesan
Department of Mechanical Engineering,
Concordia University,
Montreal, Quebec, Canada H3G 1M8

Parametric steady-state vibrations of an asymmetric rotor while passing through primary resonance and the associated stability behavior are analyzed. The undamped case is considered and the equations of motion are rewritten in a form suitable for applying the method of multiple scales. Sensitivity to the bearing as well as shaft asymmetries of the oscillations due to unbalance excitation is evaluated. Expressions for amplitude and frequency modulation functions are obtained and are specialized to yield the steady-state solutions near primary resonance. Frequency-amplitude relationships that result from combined parametric and mass unbalance excitations are derived. Stability regions in the parameter space are obtained based on the time evolution of the amplitude and phase of the steady-state motions. The effects of bearing asymmetry on the amplitude and phase of the resonant oscillations are brought out. The sensitivity of vibrational and stability characteristics to various rotor-dynamic system parameters is illustrated through a numerical investigation.

1 Introduction

Asymmetric rotor systems, in which the flexural rigidities of bearings and shafts in two principal directions are not equal, exhibit a number of peculiarities in their vibrational characteristics that cannot be observed in symmetric rotors. These include parametric oscillations, double frequency vibrations due to gravitational forces, etc., and detailed studies regarding such phenomena have been made during the past few decades. Examples of asymmetric rotor-dynamic systems include turbogenerators, two-bladed propellers, helicopter rotors, and two-pole generators. Rotor shafts of these mechanical systems usually have asymmetric cross-sectional properties, and further the support systems such as the bearing system of a turbomachine are characterized by the stiffness asymmetry between horizontal and vertical directions. In practice, rotor shafts of turbogenerators, because of their construction, have different flexural rigidities in two principal directions. Even in the case of circular prismatic rotor shafts, the appearance and growth of fatigue cracks during operation lead to a situation similar to that mentioned above. In long rotor-dynamic systems in which two shafts are connected by a coupling, a slight difference in the preloading of the shaft coupling screws causes a corresponding difference between the combined shaft-coupling stiffnesses along the two principal directions of the shaft. This way the rotor-dynamic system possesses asymmetric stiffness characteristics. A time-dependent stiffness field (with respect to stationary inertial frame of reference) is always present in the above-mentioned rotor systems, the consequences of which are of paramount importance. They are (*i*) parametric instability, (*ii*) a drastic modification in the behavior of self-excited vibrations of the rotor shaft, (*iii*) profound effects on the forced motions of the rotors, which cause significant shifts in the amplitude as well as in the frequency of critical amplitude peaks, (*iv*) appearance of pseudo-critical vibration peaks at operating speeds, thus leading to unexpected oscillations, and (*v*) pseudo-critical vibration peaks at other than synchronous frequencies. A considerable amount of research activity has taken place recently regarding the vibrational characteristics of such time-varying systems and some of the important references are given at the end of this paper as well as summarized below.

The eigenproblem arising from the free vibrations and the stability of the free motion of an asymmetric rotor supported on isotropic bearings have been paid particular attention by Yamamoto and Ota (1964, 1966). Brosens and Crandall (1961) and Ardayfio and Frohrib (1976) considered in detail the steady-state oscillations arising from the inhomogeneous problem. That a vibration vector locus in the neighborhood of a critical speed (generally known as modal circle) forms an ellipse has been indicated by Parkinson (1965). Also the observation that the amplitude and phase of vibration response are severely affected by the location of mass unbalance thus demanding a complex balancing scheme has also been suggested by Parkinson (1965). The double frequency vibrations occurring when the rotor rotational speed is 0.5 times the critical speed or in its neighborhood have been a prime concern in the study by Iwatsubo and Nakamura (1968). A suitable method of analysis for such a case was developed by Bishop and Parkinson (1965). Okijima and Kondo (1974a, b), Black (1969), and Iwatsubo et al. (1973) studied the stability of oscillations at resonance. Additional investigations on this subject include Yamamoto and Ota (1966), Parszewski et al. (1986), Inoue and Matsukura (1977), Genta (1988), and Ehrich (1992).

However, the characterization of steady-state oscillations that occur as the rotor-dynamic system passes through primary resonance and the evaluation of modulating functions for amplitude and phase of the response have not been carried out in detail. It is not uncommon in industrial practice to encounter the operation of a rotor beyond its critical speed. Rotational devices such as turbocompressors, feed pumps, textile machinery spindles, etc., have their operational frequencies well above the critical frequency. When the rotor system is operated beyond its critical speed, at the start-up or shut-down of the system the rotor is passed through resonance. This resonance is manifest by the appearance of extended amplitudes of oscillations of the rotor system and considerable amount of power is required to drive

Contributed by the International Gas Turbine Institute for publication in the JOURNAL OF ENGINEERING FOR GAS TURBINES AND POWER. Manuscript received by the International Gas Turbine Institute September 11, 1994. Associate Technical Editor: R. E. Kielb.

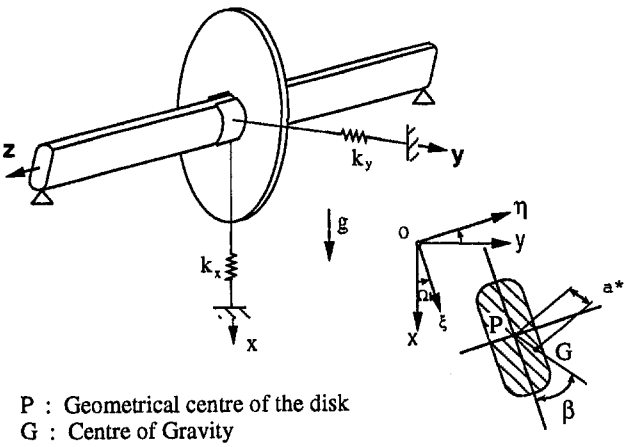

P : Geometrical centre of the disk
G : Centre of Gravity

Fig. 1 Asymmetric rotor-dynamic system

the rotor through its critical speed. Asymmetric rotors, in these situations, exhibit a highly complex behavior and so a detailed analysis of resonant oscillations becomes essential to ensure operational safety. The information regarding the vibrational characteristics of asymmetric rotor systems at resonance is also required as an input in parametric identification methods such as resonance testing and in diagnostic systems of rotating machinery that ensure early detection of incipient failures, fatigue failures, etc. Such an analytical investigation regarding the vibrational and stability behavior of asymmetric rotors is the objective of the present paper. The mathematical model of the asymmetric rotor system that has been employed in past investigations such as that of Inoue and Matsukura (1977) is being used in the present work. However, the equations of motion are recast in a form suitable to introduce the "fast" and "slow" time scales so that the method of multiple scales (Nayfeh and Mook, 1979) can be employed for obtaining the desired solution.

2 Equations of Motion

An asymmetric rotor-dynamic system as shown in Fig. 1 is considered. As can be seen from the figure, this mathematical model consists of a massless horizontal shaft, a disk, and a flexible bearing. The horizontal shaft is prismatic and the stiffnesses in two principal directions are different. Both the disk and the bearing are attached at the center of the shaft, and further, the stiffnesses of the bearing in horizontal and vertical directions are different. The mass of the disk is denoted by m. The stiffnesses of the flexible bearing in the horizontal and vertical directions are denoted by k_x and k_y, respectively. The shaft is of uniform cross section along its longitudinal axis and the two different stiffnesses along its two principal directions ξ and η are designated as K_ξ and K_η, respectively. In Fig. 1, the x–y–z triad is the stationary coordinate system such that the z axis coincides with the undeflected horizontal shaft, x axis is vertically downward and y axis is horizontal to the right; $\xi\eta z$ is the rotating coordinate system such that ξ and η axes coincide with the principal axes of the shaft cross section. As has been done in past investigations, the cross-coupled characteristics of the bearing in the horizontal and vertical directions are ignored in the present analysis.

The equations of motion representing the dynamic behavior of this rotor system are given by the following equations in the stationary coordinate system x–y–z (Inoue and Matsukura, 1977):

$$\ddot{R}_x + \omega_x^2 R_x = -\mu^* \omega_m^2 (R_x \cos 2\Omega t + R_y \sin 2\Omega t) + g + a^* \Omega^2 \cos(\Omega t + \beta) \quad (1)$$

$$\ddot{R}_y + \omega_y^2 R_y = -\mu^* \omega_m^2 (R_x \sin 2\Omega t - R_y \cos 2\Omega t) + a^* \Omega^2 \sin(\Omega t + \beta) \quad (2)$$

where R_x and R_y are the x-directional and y-directional displacement components; ω_x, ω_y, and ω_m are the natural frequencies of the shaft given by

$$\omega_x = \sqrt{\frac{k_x + K_m}{m}}; \quad \omega_y = \sqrt{\frac{k_y + K_m}{m}}; \quad \omega_m = \sqrt{\frac{K_m}{m}}$$

and K_m and μ^* are the mean stiffness and asymmetry factor of the shaft given by

$$\mu^* = \frac{K_\xi - K_\eta}{K_\xi + K_\eta}; \quad K_m = \frac{K_\xi + K_\eta}{2}$$

It may be noted that K_m and ω_m given above are the mean stiffness and the mean natural frequency of the rotor shaft. Further, the rotational speed of the shaft is denoted as Ω, g is the gravitational acceleration, a^* is the disk mass eccentricity from the z axis, and β is the phase angle of the disk eccentricity from the ξ axis. As can be seen from these expressions, the forcing functions arise from gravity, a periodic force with frequency Ω due to rotor unbalance and the parametric force due to rotor asymmetry. The flexural rigidity of the shaft varies with

Nomenclature

x, y, z = stationary frame of reference
ξ, η, z = rotating frame of reference
a^* = eccentricity of mass unbalance
a_{x0}, a_{y0} = amplitudes of vibratory motions in x and y directions, respectively
g = gravitational acceleration
k_x = stiffness of bearing in x direction
k_y = stiffness of bearing in y direction
K_ξ = stiffness of shaft in its principal direction ξ
K_η = stiffness of shaft in its principal direction η
K_m = mean stiffness of the shaft = $(K_\xi + K_\eta)/2$
m = mass of the disk
R_x = vibratory motion in the x direction
R_y = vibratory motion in the y direction
R_{x0}, R_{y0} = base solutions of the asymptotic expansions for x- and y-directional motions
t = time
T_0, T_1, T_2 = time scales of order 0, 1 and 2 respectively
T_n = time scale of order n
β = phase angle of the mass eccentricity from the ξ-axis
ϵ = asymptotic parameter corresponding to multiple time scales
η_x, η_y = phases of the vibratory motions in x- and y-directions respectively
γ_1, γ_2 = dependent variables of the autonomous system
$\lambda_{x0}, \lambda_{y0}$ = eigenvalues corresponding to the perturbed motions of a_{x0} and a_{y0} respectively
μ^* = asymmetry factor of the shaft; $\mu^* = (K_\xi - K_\eta)/(K_\xi + K_\eta)$
σ_1, σ_2 = detuning parameters that characterize the nearness of the system to resonance
ω_x, ω_y = natural frequencies of the asymmetric shaft
ω_m = mean natural frequency of the shaft
Ω = rotating speed of the shaft

frequency 2Ω, and so in one revolution of the shaft, the stiffness is maximum twice and minimum twice.

3 Steady-State Oscillations Near Resonance

The steady-state response of the rotor system is now sought. To this end, the equations of motion are rearranged into the following form and also a perturbation parameter is introduced:

$$\ddot{R}_x + \omega_x^2 R_x = -\mu\epsilon\omega_m^2(R_x \cos 2\Omega t + R_y \sin 2\Omega t) + \epsilon g^* + \epsilon a\Omega^2 \cos(\Omega t + \beta) \quad (3)$$

$$\ddot{R}_y + \omega_y^2 R_y = -\mu\epsilon\omega_m^2(R_x \sin 2\Omega t - R_y \cos 2\Omega t) + \epsilon a\Omega^2 \sin(\Omega t + \beta) \quad (4)$$

wherein the following substitutions have been made:

$$\mu = \epsilon^{-1}\mu^*; \quad g^* = \epsilon^{-1}g; \quad a = \epsilon^{-1}a^* \quad (5)$$

The perturbation parameter ϵ, $0 \le \epsilon \le 1$, has been introduced so that the method of multiple scales can now be employed to obtain the response. A new set of independent variables and time derivatives are introduced into the equations of motion, which are described by

$$T_n = \epsilon^n t; \quad D_n = \partial/\partial T_n, \quad n = 0, 1, 2, \ldots \quad (6)$$

so that the time derivatives are rewritten as

$$\frac{d}{dt} = D_0 + \epsilon D_1 + \epsilon^2 D_2 + \ldots \quad (7)$$

$$\frac{d^2}{dt^2} = D_0^2 + 2\epsilon D_0 D_1 + \epsilon^2(2D_0 D_2 + D_1^2) + \ldots \quad (8)$$

A set of compatible uniform expansions for the dependent variables is employed as follows:

$$R_x(t, \epsilon) = R_{x0}(T_0, T_1, T_2 \ldots) + \epsilon R_{x1}(T_0, T_1, T_2 \ldots) + \ldots \quad (9)$$

$$R_y(t, \epsilon) = R_{y0}(T_0, T_1, T_2 \ldots) + \epsilon R_{y1}(T_0, T_1, T_2 \ldots) + \ldots \quad (10)$$

In what follows, first-order uniform solutions for $R_x(t, \epsilon)$ and $R_y(t, \epsilon)$ are sought. Substitution of Eqs. (5)–(10) into Eqs. (3) and (4) yields, after equating coefficients of like power of ϵ, a set of differential equations as follows:

$$D_0^2 R_{x0} + \omega_x^2 R_{x0} = 0; \quad D_0^2 R_{y0} + \omega_y^2 R_{y0} = 0 \quad (11, 12)$$

$$D_0^2 R_{x1} + \omega_x^2 R_{x1} = -2D_0 D_1 R_{x0} - \mu\omega_m^2(R_{x0} \cos 2\Omega t + R_{y0} \sin 2\Omega t) + g^* + a\Omega^2 \cos(\Omega t + \beta) \quad (13)$$

$$D_0^2 R_{y1} + \omega_y^2 R_{y1} = -2D_0 D_1 R_{y0} - \mu\omega_m^2(R_{x0} \sin 2\Omega t - R_{y0} \cos 2\Omega t) + a\Omega^2 \sin(\Omega t + \beta) \quad (14)$$

Equations (11) and (12) are solved to yield

$$R_{x0} = A_{x0} \exp(i\omega_x T_0) + \bar{A}_{x0} \exp(-i\omega_x T_0) \quad (15)$$

$$R_{y0} = A_{y0} \exp(i\omega_y T_0) + \bar{A}_{y0} \exp(-i\omega_y T_0) \quad (16)$$

where A_{x0} and A_{y0} are unknown arbitrary but small solution amplitudes to be determined and further overbars indicate the complex conjugates. Substitution of Eqs. (15) and (16) into Eqs. (13) and (14) yields

$$D_0^2 R_{x1} + \omega_x^2 R_{x1} = -2i\omega_x A'_{x0} \exp(i\omega_x T_0) - (\mu\omega_m^2/2)\{A_{x0} \exp(3i\omega_x T_0 + 2i\sigma_1 T_1) + \bar{A}_{x0} \exp(i\omega_x T_0 + 2i\sigma_1 T_1)\} - (\mu\omega_m^2/2i)\{A_{y0} \exp(3i\omega_y T_0 + 2i\sigma_2 T_1) + \bar{A}_{y0} \exp(i\omega_y T_0 + 2i\sigma_2 T_1)\} + (a/2)(\omega_x + \epsilon\sigma_1)^2 \times \exp[i(\omega_x T_0 + \sigma_1 T_1 + \beta)] + cc + g^* \quad (17)$$

$$D_0^2 R_{y1} + \omega_y^2 R_{y1} = -2i\omega_y A'_{y0} \exp(i\omega_y T_0) - (\mu\omega_m^2/2i)\{A_{x0} \exp(3i\omega_x T_0 + 2i\sigma_1 T_1) + \bar{A}_{x0} \exp(i\omega_x T_0 + 2i\sigma_1 T_1)\} + (\mu\omega_m^2/2)\{A_{y0} \exp(3i\omega_y T_0 + 2i\sigma_2 T_1) + \bar{A}_{y0} \exp(i\omega_y T_0 + 2i\sigma_2 T_1)\} + (a/2i)(\omega_y + \epsilon\sigma_2)^2 \times \exp[i(\omega_y T_0 + \sigma_2 T_1 + \beta)] + cc \quad (18)$$

In Eqs. (17) and (18), cc indicates the complex conjugate part, and further

$$\omega_x + \epsilon\sigma_1 = \Omega = \omega_y + \epsilon\sigma_2 \quad (19)$$

where σ_1 and σ_2 are the detuning parameters that characterize the nearness to resonance. On setting the secular terms to zero, Eqs. (17) and (18) yield a set of first-order differential equations:

$$-2i\omega_x A'_{x0} + (a/2)(\omega_x + \epsilon\sigma_1)^2 \exp(i\sigma_1 T_1 + i\beta) = (\mu\omega_m^2/2)\bar{A}_{x0} \exp(2i\sigma_1 T_1) \quad (20)$$

$$-2i\omega_y A'_{y0} - (ai/2)(\omega_y + \epsilon\sigma_2)^2 \exp(i\sigma_2 T_1 + i\beta) = -(\mu\omega_m^2/2)\bar{A}_{y0} \exp(2i\sigma_2 T_1) \quad (21)$$

Writing A_{x0} and A_{y0} in polar form as

$$A_{x0} = (\tfrac{1}{2})a_{x0} \exp(i\eta_x) \quad (22)$$

$$A_{y0} = (\tfrac{1}{2})a_{y0} \exp(i\eta_y) \quad (23)$$

where a_{x0}, a_{y0}, η_x, and η_y are real. From Eqs. (20) and (21), it can be shown that:

$$a'_{x0} = (a\Omega^2/2\omega_x) \sin(\sigma_1 T_1 + \beta - \eta_x) - (a_{x0}\mu\omega_m^2/4\omega_x) \sin(2\sigma_1 T_1 - 2\eta_x) \quad (24)$$

$$\eta'_x = -\tfrac{1}{2}(a\Omega^2/\omega_x a_{x0}) \cos(\sigma_1 T_1 + \beta - \eta_x) + (\mu\omega_m^2/4\omega_x) \cos(2\sigma_1 T_1 - 2\eta_x) \quad (25)$$

$$a'_{y0} = -(a\Omega^2/2\omega_y) \cos(\sigma_2 T_1 + \beta - \eta_y) + (a_{y0}\mu\omega_m^2/4\omega_y) \sin(2\sigma_2 T_1 - 2\eta_y) \quad (26)$$

$$\eta'_y = -\tfrac{1}{2}(a\Omega^2/\omega_y a_{y0}) \sin(\sigma_2 T_1 + \beta - \eta_y) - (\mu\omega_m^2/4\omega_y) \cos(2\sigma_2 T_1 - 2\eta_y) \quad (27)$$

Equations (24)–(27) are the desired equations that describe the time evolution of the amplitude and phase of the steady-state motion. On substituting Eqs. (22) and (23) into Eqs. (15) and (16) and using these results in Eqs. (9) and (10), the solutions R_x and R_y are obtained to the first approximation:

$$R_x = a_{x0} \cos(\omega_x T_0 + \eta_x) + O(\epsilon) \quad (28)$$

$$R_y = a_{y0} \cos(\omega_y T_0 + \eta_y) + O(\epsilon) \quad (29)$$

where a_{x0}, a_{y0}, η_x, and η_y are governed by Eqs. (24)–(27). Since T_1 appears explicitly in Eqs. (24)–(27), they are nonautonomous systems. It is always desirable to eliminate the explicit dependence of both motion amplitudes and phases on T_1, thereby transforming Eqs. (24)–(27) into autonomous systems. Here, the transformation of Eqs. (24)–(27) into autonomous systems essentially means that the motion amplitudes and

phases are expressed as implicit functions of time scale T_1 (Nayfeh and Mook, 1979). This transformation can be accomplished by introducing a new set of dependent variables according to

$$\gamma_1 = \sigma_1 T_1 - \eta_x + \beta \tag{30}$$

$$\gamma_2 = \sigma_2 T_1 - \eta_y + \beta \tag{31}$$

As a result, from Eqs. (24)–(27), the autonomous systems are formed as

$$a'_{x0} = (a\Omega^2/2\omega_x)\sin\gamma_1 - (a_{x0}\mu\omega_m^2/4\omega_x)\sin 2(\gamma_1 - \beta) \tag{32}$$

$$\gamma'_1 = \tfrac{1}{2}(a\Omega^2/\omega_x a_{x0})\cos\gamma_1 + \sigma_1 - (\mu\omega_m^2/4\omega_x)\cos 2(\gamma_1 - \beta) \tag{33}$$

$$a'_{y0} = -(a\Omega^2/2\omega_y)\cos\gamma_2 + (a_{y0}\mu\omega_m^2/4\omega_y)\sin 2(\gamma_2 - \beta) \tag{34}$$

$$\gamma'_2 = \tfrac{1}{2}(a\Omega^2/\omega_y a_{y0})\sin\gamma_2 + \sigma_2 + (\mu\omega_m^2/4\omega_y)\cos 2(\gamma_2 - \beta) \tag{35}$$

As can be seen from Eqs. (32)–(35), both the motion amplitudes and phases are still functions of time scale T_1, but the explicit functional dependency between them is eliminated. Steady-state motions are deduced from Eqs. (32)–(35) by letting $a'_{x0} = a'_{y0} = \gamma'_1 = \gamma'_2 = 0$, as follows. For x-directional motion, one gets

$$(a\Omega^2/2\omega_x)\sin\gamma_1 = (a_{x0}\mu\omega_m^2/4\omega_x)\sin 2(\gamma_1 - \beta) \tag{36}$$

$$\sigma_1 = -(a\Omega^2/2\omega_x a_{x0})\cos\gamma_1 + (\mu\omega_m^2/4\omega_x)\cos 2(\gamma_1 - \beta) \tag{37}$$

and for y-directional motion,

$$(a\Omega^2/2\omega_y)\cos\gamma_2 = (a_{y0}\mu\omega_m^2/4\omega_y)\sin 2(\gamma_2 - \beta) \tag{38}$$

$$\sigma_2 = -(a\Omega^2/2\omega_y a_{y0})\sin\gamma_2 - (\mu\omega_m^2/4\omega_y)\cos 2(\gamma_2 - \beta) \tag{39}$$

Equations (36)–(39) are combined to yield the algebraic equations for response amplitudes:

$$[a\Omega^2/2\omega_x]^2 = [\sigma_1^2 + (\mu\omega_m^2/4\omega_x)^2 - (\sigma_1\mu\omega_m^2/2\omega_x)\cos 2(\gamma_1 - \beta)]a_{x0}^2 \tag{40}$$

$$\left[\frac{a\Omega^2}{2\omega_y}\right]^2 = \left\{\left(\frac{\mu\omega_m^2}{4\omega_y}\right)^2 \sin^2 2(\gamma_2 - \beta) + \left\{\sigma_2 + \left(\frac{\mu\omega_m^2}{4\omega_y}\right)\cos 2(\gamma_2 - \beta)\right\}^2\right\}a_{y0}^2 \tag{41}$$

Equations (40) and (41) given above are the "frequency-response equations" for the two rotor displacement components a_{x0} and a_{y0}, respectively, in terms of their respective detuning parameters and excitation amplitudes. As a result, the solutions R_x and R_y are given by

$$R_x = a_{x0}\cos(\omega_x t + \epsilon\sigma_1 t - \gamma_1 + \beta) + O(\epsilon) \tag{42}$$

$$R_y = a_{y0}\cos(\omega_y t + \epsilon\sigma_2 t - \gamma_2 + \beta) + O(\epsilon) \tag{43}$$

where a_{x0}, a_{y0}, η_x, and η_y are described through the modulating functions given by Eqs. (32)–(35).

4 Instability of Steady-State Response

Stability of nontrivial solutions of R_x and R_y can be ascertained by adding a small perturbation to the steady-state response and checking whether this perturbation grows or decays, in time. To this end, the amplitude and phase of the steady-state motion are decomposed into two parts as follows:

$$a_{x0} = {}_0a_{x0} + {}_1a_{x0} \tag{44}$$

$$a_{y0} = {}_0a_{y0} + {}_1a_{y0} \tag{45}$$

$$\gamma_1 = {}_0\gamma_1 + {}_1\gamma_1 \tag{46}$$

$$\gamma_2 = {}_0\gamma_2 + {}_1\gamma_2 \tag{47}$$

wherein each term is split into a mean term and a perturbing term; ${}_1a_{x0}$, ${}_1a_{y0}$, ${}_1\gamma_1$ and ${}_1\gamma_2$ are "small" perturbations. Substitution of Eqs. (44)–(47) into Eqs. (32)–(35) yields, after expanding the resulting equations for "small" perturbations and noting that the mean components satisfy the steady-state solutions represented by Eqs. (36)–(39),

$$+{}_1a'_{x0} = \left[\frac{a\Omega^2}{2\omega_x}\cos{}_0\gamma_1\right]{}_1\gamma_1 - \frac{\mu\omega_m^2}{2\omega_x}\cdot{}_0a_{x0}\cdot{}_1\gamma_1\cos 2({}_0\gamma_1 - \beta) - \frac{\mu\omega_m^2}{4\omega_x}\cdot{}_1a_{x0}\sin 2({}_0\gamma_1 - \beta) \tag{48}$$

$$+{}_1\gamma'_1 = -\left[\frac{a\Omega^2}{2{}_0a_{x0}\omega_x}\sin{}_0\gamma_1\right]{}_1\gamma_1 - \left[\frac{a\Omega^2}{2{}_0a_{x0}^2\omega_x}\cos{}_0\gamma_1 - \frac{\mu\omega_m^2}{4{}_0a_{x0}\omega_x}\cos 2({}_0\gamma_1 - \beta)\right]{}_1\alpha_{x0} - \frac{\mu\omega_m^2}{4{}_0a_{x0}\omega_x}[{}_1a_{x0}\cos 2({}_0\gamma_1 - \beta) - 2{}_1\gamma_1\,{}_0a_{x0}\sin 2({}_0\gamma_1 - \beta)] \tag{49}$$

The eigenvalues of the coefficient matrix formed using the right-hand side of Eqs. (48) and (49) decide the stability of motion for a_{x0}. As a result, stability of solution a_{x0} is governed by the condition:

$$\begin{vmatrix} -\dfrac{\mu\omega_m^2}{4\omega_x}\sin 2({}_0\gamma_1 - \beta) - \lambda_{x0} & \dfrac{a\Omega^2}{2\omega_x}\cos{}_0\gamma_1 - \left[\dfrac{\mu\omega_m^2}{2\omega_x}\right]_0 a_{x0}\cos 2({}_0\gamma_1 - \beta) \\ \dfrac{\sigma_1}{{}_0a_{x0}} - \dfrac{\mu\omega_m^2}{4\omega_{x_0}a_{x0}}\cos 2({}_0\gamma_1 - \beta) & +\dfrac{\mu\omega_m^2}{2\omega_x}\sin 2({}_0\gamma_1 - \beta) - \dfrac{a\Omega^2}{2\omega_{x_0}a_{x0}}\sin{}_0\gamma_1 - \lambda_{x0} \end{vmatrix} = 0 \tag{50}$$

From this condition, the algebraic eigenvalue equation for λ_{x0} is obtained to be

$$\lambda_{x0}^2 + \lambda_{x0}\left\{\frac{a\Omega^2}{2{}_0a_{x0}\omega_x}\sin{}_0\gamma_1 - \frac{\mu\omega_m^2}{4\omega_x}\sin 2({}_0\gamma_1 - \beta)\right\}$$

$$-\frac{\sigma_1 a\Omega^2}{2_0 a_{x0}\omega_x}\cos {}_0\gamma_1-\frac{1}{2}\left[\frac{\mu\omega_m^2}{2\omega_x}\right]^2\cos^2 2({}_0\gamma_1-\beta)$$

$$+\frac{\sigma_1\mu\omega_m^2}{2\omega_x}\cos 2({}_0\gamma_1-\beta)$$

$$+\frac{a\Omega^2\mu\omega_m^2}{8_0 a_{x0}\omega_x^2}\cos {}_0\gamma_1\cos 2({}_0\gamma_1-\beta)=0 \quad (51)$$

A similar analysis yields the following algebraic eigenvalue equation for a_{y0}:

$$\lambda_{y0}^2-\lambda_{y0}\left\{\frac{a\Omega^2}{2_0 a_{y0}\omega_y}\cos {}_0\gamma_2-\frac{\mu\omega_m^2}{4\omega_y}\sin 2({}_0\gamma_2-\beta)\right\}$$

$$-\frac{\sigma_2 a\Omega^2}{2_0 a_{y0}\omega_y}\sin^2 {}_0\gamma_2-\frac{1}{2}\left[\frac{\mu\omega_m^2}{2\omega_y}\right]^2\cos^2 2({}_0\gamma_2-\beta)$$

$$-\frac{\sigma_2\mu\omega_m^2}{2\omega_y}\cos 2({}_0\gamma_2-\beta)$$

$$-\frac{a\Omega^2\mu\omega_m^2}{8_0 a_{y0}\omega_y^2}\sin {}_0\gamma_2\cos 2({}_0\gamma_2-\beta)=0 \quad (52)$$

Equations (51) and (52) define the stability domain through the corresponding roots λ_{x0} or λ_{y0}. From Eq. (51) it can be shown that the roots λ_{x0} are real when the following inequality relationship is satisfied:

$$-\frac{\sigma_1 a\Omega^2}{2_0 a_{x0}\omega_x}\cos {}_0\gamma_1-\frac{1}{2}\left[\frac{\mu\omega_m^2}{2\omega_x}\right]^2\cos^2 2({}_0\gamma_1-\beta)$$

$$+\frac{\sigma_1\mu\omega_m^2}{2\omega_x}\cos 2({}_0\gamma_1-\beta)$$

$$+\frac{a\Omega^2\mu\omega_m^2}{8_0 a_{x0}\omega_x^2}\cos {}_0\gamma_1\cos 2({}_0\gamma_1-\beta)<0 \quad (53)$$

This condition corresponds to an unstable steady-state solution, since it results in one positive real root. For any set of values of rotor system parameters, such as mass unbalance, stiffness, rotor rotational speed, etc., if this condition is satisfied, the systems is unstable. A similar analysis shows that steady-state solutions near resonance R_{y0} are unstable when

$$-\frac{\sigma_2 a\Omega^2}{2_0 a_{y0}\omega_y}\sin {}_0\gamma_2-\frac{1}{2}\left[\frac{\mu\omega_m^2}{2\omega_y}\right]^2\cos^2 2({}_0\gamma_2-\beta)$$

$$-\frac{\sigma_2\mu\omega_m^2}{2\omega_y}\cos 2({}_0\gamma_2-\beta)$$

$$-\frac{a\Omega^2\mu\omega_m^2}{8_0 a_{y0}\omega_y^2}\sin {}_0\gamma_2\cos 2({}_0\gamma_2-\beta)<0 \quad (54)$$

Now it can be observed that the bearing and shaft asymmetry causes the instability of x- and y-directional steady-state response, for certain positive values of σ_2.

5 Design Aspects

It is well known that damping leads to finite-amplitude vibrations in linear systems near resonance. From Eqs. (40) and (41), it can be seen that the shaft and bearing asymmetries also lead to finite-amplitude vibrations near resonance, in the absence of damping. Further, (*i*) in some cases the bearing and shaft asymmetries help in suppressing the vibrations due to mass unbalance near resonance as can be seen from Eqs. (36) and (38), (*ii*) twice-per-revolution vibrations are caused by shaft asymmetry, which may excite half-critical speeds during start-up or shut-off operations. The rotors can be driven through their critical speeds by applying sufficient power and the magnitude of this power can be significantly reduced if nonisotropic bearings or shafts with asymmetric cross-sectional properties are present. However, as can be observed from Eq. (54), the bearing asymmetry leads to unstable vibrations near resonance when the rotor rotational speed is greater than the natural frequencies of the rotor corresponding to x- and y-directional motions, i.e., before the resonance is passed. From the above-described analytical study, the following motion characteristics are also observed: (*i*) The amplitudes of the resonant response in x- and y-directions are considerably affected by the location of the mass unbalance, thus requiring a balancing process that is more complex, (*ii*) the presence of bearing and shaft asymmetries considerably affects the stability characteristics of resonant oscillations, (*iii*) near the primary resonance, the sensitivity of x- and y-directional unbalance responses to both the bearing and shaft asymmetries is quite severe, (*iv*) no monotonically increasing or decreasing trend is observed with respect to the amplitudes of unbalance response, when the bearing or shaft asymmetries are changed, (*v*) the steady-state behavior of the rotor-dynamic system near resonance is markedly different from the motion characteristics that correspond to the excitation frequencies, which are far away from resonant frequencies, (*vi*) increasing the shaft asymmetry helps to stabilize the rotor system during run-up or run-down operations.

6 Numerical Results

The characteristics of steady-state response near resonance are illustrated through a numerical example. A rotor system that has been used for numerical study in the work of Lalanne and Ferraris (1990) is employed in the present work. It consists of a disk with an inner radius 0.01 m and outer radius 0.15 m. The thickness of the disk is 0.03 m and the material density is 7800 kg/m^3. The mass unbalance is located at a radial distance of 0.15 m. The shaft stiffnesses in the ξ and η directions are taken to be 1.57×10^6 N/m and 1.195×10^6 N/m, respectively. The stiffnesses of the flexible bearing in the x and y directions are taken to be 5.1×10^5 N/m and 2.55×10^5 N/m, respectively. Further, (*i*) the value of ϕ_0 has been taken to be zero, (*ii*) the value of ϵ has been set to unity.

To study the vibrational characteristics of the rotor as it passes through the critical speed, σ_1 is varied between -300 and $+200$. The amplitudes of x-directional and y-directional response at $t = 10$ s are plotted in Fig. 2. The abscissa, detuning parameter, denotes σ_1 in this figure. From Fig. 2 it can be observed that (*i*) the amplitude of x-directional motion is greater than that of y-directional motion, when the rotational speed of the rotor is very close to the critical speed, (*ii*) the variation of the x-directional motion amplitude, as the system passes through reso-

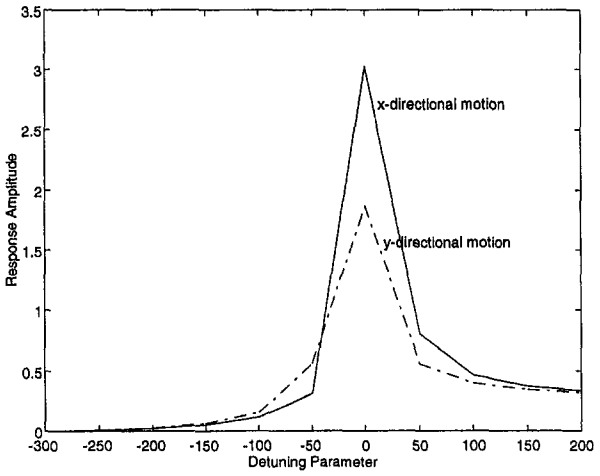

Fig. 2 Response amplitude as a function of detuning parameter

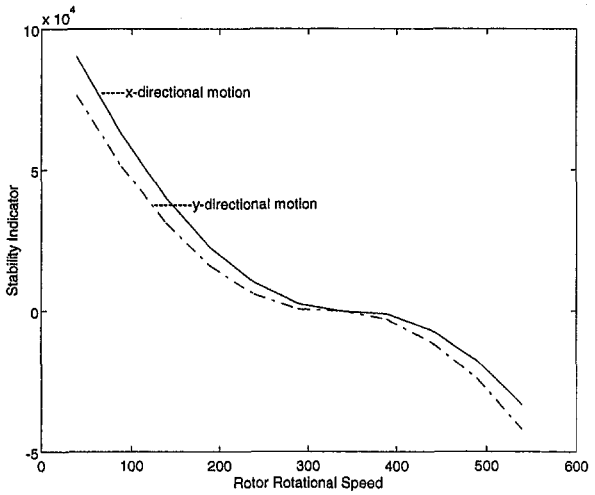

Fig. 3 Stability of the rotor near resonance

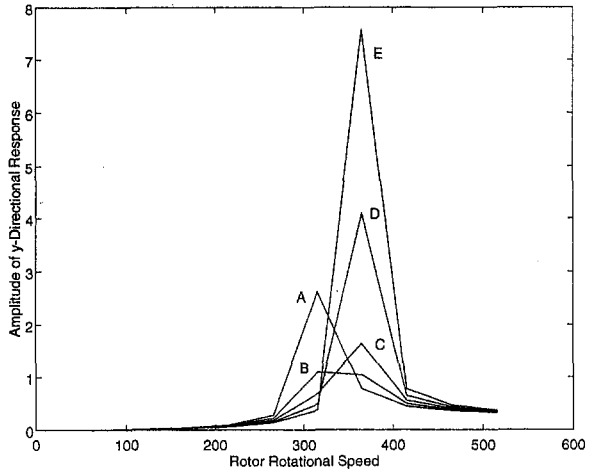

Fig. 4 Sensitivity of response amplitude a_{y0} to the bearing asymmetry

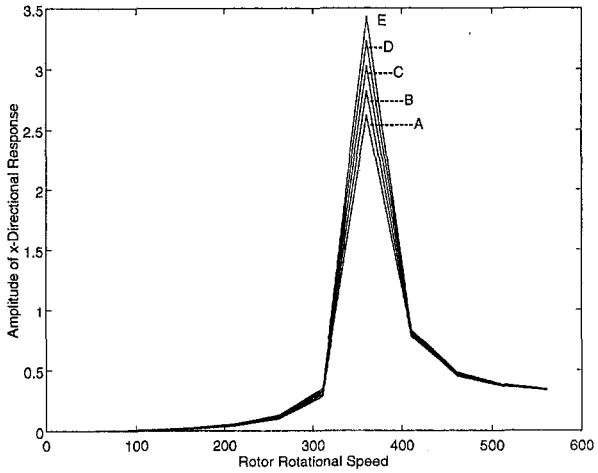

Fig. 5 Sensitivity of response amplitude a_{x0} to the bearing asymmetry

nance, is more pronounced than that of y-directional motion, i.e., x-directional unbalance motion is more sensitive to resonance. The left-hand sides of Eqs. (53) and (54) are essentially the stability indicators of x- and y-directional motions, respectively, and the stability of the rotor system is represented in Fig. 3. As can be seen, the x-directional motion is stable for the larger part of the frequency sweep through resonance. This can be explained as follows. From Eqs. (53) and (54), it can be observed that the first term of the left-hand side represents the combined effects of mass unbalance forces, system asymmetry, and nearness to resonance. In a similar manner, it can be said that (i) the second term represents the effect of asymmetry of the rotor-bearing system, (ii) the third term represents the combined effects of both nearness to resonance and asymmetry of the rotor-bearing system, and (iv) the last term represents the combined effects of both mass unbalance and asymmetry of the rotor-bearing system. The combined effects of both nearness to resonance and asymmetry of the rotor-bearing system, as represented by the third term of Eqs. (53), tend to stabilize the x-directional motion (as can be seen from the positive sign). Similarly, the x-directional motion is also stabilized by the combined effects of both mass unbalance and asymmetry of the rotor-bearing system, as represented by the fourth term of Eq. (53). But, the same combined effects tend to destabilize the y-directional motion, along with the combined effects of both mass unbalance forces and nearness to resonance, and the effect of asymmetry of the rotor-bearing system. Hence, the x-directional motion is more stable while passing through resonance conditions.

The effects of bearing asymmetry on the near-resonance response are studied next and the results are plotted in Figs. 4 and 5. In this study, first k_x is kept at the value of 2.55×10^5 N/m and the value of y-directional bearing stiffness is changed. Amplitudes of y-directional motion are plotted in Fig. 4 in which curves A, B, C, D, and E correspond to the cases when the ratio k_y/k_x is equal to 1.0, 1.5, 2.0, 2.5, and 3.0, respectively. Next the situation is reversed, i.e., k_y is taken to be equal to 2.55×10^5 N/m and the x-directional bearing stiffness is changed according to k_x/k_y = 1.0, 1.5, 2.0, 2.5, and 3.0. Corresponding curves are identified by the symbols A, B, C, D, and E, respectively, in Fig. 5. As can be observed from these figures, the response amplitudes in both cases of stiffness variation attain their maximum values when the ratio between bearing stiffnesses in the x and y directions are maximum. Further, it can be seen that (i) for a fixed value of y-directional bearing stiffness when the bearing stiffness in the x direction is reduced, the amplitude of unbalance vibration in the x direction uniformly decreases, (ii) a similar argument does not apply when the y-directional bearing stiffness is reduced and the value of x-directional bearing stiffness is fixed, (iii) the response amplitudes are highly sensitive to the bearing asymmetry when the rotational speed of the rotor lies in the range of 250–450 rpm (this region actually corresponds to the near-resonance excitation frequencies corresponding to the x- and y-directional motions), (iv) the peak of the y-directional response is shifted to the left when k_y is reduced.

The effects of shaft asymmetry are studied now, and the variation of response amplitudes with the shaft stiffness asymmetry is plotted in Figs. 6 and 7. Curves A, B, C, D, and E correspond to the cases when the ratio K_ξ/K_η is equal to 1.2, 1.4, 1.6, 1.8, and 2.0, respectively. In all five cases, the ratio k_x/k_y has been set to be 1.5 with $k_y = 2.55 \times 10^5$ N/m and further K_η is taken to be 1.195×10^6 N/m. From these two figures it can be seen that when the resonance condition is reached, the amplitudes of x- and y-directional motion are not decreased or increased in a uniform manner. Further, (i) the peak response in the x direction is shifted to the right when the ratio K_ξ/K_η is equal to 2.0, (ii) the unbalance response amplitudes are highly sensitive to the shaft asymmetry when the rotational speed of the rotor lies in the range of 300–450 rpm, i.e., near the resonance conditions corresponding to the x- and y-directional motions. The stability of the rotor system when the ratio K_ξ/K_η is equal to 1.4, 1.8, 2.2, 2.6, and 3.0 is represented in Fig. 8. From this figure it can be observed that when the shaft stiffness K_ξ is increased the system becomes stable for a larger

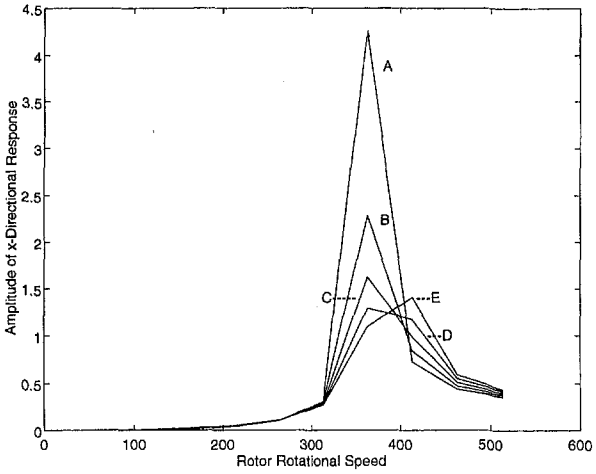

Fig. 6 Effect of shaft asymmetry on the resonant response in x direction

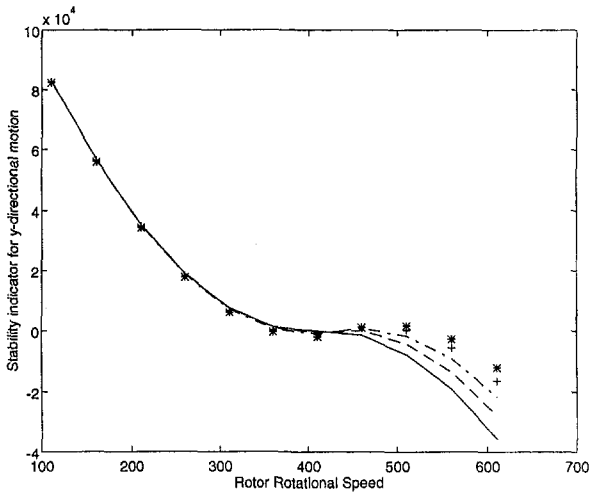

Fig. 8 Effects of shaft stiffness K_ξ on the stability of the rotor; K_ξ/K_η = 1.4 (—), 1.8 (---), 2.2 (-·-·), 2.6 (+ +), 3.0 (* *)

portion of frequency sweep through resonance. A similar effect is observed with respect to the y-directional motion.

7 Conclusions

The dynamic response of an asymmetric rotor supported on asymmetric bearings is analyzed here using the many-variable version of the multiple scales method. Particular attention has been paid to studying the motion characteristics of the rotor while passing through the primary resonance, and the modulating functions for amplitude and phase of the motion are obtained in an explicit form. The stability analysis is performed based on the time evolution of the amplitude and phase of the periodic motion and algebraic equations that define the stability domains of the rotor-dynamic system are obtained in terms of both the detuning and system parameters. An extensive numerical study regarding the impacts of both the bearing and shaft asymmetries on the vibrational behavior and stability of the rotor is also presented. The effects of bearing and shaft asymmetries on the vibrational and stability characteristics are seen to be quite complex when the excitation frequency is close to the system natural frequencies. Even without the presence of damping, the vibrational amplitudes are limited to finite values at resonance conditions, by shaft-bearing asymmetry. As has been indicated in sections four and five, the combined effects of both shaft-bearing asymmetry and the nearness to resonance tend to stabilize x-directional motion but tend to destabilize the y-directional motion. The same is the case with the combined effects of mass unbalance and shaft-bearing asymmetry. The maximum amplitude of y-directional vibration has been shown not to occur always at the resonant frequency, but to occur at a frequency that is lesser than resonant frequency. For x-directional motion, the maximum amplitude occurs at a frequency that is higher than the resonant frequency. Further, the vibration amplitudes and phases have been shown to be time-dependent and so, the amplitude-modulated and phase-modulated vibrations are seen to occur during run-up and run-down operations. All these new observations have been systematically brought out in the present paper. Expressions for amplitude and phase modulations that are derived in the present paper can be directly employed to study the effects of acceleration or deceleration through resonance wherein the excitation frequency is time dependent.

The existing works on asymmetric rotor-dynamic systems did not consider the nonstationary nature of run-up or run-down vibrations. The effects of nearness of the system to resonance have not been included in the analysis. Further, based on a stationary solution assumption, most of the works analyzed the asymmetric rotor system for the critical excitation frequencies corresponding to parametric instability. Also, the effects of asymmetries in shifting the regions of parametric instability have been the prime concern of the existing works. The objective has obviously been to operate the rotor system at a frequency other than the frequencies of parametric instability. Quantification of the vibration response during start-up or shutdown of the motor has not been performed in the existing works. Also, in existing works, the effects of bearing and shaft asymmetry on the steady-state, i.e., stationary motions of the rotor-dynamic system, have been quantified employing various assumptions and without considering the influence of nearness of the system to resonance. For instance, in the work of Black (1969), the motions of an asymmetric rotor are assumed to be "small" perturbations to the motions of a symmetric rotor with mean (isotropic) stiffness properties. Near resonance, large-amplitude vibrations occur, thus making the assumption of "small" perturbations an approximation that may yield imprecise results. Similar assumptions have been employed in other works. Vibration amplitudes and phases have been treated to be time invariant. Conclusions regarding the effects of bearing and shaft asymmetries have been then obtained based on these assumptions, which are valid only for steady-state motions at frequencies far away from resonant frequencies. This is so because, near resonant frequencies, the motions become more complicated, since the additional effects due to the nearness of the system to resonance become significant, as can be seen from the results of the present paper. Also, the combined effects of

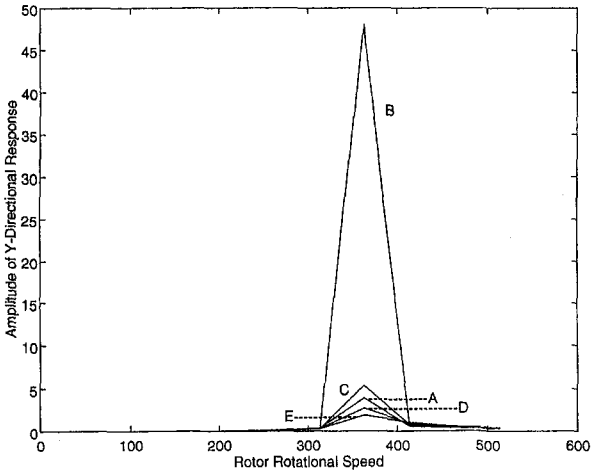

Fig. 7 Effect of shaft asymmetry on the resonant response in y direction

nearness to resonance, mass unbalance, and system asymmetry have been shown, in the present paper, to affect the motion and stability characteristics significantly.

So, under these circumstances, the conclusions drawn in the existing works, based on steady-state solutions, should not be generalized to include resonant motions. For instance, in the work of Inoue and Matsukura (1977), it is concluded that with the increase of the bearing asymmetry, the effect of the shaft asymmetry on the unbalance vibration decreases and finally converges to half of that in the case of symmetric bearing. From the results of the present work, it can be seen that such a general conclusion cannot be drawn when the resonant conditions are approached. Also, the time variation of amplitude and phase near the resonance has been shown in the present work to be significant. All these point to the need to consider the effects of bearing and shaft asymmetry separately on the vibratory motions near resonance. Further, it can also be seen that the effects of asymmetries on the vibratory motions during run-up or run-down are not the same as that of steady-state response.

The rotor system has to be accelerated or decelerated through resonant frequencies, if the rotor is to be operated at a frequency higher than the critical speeds. So, for balancing and design of rotor systems, the information about the vibration response during run-up or run-down operations is needed, and such information has been obtained in the present paper. The effects of both the bearing and shaft asymmetries on the steady-state motions near resonance are shown to be quite complex, thus demanding sophisticated designs and balancing procedures to overcome sudden failures during run-up or run-down operations. The results of the present work can be deployed in devising suitable rotor balancing procedures and developing safer designs of industrial rotor-dynamic systems that minimize the severity of vibration levels and maximize the operational safety.

References

Ardayfio, D., and Frohrib, D. A., 1976, "Instabilities of an Asymmetric Rotor With Asymmetric Shaft Mounted on Symmetric Elastic Supports," ASME *Journal of Engineering for Industry,* Vol. 98, pp. 1161–1165.

Bishop, R. E. D., and Parkinson, A. G., 1965, "Second Order Vibration of Flexible Shafts," *Proceedings Royal Society of London,* Vol. 259, pp. 1–31.

Black, H. F., 1969, "Parametrically Excited Lateral Vibrations of an Asymmetric Slender Shaft in Asymmetrically Flexible Bearings," *Journal of Mechanical Engineering Science,* Vol. 11, pp. 57–67.

Brosens, P. J., and Crandall, S. H., 1961, "Whirling of Unsymmetrical Rotor," ASME *Journal of Applied Mechanics,* Vol. 28, pp. 355–362.

Ehrich, F., 1992, "Observations of Subcritical Superharmonic and Chaotic Response in Rotor Dynamics," ASME *Journal of Vibration and Acoustics,* Vol. 114, pp. 93–100.

Genta, G., 1988, "Whirling of Unsymmetrical Rotor: A Finite Element Approach Based on Complex Coordinates," *Journal of Sound and Vibration,* Vol. 124, pp. 27–53.

Inoue, T., and Matsukura, Y., 1977, "Effect of Bearing Asymmetry on the Motion of an Asymmetric Rotor," *Proceedings 27th Japan National Congress of Applied Mechanics,* Vol. 27.

Iwatsubo, T., and Nakamura, M., 1968, "Balancing of Flexible Rotors With Asymmetric Shaft Stiffness," *Memoirs of the Faculty of Engineering,* Kobe University, No. 15.

Iwatsubo, T., Tomita, A., and Kawai, R., 1973, "Vibrations of Asymmetric Rotors Supported by Asymmetric Bearings," *Ingenieur Archive,* Vol. 42, pp. 416–432.

Lalanne, M., and Ferraris, G., 1990, *Rotordynamics Prediction in Engineering,* Wiley, New York.

Nayfeh, A. H., and Mook, D. T., 1979, *Nonlinear Oscillations,* Wiley, New York.

Okijima, K., and Kondo, Y., 1974a, "On the Critical Speed Regions of an Asymmetric Rotating Shaft Supported by Asymmetrically Elastic Pedestals (1st Report)," *Transactions Japan Society of Mechanical Engineers,* Vol. 40, pp. 2832–2842.

Okijima, K., and Kondo, Y., 1974b, "On the Critical Speed Regions of an Asymmetric Rotating Shaft Supported by Asymmetrically Elastic Pedestals (2nd Report)," *Transactions Japan Society of Mechanical Engineers,* Vol. 40, pp. 2843–2850.

Parkinson, A. G., 1965, "On the Balancing of Shafts With Axial Asymmetry," *Proceedings Royal Society of London,* Series A, Vol. 259, pp. 1095–1098.

Parszewski, Z. A., Krodekiewski, J. M., and Rucinksi, J., 1986, "Parametric Instabilities of Rotor Support Systems With Asymmetric Stiffness and Damping Matrices," *Journal of Sound and Vibration,* Vol. 109, pp. 111–125.

Yamamoto, T., and Ota, H., 1964, "On Unstable Vibrations of a Shaft Carrying an Unsymmetrical Rotor," ASME *Journal of Applied Mechanics,* Vol. 31, pp. 515–522.

Yamamoto, T., and Ota, H., 1966, "On the Forced Vibrations of the Shaft Carrying an Unsymmetrical Rotor," *Bulletin of Japan Society of Mechanical Engineering,* Vol. 9, pp. 58–66.

Yamamoto, T., Ota, H., and Kono, K., 1968, "On the Unstable Vibrations of a Shaft With Unsymmetrical Stiffness Carrying an Unsymmetrical Rotor," ASME *Journal of Applied Mechanics,* Vol. 35, pp. 313–321.

Instability Threshold and Stability Boundaries of Rotor-Bearing Systems

W. J. Chen
Centrifugal Compressor Division,
Ingersoll-Rand Company,
Mayfield, KY 42066

A direct numerical method for the determination of instability threshold and stability boundaries of flexible rotor-bearing systems is presented. The proposed procedure can also be used to improve the system stability by considering the design variables as operating parameters. The finite element method is utilized in the formulation of system equations of motion. The numerical algorithm is based on nonlinear optimization techniques. Two examples are presented to illustrate the feasibility, desirability, and ability of the proposed algorithm. A simple journal bearing system is used for the parametric study. An industrial high-speed compressor is employed to demonstrate the ability of this algorithm to deal with practical applications. The stability boundaries calculated from this algorithm are in agreement with the experimental results.

Introduction

The designs of rotor-bearing systems are becoming more complex due to the increase in rotor rotational speeds, requirements for energy conservation, and extreme operating conditions. Typical design requirements for modern compressors include the capability of operating in the unloaded condition, near-surge condition, with a wide range of oil temperatures, and with possible rotor overspeed. Very often, instabilities caused by fluid film bearings, seals, and aerodynamic forces are the only restrictions to the wide range of operating conditions. A very large and unstable vibration component, typically ranging from 20 to 80 percent of the rotor speed, can be observed by dynamic signal analyzers or FFT emulators if the system is operated beyond the instability threshold or the stability boundaries. Under the unstable condition, the linear theory is no longer valid and the motion is constrained by physical restrictions. Continuous operation under this excessive vibration usually results in machine damage. Very often, the effects of the operating parameters on the system stability are essential in the design stage. The rotor speed dictates the aerodynamic performance. The lubricant viscosity determines the oil type and operating temperature range. The bearing loads determine the range of throttling. Therefore, it is extremely useful to have an automated procedure to calculate directly the instability threshold and the stability boundaries of the operating parameters.

When a rotor is operated beyond a certain rotational speed, a very high and unstable vibration component with a fractional frequency of the rotor speed will be developed. This rotor speed is referred to as the instability threshold. At constant rotational speed, the rotor can experience the same unstable state when an operating parameter is beyond/below a certain value or outside a certain range. This limit is referred to as the stability boundary of that operating parameter. The instability threshold and stability boundary are usually determined from a stability map. A map of logarithmic decrements or damping coefficients versus the operating parameter is generated by repeated calculation of eigenvalues for a range of an operating parameter under study. Lund (1974) utilized the transfer matrix method for the calculation of damped critical speeds and instability threshold by repeatedly solving the eigenvalue polynomial equation. Later, various roots searching techniques based on the transfer matrix polynomial method were proposed by Murphy and Vance (1983) and Kim and David (1990). The instability threshold is then determined graphically by a stability map. A direct numerical procedure for the determination of the instability threshold based on the transfer matrix method was presented by Zhou and Rieger (1985). Quadratic interpolation and iteration schemes were used in their algorithm to determine the instability threshold and the corresponding whirl frequency. No stability boundaries on the operating parameters were discussed. The numerical difficulties involved with the transfer matrix method as the model size increases are well known. The possibility of missing some vibration modes still remains. A closed-form solution of the stability parameter for a rigid and symmetric rotor system supported by two identical fluid film bearings was presented by Lund and Thomsen (1978). Rao (1983) extended the work to a flexible and symmetric rotor supported by two identical bearings. Burrows and Sahinkaya (1984), and Sahinkaya and Burrows (1985) utilized eigenvalue assignment algorithm to control the onset of instability associated with oil whirl.

The development of finite element formulations for use in rotor-bearing-foundation systems has received considerable attention within the past few years (Rouch and Kao, 1979; Nelson, 1980). The capability of modeling complex systems and the stability of the numerical algorithms make the finite element method a popular and indispensable tool in the field of rotordynamics. The effects of rotatory inertia, gyroscopic moments, shear deformation, axial loads, flexible disks, and housing are included in the work. The linearized bearing and seal coefficients, aerodynamic cross-couplings, and other sources of interaction can be easily incorporated into the mathematical model. Rajan et al. (1986) presented a direct numerical algorithm for calculation of damped critical speeds using eigenvalue sensitivity based on the finite element formulation. The parameter sensitivity in the dynamics of rotor systems was discussed in their paper. The instability threshold still has to be determined by the graphic method.

A direct numerical procedure proposed in this paper allows the designers to determine the instability threshold and stability boundaries of the operating parameters if the boundaries exist. The governing system equations of motion are derived from the finite element method. The solution procedure is based on optimization techniques. The optimization techniques are very effective and suitable for this type of algorithm. The operating

Contributed by the International Gas Turbine Institute and presented at the ASME Conference on Engineering Systems Design and Analysis, London, United Kingdom, July 4–7, 1994. Manuscript received by the International Gas Turbine Institute September 11, 1994. Associate Technical Editor: R. E. Kielb.

parameters are subject to constraints as dictated by practical limitations. Examples are presented to illustrate the procedure.

Governing Equations of Motion

The finite element formulation of the rotor assembly is well documented by Ehrich (1992). The equations of motion for the rotating assembly and foundation, neglecting the material damping, are of the form

$$\begin{bmatrix} \mathbf{M}_r & \mathbf{0} & \mathbf{0} \\ \mathbf{0} & \mathbf{M}_d & \mathbf{0} \\ \mathbf{0} & \mathbf{0} & \mathbf{M}_f \end{bmatrix} \begin{Bmatrix} \ddot{\mathbf{q}}_r \\ \ddot{\mathbf{q}}_d \\ \ddot{\mathbf{q}}_f \end{Bmatrix} + \begin{bmatrix} \mathbf{G}_r & \mathbf{0} & \mathbf{0} \\ \mathbf{0} & \mathbf{G}_d & \mathbf{0} \\ \mathbf{0} & \mathbf{0} & \mathbf{0} \end{bmatrix} \begin{Bmatrix} \dot{\mathbf{q}}_r \\ \dot{\mathbf{q}}_d \\ \dot{\mathbf{q}}_f \end{Bmatrix} + \begin{bmatrix} \mathbf{K}_{rr} & \mathbf{K}_{rd} & \mathbf{K}_{rf} \\ \mathbf{K}_{dr} & \mathbf{K}_{dd} & \mathbf{0} \\ \mathbf{K}_{fr} & \mathbf{0} & \mathbf{K}_{ff} \end{bmatrix} \begin{Bmatrix} \mathbf{q}_r \\ \mathbf{q}_d \\ \mathbf{q}_f \end{Bmatrix} = \begin{Bmatrix} \mathbf{Q}_r \\ \mathbf{Q}_d \\ \mathbf{Q}_f \end{Bmatrix} \quad (1)$$

where the vectors $\mathbf{q}_r$, $\mathbf{q}_d$, $\mathbf{q}_f$ represent the displacements of shaft elements (and rigid disks), flexible disks, and flexible foundation, respectively. The mass/inertia matrix $\mathbf{M}$ is a real symmetric matrix, which is a function of structural properties. The gyroscopic matrix $\mathbf{G}$ is a real skew symmetric matrix, which is a function of structural properties and shaft rotational speed. The stiffness matrix $\mathbf{K}$ can be an arbitrary real matrix due to the nonconservative axial loads. The motion of the rotor is described by two translational and two rotational coordinate displacements at each finite element station. The motions of the flexible disks and foundation can be described by six degrees of freedom at each finite element station. The matrices of flexible disks and foundation can be obtained from any existing structural finite element computer programs, such as NASTRAN and ANSYS. The three primary structural components (shaft and rigid disks, flexible disks, and foundation) are coupled by the interconnecting components.

Fluid film bearings are commonly used in rotating machinery due to their bearing damping, stiffness characteristics, and long life of operation. The use of linearized bearing dynamic coefficients in the analysis of rotor dynamics has been widely accepted (Lund and Thomsen, 1978). The linearized governing equation of motion for a fluid film bearing connecting shaft station i and foundation j (or station j of another shaft) is given by

$$\begin{bmatrix} \mathbf{C}_b & -\mathbf{C}_b \\ -\mathbf{C}_b & \mathbf{C}_b \end{bmatrix} \begin{Bmatrix} \dot{\mathbf{q}}_i \\ \dot{\mathbf{q}}_j \end{Bmatrix} + \begin{bmatrix} \mathbf{K}_b & -\mathbf{K}_b \\ -\mathbf{K}_b & \mathbf{K}_b \end{bmatrix} \begin{Bmatrix} \mathbf{q}_i \\ \mathbf{q}_j \end{Bmatrix} = \begin{Bmatrix} \mathbf{Q}_i \\ \mathbf{Q}_j \end{Bmatrix} \quad (2)$$

where the 2×2 matrices $\mathbf{C}_b$ and $\mathbf{K}_b$ are the bearing damping and stiffness coefficients, which are determined by solving the Reynolds equation and its perturbed equations (Klit and Lund, 1986). To study the effects of bearing parameters on the system stability, the bearing dynamic coefficients are expressed in the nondimensional form and represented as functions of the Sommerfeld number. The bearing Sommerfeld number is defined as

$$S_B = \frac{\mu N_s}{(W/LD)} \left(\frac{R}{C_B}\right)^2 \quad (3)$$

and the nondimensional stiffness and damping coefficients are

$$\hat{K}_{i,j} = \frac{K_{i,j} C_B}{W}; \quad \hat{C}_{i,j} = \frac{C_{i,j} \Omega C_B}{W} \quad (i = x, y; j = x, y) \quad (4)$$

The Sommerfeld number and nondimensional coefficients are sometimes normalized with respect to the lobe radial clearance. However, the bearing radial clearance is more often used by bearing and equipment manufacturers for measurability and machinability. Hence, the bearing radial clearance is employed in this paper. The relationship between the bearing and lobe radial clearance is related by the bearing preload:

$$m = 1 - \frac{C_B}{C_L} \quad (5)$$

For a given operating condition, a Sommerfeld number is determined and the calculation of corresponding bearing stiffness and damping coefficients becomes straightforward. Thus, for a given type of bearing, the dimensional bearing coefficients in Eq. (2) are functions of rotor speed, oil viscosity, bearing load, and bearing clearance.

Other sources of self-excitation include the aerodynamic effects of impellers and seals. This type of destabilizing forces can be expressed in the form (Weiser and Nordmann, 1989)

$$\begin{bmatrix} C_a & c_a \\ -c_a & C_a \end{bmatrix} \begin{Bmatrix} \dot{x} \\ \dot{y} \end{Bmatrix} + \begin{bmatrix} K_a & k_a \\ -k_a & K_a \end{bmatrix} \begin{Bmatrix} x \\ y \end{Bmatrix} = \begin{Bmatrix} F_x \\ F_y \end{Bmatrix} \quad (6)$$

where C_a, c_a and K_a, k_a are also functions of operating parameters.

The assembled equations of motion that describe the dynamic characteristics of the system are of the form

$$\mathbf{M}\ddot{\mathbf{q}} + [\mathbf{G} + \mathbf{C}_p]\dot{\mathbf{q}} + [\mathbf{K} + \mathbf{K}_p]\mathbf{q} = \mathbf{Q} \quad (7)$$

where $\mathbf{p}$ is the vector of the operating parameters, which include rotor rotational speed, lubricant viscosity, bearing loads, bearing clearance, axial loads, etc. The matrices $\mathbf{C}_p$ and $\mathbf{K}_p$ are quite sparse and can be rearranged for minimum storage requirement.

System Stability

For a given operating condition, the stability of the dynamic system can be determined by the eigenvalue equation of the homogeneous state space form. The associated eigenvalue problem is

Nomenclature

$\mathbf{C}$ = damping matrix
C = damping
C_B = bearing radial clearance
C_L = lobe radial clearance
D = bearing diameter
F = force
f = objective function
$\mathbf{G}$ = gyroscopic matrix
$\mathbf{I}$ = identity matrix
$j = \sqrt{-1}$
L = bearing length
K = stiffness
$\mathbf{K}$ = stiffness matrix
m = preload
$\mathbf{M}$ = mass/inertia matrix
N_S = rotor speed, rps
n = degrees of freedom
$\mathbf{p}$ = operating parameter vector
$\mathbf{Q}$ = force vector
$\mathbf{q}$ = displacement vector
R = shaft radius, system modal norm
S_B = bearing Sommerfeld number
x, y = displacements
W = bearing load
δ = logarithmic decrement
ϵ = convergence tolerance
λ = eigenvalue
μ = lubricant viscosity
σ = damping exponent
ϕ = right eigenvector
φ = left eigenvector
Ω = rotor speed, rad/s
ω = natural whirl frequency

Subscripts

a = aerodynamics
b, d, r, f = bearing, disk, rotor, foundation
i, j = indices

Superscripts

L, U = lower, upper limit

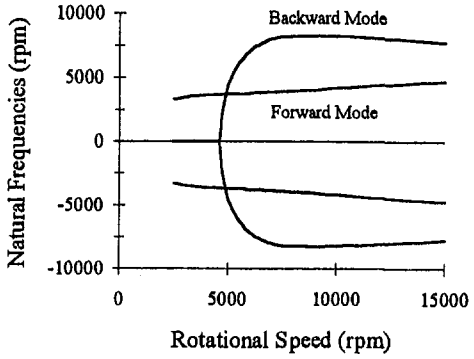

Fig. 1 Whirl speed map

$$(\lambda \mathbf{M}^* + \mathbf{K}^*)\phi = \mathbf{0} \tag{8}$$

with $2n$ eigenvalues λ_i and the associated eigenvectors ϕ_i. The state space matrices are

$$\mathbf{M}^* = \begin{bmatrix} \mathbf{M} & \mathbf{0} \\ \mathbf{0} & \mathbf{I} \end{bmatrix}; \quad \mathbf{K}^* = \begin{bmatrix} \mathbf{G} + \mathbf{C}_p & \mathbf{K} + \mathbf{K}_p \\ -\mathbf{I} & \mathbf{0} \end{bmatrix} \tag{9}$$

Since $\mathbf{M}$ is a positive definite real symmetric matrix, equation (8) can be reduced to the standard form

$$\mathbf{A}\phi = \lambda\phi \tag{10}$$

where

$$\mathbf{A} = -(\mathbf{M}^*)^{-1}\mathbf{K}^* = \begin{bmatrix} -\mathbf{M}^{-1}(\mathbf{G} + \mathbf{C}_p) & -\mathbf{M}^{-1}(\mathbf{K} + \mathbf{K}_p) \\ \mathbf{I} & \mathbf{0} \end{bmatrix} \tag{11}$$

is an arbitrary real matrix. The solution of the eigenvalue problem is complex:

$$\lambda_i = \sigma_i + j\omega_i \quad (i = 1, 2, \ldots 2n) \tag{12}$$

The stability boundary can be established by examining the variation in the real part of λ_i as a function of an operating parameter. It is very common that logarithmic decrement is used to express the degree of the stability instead of using the damping exponent:

$$\delta = \frac{-2\pi\sigma}{\omega} \tag{13}$$

When logarithmic decrement becomes negative or the damping exponent becomes positive, the system becomes unstable in the linear sense.

Numerical Algorithm

At the threshold of instability, the real part of eigenvalue is zero such that

$$\lambda_{\text{threshold}} = j\omega_{\text{threshold}} \tag{14}$$

To determine the stability boundary of an operating parameter, the problem can be stated as one of choosing an operating parameter subject to practical limitation of the design such that one of the system eigenvalues has a zero real part. The corresponding imaginary part is referred to as unstable whirl frequency. In most applications, if the system becomes unstable, the rotor whirls in its first mode (lowest whirl frequency) with forward precession. It should be noted that the first unstable mode can be either a bending mode or a rigid body mode, depending upon the potential energy distribution.

The numerical algorithm can be written mathematically as follows: to find an operating parameter, p, which minimizes

Table 1 System parameters

Journal mass = 22.766 kg (0.13 Lbf-sec^2/in.)
Bearing length = 12.7 mm (0.5 in.)
Bearing diameter = 50.8 mm (2.0 in.)
Bearing clearance = 0.0635 mm (0.0025 in.)
Bearing load = 222.4 N (50 Lbf)
Oil viscosity = 6.89478 Centipoise (1.0E-06 Reyns)

$$f(p) = |\sigma| \quad \text{or} \quad \sigma^2 \tag{15}$$

and is subject to

$$p^L < p < p^U \tag{16}$$

The operating parameters considered in this paper can be the rotor rotational speed, lubricant viscosity, bearing loads, bearing clearance, axial loads, etc. The optimization procedure is terminated at the ith iteration step if the objective function, $f(p)$, satisfies the following convergence equations:

$$f(p) < \epsilon \tag{17}$$

or

$$|f(p)^i - f(p)^{i-1}| < \epsilon \tag{18}$$

where ϵ is a small real number that defines the desired accuracy. When the convergence Eq. (17) is satisfied, the instability boundary is established. If the procedure stops due to convergence Eq. (18), no instability boundary will be established and the system is in either a stable or an unstable state throughout the limits of the operating parameter. When no instability boundary is established, caution must be taken to be certain that the converged solution is the global minimum. To ensure the solution is the global minimum, several different starting values are considered inside the computer programs. The feasible direction method (Vanderplaats, 1984) is employed as the optimization solver. The gradients required in the iterative process can be obtained analytically in the following expression (Rajan et al., 1986)

$$\frac{\partial \lambda_i}{\partial p} = \frac{-\varphi_i^T \left(\lambda_i \dfrac{\partial \mathbf{M}^*}{\partial p} + \dfrac{\partial \mathbf{K}^*}{\partial p} \right) \phi_i}{R_i} \tag{19}$$

where ϕ_i, φ_i are the corresponding right and left eigenvectors, respectively. The right eigenvector is defined in Eq. (10) and the left eigenvector is defined in the following equation

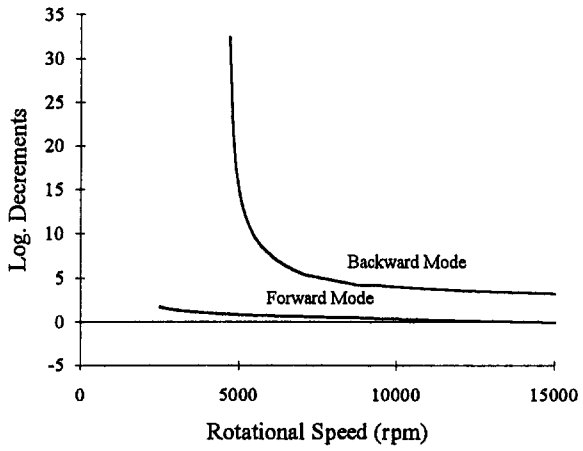

Fig. 2 Stability map

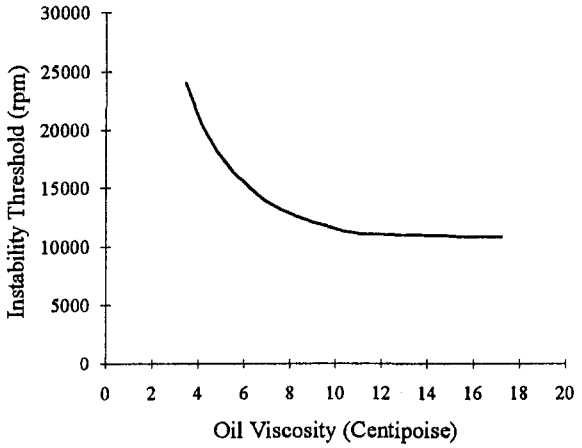

Fig. 3 Instability threshold versus oil viscosity

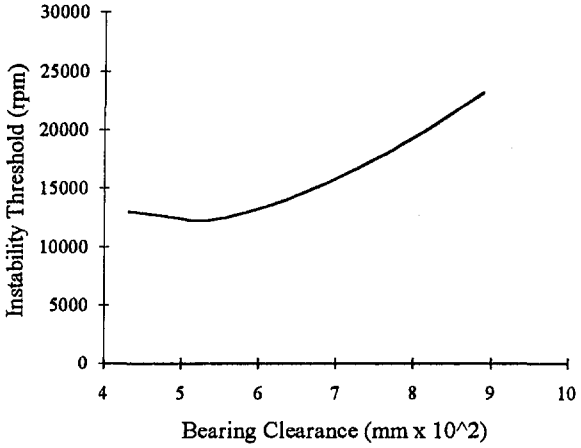

Fig. 5 Instability threshold versus bearing clearance

$$\boldsymbol{\varphi}^T\mathbf{A} = \lambda\boldsymbol{\varphi}^T \tag{20}$$

The associated modal norm is defined as

$$R_i = \boldsymbol{\varphi}_i^T\mathbf{A}\boldsymbol{\phi}_i \tag{21}$$

The matrices in Eq. (21) are quite sparse. Computational procedures may be adopted that allow for calculation of eigenvalue sensitivities with minimum computational expense (Rajan et al., 1986). To determine the instability boundary, only the real part of Eq. (19) is used.

Parametric Studies

A single journal bearing system (Kirk and Gunter, 1970) is used for the parametric studies. The physical parameters of the system are summarized in Table 1.

For a single journal bearing system, the rotor is assumed to be rigid and symmetric, which is usually not practical. This simple two-degrees-of-freedom system is only employed to demonstrate the validity of the numerical procedures proposed in this paper. The results obtained from the algorithm presented here can be easily verified by using the conventional graphic method.

Using the analytical procedures described earlier, the instability threshold can be found to be around 14,025 rpm by considering the rotational speed as the operating parameter. For the purpose of comparison, the whirl speed and stability maps shown in Figs. 1 and 2 are generated by calculating system eigenvalues over a range of rotational speed. Figure 1 shows that the backward mode is a real nonvibratory mode with zero whirl frequency from zero to 4615 rpm and becomes a vibratory mode after 4615 rpm. The forward mode is always a vibratory mode throughout the speed range. Figure 2 shows that the forward mode becomes unstable as the speed exceeds 14,025 rpm. The instability threshold determined by using the proposed procedure is in good agreement with the result obtained from the stability map. A parametric study is then carried out to understand the influence of each parameter on the instability threshold. Figure 3shows the instability threshold decreases as the oil viscosity increases and becomes very sensitive at lower viscosities (i.e., high temperature range). Figure 4 shows that decreasing the bearing load monotonously lowers the instability threshold. Figure 5 shows the lowest instability threshold occurs when the bearing clearance is around 0.0575 mm and the system stability can be improved by either decreasing or increasing the clearance from that point.

At 12,000 rpm, the stability boundaries of the bearing load and oil viscosity were calculated to be around 185 N and 9.1 Centipoise, respectively. The logarithmic decrements versus bearing load and oil viscosity at 12000 rpm are plotted in Figs. 6 and 7 for comparison purposes. Figure 6 shows the logarithmic decrement of the forward mode decreases as the bearing load decreases. In contrast, the logarithmic decrement of the backward mode slightly increases as the bearing load decreases. The forward mode becomes unstable when the bearing load is less than 185 N. Figure 7 shows the forward mode becomes unstable when the oil viscosity is larger than 9.1 Centipoise. The logarithmic decrement of the backward mode increases and the logarithmic decrement of the forward mode decreases as the oil vis-

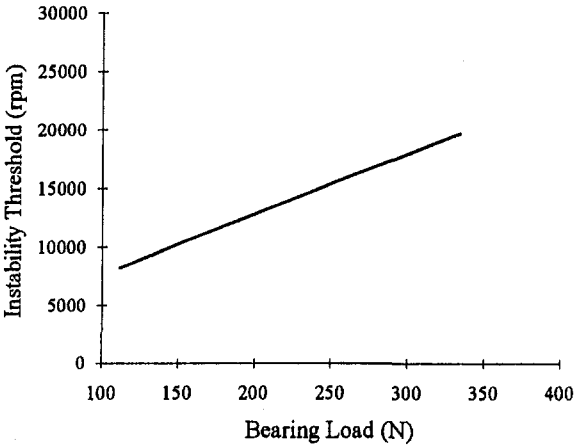

Fig. 4 Instability threshold versus bearing load

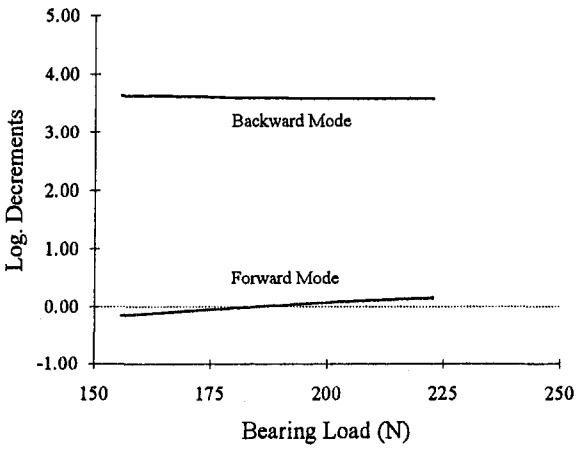

Fig. 6 Logarithmic decrements versus bearing load

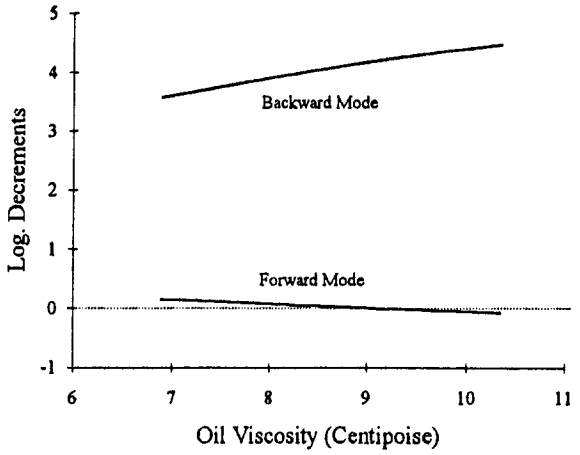

Fig. 7 Logarithmic decrements versus oil viscosity

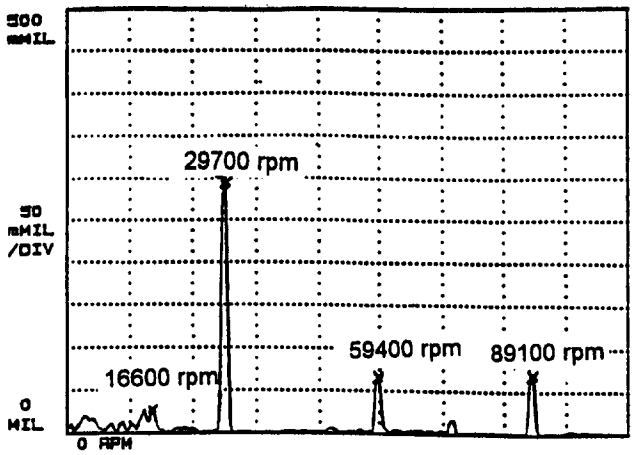

Fig. 10 Test results at 38°C loaded condition

cosity increases. The logarithmic decrements of the forward and backward modes move in opposite directions as the operating parameter varies. In general, the forward mode becomes unstable.

Applications to an Industrial Compressor

To illustrate the practical application of the algorithm, a high-speed centrifugal compressor was employed as a test vehicle. The single overhung rotor system has a length of 550 mm and a bearing diameter of 55 mm. The rotating assembly weighs about 17 kg and is supported by two three-lobe bearings as indicated in Fig. 8. ISO VG 32 mineral oil was used in the test. The bearing loads are mainly due to the gear force, which varies from 110 kg to 450 kg depending on the loading condition. Two perpendicular vibration probes were located at station 4 between the impeller and bearing. The effects of the bearing loads and oil temperature on the stability were studied. The first three forward synchronous rigid bearing critical speeds are calculated to be 17,730, 80,720, and 177,260 rpm. The rotor is operated at a constant speed of 29,700 rpm, which is above the first bending critical speed.

In the analytical model, an aerodynamic cross-coupling of 350 N/mm was included at finite element station 2. The cross-coupling was calculated from the Alford equation with a correlation factor of 1.5 (Kirk, 1988). In the analytical calculation of the bearing load instability boundary, the convergence Eq. (18) was satisfied. Hence no instability boundary was established and the system is in a stable state throughout the limits of bearing load. In the calculation of the oil temperature instability boundary, the program converged and the objective function was nearly zero. The instability boundaries were calculated to be 59°C and 61°C for the loaded and unloaded conditions, respectively. The unstable whirl frequency was calculated around 15,000 rpm. The unstable mode in this application is the first bending forward mode. The associated mode shape is plotted in Fig. 9.

The analytical results calculated from this work were compared with the experimental results. The effect of bearing load on the system stability was examined first. The oil inlet temperature was controlled to be around 38°C. Figures 10 and 11 are the spectrum plots for the fully loaded and unloaded conditions. In the loaded condition, the 1X (29700 rpm) vibration component was steady with an amplitude around 0.0075 mm, the amplitudes of subsynchronous and higher harmonics were relatively small. In the unloaded condition, the 1X (29,700 rpm)

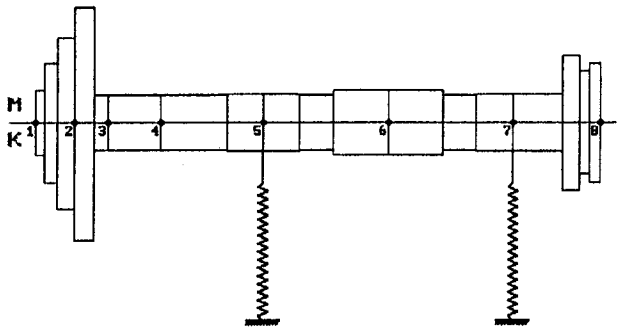

Fig. 8 Rotor configuration

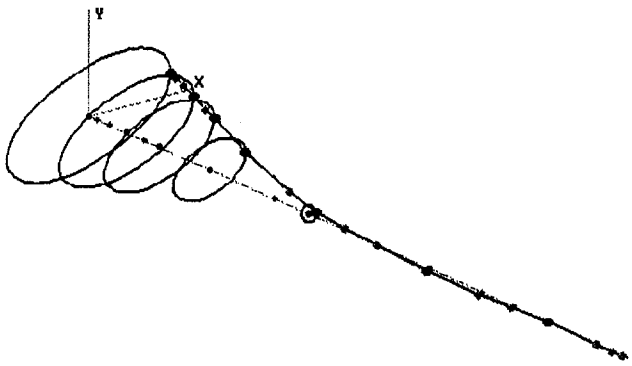

Fig. 9 Unstable forward precession mode

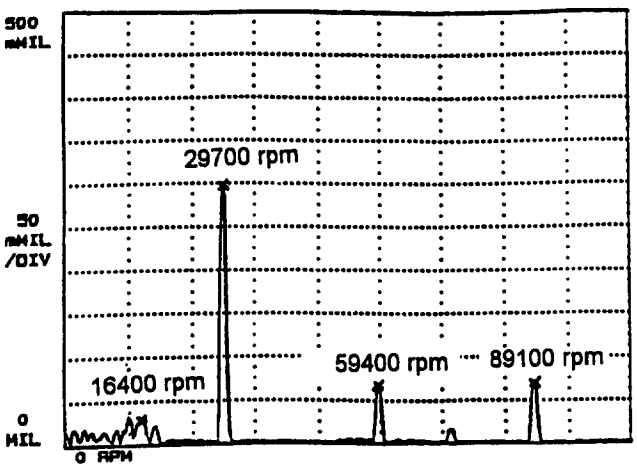

Fig. 11 Test results at 38°C unloaded condition

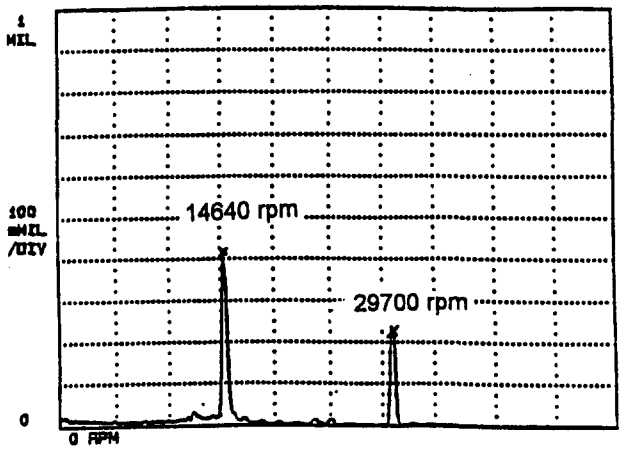

Fig. 12 Test results at 52°C loaded condition

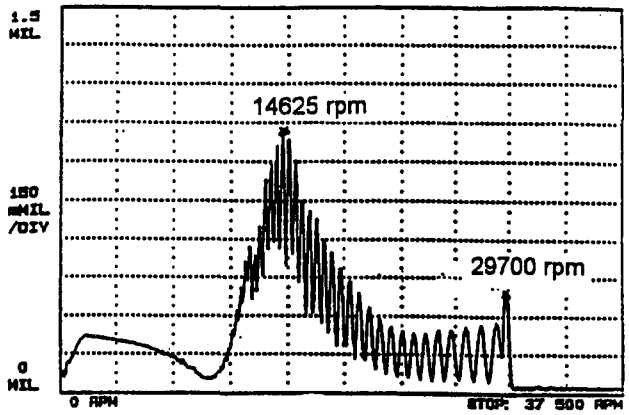

Fig. 14 Coastdown data

vibration component varied from 0.008 mm to 0.011 mm and the amplitudes of subsynchronous and higher harmonics were relatively small. In both cases, a small subsynchronous component occurred around 16,500 rpm. The system was stable for all loading conditions at 38°C inlet oil temperature. This finding is in agreement with the analytical calculation. The effect of oil temperature, i.e., oil viscosity, on the system stability was then examined by gradually increasing the oil temperature. In the loaded condition, when the oil inlet temperature approached 52°C, an unstable subsynchronous component showed up with an oscillating frequency of 14,640 rpm and a fluctuating amplitude ranging from 0.008 mm to 0.02 mm. Figure 12 shows the instantaneous spectrum plot of the loaded condition with an oil inlet temperature of 52°C. Similarly, when the oil inlet temperature exceeded 50°C in the unloaded condition, the unstable subsynchronous component showed up with an oscillating frequency of 14,760 rpm. Figure 13 shows the unstable subsynchronous component in the unloaded condition. In both cases, the amplitudes of the subsynchronous components were larger than that of synchronous components and the amplitudes were fluctuating and unstable. The unstable vibrations were constrained by the bearing clearance and continuous operation under this condition can result in bearing failure. The critical speed was found to be around 14,600 rpm from the coastdown plot as shown in Fig. 14.

The analytical and experimental results are in agreement. The instability boundaries of the oil temperature established analytically were slightly higher than the values obtained from the experiment. The difference may be attributed to the measurement of the oil inlet temperature, the assumption made in the heat balance calculation, and the estimation of the aerodynamic cross-coupling. This example illustrated the proposed algorithm can be an effective design tool in the establishment of the instability boundaries of the operating parameters.

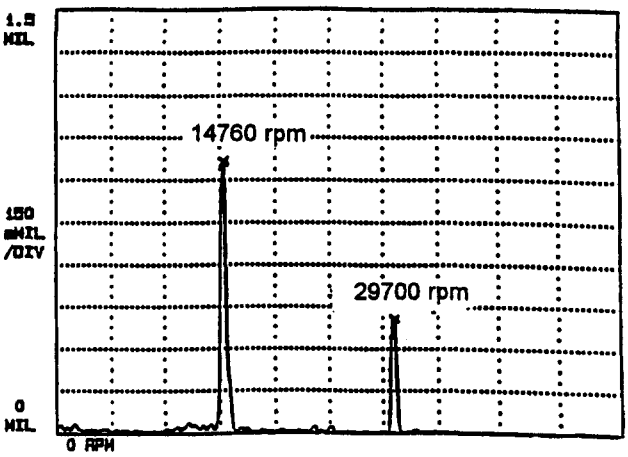

Fig. 13 Test results at 50°C unloaded condition

Conclusion

A direct numerical algorithm for determination of instability threshold and stability boundaries of operating parameters for the flexible rotor-bearing systems has been presented. The proposed algorithm can be used as a design tool for improvement of system stability and for adjustment of the operating parameters to a wide range of operation. Two examples have been presented to demonstrate the automated algorithm.

Acknowledgments

The author wishes to thank Mr. Filippo Mariani, Ingersoll-Rand Company, Italy, for his contribution to the implementation of experimental work on the industrial compressor.

References

Burrows, C. R., and Sahinkaya, M. N., 1984, "Control of Oil-Whirl by Pole Assignment," *Proceedings of the 1984 American Control Conference,* pp. 354–359.

Ehrich, F. F., 1992, *Handbook of Rotor-dynamics,* McGraw-Hill, New York, Chap. 2.

Kim, D., and David, J. W., 1990, "An Improved Method for Stability and Damped Critical Speeds of Rotor-Bearing Systems," ASME *Journal of Vibration and Acoustics,* Vol. 112, pp. 112–118.

Kirk, R. G., and Gunter, E. J., 1970, *Transient Journal Bearing Analysis,* NASA CR-1549.

Kirk, R. G., 1988, "Evaluation of Aero-dynamic Instability Mechanisms for Centrifugal Compressors—Part 1: Current Theory," ASME *Journal of Vibration, Acoustics, Stress, and Reliability in Design,* Vol. 110, pp. 201–206.

Klit, P., and Lund, J. W., 1986, "Calculation of the Dynamic Coefficients of a Journal Bearing, Using a Variational Approach," ASME *Journal of Tribology,* Vol. 108, pp. 421–425.

Lund, J. W., 1974, "Stability and Damped Critical Speeds of a Flexible Rotor in Fluid-Film Bearings," ASME *Journal of Engineering for Industry,* Vol. 96, pp. 509–517.

Lund, J. W., and Thomsen, K. K., 1978, "A Calculation Method and Data for the Dynamic Coefficients of Oil-Lubricated Journal Bearings," ASME *Topics in Fluid Film Bearing and Rotor Bearing System Design and Optimization,* pp. 1–28.

Murphy, B. T., and Vance, J. M., 1983, "An Improved Method for Calculating Critical Speeds and Rotordynamic Stability of Turbomachinery," ASME *Journal of Engineering for Power,* Vol. 105, pp. 591–595.

Nelson, H. D., 1980, "A Finite Rotating Shaft Element Using Timoshenko Beam Theory," ASME *Journal of Mechanical Design,* Vol. 102, Paper No. 79-WA/DE-5.

Rajan, M., Nelson, H. D., and Chen, W. J., 1986, "Parameter Sensitivity in the Dynamics of Rotor-Bearing Systems," ASME *Journal of Vibration Acoustics, Stress, and Reliability in Design,* Vol. 108, pp. 197–206.

Rao, J. S., 1983, "Instability of Rotors in Fluid Film Bearings," ASME *Journal of Vibration, Acoustics, Stress, and Reliability in Design,* Vol. 105, pp. 274–279.

Rouch, K. E., and Kao, J. S., 1979, "A Tapered Beam Finite Element for Rotor Dynamics Analysis," *Journal of Sound and Vibration,* Vol. 66, pp. 119–140.

Sahinkaya, M. N., and Burrows, C. R., 1985, "Control of Stability and the Synchronous Vibration of a Flexible Rotor Supported on Oil-Film Bearings," ASME *Journal of Dynamic Systems, Measurement, and Control,* Vol. 107, pp. 139–144.

Vanderplaats, G. N., 1984, *Numerical Optimization Techniques for Engineering Design With Applications,* McGraw-Hill, New York.

Weiser, H. P., and Nordmann, R., 1989, "Calculation of Rotordynamic Coefficients for Labyrinth Seals Using a Three Dimensional Finite Difference Method," *The 6th Workshop on Rotordynamic Instability Problems in High-Performance Turbomachinery,* Texas A&M University.

Zhou, S., and Rieger, N. F., 1985, "An Instability Analysis Procedure for Three-Level Multi-Bearing Rotor-Foundation Systems," *Symposium on Instability in Rotating Machinery,* Carson City, NV.

Nonlinear Analysis of Rotordynamic Instabilities in High-Speed Turbomachinery

D. S. H. Chan
Department of Marine Technology,
Kværner Engineering A. S.,
Oslo, Norway

A nonlinear approach based on the method of averaging has been developed to study unstable lateral vibrations of rotors in high-speed turbomachinery. The method makes use of an extended concept of bearing dynamic coefficients, which are defined by applying small perturbations to the dynamic equilibrium positions. The approach has been applied to determine the stability threshold of flexible rotors supported on short and tilting-pad journal bearings, respectively. Stability performance of systems supported on short journal bearings is improved by the presence of mass unbalance. However, for flexible rotors supported on tilting-pad journal bearings, increased unbalance can lead to lower rotordynamic stability margins. This has the significant implication that stability estimates from linear analysis are not always conservative. The present method provides a computationally more efficient way to understand the nonlinear vibration behavior of high-speed turbomachinery.

1 Introduction

Linearized bearing dynamic coefficients are widely used in rotordynamic analysis for calculating critical speeds, unbalance response, and stability (Lund et al., 1965; Gunter, 1966; Ehrich, 1992). The concept of such coefficients is based on a linear assumption of infinitesimally small motions about the static equilibrium position (Lund, 1987). This assumption is, however, not always valid, e.g., when the journal motion relative to the bearing clearance is fairly large due to strong dynamic forces. It is well known that the dynamic characteristics of hydrodynamic bearings are highly nonlinear for large amplitude motions. Nevertheless, linear analysis has been found to give reasonable results for the prediction of unbalance response orbits with amplitudes up to about 30-40 percent of bearing clearance (Holmes, 1970; Lund, 1987).

Despite the general success of linear analysis, it fails to cope with motions with amplitudes that approach the bearing clearance, as well as a number of nonlinear phenomena such as instability limit cycle, subharmonic vibrations, etc. These nonlinear cases are often handled by means of the time-marching numerical integration method (Adams, 1980). This method is very versatile and accurate for nonlinear analysis but its major drawback is the substantial computational time needed. Various approximate methods have been applied to reduce the computational effort for nonlinear rotordynamic analysis (Nataraj and Nelson, 1989; Hwang and Shiau, 1991; Choy et al., 1992). Most of these approximate methods are aimed at steady-state problems where it takes a long time for the numerical integration results to converge.

For the stability analysis of rotor-bearing systems with unbalance, Lund and Nielsen (1980) applied the method of averaging to rigid rotors supported on short journal bearings. The method makes use of the time-averaged bearing dynamic coefficients along the unbalance response orbit. It is computationally efficient and gives results that agree with those calculated by the time-marching numerical integration method. In this study, the method is further developed to handle flexible rotors, which are more realistic models of modern high-speed turbomachinery. Besides the bearing-induced oil whirl/whip problems (Muszynska, 1986), the method is applied to investigate the stability threshold of rotors supported on tilting-pad journal bearings and excited by aerodynamic cross-coupling forces. The aerodynamic cross-coupling represents the destabilizing influence from fluid-mechanical interactions, e.g., impeller/diffuser clearances, seals in high-speed turbomachinery (Ehrich and Childs, 1984).

Together with the extended method of averaging, the concept of quasi-linear bearing dynamic coefficients is introduced. In contrast with linearized coefficients, which depend only on the static equilibrium position, the quasi-linear coefficients are defined with reference to dynamic equilibrium positions, i.e., points along the unbalance response orbit. These quasi-linear coefficients are functions of the journal displacements and velocities at each dynamic equilibrium position. Thus, they require a modified way of calculation in the bearing design procedure, which conventionally evaluates bearing dynamic coefficients by perturbing the static equilibrium conditions.

In this paper the theory behind the extended method of averaging and quasi-linear bearing dynamic coefficients is presented briefly. A more comprehensive treatment can be found in Chan (1992). Results are then compared with predictions by the time-marching numerical integration method to verify the validity and accuracy of the present method. The assumptions and limitations of the present method for nonlinear rotordynamic analysis are also discussed.

2 Theory

2.1 Quasi-Linear Bearing Dynamic Coefficients. The concept of dynamic coefficients is extremely useful in defining the dynamic characteristics of journal bearings and is extended here to eliminate the assumption of small motions. Since unbalance is the most common cause of large-amplitude vibrations in rotor-bearing systems, the response and stability of the motion under unbalance forces are studied. The rotor is forced to whirl along a certain orbit due to unbalance and, under steady-state conditions, the rotor can be described as in a state of dynamic equilibrium at each point along the orbit. Contrary to the static equilibrium position, the rotor possesses not only displacements but also velocities at the dynamic equilibrium position. The dynamic characteristics of the bearing depend on both the journal displacements and velocities relative to the

Contributed by the International Gas Turbine Institute and presented at the 39th International Gas Turbine and Aeroengine Congress and Exposition, The Hague, The Netherlands, June 13–16, 1994. Manuscript received by the International Gas Turbine Institute February 4, 1994. Paper No. 94-GT-78. Associate Technical Editor: E. M. Greitzer.

bearing, and a new type of dynamic coefficients is obtained by linearizing the forces about the dynamic equilibrium position. The ensuing analysis using these "quasi-linear" bearing dynamic coefficients can account for the nonlinear effect in an approximate manner. This is different from a nonlinear analysis by time-marching numerical integration, where bearing dynamic coefficients are not used.

The calculation of static and dynamic characteristics of hydrodynamic journal bearings can be found in Chan (1992). The two types of bearings considered here are short journal bearings and tilting-pad journal bearings. There exists no major difference with respect to the determination of dynamic coefficients about the static or dynamic equilibrium position for the case of short journal bearings, because the analytical formulae derived for these bearing coefficients have already allowed for the journal velocities. On the other hand, the dynamic coefficients of tilting-pad journal bearings were conventionally calculated by perturbing the journal about the static equilibrium position. This perturbation procedure has to be extended to take into consideration the journal velocities at the dynamic equilibrium position.

The bearing dynamic characteristics are represented by eight sets of quasi-linear dynamic coefficients for one orbit. Each set of these quasi-linear dynamic coefficients are expanded into Fourier series. The respective Fourier series coefficients, i.e., terms related to various harmonics, are used in the subsequent rotordynamic analysis to determine the response and stability of the system. Examples of unbalance orbits and the corresponding variation of quasi-linear dynamic coefficients are shown in Figs. 1 and 2, where the number of chosen points (time steps) along the unbalance orbit is 60. Figure 1 illustrates the quasi-linear dynamic coefficients of short journal bearings. The unbalance response orbit of a flexible rotor supported on short journal bearings is shown in Fig. 1(a) where the displacements are normalized with respect to the bearing clearance C, i.e.,

$$\bar{x} = \frac{x}{C} \qquad \bar{y} = \frac{y}{C} \tag{1}$$

The dimensionless stiffness and damping coefficients are shown in Figs. 1(b) and 1(c), respectively, and they are defined by

$$\bar{K}_{ij} = \frac{CK_{ij}}{W} \qquad \bar{C}_{ij} = \frac{C\Omega C_{ij}}{W} \tag{2}$$

where W is the static load and Ω is the rotational speed. Figure 2 shows the corresponding parameters for tilting-pad journal bearings. It should be mentioned that the dynamic coefficients of tilting-pad journal bearings are reduced coefficients, which depend on the whirl frequency (White and Chan, 1992).

2.2 Method of Averaging. The basic idea of the method of averaging [see, e.g., Schmidt and Tondl (1986)] is briefly reviewed. For a nonlinear single degree-of-freedom (SDOF) system, the equation of motion can be written as

$$\ddot{y} + y = f(y) \tag{3}$$

where $f(y)$ represents the nonlinear function. The solution may be assumed in the form

$$y = a(\tau) \cos [\tau + \nu(\tau)] = a(\tau) \cos \phi(\tau) \tag{4}$$

where $a(\tau)$ and $\phi(\tau)$ are, respectively, slowly varying amplitude and phase functions of dimensionless time τ. The equation of motion is rearranged to yield the standard form of two differential equations of first order, i.e.,

$$\begin{cases} \dot{a} = g(a, \phi) \\ \dot{\phi} = h(a, \phi) \end{cases} \tag{5}$$

The stationary solution is then obtained by averaging the terms on the right-hand sides (containing the phase ϕ) over one period and equating them to zero. Thus, the nonlinear equation of motion is solved approximately and the solution method is known as the method of averaging.

A detailed mathematical formulation of the extended method can be found in Chan (1992). Here a brief description of the calculation procedure is given. The calculation procedure can be divided into three main stages: (1) matrix reduction, (2) response calculation, and (3) stability determination.

(1) Matrix Reduction. The equations of motion, including the mass and stiffness matrices, are established in terms of all the rotor degrees of freedom in the x direction,

$$M\ddot{x} + Kx = F_x + f_x \tag{6}$$

where F_x is the bearing force vector and f_x is the mass unbalance force vector in the x direction. Note that the nonlinearity lies in the bearing force vector F_x, which will be represented as a function of the quasi-linear bearing stiffness and damping coefficients (K_{ij} and C_{ij}).

Then the matrices are partitioned into two groups. One group (the master coordinates) contains all the journal degrees of

Nomenclature

$a(\tau)$ = slowly varying amplitude function
C_{ij} = bearing damping coefficients
C = bearing clearance
C_p = pad circle clearance
C_r = coefficient matrix in Eq. (7)
D = bearing diameter
F_x, F_y = bearing force vectors
f_x = mass unbalance force vector (in x direction)
g = const = acceleration due to gravity
K = shaft stiffness or shaft stiffness matrix
K_r = reduced shaft stiffness matrix
K_{ij} = bearing stiffness coefficients
L = bearing length
LOP = load-on-pad tilting-pad journal bearings
M = disk mass or shaft mass matrix
M_r = reduced shaft mass matrix
m = bearing disk mass or bearing preload
N = rotational speed, rev/s
Q = aerodynamic cross-coupling coefficient
R = bearing radius
r_u = radius of unbalance
S = Sommerfeld number
W = static bearing load
x = displacement in vertical direction
x_r = journal displacement vector (in x direction)
x_1, x_2 = journal displacements at bearings (in x direction)
x_{1c}, x_{1s} = slowly varying parameters in Eq. (9)
y = displacement in horizontal direction
y_1, y_2 = journal displacements at bearings (in y direction)
y_{1c}, y_{1s} = slowly varying parameters in Eq. (9)
ϵ_0 = static eccentricity ratio
μ = lubricant viscosity
ρ = dimensionless unbalance parameter
σ = modified Sommerfeld number for short bearings
τ = dimensionless time
$\phi(\tau)$ = slowly varying phase function
Ω = rotational speed, rad/s
Ω_G = normalizing factor in Eq (12)

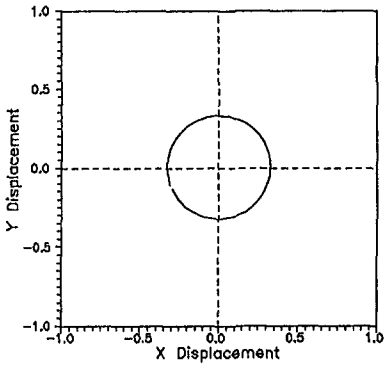

(a) Orbit Plot

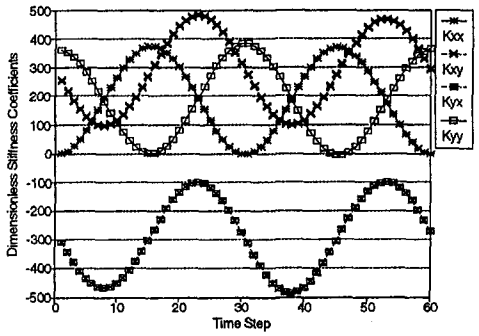

(b) Stiffness Coefficients

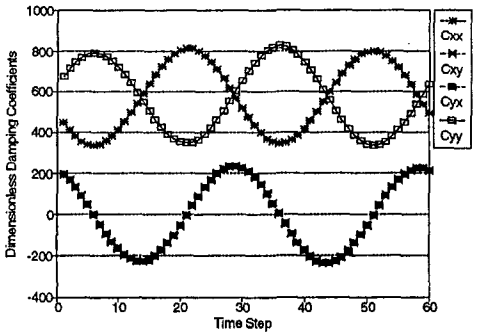

(c) Damping Coefficients

Fig. 1 Variation of quasi-linear dynamic coefficients of short journal bearing ($\epsilon_0 = 0.008$, $\rho = 0.3$)

freedom at the bearing stations, the other group (the slave coordinates) consists of all the remaining rotor degrees of freedom. The purpose of the partition is to find the linear relationship between these two groups of coordinates. Note that their relationship does not depend on the nonlinear bearing forces. The rotor degrees of freedom are then expressed in terms of the journal degrees of freedom. The derivation here assumes that the system contains two bearings. Hence, the original equations are reorganized so that only two equations contain the nonlinear bearing forces on the right hand side. These two equations are extracted for applying the method of averaging and the reduced stiffness and mass matrices of order 2 × 2 are obtained. The matrix equation is given by

$$M_r\ddot{x}_r + K_r x_r = F_x + C_r f_x \tag{7}$$

(2) Response Calculation. The equations of motion for the x and y directions are combined.

$$\begin{bmatrix} M_r & 0 \\ 0 & M_r \end{bmatrix}\begin{pmatrix} \ddot{x}_r \\ \ddot{y}_r \end{pmatrix} + \begin{bmatrix} K_r & 0 \\ 0 & K_r \end{bmatrix}\begin{pmatrix} x_r \\ y_r \end{pmatrix} = \begin{pmatrix} F_x \\ F_y \end{pmatrix} + \begin{bmatrix} C_r & 0 \\ 0 & C_r \end{bmatrix}\begin{pmatrix} f_x \\ f_y \end{pmatrix} \tag{8}$$

By applying the method of averaging, the unknown journal displacements are expressed in terms of eight slowly varying parameters x_{1c}, x_{1s}, x_{2c}, x_{2s}, y_{1c}, y_{1s}, y_{2c}, y_{2s} as given by

$$\begin{aligned} x_1 &= x_{1c}\cos\tau - x_{1s}\sin\tau \\ x_2 &= x_{2c}\cos\tau - x_{2s}\sin\tau \\ y_1 &= y_{1c}\cos\tau - y_{1s}\sin\tau \\ y_2 &= y_{2c}\cos\tau - y_{2s}\sin\tau \end{aligned} \tag{9}$$

These eight slowly varying parameters can be physically interpreted as the in-phase and out-of-phase components of the jour-

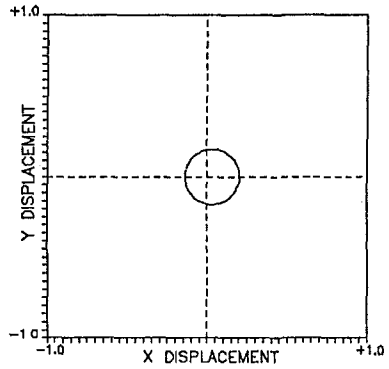

(a) Orbit Plot

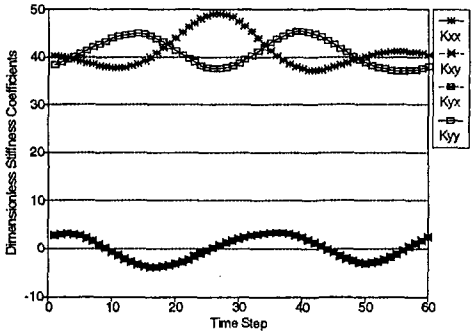

(b) Stiffness Coefficients

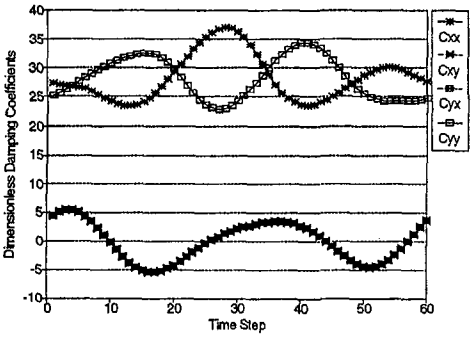

(c) Damping Coefficients

Fig. 2 Variation of quasi-linear dynamic coefficients of tilting-pad journal bearing ($\epsilon_0 = 0.05$, $\rho = 0.2$)

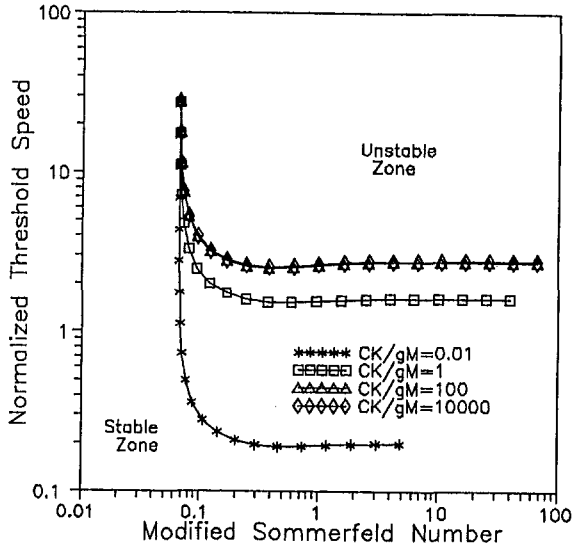

Fig. 3 Stability threshold speed curves of balanced rotors on short journal bearings

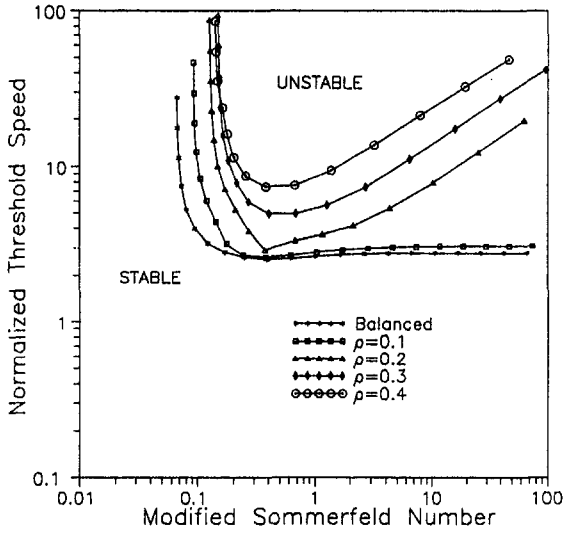

Fig. 4 Stability threshold speed curves of unbalanced rotors (CK/gM = 10000) on short journal bearings

nal displacements x_1, x_2, y_1, and y_2 at the bearing positions. Similar to the two parameters a and ϕ for an SDOF system, the eight parameters here represent the solution to the equations of motion for a reduced system with four degrees-of-freedom, i.e., the journal displacements x_1, x_2, y_1, and y_2.

Then a set of eight homogeneous equations of first order involving the slowly varying parameters is set up (cf. Eq. (5)). Averaging is applied to these equations, which contain the nonlinear bearing forces, and hence the quasi-linear bearing dynamic coefficients are utilized here in the computation. A Newton–Raphson iteration scheme is needed to estimate the eight slowly varying parameters, and the unbalance whirl orbit amplitudes are obtained by computing the journal displacements for a number of time intervals over one period.

(3) Stability Determination. The following variational equations of motion are formed:

$$\begin{bmatrix} M & 0 \\ 0 & M \end{bmatrix}\begin{pmatrix} \Delta\ddot{x} \\ \Delta\ddot{y} \end{pmatrix} + \begin{bmatrix} K & 0 \\ 0 & K \end{bmatrix}\begin{pmatrix} \Delta x \\ \Delta y \end{pmatrix} = \begin{pmatrix} \Delta F_x \\ \Delta F_y \end{pmatrix} \quad (10)$$

The time-averaged (quasi-linear) bearing dynamic coefficients are substituted for the bearing forces and hence yield the bearing damping and stiffness matrices, i.e.,

$$\begin{pmatrix} \Delta F_x \\ \Delta F_y \end{pmatrix} = -\begin{bmatrix} C_{xx} & C_{xy} \\ C_{yx} & C_{yy} \end{bmatrix}\begin{pmatrix} \Delta x \\ \Delta\dot{y} \end{pmatrix} - \begin{bmatrix} K_{xx} & K_{xy} \\ K_{yx} & K_{yy} \end{bmatrix}\begin{pmatrix} \Delta x \\ \Delta y \end{pmatrix} \quad (11)$$

A total matrix equation of second-order (derivatives in x and y) is formed by combining Eqs. 10 and 11. It is then converted to a first-order matrix equation in order to evaluate the eigenvalues. The system is stable if the real parts of all eigenvalues are negative and otherwise unstable. It should be mentioned that the quasi-linear bearing dynamic coefficients are utilized in both the iteration process of the response calculation and the eigenvalue calculation of the stability determination stage.

3 Analysis Results

Results obtained in this paper are based on flexible rotor models. In order to obtain generalized data for comparison, two rotor models are used. The first one is the well-known Jeffcott rotor model where there is only one disk mounted on a massless elastic shaft, which is supported by bearings at its two ends. The disk mass is M and the simply supported shaft stiffness is K. This is the rotor model used in Figs. 3 to 6. The second rotor model is the symmetrical three-disk rotor where there is one disk at each of the two bearing positions, in addition to the midspan rotor. The ratio of bearing disk mass m to midspan disk mass M introduces an additional parameter to the system. This three-disk model is used in Figs. 7 to 12.

The stability threshold of flexible rotors supported on short journal bearings is first considered. The threshold depends on factors such as the shaft stiffness and the amount of unbalance, etc. In Fig. 3 the stability threshold speed curves of rotors with different shaft stiffnesses are shown. The stability threshold speed is normalized as

$$\bar{\Omega} = \frac{\Omega}{\Omega_G} \qquad \Omega_G = \sqrt{\frac{g}{C}} \quad (12)$$

where g is the acceleration due to gravity and the normalized shaft stiffness is given by the dimensionless parameter

$$\bar{K} = \frac{CK}{gM} \quad (13)$$

where M is the disk mass. Figure 4 shows the stability threshold

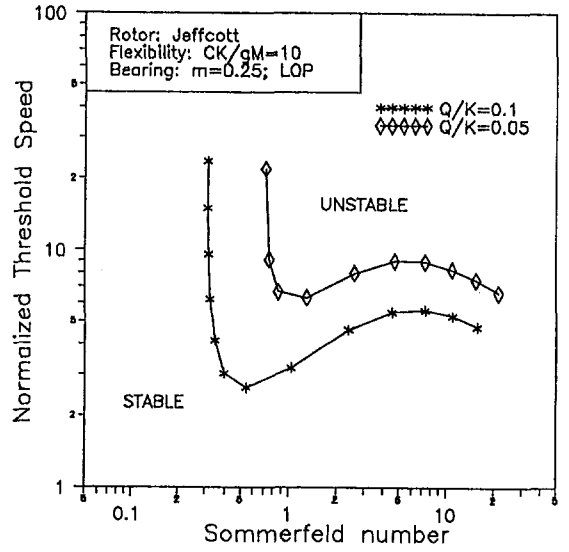

Fig. 5 Stability threshold speed curves of balanced rotors on tilting-pad journal bearings

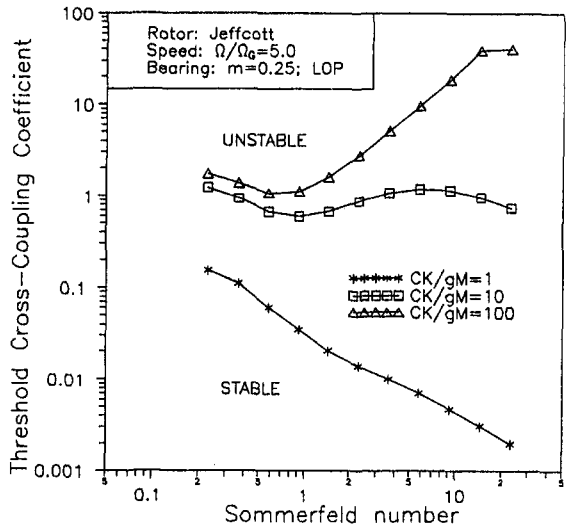

Fig. 6 Stability threshold cross-coupling curves of balanced rotors on tilting-pad journal bearings

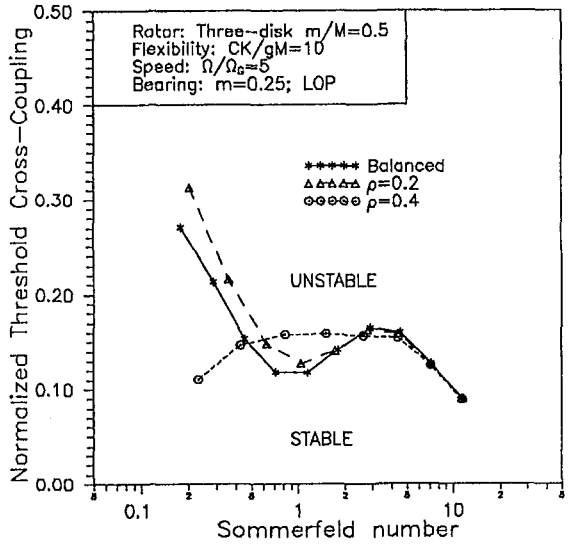

Fig. 8 Stability threshold cross-coupling curves of unbalanced rotors (*CK/gM* = 10) on tilting-pad journal bearings

speed curves for rotors of a particular shaft stiffness but carrying different amounts of unbalance. The dimensionless unbalance parameter is given by

$$\rho = \frac{r_u}{C} \tag{14}$$

where r_u is the radius of unbalance.

For rotors supported on tilting-pad journal bearings, instability problems can be caused by aerodynamic cross-coupling forces. The stability threshold of such rotor-bearing systems can be expressed in terms of the same threshold speed parameter as above. Figure 5 shows the threshold speed curves for two different levels of aerodynamic cross-coupling, which is nondimensionalized as

$$\bar{Q} = \frac{Q}{K} \tag{15}$$

where K is the shaft stiffness. Alternatively, the stability threshold can be displayed by plotting the threshold cross-coupling parameter, which is the level of aerodynamic cross-coupling when the system is on the borderline between stable and unstable conditions. Figure 6 is a plot of threshold cross-coupling curves for rotors of different shaft stiffnesses.

For all the results given above, the Jeffcott rotor model has been used. On the other hand, the flexible rotors employed in the following figures are the three-disk rotor model with a *m/M* ratio of 0.5. Figures 7 to 9 give the threshold cross-coupling curves for rotors carrying different amounts of unbalance. The normalized shaft stiffness (Eq. (13)) varies from 100 in Fig. 7 to 10 in Fig. 8 and 1 in Fig. 9. It is noted that the modified Sommerfeld number σ is used for short bearing cases and the conventional Sommerfeld number S is employed for tilting-pad bearing cases. They are defined by the equations

$$\sigma = \frac{1}{8}\frac{\mu\Omega DL}{W}\left(\frac{L}{C}\right)^2$$

$$S = \frac{\mu NDL}{W}\left(\frac{R}{C_p}\right)^2 \tag{16}$$

The whirl/speed ratio curves are shown in Fig. 10 for rotors of

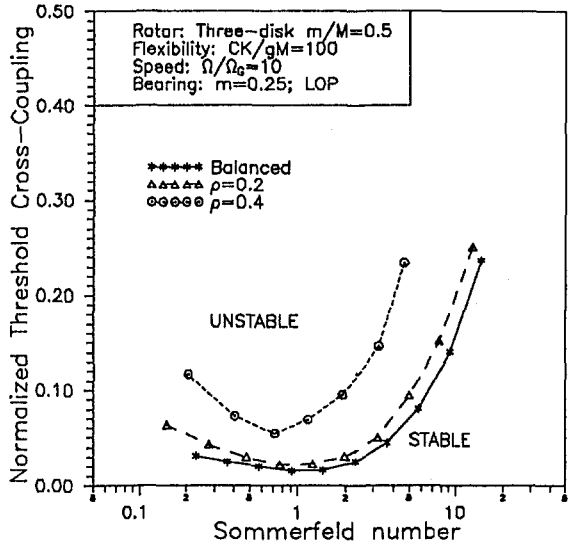

Fig. 7 Stability threshold cross-coupling curves of unbalanced rotors (*CK/gM* = 100) on tilting-pad journal bearings

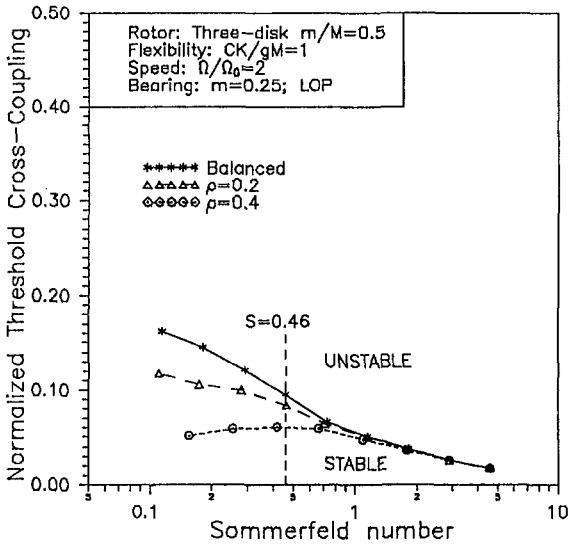

Fig. 9 Stability threshold cross-coupling curves of unbalanced rotors (*CK/gM* = 1) on tilting-pad journal bearings

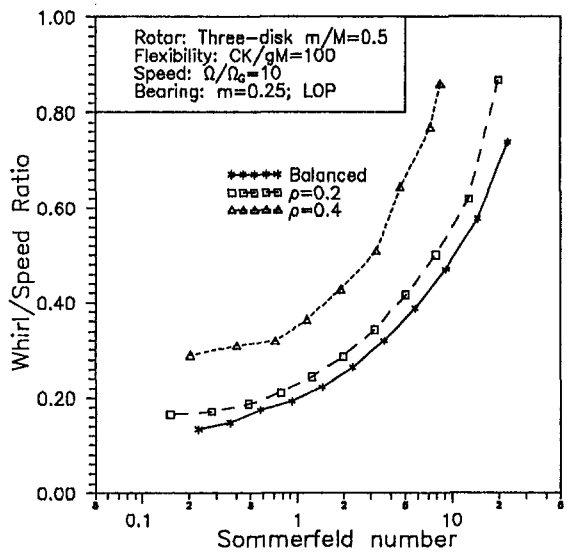

Fig. 10 Whirl/speed ratios at instability threshold of unbalanced rotors (CK/gM = 100) on tilting-pad journal bearings

a particular shaft stiffness but carrying different amounts of unbalance.

Finally, the results obtained by the time-marching numerical integration method are shown in Figs. 11 and 12 to verify the predictions of the method of averaging. These results can be compared with those intersection points along the line $S = 0.46$ in Fig. 9, which gives the threshold cross-coupling curves for the same rotor-bearing system configuration. Figure 11 shows the vibration orbit and frequency spectrum for a rotor with negligibly small unbalance ($\rho = 0.004$) and subjected to a normalized aerodynamic cross-coupling of 0.10. The corresponding orbit and spectrum for the same rotor with a larger unbalance ($\rho = 0.4$) under an aerodynamic cross-coupling of 0.06 are plotted in Fig. 12.

4 Discussion

It can be seen from Figs. 1 and 2 that the quasi-linear bearing dynamic coefficients vary along the unbalance response orbit. They are not only functions of the journal displacements but also functions of the journal velocities. That is, even if the journal passes through the same position, but with different velocities, the dynamic coefficients do not have the same values. In contrast with short journal bearings, which have cross-coupled stiffness coefficients in the same order of magnitude as the direct coefficients, the cross-coupled stiffness coefficients of tilting-pad journal bearings are in general an order of magnitude smaller than their direct counterparts. Moreover, the cross-coupled stiffness coefficients K_{xy} and K_{yx} of tilting-pad journal bearings are equal, and their variation over one cycle with almost equal positive and negative contributions yields average values close to zero. When only the time-averaged coefficients are considered in the stability analysis, the destabilizing effect of bearing cross-coupled stiffness is negligible in the case of tilting-pad journal bearings.

For rotors supported on short journal bearings, the bearing cross-coupled stiffness will generate an instability at high shaft rotational speeds commonly referred to as oil whirl/whip (Muszynska, 1986). The parameter of interest is usually the stability threshold speed, i.e., the speed above which the rotor will be dynamically unstable. As shown in Fig. 3, the threshold speed of flexible rotors is dependent on the shaft stiffness. The more flexible the shaft is, the lower the threshold speed. This is because the natural frequency of the rotor is lower for a more flexible shaft and instability occurs often when the rotational speed is above two times the rotor's natural frequency. When the rotor is unbalanced, the stability threshold is affected by the unbalance response since the dynamic characteristics of the bearings is nonlinear. The effect depends on the shaft stiffness but, broadly speaking, the stability threshold speed is increased when there is unbalance in the rotor. The larger the mass unbalance is, the higher the threshold speed as shown in Fig. 4. This is in agreement with predictions based on the rigid rotor model (Lund and Nielsen, 1980). The improvement in stability characteristics for unbalanced rotors can be qualitatively explained by an increase in the natural frequency due to a larger effective bearing direct stiffness, especially at high Sommerfeld numbers or lightly loaded conditions.

For rotors supported on tilting-pad journal bearings, instability problems arise often because of fluid-mechanical interaction forces, which can be represented by aerodynamic cross-coupling coefficients. The stability threshold speed of such rotor-bearing systems depends on the level of aerodynamic cross-coupling. The higher the level of aerodynamic cross-coupling is, the lower the threshold speed, as shown in Fig. 5. Alternatively, the maximum level of aerodynamic cross-coupling the system can endure before becoming dynamically unstable is a measure of the stability performance of these rotor-bearing

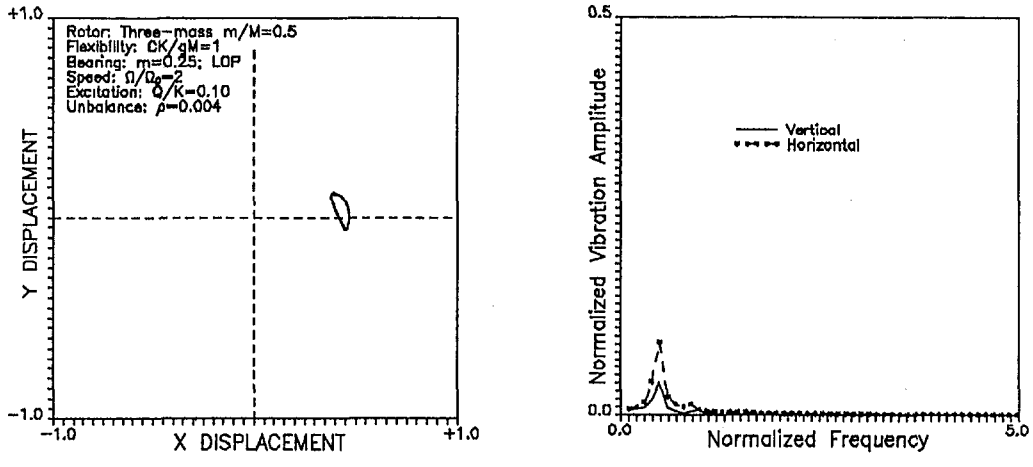

(a) Response plot (Q/K=0.10) (b) Frequency spectrum

Fig. 11 Response plot obtained by numerical integration and frequency spectra for balanced rotor (CK/gM = 1, ρ = 0.004) on tilting-pad journal bearings

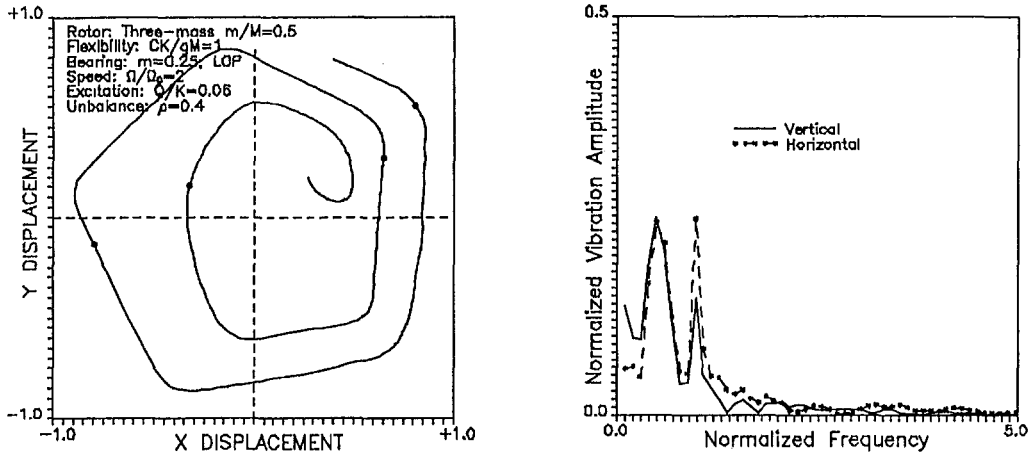

(a) Response plot (Q/K=0.06) (b) Frequency spectrum

Fig. 12 Response plot obtained by numerical integration and frequency spectra for unbalanced rotor (CK/gM = 1, ρ = 0.4) on tilting-pad journal bearings

systems. That a system can stand a larger threshold cross-coupling implies that the system is more stable against aerodynamic excitation. Similar to the short bearing cases, the shaft stiffness influences the stability threshold. As can be observed from Fig. 6, the system threshold cross-coupling is smaller when the shaft is more flexible. This can be explained by the fact that the stabilizing influence in the system comes from the bearing damping. The damping effect is reduced if the shaft becomes more flexible and the journal motions at the bearings get smaller in amplitude. Note that the threshold cross-coupling curves are calculated at a fixed operating speed. They change with different operating speeds, but the general trend is similar.

One of the most interesting results discovered in this study is the effect of unbalance on the stability of flexible rotors supported on tilting-pad journal bearings. The stability behavior of unbalanced rotors also depends on the shaft stiffness. For relatively stiff shafts (CK/gM = 100 in Fig. 7), the presence of mass unbalance improves the stability threshold, i.e., the unbalanced system can endure a higher level of aerodynamic cross-coupling without turning unstable. For medium shaft stiffness (CK/gM = 10 in Fig. 8), the effect is more difficult to generalize. A small amount of mass unbalance can slightly improve the stability threshold, but a large amount can have the opposite effect. When the shaft is fairly flexible (CK/gM = 1 in Fig. 9), the addition of mass unbalance causes a deterioration in the stability threshold. In effect, the unbalanced rotor becomes unstable at a lower level of aerodynamic cross-coupling than a balanced rotor. This is important since the linearized analysis then does not always yield a conservative estimate of the stability boundary. In practice, it will be advantageous to minimize the residual unbalance in view of the stability consideration.

A useful diagnosis tool in vibration monitoring is the spectrum analysis of the rotor vibration. The characteristics of unstable vibrations due to aerodynamic cross-coupling forces is revealed by the ratio of whirl frequency to rotational speed. It has been found that the whirl frequency in such instability problems is typically subsynchronous, i.e., the whirl/speed ratio is less than unity and usually varies from 0.3 to 0.8. This is also the reason why the subsynchronous behavior of tilting-pad journal bearings is of interest (White and Chan, 1992).

The accuracy of the method of averaging is dependent on such factors as the slowly varying parameters, number of averaging points in one cycle, deviation from the assumption of quasi-harmonic response, etc. It varies from case to case and cannot be established generally. Nevertheless, the validity of the results in this study has been confirmed by cross-checking with results from the time-marching numerical integration method, for example, results shown in Figs. 11 and 12. By comparing Figs. 11 and 12, the stability threshold of the unbalanced flexible rotor is obviously lower than that of the well-balanced rotor. They clearly demonstrate the negative effect of mass unbalance on stability under such conditions. The operating conditions for the rotor-bearing system in Figs. 11 and 12 are close to the line S = 0.46 in Fig. 9. The good agreement of the normalized threshold cross-coupling at the intersection points in Fig. 9 with those in Figs. 11 and 12 also verifies the accuracy of the present method.

5 Conclusions

The following conclusions can be drawn from the results in this study:

1 The concept of quasi-linear bearing dynamic coefficients is explained and utilized in the method of averaging, which accounts for the effect of bearing nonlinearity in an approximate manner. Their usefulness is reflected in the stability prediction using the method of averaging.

2 The method of averaging has been extended to calculate the stability threshold of flexible rotors supported on short journal bearings. The effect of shaft stiffness on the stability threshold has been investigated and it is found that the more flexible the shaft is, the lower the threshold speed. The stability threshold is found to be improved by the presence of mass unbalance on the rotor. The threshold speed becomes higher when the amount of unbalance increases. This is explained by an increase in system natural frequency due to a larger effective bearing direct stiffness.

3 The method of averaging is also applied to investigate the stability threshold of rotors supported on tilting-pad journal bearings and subjected to aerodynamic cross-coupling. The threshold speed of such systems decreases when the cross-coupling becomes larger. The threshold cross-coupling is used as an alternative measure of stability performance for such systems. The stability threshold is lower for rotors with higher shaft flexibility because the effective bearing damping effect, which stabilizes the rotor-bearing system, is reduced by a smaller journal amplitude. The presence of mass unbalance is not necessarily beneficial to the stability of such systems. For fairly flexible rotors, increasing the unbalance can lead to a deterioration of the stability threshold.

4 It has been shown that the main characteristic of rotordynamic instabilities due to aerodynamic cross-coupling is the

subsynchronous vibration frequency, i.e., a whirl/speed ratio of less than unity. This is a useful diagnosis tool in the vibration monitoring of high-speed turbomachinery.

5 The results from the time-marching numerical integration method confirm the validity and accuracy of the predictions by using the method of averaging. Therefore, the method of averaging offers a computationally efficient method for nonlinear rotordynamic analysis.

Acknowledgments

The author is most grateful to the Kværner Engineering A.S for giving the opportunity and support during the period over which this paper was written. Thanks must also be given to Professor Maurice White and the Department of Marine Engineering at the Norwegian Institute of Technology (NTH), University of Trondheim, where the main part of this study has been carried out.

References

Adams, M. L., 1980, "Non-linear Dynamics of Flexible Multi-bearing Rotors," *Journal of Sound and Vibration,* Vol. 71, No. 1, pp. 129–144.

Chan, S. H., 1992, "Nonlinear Analysis of Rotordynamic Instabilities in High-Speed Turbomachinery," Doctoral Thesis, Norwegian Institute of Technology, University of Trondheim.

Choy, F. K., et al., 1992, "Nonlinear Transient and Frequency Response Analysis of a Hydrodynamic Journal Bearing," ASME *Journal of Tribology,* Vol. 114, pp. 448–454.

Ehrich, F. F., and Childs, D., 1984, "Self-Excited Vibrations in High-Performance Turbomachinery," *Mechanical Engineering,* May, pp. 66–79.

Ehrich, F. F., 1992, *Handbook of Rotordynamics,* McGraw-Hill, New York.

Gunter, E. J., 1966, "Dynamic Stability of Rotor-Bearing Systems," NASA Report SP-113, Washington, DC.

Holmes, R., 1970, "Non-linear Performance of Turbine Bearings," *Journal of Mechanical Engineering Science,* Vol. 12, No. 6, p. 377.

Hwang, J. L., and Shiau, T. N., 1991, "An Application of the Generalized Polynomial Expansion Method to Nonlinear Rotor Bearing Systems," ASME *Journal of Vibration and Acoustics,* Vol. 113, pp. 299–308.

Lund, J. W., et al., 1965, "Rotor-Bearing Dynamics Design Technology, Pt. III: Design Handbook for Fluid Film Type Bearings," Technical Report AFAPL-TR-65-45, Aero Propulsion Lab, Wright-Patterson Air Force Base, Ohio.

Lund, J. W., and Nielsen, H. B., 1980, "Instability Threshold of an Unbalanced Rigid Rotor in Short Journal Bearings," *Proc. 2nd International Conference on Vibrations in Rotating Machinery,* Institution of Mechanical Engineers, Cambridge, Paper No. C263/80, pp. 91–95.

Lund, J. W., 1987, "Review of the Concept of Dynamic Coefficient for Fluid Film Journal Bearings," ASME *Journal of Tribology,* Vol. 109, pp. 37–41.

Muszynska, A., 1986, "Whirl and Whip-Rotor/Bearing Stability Problems," *Journal of Sound and Vibration,* Vol. 110, No. 3, pp. 443–462.

Nataraj, C., and Nelson, H. D., 1989, "Periodic Solutions in Rotor Dynamic System With Nonlinear Supports: A General Approach," ASME *Journal of Vibration, Acoustics, Stress, and Reliability in Design,* Vol. 111, pp. 187–193.

Schmidt, G., and Tondl, A., 1986, *Non-linear Vibrations,* Cambridge University Press, Cambridge, United Kingdom.

White, M. F., and Chan, S. H., 1992, "The Subsynchronous Dynamic Behaviour of Tilting-Pad Journal Bearings," ASME *Journal of Tribology,* Vol. 114, pp. 167–173.

Forced Harmonic Response of Grouped Blade Systems: Part I — Discrete Theory

L. F. Wagner
Power Generation Technology Division,
Westinghouse Electric Corporation,
Pittsburgh, PA 15235

J. H. Griffin
Department of Mechanical Engineering,
Carnegie Mellon University,
Pittsburgh, PA 15213

The vibration of grouped blades on a flexible disk cannot be analyzed using procedures developed for individual, uncoupled groups. The bladed-disk system must be considered either in whole, or as a structure composed of cyclically symmetric sectors. The latter approach, while being computationally more economical, is more complicated to implement because both the structural system and the applied forces must be transformed to a system based on the geometry of a single sector. However, the sector transformation permits a natural ordering of the modes that cannot be obtained from a complete system model. This paper describes the development of the sector model, and the associated transformation of the applied harmonic forces typically prevalent in turbomachinery. The displacements are expressed in a series of the natural modes of a transformed sector, and expressions are developed for maximum displacements of the complete structure. This approach leads to an easier interpretation of the analytical results and an improved physical understanding of the response. For example, it is shown that a single harmonic, or engine-order excitation, can cause response in only a restricted subset of modes.

Introduction

An effective technique for decreasing the vibratory response of turbine blades is to assemble the blades into groups or packets. The interblade constraints imposed by the grouping mean that no individual blade need withstand the maximum force amplitudes resulting from harmonic excitation or local transients. The grouping is accomplished by mechanically coupling the blades together using lashing wires or shrouds. In addition to its function of coupling, a shroud typically functions as a sealing surface to help direct flow through the blade passages by keeping the radial flow components as small as possible. Lashing wires are used almost exclusively for connecting adjacent blades, but also occasionally to provide friction damping by fitting the wires through close clearance holes in the blades.

While imparting increased mechanical strength to each blade, grouping also tends to desensitize the thermodynamic performance to changes in blade passage geometry brought on by the centrifugal effects of the untwisting of a pretwisted blade. Vibratory characteristics are generally improved, as evidenced by an increase in the natural frequencies of modes that are mostly tangentially directed (i.e., in the plane of the disk). A particularly desirable benefit of blade grouping is the possible minimization of vibratory response of certain modes to specific orders of harmonic excitation (see, e.g., Ortolano et al., 1981; Wagner and Griffin, 1993). Grouping will also reduce the sensitivity of individual blades to mistuning, because the blades that would otherwise respond would be constrained by adjacent blades.

Although the benefits of blade grouping are notable, grouping is not, by any means, a panacea. Shrouds and lashing wires increase the steady-state centrifugal loading on each blade, and radial extension due to centrifugal force causes the end blades to bend toward the center of the group because of shroud or lashing wire tangential constraints. Although untwisting of individual blades can be controlled by grouping, coupling between torsion and bending may result in nonuniform positioning of the blades relative to the flow field (i.e., gross twisting of the group). However, it is of most significance to blade designers that grouping of blades causes problems for dynamic analysis, resulting in more complex modeling with more degrees of freedom and consequently more computing effort. The geometric complexity of the blade-group system, that is, the nonaxisymmetry, also makes an understanding of the vibratory phenomena extremely difficult to obtain.

Many investigators have modeled blade groups by ignoring the disk and fixing the blades at the roots (e.g., Thomas and Belek, 1977; Sabuncu and Thomas, 1992). The assumption that the disk can be ignored is only appropriate if the disk stiffness is high compared to that of the group. If these stiffnesses are comparable, the blade groups and disk must be modeled as a system. If the system is nearly rotationally symmetric (i.e., a large number of blades on an axisymmetric disk), it would seem very reasonable to exploit the symmetry, and assume that the variation in circumferential displacement for any mode would be sinusoidal. This is, in fact, a popular and efficient technique (Kirkhope and Wilson, 1976), giving rise to mode shapes characterized by equally spaced, zero displacement diametral lines or "nodal diameters," and by circles of zero displacement referred to as "nodal circles." Thus, individual freestanding blades on a flexible disk, or blades continuously coupled with a shroud, can be reasonably well modeled by assigning each mode to a given nodal diameter of the disk. For each desired nodal diameter, this type of semi-analytical model allows the disk to be considered as a one-dimensional extension from the blade attachment point to the disk bore. This idea is extremely convenient, but is not generally applicable to the modal description of grouped-bladed disks, which depart from rotational symmetry and have modes that may be composed of more than one nodal diameter component. It must be emphasized that assigning the nodal diameters amounts to creating a *constraint* for the system, which for grouped blades does not always allow the occurrence of the natural modal patterns. Thus, grouped blade analysis using the assigned nodal diameter method will lead to errors in modal and response calculations, such as the identification of false modes (Ewins and Imregun, 1984), and it also tends to create difficulties in concise categorization of the modes.

Contributed by the International Gas Turbine Institute and presented at the 39th International Gas Turbine and Aeroengine Congress and Exposition, The Hague, The Netherlands, June 13 – 16, 1994. Manuscript received by the International Gas Turbine Institute February 15, 1994. Paper No. 94-GT-203. Associate Technical Editor: E. M. Greitzer.

The most direct method for analysis of assemblies of grouped blades attached to a flexible disk is to model the full system. This analysis will generally result in many modes, including repeated and closely spaced roots, which can be nearly impossible to interpret. Additionally, computation of the full system modes is often prohibitively expensive. An equally accurate, but far less costly, alternative is to take advantage of the rotationally periodic, or cyclically symmetric, nature of the structure. Such an analysis makes use of a single blade-group sector model, and seeks solutions for a series of problems, each based on separate, but related, boundary constraints (an early example of calculating modes using a sector model is given by Salama et al., 1976). Thus, a full system computation is replaced with a series of much smaller and significantly less expensive calculations, which yield the same results, and additionally provide a natural and convenient ordering of the modes that the full system model cannot (Wagner and Griffin, 1993). A recent related technique for determining the transient response of cyclically symmetric structures, based on the Ritz-Wilson technique, has been presented by Balasubramanian et al. (1993).

This paper describes a discrete sector model for a cyclically symmetric, bladed-disk system, along with the associated transformation of the harmonic exciting forces typically found in turbomachinery. Expressions are developed, via modal participation factors, for the blade displacements, with stress determination being a forthright extension. The core of this work is based on that of Thomas (1979), who developed a theory for calculating the modes of a cyclically symmetric structure by analyzing a single sector, and on the numerical procedures of Cai et al. (1990), who treated the uncoupling of discretized equations for structures with general periodic properties. A similar uncoupling technique, using a method of complex constraints, was developed by Wildheim (1981). The current research is an extension of Wildheim's work in that it develops explicit expressions for the resonant response of grouped blades, and a specialization and extension of the work of Cai et al. to cyclic symmetric systems. A companion paper (Wagner and Griffin, 1996) demonstrates the application of this numerical model.

Modes of Cyclically Symmetric Structures

Effective vibration analysis of grouped blades is intimately associated with an understanding of the system modal characteristics. A system composed of multiple groups of blades supported by a flexible disk provides an example of a rotationally periodic, or cyclically symmetric structure, and such a system can be efficiently analyzed by making use of this symmetry. Thomas (1979) has shown that the modes of such a repeating structure can be found by imposing constraints on the equations of motion for a single substructure, such as that shown in Fig. 1. The displacement constraints are of the form

$$\{d_R\} = e^{\mu}\{d_L\} \tag{1}$$

where $\{d_R\}$ and $\{d_L\}$ are displacement vectors on the right- and left-hand boundaries, with similar constraints for the forces. μ has been termed the "propagation constant" and must be purely imaginary with values between $-i\pi$ and $i\pi$. Thomas shows that any normal mode of vibration for such a structure can be regarded as a standing wave, and that for N substructures, the propagation constant must satisfy

$$e^{N\mu} = 1 \tag{2}$$

which is simply a constraint that enforces periodicity. There are N independent values of the imaginary part of μ, which is referred to as the "phase constant," but the negative values are associated with mode shapes of the same form as those for the corresponding positive values, with the circumferential direction reversed. The frequencies associated with the positive and negative propagation constants are also identical. Thus, all the natural frequencies for the complete cyclically symmetric structure can be obtained by consideration of a single substructure which is subject to the constraints imposed by Eq. (1), and by considering only positive (or negative) propagation constants, with the inclusion of $\mu = 0$. Note that for N even, the imaginary part of μ must take the $N/2 + 1$ values

$$0, 2\pi/N, 4\pi/N, \ldots 2\pi(N/2 - 1)/N, \pi$$

and for N odd, the $(N + 1)/2$ values

$$0, 2\pi/N, 4\pi/N, \ldots 2\pi(N - 1)/2N$$

Although it is sufficient to consider only nonnegative values of μ for definition of the modes, modal summation techniques used for forced response analysis require the consideration of all N independent values of the phase constant.

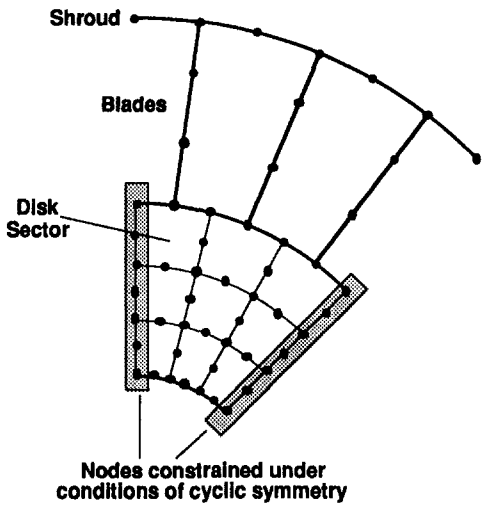

Fig. 1 Discrete cyclically symmetric sector model of a blade group on a flexible disk

The mode shapes of cyclically symmetric structures are of the following three different types:

(a) All substructures vibrate with identical shapes. Rotating the mode shape for a given substructure through any integral number of substructures leaves the mode unchanged. This shape occurs for $\mu = 0$, and is completely described by a single eigenvalue and eigenvector.

(b) Each substructure has the same shape as its neighbor, but vibrates in antiphase. This mode shape is unchanged for rotation through an even number of substructures. Rotation through an odd number of substructures changes the phase of the vibration by π. This phase change, however, does not constitute a new shape for the mode, and thus, as with case (a), this mode is also represented by a single eigenvalue and eigenvector. This mode shape is possible only for an even number of substructures with either $\mu = -i\pi$ or $i\pi$.

(c) All remaining substructure modes are degenerate and occur in orthogonal pairs. These modes can be conveniently represented by a pair of complex modes, which can be shown to be conjugates. This property can be used to great advantage for simplification of the numerical computation of harmonic response.

These modes can be further described by noting that, in any normal mode, the displacements of adjacent substructures must differ in phase by a constant value Ψm, where Ψ is the angular extent of a single substructure, and m is an integer ($m = 0, 1, 2, \ldots N/2$ for N even, and $m = 0, 1, 2, \ldots (N - 1)/2$ for N odd), which facilitates incrementation of the imaginary part of the propagation constant. The values of m are thus used as phase

indices and will be referred to as "mode harmonics." Although a given value for m will impose constraints on the substructure boundaries, a complete set of modes is associated with each value of m.

Reduction of the Full System Model to a Sector Model

Computational efficiency is an important factor for the analysis of grouped blades, and taking advantage of cyclic symmetry is the best way to reduce computation. Thus, following the theory of Thomas (1979), and of Cai et al. (1990), it will be shown that the full system discretized equations can be decoupled to form a reduced system for a single sector. In addition, the applied harmonic forces will also be reduced in a manner that shows dependence upon bladed-disk mode harmonics.

Decoupling of the Sectors. The matrix equation for undamped, forced vibration of a complete bladed-disk structure, composed of N cyclically symmetric substructures (blade groups), can be written

$$[M]\{\ddot{X}\} + [K]\{X\} = \{P\} \tag{3}$$

where $[K]$ and $[M]$ are symmetric and cyclic, stiffness and mass matrices. This equation has eigenvalues $\lambda_k^{(m)}$, which are the squares of the system natural frequencies, and eigenvectors $\tilde{\Phi}_k^{(m)}$ corresponding to the kth mode of the mth mode harmonic. The stiffness matrix has the following form:

$$[K] = \begin{bmatrix} K_{11} & K_{12} & \cdots & K_{1N} \\ K_{21} & K_{22} & \cdots & K_{2N} \\ \vdots & & & \vdots \\ K_{N1} & K_{N2} & \cdots & K_{NN} \end{bmatrix} \tag{4}$$

and similarly for $[M]$. $\{P\}$ and $\{X\}$ are forcing and displacement vectors given by

$$\{X\} = \{X_1\ X_2 \ldots X_N\}^T, \quad \{P\} = \{P_1\ P_2 \ldots P_N\}^T$$

Here $\{X_j\}$ and $\{P_j\}$ are the displacement and force vectors for the jth substructure. Due to the periodicity of the structure, each of the submatrices $[K_{rs}]$ can be shown to possess the following dependencies:

$$\begin{aligned} [K_{11}] &= [K_{22}] = \ldots = [K_{NN}] \\ [K_{rs}] &= [K_{sr}]^T \quad s, r = 1, 2, \ldots, N \\ [K_{1s}] &= [K_{2,s+1}] = \ldots = [K_{N-s+1,N}] \\ &= [K_{N-s+2,1}] = \ldots = [K_{N,s-1}] \\ & \qquad s = 2, 3, \ldots, N \end{aligned} \tag{5}$$

and similarly for $[M_{rs}]$.

Recalling the work of Thomas (1979), it was shown that the deflection of one substructure of a rotationally periodic structure vibrating in a given mode has the same amplitude, but a constant phase difference, relative to the deflection of the preceding substructure. This can be written in discretized form for the jth substructure vibrating in the kth mode of the mth mode harmonic family as

$$\{\Phi_k^{(m)}\}_j = e^{im\Psi}\{\Phi_k^{(m)}\}_{j-1} \tag{6}$$

and the eigenvector for the complete structure can thus be expressed as

$$\{\tilde{\Phi}_k^{(m)}\}_j = [U_m]\{\Phi_k^{(m)}\} \tag{7}$$

where $\{\Phi_k^{(m)}\}$ refers to the first (arbitrary) substructure and

$$[U_m] = \frac{1}{\sqrt{N}}[e^{im\Psi}I_J\ e^{2im\Psi}I_J \ldots e^{i(N-1)m\Psi}I_J]^T$$

Note that there are J degrees of freedom in each substructure, and $[I_J]$ denotes a unit matrix of order J. The value $\sqrt{N}$ is a normalizing factor.

According to the expansion theorem commonly used in vibration theory, all possible displacements of a structure can be expressed in a series of the natural modes, and thus for the present problem,

$$\{X\} = \sum_{m=1}^{N}\sum_{k=1}^{J} \eta_{mk}[U_m]\{\Phi_k^{(m)}\} \tag{8}$$

This may be more succinctly written as

$$\{X\} = [U]\{q\} \tag{9}$$

where

$$[U] = [U_1\ U_2\ U_3 \ldots U_N]$$

and

$$\{q\} = \{q_1\ q_2\ q_3 \ldots q_N\}^T$$

with the sector reduced coordinates given by

$$\{q_m\} = \sum_{k=1}^{J} \eta_{mk}\{\Phi_k^{(m)}\} \tag{10}$$

which are also referred to as "mode subspace coordinates" (Cai et al., 1990). Substituting Eq. (9) into Eq. (3) and premultiplying by $[U^*]^T$, with the * denoting the complex conjugate, yields the following transformed system:

$$[m]\{\ddot{q}\} + [k]\{q\} = \{p\} \tag{11}$$

where

$$\begin{aligned} [m] &= [U^*]^T[M][U], \\ [k] &= [U^*]^T[K][U], \\ \{p\} &= [U^*]^T\{P\} \end{aligned}$$

In general, the matrix $[k]$ has the same form as Eq. (4), namely,

$$[k] = \begin{bmatrix} k_{11} & k_{12} & \cdots & k_{1N} \\ k_{21} & k_{22} & \cdots & k_{2N} \\ \vdots & & & \vdots \\ k_{N1} & k_{N2} & \cdots & k_{NN} \end{bmatrix} \tag{12}$$

with $[m]$ taking the same form. The block partitions of matrices $[k]$ and $[m]$ can be shown to be as follows:

$$[k_{rs}] = [U_r^*]^T[K][U_s] = [0], \quad r \neq s \tag{13}$$

and

$$\begin{aligned} [k_{mm}] &= [U_m^*]^T[K][U_m] = [k_m] \\ &= [K_{11} + K_{12}e^{im\Psi} + K_{12}^T e^{-im\Psi}] \end{aligned} \tag{14}$$

and again with similar forms for $[m]$. Thus, it is clear that $[k]$ and $[m]$ are block-diagonal matrices of complex elements, dependent on the mode harmonic m, which make up N independent systems of equations. In fact, $[k]$ and $[m]$ are also *Hermitian* in form, that is,

$$[k] = [k^*]^T \quad \text{and} \quad [m] = [m^*]^T \tag{15}$$

The eigenvalues of the homogeneous Hermitian system for each sector are real, and the eigenvectors are complex and orthogonal relative to the mass and stiffness matrices in the Hermitian sense (Hildebrand, 1965), viz.,

$$\begin{aligned} \{\Phi_r^{(m)*}\}^T[m_m]\{\Phi_s^{(m)}\} &= 0 \\ \{\Phi_r^{(m)*}\}^T[k_m]\{\Phi_s^{(m)}\} &= 0 \end{aligned} \tag{16}$$

where $r \neq s$. We can now write an equation for the reduced system as

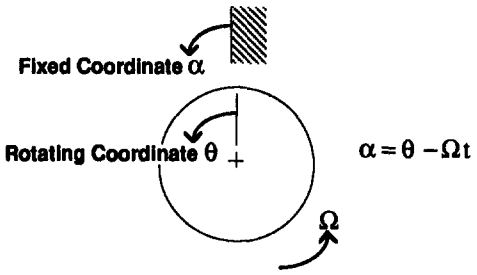

Fig. 2 Fixed and rotating coordinate systems

$$[m_m]\{\ddot{q}_m\} + [k_m]\{q_m\} = \{p_m\} \tag{17}$$

and an expression for the effective sector forces, given by

$$\{p_m\} = [U_m^*]^T\{P\} = \frac{1}{\sqrt{N}}\sum_{r=0}^{N-1} e^{-irm\Psi}\{P_r\} \tag{18}$$

where $r = 0$ refers to the first substructure.

A different approach to this decoupling problem, which results in the same reduced set of equations was presented by Wildheim (1981).

Solution of the Reduced System. The reduced system of Eq. (17) can readily be solved by methods of coordinate decoupling with an extension to Hermitian systems. Thus, making the following substitution for the reduced sector coordinate:

$$\{q_m\} = [\Phi^{(m)}]\{\eta_m\} \tag{19}$$

where it has been assumed that the reduced system eigenvalue problem has been solved, and $[\Phi^{(m)}]$ is the sector modal matrix with columns composed of the complex eigenvectors. The eigenvectors have been normalized so that the maximum modulus value has been set to unity. By making use of the orthogonality condition (16), the system (17) is transformed to a new system of uncoupled equations, which can be written in component form for mode n as

$$\ddot{\eta}_{mn} + \omega_n^{(m)2}\eta_{mn} = \frac{1}{M_{mn}}\{\Phi_n^{(m)*}\}^T\{p_m\} \tag{20}$$

with the generalized mass given by

$$M_{mn} = \{\Phi_n^{(m)*}\}^T[m_n]\{\Phi_n^{(m)}\} \tag{21}$$

which, being a Hermitian product, is real and also positive.

The steady-state solution to Eq. (20) for the reduced sector modal coordinates can be written

$$\eta_{mn} = \frac{\{\Phi_n^{(m)*}\}^T\{p_m\}}{M_{mn}(\omega_n^{(m)2} - \omega^2)} \tag{22}$$

where the forces have been assumed to be harmonic. This expression can only be practically used after transformation back to physical coordinates and by accounting for the effects of damping. Furthermore, we must still define a usable, discretized form for the effective forces imposed on a sector.

Equivalent Forces Over a Sector. The most prevalent form of blade excitation found in a rotating machine is developed by the rotation of the bladed disk through the steady-state flow pattern, which is fixed in space. This pattern is generally circumferentially nonuniform around the blade annulus. Thus, each blade will experience a superposition of steady forces, and periodically time-varying forces, which are directly related to the speed of rotation. The steady forces, in concert with rotation, provide the required work for the desired energy transformation. The time-varying excitation is made up of one or more frequencies that are integer multiples or "harmonics" of the rotating speed. The harmonics are also referred to, primarily in the aircraft industry, as "engine-order" excitation.

With reference to Fig. 2, the fixed-in-space pressure field, $P(r, \alpha)$, immediately upstream of the blade annulus, ignoring random deviations, can be described in the form of a Fourier series as

$$P(r, \alpha) = \sum_{n=1}^{\infty}(a_n(r)\cos n\alpha + b_n(r)\sin n\alpha) \tag{23}$$

where r is radius, α is a fixed-in-space circumferential coordinate, and a_n and b_n are known functions of radius. A general response analysis, which relies on mode summation, would require consideration of both sine and cosine terms in this expression, thus including phasing information. However, the following analyses will be based on single-mode response to an individual harmonic, and since the structure is periodic and response amplitudes are sought, the phase can be shown to be irrelevant. Under these conditions, and noting that transformation from fixed coordinates to coordinates rotating with the disk at rotational speed Ω is given by $\alpha = \theta - \Omega t$, the force distribution due to a given excitation harmonic h can be written

$$f(r, \theta, t) = A(r)\cos h(\theta - \Omega t) \tag{24}$$

which can be expanded to give

$$f(r, \theta, t) = A(r)[\cos h\theta \cos \omega t + \sin h\theta \sin \omega t] \tag{25}$$

where $\omega = h\Omega$. We see that the rotation gives rise to a periodic time variation of the forces applied to the blades, and thus a vibratory excitation. The time variation components are linearly independent and will be considered separately in the remaining work. Looking at just the cos ωt part of Eq. (25), and writing the force applied to the first sector, we have,

$$f_1^c(r, \theta') = A(r)\cos h\theta' \tag{26}$$

noting again that h is the excitation harmonic, and that θ' is a local sector circumferential coordinate. The force applied to the second sector is then

$$f_2^c(r, \theta') = A(r)\cos h(\theta' + \Psi) \tag{27}$$

and by extension to the jth arbitrary sector followed by trigonometric expansion, we have

$$f_j^c(r, \theta') = A(r)[\cos h\theta' \cos h(j-1)\Psi - \sin h\theta' \sin h(j-1)\Psi] \tag{28}$$

and similarly for the sin ωt component,

$$f_j^s(r, \theta') = A(r)[\sin h\theta' \cos h(j-1)\Psi + \cos h\theta' \sin h(j-1)\Psi] \tag{29}$$

Using the same transformation of forces from the full system to a sector as that given by Eq. (18), we can write the following expression for the effective distributed force, $\hat{f}$, over one sector, i.e.,

$$\hat{f}(m, r, \theta) = \frac{1}{\sqrt{N}}\sum_{q=0}^{N-1} e^{-iqm\Psi}\cdot(f_q^c\cos\omega t + f_q^s\sin\omega t) \tag{30}$$

where $q = j - 1$, and the prime has been dropped from θ for convenience. Note that the effective force is a function of the mode harmonic. Looking at just the cos ωt component in Eq. (30), we find by expansion,

$$\hat{f}^c(m, r, \theta) = \frac{A(r)}{\sqrt{N}}(\cos h\theta \sum_{q=0}^{N-1}\cos hq\Psi e^{-iqm\Psi} - \sin h\theta \sum_{q=0}^{N-1}\sin hq\Psi e^{-iqm\Psi}) \tag{31}$$

Now we can write more concise expressions for the components of $\hat{f}$, namely,

$$\hat{f}^c = \frac{A(r)}{\sqrt{N}} (\cos h\theta \Sigma_c - \sin h\theta \Sigma_s) \tag{32}$$

and

$$\hat{f}^s = \frac{A(r)}{\sqrt{N}} (\sin h\theta \Sigma_c + \cos h\theta \Sigma_s) \tag{33}$$

with

$$\Sigma_c = \sum_{q=0}^{N-1} \cos hq\Psi e^{-iqm\Psi}$$

and

$$\Sigma_s = \sum_{q=0}^{N-1} \sin hq\Psi e^{-iqm\Psi}$$

It is very clear that these summation terms are not dependent on the mass and stiffness properties of the system. These terms can be further simplified by trigonometric substitution, e.g.,

$$\Sigma_c = \tfrac{1}{2}[\sum_{q=0}^{N-1} e^{iq\Psi(h-m)} + \sum_{q=0}^{N-1} e^{-iq\Psi(h+m)}] \tag{34}$$

and by using the theory of the discrete Fourier transform to evaluate the summation terms, the following result is obtained:

$$\sum_{q=0}^{N-1} e^{-i(2\pi/N)(m-h)q} = \begin{Bmatrix} 0, & m \neq h \\ N, & m = h \end{Bmatrix} \tag{35}$$

In general, since the discrete Fourier transform is periodic, the Σ_c and Σ_s terms are nonzero only under the following conditions,

$$h = jN + m$$

or

$$h = jN - m \tag{36}$$

where $j = 0, 1, 2, \ldots$, with the further conditions that h cannot be negative, and that negative values of m need not be considered. The Σ_c and Σ_s terms depend only on the forcing harmonic, the mode harmonic, and the sector extent, and not on the dynamic characteristics of the system. This result was also found for a continuous system (Wagner and Griffin, 1993), and noting that m cannot exceed $N/2$, its physical significance is that an h order excitation can excite only a single mode or degenerate mode pair. Using the above results, the effective sector forces can be simplified as shown for the following conditions:

1. $m = 0, h = 0, N, 2N, \ldots$ or $m = N/2, h = N(j + \frac{1}{2})$, $j = 0, 1, 2, \ldots$

$$\hat{f}(r, \theta) = \sqrt{N} A(r) \cos (h\theta - \omega t) \tag{37}$$

2. $h = jN + m, j = 0, 1, 2, \ldots$

$$\hat{f}(r, \theta) = \frac{\sqrt{N}}{2} A(r) e^{i(h\theta - \omega t)} \tag{38}$$

3. $h = jN - m, j = 1, 2, 3, \ldots$

$$\hat{f}(r, \theta) = \frac{\sqrt{N}}{2} A(r) e^{-i(h\theta - \omega t)} \tag{39}$$

All other relationships between h and m will result in zero response in the mth mode harmonic. The forcing function associated with case 1, Eq. (37), is real, and the corresponding modes for $m = 0$ and $m = N/2$ are also real. Thus, it follows that the response for case 1 must be real. The form of the response for the remaining two cases is not as evident. This problem will be considered in the next section.

The forcing conditions given by Eqs. (37), (38), and (39) are written in distributed form, and thus must be discretized for use in Eq. (22). These effective sector forces are expressed in polar coordinates, but finite element models use degrees of freedom as unknowns that are usually numbered in a manner that will reduce computation intensity (i.e., reduced matrix profile, wavefront, or bandwidth). Thus, force expressions that are continuous in their distributed coordinates will, after finite element discretization, be most conveniently expressed relative to the degree-of-freedom numbers. The discretization is ideally done by representing the forces as linear combinations of the individual element shape functions, but for purposes here, each structure node, with associated degrees of freedom, will be represented simply by an r and θ coordinate. Thus, the jth degree of freedom will have coordinates r_j and θ_j. These coordinates will also be shared with other DOF at the same node point of the model.

Computation of the Participation Factors

The recovery of the physical displacements from the modal coordinates requires two transformations as defined by Eqs. (19) and (9). Thus, the reduced sector coordinates for mode n are found to be

$$\{q_m\} = \frac{\{\Phi_n^{(m)}\} \{\Phi_n^{(m)*}\}^T \{p_m\}}{M_{mn}(\omega_n^{(m)2} - \omega^2)} \tag{40}$$

where $\{p_m\}$ is the discrete form of the loads corresponding to the continuous loading as specified in Eqs. (37), (38), and (39). The physical displacement in the first sector is,

$$\{X_{1n}\} = \frac{1}{\sqrt{N}} \sum_{m=0}^{N-1} \{q_{mn}\}$$
$$= \frac{1}{\sqrt{N}} \sum_{m=0}^{N-1} \frac{\{\Phi_n^{(m)}\} \{\Phi_n^{(m)*}\}^T \{p_m\}}{M_{mn}(\omega_{(n)}^{(m)2} - \omega^2)} \tag{41}$$

The displacements for the remaining sectors differ from this result only in phase.

When a given forcing harmonic is involved, only certain terms in the series of Eq. (41) are nonzero. These terms can be identified from the conditions defined for cases 2 and 3, thus fixing the value or values of m. We see that if the forcing harmonic corresponds to case 1, i.e., a force distribution given by Eq. (37), there can be only a single term of Eq. (41) that does not equal zero. However, other forcing harmonics result in the forces represented by both Eqs. (38) and (39) contributing at two possible mode harmonics. Due to periodicity, these mode harmonics turn out to be identical, but the forces for cases 2 and 3 are each associated with a different mode of the conjugate, degenerate mode pair. Since the modes are conjugates, and the related forces of Eqs. (38) and (39) are conjugates, it is readily seen that the two nonzero terms of Eq. (41) are also conjugates. Thus, for cases 2 and 3, the summation resulting in the vector of physical displacements becomes simply twice the real part of one of the terms, namely,

$$\{X_{1n}\} = \frac{2}{\sqrt{N}} \frac{\mathrm{Re}[\{\Phi_n^{(m)}\} \{\Phi_n^{(m)*}\}^T \{p_m\}]}{M_{mn}(\omega_n^{(m)2} - \omega^2)} \tag{42}$$

where m has now been constrained to a particular value associated with the forcing harmonic. The physical displacements are thus *real* quantities.

The vector $\{p_m\}$ in Eq. (42) is the discrete form of the continuous force given by Eq. (38). After separating sin ωt and cos ωt parts, the vector product of the conjugate eigenvector and the force vector in Eq. (42) results in summations of the products of the real and imaginary eigenvector components with either sin $h\theta$ or cos $h\theta$. These terms are then "scaled" by the eigenvector itself, after which the real part is taken to finally

obtain the physical displacement vector for the first sector of the bladed disk. Thus, we can rewrite Eq. (42) in component form for the kth DOF as

$$X^k_{1n} = \frac{S^k_c \cos \omega t + S^k_s \sin \omega t}{M_{mn}(\omega_n^{(m)^2} - \omega^2)} \tag{43}$$

with

$$S^k_c = \phi^k_r(\sigma_{rc} + \sigma_{is}) + \phi^k_i(\sigma_{ic} - \sigma_{rs})$$

and

$$S^k_s = \phi^k_r(\sigma_{rs} - \sigma_{ic}) + \phi^k_i(\sigma_{is} + \sigma_{rc})$$

and where ϕ_r and ϕ_i refer to the real and imaginary parts of the eigenvector, and the summation terms are given by

$$\sigma_{rc} = \sum_{j=1}^{J} A_j \phi^j_r \cos h\theta_j, \quad \sigma_{rs} = \sum_{j=1}^{J} A_j \phi^j_r \sin h\theta_j,$$
$$\sigma_{ic} = \sum_{j=1}^{J} A_j \phi^j_i \cos h\theta_j, \quad \sigma_{is} = \sum_{j=1}^{J} A_j \phi^j_i \sin h\theta_j,$$

with A_j being the amplitude of the applied force at DOF j. Recalling that the eigenvectors were normalized to give a maximum modulus value of unity, we can now define a mode participation factor based on maximum displacement in the nth mode of the mth mode harmonic family as

$$\Lambda_{mn} = \frac{1}{K_{mn}} \{[\phi_r^{\max}(\sigma_{rc} + \sigma_{is}) + \phi_i^{\max}(\sigma_{ic} - \sigma_{rs})]^2 + [\phi_r^{\max}(\sigma_{rs} - \sigma_{ic}) + \phi_i^{\max}(\sigma_{is} + \sigma_{rc})]^2\}^{1/2} \tag{44}$$

where $K_{mn} = M_{mn}\omega_n^{(m)^2}$ is the mode generalized stiffness, and $\phi_r^{\max}$ and $\phi_i^{\max}$ are the components of the modal displacement having maximum modulus value. Note that the denominator of Eq. (43) can be rewritten as

$$K_{mn}\left[1 - \left(\frac{\omega}{\omega_n^{(m)}}\right)^2\right]$$

and therefore the maximum response obtained in any single mode is given by

$$|X_{1n}|^{\max} = \frac{\Lambda_{mn}}{\left[1 - \left(\frac{\omega}{\omega_n^{(m)}}\right)^2\right]} \tag{45}$$

It is clear that this expression does not correctly consider resonance, where the response is limited by the damping in the system.

It can be easily shown that excitation corresponding to harmonics represented by the effective forces of case 1 (Eq. (37)), and the associated single, real modes, result in participation factors that are also given by Eq. (44). However, in this case, all imaginary components are zero, and Λ_{mn} takes the following, simpler form:

$$\Lambda_{mn} = \frac{\sqrt{\sigma^2_{rc} + \sigma^2_{rs}}}{K_{mn}} \tag{46}$$

This equation also holds for the case of a rigid disk, with the mode harmonic value m becoming irrelevant.

The Inclusion of Damping. Since damping in blade systems is generally small, this analysis has been, up to this point, undertaken by ignoring damping and studying the undamped blade system. However, although damping is not important for an understanding of the modes, it must be included for consideration of resonant or near-resonant response. In this work, the damping will be assumed to be of *proportional* form (Meirovitch, 1986), which continues to allow the reduced system of equations for a sector to be decoupled. The decoupled system can be written in component form as

$$\ddot{\eta}_{mn} + 2\zeta_n^{(m)}\omega_n^{(m)}\dot{\eta}_{mn} + \omega_n^{(m)^2}\eta_{mn} = \frac{1}{M_{mn}}\{\Phi_n^{(m)*}\}^T\{p_m\} \tag{47}$$

which simply incorporates a diagonal damping term in the system of equations given by Eq. (20), with $\zeta_n^{(m)}$ being the viscous damping factor for the mode. Making use of the undamped modes and their associated conditions of orthogonality, it can easily be shown that the maximum response in a mode, including light damping, can be effectively approximated by

$$|X_{1n}|^{\max} = \frac{\Lambda_{mn}}{\sqrt{\left[1 - \left(\frac{\omega}{\omega_n^{(m)}}\right)^2\right]^2 + \left[2\zeta_n^{(m)}\frac{\omega}{\omega_n^{(m)}}\right]^2}} \tag{48}$$

This is an intuitive extension of Eq. (45), and damping is assumed to have no effect on the participation factor in a mode.

Conclusion

A numerical development has been presented for the harmonic response analysis of grouped-blade and flexible disk systems. The analysis is based on the reduction of the complete, cyclically symmetric system to an equivalent system comprised of a single sector. Typical excitation forces, harmonically related to the rotational speed, are also transformed to an equivalent distribution of forces over the sector. These transformations, while resulting in computational efficiency, also permit computation of the complete system modes in a fashion which emphasizes a natural ordering, thus being helpful for an improved understanding of the system modal spectra, and for depicting the relationship between the modes and harmonic forcing.

This paper presents expressions, based on modal participation factors, for the maximum physical response in any mode due to an applied harmonic force. The sector eigenvectors and transformed forces, while complex in form, result in system displacements which are real. Similar expressions can be found for description of the maximum stresses in any mode. It was further shown that, due to the constraints of orthogonality between the forces and the modes, a given excitation order can excite only a restricted subset of the system modes, i.e., those found by specifying a particular value of the cyclic phase angle or mode harmonic.

Application of the theory developed in this paper will be presented in Part II (Wagner and Griffin, 1996).

References

Balasubramanian, P., Jagadeesh, J. G., Suhas, H. K., Srivastava, A. K., and Ramamurti, V., 1993, "On the Use of the Ritz-Wilson Method for the Dynamic Response Analysis of Cyclic Symmetric Structures," *Journal of Sound and Vibration,* Vol. 164, pp. 193–206.

Cai, C. W., Cheung, Y. K., and Chan, H. C., 1990, "Uncoupling of Dynamic Equations for Periodic Structures," *Journal of Sound and Vibration,* Vol. 139, pp. 253–263.

Ewins, D. J., and Imregun, M., 1984, "Vibration Modes of Packeted Bladed Discs," ASME *Journal of Vibration, Acoustics, Stress, and Reliability in Design,* Vol. 106, pp. 175–180.

Hildebrand, F. B., 1976, *Advanced Calculus for Applications,* 2nd ed., Prentice-Hall, Englewood Cliffs, NJ.

Kirkhope, J., and Wilson, G. J., 1976, "A Finite Element Analysis for the Vibration Modes of a Bladed Disc," *Journal of Sound and Vibration,* Vol. 49, pp. 469–482.

Meirovitch, L., 1986, *Elements of Vibration Analysis,* 2nd ed., McGraw-Hill, New York.

Ortolano, R. J., LaRosa, J. A., and Welch, W. P., 1981, "Long Arc Shrouding—A Reliability Improvement for Untuned Steam Turbine Blading," ASME JOURNAL OF ENGINEERING FOR POWER, Vol. 103, pp. 522–531.

Sabuncu, M., and Thomas, J., 1992, "Vibration Characteristics of Pretwisted Aerofoil Cross-Section Blade Packets Under Rotating Conditions," *American Institute of Aeronautics and Astronautics Journal,* Vol. 30, No. 1, pp. 241–250.

Salama, A. M., Petyt, M., and Mota Soares, C. A., 1976, "Dynamic Analysis of Bladed Disks by Wave Propagation and Matrix Difference Techniques," *Structural Dynamic Aspects of Bladed Disk Assemblies,* A. V. Srinivasan, ed., ASME, New York, pp. 45–56.

Thomas, D. L., 1979, "Dynamics of Rotationally Periodic Structures," *International Journal for Numerical Methods in Engineering,* Vol. 14, pp. 81–102.

Thomas, J., and Belek, H. T., 1977, "Free Vibration of Blade Packets," *Journal of Mechanical Engineering Science,* Vol. 19, No. 1, pp. 13–21.

Wagner, L. F., and Griffin, J. H., 1993, "A Continuous Analog Model for Grouped-Blade Vibration," *Journal of Sound and Vibration,* Vol. 165, No. 3, pp. 421–438.

Wagner, L. F., and Griffin, J. H., 1996, "Forced Harmonic Response of Grouped Blade Systems: Part II—Application," ASME JOURNAL OF ENGINEERING FOR GAS TURBINES AND POWER, Vol. 118, this issue, pp. 137–145.

Wildheim, J., 1981, "Vibrations of Rotating Circumferentially Periodic Structures," *Quarterly Journal of Mechanics and Applied Mathematics,* Vol. 34, No. 2, pp. 213–229.

Forced Harmonic Response of Grouped Blade Systems: Part II—Application

L. F. Wagner
Power Generation Technology Division,
Westinghouse Electric Corporation,
Pittsburgh, PA 15213

J. H. Griffin
Department of Mechanical Engineering,
Carnegie Mellon University,
Pittsburgh, PA 15213

The vibration of grouped blades on a flexible disk should, for purposes of economy and clarity of modal identification, be analyzed using procedures developed for cyclically symmetric structures. In this paper, a numerical model, based on the theory of cyclically symmetric structures, is applied to the vibration analysis, and in particular, the harmonic response, of a flexible disk supporting a number of groups, or packets, of turbine blades. Results are presented to show variations in the modal participation factors as a function of such parameters as disk flexibility, blade density, and the total number of assembled groups. It is also shown that many characteristics of the system spectra of natural frequencies are strongly dependent on the number of blade groups.

Introduction

The techniques of modal analysis and the study of the modal characteristics of blades and bladed-disk assemblies have received significant attention in the literature (e.g., see Platzer and Carta, 1988). Few investigations, however, have been concerned with the forced response of such structures, and this is particularly evident for the study of grouped, or packeted, blades. Compared to individual blades, the vibration spectrum for blade groups is typically composed of many more modes with the potential to respond to harmonically generated excitation. The situation heightens in complexity with the inclusion of a flexible disk, which requires consideration of the entire system of disk and blades for analysis, and is accompanied by an increase in the number of modes. However, it has been shown (Wagner and Griffin, 1993) that not all of these modes have the potential to respond to harmonic forcing.

One of the earliest notable studies of grouped-blade harmonic response was presented by Weaver and Prohl (1958), who used a newly developed calculation procedure to categorize mode patterns, single mode resonant response factors, and stresses for tangential, axial, and torsional stimuli due to nozzle wake excitation. Although limited to groups of parallel blades, this work was notable for its early use of the digital computer, and the development of a technique that has been widely used in the industry for many years.

In 1977, Thomas and Belek used a finite element model for free-vibration parameter studies of shrouded blade groups with parallel blades. The effects of various weight, flexural rigidity, and length ratios on the tangentially directed (i.e., in the plane of the supporting disk) natural frequencies were categorized. They also showed that the in-plane vibration characteristics of a symmetric cross-sectional blade group could be predicted from an inference diagram for a two-blade group. Salama and Petyt (1978) did a similar study, but additionally examined the effects of various positioning arrangements for coupling wires between blades, the effects of finite radius of the disk (i.e., radially oriented blades), and the stiffening effects of rotation. This analysis constrained the geometry, and thus the mode shapes, to be symmetric. Of significant note are the findings that grouping tends to cause natural frequencies to occur in families of M frequencies, where M is the number of blades in a group, and each family tends to be closely related to the various modes of an individual blade with tip mass. Since the rigidity of the shroud is usually high relative to the blades, there also results a subdivision of frequencies within a family, causing one isolated natural frequency and a relatively narrow band of $M - 1$ frequencies. The isolated mode occurs at the lowest frequency with all blades in-phase, and the other modes have various out-of-phase mode patterns. The same conclusions were drawn by Bernante et al. (1982), without the constraint of symmetric group geometry.

Sabuncu and Thomas (1992) developed a comprehensive finite element, beam-based model for a grouped blade system. The effects of pretwist, stagger angle, rotational speed, shroud length, shroud thickness, shroud width, and the distance of the shear center from the centroid were investigated. One interesting finding is that increasing the shroud mass decreases the fundamental frequency under zero rotation, but as a result of centrifugal stiffening, a heavier shroud tends to *raise* the fundamental frequency as rotational speed increases. Comparisons between theoretical and experimental results showed good agreement.

One of the first in-depth investigations into the excitation of rotationally periodic structures, such as blade groups on a flexible disk, was done by Wildheim (1979), who examined the response of such structures to a concentrated, rotating force. He noted that a resonance condition exists in an n nodal diameter mode whenever the natural frequency ω_n is given by

$$\omega_n = (kN \pm n)\Omega \tag{1}$$

where Ω is the angular velocity of the force, N is the number of substructures, and $k = 0, 1, 2, \ldots$. Wildheim introduced a frequency versus nodal diameter diagram, coined the ZZENF diagram (Zig-Zag Excitation line in Nodal diameters versus Frequency), that indicates potential responses at points of intersection of the natural frequency curves and the excitation lines. The work of Singh and Vargo (1989) made use of a graph similar to the ZZENF diagram, referred to as the SAFE diagram, to elucidate certain grouped-blade experimental results presented by Weaver and Prohl (1958), and others.

In 1980, Ewins published a study of blade groups on a flexible disk, concluding that the grouping of blades leads to a gross form of mistuning, causing many diametral components. This implies that a given harmonic does not excite a pure mode. However, Ewins found that grouping can also cause the response of certain diametral modes to be suppressed for harmonic excitation. This was also the conclusion of Ortolano et

Contributed by the International Gas Turbine Institute and presented at the 39th International Gas Turbine and Aeroengine Congress and Exposition, The Hague, The Netherlands, June 13–16, 1994. Manuscript received by the International Gas Turbine Institute February 15, 1994. Paper No. 94-GT-204. Associate Technical Editor: E. M. Greitzer.

al. (1981), who undertook an industry-oriented study of long blade groups. They showed, both theoretically and by several practical examples, that if a blade group is of the same circumferential length as the period of the excitation, response in the lowest frequency, in-phase mode will be minimized. This form of grouping has been referred to as "harmonic shrouding."

Several of the previously cited investigators have presented experimental results for individual blade groups on a relatively rigid disk, but results from experimental studies of grouped blade and disk system dynamics have seldom been reported in the literature. One such study by Ewins and Imregun (1984) presented the results of a comparison of experiment with two methods of modal analysis for grouped-blade vibration. A series of experiments using constant thickness beam and plate models were conducted primarily to confirm the numerical predictions. The direct method of analysis, which considered the entire structure without using symmetry arguments, proved to match the experimental results quite well. The second method of analysis used assumed nodal diameters, and although many of the results agreed with the measurements, additional modes were predicted (i.e., "ghost" modes) that could not be found experimentally. A method was presented for predicting the nodal diameter components by the construction of a modal interference diagram using the basic geometry of the bladed assembly.

In 1985, Pfeiffer experimentally investigated the vibratory behavior of coupled steam turbine blades. Resonant stresses were measured for free-standing and coupled blades using strain gages mounted on the blades. Vibratory response patterns were illustrated using holographic techniques. It was observed that grouping caused each of the group modes to be constrained to a limited range of nodal diameters with little change in natural frequency, and as the stage responded to higher harmonic excitations, each of the frequency ranges would "step" to the next range. At each of the steps, there were also two natural frequencies corresponding to the same nodal diameter. The lower frequency could be viewed, for example, as a mode with nodes between groups, while the higher frequency exists with nodes within the groups. Similar experimental observations were reported by Ewins and Imregun (1984) using simple beam and plate models.

It is fair to say that grouped-blade systems, being structures that possess rotational periodicity, require significantly more complex analysis than individual cantilevered blades. Although much research has been devoted to faster and more comprehensive numerical techniques, much less effort has been directed toward studies of the vibratory behavior of a cyclic system. One example of such an investigation was recently undertaken by Wagner and Griffin (1993) using a continuous string model to represent the motion of a system of grouped blades on a flexible disk. This work emphasized that an understanding of the associated vibratory phenomena must be available to turbine design engineers before blade groups can be optimally designed for efficiency and reliability. Accordingly, the objective of the present work is to study certain aspects of grouped blade dynamics qualitatively by varying a number of significant parameters. The "mode participation factor" is used as a relative measure of response to harmonic excitation, and the computation of this factor is based on the methods presented in the Part I companion paper (Wagner and Griffin, 1996). When this factor is combined with damping and the frequency margin from resonance, stresses and displacements can be computed for each mode. Since the participation factor is loosely defined as the inner product of the excitation distribution and mode shape, it is clear that modal analysis must be the initial priority.

In the present paper, the theory of cyclically symmetric structures is applied to a representative problem of grouped blades on a flexible disk. After defining the geometry and material characteristics for the model problem, and comparing certain results to those of a continuous analog model for grouped blades, results for both modal and response analyses are presented. The response analyses are based on the use of participation factors. Mathematically, the amplitude of the resonant response is equal to the participation factor multiplied by the dynamic magnification factor for the mode of interest. Consequently, the participation factors provide a convenient method for assessing the relative level of vibration that would result from design changes. Furthermore, they would provide a reasonably accurate quantitative assessment of the resonant response if the magnitude of the excitation[1] and the modal damping were accurately known.

Determination of the Excited Modes

As discussed in Part I (Wagner and Griffin, 1996), the modes of a system of grouped blades can be organized into groupings of modes; each grouping, or "mode harmonic," related to a particular value of circumferential displacement phase between boundaries of a cyclically symmetric sector of the structure, which contains a single blade group. The modes within a mode harmonic grouping have mode shapes similar to the various bending or torsional modes of a single beam, but generalized to the group motions (e.g., first group bending, group torsional or X mode). A "mode family" will be defined, for the purposes of this study, as the set of modes having similar group motions, but with each family member having a different mode harmonic value. Thus, for example, a group bending mode moving in phase with adjacent groups and having all intergroup blades moving in phase, is in the same family as a similar intergroup mode that is out of phase with adjacent groups. The mode families can be identified by the order of frequencies, with the first family having the lowest set of frequencies, the second family the next highest, etc.

Typical grouped-blade modal results tend to show natural frequencies that are relatively tightly clustered. However, the modes within these clusters belong to different mode harmonic groupings, and it has been shown (Wagner and Griffin, 1996) that different mode harmonics respond independently to various orders of harmonic excitation. In fact, if a mode responds to a given excitation harmonic, it tends to be orthogonal to the excitation patterns of nearby excitation harmonics. Thus, the individual modes with the potential to respond to given exciting harmonics tend to have well isolated natural frequencies, and it follows that the use of participation factors for harmonic stress and displacement response calculation, which depends upon mode separation, should be very effective.

It was shown in Part I that the condition required for an N group bladed disk to respond to an excitation harmonic h while constrained to mode harmonic m is given by

$$h = jN \pm m \tag{2}$$

where $j = 0, 1, 2, \ldots$, with the further condition that h cannot be negative, and that negative values of m need not be considered. This condition was expressed in tabular form by Wagner and Griffin (1993) in a mode-excitation orthogonality diagram, which is shown for the first mode family (i.e., all blades within a group vibrating in phase) in Fig. 1. The cells containing an X indicate intersecting values of h and m that combine for nonzero response. All other combinations result in mode and excitation patterns which are orthogonal, leading to zero response in the mode. The diagram shows that although a multiplicity of excitation harmonics can excite a given mode, a particular excitation harmonic must excite a unique mode. Thus, the relationship between the mode harmonics (and therefore the natural frequencies) and the excitation harmonics is periodic. This observation will later be demonstrated graphically based on numerical computations.

[1] In this study it is assumed that the magnitude of the harmonic excitation is constant. This is usually a reasonable assumption provided the rotational speed of the machinery is limited in range.

h / m	0	1	2	...	N/2	...	N-2	N-1	N	N+1	...
0	X	-	-	...	-	...	-	-	-	-	...
1	-	X	-	...	-	...	-	X	-	X	...
2	-	-	X	...	-	...	X	-	-	-	X
...	...	...	...	X	-	X	...	...	...	...	...
N/2	-	-	-	...	X	...	-	-	-	-	...

a) Even number of blade groups

h / m	0	1	2	...	(N-1)/2	(N+1)/2	...	N-2	N-1	N	N+1	...
0	X	-	-	...	-	-	...	-	-	-	-	...
1	-	X	-	...	-	-	...	-	X	-	X	...
2	-	-	X	...	-	-	...	X	-	-	-	X
...	...	...	...	X	...	...	X	...	...	...	...	...
(N-1)/2	-	-	-	...	X	X	...	-	-	-	-	...

b) Odd number of blade groups

Fig. 1 Mode-excitation orthogonality diagram for mode family 1

Out of the many modes available in the complex, grouped-blade system, the establishment of the only mode (or degenerate mode pair) within a mode family that will respond to a given harmonic input can be found using Eq. (2) or the diagram of Fig. 1. Determining the level of the response can accomplished by computing the participation factors as described in Part I. These theoretical concepts will be used in the remainder of this paper to study the grouped-blade model problem parametrically.

Definition of the Model Problem Characteristics

The bladed-disk system used in the model problem is a simplified, but representative, grouped-bladed disk model for a constant-speed, low-pressure, steam-turbine stage. The "blades" in the model have a rectangular cross section that is radially unchanged. The total number of blades equals 120, and the number of blades per group will be a variable. Any departures from the geometry of the nominal model will be noted. The shroud is positioned at the blade tips, and has the same cross section as the blades. The long axes of both blade and shroud cross sections are parallel to the disk spin axis, and the "root" of each blade is fixed to the disk rim. The disk is of constant thickness and is fixed at the inner radius. The geometric and material characteristics for the nominal blade, shroud, and the disk are listed in Table 1.

Each blade has been discretized into five, equal-length, beam-type finite elements based on Bernoulli–Euler theory. The shroud is represented by two beam elements between each blade. The disk is constructed from eight-noded isoparametric plate elements, with three rows of elements radially, and one element column for each blade. A schematic illustration of the discretized, bladed-disk model is shown in Fig. 2. Steady loads on the blades have been ignored. The applied harmonic forces are distributed over the length of each blade, with a total amplitude per blade that equals 100 lb. This force level is assumed to be the same for each harmonic. The model thus constructed can be shown to provide participation factors that have converged to within 1 percent accuracy for the first two mode families.

Throughout the analysis of the model problem, only the modes that are out-of-plane of the disk, and thus involve disk coupling, will be considered. The modes that are in-plane (i.e., tangential modes) will be ignored, but these modes will behave in a similar manner and fall into families defined by the mode harmonics whenever disk flexibility is a factor in their development. The simplified model used precludes disk flexibility effects from influencing the tangential modes. Thus, each tangential mode will behave as on a rigid disk, and neither the natural frequency nor the group mode shape will change with mode harmonic.

Table 1 Nominal discrete model characteristics

Rotational Speed:	3600 rpm
Blade	
Length:	10 in.
Width:	2 in.
Thickness:	1 in.
Shroud	
Width:	2 in.
Thickness:	1 in.
Disk	
Inner radius:	20 in.
Outer radius:	40 in.
Thickness:	5 in.
Material Properties (All components)	
Elastic modulus:	30×10^6 lb/in^2
Poisson's ratio:	0.3
Weight density:	0.3 lb/in^3

Comparison to Continuous, Analog Model Results

Wagner and Griffin (1993) offered a continuous string analogy as a simple model for understanding the vibratory behavior of grouped blades. The normalized participation factors, Λ_{mn}, were presented as a function of h/N, where the index n refers to the particular mode within the mth mode harmonic grouping. The participation factor results, similarly normalized, for the first two modes of a discrete model with eight blades per group

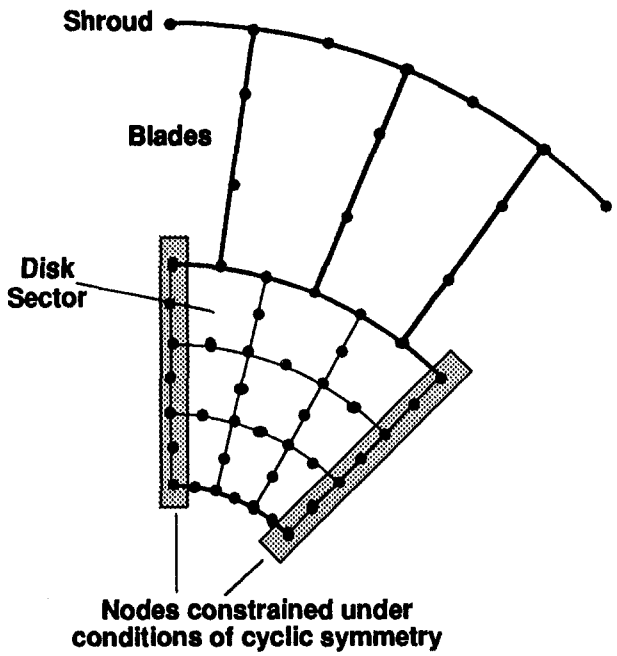

Fig. 2 Discrete cyclically symmetric sector model of a blade group on a flexible disk

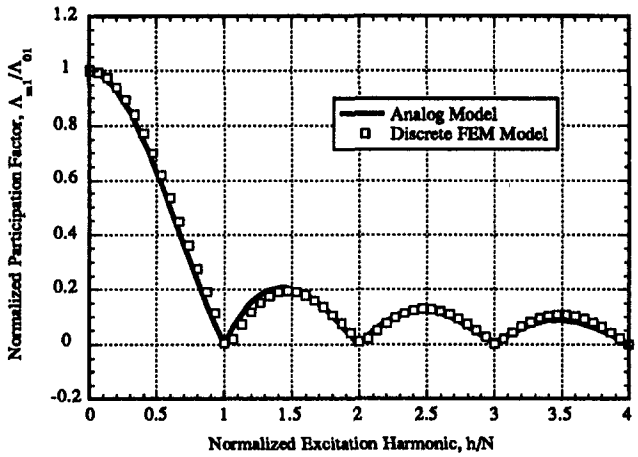

Fig. 3 Analog and discrete model comparison of participation factors—mode family 1

on a relatively stiff disk (12 in. thick),[2] are presented with comparison to the analog results in Figs. 3 and 4. These results can also be considered as baseline, to which the results of the later parameter studies can be directly compared. The relative differences between the first and second mode family results for the two models can be shown to be attributed to the ability of the discrete model to independently consider more detailed blade characteristics (i.e., moments of inertia, torsional stiffness, etc.). For example, the second mode is sensitive to the blade torsional stiffness, which is nearly irrelevant to the first mode response. Consideration of this type of detail is not possible with the analog model.

Although the absolute magnitudes have not been compared, and cannot be without calibration of the analog model, this comparison indicates that the analog model is adept at identifying the basic vibratory phenomenon, particularly the excitation harmonics that result in maximum and minimum response for each mode. However, the shape of the analog model curves will not change when coupling stiffness (i.e., "disk" flexibility) is changed. It will be seen from the discrete model results that disk flexibility and mass does indeed change the shape of the participation factor curves. The analog model is incapable of accurately simulating a relatively flexible disk because of the simple nature of the analog model coupling, and because "disk" mass has been ignored.

[2]It is questionable whether a disk of this thickness with the given radial dimensions could, within the associated theory, lead to accurate results for the disk dynamics alone. However, for the purposes here, the thick disk serves simply to provide a very stiff, effectively rigid, constraint at the blade roots.

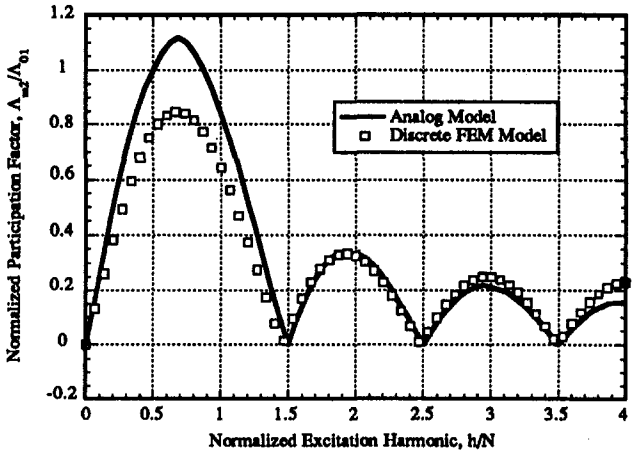

Fig. 4 Analog and discrete model comparison of participation factors—mode family 2

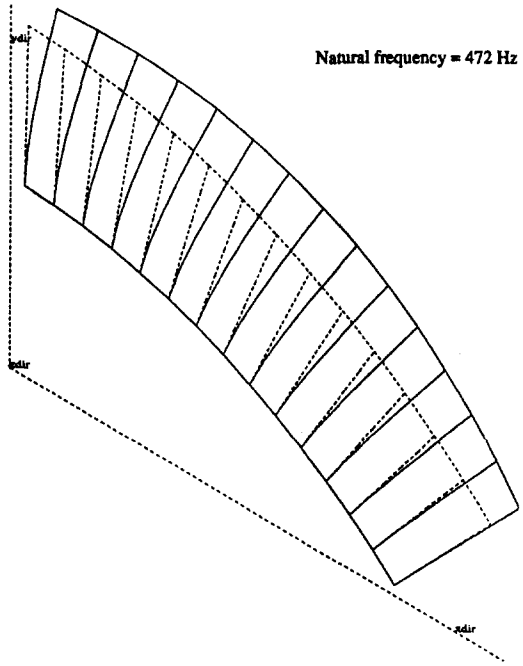

Fig. 5 First out-of-plane, rigid-disk group mode (in-phase mode)

Modal Analysis of the Discrete Model

Accurate modal analysis is important to turbine design because, first, this will permit identification of natural frequencies which, if possible, should be avoided during operation. Second, both the natural frequencies and the mode shapes are required for the computation of the participation factors.

The purpose here will be to illustrate some of the general characteristics found in the modes of a grouped-blade system, and in particular, the changes in the system modes as the mode harmonic is varied. The model used is the nominal model with eight groups on the disk (15 blades per group). This model was chosen because of the long group length, which permits better visual resolution of the phase differences between groups.

The first two modes, illustrated in Figs. 5 and 6, are for the blade group rigidly supported at the base of the blades. The displaced position of the group is indicated by the solid lines, while the undisplaced position is dashed. The first mode has all blades moving in phase, and the second mode occurs with ends out-of-phase (often called the X mode).[3] These modes, because of the rigid constraints at the bases of the blades, have natural frequencies that are upper bounds on the system frequencies.

The bladed-disk system mode shapes for the first two mode families (m = 0, 2, 4) are shown in Figs. 7, 8, and 9. (For further illustration, see Wagner, 1993.) The modes shown, and those for m = 1 and 3, are the only possible modes that can be associated with the rigid-disk in-phase mode, and the rigid-disk X mode. Since the disk has eight groups, there can be only 5 mode harmonics in each family, numbered 0 through 4. Thus, the in-phase mode family cannot exist with any number of nodal diameters greater than 4, and the X mode family does not exist beyond 8 nodal diameters.

In general, we see that as the mode harmonic increases, the in-phase mode becomes more locally constrained near the sector

[3]Hereafter, the first mode will be referred to as the "in-phase mode," and the second mode as the "X mode."

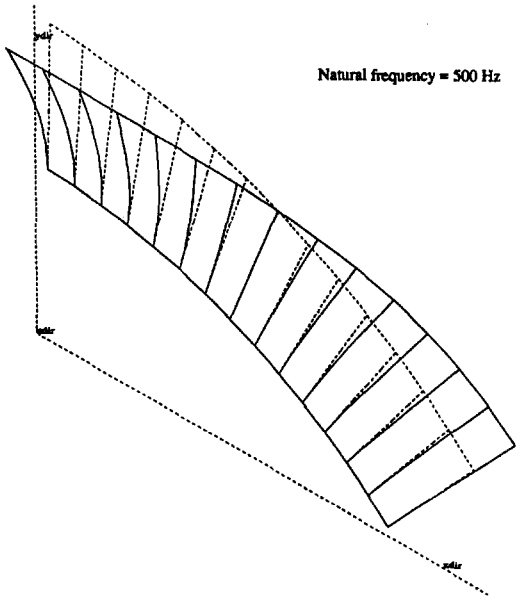

Fig. 6 Second out-of-plane, rigid-disk group mode (*X* mode)

boundaries, and thus increases in natural frequency. This is in contrast to the *X*-mode family behavior, which is less constrained at the higher mode harmonic (Fig. 9, $m = 4$), with antinodes at the sector boundary positions, and develops greater constraint, and higher frequencies, with decreasing mode harmonic until a node develops at the sector boundaries for the zeroth mode harmonic (Fig. 7). This type of alternating constraint behavior persists with the higher mode families, and is

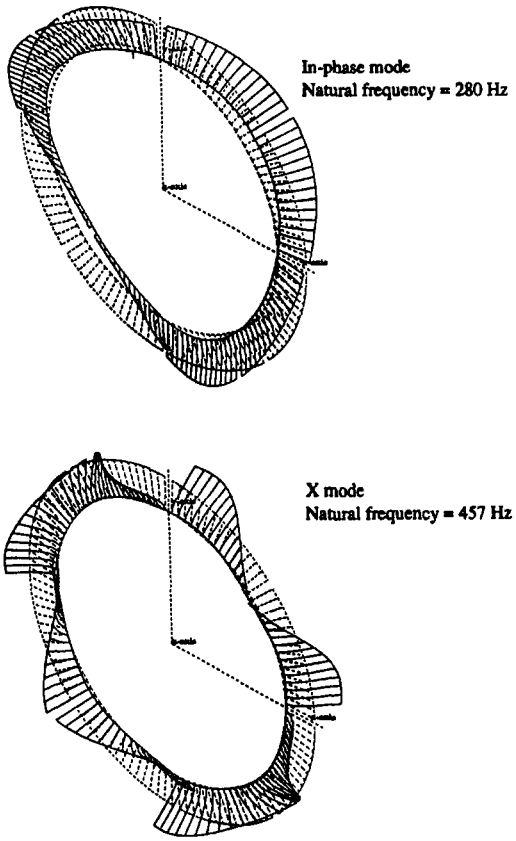

Fig. 8 System mode shapes for second mode harmonic ($m = 2$)

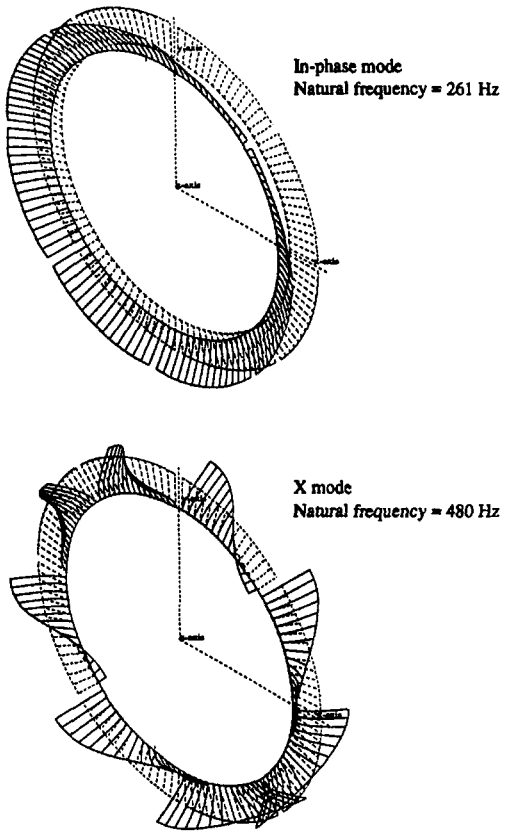

Fig. 7 System mode shapes for zeroth mode harmonic ($m = 0$)

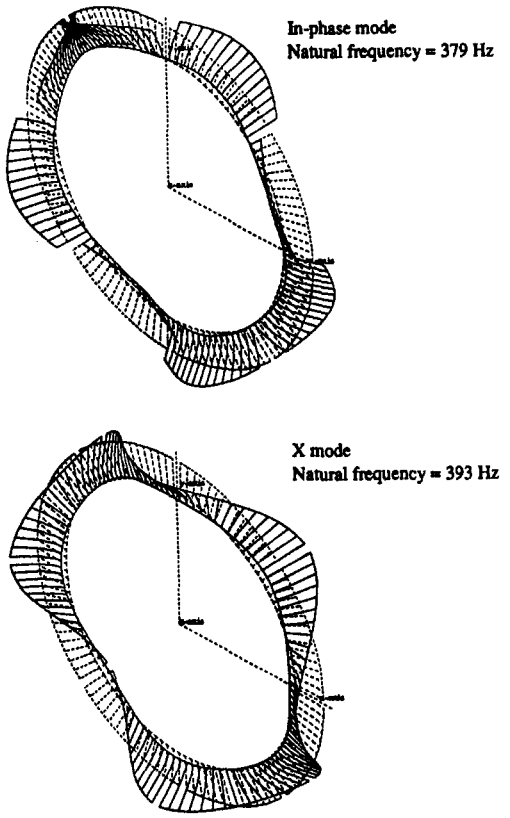

Fig. 9 System mode shapes for fourth mode harmonic ($m = 4$)

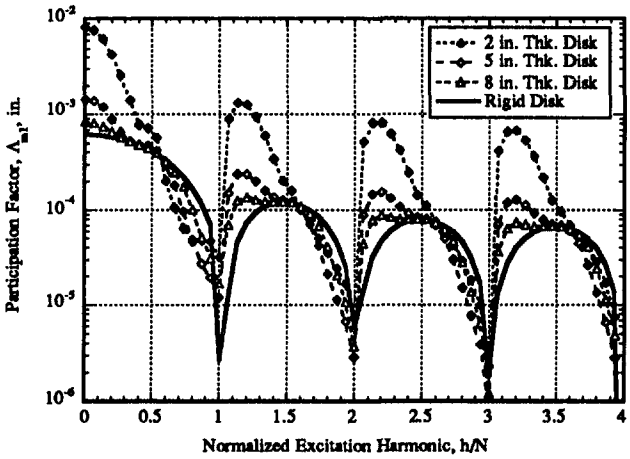

Fig. 10 Effect of disk flexibility on the dimensional participation factor—mode family 1

closely related to the number of displacement phase changes occurring within an individual group.

The zeroth mode harmonic ($m = 0$) results are shown in Fig. 7. By setting $m = 0$, each group is required to have identical deflections at the edges of the sector. It is clear that this is so for the first mode family with all blades in phase, but the only way for this to occur for the X mode family is for the sector boundary displacements to be zero. The first mode family with $m = 0$ also corresponds to the lowest zero nodal diameter mode for the system. However, the X mode with $m = 0$ corresponds to an eight nodal-diameter mode. Thus, the nodal diameters and the mode harmonics are not, in general, numerically identical. The zero mode harmonic will include modes with 0, N, $2N$, . . . nodal diameters, and is the *only* mode harmonic that will always have clearly delineated nodal diameter modes (i.e., a single nodal diameter Fourier component) regardless of whether the number of groups is odd or even.

A common conception in industry is that as the number of nodal diameters increases, the corresponding natural frequencies will also increase toward an asymptote defined by the rigid-disk, upper-bound frequency. This is a reasonably practical assumption for a large number of individual blades on a flexible disk, but there are problems with this concept when it is applied to grouped-blade systems. The first problem with this idea is that there are many modes that are made up of a combination of nodal diameter components, so that it may be difficult to identify a unique nodal diameter number with any given mode. Secondly, and more importantly, the natural frequency upper limit for any given mode family is usually much lower than the rigid-disk upper bound. This is apparent from the example problem, in-phase mode, upper-limit natural frequency ($m = 4$) of 379 Hz indicated in Fig. 9, when compared to the rigid-disk frequency of 472 Hz (Fig. 5) for the in-phase mode. The upper limit natural frequency for the X-mode family is 480 Hz, which occurs at the zeroth mode harmonic ($m = 0$). The corresponding rigid-disk natural frequency is 500 Hz. It is not possible to find modes that will bridge these "gaps" and tend toward an asymptotic relationship. It is clear that the fewer cyclically symmetric sectors a "tuned" structure[4] has, the more difficult it becomes to associate the frequency variation within a family with an upper-bound asymptote. However, if a structure is "mistuned," that is, possessing some imperfection in rotational periodicity, many more modes may become apparent in the frequency spectrum, and in such a case, it may be possible to measure resonances that occur near the upper-bound frequency.

Parameter Variation Using the Discrete Model

As a demonstration of the ability of the discrete model to consider practical design alternatives, the results of several parameter variation studies are presented. These studies will concentrate on participation factor variation as a parameter of interest is changed. Since the participation factor, as defined in this work, is related to the displacement response, no concurrent conclusions can be drawn regarding stress response without additional considerations. With disk flexibility variation, for example, greater disk flexibility generally results in participation factors of greater magnitude in the lower frequency modes, which implies greater blade-tip displacements. However, stresses at the blade root may tend to reduce as disk flexibility is increased, since the *relative* blade-tip to disk-rim displacements become smaller. Both the disk flexibility and blade density studies in the following two subsections are based on perturbations of the nominal geometry.

Effect of Disk Flexibility. As seen from Figs. 10 and 11, increasing the disk flexibility causes an increase in the maximum displacement response of the nominal blade group if the normalized excitation harmonic (h/N) takes on values between an integer and an integer plus one-half. However, response tends to decrease for other values of h/N. The normalized harmonic excitation values for zero response do not change position, but in the first mode family, the harmonics associated with the peak displacements shift to lower values of h/N. These same results have been normalized and plotted on a linear scale in Figs. 12 and 13, and here the nearly monotonic variations in the participation factors with disk thickness are easily seen.

An interesting variation can be observed in the second mode family participation factor plots for the two-inch thick disk (Figs. 11 and 13). A number of "dips" in the curves can be seen at various h/N values. These apparent anomalies are generated by the close proximity of the X mode, second mode harmonic natural frequency, and a nodal circle mode natural frequency, which is much higher for thicker disks. The mode shapes for these two modes share proportions of the normal characteristics of each, making categorization difficult. The phenomenon associated with these effects is described in the theory of frequency curve crossing or veering (Perkins and Mote, 1986).

Effect of Blade Density. The harmonic forces applied to the beam-type, blade model have been simply "sampled" from the harmonic distribution. No attempt has been made to inte-

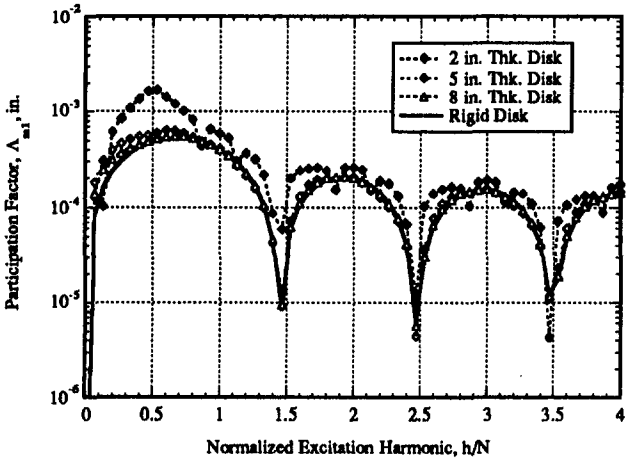

Fig. 11 Effect of disk flexibility on the dimensional participation factor—mode family 2

[4]A "tuned" structure, in this case, refers to perfect rotational periodicity, with all groups identical. This terminology is often used in the literature, and is distinct from the "tuning" required to position a natural frequency relatively in a desired way.

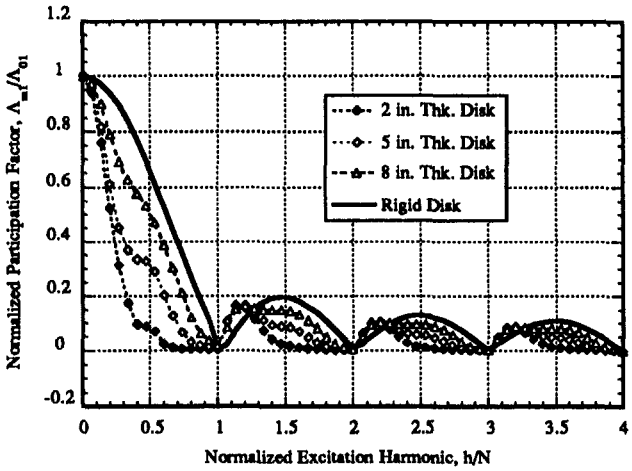

Fig. 12 Effect of disk flexibility on the normalized participation factor—mode family 1

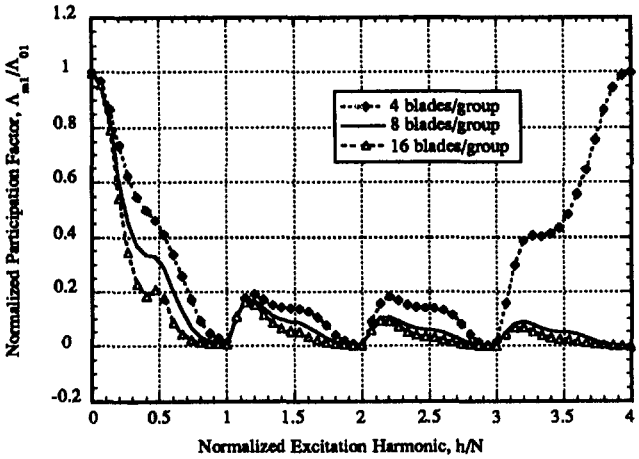

Fig. 14 Effect of group solidity by changing number of blades per group—mode family 1

grate the forces circumferentially, and to apply them as a resolved force and moment pair. Thus, under these conditions, changing the number of blades per unit circumferential length causes an effect that is similar to changing the group's solidity.

The plots of Figs. 14 and 15 indicate the effects of blade density for 4, 8, and 16 blades per group, while keeping the total number of groups equal to 15. The most notable effect in the first mode family is that low values of blade density result in unusually high participation factors for higher harmonic excitations. This is also apparent for the second mode family, and is a result of "aliasing," which is a term used in the theory of signal processing, and refers to the inability of the groups to discern differences between the sampling of certain lower harmonics and related higher harmonics (see Chap. 15 of Platzer and Carta, 1988). Lower blade density also introduces new minima at integral values of h/N in the second mode family.

The four blades per group results appear to "fold" or "mirror" as a result of aliasing at an h/N value of about 2. Although not shown, numerical results for higher h/N values show that the eight blades per group results fold at $h/N = 4$.

Effect of Number of Groups. Once the blade aerodynamic designers have finalized the details for the blade passages, the mechanical designers must decide on the blade structural details that will provide optimum reliability. One way to accomplish this task, without affecting the shape of the blade passages, is to evaluate alternative grouping arrangements. It may often be the case that one or more dominant harmonic excitations are known to exist, due to some upstream blockage condition, with some form of harmonic shrouding being the best choice for grouping. Otherwise, grouping can be chosen to avoid resonance conditions, and to provide the lowest possible participation factors in modes of interest.

Selection of an appropriate number of groups is a matter of keeping track of the excitation harmonic h, and the associated mode harmonic m, along with the natural frequencies and participation factors. The excitation and mode harmonics are related as indicated either by Eq. (2) or the mode-excitation orthogonality diagram of Fig. 1. Also, as previously indicated, each mode family can have only one mode for each mode harmonic. Thus, as the excitation harmonic number increases, the mode harmonic number cycles periodically between the limits 0 and $N/2$ (or $(N-1)/2$ for N odd). This upper limit value of the mode harmonic will be referred to as the "cutoff harmonic." Any excitation harmonic number that is larger than the cutoff value will potentially cause response *only* in the modes that have already been defined below the cutoff, albeit with a different participation.

A plot that clearly shows the periodic nature of the natural frequencies when plotted versus the excitation harmonic is shown in Fig. 16. Curves are displayed for five different group lengths, and the cutoff harmonic values are indicated. The points shown on these curves represent the available modes in the system, and the connecting lines are shown only to emphasize

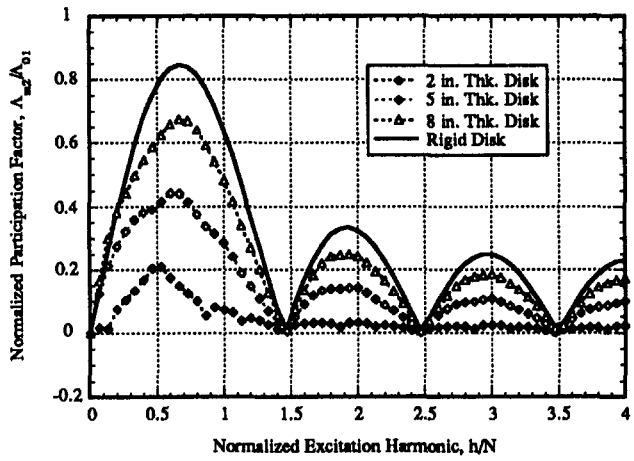

Fig. 13 Effect of disk flexibility on the normalized participation factor—mode family 2

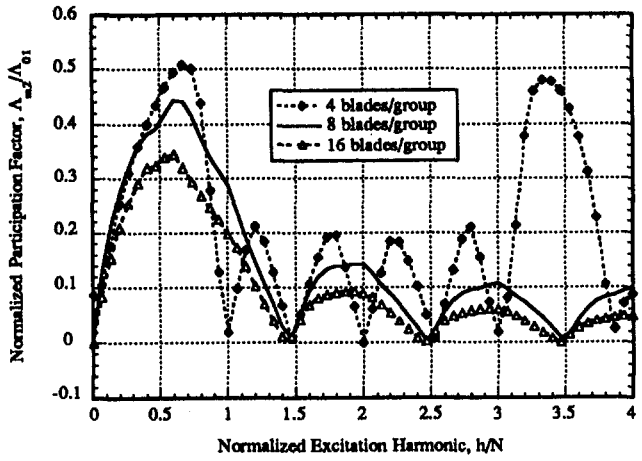

Fig. 15 Effect of group solidity by changing number of blades per group—mode family 2

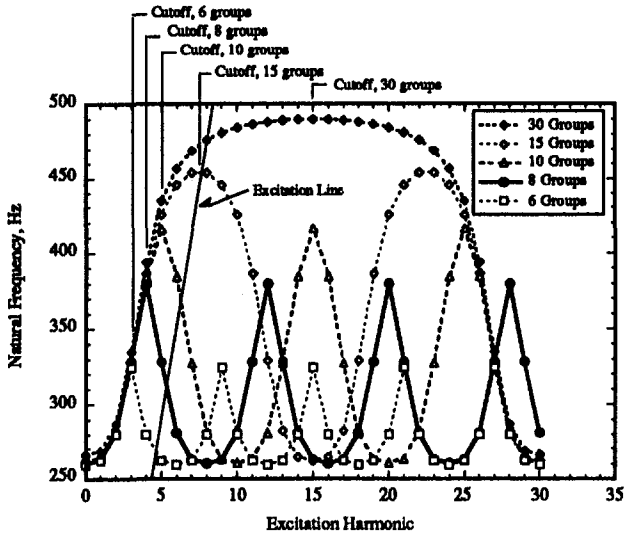

Fig. 16 Effect of group length variation on system natural frequency

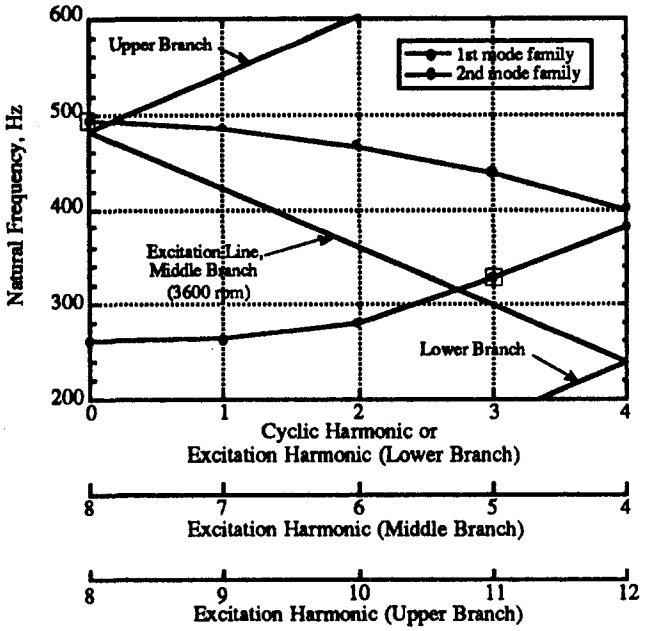

Fig. 17 ZZENF diagram for the lower two mode families of an eight-group bladed disk

association. Also shown is the excitation line, which defines the excitation frequency as a function of the excitation harmonic for the fixed rotational speed of 3600 rpm. Thus, any mode points on the various curves, lying on or near the excitation line, define potential resonance or near-resonance conditions.

Examination of Fig. 16 shows that a greater number of groups tends toward a broader range of frequencies available for excitation. For the cases shown, a disk having 30 groups has a frequency range of 223 Hz, while a 6-group system has a frequency range of only 64 Hz. These ranges are, of course, a strong function of the disk flexibility.

The choice of an appropriate group length also depends on minimizing the participation factor for the most important modes. Table 2 gives a list of mode characteristics for those modes that are closest to the excitation line for each of the chosen group lengths. The participation factors listed are proportional to the blade stresses in these lower modes, and are directly comparable since the disk is the same for each group length case.

Table 2 shows that minimum response in the first mode family would be obtained using 6 groups, while minimum response in the second mode family requires 30 groups. At this point, either a compromise is required, with more detailed computation of the stress levels, or the designer must provide some weighting to the participation factors based on expected excitation or experience.

A more convenient presentation of the information shown in Fig. 16, for a given number of groups, can be obtained by "folding" the curves about the cutoff harmonic value. Such a construction is shown in Fig. 17 for eight groups, and is referred to as a ZZENF diagram as originally proposed by Wildheim (1979). The folding makes no change in the mode frequency values, due to their periodicity relative to the cutoff harmonic, but the excitation harmonic line becomes a "zig-zag" with various branches; each branch representing a range of excitation harmonic values. For the 8-group case shown, we can see that the first mode family can potentially be excited by a fifth excitation harmonic in the third mode harmonic, and the second mode family is most vulnerable to the eighth excitation harmonic in the zeroth mode harmonic.

Table 2 Natural frequencies and participation factors for responding modes with different group lengths

	Mode Family 1				Mode Family 2			
No. Groups	m	h	Frequency (Hz)	Partic. Factor (in)	m	h	Frequency (Hz)	Partic. Factor (in)
6	1	5	262.5	1.85×10^{-5}	1	7	435.7	5.39×10^{-4}
8	3	5	327.9	6.63×10^{-5}	0	8	491.8	4.80×10^{-4}
10	4	6	384.7	1.30×10^{-4}	2	8	490.5	6.60×10^{-4}
15	7	8	453.6	4.13×10^{-4}	6	9	534.4	6.34×10^{-4}
30	8	8	476.0	5.69×10^{-4}	13	13	753.4	2.55×10^{-4}

Conclusion

A given excitation harmonic can excite only a limited subset of the structural modes of a perfectly periodic, packeted bladed disk. The modes that can be excited are most easily calculated by analyzing a single blade group and disk segment with a specific cyclic symmetric boundary condition, i.e., the only modes that can be excited are those that have a phase difference across the segment that is identical to the phase difference associated with the excitation harmonic.

Once a structural mode is identified as capable of responding to a given harmonic excitation, then the relative strength of its resonant response is given in terms of its participation factor. Its participation factor may be efficiently calculated by using the modal information from a cyclically symmetric, finite element analysis of a single group. This approach is utilized in order to illustrate how various design parameters affect the resonant response of grouped blades.

The structural modes can be classified as belonging to families that exhibit similar behavior. When the participation factors of a family are plotted as a function of the excitation harmonic divided by the number of groups, they show a trend similar to that of the magnitude of a decaying cosine function. In the case of the lowest frequency family, the first zero occurs when the excitation harmonic equals the number of groups. This condition, and the associated grouping configuration called *harmonic shrouding,* is well known and frequently exploited to minimize the response of the system's first mode to a known harmonic excitation. In fact, the participation factors of all modal families exhibit similar trends and the harmonic shroud concept can be readily applied to any mode and excitation harmonic pair once the participation factors for a family are calculated as a function of the normalized excitation harmonic.

In general, however, the designer is often concerned with more than a single mode/excitation harmonic pair, and trade-offs must be made. If a participation factor is not zero, then its value is affected by parameters such as the thickness of the disk and the blade density of the stage. In fact, under these more general circumstances, there is no simple rule for optimally choosing the number of groups. However, an approach has been defined that allows the designer to establish which cases are critical, and then the participation factors can be calculated for each case to establish the number of groups that will result in the most robust design.

References

Bernante, R., Macchi, A., and Magneachi, P., 1982, "Effect of Packeting on Turbine Blade Vibrations," *Rotordynamic Problems in Power Plants,* International Federation for the Theory of Machines and Mechanisms, pp. 247–257.

Ewins, D. J., 1980, "Further Studies of Bladed Disk Vibration: Effects of Packeting," *Vibrations in Rotating Machinery,* Institution of Mechanical Engineers Conference Publications 1980-4, pp. 97–102.

Ewins, D. J., and Imregun, M., 1984, "Vibration Modes of Packeted Bladed Discs," ASME *Journal of Vibration, Acoustics, Stress, and Reliability in Design,* Vol. 106, pp. 175–180.

Kirkhope, J., and Wilson, G. J., 1976, "A Finite Element Analysis for the Vibration Modes of a Bladed Disc," *Journal of Sound and Vibration,* Vol. 49, pp. 469–482.

Ortolano, R. J., LaRosa, J. A., and Welch, W. P., 1981, "Long Arc Shrouding—A Reliability Improvement for Untuned Steam Turbine Blading," ASME JOURNAL OF ENGINEERING FOR POWER, Vol. 103, pp. 522–531.

Perkins, N. C., and Mote, C. D. Jr., 1986, "Comments on Curve Veering in Eigenvalue Problems," *Journal of Sound and Vibration,* Vol. 106, No. 3, pp. 451–463.

Pfeiffer, R., 1985, "Blade Vibrations of Continuously Coupled and Packeted Steam Turbine LP-Stages," *Vibrations of Blades and Bladed Disk Assemblies,* ASME Publication, pp. 57–63.

Platzer, M. F., and Carta, F. O., eds, 1988, *AGARD Manual on Aeroelasticity in Axial-Flow Turbomachines, Vol. 2, Structural Dynamics and Aeroelasticity,* AGARDograph No. 298, Advisory Group for Aerospace Research and Development.

Sabuncu, M., and Thomas, J., 1992, "Vibration Characteristics of Pretwisted Aerofoil Cross-Section Blade Packets Under Rotating Conditions," *American Institute of Aeronautics and Astronautics Journal,* Vol. 30, No. 1, pp. 241–250.

Salama, A. M., Petyt, M., and Mota Soares, C. A., 1976, "Dynamic Analysis of Bladed Disks by Wave Propagation and Matrix Difference Techniques," *Structural Dynamic Aspects of Bladed Disk Assemblies,* A. V. Srinivasan, ed., ASME, New York, pp. 45–56.

Salama, A. M., and Petyt, M., 1978, "Dynamic Response of Packets of Blades by the Finite Element Method," ASME *Journal of Mechanical Design,* Vol. 100, pp. 660–666.

Singh, M. P., and Vargo, J. J., 1989, "Reliability Evaluation of Shrouded Blading Using the SAFE Interference Diagram," ASME JOURNAL OF ENGINEERING FOR GAS TURBINES AND POWER, Vol. 111, pp. 601–609.

Thomas, D. L., 1979, "Dynamics of Rotationally Periodic Structures," *International Journal for Numerical Methods in Engineering,* Vol. 14, pp. 81–102.

Thomas, J., and Belek, H. T., 1977, "Free Vibration of Blade Packets," *Journal of Mechanical Engineering Science,* Vol. 19, No. 1, pp. 13–21.

Wagner, L. F., 1993, "Vibration Analysis of Grouped Turbine Blades," PhD Dissertation, Carnegie Mellon University, Pittsburgh, PA.

Wagner, L. F., and Griffin, J. H., 1993, "A Continuous Analog Model for Grouped-Blade Vibration," *Journal of Sound and Vibration,* Vol. 165, No. 3, pp. 421–438.

Wagner, L. F., and Griffin, J. H., 1996, "Forced Harmonic Response of Grouped Blade Systems: Part I—Discrete Theory," ASME JOURNAL OF ENGINEERING FOR GAS TURBINES AND POWER, Vol. 118, this issue, pp. 130–136.

Weaver, F. L., and Prohl, M. A., 1958, "High-Frequency Vibration of Steam-Turbine Buckets," *ASME Transactions,* Vol. 80, pp. 181–194.

Wildheim, J., 1979, "Excitation of Rotationally Periodic Structures," ASME *Journal of Applied Mechanics,* Vol. 46, pp. 878–882.

Wildheim, J., 1981, "Vibrations of Rotating Circumferentially Periodic Structures," *Quarterly Journal of Mechanics and Applied Mathematics,* Vol. 34, No. 2, pp. 213–229.

Aircraft Crash Caused by Stress Corrosion Cracking

H. J. Kolkman

G. A. Kool

R. J. H. Wanhill

Department of Materials,
National Aerospace Laboratory, NLR,
Emmeloord, The Netherlands

An aircraft crash in the Netherlands was caused by disintegration of a jet engine. Fractography showed that the chain of events started with stress corrosion cracking (SCC) of a pin attached to a lever arm of the compressor variable vane system. Such a lever arm–pin assembly costs only a few dollars. Investigation of hundreds of pins from the accident and a number of identical engines revealed that this was not an isolated case. Many pins exhibited various amounts of SCC. The failed pin in the accident engine happened to be the first fractured one. SCC requires the simultaneous presence of tensile stress, a corrosive environment, and a susceptible material. In this case the stress was a residual stress arising from the production method. There was a clear correlation between the presence of salt deposits on the levers and SCC of the pins. It was shown that these deposits were able to reach the internal space between the pin and lever arm, thereby initiating SCC in this space. The corrosive environment in Western Europe explains why the problem manifested itself in the Netherlands at a relatively early stage in engine life. The main point is, however, that the manufacturer selected an SCC-prone material in the design stage. The solution has been to change the pin material.

Introduction

Recently an aircraft powered by a single turbofan jet engine crashed in the Netherlands. An initial investigation revealed that the crash was due to disintegration of the jet engine. Destroyed blades and vanes were found from the sixth compressor rotor stage onward. This made the fifth stator stage, located in front of the sixth rotor stage, particularly suspect.

The third, fourth, and fifth compressor stator stages of the engine under consideration contain variable stator vanes. The variable vanes are connected to the actuator rings by means of levers. Each lever is an assembly of an arm and a pin; see Fig. 1. The pins fit into the holes of an actuator ring. One of the fifth-stage levers exhibited a broken pin. The fracture face was along AA in Fig. 1. A fractographic investigation was performed in order to determine whether the pin failure was a consequence or the cause of the crash.

Fractography

Macroscopic study of the fracture face revealed that little deformation had taken place, and the fracture face was very flat. In other words, it was highly unlikely that the fracture was created by overload during the crash. The fracture face of the pin was studied in more detail by means of SEM (*S*canning *E*lectron *M*icroscopy). It was found that almost the entire fracture face showed the characteristics of transcrystalline SCC (*S*tress *C*orrosion *C*racking); see Fig. 2. Characteristic corrosion pits, tunnels and slots [1, 2] were found near both the pin inner and outer perimeters; see Fig. 3.

SCC Tests

SCC requires the *simultaneous* presence of:

- a (tensile) stress
- a susceptible material
- a corrosive environment.

Initially it was unclear whether and how all these conditions were fulfilled. The driving stress for SCC might be the residual stress introduced during the upsetting of the pin heads. But it

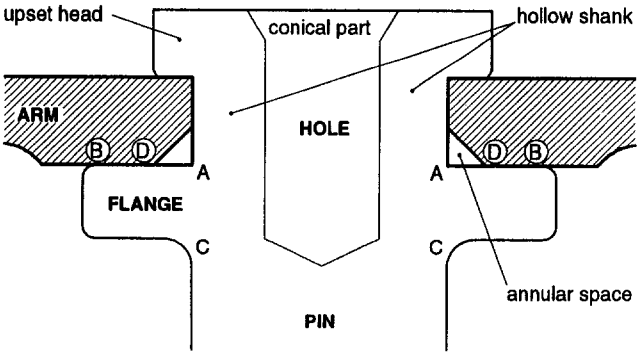

Fig. 1 Schematic cross section of the vane arm assembly

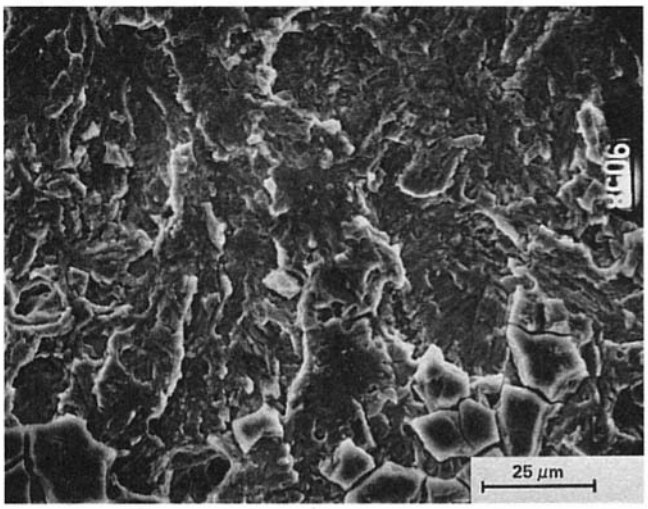

Fig. 2 Example of corrosion products on top of transcrystalline stress corrosion cracking (SCC) of the pin

Contributed by the International Gas Turbine Institute and presented at the 39th International Gas Turbine and Aeroengine Congress and Exposition, The Hague, The Netherlands, June 13–16, 1994. Manuscript received by the International Gas Turbine Institute February 26, 1994. Paper No. 94-GT-298. Associate Technical Editor: E. M. Greitzer.

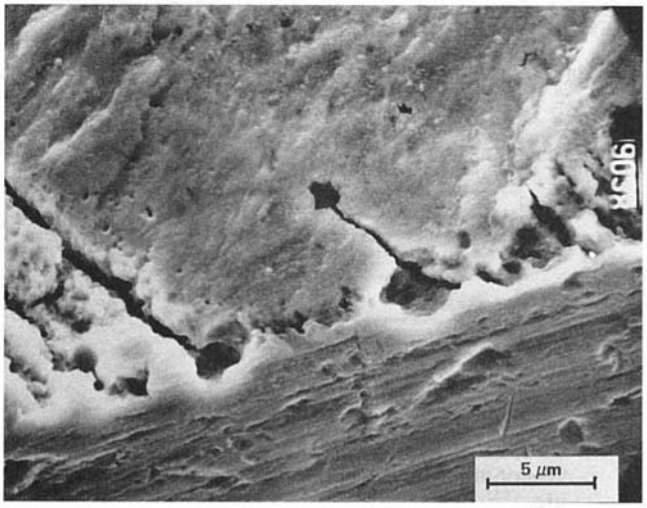

Fig. 3 Example of corrosion pits and slots: the lower part of the fractograph shows the inner perimeter and part of the surface of the central hole in the pin

was unknown whether this stress was high enough to initiate SCC. The pin material was the nitrogen-strengthened stainless steel Nitronic 60. No definitive literature data on the SCC susceptibility of Nitronic 60 could be found [3, 4]. The West European environment is certainly corrosive, see, e.g., [5, 6]. However, in view of the manufacturing process, it was supposed that the annular space (see Fig. 1), where the SCC cracks were initiated, was (mechanically) sealed from the environment. In that case the corrosive medium would have to have been introduced during the production process, e.g., by cleaning with chloride-containing solvents or by a chloride-containing grease used during the upsetting.

In view of these uncertainties it was decided to perform SCC tests according to ASTM Standard Practice G36-87, which involves exposure in boiling $MgCl_2$. The test articles were 15 levers, including some new ones. No external stresses were applied. The test duration was seven days. After the test the pins of all levers exhibited cracks and $MgCl_2$ was found in all internal spaces investigated. This shows that:

- The required stress for SCC was the residual stress arising from the production method.
- Nitronic 60 *is* prone to SCC.
- The internal annular space was not sealed from the environment. Hence it is possible that the corrosive environment penetrated into these internal spaces. Evidence that this really occurred during service will be given later.

Condition of Unfailed Pins

Quantitative Results. A major point was whether an isolated case was concerned. Hence a number of techniques were

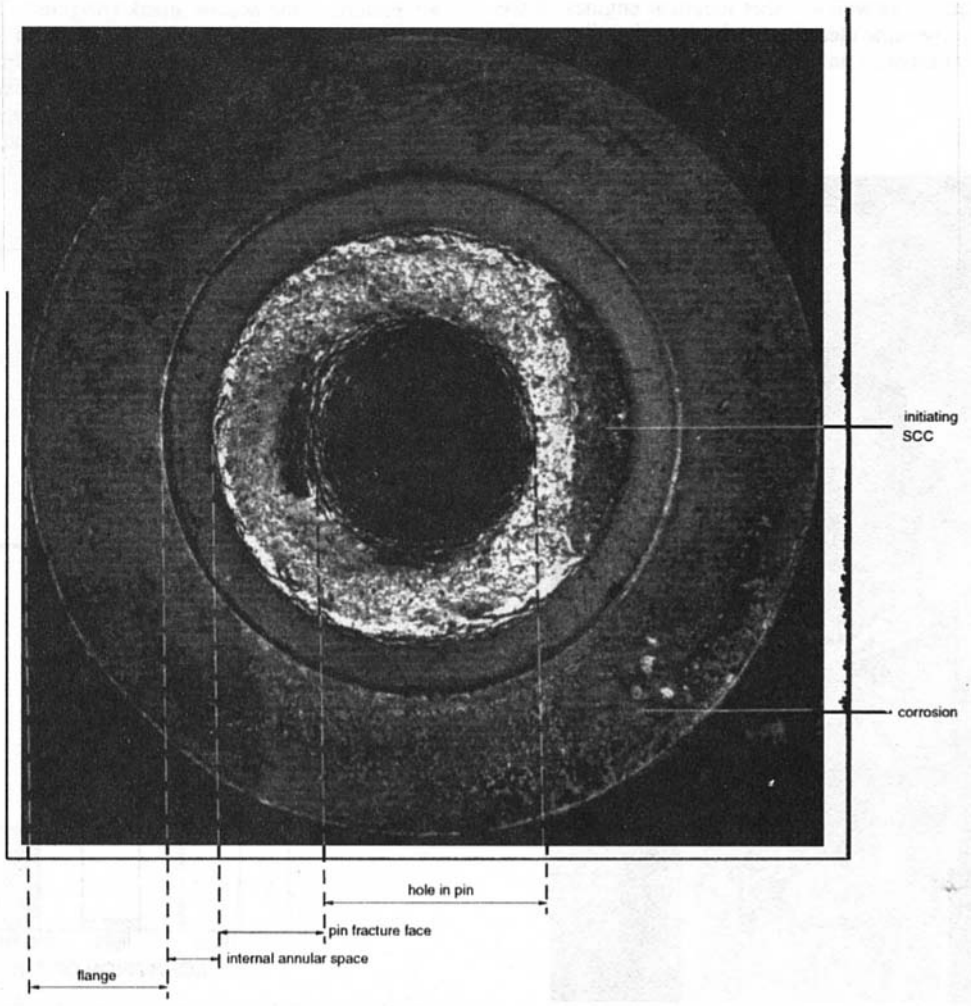

Fig. 4 Result of tensile test. The plane of the photograph is along AA in Fig. 1; the viewing direction is downward.

Table 1 Number of pins with SCC as fraction of the total number of pins tested

Engine cycles	3th stage	4th stage	5th stage
550	14 %	20 %	13 %
850	9 %	28 %	3 %
1250 (mishap)	20 %	not tested	63 %
1650	20 %	72 %	12 %

Table 2 Maximum area fraction of SCC in fracture face

Engine cycles	3th stage	4th stage	5th stage
550	52 %	64 %	39 %
850	64 %	78 %	< 20 %
1250 (mishap)	11 %	not tested	94 %
1650	86 %	90 %	75 %

used to investigate whether SCC had been active in other pins of the accident engine as well as other identical engines of the same user. After it became clear from laborious metallographic sectioning that a number of unfailed pins exhibited SCC, it was decided to:

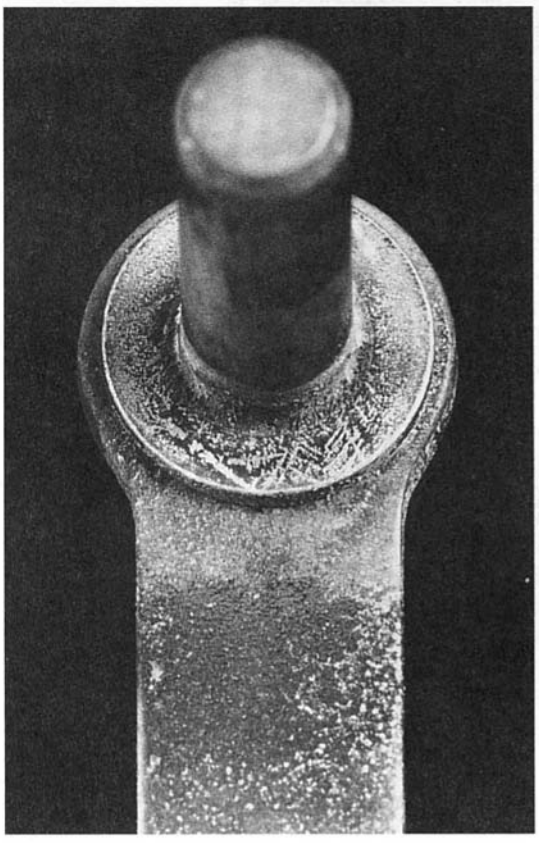

Fig. 5 Extreme example of salt on vane arm

Table 3 Relationship between external salts and SCC for the third stage levers of the 850 cc engine

		pins with SCC	pins with no SCC	Total
arms with	salt	8	10	18
	no salt	0	72	72
	Total	8	82	92

1 Inspect all levers frequently.
2 Continue the investigation to determine whether the occurrence of SCC was dependent on factors such as the vendor of the levers, the compressor stage, or the service life.

X-ray inspection was found to be very unreliable due to the complicated geometry. Optical metallography of cross sections through the pins could also give unreliable results for other crack geometries than perfectly annular, and also the preparation of cross sections of hundreds of pins would have been very time consuming. The engine manufacturer came up with the excellent idea to perform tensile tests on the pins, using a simple jig fitting with the grips of the tensile machine. Hydraulic grips enabled a rapid change of the test articles. 643 pins were tensile tested. There were different pin failure types, namely:

- Failure of the hollow shank (88 pins). This fracture type occurred when an stress corrosion crack of some length was already present in the plane AA in Fig. 1. Figure 4 illustrates the resulting fracture face. The dull pre-existing SCC can be clearly distinguished from the shinier grey overload area caused by the tensile test. The amount of SCC could be quantified by determining the percentage of SCC in the fracture face by means

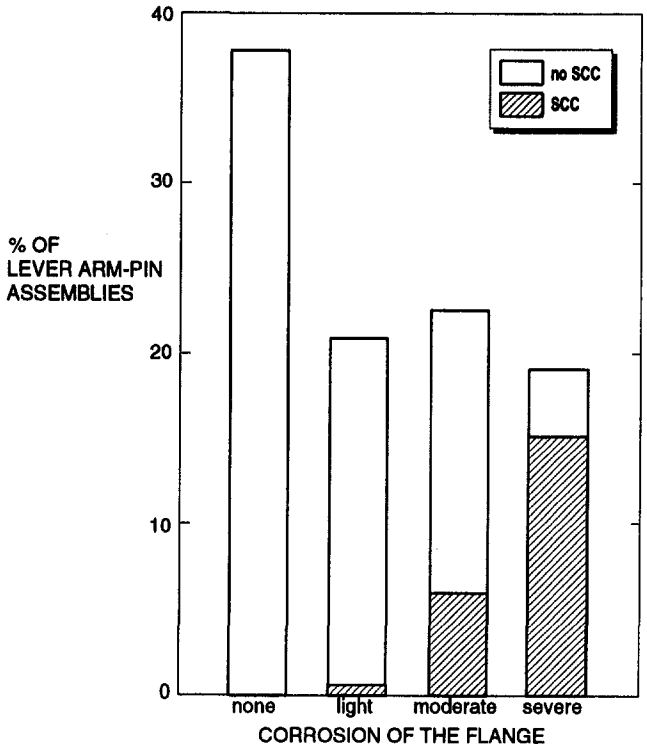

Fig. 6 Relationship between the occurrence of SCC and corrosion of the flange

of an image analyzer or from the decreased fracture load, or by measuring the maximum stress corrosion crack length (as percentage of the wall thickness).

- Shearing of the upset head (550 pins). This fracture type occurred mainly when no stress corrosion crack was present (494 pins). However, more rarely (56 pins) this crack type was also observed if the stress corrosion crack was too small for crack initiation of the shank type, as revealed by careful inspection after the tensile tests. In order to determine the size of these small cracks, a number of them were forcibly opened or cross-sectioned.
- Very rarely (5 pins) sound pins failed in the radius near C in Fig. 1.

Tables 1 and 2 provide examples of the data obtained. It is seen that SCC was found for all variable vane compressor stages in all engines investigated. It might have been expected that the severity of SCC would depend on the stage number and would increase with the number of cycles (which would be very useful in establishing an inspection interval), but such tendencies were absent.

The manufacturer performed similar tests on pins originating from engines that had been operating in other regions than Western Europe. Severe SCC was found, but only after much longer service lives.

Other Observations

- Figure 4 illustrates the observation that SCC always initiated in the annular internal space.
- On a number of lever arms salt deposits were present, e.g. see Fig. 5. EDX (*E*nergy *D*ispersive analysis of *X*-rays) in the SEM revealed that these deposits consisted of the harmless $CaSO_4$ and the corrosive NaCl. Because of aerodynamic reasons (stagnation of the bypass air near obstacles), this salt had not been deposited on all lever arms. There was a close relationship between the presence of these deposits and the occurrence of SCC; see Table 3.
- For a number of levers, the sides of the flanges facing the arms (BD in Fig. 1) were corroded; the other sides of the flanges were always in good condition. There was a close relationship between corrosion of the flange of a particular pin and the occurrence of SCC, Fig. 6. The aforementioned salts were also found on the corroded flanges.
- For some levers, many NaCl crystals were found in the internal annular space. Although this observation was relatively rare, it seems unlikely that this NaCl was introduced during production.

Discussion

From the forementioned observations we obtain the following scenario. During flight the salt in the bypass air deposited on a number of lever arms (Fig. 5). During shutdown periods with high relative humidity the deposits absorbed moisture from the air so that a concentrated salt solution was obtained. This salt solution was able to penetrate any opening between the vane arm and the flange of the pin (along BD in Fig. 1). Hence the observed flange corrosion (Fig. 6) can be explained by crevice corrosion of the relatively less noble pin material. Finally the salt solution reached the unsealed annular internal space (see Fig. 1) and supplied the aggressive environment for SCC of pin material in the highly stressed area near A.

The failed pin in the accident engine happened to be the first one. Differences between different engines can be explained by different flight types (e.g., over sea or coastal regions or not) and different humidities during shutdown periods, rather than by differences in service life.

Conclusions

The main cause of the crash was that the engine manufacturer selected an SCC-prone material (Nitronic 60) for the pins of the levers of the compressor variable vanes in the design stage. The solution has been to change the pin material. The first levers with the new pin material were delivered less than five months after the accident. The frequent inspections on the levers with the old pins were continued until all these levers had been replaced.

References

1 Swann, P. R., and Embury, J. D., "Microstructural Aspects of Stress-Corrosion Failure," in: *High-Strength Materials,* V. F. Zackay, ed., Wiley, New York, 1965, pp. 327–363.

2 Nielsen, N. A., "Nature of Initial Corrosion of Stressed Stainless Steels by Chloride Ions," *Corrosion,* Vol. 20, 1964, pp. 104–109t.

3 Douthet, J. A., "Nitronic Family of Nitrogen-Bearing Stainless Steels," *Metal Progress,* Vol. 108, 1975, pp. 50–54.

4 Kirchner, R. W., Crook, P., and Asphani, A. J., "Corrosion Resistant, High Performance Alloys for the Food Industry," *Corrosion 84,* NACA, 1984, Paper 102.

5 Kolkman, H. J., and Mom, A. J. A., "Corrosion and Corrosion Control in Gas Turbines, Part I: The Compressor Section," ASME Paper No. 84-GT-225, 1984.

6 Kolkman, H. J., "Coatings for Gas Turbine Compressors," in: *Materials Development in Turbo-Machinery Design,* D. M. R. Taplin, J. F. Knott, and M. H. Lewis, eds., The Institute of Metals, London, Book 456, 1989, pp. 224–230.

N. N. Nemeth
NASA Lewis Research Center,
Cleveland, OH 44135

L. M. Powers
Department of Civil Engineering,
Cleveland State University,
Cleveland, OH 44135

L. A. Janosik

J. P. Gyekenyesi

NASA Lewis Research Center,
Cleveland, OH 44135

Durability Evaluation of Ceramic Components Using CARES/LIFE

The computer program CARES/LIFE calculates the time-dependent reliability of monolithic ceramic components subjected to thermomechanical and/or proof test loading. This program is an extension of the CARES (Ceramics Analysis and Reliability Evaluation of Structures) computer program. CARES/LIFE accounts for the phenomenon of subcritical crack growth (SCG) by utilizing the power law, Paris law, or Walker equation. The two-parameter Weibull cumulative distribution function is used to characterize the variation in component strength. The effects of multiaxial stresses are modeled using either the principle of independent action (PIA), the Weibull normal stress averaging method (NSA), or the Batdorf theory. Inert strength and fatigue parameters are estimated from rupture strength data of naturally flawed specimens loaded in static, dynamic, or cyclic fatigue. Application of this design methodology is demonstrated using experimental data from alumina bar and disk flexure specimens, which exhibit SCG when exposed to water.

Introduction

Advanced ceramic components designed for gasoline, diesel, and turbine heat engines are leading to lower engine emissions, higher fuel efficiency, and more compact designs due to their low density and ability to retain strength at high temperatures. Ceramic materials are also used for wear parts (nozzles, valves, seals, etc.), cutting tools, grinding wheels, bearings, coatings, electronics, and human prostheses. Among the many requirements for the successful application of advanced ceramics are the proper characterization of material properties and the use of a mature and validated brittle material design methodology.

Ceramics are brittle and the lack of ductility leads to low strain tolerance, low fracture toughness, and large variations in observed fracture strength. The material as processed has numerous inherent randomly distributed flaws. The observed scatter in fracture strength is caused by the variable severity of these flaws. The ability of a ceramic component to sustain a load also degrades over time. This is due to a variety of effects such as oxidation, creep, stress corrosion, and cyclic fatigue. Stress corrosion and cyclic fatigue result in a phenomenon called subcritical crack growth (SCG). SCG initiates at an existing flaw and continues until a critical length is reached, causing catastrophic crack propagation. The SCG failure mechanism is a load-induced phenomenon over time. It can also be a function of chemical reaction, environment, debris wedging near the crack tip, and deterioration of bridging ligaments. Because of this complexity, models that have been developed tend to be semi-empirical and approximate the behavior of subcritical crack growth phenomenologically.

The objective of this paper is to present a description of the integrated design computer program, CARES/LIFE [1] (Ceramics Analysis and Reliability Evaluation of Structures LIFE prediction program). The theory and concepts presented in this paper reflect the capabilities of the CARES/LIFE program for time-dependent probabilistic design. To determine the validity of the design methodology utilized in this software, time-dependent reliability predictions from CARES/LIFE are compared with experimental data [2] from uniaxially and biaxially loaded alumina flexure bars and disks, which are known to exhibit slow crack growth in water.

Contributed by the International Gas Turbine Institute and presented at the 39th International Gas Turbine and Aeroengine Congress and Exposition, The Hague, The Netherlands, June 13–16, 1994. Manuscript received by the International Gas Turbine Institute February 11, 1994. Paper No. 94-GT-362. Associate Technical Editor: E. M. Greitzer.

Program Capability and Description

Probabilistic component design involves predicting the probability of failure for a thermomechanically loaded component from specimen rupture data. Typically these experiments are performed using many simple geometry flexural or tensile test specimens. A static, dynamic, or cyclic load is applied to each specimen until fracture. Statistical strength and SCG (fatigue) parameters are then determined from these data. Using these parameters and the results obtained from a finite element analysis, the time-dependent reliability for a complex component geometry and loading is then predicted. Appropriate design changes are made until an acceptable probability of failure has been reached. This design methodology combines the statistical nature of strength-controlling flaws with the mechanics of crack growth to allow for multiaxial stress states, concurrent (simultaneously occurring) flaw populations, and scaling effects. These issues are addressed within the CARES/LIFE program.

CARES/LIFE predicts the probability of failure of a monolithic ceramic component as a function of service time. It assesses the risk that the component will fracture prematurely as a result of subcritical crack growth. The effect of proof testing components prior to service is also considered. CARES/LIFE is coupled to commercially available finite element programs such as ANSYS, ABAQUS, MSC/NASTRAN, and COSMOS/M. CARES/LIFE is an extension of the CARES [3, 4] program. It retains all of the capabilities of the previous CARES code, which include fast-fracture component reliability evaluation and Weibull parameter estimation from inert strength (without SCG contributing to failure) specimen data. CARES/LIFE can estimate parameters that characterize SCG from specimen data as well.

Finite element heat transfer and linear-elastic stress analyses are used to determine the component's temperature and stress distributions. The reliability at each element is calculated assuming that randomly distributed volume flaws and/or surface flaws control the failure response. The probability of survival for each element is assumed to be a mutually exclusive event, and the overall component reliability is then the product of all the element survival probabilities. CARES/LIFE generates a data file containing element risk-of-rupture intensities (a local measure of reliability) for graphical rendering of the structure's critical regions.

CARES/LIFE describes the probabilistic nature of material strength, using the Weibull cumulative distribution function. The effect of multiaxial stresses on reliability is predicted using

the principle of independent action (PIA) [5, 6], the Weibull normal stress averaging method (NSA) [7], or the Batdorf theory [8, 9]. The Batdorf theory combines the weakest link theory and linear elastic fracture mechanics (LEFM). Conventional fracture mechanics analysis requires that both the size of the critical crack and its orientation relative to the applied loads determine the fracture stress. The Batdorf theory includes the calculation of the combined probability of the critical flaw being within a certain size range and being located and oriented so that it may cause fracture. A user-selected flaw geometry and a mixed-mode fracture criterion are required to model volume or surface-strength-limiting defects. Mixed-mode fracture refers to the ability of a crack to grow under the combined actions of a normal load (opening mode) and shear load (sliding and tearing modes) on the crack face. CARES/LIFE includes the total strain energy release rate fracture criterion, which assumes a crack will extend in its own plane (coplanar) [9]. Out-of-plane crack extension criteria are approximated by a simple semi-empirical equation [10, 11]. Available flaw geometries include the Griffith crack, penny-shaped crack, semicircular crack, and notched crack. The Batdorf theory is equivalent to the probabilistic multiaxial theories proposed by Evans [12] and Matsuo [13].

Subcritical crack growth is difficult to model, because it is a complex phenomenon often involving a combination of failure mechanisms. Existing models usually involve empirically derived crack propagation laws that describe the crack growth in terms of the stress intensity factor at the crack tip plus additional parameters obtained from experimental data.

In CARES/LIFE, the relations describing subcritical crack growth are directly incorporated into the PIA, NSA, and Batdorf theories. Subcritical crack growth is modeled with the power law [14, 15], the Paris law [16], and the Walker law [17, 18] for static and constant-amplitude cyclic loading. These laws use experimentally determined parameters, which are material and environment sensitive. The power law is used to model stress corrosion cracking in materials such as glasses and alumina exposed to H_2O. Elevated-temperature slow crack growth of silicon nitrides, silicon carbides, and alumina also follows power law behavior.

Some polycrystalline ceramics are prone to strength degradation due to mechanical damage induced by cyclic loading. The Paris and Walker laws have been suggested as models to account for this behavior [18]. The Walker equation is functionally similar to the Paris equation with additional terms to account for the effect of the R-ratio (minimum cycle stress to maximum cycle stress) on lifetime.

CARES/LIFE is capable of predicting the change in a surviving component's reliability after proof testing is performed. Proof testing is the loading of all components prior to service to eliminate those that may fail prematurely. The components that survive the proof test will have a lower (attenuated) risk of failure in service. In CARES/LIFE the attenuated failure probability is calculated using the PIA, the Weibull normal stress averaging, and the Batdorf theories. The Batdorf model is used to calculate the attenuated failure probability when the proof test load and the service load are not in line or have different multi-axial stress states. This feature is useful when the proof test does not identically simulate the actual service conditions on the component. The durations of the proof test and the service load are also considered in the analysis.

Predicted lifetime reliability of structural ceramic components depends on Weibull and fatigue parameters estimated from widely used tests involving flexural or tensile specimens. CARES/LIFE estimates fatigue parameters from naturally flawed specimens ruptured under static, cyclic, or dynamic (constant stress rate) loading. Fatigue and Weibull parameters are calculated from rupture data of three-point and four-point flexure bars, as well as tensile specimens. For other specimen geometries, a finite element model of the specimen is also required when estimating these parameters.

Theory

Time-dependent reliability is based on the mode I equivalent stress distribution transformed to its equivalent stress distribu-

Nomenclature

A = surface area; material-environmental fatigue constant
a = crack half length
B = subcritical crack growth constant
$\bar{C}$ = Shetty's constant in mixed-mode fracture criterion
g = g-factor
H = step function
i = ranking of ordered fracture data in statistical analysis
K = stress intensity factor
k = crack density coefficient
m = Weibull modulus, or shape parameter
N = material-environmental fatigue constant
n = number of cycles
P_f = cumulative failure probability
Q = cyclic fatigue parameter
R = ratio of minimum to maximum effective stress in a load cycle
T = period of one cycle
t = time
t_o = time-dependent scale parameter
V = volume; crack velocity
x, y, z = Cartesian coordinate directions
Y = crack geometry factor
α = angle between σ_n and the stress σ_1
β = angle between σ_n projection and the stress σ_2 in plane perpendicular to σ_1
Δ = increment
η = crack density function
π = 3.1416
σ = applied stress distribution
σ_o = Weibull scale parameter
$\sigma_1, \sigma_2, \sigma_3$ = tensor stress components; principal stresses ($\sigma_1 \geq \sigma_2 \geq \sigma_3$)
τ = shear stress acting on oblique plane whose normal is determined by angles α and β
Ψ = spatial location (x, y, z) and orientation (α, β) in a component
Ω = solid angle in three-dimensional principal stress space for which $\sigma_e \geq \sigma_{cr}$
ω = angle in two-dimensional principal stress space for which $\sigma_e \geq \sigma_{cr}$

Subscripts

B = Batdorf
c = cyclic; critical
ch = characteristic
cr = critical
d = dynamic fatigue
e, ef = effective
eq = equivalent
f = failure; fracture
I = crack opening mode
II = crack sliding mode
III = crack tearing mode
i = ith
max = maximum
min = minimum
n = normal; normal stress averaging
S = surface
T = transformed
u = uniaxial
V = volume
w = Weibull
θ = characteristic

Superscripts

$\tilde{}$ = modified parameter
$\bar{}$ = normalized quantity

tion at time $t = 0$. Investigations of mode I crack extension [19] have resulted in the following relationship for the equivalent mode I stress intensity factor:

$$K_{Ieq}(\Psi, t) = \sigma_{Ieq}(\Psi, t) Y \sqrt{a(\Psi, t)} \quad (1)$$

where $\sigma_{Ieq}(\Psi, t)$ is the equivalent mode I stress on the crack, Y is a function of crack geometry, $a(\Psi, t)$ is the appropriate crack length, and Ψ represents a location (x, y, z) within the body and the orientation (α, β) of the crack. In some models such as the Weibull and PIA, Ψ represents a location only. Y is a function of crack geometry; however, herein it is assumed constant with subcritical crack growth. Crack growth as a function of the equivalent mode I stress intensity factor is assumed to follow a power law relationship:

$$\frac{da(\Psi, t)}{dt} = AK^N_{Ieq}(\Psi, t) \quad (2)$$

where A and N are material/environmental constants. The transformation of the equivalent stress distribution at the time of failure, $t = t_f$, to its critical effective stress distribution at time $t = 0$ is expressed as [20, 21]

$$\sigma_{Ieq,0}(\Psi, t_f) = \left[\frac{\int_0^{t_f} \sigma^N_{Ieq}(\Psi, t) dt}{B} + \sigma^{N-2}_{Ieq}(\Psi, t_f) \right]^{1/(N-2)} \quad (3)$$

where

$$B = \frac{2}{AY^2 K^{N-2}_{IC}(N-2)}$$

is a material/environmental fatigue parameter, K_{Ic} is the critical stress intensity factor, and $\sigma_{Ieq}(\Psi, t_f)$ is the equivalent stress distribution in the component at time $t = t_f$. The dimensionless fatigue parameter N is independent of fracture criterion. B is adjusted to satisfy the requirement that for a uniaxial stress state, all models produce the same probability of failure. The parameter B has units of stress^2 $\times$ time.

Volume Flaw Analysis. The probability of failure for a ceramic component using the Batdorf model [8, 9, 22] for volume flaws is

$$P_{fV} = 1 - \exp\left\{ -\int_V \left[\int_0^{\sigma_{e_{\max}}} \frac{\Omega}{4\pi} \frac{d\eta_V(\sigma_{cr})}{d\sigma_{cr}} d\sigma_{cr} \right] dV \right\} \quad (4)$$

where V is the volume, η_V is the crack density function, $\sigma_{e_{\max}}$ is the maximum value of $\sigma_{Ieq,0}$ for all values of Ψ, and Ω is the area of a solid angle projected onto a unit radius sphere in principal stress space containing all crack orientations for which the effective stress is greater than or equal to the critical mode I strength, σ_{cr}. The crack density distribution is a function of the critical effective stress distribution. For volume flaw analysis, the crack density function is expressed as

$$\eta_V(\sigma_{cr}(\Psi)) = k_{BV} \sigma^{m_V}_{cr} \quad (5)$$

where k_{BV} and m_V are material constants. The solid angle is expressed as

$$\Omega = \int_0^{2\pi} \int_0^{\pi} H(\sigma_{Ieq,0}, \sigma_{cr}) \sin \alpha d\alpha d\beta \quad (6)$$

where

$$H(\sigma_{Ieq,0}, \sigma_{cr}) = \begin{cases} 1 & \sigma_{Ieq,0} \geq \sigma_{cr} \\ 0 & \sigma_{Ieq,0} < \sigma_{cr} \end{cases}$$

and α and β are the radial and azimuthal angles, respectively, on the unit radius sphere. The transformed equivalent stress $\sigma_{Ieq,0}$ is dependent on the appropriate fracture criterion, crack shape, and time to failure, t_f. Equation (4) can be simplified by performing the integration of σ_{cr} [22], yielding the time-dependent probability of failure for volume flaw analysis

$$P_{fV}(t_f) = 1 - \exp\left[-\frac{k_{BV}}{2\pi} \int_V \int_0^{2\pi} \int_0^{\pi/2} \sigma^{m_V}_{Ieq,0}(\Psi, t_f) \sin \alpha d\alpha d\beta dV \right] \quad (7)$$

Fracture criteria and crack shapes available for time-dependent analysis are identical to those used for fast fracture analysis in CARES [3, 4]. These fracture criteria include Weibull normal stress averaging (a shear-insensitive case of the Batdorf theory), the total coplanar strain energy release rate, and the noncoplanar crack extension (Shetty) criterion.

For a stressed component, the probability of failure for volume flaw analysis is calculated from Eq. (7). The finite element method enables discretization of the component into incremental volume elements. CARES/LIFE evaluates the reliability at the Gaussian integration points of the element or, optionally, at the element centroid. Subelement volume is defined as the contribution of the integration point to the element volume in the course of the numerical integration procedure. The volume of each subelement (corresponding to a Gauss integration point) is calculated using shape functions inherent to the element type [4]. Assuming that the probability of survival for each element is a mutually exclusive event, the overall component reliability is then the product of all the calculated element (or subelement) survival probabilities.

Surface Flaw Analysis. The probability of failure for a ceramic component using the Batdorf model [8, 9, 22] for surface flaws is

$$P_{fS} = 1 - \exp\left\{ -\int_A \left[\int_0^{\sigma_{e_{\max}}} \frac{\omega}{\pi} \frac{d\eta_S(\sigma_{cr})}{d\sigma_{cr}} d\sigma_{cr} \right] dA \right\} \quad (8)$$

where A is the surface area, η_S is the crack density function, $\sigma_{e_{\max}}$ is the maximum value of $\sigma_{Ieq,0}$ for all values of Ψ, and ω is the arc length of an angle α projected onto a unit radius semi-circle in principal stress space containing all of the crack orientations for which the effective stress is greater than or equal to the critical stress. Analogous to the argument for volume flaws, Eq. (8) can be reformulated, yielding [22]

$$P_{fS}(t_f) = 1 - \exp\left[-\frac{k_{BS}}{\pi} \int_A \int_0^{\pi} \sigma^{m_S}_{Ieq,0}(\Psi, t_f) d\alpha dA \right] \quad (9)$$

The transformed equivalent stress $\sigma_{Ieq,0}$ is dependent on the appropriate fracture criterion, crack shape, and time to failure, t_f. The fracture criteria and crack shapes available for time-dependent analysis are identical to those used for fast fracture analysis. These fracture criteria include Weibull normal stress averaging (a shear-insensitive case of the Batdorf theory), the total coplanar strain energy release rate, and the noncoplanar crack extension (Shetty) criterion.

The finite element method enables discretization of the surface of the component into incremental area elements. CARES/LIFE evaluates the failure probability at the Gaussian integration points of shell elements or, optionally, at the element centroids. The area of each subelement (corresponding to a Gaussian integration point) is calculated using shape functions inherent to the element type [4]. Assuming that the probability of survival for each element is a mutually exclusive event, the overall component reliability is then the product of all the calculated element (or subelement) survival probabilities.

Static Fatigue. Static fatigue is defined as the application of a nonvarying load over time. For this case the mode I equivalent stress, $\sigma_{Ieq}(\Psi, t)$, is independent of time and is thus denoted by $\sigma_{Ieq}(\Psi)$. Integrating Eq. (3) with respect to time yields

$$\sigma_{leq,0}(\Psi, t_f) = \sigma_{leq}(\Psi)\left[\frac{t_f \sigma^2_{leq}(\Psi)}{B} + 1\right]^{1/(N-2)} \quad (10)$$

Dynamic Fatigue. Dynamic fatigue is defined as the application of a constant stress rate $\dot{\sigma}(\Psi)$ over a period of time, t. Assuming the applied stress is zero at time $t = 0$, then

$$\sigma_{leq}(\Psi, t) = \dot{\sigma}(\Psi)t \quad (11)$$

Substituting Eq. (11) into Eq. (3) results in an expression for effective stress at the time of failure:

$$\sigma_{leq,0}(\Psi) = \left[\frac{\sigma^N_{leq}(\Psi, t_f)t_f}{(N+1)B} + \sigma^{N-2}_{leq}(\Psi, t_f)\right]^{1/(N-2)} \quad (12)$$

Cyclic Fatigue. Cyclic fatigue is defined as the repeated application of a loading sequence. Analysis of the time-dependent probability of failure for a component subjected to various cyclic boundary load conditions is simplified by transforming that type of loading to an equivalent static load. The conversion satisfies the requirement that both systems will cause the same crack growth [23]. Implicit in this conversion is the validity of Eq. (2) for describing the crack growth. The probability of failure is obtained with respect to the equivalent static state.

Evans [24] and Mencik [23] defined g factors, $g(\Psi)$, for various types of cyclic loading, that are used to convert the cyclic load pattern to an equivalent static load. For periodic loading, T is the time interval of one cycle, and $\sigma_{leq}(\Psi)$ is the equivalent static stress acting over the same time interval, t_1, as the applied cyclic stress, $\sigma_{leqc}(\Psi, t)$, at some location Ψ. The equivalent static stress is related to the cyclic stress by

$$\sigma^N_{leq}(\Psi)t_1 = \int_0^{t_1} \sigma^N_{leqc}(\Psi, t)dt = t_1\left[\frac{\int_0^T \sigma^N_{leqc}(\Psi, t)dt}{T}\right]$$
$$= g(\Psi)\sigma^N_{leqc_{\max}}(\Psi)t_1 \quad (13)$$

The CARES/LIFE program uses the maximum cyclic stress, $\sigma_{leqc_{\max}}(\Psi)$, of the periodic load as a characteristic value to normalize the g factor. For a periodic load over a time t_1, the mode I static equivalent stress distribution is

$$\sigma_{leq,0}(\Psi, t_f) = \sigma_{leqc_{\max}}(\Psi)\left[\frac{g(\Psi)t_f \sigma^2_{leqc_{\max}}(\Psi)}{B} + 1\right]^{1/(N-2)} \quad (14)$$

The use of g factors for determining component life is an unconservative practice for materials prone to cyclic damage. The Walker equation [17], which has traditionally been used in metals design, has been suggested as a model of fatigue damage for some ceramic materials [18]. The Walker equation describes the crack growth increment per cycle, n, as

$$\frac{da(\Psi, n)}{dn} = AK^{N-Q}_{Ie_{\max}}(\Psi, n)\Delta K^Q_{Ie}(\Psi, n) \quad (15)$$

where

$$K_{Ie_{\max}}(\Psi, n) = \sigma_{leqc_{\max}}(\Psi, n)Y\sqrt{a(\Psi, n)}$$

and $\Delta K_{Ie}(\Psi, n)$ represents the range of the stress intensity factor over the load cycle. The subscript max indicates the maximum cycle stress. The cyclic fatigue parameters A, N, and Q are experimentally determined. The Walker equation reduces to the Paris law [16] when N and Q are equal in value. The integration of Eq. (15) parallels that of Eq. (2), yielding the cyclic fatigue equivalent stress distribution

$$\sigma_{leqc,0}(\Psi, n_f) = \left[\frac{\int_{n=0}^{n_f}[1 - R(\Psi, n)]^Q \sigma^N_{leqc_{\max}}(\Psi, n)dn}{B} + \sigma^{N-2}_{leqc_{\max}}(\Psi, n_f)\right]^{1/(N-2)} \quad (16)$$

where $R(\Psi, n)$ is the ratio of the minimum to maximum cyclic stress, n_f is the number of cycles to failure, and B is now expressed in units of stress^2 × cycle. The parameters B and N are determined from cyclic data.

Evaluation of Fatigue Parameters From Inherently Flawed Specimens. Lifetime reliability of structural ceramic components depends on the history of the loading, the component geometry, the distribution of pre-existing flaws, and the parameters that characterize subcritical crack growth. These crack growth parameters must be measured under conditions representative of the service environment. When determining fatigue parameters from rupture data of naturally flawed specimens, the statistical effects of the flaw distribution must be considered along with the strength degradation effects of subcritical crack growth. In the following discussion, fatigue parameter estimation methods are described for surface flaw analysis using the power law formulation for constant stress rate loading (dynamic fatigue). Analogous formulations for volume flaws, static fatigue, and cyclic fatigue have also been developed [1].

For the uniaxial Weibull distribution, the probability of failure is expressed as

$$P_{fS}(t_f) = 1 - \exp\left[-k_{wS}\int_A \sigma^{m_S}_{1,0}(\Psi)dA\right] \quad (17)$$

where Ψ represents a location (x, y) and $\sigma_{1,0}$ denotes the transformed uniaxial stress analogous to $\sigma_{leq,0}$ as defined in Eq. (9). The Weibull crack density coefficient is given by

$$k_{wS} = \frac{1}{\sigma^{m_S}_{oS}} \quad (18)$$

The Weibull scale parameter, σ_{oS}, corresponds to the stress level where 63.21 percent of specimens with unit area would fail and has units of stress × area$^{1/m_S}$. CARES/LIFE normalizes the various fracture criteria to yield an identical probability of failure for the uniaxial stress state. This is achieved by adjusting the fatigue constant B. For the uniaxial Weibull model this adjusted value is denoted by B_w and for the Batdorf model it is denoted by B_B. From the dynamic fatigue Eq. (12), substituting B_{wS} for B, N_S for N, the uniaxial stress σ_1 for σ_{leq}, and rearranging Eq. (17) while assuming that

$$\frac{\sigma^2_1(\Psi, t_f)t_f}{(N_S + 1)B_{wS}} \gg 1 \quad (19)$$

the median behavior of the experimental dynamic fatigue data can be described by

$$\sigma_{f_{0.5}} = A_d \dot{\sigma}^{1/(N_S+1)} \quad (20)$$

where $\sigma_{f_{0.5}}$ is the median rupture stress of the specimen and $\dot{\sigma}$ represents the stress rate at the location of maximum stress. The constant A_d is

$$A_d = \left\{\frac{(N_S + 1)B_{wS}\sigma^{N_S-2}_{oS}}{\left[\frac{A_{ef}}{\ln\left(\frac{1}{1 - 0.50}\right)}\right]^{1/\tilde{m}_S}}\right\}^{1/(N_S+1)} \quad (21)$$

where

$$\tilde{m}_S = \frac{m_S}{N_S - 2}$$

Table 1 Weibull parameters estimated from inert data

Specimen	Weibull modulus, m_S	90% confidence bounds on m_S	Characteristic strength, $\sigma_{\theta S}$ MPa	90% confidence bounds on $\sigma_{\theta S}$ MPa	Scale parameter, σ_{oS} MPa · mm$^{2/m_S}$
3-point	25.43	20.47, 29.91	385.9	382.0, 389.9	414.7
4-point	23.76	19.13, 27.95	353.4	349.6, 357.3	425.8
Disk	22.25	17.12, 26.81	338.7	334.1, 343.5	436.4
Disk (batch 2)	28.98	13.28, 40.88	351.4	341.5, 362.2	423.2

The constants A_d and A_{ef} are obtained by equating risks of rupture. A_{ef} is a modified effective area required for the time-dependent formulation. For the uniaxial Weibull distribution, the expression for the modified effective area is

$$A_{ef} = \int_A \left(\frac{\sigma_1(\Psi, t_f)}{\sigma_f} \right)^{\tilde{m}_S N_S} dA \tag{22}$$

where $\sigma_1(\Psi, t_f)$ denotes the maximum principal stress distribution. For multiaxially stressed components, the Batdorf technique is used to evaluate fatigue parameters. The analogous formulation for A_{ef} is then

$$A_{ef} = \frac{2\bar{k}_{BS}}{\pi} \int_A \left[\int_0^{\pi/2} \left(\frac{\sigma_{leq}(\Psi, t_f)}{\sigma_f} \right)^{\tilde{m}_S N_S} d\alpha \right] dA \tag{23}$$

where the normalized Batdorf crack density coefficient is $\bar{k}_{BS} = k_{BS}/k_{wS}$. Equation (21) is applicable except that B_{BS} replaces B_{wS}. The relationship between B_{BS} and B_{wS} for a uniaxial load is established by equating the risk of rupture of the Batdorf model with that of the uniaxial Weibull model [1]

$$\frac{B_{wS}}{B_{BS}} = \left\{ \frac{\pi \int_A \sigma_1^{\tilde{m}_S N_S}(\Psi, t_f) dA}{2\bar{k}_{BS} \int_A \int_0^{\pi/2} \sigma_{leq}^{\tilde{m}_S N_S}(\Psi, t_f) d\alpha dA} \right\}^{1/\tilde{m}_S} \tag{24}$$

As N_S becomes large, Eq. (24) approaches unity.

The terms A_d and N_S in Eq. (21) are determined from experimental data. Taking the logarithm of Eq. (20) yields

$$\ln \sigma_{f_{0.5}} = \ln A_d + \frac{1}{N_S + 1} \ln \dot{\sigma} \tag{25}$$

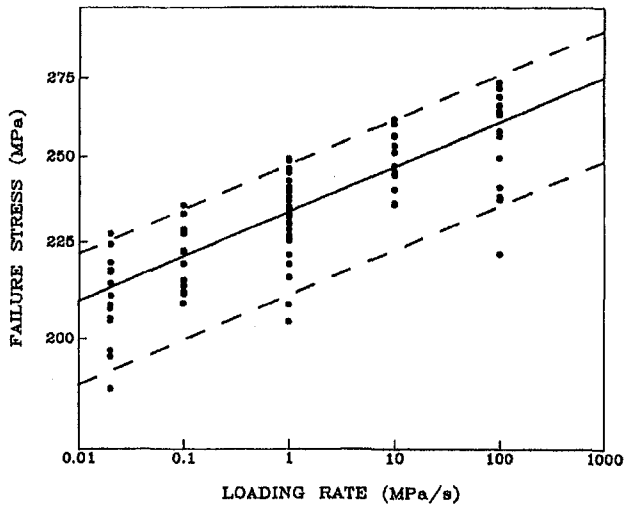

Fig. 1 Dynamic fatigue of alumina four-point flexure bars in water. Median regression line (solid), and 5 and 95 percent regression lines (dashed) estimated with the median deviation technique.

Linear regression analysis of the experimental data is used to solve Eq. (25). The median value method is based on least-squares linear regression of median data points for various stress rates. Another technique uses least-squares linear regression on all the data points. A third option for estimating fatigue parameters is a modification to a method used by Jakus [25]. In this procedure, fatigue parameters are determined by minimizing the median deviation of the logarithm of the failure stress. The median deviation is the mean of the residuals, where the residual is defined as the absolute value of the difference between the logarithm of the failure stress and the logarithm of the median value. In CARES/LIFE this minimization is accomplished by maximizing $\tilde{m}_S(N_S + 1)$ estimated from the data versus the fatigue exponent.

To obtain A_d based on the median line of the distribution the following steps are taken. Experimental data at a sufficient number of discrete levels of applied stressing rate are transformed to equivalent failure times t_{Ti} at a fixed stress rate $\dot{\sigma}_T$ (equating failure probabilities using Eq. (17))

$$t_{Ti} = t_{fi} \left(\frac{\dot{\sigma}_i}{\dot{\sigma}_T} \right)^{N_S/(N_S+1)} \tag{26}$$

where the subscript T indicates a transformed value, the subscript i denotes each observed data number, and $t_{fi} = \sigma_{fi}/\dot{\sigma}_i$. In CARES/LIFE the value of $\dot{\sigma}_T$ is taken as the lowest level of stressing rate in the data set. With the data defined by a single Weibull distribution, parameter estimation is performed on the transformed data using

$$P_{fi} = 1 - \exp\left[-\left(\frac{t_{Ti}}{t_{\theta S}} \right)^{\tilde{m}_S(N_S+1)} \right] \tag{27}$$

where the characteristic time is

$$t_{\theta S} = \left[\frac{(N_S + 1) B \sigma_{oS}^{N_S - 2}}{A_{ef}^{1/\tilde{m}_S} \dot{\sigma}_T^{N_S}} \right]^{1/(N_S+1)} \tag{28}$$

CARES/LIFE performs least-squares or maximum likelihood Weibull parameter estimation as described by Pai [26] to solve Eq. (27) for $\tilde{m}_S(N_S + 1)$ and $t_{\theta S}$. Substituting $\dot{\sigma}_T$ for $\dot{\sigma}$ in Eq. (20) and solving for the rupture stress in Eq. (27) corresponding to a 50 percent probability of failure, $\sigma_{T_{0.50}}$, yields

$$A_d = t_{\theta S} \left\{ \dot{\sigma}_T^{N_S} \left[\ln \left(\frac{1}{1 - 0.50} \right) \right]^{1/\tilde{m}_S} \right\}^{1/(N_S+1)} \tag{29}$$

This value of A_d is used with the fatigue exponent N_S estimated either with the least-squares (using all experimental rupture stresses) or median deviation method. The fatigue constant B is obtained from Eqs. (21) or (28).

Example

This example demonstrates the use of CARES/LIFE to predict the time-dependent reliability of components under multiaxial loads. The data for this example are from experimental work performed by Chao and Shetty [2] on alumina disks and bars exposed to water at room temperature. Chao and Shetty

Table 2 Fatigue parameters for four-point bend bars

Estimation method	Fatigue constant, A_d	Fatigue exponent, N_S	Fatigue constant, B_{wS} MPa^2 · s	Fatigue constant, B_{BS} MPa^2 · s	Crack velocity, V_c m · s^{-1}
Median Value	2.339 x 10^2	36.04	4.590 x 10^{-1}	4.579 x 10^{-1}	1.162
Least Squares	2.336 x 10^2	40.84	5.631 x 10^{-2}	5.617 x 10^{-2}	8.176
Med Deviation	2.337 x 10^2	41.23	4.783 x 10^{-2}	4.771 x 10^{-2}	9.373
Reference 2	---	40.7	---	---	9.1

investigated the relationship between stress state and time-dependent strength degradation, specifically to determine whether strength degradation due to slow crack growth in biaxial flexure can be predicted from inert fracture stresses and dynamic fatigue assessed in simple uniaxial tests. Time-dependent reliability predictions for the alumina from CARES/LIFE are compared to the results obtained by Chao and Shetty.

Details regarding specimen preparation and testing are given in [2]. Two batches of an alumina ceramic were purchased from the same vendor. The first batch was in the form of plates (127 × 127 × 5 mm) and rods (50.8 mm diameter, 76.2 mm length). The plates and rods were made from the same powder lot with identical isostatic pressing and sintering conditions. The second batch of alumina, in the form of rods, was purchased subsequently to examine dynamic fatigue under biaxial stresses. This material had identical chemistry and preparation to the first batch. The measured properties of the first batch include a fracture toughness, K_{Ic}, of 4.13 MPa·$\sqrt{m}$, Young's modulus, E, of 297.2 GPa, and a Poisson ratio, ν, of 0.23.

Bar specimens were cut from the plate stock and disks were cut from the rod stock. Specimens were either tested in a dry nitrogen environment at 100 MPa/s to obtain inert (fast-fracture) strengths, or in deionized water at various stress rates to obtain the time-dependent fracture strengths. The specimens were carefully prepared to minimize machining damage or failure from edge flaws. The uniaxial specimens were nominally 3 × 4 × 45 mm. These specimens were loaded in either four-point flexure with an outer support span of 40 mm and an inner load span of 20 mm, or in three-point flexure using a 40 mm support span. The disk specimens were nominally 3.175 mm in thickness and 50.8 mm in diameter. They were loaded under uniform pressure on one face and supported on the other face by 40 freely rotating ball bearings spaced uniformly along a 49.53 mm diameter circle. Fractography showed that all specimens broke due to a single population of randomly oriented surface flaws.

Table 1 lists the fast-fracture Weibull parameters, estimated using the maximum likelihood method, for the various specimen configurations and loads. The values shown correlate very well to those of [2] for the Weibull shape parameter and characteristic strength. The results for the 90 percent confidence intervals differ somewhat from [2] due to the methods of estimation. CARES/LIFE uses the technique from Thoman et al. [27], while [2] uses a bootstrap technique. The 90 percent confidence interval on the Weibull modulus significantly overlaps for both bar and disk tests. This is an indication that the strength response is controlled by the same flaw population. Confidence bands on the characteristic strength may only be compared for identical specimen loading and geometry due to the size effect. The confidence intervals obtained for the two disk tests using CARES/LIFE are shown to overlap. The large confidence interval for the batch 2 specimens is due to the small sample size of 7 specimens. In [2] the discrepancies in average strength between batch 1 and batch 2 disks were attributed to material processing differences. This will be further discussed.

Fatigue parameters were estimated from four-point bend bar specimens loaded in dynamic fatigue in water. At least 15 specimens each were tested at stress rates of 0.02, 0.1, 1.0, 10.0, and 100.0 MPa/s. Figure 1 shows a plot of the individual failure stresses of the 95 specimens tested. Superimposed on this figure are median lines and 5 and 95 percent confidence bounds on this data as estimated with the median deviation technique. Table 2 lists the estimated fatigue parameters using the median value, least-squares, and median deviation techniques. The median deviation technique shows best agreement with Chao and Shetty for this case. In [2] the power law is used in the following form:

$$\frac{da(t)}{dt} = V_c\left(\frac{K_{Ieq}}{K_{Ic}}\right)^N \tag{30}$$

where V_c is the critical crack velocity. The CARES/LIFE program is formulated using the fatigue constant B and, therefore, V_c is not explicitly calculated. However, for comparison, V_c can be computed from CARES/LIFE results using the fracture strength relation [2]

$$\sigma_f = \dot{\sigma}\left[\frac{2K_{Ic}^{N_S}(N_S+1)}{V_c Y^{N_S}(N_S-2)\dot{\sigma}^{N_S}}\left(a_i^{1-N_S/2} - a_f^{1-N_S/2}\right)\right]^{1/(N_S+1)} \tag{31}$$

where a_i is initial crack size and a_f is the crack size at failure. The subscript S denotes surface-flaw-dependent properties. Assuming $a_i \gg a_f$ and rearranging this expression yields

$$\sigma_f = \left[\frac{2K_{Ic}^{N_S}(N_S+1)a_i^{1-N_S/2}}{V_c Y^{N_S}(N_S-2)}\right]^{1/(N_S+1)} \dot{\sigma}^{1/(N_S+1)} \tag{32}$$

Equating Eqs. (32) and (20) results in

$$V_c = \frac{2K_{Ic}^{N_S}(N_S+1)a_i^{1-N_S/2}}{A_d^{N_S+1}Y^{N_S}(N_S-2)} \tag{33}$$

Table 3 Fatigue parameters for disk (batch 2) specimens

Estimation method	Fatigue constant, A_d	Fatigue exponent, N_S	Fatigue constant, B_{BS} MPa^2 · s	Crack velocity, V_c m · s^{-1}
Median Value	2.293 x 10^2	35.68	2.675 x 10^{-1}	1.894
Least Squares	2.313 x 10^2	41.79	3.959 x 10^{-2}	16.22
Med Deviation	2.304 x 10^2	36.23	2.649 x 10^{-1}	1.988
Reference 2	---	36.6	---	2.4

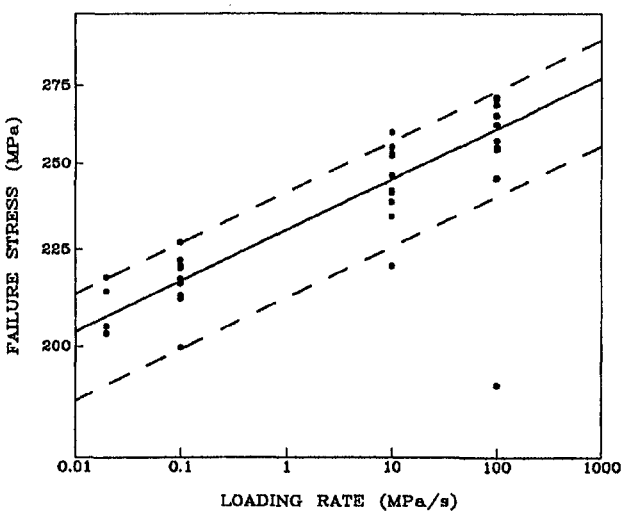

Fig. 2 Dynamic fatigue of alumina pressure-on-disk flexure specimens in water. Median regression line (solid), 5 and 95 percent regression lines (dashed) estimated with the median deviation technique.

The initial crack length a_i and fatigue constant A_d are evaluated here for a failure probability of 50 percent. The crack geometry factor Y for a semicircular crack is 1.366 [3]. Crack length a_i was determined from Eq. (1) using the strength determined from inert testing (Table 1) for a 50 percent probability of failure. Chao and Shetty [2] estimated that N_S was 40.7 and V_c was 9.1 m/s for Y equal to 1.24. The differences between the various parameter estimates in CARES/LIFE and [2] are not considered significant. The fatigue velocity V_c is particularly sensitive to N_S, as shown in Eq. (33). Table 2 also lists the fatigue constants B_{wS} and B_{BS}. B_{BS} is determined for a semicircular crack and noncoplanar crack extension with a shear sensitivity constant of $\bar{C} = 0.82$ [3]. The differences between B_{wS} and B_{BS} are small since N_S is relatively large. Finally, the Weibull modulus can be directly estimated from the fatigue data using the relation $\tilde{m}_S = m_S/(N_S - 2)$ when N_S and $\tilde{m}_S$ are known. For example, using the median deviation method, $m_S = 25.0$, which is consistent with the results shown in Table 1.

To obtain disk specimens for dynamic fatigue tests, a second batch of material (of identical dimensions as the first material batch) was secured by Chao and Shetty [2]. Seven of these specimens were broken under inert conditions and a total of 35 specimens were broken at stressing rates of 0.02, 0.1, 10.0, and 100.0 MPa/s. Table 1 lists the fast-fracture Weibull parameters of the (batch 2) disks and Table 3 gives the estimates for the fatigue parameters. Table 3 shows only B_{BS}, since B_{wS} is formulated only for the uniaxial stress state. Figure 2 shows a plot of the individual failure stresses as well as the median line and 5 and 95 percent confidence bounds estimated with the median deviation technique. One data point was flagged as an outlier (at 100 MPa/s); however, it was not rejected and had little effect on the overall results. Batch 2 material showed a stronger than expected average strength relative to the batch 1 material. Chao and Shetty [2] attributed this to a small increase of K_{Ic} in the material. Although batch 2 was unexpectedly strong, the rate of strength degradation was similar to that of the batch 1 four-point flexure data. Reference [2] reported that the 90 percent confidence intervals of N_S for both batches showed significant overlap. This was further confirmed in Table 4, which shows the ratio of the natural logarithm of the characteristic strength of the batch 2 disks to the natural logarithm of the characteristic strength of the batch 1 four-point flexure specimens at each stressing rate (maximum likelihood estimates). If the rate of change of strength degradation were stress-state dependent, then the strength ratio would systematically change with stressing rate. However, Table 4 shows no such change. Therefore, the differences between fatigue exponents N_S in Table 3 and Table 2 appear to be reflecting expected statistical variation.

Table 4 Comparison of four-point and disk (batch 2) characteristic strengths

Stressing rate, $\dot{\sigma}$ MPa · s^{-1}	4-point strength, $\sigma_{\theta S}$ MPa	Disk strength, $\sigma_{\theta S}$ MPa	Strength ratio, $\frac{\ln \sigma_{\theta S_{disk}}}{\ln \sigma_{\theta S_{4\text{-point}}}}$
0.020	2.145×10^2	2.116×10^2	0.9975
0.100	2.250×10^2	2.195×10^2	0.9954
10.00	2.531×10^2	2.492×10^2	0.9972
100.0	2.628×10^2	2.620×10^2	0.9995
Inert	3.534×10^2	3.514×10^2	0.9990

The effect of multiaxial stress states on the material is assessed by comparing the difference in inert strength between the uniaxially loaded four-point bend specimen and the biaxially loaded disk. Assuming that small cracklike imperfections control the failure, the material strength in multiaxial stress states can be correlated to the effects of mixed-mode loading on the individual cracks [8, 9]. Shetty [11] developed a simple equation describing the ability of a crack to extend under the combined actions of a normal and shear load on the crack face using an empirically determined parameter, $\bar{C}$. For a semicircular crack this equation is [3]

$$\sigma_{Ieq} = \frac{1}{2}\left[\sigma_n + \sqrt{\sigma_n^2 + 3.301\left(\frac{\tau}{\bar{C}}\right)^2}\right] \tag{34}$$

where σ_n and τ are the normal and shear stresses, respectively, acting on the flaw plane.

The failure response of the biaxial flexure specimens and the three-point flexure bars is predicted using the Weibull parameters (Table 1) and fatigue parameters (Table 2; median deviation results) estimated from the four-point flexure bar rupture tests. The prediction for the three-point bars is compared to experimental results to confirm the expected Weibull size effect. The disk prediction is compared to experimental results in order to make assertions regarding the effect of multi-axial stress states on the fast-fracture and fatigue fracture of the material.

For this analysis, the disk predictions are based on a finite element model of the disk as shown in Fig. 3. Brick and wedge solid elements are used to model a 7.5 deg sector of the disk and appropriate boundary conditions are applied corresponding to a 49.53-mm-diam ring support and a pressure load on one face. A gradient is imposed on the nodal spacing such that the smallest elements have the highest tensile stresses. This is required to obtain a satisfactory convergence of the reliability solution and is independent of the mesh size needed to obtain accurate nodal stresses. To perform surface flaw reliability analysis, quadrilateral and triangular shell elements are attached to the surface nodes on the disk tensile face in order to obtain surface stresses and areas. The shell elements are very thin and

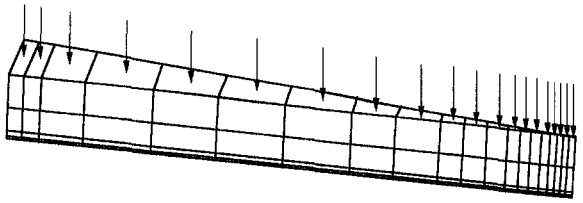

Fig. 3 Finite element model of a 7.5 deg sector of the disk. Arrows indicate pressure load on disk.

Table 5 Weibull parameters estimated in water (1 MPa/s)

Specimen	Weibull modulus, m_{dS}	90% confidence bounds on m_{dS}	Characteristic strength, σ_{0S} MPa	90% confidence bounds on σ_{0S} MPa
3-point	27.83	21.20, 33.70	255.6	252.7, 258.5
4-point	26.70	20.54, 32.17	236.3	233.6, 239.0
Disk	32.66	24.87, 39.53	215.9	213.8, 218.1

have membrane properties only. These elements are such that they contribute negligible stiffness to the model. Verification of the accuracy of the finite element model is obtained by comparison to available closed form solutions. Chao and Shetty [2] calibrated the applied pressure on the disk to the measured strain at the center of the disk. The strain calibration was used to correlate the fracture stress with the fracture pressure. The CARES/LIFE analysis uses these reported fracture stresses rather than the actual applied pressure on the disk. Reliability predictions for the three-point flexure bar are obtained from closed-form solutions of the effective area [1, 3].

Probability of failure predictions are made for the disk and three-point bar in the fast-fracture condition and also for dynamic loading at a stressing rate of 1 MPa/s in water. The fracture strength distribution of dynamically (constant stress rate) loaded specimens is characterized by a Weibull distribution with a Weibull modulus, m_{dS}, of

$$m_{dS} = \left(\frac{N_S + 1}{N_S - 2}\right) m_S \tag{35}$$

For this analysis m_{dS} has a value of 25.58. Table 5 lists the estimated Weibull parameters obtained from bars and disks loaded in this condition. In all cases the estimated Weibull modulus is somewhat higher than predicted; however, the predicted value was within the 90 percent confidence bounds. Table 5 shows that the Weibull modulus did increase from the inert condition, as expected. If the Weibull modulus value of m_S = 25.0 obtained directly from the four-point fatigue data were considered, then m_{dS} would be 26.9, which is in better agreement with Table 5.

The CARES/LIFE program is designed to predict reliability for static fatigue or constant-amplitude cyclic loading. To predict reliability for dynamic loading, an equivalent static loading time is computed using the approach given in Eq. (13). In this case, the g factor is equal to $1/(N_S + 1)$ multiplied by the time to failure. Figures 4 and 5 are the resulting Weibull plots of these predictions for various levels of shear sensitivity parameter $\bar{C}$. In Fig. 4 a value of $\bar{C}$ of 0.82 is used, which corresponds to an approximation of the maximum tangential stress mixed-mode fracture criterion. The dashed line in the figure denotes the results from [2]. The small differences indicated are mainly due to the different $\bar{C}$ and crack geometry factor, Y, used and are not due to the different values used for the fatigue parameters. This figure also shows a good correlation between predicted and experimental results for the three-point flexure bars, which confirms the size effect expected in fast-fracture and fatigue. The CARES/LIFE prediction lines for the three-point flexure bars superimpose on the three-point bar prediction lines of [2].

Figure 5 shows predictions for $\bar{C}$ values of 0.82, 0.90, and $\gg 1$ (solid, long dashed, and short dashed line, respectively). Since in this example the CARES/LIFE fracture predictions are normalized to the (uniaxial stress state) four-point flexure data, then the choice of a fracture criterion only effects the predictions for the (biaxial stress state) disks. The $\bar{C}$ values of 0.82 and much greater than one represent the extreme bounds on the expected mixed-mode shear sensitivity of the flaws in the material. The value of $\bar{C} \gg 1.0$ represents a shear-insensitive fracture criterion, while $\bar{C} = 0.82$ is highly shear sensitive. The 0.90 value represents a choice of $\bar{C}$ that best fits both inert and fatigue disk data. Optimizing $\bar{C}$ in this manner was not considered in [2]. From this figure stress state effects are adequately accounted for, both in fast-fracture and subcritical crack growth conditions.

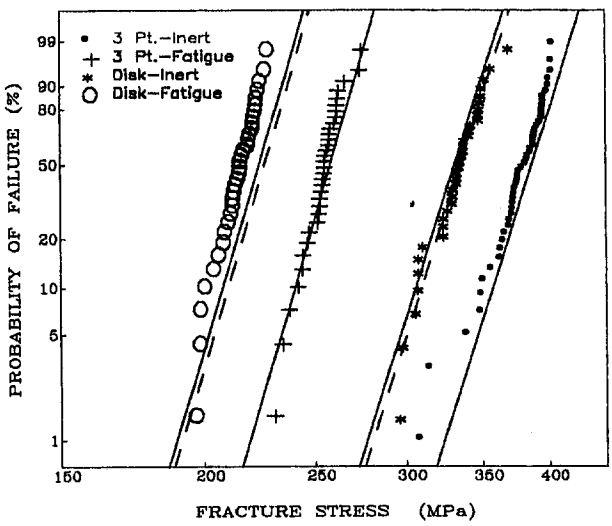

Fig. 4 Weibull plot showing fast-fracture three-point and disk specimen strengths measured in an inert environment, as well as three-point and disk specimen fracture strengths dynamically loaded at a rate of 1 MPa/s. Solid lines are corresponding CARES/LIFE predictions for $\bar{C}$ = 0.82. Dashed lines are corresponding predictions from [2].

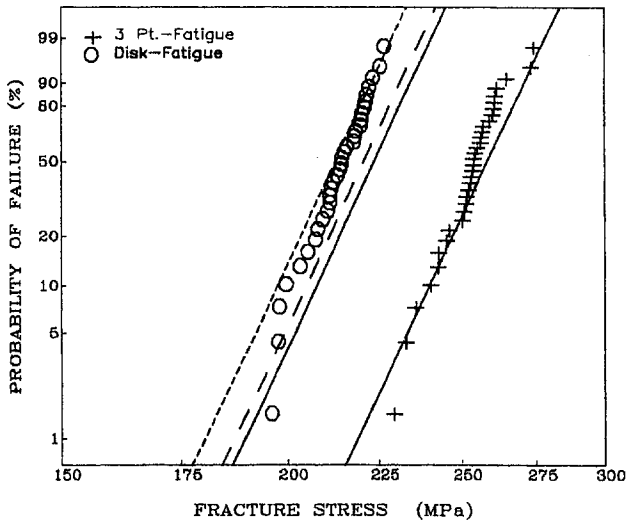

Fig. 5 Weibull plot showing three-point and disk specimen dynamic fatigue strengths that were loaded at a rate of 1 MPa/s. Solid line corresponds to CARES/LIFE prediction for $\bar{C}$ = 0.82 (shear-sensitive criterion). Long dashed line corresponds to the disk prediction for $\bar{C}$ = 0.90 and the short dashed line corresponds to the disk prediction for $\bar{C} \gg 1.0$ (shear-insensitive criterion).

Conclusion

The use of structural ceramics for high-temperature applications depends on the strength, toughness, and reliability of these materials. Ceramic components can be designed for service if the factors that cause material failure are accounted for. This design methodology must combine the statistical nature of strength controlling flaws with fracture mechanics to allow for multiaxial stress states, concurrent flaw populations, and subcritical crack growth. This has been accomplished with the CARES/LIFE public domain computer program for predicting the time-dependent reliability of monolithic structural ceramic components. An example has been given to illustrate the use of this design methodology in CARES/LIFE for predicting the effects of component size, stress distribution, stress state, and subcritical crack growth on the lifetime reliability. Potential enhancements to the code include the capability for transient analysis, three-parameter Weibull statistics, creep and oxidation modeling, flaw anisotropy, threshold stress behavior, and parameter regression for multiple specimen sizes.

References

1 Nemeth, N. N., Powers, L. M., Janosik, L. A., and Gyekenyesi, J. P., "Ceramics Analysis and Reliability Evaluation of Structures LIFE prediction program (CARES/LIFE) Users and Programmers Manual," TM-106316, to be published.

2 Chao, L. Y., and Shetty, D. K., "Time-Dependent Strength Degradation and Reliability of an Alumina Ceramic Subjected to Biaxial Flexure," Life Prediction Methodologies and Data for Ceramic Materials, ASTM STP 1201, C. R. Brinkman and S. F. Duffy, eds., American Society for Testing and Materials, Philadelphia, 1993.

3 Nemeth, N. N., Manderscheid, J. M., and Gyekenyesi, J. P., "Ceramics Analysis and Reliability Evaluation of Structures (CARES)," NASA TP-2916, Aug., 1990.

4 Powers, L. M., Starlinger, A., and Gyekenyesi, J. P., "Ceramic Component Reliability With the Restructured NASA/CARES Computer Program," NASA TM-105856, Sept., 1992.

5 Barnett, R. L., Connors, C. L., Hermann, P. C., and Wingfield, J. R., "Fracture of Brittle Materials Under Transient Mechanical and Thermal Loading," U.S. Air Force Flight Dynamics Laboratory, AFFDL-TR-66-220, (NTIS AD-649978), 1967.

6 Freudenthal, A. M., "Statistical Approach to Brittle Fracture," in: *Fracture, Vol. 2: An Advanced Treatise, Mathematical Fundamentals,* H. Liebowitz, ed., Academic Press, 1968, pp. 591–619.

7 Weibull, W. A., "The Phenomenon of Rupture in Solids," *Ingenoirs Vetenskaps Akadanien Handlinger,* No. 153, 1939.

8 Batdorf, S. B., and Crose, J. G., "A Statistical Theory for the Fracture of Brittle Structures Subjected to Nonuniform Polyaxial Stresses," ASME *Journal of Applied Mechanics,* Vol. 41, No. 2, June, 1974, pp. 459–464.

9 Batdorf, S. B., and Heinisch, H. L., Jr., "Weakest Link Theory Reformulated for Arbitrary Fracture Criterion," *Journal of the American Ceramic Society,* Vol. 61, No. 7–8, July-Aug., 1978, pp. 355–358.

10 Palaniswamy, K., and Knauss, W. G., "On the Problem of Crack Extension in Brittle Solids Under General Loading," *Mechanics Today,* Vol. 4, 1978, pp. 87–148.

11 Shetty, D. K., "Mixed-Mode Fracture Criteria for Reliability Analysis and Design With Structural Ceramics," ASME JOURNAL OF ENGINEERING FOR GAS TURBINES AND POWER, Vol. 109, No. 3, July, 1987, pp. 282–289.

12 Evans, A. G., "A General Approach for the Statistical Analysis of Multiaxial Fracture," *Journal of the American Ceramic Society,* Vol. 61, 1978, pp. 302–306.

13 Matsuo, Y., *Trans. of the Japan Society of Mechanical Engineers,* Vol. 46, 1980, pp. 605–611.

14 Evans, A. G., and Wiederhorn, S. M., "Crack Propagation and Failure Prediction in Silicon Nitride at Elevated Temperatures," *Journal of Material Science,* Vol. 9, 1974, pp. 270–278.

15 Wiederhorn, S. M., *Fracture Mechanics of Ceramics,* R. C. Bradt, D. P. Hasselman, and F. F. Lange, eds., Plenum, New York, 1974, pp. 613–646.

16 Paris, P., and Erdogan, F., "A Critical Analysis of Crack Propagation Laws," ASME *Journal of Basic Engineering,* Vol. 85, 1963, pp. 528–534.

17 Walker, K., "The Effect of Stress Ratio During Crack Propagation and Fatigue for 2024-T3 and 7075-T6 Aluminum," ASTM STP 462, 1970, pp. 1–14.

18 Dauskardt, R. H., James, M. R., Porter, J. R., and Ritchie, R. O., "Cyclic Fatigue Crack Growth in SiC-Whisker-Reinforced Alumina Ceramic Composite: Long and Small Crack Behavior," *Journal of the American Ceramic Society,* Vol. 75, No. 4, 1992, pp. 759–771.

19 Paris, P. C., and Sih, G. C., *Stress Analysis of Cracks,* ASTM STP 381, 1965, pp. 30–83.

20 Thiemeier, T., "Lebensdauervorhersage fun Keramische Bauteile Unter Mehrachsiger Beanspruchung," Ph.D. dissertation, University of Karlesruhe, Germany, 1989.

21 Sturmer, G., Schulz, A., and Wittig, S., "Lifetime Prediction for Ceramic Gas Turbine Components," ASME Preprint 91-GT-96, June 3–6, 1991.

22 Batdorf, S. B., "Fundamentals of the Statistical Theory of Fracture," *Fracture Mechanics of Ceramics,* Vol. 3, R. C. Bradt, D. P. H. Hasselman, and F. F. Lange, eds., Plenum Press, New York, 1978, pp. 1–30.

23 Mencik, J., "Rationalized Load and Lifetime of Brittle Materials," *Communications of the American Ceramic Society,* Mar., 1984, pp. C37–C40.

24 Evans, A. G., "Fatigue in Ceramics," *International Journal of Fracture,* Dec., 1980, pp. 485–498.

25 Jakus, K., Coyne, D. C., and Ritter, J. E., "Analysis of Fatigue Data for Lifetime Predictions for Ceramic Materials," *Journal of Material Science,* Vol. 13, 1978, pp. 2071–2080.

26 Pai, S. S., and Gyekenyesi, J. P., "Calculation of the Weibull Strength Parameters and Batdorf Flaw Density Constants for Volume and Surface-Flaw-Induced Fracture in Ceramics," NASA TM-100890, 1988.

27 Thoman, D. R., Bain, L. J., and Antle, C. E., "Inferences on the Parameters of the Weibull Distribution," *Technometrics,* Vol. 11, No. 3, Aug., 1969, pp. 445–460.

Plasticity Considerations in Probabilistic Ceramic-to-Metal Joint Design

D. A. ONeil

J. H. Selverian

Central Research and Development,
OSRAM Sylvania Inc.,
71 Cherry Hill Drive,
Beverly, MA 01915

K. S. Kim

Division of Engineering,
Brown University,
Providence, RI 02912

A new probabilistic failure criterion was developed for the design of high-temperature ceramic-to-metal joints. The essential feature of the theory is the inclusion of the energy dissipated during plastic deformation of the adjacent braze layer in the joint. A large number of bimaterial interface fracture simulations were performed for different crack positions and orientations near the bimaterial interface to determine the effect on stresses in the ceramic near the interface. The effective stress values were then ported to a probabilistic failure analysis code, which permitted simple inclusion of the new failure criterion. Brazed joints were made and failure tested in torsion to verify the failure criterion. Results show that the new failure criterion more closely approximates the failure of the ceramic-to-metal joints over the entire range of ultimate loads, and is a significant improvement in the failures criteria previously used for this type of joint design. Aspects of the failure criterion, material systems, residual stresses, mechanical behavior, and strength predictions will be presented.

Introduction

Ceramic materials are being developed for use in advanced heat engine applications. A key issue in their design and manufacture is joining the ceramic rotor to a metal shaft to transmit power. Design concepts for ceramic-to-metal joints were described in an earlier paper (Selverian et al., 1992).

The goals of this work were to develop new methods for the design and analysis of ceramic-to-metal joints, to predict performance of the joint, and to construct and test ceramic-to-metal joints that could support a 20.9 N-m (50 MPa) torque load at 650°C and 950°C with a braze area of 2.0 cm^2. Some expectation of the strength of the ceramic joint was necessary so that different joint geometries and materials could be explored without the difficulty of making each different design. The difficulty with realizing a predictive design tool for these joints was the probabilistic nature of the ceramic material properties, and the interaction between the metal, ceramic, and braze materials.

The heat engine applications of the joints considered here are primarily loaded with high-temperature torsional stresses. Therefore, the test joints were evaluated in torsion, torsional fatigue, and thermal fatigue tests. At the completion of the work, it was desired to not only have a prototype joint design manufactured, but also to confirm the analytical models derived for joint design by comparison with life-tests of the final joint prototypes.

Experimental Procedure

Material Systems. A detailed discussion of the material systems used here is given by Selverian et al. (1994). For the 650°C application an Fe-based superalloy, Incoloy 909, was selected because of its low coefficient of thermal expansion (CTE) as well as its high-temperature properties. For the 950°C application a Ni-based superalloy, Inconel 718, was chosen solely for its high-temperature capabilities. The CTE of Inconel 718 is approximately 50 percent greater than that of Incoloy 909. In the remainder of the paper Incoloy 909 and Inconel 718 together are referred to as structural alloys.

Silicon nitride (Si_3N_4 + 6 percent Y_2O_3) was selected as the structural ceramic material. The silicon nitride shaft was polished to a 0.1 mm surface finish. A 3-mm-thick Ti-coating was electron beam evaporated onto one end of the silicon nitride shaft. This Ti coating served to promote wetting and adhesion between the ceramic and braze alloy.

Nickel and molybdenum were used as interlayer materials between the ceramic and the structural alloy, and a Au-5Pd-2Ni (in wt %) braze alloy was used. The two material systems studied were Si_3N_4/Ni/Incoloy 909 as the 650°C system and Si_3N_4/Mo/Inconel 718 as the 950°C system. The Au-5Pd-2Ni braze alloy was used in both systems.

Joint Geometry. Several ceramic-to-metal braze joint configurations were studied in the initial phases of this work. Geometries included butt, tapered and cylindrical type joints, and are detailed by Selverian et al. (1992). Stress analysis and manufacturing/brazing considerations, as well as material interaction, pointed to the cylindrical configuration for further consideration. Subsequent manufacture, experimental joint testing, and modeling considerations were focused on the following cylindrical joint geometry:

The joint consists of a 1.27-cm-dia. silicon nitride rod brazed to a 1.946 cm outer diameter metal shaft with a 2.0 cm^2 brazed area. The ceramic rod fits into a cup machined into the end of the metal shaft. A schematic of the ceramic-to-metal joint geometry is shown in Fig. 1.

Testing of Brazed Joints. Figures 2(*a*) and 2(*b*) show a brazed joint between silicon nitride and Incoloy 909. This type of joint was used for the torsion and torsion fatigue tests. All of the mechanical testing of the brazed joints was carried out on a servohydraulic axial/torsional machine. The top and bottom gripping axes were axially aligned to within 40 μm of one another. Torsion load to failure and fatigue torsion tests were performed on the brazed joints; all tests were performed in air. Details of the torsion test procedures are given by Selverian et al. (1994). The results for the tests are given in Tables 1–4.

In Tables 1–4 one of the failure modes is described as "slippage." Slippage here refers to excessive relative rotational motion between the ceramic and superalloy parts of the joint such that the test had to be stopped. One of these failure surfaces

Contributed by the International Gas Turbine Institute and presented at the 39th International Gas Turbine and Aeroengine Congress and Exposition, The Hague, The Netherlands, June 13–16, 1994. Manuscript received by the International Gas Turbine Institute February 26, 1994. Paper No. 94-GT-229. Associate Technical Editor: E. M. Greitzer.

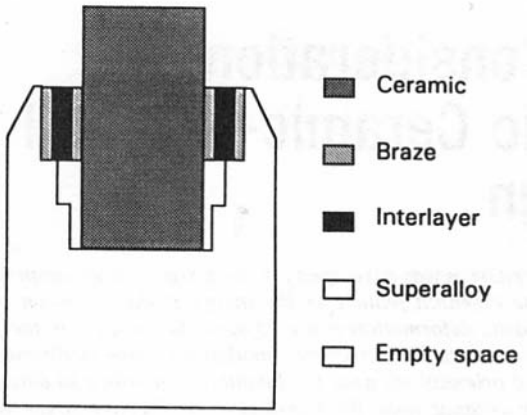

Fig. 1 Schematic of the ceramic-to-metal joint geometry

was examined by Auger spectroscopy. This revealed that the failure occurred in the near-interfacial regions; braze, ceramic, and reaction zone products were observed. As detailed by Selverian et al. (1994), at elevated temperatures (when the shrink-fit stresses become tensile) the brittle interfacial reaction zone fails. This result was predicted by Selverian et al. (1993).

Torsion tests were run at a rate of 0.2°/s and the axial load was controlled to within ±4.5 N of zero to maintain pure torsional loading. An induction furnace, with a SiC susceptor, was used to heat the joints for the elevated temperature tests. Torsion fatigue tests were carried out at minimum and maximum torques of 3.95–20.9 N-m, 6.0–31.7 N-m, or 8.0–42.2 N-m, all with a 1.5 Hz loading frequency. Torques of 3.95–20.9 N-m are typical values found in heat engines currently under development.

The temperature versus time profile used for the 650°C thermal fatigue testing consisted of a maximum temperature of 650°C and a minimum temperature of 335°C with a frequency of 0.07 Hz. The temperature versus time profile used for 950°C thermal fatigue testing consisted of a maximum temperature of 950°C and a minimum temperature of 545°C with a frequency of 0.11 Hz. The thermal fatigue conditions were also developed with the idea of simulating the stresses developed in a heat engine. All the mechanical and thermal tests were conducted in air.

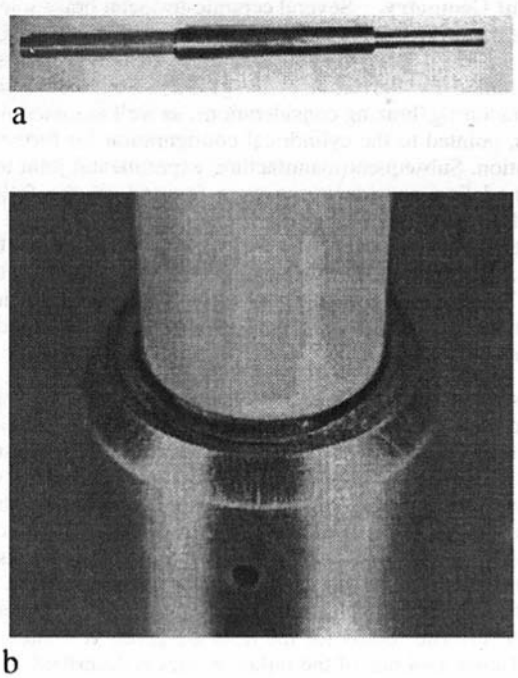

Fig. 2 Brazed Si_3N_4/Ni/Incoloy 909 joint. Test sample for torsion and mechanical fatigue testing. The ceramic is 1.27 cm in diameter and the metal is 1.946 cm in diameter.

Table 1 Results of the torsion tests of Si_3N_4/Ni/Incoloy 909 brazed joints

Test Temp. (°C)	Torque (N-m)	Shear Strength (MPa)	Bending Moment (N-m)	Rotation (°)
25	61	151*	7	2.22
	97	242*	14	3.52
	53	132*	11	1.98
	30	75*	13	1.15
	60	148*	10	1.05
	49	121*	23	2.55
	64	158*	14	3.05
	90	222*	12	4.3
	45	111*	2	2.05
650	4.	11.5#	---	---
	1.6	3.9#	---	0.10
	7.0	17.4#	---	---
	4.9	12.1#	---	0.21°

* broke in ceramic.
# ceramic slipped in joint.

Fatigue Testing. Thermal and mechanical fatigue tests were used to evaluate the effects of repeated thermal and mechanical loading on the long-term performance of the brazed joints. Brazed joints were made for thermal fatigue tests at 650°C and 950°C. The same joint geometry was used as in Fig. 1. The initial crack distribution in the joint was checked by microfocus x-ray. No cracks were detected in the silicon nitride. The apparent lack of cracks in the silicon nitride could be due to either no cracking or to the cracks being smaller than the 40 mm detection limit of the x-ray equipment. The samples were

Table 2 Results of the torsion tests of Si_3N_4/Mo/Inconel 718 brazed joints

Test Temp. (°C)	Torque (N-m)	Shear Strength (MPa)	Bending Moment (N-m)	Rotation (°)
25	12	30	25*	0.38
	40	98	13*	1.19
	23	56	17*	0.70
	51	127	16*	0.80
	41	101	16*	0.64
950	0.34	0.84#	---	---

* broke in ceramic.
# ceramic slipped in joint.

Table 3 Room temperature fatigue tests of Si_3N_4/Ni/Incoloy 909 and Si_3N_4/Mo/Inconel 718 brazed joints

Joint	Torque (N-m)	Rotation (°)	Number of Cycles for Failure
Si_3N_4/Ni/ Incoloy 909	3.95-20.9	±0.31	$> 10^3$*
	"	±0.32	$> 10^3$*
	"	±0.31	$> 10^3$*
	"	±0.32	$> 10^3$*
	"	±0.31	$> 10^6$
	6.0 - 31.7	---	$> 10^6$
	8.0 - 42.2	---	$> 10^6$
Si_3N_4/Mo/ Inconel 718	3.95 - 20.9	---	$> 10^3$*
	"	±0.26	$> 10^3$

* These samples were heated to 650-700°C, then gripped in the testing machine, and then cooled to room temperature before testing, to realign the sample. These samples were stopped at 10^3 cycles due to time limitations, not failure of the joint.

reexamined by microfocus x-ray after 10, 100, and 1000 cycles. The Si_3N_4/Ni/Incoloy 909 joints survived all 1000 cycles without evidence of cracking. Severe oxidation of the molybdenum interlayer in the Si_3N_4/Mo/Inconel 718 joints prevented their complete testing.

Several Si_3N_4/Ni/Incoloy 909 and Si_3N_4/Mo/Inconel 718 joints were torsion fatigue tested at room temperature, Table 3. A Si_3N_4/Ni/Incoloy 909 joint was first fatigued at room temperature for 10^3 cycles then fatigued at room temperature for 10^6 cycles. All the joints survived 10^6 fatigue cycles at a torque amplitude of 3.95–20.9 N-m. The joints showed no signs of degradation; the rotation required to maintain these torques was unchanged at ±0.32 deg from the start of the test. The torque amplitudes were increased to 6.0–31.7 N-m and to 8.0–42.2 N-m. One joint was tested at each torque level and joints survived 10^6 cycles, Table 3.

The joints that failed in the ceramic were compared to modeling predictions of the joint strength. Since the new failure criterion is applicable only in brittle materials having a distribution of strengths, the experimental failures due slippage were not included in the experimental failure distribution.

Modeling Approach

Previous work (Selverian et al., 1994) has shown the applicability of probabilistic failure analysis in the design of ceramic components. As a result of this work, the mode of failure in the ceramic material was qualitatively known by failure surface and location of initiation (using various microscopy methods). However, the probabilistic failure methods used by Nemeth et al. (1989) (which were used in previous ceramic-to-metal joint designs) do not include energy dissipation by plastic work. Plastic energy was dissipated in the braze layer during cool down from the brazing temperature, and also in service conditions of the joint. Our aim here, therefore, was to consider the effect of the plasticity of the braze layer on crack propagation when the cracks are at or near the ceramic–braze interface. Once the effect on cracks near the interface was quantitatively understood, it was incorporated into the probabilistic failure analysis code as stress modification factors. By including the plasticity effect in this way, modifications to the probabilistic failure code were precluded. A discussion of the new failure criterion follows, but detailed structure of the technique is given by Kim et al. (1992), Yang and Kim (1993), and Kang et al. (1992).

It is useful to describe the reasoning behind our approach. In previous probabilistic failure analyses of the entire joint system (Selverian et al., 1992), stress results from finite element studies of the joint were post-processed through a probabilistic ceramic failure analysis code, NASA CARES (Nemeth et al., 1989). The stresses and volumes of each of the ceramic finite elements were combined with Weibull strength data for the ceramic finite elements to give the probability of failure at each position in the ceramic body. In addition, a cumulative probability of failure for the entire joint was also calculated. The drawback with this method was that of all the ceramic failure models included in the CARES code, none included the effect of having a ductile layer near the surface of the ceramic body. This ductile layer (the braze) has been shown to absorb some of the energy in the system that may be otherwise used for further crack growth.

In our current modeling work, we calculated this effective toughening of the system by evaluating the energy release rate at the crack tip (which is near the elasto-plastic interface of the ceramic–braze zone) relative to the energy release rate at a crack tip away from the interface. This series of finite element calculations can then be performed for a range of crack-tip orientations relative to the interface, and also for a range of distances of the crack-tip to the interface. Finally, these data are interfaced with the CARES probabilistic failure analysis code in the form of a new failure model specific to ceramic components joined to plastically deforming materials. The derivation of the "T-stress" component for the braze joint and some results showing the mode-dependent toughening of the interface follow.

T-Stress Component Evaluation. Work has been being carried out to evaluate the so-called T-stress at the tip of a crack at or near a bimaterial interface with one of the interface layers modeled as an elastic-strain hardening material. For a tensile specimen with a crack parallel to the tensile direction, the stress at the crack tip can be written as

$$\sigma_{\alpha\beta}(r, \theta) = \frac{K_I}{\sqrt{2\pi r}} f_{\alpha\beta}(\theta) + \sigma^o_{\alpha\beta}(\theta) + a_1 \sqrt{r} g_{\alpha\beta}(\theta) + \ldots a_2 r h_{\alpha\beta}(\theta) + a_n (\sqrt{r})^n h_{\alpha\beta}(\theta) \quad (1)$$

The first term, $(K_I/\sqrt{2\pi r}) f_{\alpha\beta}(\theta)$, is usually described as the singular term in linear elastic fraction mechanics, and the first nonsingular term is known as the T-stress, or σ_{ox} among experimentalists. So

$$\sigma^o_{\alpha\beta}(\theta) \equiv \sigma_{ox} \equiv T\text{-stress}. \quad (2)$$

Cotteral and Rice (1980) have shown the instability of the

Table 4 Results of the 500°C torsion tests of Si_3N_4/Ni/Incoloy 909 brazed joints. All of these joints were fatigued tested at room temperature before testing at 500°C.

Torque (N-m)	Shear Strength (MPa)	Previous Fatigue Test Conditions (cycles at stress)	Fracture Mode
49.7	123	10^3 at 3.95-20.9	slipped
24.8	61	10^6 at 3.95-20.9	cer. broke
15.3	38	10^6 at 6.0 - 31.7	slipped

crack path depends on the T-stress term. In addition, it has been speculated that the nonsingular term may play a significant role in crack branching. For the design of the ceramic-to-metal brazed joint, the description of the instability of the crack path due to the T-stress term will permit numerical study of the fracture surface by following crack propagation and allow joint design that takes into account the effect of this nonsingular term coupled to the elasto-plastic interface (the ceramic-braze interface). The T-stress term in further discussion refers to the first nonsingular term in the crack tip stress series description.

The method used to find the nonsingular stress term (the T-stress) at the crack tip uses an application of an energetic force on a point load in the development of an interaction (or mutual) integral to extract this term. This work is detailed in Kim (1992).

Following is the description of the general method for the study of an interaction integral of a point load. The conservation force on an object such as an inclusion, a crack tip, a dislocation, or a point force is referred to as an *energetic force* or an *energy release rate.* The energetic force, G, is defined as the negative gradient of the potential energy of a body with respect to a virtual displacement of the object. Denoting the virtual displacement of the object by $\rho\mathbf{e}$ for which $\mathbf{e}$ is a unit vector, the definition of the energetic force is expressed as

$$G = \lim_{\rho \to 0} \frac{II(\mathbf{r} + \rho\mathbf{e}) - II(r)}{\rho} \mathbf{e}, \tag{3}$$

where II represents the potential energy of the body. The energetic force often can be calculated by the $\mathbf{J}$ integral. Provided the mechanical response function, i.e., the elastic properties, are invariant in the direction of G, the energetic force, G, can be evaluated by a surface integral (or a contour integral for two dimensional cases) in terms of the field quantities. The elastic equilibrium field surrounding the object is represented by the field quantities of the stress, σ, the strain, ϵ, and the displacement, u. Denoting the equilibrium field, $\{\sigma, \epsilon; u\}$, by S, the surface integral is depicted by $\mathbf{J}_\Gamma(\mathbf{S})$, where Γ indicates the integrating surface (or contour). A Cartesian component of the $\mathbf{J}$ integral is expressed as

$$J_i = \int (Wn_i - \sigma_{kj} n_k u_{j,i}) d\Gamma, \tag{4}$$

where the summation convention is assumed on the repeated indices, the strain energy density function is represented by W and the out normal of the surface, Γ, is indicated by $\mathbf{n}$.

The energetic forces of various singular objects have many interesting properties. Those of dislocations, point defects, and cracks have been applied to many engineering problems in plasticity, diffusion, and fracture mechanics. However, not much attention has been paid to those of point forces.

The stress state around a point load in a linear elastic medium can be separated into two parts. One is the singular stress field corresponding to the point load in an infinite medium, denoted by superscript p, e.g., S^p. The remaining stress field corresponds to the image effect of the limited geometry and other sources of stresses. This remaining field is denoted without superscripts, e.g., S. In order to get a useful expression of the energetic force of a point load in such a superposed field, an alternative expression of the $\mathbf{J}$ integral of a general superposed field is derived first, and then some properties of the $\mathbf{J}$ integral related to the energetic force of a point load will be discussed next.

Consider the superposition of two general equilibrium fields, S^A and S^B. Substituting the field quantities of the total field, $S^A + S^B$, into Eq. (2), the $\mathbf{J}$ integral of the total field over a Γ is expressed as

$$\mathbf{J}_r(S^A + S^B) = \mathbf{J}_r(S^A) + \mathbf{J}_r(S^B) + \mathbf{J}^{\text{int}}_\Gamma(S^A, S^B), \tag{5}$$

where the superscript int indicates the interaction integral. A Cartesian component of the interaction integral is given by

$$\mathbf{J}^{\text{int}}_\Gamma(S^A, S^B) = \int_\Gamma (W^{\text{int}} n_i - \sigma^A_{kj} n_k u^B_{j,i} - \sigma^B_{kj} n_k u^A_{j,i}) d\Gamma, \tag{6}$$

where the interaction strain energy, W^{int}, has the relationship

$$W^{\text{int}} = \tfrac{1}{2}(\sigma^A_{ij}\epsilon^B_{ij} + \sigma^B_{ij}\epsilon^A_{ij}) = \sigma^A_{ij}\epsilon^B_{ij} = \sigma^B_{ij}\epsilon^A_{ij}. \tag{7}$$

The last two equalities hold due to the symmetry of the elastic moduli tensor. Therefore, the interaction integral can be expressed in a convenient form:

$$J^{\text{int}}_i(S^A, S^B) = \int_\Gamma (\sigma^B_{kj}\epsilon^A_{kj} n_i - \sigma^B_{kj} n_k u^A_{j,i}) d\Gamma - \int_\Gamma (\sigma^A_{kj} n_k u^B_{j,i}) d\Gamma, \tag{8}$$

Interaction Integrals for Extracting Stress Intensity Factor and *T*-Stress. In the previous section we outlined a method for evaluating the so-called T-stress component of the stress field at or near an interface crack. In this section, the method for numerically evaluating the stress field of a crack near the interface of a multilayered structure (the ceramic-to-metal braze joint) is described, especially when plastic deformation of one of the layers (the braze layer) occurs.

In order to extract the complex stress intensity factor, K, and T-stress, the interaction integral based on the path-independent J-integral is used by several authors (Moran and Shih, 1987; Kim et al., 1992). To define the interaction integral, consider two general equilibrium fields as before, S^A and S^B. The J-integral of the superposed field, $S^A + S^B$, over a contour Γ can be expressed as

$$J(S^A + S^B) = J(S^A) + J(S^B) + J^{\text{int}}(S^A, S^B) \tag{5}$$

where the superscript int indicates the interaction integral.

First, to extract the complex stress intensity factor K near an interface crack, consider an interaction integral between the actual field S (given by Eq. (1)) and the auxiliary field $S^{\tilde{K}}$, which is the $(1/\sqrt{r})$ singular field and whose strength is $\tilde{K} = |\tilde{K}| e^{i\phi}$. Then by calculating each J-integral in Eq. (5), the interaction integral $J^{\text{int}}(S, S^{\tilde{K}})$ can be expressed in terms of two stress intensity factors, K and $\tilde{K}$, as

$$J^{\text{int}}(S, S^{\tilde{K}}) = \frac{|\tilde{K}| h_{22}}{2 \cosh^2 \pi\epsilon} (K_1 \cos\phi + K_2 \sin\phi) \tag{9}$$

for an anisotropic bimaterial interface crack where h_{22} is defined by Eq. (A.10) in Choi et al. (1991). Therefore, the complex stress intensity factor can be completely obtained (i.e., K_1 and K_2 separately) by applying Eq. (9) twice with the different mode, ϕ, of the auxiliary field $S^{\tilde{K}}$, and then by solving for K_1 and K_2. In each case, the interaction integral, $J^{\text{int}}(S, S^{\tilde{K}})$, is calculated by Eq. (9).

Now, to extract the T-stress at an interface crack, consider an interaction integral between the actual field S and the auxiliary field $S^{\tilde{T}}$, which is the $(1/r)$ singular field of the point force, $\tilde{T}$, located at a crack tip and directed to x-axis. Noting that, for the in-plane problem, only the nonsingular stress at the crack tip is σ^o_{xx}, Kim et al., (1992) have shown that the interaction integral between S and $S^{\tilde{T}}$ field is reduced to

$$J^{\text{int}}(S, S^{\tilde{T}}) = \tilde{T}\epsilon^o_{xx}. \tag{10}$$

Once ϵ^o_{xx} is obtained through this equation, the nonsingular stress term σ^o_{xx} can be easily calculated using Hookes' law. Note that, for the interface cracks, the T-stress can have a jump across the interface. The jump quantities are determined from the compatibility condition that the corresponding strain ϵ^o_{xx} should be continuous across the interface.

Both fundamental fields of $S^{\tilde{K}}$ and $S^{\tilde{T}}$ in the above were presented in Choi et al. (1991) for an interface crack between

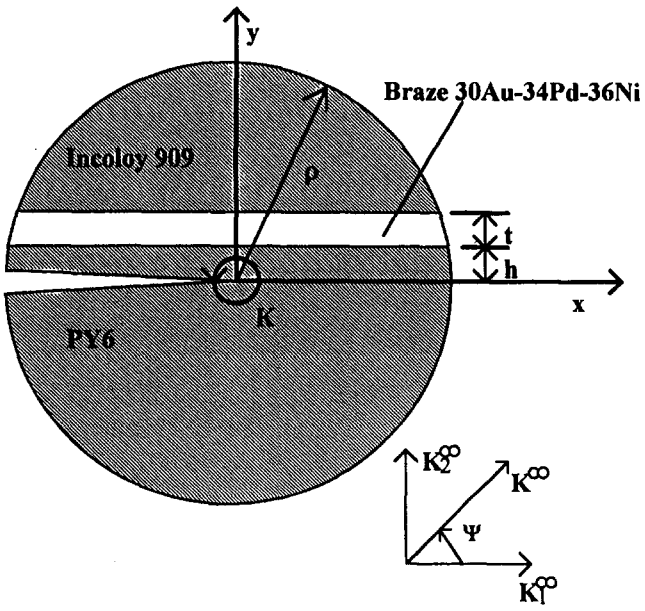

Fig. 3 Geometry of the model used to find the effect of a plastic region on bimaterial fracture in the ceramic-to-metal brazed joint. Note material system studied, and definition of h and t. In the figures, $\bar{\sigma}^{o}_{xx} = \sqrt{\rho}\sigma^{o}_{xx}/|K^{\infty}|$, and $|\bar{K}^{\infty}| = |K^{\infty}|/(\sigma_o\sqrt{\rho})$.

an anisotropic bimaterial, but they can also be used for the isotropic cases.

Toughening of the Brazing Structure. These methods have been implemented into a two-dimensional finite element program, and results obtained for the material system specific to the ceramic-to-metal joint. The geometry of the metal-braze-ceramic region is shown in Fig. 3. Material properties of each of the materials were:

1 Structural Alloy; Incoloy 909
E_s = 158.6 GPa, υ_s = 0.34
2 Braze Material; 30Au-34Pd-36Ni
E_b = 32.4 GPa, υ_b = 0.3
Yield stress σ_o = 626.0 MPa
3 Ceramic; PY6 (Si_3N_4)
E_c = 296.5 GPa, υ_c = 0.2

The distance h/t and mode mixity, Ψ, were varied over a wide range of values typical for the ceramic-to-metal braze joint. These analyses were performed using two-dimensional finite element methods. Typical results for a crack parallel to the ceramic-braze interface are shown in Fig. 4. Figure 4(a) shows the increasing energy release rate when the crack gets closer to the interface. Note also the energy release rate increases as fracture tends to mode *II* loading. The change in the *T*-stress factor for the same cases of mode mixity and crack position are illustrated in Fig. 4(b).

In summary, we have seen that not only is the interface tougher in mode *II* loading (as it is near an elastic-elastic interface), but also that the plastic deformation of braze material also acts as a toughening agent, particularly in mode *II* loading. The result is a failure model for ceramics, which is significantly different from existing models.

Detailed Description of Implementation. One goal in this work was to implement a failure condition that includes the plasticity of the braze layer into an existing probabilistic failure code, the NASA CARES program. The method by which the failure criterion is implemented into the existing FE protocol is described here.

The underlying method we used is as follows: The effective increase in energy release rate due to plasticity was calculated (via FEA techniques) for which a wide range of far-field mode mixities and distances of the crack from the braze-ceramic interface. Collecting these data onto a G versus crack distance plot (Fig. 5), a family of mode mixity points results. A best-fit curve is then passed through the points and the coefficients of these curves are used to weight the stress values calculated for the experimental joint system. These weights (described in detail below) effectively *reduce* the stress near the interface region of the ceramic, thereby decreasing the probability of failure.

The correction factor for stress was estimated using energy release data obtained from finite element calculations. Data were obtained for cracks at different distances h from the interface (with a constant brazing thickness t) under various far-field loading conditions. The ratio of the total energy release rate due to far-field loading G^{∞} to the actual energy release rate calculated at the crack tip G is a measure of the amount of energy consumed by plastic yielding in the brazing layer. The behavior of this ratio was plotted as a function of h/t for various angles of far-field loading incidence Ψ. These plots were made for different loading magnitudes $|K|$, where the magnitude has been normalized as follows (Figs. 3, 4, and 5). A detail of the stress components affected by the stress factors is shown in Fig. 6. The far-field stress intensity factor was defined as:

$$|K^{\infty}| \equiv \frac{K_{IC}}{\sigma_o\sqrt{t}} \tag{11}$$

These data show the dependence of G^{∞}/G on $|K^{\infty}|$ and h/t for each angle of incidence. Thus, the effective stresses we seek should assume this form:

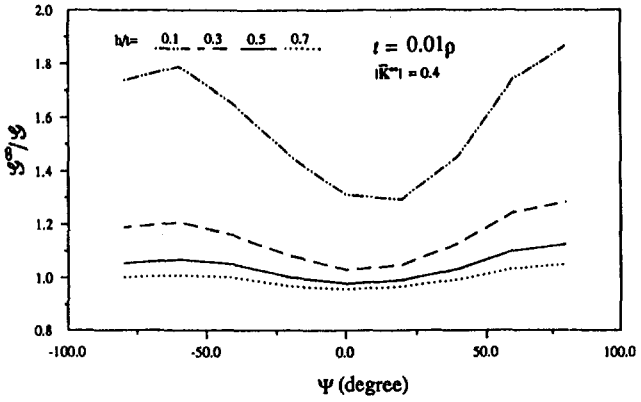

(a) Mode-dependent Toughening

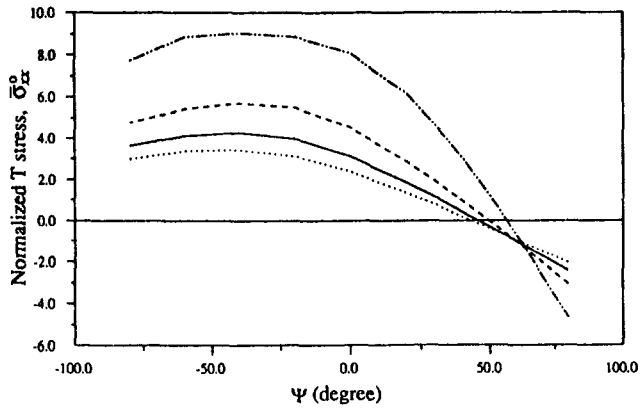

(b) T stress

Fig. 4 Toughening effect of plastic interlayer (a), and *T*-stress component values as a function of mode mixity and distance of crack tip from interface (b)

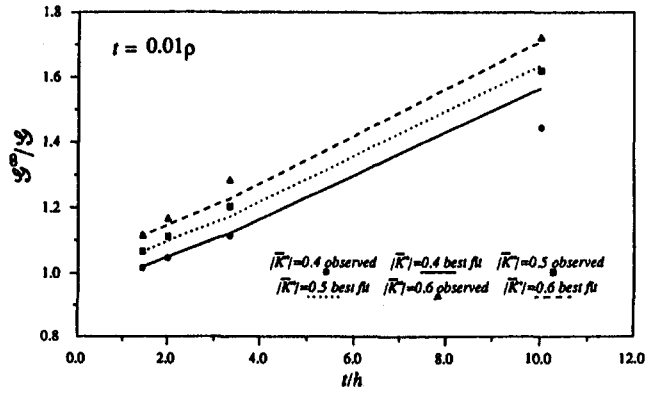

(a) Best Fit Function for Toughening Factor

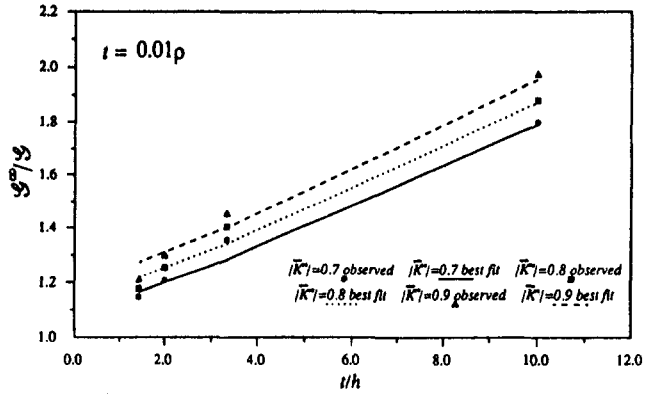

(b) Best Fit Function for Toughening Factor

Fig. 5 Best-fit curves used for stress weighting factors. These curves are specific to a given material system.

$$\sigma_{yy}^{\text{eff}} = \frac{\sigma_{yy}}{\sqrt{f_c}} \tag{12}$$

$$\sigma_{xy}^{\text{eff}} = \frac{\sqrt{\lambda}\sigma_{xy}}{\sqrt{f_c}} \tag{13}$$

$$\sigma_{zy}^{\text{eff}} = \frac{\sqrt{\lambda}\sigma_{zy}}{\sqrt{f_c}} \tag{14}$$

$$\sigma_{xx}^{\text{eff}} = \sigma_{xx}$$

$$\sigma_{zz}^{\text{eff}} = \sigma_{xz}$$

$$\sigma_{zz}^{\text{eff}} = \sigma_{zz}$$

where

$$f_c = \frac{G^\infty}{G} = f\left(\frac{t}{h}, |K^\infty|\right)$$

and

$$\lambda = 0.3$$

Notice that in the xx, xz, and zz directions, no toughening effects are considered, since the metal plasticity model affects shear coupons only (Fig. 6).

To find f_c, numerous function forms were assumed and tested using a least-squares approximation. The following exponential form was eventually settled on because it provided the best fit to the data with the smallest number of independent parameters (three):

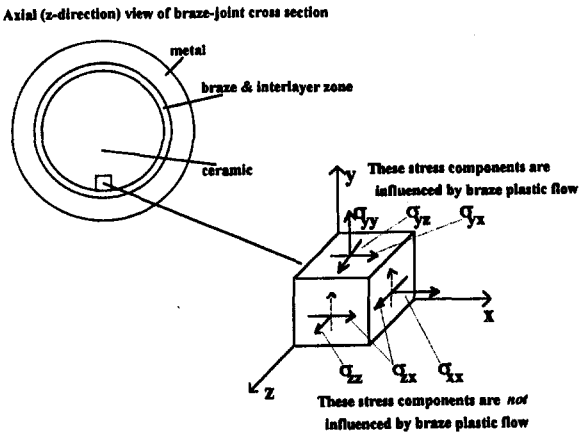

Fig. 6 Detail of stress components in the ceramic-to-metal joint affected braze layer plasticity

$$f_c = \exp\left(A\left(\frac{t}{h}\right) + B(|K^\infty|) + C\right) \tag{15}$$

Using data for $\psi = 0$ deg, $0.4 \leq |K^\infty| \leq 1.0$, and $1.44 \leq t/h \leq 10$, the least-squares approximation yields:

$$A = 0.0837$$

$$B = 0.0447$$

$$C = 0.0711$$

With these values, Eq. (15) predicts the toughness correction factor with a standard error of approximately 0.032723.

Equations (12) – (14) can now be used to modify the stress readings given the magnitude of far-field loading and the ratio of the brazing layer thickness to the distance from the interface to a crack imperfection.

Results and Discussion

An applied torque was superimposed with the calculated residual stress field as a shear stress. Figure 7 shows the torque distribution used to determine the shear stress. A stress concentration due to the change in cross section at the joint was included as before. The stress concentration was 1.7 at the top of the joint and tapered off to 1.0 a distance of one ceramic diameter away from the joint. Selection of the stress concentration factor depended on the radius of the fillet formed by the braze alloy. A fillet radius of 1 mm was selected; however, the fillet radius varied over the joint area. The stress concentration factor was estimated from Rourk (1971).

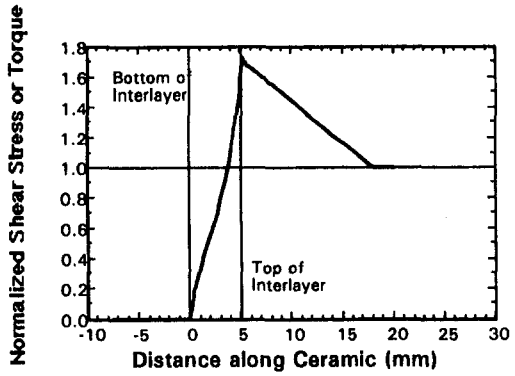

Fig. 7 Plot of the torque distribution in the ceramic portion of the brazed joint. Torque values are normalized to the applied torque.

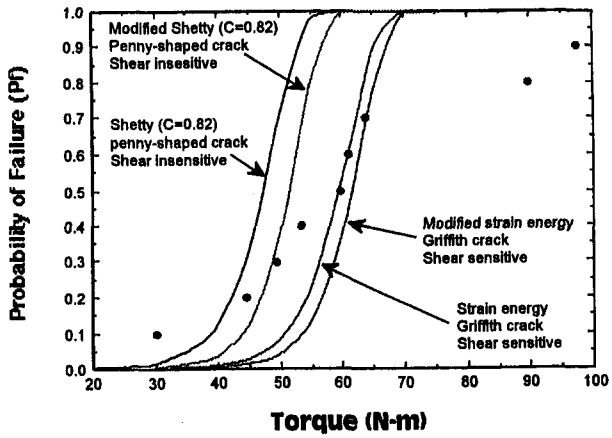

Fig. 8 Predicted and experimental values of the brazed joint strength measured in torsion (Si_3N_4/Ni/Incoloy 909). Two failure theories were used: (1) Shetty criterion with $\bar{c}$ = 0.82, penny-shaped crack, and a shear-insensitive Batdorf crack density, and (2) coplanar strain energy release rate, Griffith crack, and a shear-sensitive Batdorf crack density.

The fraction of torque carried by the ceramic and metal components in the joint region was calculated based on the material properties and was also factored into the torque distribution shown in Fig. 7. Once the torque was added to the residual stress field, the combined stress field was used as input to the CARES probabilistic failure computer code (Nemeth et al., 1989) to obtain the probability of survival for the joint at the applied torque level. This same procedure was performed at several different torques. The probability of failure (P_f) values were calculated as a function of applied torque. This probabilistic approach to joint strength, unlike a maximum principal stress approach, provided a method to estimate the strength distribution of a ceramic-to-metal brazed joint and can be used as a design aid.

Two failure theories were used to predict the behavior of the ceramic-to-metal joints for comparison. These were: (1) Shetty criterion, with $\bar{c}$ = 0.82, a penny-shaped crack, and a shear-insensitive Batdorf crack density coefficient, and (2) coplanar strain energy release rate, with a Griffith crack, and a shear-sensitive Batdorf crack density coefficient. For these failure theories the Weibull modulus (m_v), the normalized Weibull scale parameter (σ_{ov}), and the Batdorf crack density coefficient (k_{BV}) were calculated from four-point bend tests of the silicon nitride material used in the ceramic-to-metal brazed joints. Twenty-four samples were tested and 1 outlier was detected in the data (Selverian et al., 1992).

A Weibull modulus (m_v) of 21.2 and a normalized Weibull scale parameter (σ_{ov}) of 369.8 MPa(m)$^{3/21.2}$ were used for both failure theories. A shear-insensitive Batdorf crack density coefficient of 43.4 and a shear-sensitive Batdorf crack density coefficient of 22.2 were used for the Shetty and coplanar strain energy release rate theories, respectively. The maximum likelihood method was used to fit the experimental data. The constants described above were required as input variables by the CARES program and are further described by Nemeth et al. (1989).

The new failure criterion was tested on ceramic-to-metal joints containing nickel and moly interlayers with Incoloy 909 and Inconel 718 structural components, respectively. Figures 8 and 9 show the probability of failure versus applied torque on the two joint systems with experimental results. Both penny-shaped crack and Griffith crack were assumed to find the failure envelope. The new model shifted the failure curves, resulting in a less conservative failure prediction for both joint systems, and for both penny-shaped and Griffith cracks. The reason for the shift in new model (or "modified" as indicated on Figs. 8 and 9) was that previous models did not account for the fracture energy absorbed by plastic work of an adjoining material (the braze layer). Therefore, it predicted that a larger applied torque could be tolerated for a specified probability of failure. It is to be noted that, especially for the Incoloy 909 material system, the new failure model predicts the experimental results more closely. It is believed that the new failure model will provide more accurate prediction for ceramic failure where some plastic work is encountered in manufacturing or service.

In Figs. 8 and 9, the predicted strength distributions surrounded the experimental values and intermediate values of P_f, where $P_f = 1 - P_s$. However, at the low and high regions of the probability distributions, the predictions deviated from the experimentally measured strengths. Also, the predicted probability distributions were much steeper (higher Weibull modulus) than the experimental probability distribution. The Weibull modulus decreased from 21.2 for the unbrazed ceramic to ~4 for the Si_3N_4/Ni/Incoloy 909 brazed joints. A similar decrease in Weibull modulus was seen in shear testing of ceramic-to-metal lap joints (Selverian et al., 1992) and in four-point bend tests of ceramic-to-metal butt joints. The cause of the difference in the slopes (Weibull modulus) of the probability distributions was unknown.

Summary

Material systems designed for 650°C and 950°C applications were evaluated in terms of torsion, torsion fatigue, and thermal fatigue. Si_3N_4/Ni/Incoloy 909 was selected as the 650°C system while Si_3N_4/Mo/Inconel 718 was selected as the 950°C system. The Au-5Pd-2Ni braze alloy was used in both systems. A cylindrical cup joint geometry with an interlayer was selected for these joints.

Room temperature and 500°C torsion strengths of the 650°C system were measured in the range of 30–100 N-m with a 2 cm^2 brazed area while the strength at 650°C was significantly lower (1.6–7.0 N-m). This was attributed to a reduction in the shrink-fit at 650°C (Selverian et al., 1992). The Si_3N_4/Ni/Incoloy 909 joints showed excellent room temperature fatigue behavior. A similar trend was seen in the high-temperature strength of the Si_3N_4/Mo/Inconel 718 joints, which had lower strength than the Si_3N_4/Ni/Incoloy 909 joints due to the high CTE of Inconel 718.

A new failure criterion, based on the energy dissipated by plastic deformation of the braze material, was developed. A wide range of finite element calculations varying the position of the crack from the interface, and varying the mode mixity

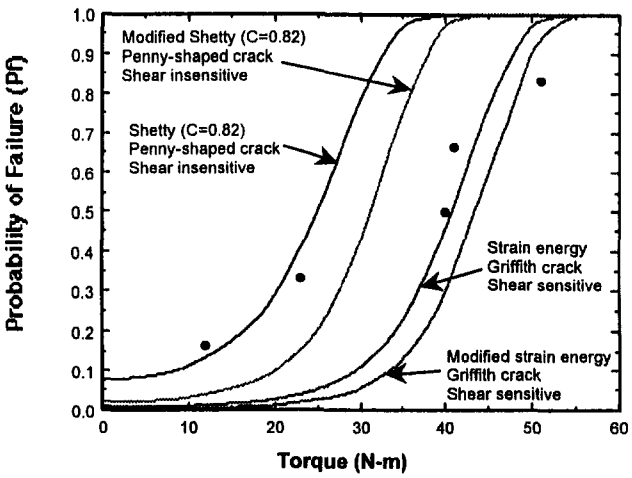

Fig. 9 Predicted and experimental values of the brazed joint strength measured in torsion (Si_3N_4/Mo/Inconel 718). Two failure theories were used: (1) Shetty criterion with $\bar{c}$ = 0.82, penny-shaped crack, and a shear-insensitive Batdorf crack density, and (2) coplanar strain energy release rate, Griffith crack, and a shear-sensitive Batdorf crack density.

of the crack, were performed. These analyses provided the effective toughening factors near the interface due to the plastic deformation of the braze material. Using these toughening values, the new failure criterion was simply integrated into an existing probabilistic failure analysis code by including the energy absorption as stress factors on stress components, which were affected by permanent braze deformation. The criterion showed better fit to the experimental joint failure statistics than the existing failure criteria in the probabilistic code. Probabilistic failure predictions for ceramic materials adjacent to plastically deforming materials should include this factor.

The strength predictions of the finite element analysis were compared with experimental results. Scatter in the measured strengths and the difference between measured and predicted strengths indicated the importance of processing effects and the probabilistic nature of ceramic failure on the fracture process. However, the probabilistic approach for the ceramic-to-metal brazed joints was a better method for comparing the performance of various brazed joints due to the statistical nature of ceramic failure, and it provided an estimate of the strength distribution of the joint for design considerations. The new failure criterion provided better guidelines for constructing high-temperature ceramic-to-metal joints than previous models. The model is best applied to ceramic components where the failure of the ceramic is affected by plastic deformation of nearby materials.

Acknowledgments

This research was sponsored, in part, by the U.S. Department of Energy, Assistant Secretary for Conservation and Renewable Energy, Office of Transportation Systems, as part of the Ceramic Technology for Advanced Heat Engines Project of the Advanced Materials Development Program, under contract DE-AC05-840R21400 with Martin Marietta Energy Systems, Inc. Special thanks go to M. Santella and D. R. Johnson at ORNL. The support of R. Schulz at the DOE is also appreciated.

The authors wish to thank H. Kim for his support and contributions. The participation in the experimental program by D. Bazinet and G. McCloud is gratefully acknowledged. A significant contribution to program management and braze alloys was made by Shinhoo Kang, Dept. of Inorganic Materials Engineering, School of Engineering, Seoul National University, Seoul, Korea.

References

Choi, H. C., Kim, K. S., and Shih, C. F., 1991, "A Study on Interlayer Effect on Interface Toughness, Parts I & II," ASME *Journal of Applied Mechanics,* Vol. 58.

Cotterall, B., and Rice, J. R., 1980, "Slightly Curved or Kinked Cracks," *Int. Journal of Fracture Mechanics,* Vol. 16, pp. 155–169.

Kang, S., Selverian, J. H., and O'Neil, D., 1992, Oak Ridge National Laboratory, Final report, Subcontract No. 86X-SB047C.

Kim, K. S., Stigh, U., and Choi, H. C., 1992, "A Study of the Energetic Force of a Point Load," ASME *Journal of Applied Mechanics,* Vol. 59, pp. xx–00.

Moran, B., and Shih, C. F., 1987, "Crack-Tip and Associated Domain Integrals From Momentum and Energy Balance," *Engineering Fracture Mechanics,* Vol. 27, pp. 615–642.

Nemeth, N. N., Mandersheid, J. M., and Gyekenyesi, J. P., 1989, "Ceramic Analysis and Reliability Evaluation of Structures (CARES)—User's Guide," NASA Technical Paper 2916.

Rourk, R. J., 1971, *Formulas for Stress and Strain,* 4th ed, McGraw-Hill, New York.

Selverian, J. H., ONeil, D. A., and Kang, S., 1992, *The American Ceramic Society Bulletin,* Vol. 71(9).

Selverian, J. H., O'Neil, D. A., and Kang, S., 1994, "Performance Testing and Strength Prediction of Ceramic-to-Metal Joints," ASME JOURNAL OF ENGINEERING FOR GAS TURBINES AND POWER, Vol. 116, pp. 622–628.

Yang, M., and Kim, K. S., 1993, "On the Behavior of Sub-interface Cracks With Crack-Face Contact," *Journal of Engineering Fracture Mechanics,* Vol. 44, No. 1, pp. 155–165.

H. Kumakura

M. Sasaki

D. Suzuki

H. Ichikawa

Nissan Motor Co., Ltd.;
Japan Automobile Research Institute, Inc.,
Tsukuba, Japan

Development of a Low-Emission Combustor for a 100-kW Automotive Ceramic Gas Turbine (II)

Performance tests were conducted on a low-emission combustor, which has a prevaporization–premixing lean combustion system and is designed for a 100 kW automotive ceramic gas turbine. The results of steady-state combustion tests performed at an inlet temperature of 1000–1200 K and pressure of 0.1–0.34 MPa indicate that the combustor would meet Japan's emission standards for gasoline engine passenger cars without using an aftertreatment system. Flashback was suppressed by controlling the mixture velocity and air ratios. Strength tests conducted on rings and bars cut from the actual ceramic parts indicate that the combustor has nearly the same level of strength as standard test specimens.

Introduction

There are strong demands in the motor vehicle sector today to achieve more efficient use of petroleum and to reconcile vehicle use with preservation of the global environment. In this connection, the ceramic gas turbine is regarded as a promising candidate for the next generation of automotive engines because of its multifuel capability, low emission levels, and potential for improving thermal efficiency through the use of ceramics. In Japan, the Petroleum Energy Center has been proceeding with a project to develop an automotive ceramic gas turbine (CGT) since fiscal 1990 under the auspices of the Ministry of International Trade and Industry. Japan Automobile Research Institute Inc. (JARI) is participating in this project together with members of the domestic petroleum industry and is responsible for developing the CGT engine. Figure 1 shows the construction of the CGT engine under development. This 100-kW engine is built with a single-shaft regenerative turbine and is designed to operate at a turbine inlet temperature of 1623 K. A major performance objective is to attain engine efficiency of 40 percent. The emission performance objective is to meet Japan's 10 and 15 mode emission standards for gasoline engine passenger cars without using an aftertreatment system. This means that the performance of the combustor will directly govern the emission levels of the CGT engine.

With the aim of maintaining acceptable part-load fuel economy, the CGT engine is equipped with two high-efficiency regenerators, which results in an exceptionally high combustor inlet temperature, T_{in}, of 1150–1300 K. Since this high inlet temperature promotes the formation of thermal NO_x, one of the critical development challenges is to control NO_x emissions.

In a previous study of three types of low-NO_x combustion systems, it was found that a prevaporization–premixing lean combustion system was a promising practical combustor candidate for meeting the gasoline engine passenger car emission standards [1]. This combustion system was therefore adopted to design and engineer a prototype ceramic combustor in the CGT development project [2].

This paper presents the results of tests conducted to evaluate the performance of the first combustor prototype, called PPL-1. It also describes various problems that were revealed and the design measures that have been devised to overcome them.

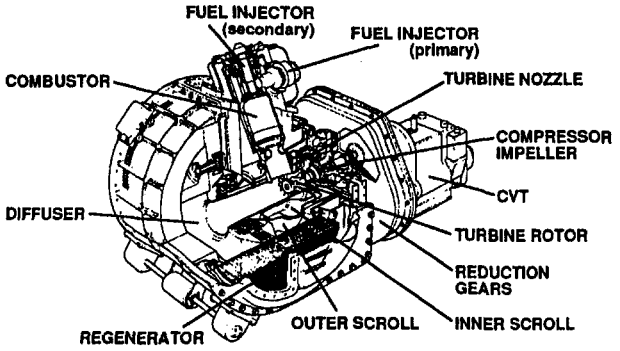

Fig. 1 Construction of 100-kW CGT engine

Combuster Design

The construction of the prevaporization–premixing lean (PPL) combustor is shown schematically in Fig. 2. The technical issues that had to be addressed in designing the fuel injectors, prevaporization–premixing section, primary (lean) combustion section, dilution section, and variable mechanism noted in the figure are summarized in Table 1 along with their respective

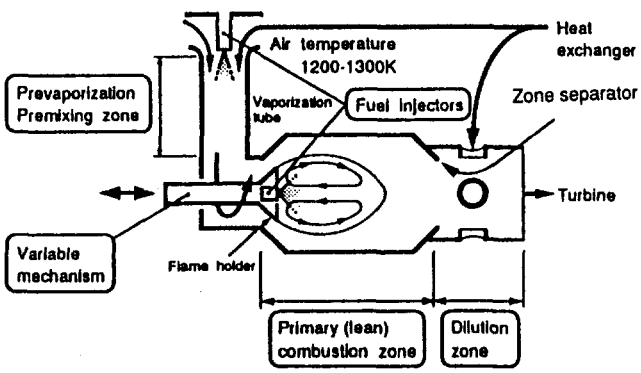

Fig. 2 Construction of prevaporization-premixing lean combustor

Contributed by the International Gas Turbine Institute and presented at the 39th International Gas Turbine and Aeroengine Congress and Exposition, The Hague, The Netherlands, June 13–16, 1994. Manuscript received by the International Gas Turbine Institute February 4, 1994. Paper No. 94-GT-33. Associate Technical Editor: E. M. Greitzer.

Table 1 Technical issues and design measures for prevaporization–premixing lean combustor

Component / Region	Technical Issues	Target Values	Measures Adopted in Preliminary Design
Fuel injectors	· High turn-down ratio · Improvement of atomization · Improvement of thermal resistance	· 45 · 60 μm (for 90% of droplets by volume) · Combustor inlet gas temperature of 1323K	· Use of injectors at two stages · Increase in atomization pressure and optimization of air-assist action · Optimization of cooling effect through air assist
Prevaporization-premixing region	· Acceleration of vaporization and mixing · Control of autoignition and flashback	· More than 95% · Complete suppression	· Adoption of a swirl and louver to promote turbulent mixture · Optimum design length of prevaporization tube
Lean combustion region	· Assurance of lean combustion stability · Attainment of low NOx and CO combustion · Improvement of load factor	· Stable combustion in all operating ranges · Compliance with domestio emission standards · Vehicle mountable configuration	· Optimization of flame-sustaining swirl · Adoption of prevaporization-premixing lean combution and discontinuation of torching · Recirculation zone control
Dilution region	· Uniform temperature distribution	· Within ±50K	· Control of combustor flow
Variable mechanism	· Assurance of reliable control of excess air ratio (λ) in lean combustion region	· Stable combustion in all operating ranges · Compliance with domestic emission standards	· Control of area of air induction hole into prevaporization region
Ceramic components	· Assurance of reliability and durability	· Required service life of 10 years	· Adoption of pull-up support structure · Service life prediction based on stress analysis

performance targets. Specific studies were made of these issues in the course of executing the combustor design. The right-hand column of the table shows the measures that were incorporated in the preliminary combustor design with the aim of attaining the performance targets.

The design details of typical measures were described in the previous report [2]. For instance, in order to promote better fuel atomization and mixing, a swirler and a louver were installed at the inlet to the prevaporization tube and the tube was positioned tangentially to the longitudinal axis of the lean combustion section. A zone separator was incorporated in the construction of the lean combustion section in order to shorten the length of the recirculation region. The variable mechanism was obtained by the movement of the flame holder along the central axis of the combustor, which varies the throat area and thereby changes the air distribution ratio, np, in the prevaporization–premixing section. A value of $np = 0.21$ was used throughout the present work. In connection with the application of ceramics, the combustor was divided into several pieces to avoid mechanical and thermal stress concentrations that could cause damage. After being formed, the pieces were assembled in a stack-up fashion. The entire combustor has been given a flexible self-supporting design as a result of adopting a pull-up construction.

Table 2 summarizes the design specifications of the first combustor prototype based on the preliminary design.

Fabrication and Strength Test of Ceramic Component

Prototyping of Ceramic Parts. A ceramic subassembly fabricated for the PPL-1 combustor is shown in Fig. 3, and the swirler and flame holder are shown in Fig. 4. Because of the complex shape of the swirler installed at the inlet to the prevaporization section, it was divided into 16 pieces, which were produced by injection molding.

Radial Crushing Strength Test of Combustor Liner. A test procedure was reported [3, 4] for assessing the actual strength of ceramic components such as the combustor liner, which has a thin, shell-like construction. It was shown that more accurate strength and service life predictions can be obtained for such components by determining the radial crushing strength of disk-shaped test pieces cut from actual components.

In the present work, eight disk-shaped test pieces were cut from each of two lean combustion section liners made of silicon carbide (C-600A) and subjected to radial crushing strength tests. The test results were then compared with the three-point bending strength of a standard test piece specified by the Japan Industrial Standards (JIS).

Figure 5 illustrates the radial crushing strength test procedure. Copper plates 0.3 mm in thickness were inserted between a disk-shaped test piece and the test apparatus. A vertical load was applied at a constant displacement velocity of 0.3 mm/min and the rupture load of the test piece was measured. All the measured results were arranged in Weibull plots and the Weibull distribution factor was found by the least-squares method. In addition, the radial crushing strength of the disk-shaped test pieces was converted to an equivalent value in terms of effective volume for comparison with the measured bending strength of the JIS specimen.

Table 2 Design specification of first combustor prototype

Prevaporization-premixing region	
Prevaporization tube length	52mm (straight segment immediately after swirler)
Prevaporization tube diameter	34mm
Turbulent mixture promoters	Swirler + louver
Swirl number	0.17
Fuel injectors	
Fuel droplet Size	60 μm max. (90% of droplets by volume)
Spray angle	60 deg
Flame-sustainig swirler	Positioned tangentially to prevaporization tube
Lean combustion region	
Air load capacity	250kg/m^{3}s MPa
Axial length	150mm
Lean combustion tube diameter	100mm
Flame-sustainig swirl number	1.0
Recirculation zone control	Zone separator
Variable mechanism	
Control method	Control of area of opening to prevaporization tube
Working principle	Area varied by moving flame holder along its axis
Ceramic components	
Low stress design	Discontinuation of secondary air holes
	Stress relief through component segmentation
	Extensive use of axisymmetric components

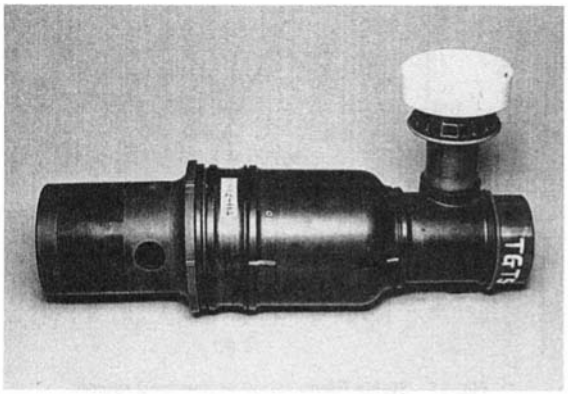

Fig. 3 Subassembly of combustor prototype (PPL-1)

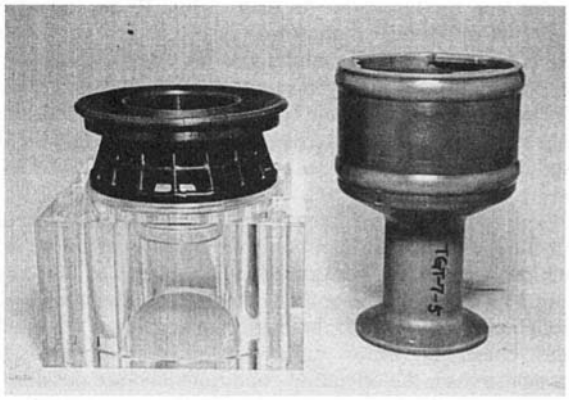

Fig. 4 Swirler of prevaporization section and flame holder

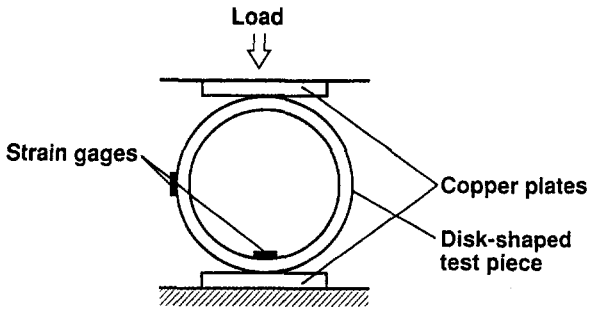

Fig. 5 Radial crushing strength test setup

Typical results of the radial crushing strength tests are shown in Table 3. The rupture strength and Weibull distribution factor of the two test ceramic liners (S/N No. 2 and S/N No. 3) are given as average values, as no significant difference was observed in their strength. The Weibull distribution factor of the

Table 3 Radial crushing strength test results

Test piece	Rupture strength MPa	Weibull distribution factor m	Equivalent strength of effective volume, σ 3P
S/N2 S/N3	455	8.9	(566)
3-point bending strength of JIS test pice	(605)	15	———

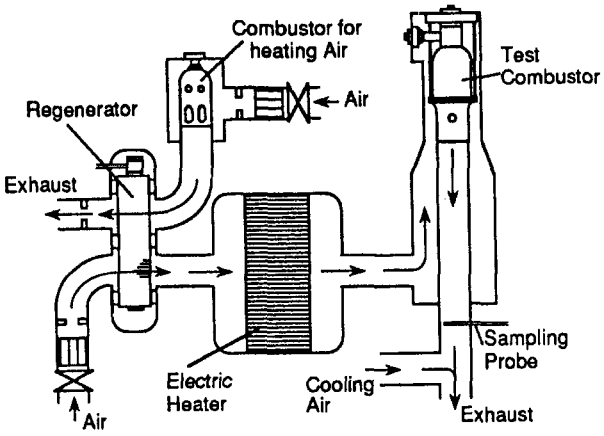

Fig. 6 Configuration of combustion test setup

radial crushing strength of the disk-shaped test pieces was lower than that of the JIS test piece. However, their equivalent strength computed in terms of effective volume, σ $3P$, was 94 percent of the rupture strength measured for the JIS specimen. Since that value was judged to be sufficient for an actual combustor liner, it was decided to proceed with the combustion tests as described in the following section.

Steady-State Combustion Tests of Prevaporization–Premixing Lean Combustor

The experimental apparatus used in conducting steady-state combustion tests is shown schematically in Fig. 6. A two-stage heating system was adopted to raise the combustor inlet air temperature to 1200 K. The air was heated in the first stage by a rotary heat regenerator and in the second stage by a 250-kW electric heater. The fuel used in the combustion tests was JIS No. 1 kerosene. All the fuel was injected from the primary injector to accomplish PPL combustion, and the secondary injector (used for diffusion combustion) was not employed.

The condition of the combustion flame is shown in Fig. 7. During combustion of the premixed mixture, the red heat of the ceramic liner stands out and the flame itself is virtually invisible to the unaided eye.

Stable Combustion Range of the First Combustor Prototype. The stable combustion range of the first combustor prototype is shown in Fig. 8 as a function of the combustor inlet temperature, T_{in}, and in Fig. 9 as a function of the combustor inlet pressure, P_{in}. In these figures, the vertical axis indicates the mean axial flow velocity, $\mathbf{u}_{ax}$, of the premixed mixture as it flows through the throat area into the combustion chamber, and the horizontal axis indicates the air ratio, λ_p ($= np \times \lambda_{\text{overall}}$), in the lean combustion section. It was observed that the

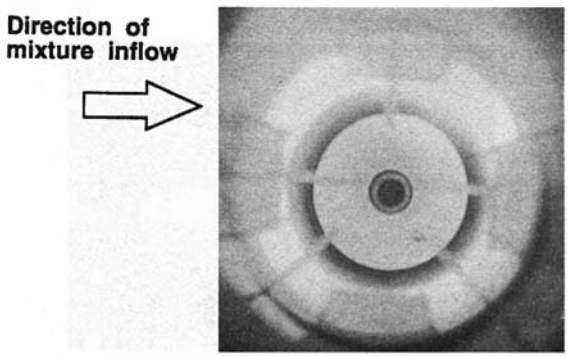

Fig. 7 Flame photograph (taken from combustor outlet)

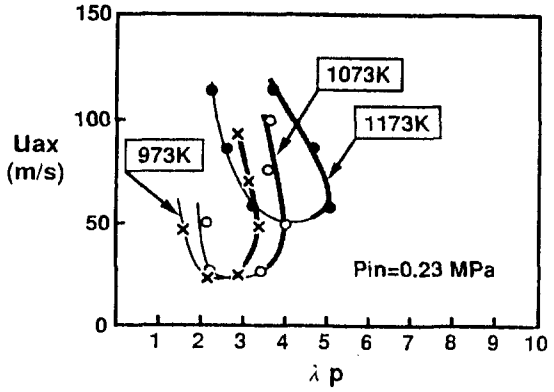

Fig. 8 Stable combustion region versus combustor inlet temperature

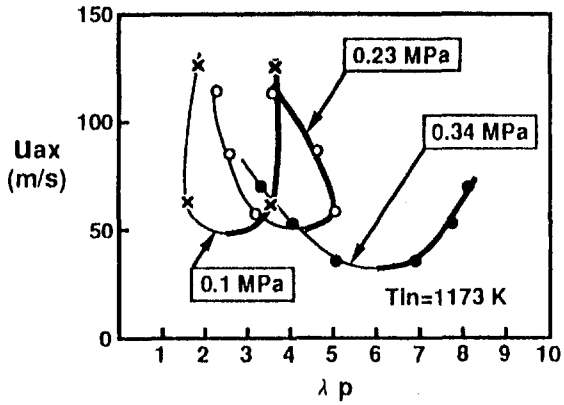

Fig. 9 Stable combustion region versus combustor inlet pressure

limits for the occurrence of flashback and flame blowout changed greatly when the throat area was varied by moving the flame holder. Therefore, it was decided to express the stable combustion range in terms of the mean axial flow velocity, u_{ax}, of the mixture in the throat area, which was thought to govern the flashback limit. The limit of stable combustion on the rich mixture side (fine lines in the figure) indicates the flashback limit while the limit on the lean mixture side (boldface lines) represents the lean blowout limit.

A flame holder that was damaged by flashback is shown in Fig. 10. Flashback must be avoided as much as possible because, in addition to causing a noticeable increase in NO_x emissions, it can also be a direct cause of damage to ceramic components.

As shown in Fig. 8, the stable combustion range shifted a little toward the lean mixture side when the combustor inlet temperature was raised from 973 K to 1073 K. However, when the temperature was increased further from 1073 K to 1173 K,

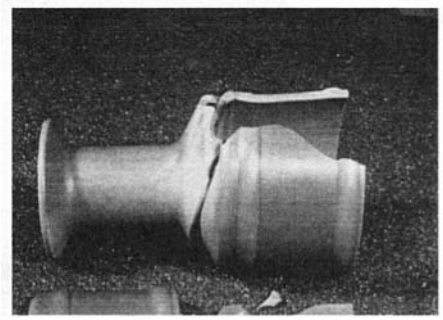

Fig. 10 Flame holder damaged by flashback

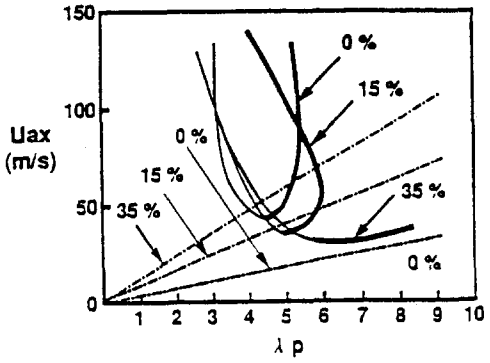

Fig. 11 Stable flame range in low-load region

it showed a large shift toward the fast flow velocity side and also the lean mixture side. As seen in Fig. 9, the lowest flow velocity of the stable combustion range changed very little in relation to changes in the combustor inlet pressure. However, when the combustor inlet pressure rose from 0.23 to 0.34 MPa, the blowout limit of the stable combustion region shifted considerably toward the lean mixture side. This indicates that the limit of stable combustion for a lean mixture expands greatly as the pressure rises to a high level.

Based on these experimental results, a suitable operating point for the combustor can be found by estimating the stable combustion range for various operating points of the engine. Figure 11 shows the stable flame range estimated for the load regions needed to operate the engine under Japan's 10 and 15 modes. Once the various dimensions of the combustor have been determined, the operating conditions that are possible can be selected on the basis of the straight lines corresponding to the different load factors noted in the figure. The results show, for instance, that it would be impossible to obtain a stable flame region under the operating conditions for a load factor of 0 percent. Since the straight lines representing the operating conditions do not cross the stable flame region, it was concluded it would be hard to prevent flashback in the first combustor prototype, especially under a low load condition with an exceptionally high combustor inlet temperature of approximately 1250–1350 K.

Emission Performance. Typical examples of the NO_x and CO emission characteristics of the prevaporization–premixing lean combustor are shown in Figs. 12 and 13, respectively. Hydrocarbon emissions will not be treated in this discussion as only very small quantities less than $\frac{1}{40}$ of these substances were produced.

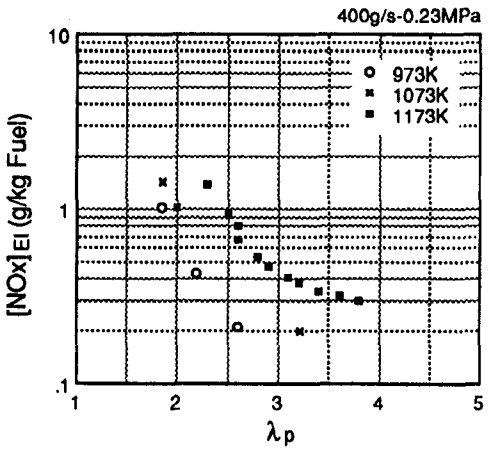

Fig. 12 NO_x emission characteristics

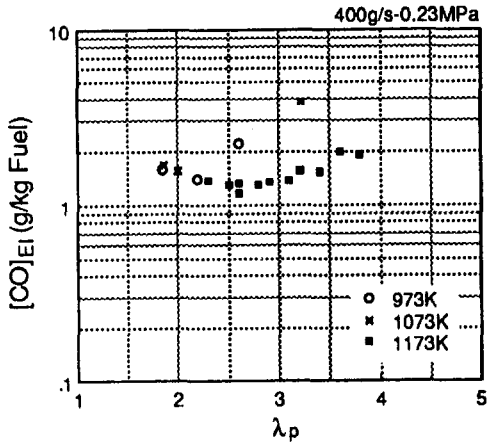

Fig. 13 CO emission characteristics

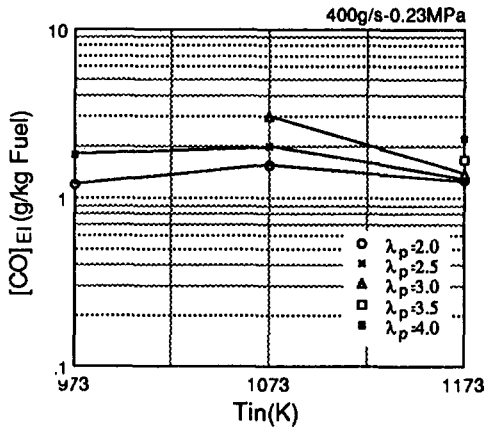

Fig. 15 Temperature dependence characteristics of CO emissions

Taking a combustor inlet temperature of 1173 K (■) in Fig. 12 as an example, NO_x emission levels have been plotted in a range defined by the flashback limit (air ratio in the lean combustion section of λ_p = approximately 2.2) and the blowout limit (λ_p = approximately 3.8). The results show that, as the combustor inlet temperature rose, the stable combustion range shifted to the lean mixture side, and the NO_x emission level increased. On the other hand, the CO emission level rose sharply near the flame blowout limit.

Generally, NO_x emissions are strongly dependent on the combustor inlet temperature, T_{in}, and combustor inlet pressure, P_{in}, and can be given by Eq. (1) [1]:

$$\langle NO_x \rangle EI = \langle NO_x \rangle EIREF \cdot (P/P_{REF})^m \cdot \exp\{k(T_{in} - T_{inREF})\} \quad (1)$$

$$\langle NO_x \rangle EIREF = a \cdot \lambda_p^b \quad (2)$$

where *REF* stands for the reference condition. The temperature dependence characteristics of the NO_x and CO emissions are shown in Figs. 14 and 15, respectively. It is seen that NO_x emissions increased with an increasing combustor inlet temperature, T_{in}, irrespective of the air ratio, λ_p. The temperature dependence index, k, shows virtually a constant increase in a range of $k = 5.2 \times 10^{-3} - 6.1 \times 10^{-3}$ for an air ratio of $2.0 < \lambda_p < 4.0$. This value of k was considerably larger than that reported earlier ($k = 1.8 \times 10^{-3}$) for combustion of a completely prevaporized and premixed air–fuel mixture at an air ratio of $\lambda_p = 2$, which suggests the effect of a nonuniform mixture, among other possible factors. Within this temperature range, the CO emission level showed little dependence on the combustor inlet temperature.

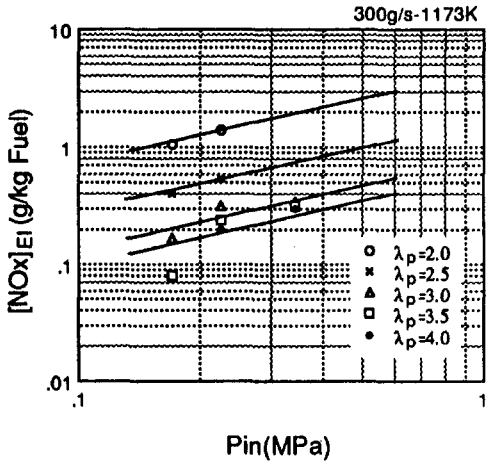

Fig. 16 Pressure dependence characteristics of NO_x emissions

Figures 16 and 17 show the inlet pressure dependence characteristics of NO_x and CO emissions, respectively. The NO_x emission level increased with increasing inlet pressure. The inlet pressure dependence index, m, shows a little decrease in a high-pressure range ($P = 0.34$ MPa). It will be necessary to examine this tendency over a wide pressure range for NO_x emissions in

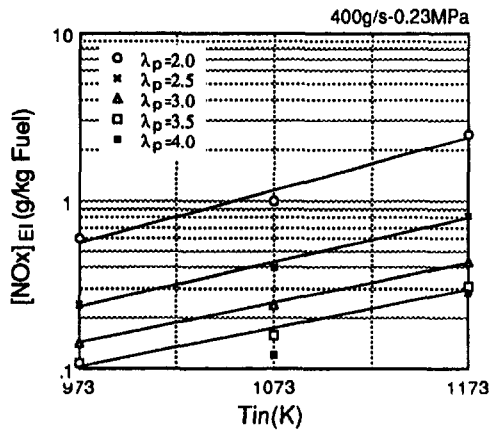

Fig. 14 Temperature dependence characteristics of NO_x emissions

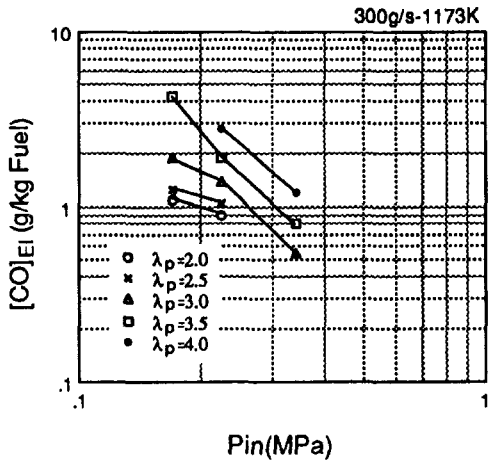

Fig. 17 Pressure dependence characteristics of CO emissions

Table 4 Predicted 10 and 15 mode NO_x emissions

λ p setting	Predicted NOx level
2.5	0.09 g/km
3.0	0.05 g/km

future work. The CO emission level, on the other hand, tended to decrease with increasing inlet pressure, irrespective of λ_p.

Based on the experimental results, a NO_x emission model was created around Eq. (1) and used to conduct NO_x emission simulations under Japan's 10 and 15 modes. The values input into the model for the air mass flow rate at the combustor inlet, fuel flow rate, combustor inlet temperature, and combustor inlet pressure were those obtained in vehicle emission simulations under the 10 and 15 mode conditions. The pressure dependence index was given a value of $m = 0.3$, which was the value reported earlier for combustion of a completely prevaporized and premixed air–fuel mixture [1].

The simulation results are shown in Table 4. The predicted CO emission level was noticeably lower (only about $\frac{1}{30}$) than the 10 and 15 mode standard. The predicted NO_x emission levels for λ_p values of 2.5 and 3.0 were both well below the NO_x emission standard of 0.25 g/km. These values would allow a sufficient margin for the increase in NO_x emissions that would likely occur under transient operating conditions due to the response lag of the variable mechanism. It will be necessary to examine transient emission performance in future work.

Problems in the First Combustor Prototype and Related Design Improvements. The results of the steady-state combustion tests revealed several problems in the first combustor prototype (PPL-1), which are outlined in Table 5 along with design measures for addressing them.

First, the flame holder must be optimally positioned to prevent flashback. That means the mechanism for varying the air ratio distribution between the primary combustion section and dilution section should be designed as a variable throttling device at the inlet to the prevaporization tube. Moreover, simply using a leaner mixture ($\lambda_p = 5.0$) to control flashback will not work because it will lead to excessive pressure losses in the low-load region, as indicated in Fig. 18. Other design measures will have to be considered for preventing flashback even under a condition of a slightly richer mixture ($\lambda_p = 3.0$) than shown above. Effective measures for this purpose include lowering the combustor inlet air temperature and providing a more uniform flow in the premixing section along with a more uniform mixture ratio distribution. For instance, reducing the combustor inlet temperature by a uniform 100 K would shift the stable flame region shown in Fig. 11 from the present limits of $\lambda_p = 4$ and $\mathbf{u}_{ax} = 60$ m/s toward the rich mixture side by a λ_p value of approximately 1.5 and toward the low-flow velocity side by a $\mathbf{u}_{ax}$ value of approximately 20 m/s. In addition, if the nonuniform flow velocity through the throat area could be eliminated by providing a uniform flow in the premixing section, the stable flame region shown in Fig. 11 would shift toward the low-flow velocity side by a $\mathbf{u}_{ax}$ value of about 15 percent. The reason for that is the variation in the mixture velocity at the entrance to the combustion region has been estimated to be about 20 percent [5].

Table 5 Problem in first combustor prototype and related design measures

Problems	Design Measures
Variable mechanism: It is impossible to obtain the desired adjustment of air distribution and prevent flashback at the same time	A stationary flame holder and a variable area into the prevaporization tube
Swirl chamber: Flow velocity into the combustion chamber was not uniform	Assure a uniform flow velocity (Redesign of swirl chamber)
Swirl for prevaporization-premixing: Too complex swirler	A block-type swirler

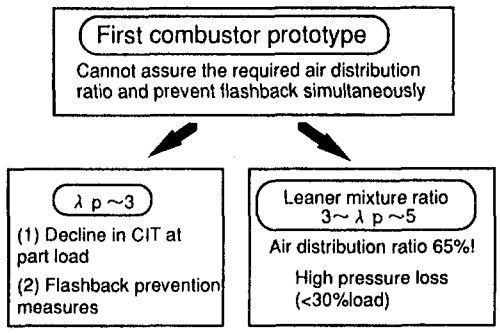

Fig. 18 Study of design measures for preventing flashback

As a final measure for preventing flashback, we will consider dilution of the boundary layer. The simulation results suggested that a lower flow velocity in some areas near the walls of the throat may have caused localized reductions of the air ratio [5]. It is possible that flashback may have originated in those areas. In that case, flashback could be prevented by introducing air into those areas to dilute the boundary layer. It is planned to incorporate the foregoing design measures into an improved combustor prototype.

Conclusion

Steady-state combustion tests were conducted to evaluate a low-emission combustor for a 100-kW automotive ceramic gas turbine. The results showed that there was a good prospect of meeting Japan's 10 and 15 mode emission standards.

The experimental results obtained with this first combustor prototype (PPL-1) indicated that the flashback limit made it exceptionally difficult to operate the combustor at acceptable performance levels in the low-load region. The results suggested several approaches to improving the combustor design in order to resolve that problem.

In future work, it is planned to incorporate those design improvements into the combustor to prevent flashback and to conduct evaluations of transient emission performance.

References

1 Sasaki, M., Kumakura, H., and Suzuki, D., "Low NO_x Combustor for Automotive Ceramic Gas Turbine—Conceptual Design," ASME Paper No. 91-GT-369, 1991.

2 Sasaki, M., Kumakura, H., Suzuki, D., Sugiyama, K., and Okubo, Y., "Development of a Low Emission Combustor for a 100-kW Automotive Ceramic Gas Turbine (I)," ASME Paper No. 93-GT-63, 1993.

3 Sasaki, M., et al., "Development of a Reaction Sintered SiC Combustor Liner and Issues Remaining to Be Solved," GTSJ 16-23 [in Japanese], 1988.

4 Kumakura, H., Sasaki, M., and Suzuki, D., "Low NO_x Combustor for Automotive Ceramic Gas Turbine—Reliability Assurance," ASME JOURNAL OF ENGINEERING FOR GAS TURBINES AND POWER, Vol. 115, 1993, pp. 547–553.

5 Nomura, K., and Ohkubo, Y., "Combustion Analysis of a Combustor for a 100-kW Automotive Ceramic Gas Turbine," presented at the Fall Conference of GTSJ [in Japanese], 1993.

Hybrid Bearing Technology for Advanced Turbomachinery: Rolling Contact Fatigue Testing

J. F. Dill
Mechanical Technology Inc.,
Latham, NY 12110

The purpose of this paper is to describe the basic structure and results to date of a major ARPA funded effort to provide a tribological performance database on ceramic bearing materials and their interaction with standard bearing steels. Program efforts include studies of material physical properties, machining characteristics, and tribological performance. The majority of the testing completed to date focuses on rolling contact fatigue testing of the ceramic materials, including efforts to arrive at optimum approaches to evaluating ceramic/steel hybrid combinations in rolling contact fatigue.

Introduction

Over the last 10 years ceramic materials technology has advanced to the point where advanced silicon nitride materials are being considered for application in hybrid bearings (ceramic rolling elements with steel races) in a wide range of turbomachinery applications. While there are a number of materials that can meet the performance requirements of advanced turbomachines, at present each material supplier has its own proprietary composition and manufacturing process, making the selection of the ceramic material confusing for the applications engineer.

At the same time, there are insufficient comparative data available in the literature on the performance of different ceramic materials to guide this selection process. This lack of information raises serious questions in the application of hybrid bearings when material suppliers too frequently "improve" (i.e., change) their compositions or there is a desire to change the ceramic material supplier either because of cost or availability of material.

It is not always clear from a performance viewpoint that the material supplier changes are improvements. In recent years, one ceramic supplier made changes that increased the purity of its material, but those same changes also reduced the fracture toughness, which can only be regarded as a potential performance reducer. The other result of the frequent composition changes in ceramic bearing materials is a lack of batch-to-batch consistency in material performance, which reduces user confidence in noncritical applications and can preclude the use of certain materials in applications such as aircraft turbine engines or rocket engine turbopumps where consistency of performance is critical.

In addition to such user-oriented application questions, which arise from composition changes in ceramic bearing materials, the bearing ball finisher is faced with issues related to varying material machining properties due to the different physical properties of ceramics from each supplier. While each ceramic may have the potential to perform well in a bearing application, the optimum ball manufacturing process can differ significantly depending on the specific properties of the ceramic. As shown by Gardos and Hardisty (1993), the polishing rate of the ceramic ball blank material at a fixed set of conditions can vary by at least a factor of three among known acceptable ceramic materials. The ball finisher must go through costly process development efforts each time the material changes, because the relationship between material properties and machinability is poorly defined for these materials. This need to vary finishing process can affect both the quality and cost of the ball supplied when changes are made in the ceramic material used.

ARPA has awarded a contract to Mechanical Technology Inc. (MTI) to address the requirement for comparative processing data on currently available silicon nitride bearing materials, and to develop an understanding of the rolling and sliding contact performance of these materials. The goal of this effort is to permit users to evaluate materials selections based on material properties and the results of selected tribological tests. In this program, MTI is teamed with Hughes Aircraft and Spheric Engineering Ltd. to study the mechanical, finishing, and tribological properties of silicon nitride bearing materials. Upon completion of the effort, the results of the testing will be published in a Hybrid Bearing User's Guide, along with specifications for the testing of ceramic bearing materials. This paper will present the results of this test program to date and the implications of those results in the evaluation of ceramic bearing materials.

Program Outline

There are three major technical focuses of the program that MTI is currently conducting under ARPA funding. These focuses include: (1) evaluating material properties such as fracture toughness and hardness, (2) defining ball blank finishing characteristics, and (3) defining the relationships between materials properties and their tribological performance.

Efforts to evaluate the fracture toughness and hardness of various ceramic ball blank materials along with the uniformity of those properties throughout the ball blank are being conducted by M. Gardos of Hughes Aircraft. There were some indications in previous efforts by Hughes Aircraft and Spheric Engineering Ltd. on ball polishing as reported by Gardos and Hardisty (1993) that the final quality of the ball (in terms of sphericity and waviness) could be affected by small nonuniformities in the ball blank material (possibly even in HIPPed materials). Efforts currently underway at Hughes Aircraft are investigating these effects further via precision micro-indentation studies of ball blank materials from various suppliers. All ball blanks are also being inspected using a range of advanced NDI techniques, which are also being funded by ARPA, including acoustic resonance studies by Quatro and laser material evaluation techniques by Argonne National Laboratory. It is hoped that use of both techniques will permit the more advanced NDI results to be correlated with conventional indentation evaluation techniques.

Contributed by the International Gas Turbine Institute and presented at the 39th International Gas Turbine and Aeroengine Congress and Exposition, The Hague, The Netherlands, June 13–16, 1994. Manuscript received by the International Gas Turbine Institute March 5, 1994. Paper No. 94-GT-386. Associate Technical Editor: E. M. Greitzer.

Table 1 Characteristics of ceramic materials tested to date

Material Tested	Additive	Process	Vickers Hardness (kg/mm^2)	K_{IC} MPa $(m)^{1/2}$
A	MgO	Si_3N_4 Powder HIP	1509-1586	4.34-5.05
B	$Y_2O_3 + Al_2O_3 + TiO_2 + C$	Si_3N_4 Powder HIP	1461-1494	6.4-7.1
C	$Y_2O_3 + SrO$	Si_3N_4 Powder HIP	1580	8.6
D	$Y_2O_3 + Al_2O_3$	Si Powder Reaction Bond	1550	6-7.5
E	MgO	Si_3N_4 Powder HIP	1550	6.5
F	$Y_2O_3 + Al_2O_3$	Si Powder Reaction Bond HIP	1468 ± 6	$5.3 \pm .16$
G	$Y_2O_3 + Al_2O_3$	Si Powder Reaction Bond HIP	1433-1468	5.26-5.38

Ball blank finishing studies are designed to give further detail of the relationship between material finishing rate under controlled conditions and material properties such as that discussed by Gardos and Hardisty (1993). In an expansion of the prior work, studies will be done during both grinding and polishing portions of the finishing process. To provide more precise information than that initial study, a group of instrumented ball finishing machines were developed by Spheric. These machines include load cells and gas pressure load cylinders for load control, precise speed control and measurement, variable speed capability through use of a variable speed motor, computer-controlled lubricant and abrasive addition, and computer-controlled machine shutdown at specified inspection or process change intervals. These machines are being used to evaluate further the relationship between ball finishing rate and material properties.

Studies are also being conducted of finishing process optimization for materials with varying properties. In these studies, finishing conditions are being varied to achieve as nearly as possible an optimum condition for both the grinding and polishing stages of ball finishing. It is hoped that these studies, when coupled with the relative machining studies under fixed conditions, will provide a database for ball finishers, which can be used to select finishing conditions for new ball blank materials based on the material's physical properties.

The third area of technical investigation includes a wide range of tribological studies. These studies focus on hybrid material combinations including M-50 and 440C bearing steels with six different ceramic materials. These tribological studies include rolling contact fatigue, sliding wear, and lubricant degradation tests. Rolling contact fatigue evaluations investigate both the fatigue properties of the ceramic materials and the effects of the ceramic material composition on the fatigue performance of the mating metallic component. Sliding wear studies are being conducted over a range of conditions to evaluate the relative wear resistance of different ceramic compositions. Both the fatigue and wear studies are being conducted primarily at MTI, although some wear evaluations will be done by Hughes Aircraft also.

The effects of all metallic versus hybrid ceramic/metallic contacts on the degradation of perfluoropolyalkylether (PFPAE) lubricants is being evaluated by Hughes. To conduct these studies a simple lubricant test has been developed, which has demonstrated the ability to produce lubricant degradation in an all-metal system. Studies by Carré (1990) have shown that use of hybrid ceramic contacts reduces PFPAE lubricant degradation. However, those studies used a single composition of ceramic. Upon completion of metallic baseline tests, the effects of ceramic composition on the reduction in PFPAE lubricant degradation will be evaluated.

The efforts described above will involve full evaluation of up to six ceramics, although to date as shown in Table 1, seven different materials have been screened using rolling contact fatigue testing. Values of hardness and fracture toughness in Table 1 are those provided by the material suppliers as part of the certification of their material and are included only to roughly classify the materials. Since these values have not been measured in a consistent manner, Hughes Aircraft is making measurements with a standardized procedure for all test materials. The Hughes measured values will be used in all analysis of the program data. Rolling contact fatigue testing is being used as a benchmark for selecting materials to be included in other tests. Upon completion of all the testing under this program, the goal is to assemble the data into a handbook for users, finishers, and material suppliers. With the breadth of the data being obtained, the goal will be to tie physical properties, NDI performance, finishing characteristics, and tribological performance into a complete picture of silicon nitride behavior in hybrid bearing applications. The following sections discuss the results of this research to date in one key area, the area of rolling contact fatigue testing of ceramics.

Toward Sensible RCF Testing of Ceramic and Metallic Materials

As the RCF performance of ceramic materials has improved, the tendency has been to increase the applied load or stress in the contact to accelerate the testing further and maintain a manageable test time. This and the following sections will discuss some of the issues associated with rolling contact fatigue testing of ceramics in hybrid combination and the results of a number of specific studies undertaken to arrive at a consistent approach to such testing.

Issues that must be addressed include the fact that in some cases, experimental evidence shows that the failure mode in the ceramic rod can change over from the fatigue spalling type of failure, which is typical of bearing applications of this material, to a flaking wear type of failure when very high stresses are used. When the fatigue testing involves a hybrid material combination, i.e., steel balls on ceramic test rods, the steel balls can exhibit very high wear at high loads, resulting in a rapid drop in stress from the initial high value. Both of these phenomena can significantly affect the results of rolling contact fatigue tests in ceramics. The following sections will discuss the results of tests that have been conducted to evaluate these phenomena in the rolling contact fatigue testing of ceramic materials.

Rolling contact fatigue testing in this program is being conducted using the RCF tester developed by NTN-Bower Corp., as described by Glover (1982). As shown in Fig. 1, the test consists of a $\frac{3}{8}$ in. diameter rod sample of the test material to which rolling contact stresses are applied using standard $\frac{1}{2}$-in. dia bearing grade balls. Loads are applied to the ball/rod combination through two standard tapered roller bearing cups using three equally spaced springs whose tension is set to provide a fixed contact load. Because of the large amount of compression in the springs at the loads used, the small amounts of wear in the contacts measured here do not affect the applied load. As will be discussed later, however, the wear can significantly reduce the applied stress by increasing the Hertzian contact area over which the load is spread.

RCF testing with the NTN-Bower rig is being used to screen materials for further more detailed evaluations in other portions of the program. In these tests, roughened M-50 balls are used along with an initial stress of 786 ksi (5.42 GPa) to evaluate the basic integrity of various ceramic materials. To date preliminary evaluations have been conducted on the seven materials described in Table 1.

High Stresses and Accelerated Ceramic Wear

As ceramic materials have gotten better, the stresses used in evaluating their fatigue performance have been steadily in-

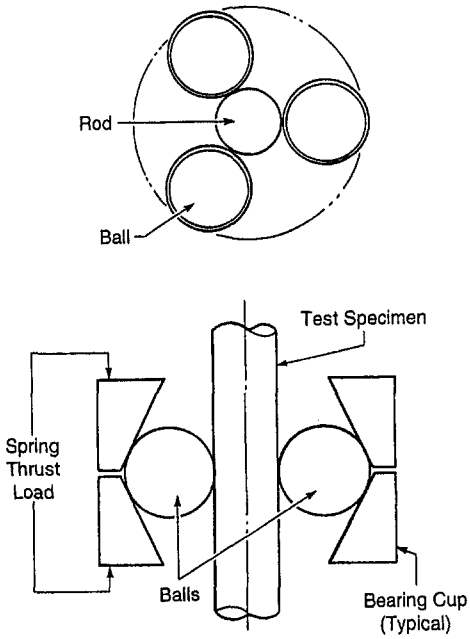

Fig. 1 Basic layout of NTN-Bower RCF tester

creased in an effort to keep test times reasonable. While for some materials, this approach still gives reasonable results even at stresses of over 900 ksi (6.20 GPa), testing of some materials results in a rapidly increasing wear rate with contact stress at high stresses. An example of the differing wear behavior during rolling contact fatigue testing of two ceramic materials is given in Fig. 2.

Wear measurements on the ceramic rods were made by running two tests at each initial stress level for a fixed period of time. Only tracks where no spalling occurred were used for wear measurements. By limiting the test time of the measurements, both ball and rod spalling were avoided. Wear values on the ceramic rods were measured by using a profilometer to trace across the track profile in three regions approximately 120 deg apart on each rod. The three values for each track were then averaged to give the average wear for that track, and the values for the two tracks at each stress were averaged to produce the wear values plotted in Fig. 2.

For material A, the wear rate is very low and the change with stress is minimal up to the highest test stress of 935 ksi (6.45 GPa). For material B, while its wear at 650 ksi (4.48 GPa) is comparable to that of material A, as stress increases there is a rapid increase in wear especially above 800 ksi (5.52 GPa). At the maximum stress of 935 ksi (6.45 GPa), the wear rate of

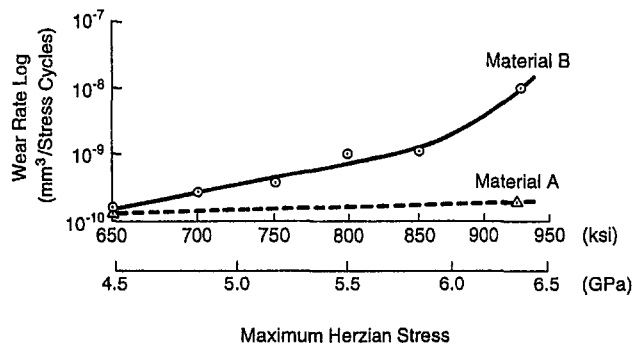

Fig. 2 Rolling contact wear of two ceramics versus maximum Hertzian contact stress

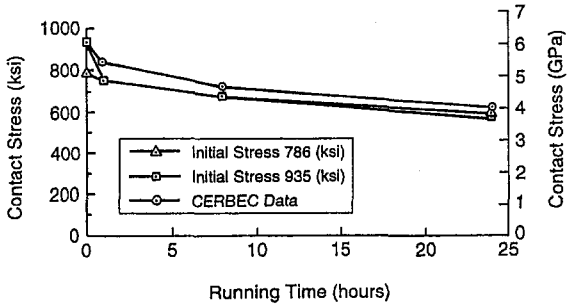

Fig. 3 Stress reduction in rolling contact fatigue tests due to steel ball wear

material B is almost two orders of magnitude higher than that of material A.

In the past such testing has been used to differentiate between the viability of various ceramic candidates for bearing applications and in developing advanced ceramic formulations. However, in this case, both materials A and B are known to perform well in actual bearing applications. The accelerated wear of material B seems to be connected to a change in the fundamental wear mode of that material. At 650 ksi (4.48 GPa), wear of the ceramic material is minor even in very long tests (60 million cycles and higher), but as stress increases above that value the wear increases significantly. The mode of wear also changes over to a shallow flaking type wear at the highest stress levels.

It is known that this material performs well in actual bearings, and the wear is comparable to other materials below 650 ksi (4.48 GPa). Based on this knowledge, it can be concluded that the change in wear mode at high stresses may not be relevant to realistic applications where stresses would be much lower. At realistic bearing stresses of 200–300 ksi (1.38–2.07 GPa), it should be impossible to tell the difference in the rolling contact wear characteristics of the two materials. In investigating the rolling contact fatigue performance of ceramics, this laboratory has adopted the approach of evaluating the effect of stress level on a material's wear prior to setting the stress value to be used in rolling contact fatigue testing. By evaluating the stress dependence of rolling contact wear, it is possible to avoid rejecting a material due to high wear at high stresses when that wear is more related to the test technique than to the actual expected performance of the material in a bearing application.

Ball Wear and Stress Reduction in Testing RCF of Ceramic Rods With Steel Balls

In addition to possible increased ceramic rod wear at high stresses in RCF-type fatigue testing, the wear of the metal balls used in combination with the ceramic rod also increases significantly as stresses increase over 800 ksi (5.52 GPa). To evaluate these effects, a series of experiments were run using material A in Table 1 to evaluate steel ball wear during RCF testing of ceramic rods.

The increased wear of the steel balls in RCF testing of ceramics is critical because it leads to a stress reduction as a function of time. As shown by Curve A in Fig. 3, when starting at an initial stress of 935 ksi (6.45 GPa), after only 1 hour of running time the stress can decrease to approximately 700 ksi (4.83 GPa) when running surface roughened M-50 balls against a ceramic rod. Due to the inverse ninth power dependence of life on stress, such a stress reduction can account for an increase in the measured rod life by a factor of over 13 relative to the life that would be obtained if the initial high stress level were maintained.

Ball wear was measured using an optical microscope with a reticle scale. Because of the ball wear in the ceramic/metallic contact, the contact track is clearly visible on each ball. For

Table 2 Rolling contact fatigue and wear performance of seven ceramics

Material Tested	Ball Wear at 786 ksi (5.42 GPa)	Rod Wear	Ball Spall	Rod Spall
A	normal	none	5	none
B	normal	none	10	none
C	normal	none	none	large
D	heavy (2xnorm)	none	2	none
E	normal	none	none	none
F	normal	none	none	none
G	normal	none	none	none

each RCF test, the Hertzian contact track width is measured at three places on each of the three test balls, which have run in contact with the ceramic rod. In all cases the track widths were found to be very uniform on each individual ball at the three measuring spots and also on all three balls used in an individual test. The measured values from all three balls are then averaged to give an average wear value. Previous studies in this laboratory have shown that this technique provides reliable correlation with measurements made using profilometer tracing. The increase in contact track width can then be used to calculate the stress reduction with time in the contact.

This reduction in stress with time found in RCF testing of ceramics with steel balls is particularly significant when trying to compare steel ball on ceramic rod results with comparable steel on steel tests. In steel on steel tests with both M-50 and 52100 balls running on M-50 rods, track measurements indicate that even after 120 hours of running the contact width is equal to the calculated Hertzian contact width. Thus in steel-on-steel RCF tests, the stress reduction with time is minimal. The difference in stress behavior with time in the steel-on-steel tests versus steel-on-ceramic tests can account for a reasonable portion of the reported longer life of ceramic materials in RCF-type testing when using roughened steel balls.

As shown in Fig. 3, the ball wear measured here for material A roughly duplicates that reported by Lucek (1990) for steel ball wear in his RCF testing of a similar silicon nitride. Values of stress versus time were taken as approximate values from Fig. 6 of Lucek (1990). The relative agreement on the stress reduction is good considering the variability seen from test to test on ball wear, and recognizing possible small material property differences between material A and that evaluated by Lucek (1990). The values of stress reduction shown in Fig. 2 are meant to show trends rather than provide exact values at this time. The results are also only applicable to one particular silicon nitride ceramic/metallic material combination since there is clear evidence that the ball wear experienced in RCF testing is affected by the ceramic material used as shown in Table 2. Obviously the wear would also change in the ball material were changed.

The rapid stress drop at short time reported here is felt to represent more closely the actual experimental situation than the linear relationship assumed by Lucek (1990). In these tests, measurements were made by terminating tests at 1, 8, and 24 hour periods and measuring the ball track widths. All cases used were terminated tests since it was felt that the wear track width might be affected by the presence of a spall on either the balls or the rod. In contrast, Lucek (1990) made his measurements on tracks from spalling failures, but outside the region of failure. Considering these differences in the testing, the agreement is quite good, especially since small differences in assumed elastic modulus and Poisson's ratio in the stress calculations could easily account for the differences in the curves at longer test times.

More extensive studies have shown that the ball wear is variable from test to test with a given material and thus different tests will experience varying degrees of stress reduction with time. On the other hand, if the same tests are started at 786 ksi (5.42 GPa), only minor ball wear is experienced. In general, ball/rod Hertzian contact widths are within 15–20 percent of the calculated values even after 120 hours when tests are started at 786 ksi (5.42 GPa). By starting the tests at lower stress, a more consistent stress level is maintained over a longer period of time than when starting at the highest stress levels.

The details of the ball wear also seem to differ depending on the properties of the ceramic material being tested. Table 2 summarizes the ball wear for a group of seven silicon nitride ceramic bearing materials tested at a starting stress of 786 ksi (5.42 GPa). All of these materials were evaluated following the same test procedure using the same RCF test machine. All the samples were machined by the same machining vendor, but one material clearly produced higher steel ball wear than the others. The causes for this difference are being evaluated in further testing. At the present time, it is not clear if the higher wear exhibited with one ceramic material is related to some basic material compatibility issue between the ceramic and metal parts, or if the higher metal wear can be attributed to a difference in the detailed surface finishability of the ceramic material. Initial inspection of the various ceramic rods shows no fundamental geometric differences (roundness, straightness, surface finish) between the materials studied, which could account for the differences in wear in the tests.

In addition to differences in the wear of the steel balls, two materials showed a significantly poorer performance of the steel balls in terms of fatigue spalling. For these materials (B and D), there was a much higher frequency of ball spalling during tests, which were scheduled to be terminated at the same time up period as all other tests. For most of the materials tested, no ball or rod spalls occurred during the 120 hour time up period. However, for the two materials just identified, B and D, significant ball spalling occurred. This is particularly true for material B, where half of the fatigue tests terminated prior to the 120 hour time up because of ball spalling.

The ceramic fatigue test rods were all finished by the same machining vendor and all met the machining specification for straightness, roundness, and surface finish, which are generally regarded as the key geometric features that must be controlled in the manufacture of the test specimen. The rod wear was also comparable for all materials at the end of the tests so the ball spalling couldn't be attributed to a roughening of the rod causing a life reduction in the balls. The balls used were all from the same lot of M-50 material and were roughened by grit blasting using the same process. Further investigations are under way to understand these differences. One key series of test that will be performed in the future will involve rolling contact fatigue tests using steel rods and ceramic balls to evaluate whether there is a difference in the life of the steel material with different ceramic ball materials.

RCF Testing With Roughened Versus Smooth Balls

Standard practice with the NTN-Bower RCF tester is to use roughening of the steel balls to accelerate the tests by reducing the relative EHD film thickness in the contact. Testing during the development of the rig as discussed by Glover (1982) showed that this approach gave significantly reduced test times. The standard roughening increases the contact composite roughness to 4 μin. from the value of 2 μin., which is obtained with a smooth (approximately 0.5 μin. finish) ball running on the standard 4 μin. roughness rod. Since the calculated EHD

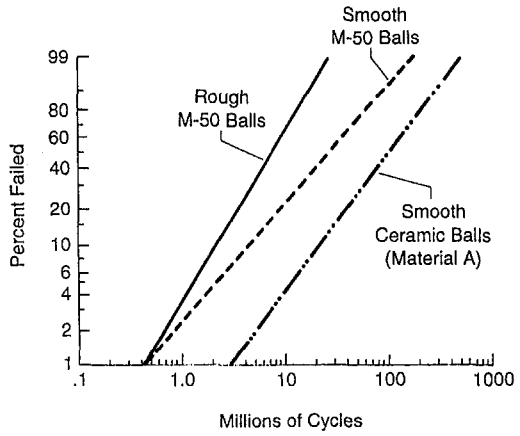

Fig. 4 RCF test Weibull data comparing M-50 life obtained with different balls as indicated

film thickness with MIL-L-23699 lubricant generally used in this test is approximately 2 μin., this is a factor of two change in the ratio of film thickness to surface roughness.

Using the standard curve for estimating the effect of film thickness on fatigue life such as that given by Zaretsky (1992), the use of smooth balls should result in a life increase of a factor of about 2, although at the low film thickness to surface roughness ratios involved the exact effect is difficult to determine other than by direct measurement. Data taken under this current program indicate that the use of smooth balls in place of the standard roughened balls significantly extends the test time, although the percent of rod spalls remains high with smooth M-50 balls at 786 ksi (5.42 GPa) on M-50 rods, despite the comments of the original rig designers, as reported by Glover (1982) to the contrary. The Weibull curves for roughened M-50 balls on M-50 rods, smooth M-50 balls on M-50 rods, and smooth ceramic balls (material A) on M-50 rods are given in Fig. 4. All of the M-50 rods were from one batch of material, and the M-50 balls were also from one batch whether roughened or smooth.

For rough M-50 balls on M-50 rods a L10 life of 2 million cycles and a Weibull slope of 1.5 was found over a baseline of 23 tests. For smooth M-50 on M-50, there were 18 rod spalls out of 20 tests with a L10 value of 4.5 million cycles and a Weibull slope of 1.0. The use of smooth M-50 balls in the fatigue testing of the M-50 rods results in approximately a 2 $\times$ increase in the measured L10 life for this material combination as expected because of the increase in relative EHD film thickness.

Because we were interested in evaluating the use of this same test for investigating the performance of ceramic balls on steel rods, a series of these tests were also run using material A. Material A was selected for these initial evaluation tests because we had the material available as finished balls. In these tests, a further increase was found in the L10 fatigue life of the M-50 rods by a factor of over 4 when the tests were run with the load adjusted to provide the same maximum Hertzian contact stress as was used in the steel on steel tests. The measured L10 life for 20 failures was 20 million cycles with a Weibull slope of 1.2.

Statistically, this difference at the L10 level appears to be significant. The ball grades for both steel and ceramic balls were grade 5 although details of the waviness have not been checked at this time. While the contact area, and hence stressed volume is less for the ceramic on steel contact (because of the higher modulus of the ceramic material), the depth of the maximum shear stress and hence the distance a crack must propagate to form a spall is also less leading to roughly compensating effects on the expected relative fatigue life of the two material combinations. As compared to the tests with roughened steel balls on ceramic rods, both ball and rod wear was negligible in all smooth ball tests with track widths being equivalent to the calculated Hertzian contact width where they could be determined. On the smooth balls, it is frequently difficult to detect the ball rod track even with microscopic inspection. Further tests are in progress to investigate the effect of ceramic materials on the fatigue life of bearing steels at high stresses and low speeds.

Material Failure Due to Inclusions

Only one material, material C, exhibited a problem with rod spalling in the ceramic material. In this material, the failure was found in only one rod specimen out of four tested, and all of the spalls were on the same side of the rod. The suspicious nature of the failures being so closely aligned on the same side of the same rod led to a concern that either something had happened in the manufacture or the machining of the rod. Detailed investigations led to the determination of the fact that this rod contained a significant region of ZrN inclusions and that these inclusions had led to the observed spalling failures. The origin of the inclusions was traced back to the ceramic material processing where ZrO_2 balls were used during the powder milling process.

Obviously some debris from the powder milling ended up in the rod material and was converted to a nitride form during the subsequent processing of the material. Except for this one region of inclusions, this material performed well in the rolling contact fatigue testing. If the manufacturer should choose to change the basic powder milling process, and keep the rest of the composition and processing the same, it is expected that this material could perform very well in future tests.

General Comments on Rolling Contact Fatigue Testing of Ceramic/Steel Bearing Material Combinations

A wide range of silicon nitride ceramic materials are currently available, which exhibit excellent performance in rolling contact fatigue. In general, these materials have fatigue lives either comparable to or exceeding that of the M-50, 52100, and 440C steel bearing materials, which they may be paired with in a hybrid bearing. RCF-type testing is one useful test, which can be used to evaluate the potential performance of various ceramic material combinations prior to advancing to full-scale bearing tests. With reasonable test acceleration, RCF testing can provide insight into a material's expected performance relative to other ceramics known to be acceptable in bearing applications.

However, RCF tests are only one of many screening tests that should be employed in evaluating ceramic materials for bearing applications. One deficiency of the test is that it samples a relatively small amount of material, thus reducing the probability of detecting material deficiencies such as inclusions, although in the worst cases even this type of defect can clearly be found. A combination of steel ball on ceramic rod, and ceramic ball on steel rod tests should provide a reasonable picture of the anticipated performance of hybrid bearing material pairs.

Conclusions

All of the ceramics tested here should give adequate performance in bearings except material C, and even that material should perform well if the inclusions are eliminated. Ceramics can be used to replace steel balls in rolling element bearings and provide a range of performance benefits. Depending on the severity of the application, substitution can be made either routinely (in uses such as machine tool spindles, dental drills, etc.) or may require significant testing to quantify and verify performance in the most difficult applications (uses such as turbine engine mainshaft bearings and cryogenic turbopumps).

In general, after many years of development, it is possible to find many adequate ceramic bearing materials. The key issue for all of the materials that meet performance requirements at this point is reducing the costs to a level that is acceptable for the performance benefit that can be achieved.

Acknowledgments

The efforts described in this paper are primarily based on data funded by ARPA as part of their Ceramic Bearing Technology Initiative. Initial studies of the effects of stress on rolling contact wear of ceramics were funded with MTI internal funding. The MTI/ARPA Ceramic Bearing Technology Program is technically monitored by Mr. Karl Mecklenburg of the Air Force Materials Laboratory at Wright Patterson Air Force Base.

References

Carré, D. J., 1990, "The Use of Solid Ceramic and Ceramic Hard-Coated Components to Prolong the Performance of Perfluoropolyalkylether Lubricants," The Aerospace Corporation Report No. SSD-TR-90-32, Sept.

Gardos, M. N., and Hardisty, R. G., 1993, "Fracture Toughness- and Hardness-Dependent Polishing Wear of Silicon Nitride Ceramics," *STLE Tribology Transactions,* Vol. 36 (1993), No. 4, pp. 652–660.

Glover, D., 1982, "A Ball-Rod Rolling Contact Fatigue Tester," *Rolling Contact Fatigue Testing of Bearing Steels,* J. J. C. Hoo, ed., ASTM STP 771, pp. 107–124.

Lucek, J. W., 1990, "Rolling Wear of Silicon Nitride Bearing Materials," ASME Paper No. 90-GT-165.

Zaretsky, E. V., 1992, "STLE Life Factors for Rolling Bearings," STLE Publication SP-34, p. 200.

SPSLIFE: A User-Friendly Approach to the Structural Design and Life Assessment of Ceramic Components

T. Bornemisza

A. Saith

Sundstrand Power Systems,
San Diego, CA 92186

In order to expedite the structural analysis of ceramic components, Sundstrand Power Systems has developed a proprietary computer code called "SPSLIFE," which can substantially reduce the time spent on the design assessment of ceramic components. The life assessment computations for the various failure modes are performed using the structural analysis and materials files as input data. A number of "menus" are incorporated to request user input data and to guide the user through the problem definition process. The user has the capability to select existing material data files or create new ones. The computational modules are based on the analytical approaches currently used in the industry. The modular construction of the code facilitates making revisions or adding new modules. Graphic display is used to provide a visual summary of the life assessment calculations for the various failure modes. The output files generated provide a detailed review of the results, which is helpful for design optimization. Independently derived component fast fracture and static fatigue survival probabilities using the NASA CARES and CARES/LIFE codes are displayed for reference. The paper provides an application example using a patented design of a ceramic monorotor for the Sundstrand Power Systems TJ-50 small gas turbine engine.

1.0 Introduction

Recent improvements in the structural properties of advanced ceramics have significantly increased the potential for the successful application of monolithic ceramic components in the hot sections of gas turbines. Worldwide materials research on advanced ceramics, especially during the last decade, has resulted in excellent high-temperature strength and good resistance to oxidation and corrosion, exceeding those of the best superalloys. The previously wide distribution of the material strength in experimental monolithic ceramic parts has been narrowed to a more acceptable range, with many manufacturers reporting Weibull statistical strength distribution shape parameters in excess of 20. This progress is largely due to the improved control of manufacturing processes. For example, reduction in the size and frequency of flaws has enabled the high yield and cost-effective mass production of reliable ceramic turbocharger rotors for the Japanese automobile market.

As the new ceramic materials progress from the materials research laboratory into the advanced product design and development phase, the long-term performance of the ceramic components becomes increasingly important for the gas turbine designer. The analytical assessment of the expected component life requires the statistical characterization of the material properties in the various failure modes as well as the predicted stress–temperature distribution within the component as a function of the structural and thermal loads.

The design and analysis of the experimental ceramic turbine components at Sundstrand Power Systems have highlighted the need for an expeditious approach to the statistical life assessment analysis. The design optimization of highly stressed ceramic components frequently requires several iterations, which are extremely time consuming. The analyst has to review and study a number of large files containing the detailed results of the finite element stress, temperature, and life assessment analysis. The extent of the analytical work required can be illustrated by using the integrally bladed monolithic ceramic turbine rotor of a small gas turbine as an example.

Due to the various loading mechanisms, the rotor material is subjected to high transient and steady-state stresses and temperatures during a single operating cycle. The numerous loading mechanisms and failure modes of a ceramic turbine wheel have been discussed in [1] and are summarized here in Table 1.

The designer of a turbine wheel has to evaluate which of the potential failure modes is applicable, and perform the analyses required to assess the probability of success for the design.

The structural life assessment analysis for the various failure modes involves a considerable number of finite element files containing thousands of numbers describing the stress and temperature distribution within the wheel during the start, shutdown, on- and off-loading transients and at steady-state operating conditions. These files are processed through fast fracture and life assessment codes to perform the statistical analysis of the percent probability of success of the design for the selected failure mode and material. Sundstrand Power Systems has been using the structural ceramics reliability codes developed by NASA [2–4] for the statistical assessment of failure probability. Frequently the optimization of the turbine wheel structural design involves several design iterations and may require extensive revisions of the aerodynamic configuration as well as the finite element model.

2.0 Program Objectives

In order to provide the design engineers with an effective design tool and to save analysis time, Sundstrand Power Systems, under internal funding, has developed a proprietary computer code called "SPSLIFE" to perform the life assessment analysis of monolithic ceramic components. The basic objectives of SPSLIFE can be summarized as follows:

Contributed by the International Gas Turbine Institute and presented at the 39th International Gas Turbine and Aeroengine Congress and Exposition, The Hague, The Netherlands, June 13–16, 1994. Manuscript received by the International Gas Turbine Institute March 4, 1994. Paper No. 94-GT-486. Associate Technical Editor: E. M. Greitzer.

Table 1 Ceramic turbine wheel structural failure modes

Loading Mechanism	Failure Mechanism: Fast Fracture	Static Fatigue	Cyclic Fatigue	Creep Fracture	Environmental Damage (Oxidation)
Centrifugal Load	✓	✓		✓	
Rotor Dynamics	✓		✓		
Blade Rub	✓				
Aerodynamic			✓		
Foreign Object Damage	✓				
Thermal Gradient				✓	
Thermal Shock	✓	✓			✓
High Temperature				✓	✓
Combustion Prod.		✓			✓

- User friendly. Provide a guided user-driven analytical tool for the "non-ceramic expert," but knowledgeable design engineers and stress analysts to perform the life assessment analysis of ceramic components during the preliminary design and structural design optimization phases of a particular project.
- Modularized construction to facilitate expansion of the capabilities and accommodate changes and revisions to the individual modules.
- The visual display of the analysis results should be clear and easy to interpret.
- The output files should be organized to facilitate the detailed review of the results for the purpose of design optimization.
- Provide for the easy revision of the data files but provide the capability to limit accessibility to different levels of users.

It should be pointed out that it was not the objective of this effort to develop new analytical approaches to ceramic component life assessment. However, the capability was provided to modify, exchange, or add new computational modules in a relatively easy way.

3.0 Program Structure

The conceptual design of the SPSLIFE modularized computer code for the life assessment of ceramic components is shown in Fig. 1. The program links ANSYS structural analysis files and materials data files with life assessment modules for different modes of failure to provide quantitative estimates of component life and survival probability. In addition, the program produces presentation quality design assessment maps depicting stress and temperature distributions for the components, together with design envelopes for fast fracture, slow crack growth, creep, and oxidation. Cyclic fatigue, proof testing, and wear modules are also planned.

SPSLIFE is a user-friendly, interactive program. Helpful menus guide the user through the program. The "Welcome to SPSLIFE" menu allows the user to select whether the objective

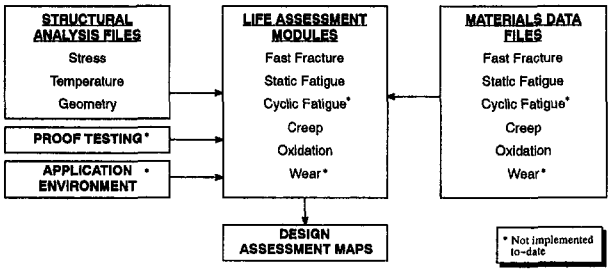

Fig. 1 SPSLIFE design concept

is to define a new problem, to execute an analysis, or to plot analysis results. The "Application Defaults" menu allows the user to specify the problem, select a design life, materials data, and related parameters. The "Applications" menu permits a choice of different analysis types: fast fracture, slow crack growth, creep, oxidation, etc. The "Plot" menu permits graphic superposition of results for different analysis types on the stress–temperature plot, resulting in a Design Assessment Map.

SPSLIFE Design Assessment Maps are component-specific, and provide a graphic overview of the design evaluation results. The maps are based on the "fracture map" concept discussed in the ceramics literature (e.g., [5]) and follow the general layout of [6]. Design envelopes for different failure modes are superimposed on a plot of maximum principal stress versus temperature for all the nodes in the finite element model. Specific equations and procedures used in SPSLIFE are proprietary to Sundstrand Power Systems.

4.0 Analysis Modules

The Fast Fracture Module uses enhanced uniaxial Weibull methodology [7], distinguishing between three different categories of flaws: internal or "volume" flaws, as-fired surface flaws and machined surface flaws.

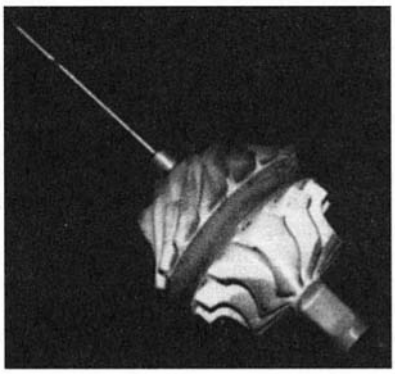

Fig. 2 Ceramic monorotor

Nomenclature

B = subcritical crack growth constant
F_x = preselected component failure probability
m_{afs} = Weibull modulus, as-fired surface flaw population
m_{ms} = Weibull modulus, machined surface flaw population
m_v = Weibull modulus, internal or volume flaw population
n = subcritical crack growth exponent
S = number of segments in cyclic symmetry problem
T_f = time to failure
$\Delta A_{afs,\text{sub}}$ = subelement area, as-fired surface
$\Delta A_{ms,\text{sub}}$ = subelement area, machined surface
ΔV_{sub} = subelement volume
σ_{ff} = maximum principal stress in the component corresponding to a specified component fast fracture failure probability
σ_{sf} = maximum principal stress in the component corresponding to a specified component static fatigue failure probability
σ_{sub} = subelement maximum principal stress
$\sigma_{o,afs}$ = unit area characteristic strength, or scale parameter, as-fired surface
$\sigma_{o,ms}$ = unit area characteristic strength, or scale parameter, machined surface
$\sigma_{o,V}$ = unit volume characteristic strength, or scale parameter
$\sigma_{1\max}$ = maximum principal stress in the component

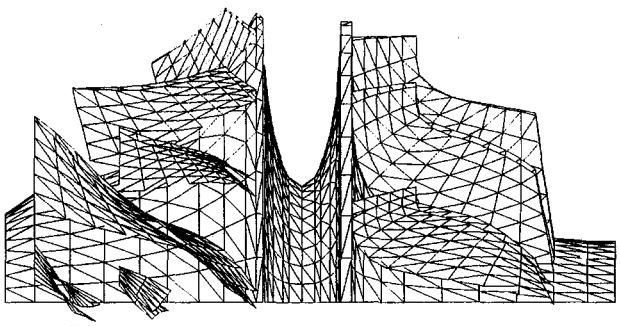

Fig. 3 Ceramic monorotor finite element analysis model

For volume flaws

$$\ln\left(\frac{1}{1-F}\right) = \sum_{V}\left(\frac{\sigma_{\text{sub}}}{\sigma_{o,V}}\right)^{m_v}\cdot\Delta V_{\text{sub}} \quad (1)$$

Adding terms for machined surface flaws and as-fired surface flaws,

$$\ln\left(\frac{1}{1-F}\right) = S\cdot\sum_{V}\left(\frac{\sigma_{\text{sub}}}{\sigma_{o,V}}\right)^{m_v}\cdot\Delta V_{\text{sub}} + S\cdot\sum_{A}\left(\frac{\sigma_{\text{sub}}}{\sigma_{o,ms}}\right)^{m_{ms}} \times \Delta A_{ms,\text{sub}} + S\cdot\sum_{A}\left(\frac{\sigma_{\text{sub}}}{\sigma_{o,afs}}\right)^{m_{afs}}\cdot\Delta A_{afs,\text{sub}} \quad (2)$$

where S is the number of segments in a cyclic symmetry problem.

Equation (2) can be rewritten as

$$\ln\left(\frac{1}{1-F_x}\right) = \left(\frac{\sigma_{ff}}{\sigma_{o,V}}\right)^{m_v}\cdot S\cdot\sum_{V}\left(\frac{\sigma_{\text{sub}}}{\sigma_{1\,\max}}\right)^{m_v}\cdot\Delta V_{\text{sub}} + \left(\frac{\sigma_{ff}}{\sigma_{o,\text{ms}}}\right)^{m_{ms}}\cdot S\cdot\sum_{A}\left(\frac{\sigma_{\text{sub}}}{\sigma_{1\,\max}}\right)^{m_{ms}}\cdot\Delta A_{ms,\text{sub}} + \left(\frac{\sigma_{ff}}{\sigma_{o,afs}}\right)^{m_{afs}} \times S\cdot\sum_{A}\left(\frac{\sigma_{\text{sub}}}{\sigma_{1\,\max}}\right)^{m_{afs}}\cdot\Delta A_{afs,\text{sub}} \quad (3)$$

Fast fracture stress contours can then be drawn for σ_{ff} for any preselected component failure probability F_x. Equation (3) is satisfied only for the contour that passes through the $\sigma_{1\,\max}$ location, i.e., when $\sigma_{ff} = \sigma_{1\,\max}$.

The program requests separate materials data file entries for each category of flaws to ensure that proper attention is given to surface properties. The data files are selected from a materials library that contains background information on each data set. Three fast fracture design envelopes are shown on the Design Assessment Map corresponding to three different survival probabilities; any nodes outside of these contours show that the design goal is not being met. For reference, independently derived component fast fracture survival probabilities using the NASA CARES and CARES/LIFE codes are shown in the top right hand corner of SPSLIFE Design Assessment Maps.

The Slow Crack Growth or Static Fatigue Module uses Evans–Wiederhorn methodology (8), again distinguishing between internal flaws, as-fired surface flaws and machined surface flaws.

For steady-state loading of volume flaws,

$$\ln\left(\frac{1}{1-F}\right) = \left(\frac{T_f}{B_v}\right)^{(m_v/(n_v-2))}\cdot\frac{1}{\sigma_{o,V}^{m_v}}\cdot\sum_{V}\sigma_{\text{sub}}^{(m_v n_v/(n_v-2))}\cdot\Delta V_{\text{sub}} \quad (4)$$

Adding terms for machined surface flaws and as-fired surface flaws,

$$\ln\left(\frac{1}{1-F_x}\right) = \left(\frac{T_f}{B_v}\right)^{(m_v/(n_v-2))}\cdot\frac{1}{\sigma_{o,V}^{m_v}}\cdot S\cdot\sum_{V}\sigma_{\text{sub}}^{(m_v n_v/(n_v-2))}\cdot\Delta V_{\text{sub}} + \left(\frac{T_f}{B_{ms}}\right)^{(m_{ms}/(n_{ms}-2))}\cdot\frac{1}{\sigma_{o,ms}^{m_{ms}}}\cdot S\cdot\sum_{A}\sigma_{\text{sub}}^{(m_{ms}n_{ms}/(n_{ms}-2))}\cdot\Delta A_{ms,\text{sub}} + \left(\frac{T_f}{B_{afs}}\right)^{(m_{afs}/(n_{afs}-2))}\cdot\frac{1}{\sigma_{o,afs}^{m_{afs}}}\cdot S\cdot\sum_{A}\sigma_{\text{sub}}^{(m_{afs}n_{afs}/(n_{afs}-2))}\cdot\Delta A_{afs,\text{sub}} \quad (5)$$

where S is the number of segments in a cyclic symmetry problem. This equation can be rewritten as

$$\ln\left(\frac{1}{1-F_x}\right) = \left(\frac{T_f}{B_v}\right)^{(m_v/(n_v-2))}\cdot\frac{\sigma_{sf}^{(m_v n_v/(n_v-2))}}{\sigma_{o,V}^{m_v}} \times S\cdot\sum_{V}\left(\frac{\sigma_{\text{sub}}}{\sigma_{1\,\max}}\right)^{(m_v n_v/(n_v-2))}\cdot\Delta V_{\text{sub}} + \left(\frac{T_f}{B_{ms}}\right)^{(m_{ms}/(n_{ms}-2))}$$

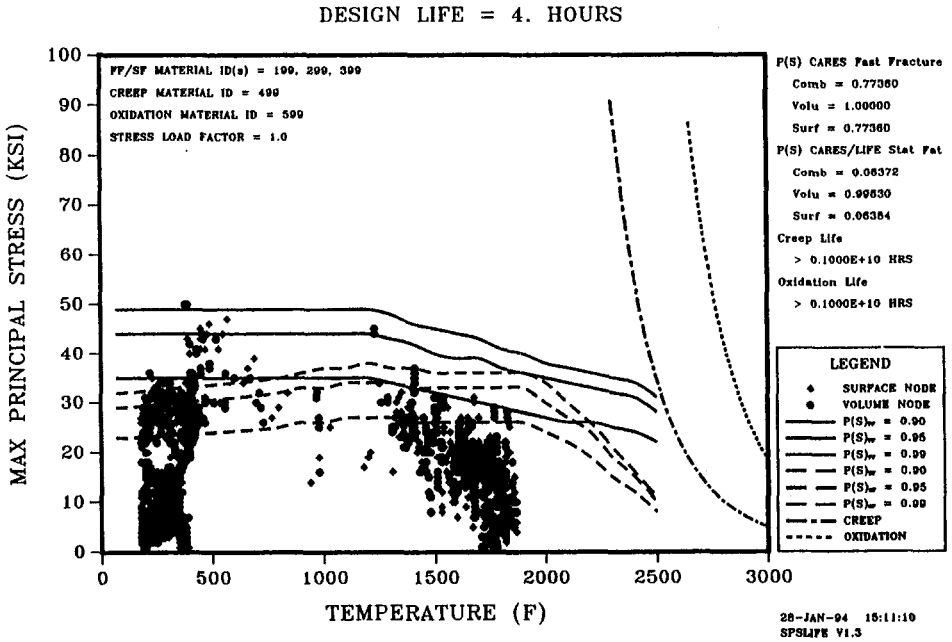

Fig. 4 TJ-50 monorotor design assessment map, material A, condition 1, design life = 4 h

Table 2 Fast fracture and slow crack growth parameters for material A

Temperature (°F)	Volume		Machined Surface		As-Fired Surface		Slow Crack Growth (All Flaws)	
	m_v	$\sigma_{o,v}$	m_{ms}	$\sigma_{o,ms}$	m_{afs}	$\sigma_{o,afs}$	n	B
70	13.0	111000	8.7	104900	6.8	59800	0.2502E+02	0.7597E+09
800	13.0	111000	8.7	104900	6.8	59800	0.3435E+02	0.4612E+09
900	13.0	109900	8.7	104900	6.8	59800	0.3627E+02	0.4254E+09
1000	13.0	108800	8.7	104900	6.8	59800	0.3893E+02	0.3858E+09
1100	13.0	107700	8.7	104900	6.8	59800	0.4149E+02	0.3526E+09
1200	13.0	105500	8.7	103900	6.8	59200	0.4444E+02	0.3203E+09
1300	13.0	102200	8.7	101800	6.8	58000	0.4725E+02	0.2943E+09
1400	13.0	98800	8.7	98600	6.8	56200	0.5123E+02	0.2642E+09
1500	13.0	95500	8.7	95500	6.8	54400	0.5600E+02	0.2351E+09
1600	13.0	92200	8.7	93400	6.8	53200	0.6305E+02	0.2029E+09
1700	13.0	88800	8.7	91300	6.8	52000	0.7065E+02	0.1760E+09
1800	13.0	85500	8.7	88100	6.8	50200	0.9405E+02	0.1259E+09
1900	13.0	82200	8.7	85000	6.8	48400	0.1302E+03	0.8664E+08
2000	13.0	79900	8.7	81800	6.8	46600	0.9010E+02	0.1211E+09
2100	13.0	76600	8.7	79700	6.8	45400	0.5486E+02	0.1940E+09
2200	13.0	73300	8.7	77600	6.8	44300	0.3349E+02	0.3134E+09
2300	13.0	68800	8.7	75500	6.8	43100	0.2093E+02	0.4936E+09
2400	13.0	64400	8.7	72400	6.8	41300	0.1392E+02	0.7403E+09
2500	13.0	56600	8.7	66100	6.8	37700	0.9510E+01	0.1100E+10

Notes:

1. Weibull modulus (shape parameter) and characteristic strength (scale parameter) are listed separately for volume flaws (m_v, $\sigma_{o,v}$) machined surface flaws (m_{ms}, $\sigma_{o,ms}$), and as-fired surface flaws (m_{afs}, $\sigma_{o,afs}$).
2. Slow crack growth parameters n and B are applied to all flaws, due to absence of more specific data.
3. Units

   Scale parameter $\sigma_{o,v}$: psi. in^{3/m_v}; $\sigma_{o,ms}$: psi. $in^{2/m_{ms}}$; $\sigma_{o,afs}$: psi. $in^{2/m_{afs}}$

   Slow crack growth coefficient B: psi^2 sec

$$\times \frac{\sigma_{sf}}{\sigma_{o,ms}^{m_{ms}}}^{(m_{ms}n_{ms}/(n_{ms}-2))} \cdot S \cdot \sum_{ms} \left(\frac{\sigma_{\text{sub}}}{\sigma_{1\,\max}}\right)^{(m_{ms}n_{ms}/(n_{ms}-2))} \cdot \Delta A_{ms,\text{sub}}$$

$$+ \left(\frac{T_f}{B_{afs}}\right)^{(m_{afs}/(n_{afs}-2))} \cdot \frac{\sigma_{sf}}{\sigma_{o,afs}^{m_{afs}}}^{(m_{afs}n_{afs}/(n_{afs}-2))}$$

$$\times S \cdot \sum_{afs} \left(\frac{\sigma_{\text{sub}}}{\sigma_{1\,\max}}\right)^{(m_{afs}n_{afs}/(n_{afs}-2))} \cdot \Delta A_{afs,\text{sub}} \quad (6)$$

Slow crack growth contours can then be drawn for σ_{sf} for any preselected component failure probability F_x. Equation (6) is satisfied only for the contour that passes through the $\sigma_{1\,\max}$ location, i.e., when $\sigma_{sf} = \sigma_{1\,\max}$. Again, three different design envelopes are shown corresponding to three different survival probabilities; for reference, independently derived component slow crack growth survival probabilities using the NASA CARES/LIFE code are shown below the corresponding fast fracture probabilities (in the top right-hand corner of the Design Assessment Map).

The Creep-Fracture Module uses Monkman–Grant methodology [9]; a design envelope is shown on the Design Assessment Map, and the calculated creep life corresponding to actual stresses and temperatures is tabulated on the right-hand side of the map. The Oxidation Module uses the fracture mechanics approach described by Soma et al. [6]. A design envelope is shown corresponding to the selected design life, and the calculated oxidation life is tabulated on the right-hand side ofthe map.

5.0 Applications

SPSLIFE was initially applied to the TJ-50 ceramic monorotor discussed below in greater detail. Since then, the program has been used for preliminary design evaluation and life assessment of several ceramic components on the Ceramic Stationary Gas Turbine Program, including two blade designs, one nozzle design and three combustor liner designs. Reference [10] documents the results for the CSGT components.

TJ-50 Monorotor

The ceramic monorotor is shown in Fig. 2. A three-dimensional finite element model (Fig. 3) of the rotor was built using brick elements, and triangular shell elements were placed on the surfaces. Separate files were written in ANSYS for the as-fired and machined surface elements. These files are used by SPSLIFE to allow for property differences between as-fired and machined surfaces.

Figure 4 shows the Design Assessment Map for the monorotor for a turbine inlet temperature of 2050°F. The temperatures and stresses shown on the node plot are for steady-state operation at a speed of 130,000 rpm. The analysis was run for a design life of 4 hours and using a material designated as Material A. Fast fracture and slow crack growth parameters for this material are shown in Table 2. The rotor was analyzed in the normally machined condition (Condition 1), i.e., the rims and undercut areas were in the machined condition, and the hubs and airfoils were in the as-fired condition. The map shows that creep and oxidation are not a problem for this design. However, selected design goals of 90, 95, and 99 percent survival probability are not met in fast fracture and in slow crack growth. In fast fracture,

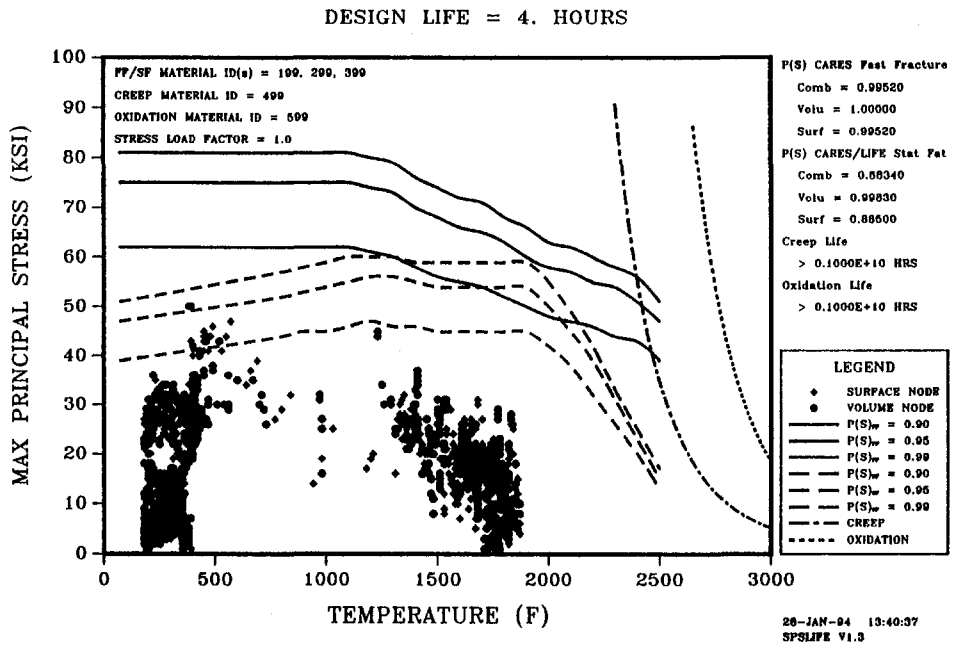

Fig. 5 TJ-50 monorotor design assessment map, material A, condition 2, design life = 4 h

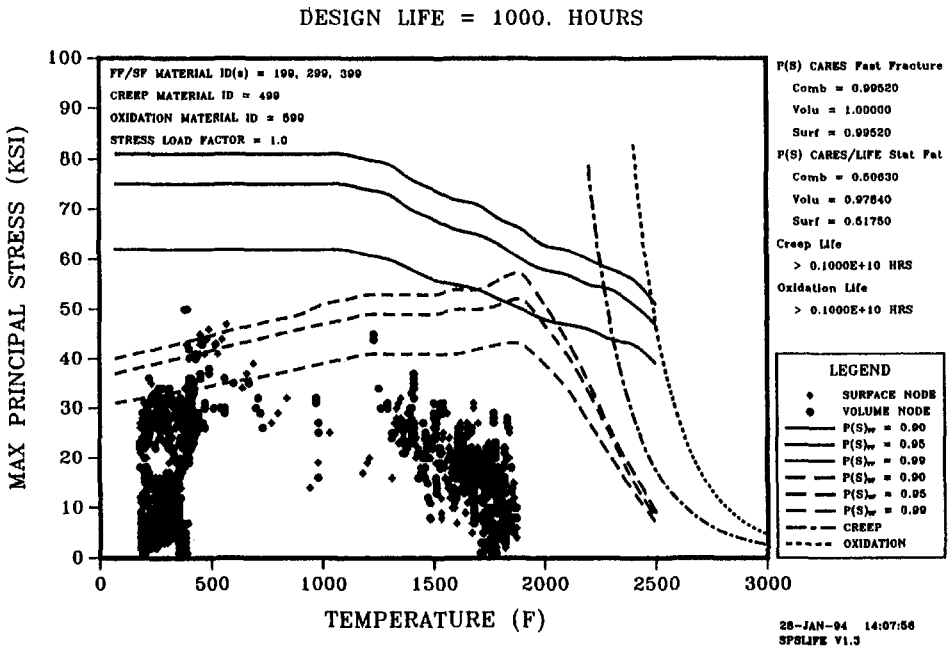

Fig. 6 TJ-50 monorotor design assessment map, material A, condition 2, design life = 1000 h

the three solid lines represent component survival probabilities of 90, 95, and 99 percent, respectively, and the node plot crosses the highest of these lines, indicating a survival probability of less than 90 percent. The top right-hand corner of the map shows the survival probability determined by the NASA CARES program to be 77 percent. In slow crack growth, the node plot crosses the three dashed lines, indicating that the lowest design goal of 90 percent is far from being met. The map shows the slow crack growth survival probability determined by the NASA CARES/LIFE program to be 6 percent.

Figure 5 is a Design Assessment Map for the same component and material, but with better surface properties (Condition 2). For this case, all of the surface elements are assigned the machined surface properties shown in Table 2. In fast fracture, all three solid lines are now above the node plot, indicating that the highest selected design goal of 99 percent fast fracture survival probability has been met. CARES shows a survival probability of 99.52 percent. In slow crack growth, two of the lines are crossed, resulting in an estimated survival probability of 94 percent. CARES/LIFE shows a survival probability of 88.34 percent.

Figure 6 shows a map for the monorotor using Material A (Condition 2) and a design life of 1000 hours. The slow crack growth survival probability goals are no longer met. CARES/LIFE shows a slow crack growth survival probability of 50.63 percent.

The designer has access to several files created by SPSLIFE to expedite redesign. Design improvements can be made by redesigning the component in areas that cross the design envelopes. In the case of the monorotor, stresses need to be reduced at the highest stress location on the compressor.

Acknowledgments

Advice and assistance received from D. G. Eastman and T. G. Egbert of Sundstrand Power Systems (SPS) and from Dr. J. Gyekenyesi, N. Nemeth, and L. Powers of NASA Lewis Research Center are gratefully acknowledged. R. J. Geiser, J. J. McLaughlin, and Dr. N. G. Shah of SPS also made significant contributions to the development of SPSLIFE. Funding for program development was provided by SPS. Dr. A. E. Caldwell of SPS provided the ANSYS model for the TJ-50 monorotor. The authors thank MICOM and ARPA for permission to include the TJ-50 monorotor as an example in the paper.

References

1 Bornemisza, T., "Ceramic Small Gas Turbine Technology Demonstrator," ASME Paper No. 90-GT-306, 1990.

2 Gyekenyesi, J. P., "SCARE: A Postprocessor Program to MSC/NASTRAN for the Reliability Analysis of Structural Ceramic Components," ASME JOURNAL OF ENGINEERING FOR GAS TURBINES AND POWER, Vol. 108, 1986, pp. 540–546.

3 Gyekenyesi, J. P., and Nemeth, N. N., "Surface Flaw Reliability Analysis of Ceramic Components With the SCARE Finite Element Postprocessor Program," ASME JOURNAL OF ENGINEERING FOR GAS TURBINES AND POWER, Vol. 109, 1987, pp. 274–281.

4 Nemeth, N. N., et al., "Time-Dependent Reliability Analysis of Monolithic Ceramic Components Using the CARES/LIFE Integrated Design Program," presented at the ASTM Symposium on Life Prediction Methodologies for Ceramic Materials in Advanced Applications—A Basis for Standards, Cocoa Beach, FL, Jan. 11–13, 1993.

5 Quinn, G. D., and Wiederhorn, S. M., "Structural Reliability of Ceramics at Elevated Temperatures," presented at the ASTM Symposium on Life Prediction Methodologies for Ceramic Materials in Advanced Applications—A Basis for Standards, Cocoa Beach, FL, Jan. 11–13, 1993.

6 Soma, T., Ishida, Y., et al., "Ceramic Component Design for Assuring Long-Term Durability," *Advanced Ceramic Materials*, Vol. 2, No. 4, Oct. 1987.

7 Weibull, W., "A Statistical Distribution Function of Wide Applicability," ASME *Journal of Applied Mechanics*, Vol. 18, No. 3, 1951, pp. 293–297.

8 Wiederhorn, S. M., "Subcritical Crack Growth in Ceramics," in: *Fracture Mechanics of Ceramics*, R. C. Bradt et al., eds., Plenum, New York, 1974, pp. 613–646.

9 Wiederhorn, S. M., et al., "Tensile Creep Testing of Structural Ceramics," *Proc., Annual Automotive Technology Development Contractors' Coordination Meeting*, Dearborn, MI, Oct. 28–31, 1991.

10 Saith, A., Norton, P., and Parthasarathy, V., "Application of SPSLIFE to Preliminary Design Evaluation and Life Assessment of CSGT Components," ASME Paper No. 94-GT-420, 1994.

Ceramic Hybrid Bearings in Air-Cycle Machines

L. Burgmeier
AlliedSignal Aerospace Company,
Cypress, CA 90630

M. Poursaba
Tinker AFB, OK 73145

Extensive research in the field of ceramic rolling contact bearings has been conducted over the past several years. The results of this research indicate that silicon nitride may offer significant improvements in rolling fatigue life and a possible increase in operating temperature. AlliedSignal Aerospace Systems & Equipment (ASE) and the Air Force Item Management Engineering Branch at Tinker Air Force Base are conducting a development program under contract to ARPA to introduce ceramic hybrid bearings into existing F-15, F-111, and C-130 aircraft fleets in a near-term program involving retrofitting mature air-cycle machines with such bearings. The air-cycle machine (ACM) is a complex bearing application, operating at very high speeds (up to 100,000 rpm) and at high temperatures. In more severe military ACM applications, mean times between failures (MTBFs) of 2000 and 3000 hours are common. The fleet would see an immediate benefit from improved bearing life. This paper describes the analytical approach to evaluating and comparing ceramic to steel bearings, describes the laboratory test program to verify performance, and discusses the life-cycle cost improvement and the flight test program.

I Introduction

In modern jet aircraft, cabins and avionics are pressurized and cooled to a comfortable "shirt-sleeve" environment using compressed air bled from the main propulsion turbine engines. The hot, high-pressure engine bleed is conditioned utilizing an air-cycle environmental control system (ECS). Figure 1 shows a typical air-cycle ECS. The engine bleed is cooled to about 230°C in a precooler. The bleed temperature is further cooled to about 120°C in the primary heat exchanger before it enters the compressor of the ACM. The compressor adiabatically compresses the air, increasing its temperature to about 200°C, until it enters the secondary heat exchanger, and is cooled to 65°C. The turbine cools the air further by extracting energy to drive the compressor. Adiabatic expansion in the turbine reduces the air temperature to subfreezing, and this subfreezing air is then mixed with recirculated cabin air to yield a comfortable temperature.

To run efficiently, the ACMs operate at very high speeds, from 50,000 to well above 100,000 rpm. A self-contained bearing and lubrication system results in a compact, simple machine easily packaged in an aircraft. Figure 2 shows a cross section of an F-15 ACM, which is typical of ball bearing ACMs. The ball bearings are selected to keep the surface speed *DN* to less than 1.2 million. (*DN* is the bearing inside diameter in millimeters times the speed in revolutions per minute.) The 1.2 million *DN* results in the best compromise of size and speed.

The simplest, most compact and lightweight lubrication system is the wick system, which eliminates the need for oil pumps. Lubrication and cooling are accomplished by wicking the oil to the shaft adjacent to the bearing, where the rotation of the shaft slings the oil into the air to be drawn through the bearing by slingers on the outboard side of the bearing. The oil sump capacity is typically 200 cc. The wicks deliver oil at the rate of approximately 2 to 6 cc per hour. A labyrinth seal outboard of the slinger, combined with a depressed sump pressure, prevents oil from leaking out of the sump. Details of the compressor end bearing, resilient mount, wick, and seal are shown in Fig. 3.

Contributed by the International Gas Turbine Institute and presented at the 39th International Gas Turbine and Aeroengine Congress and Exposition, The Hague, The Netherlands, June 13–16, 1994. Manuscript received by the International Gas Turbine Institute March 4, 1994. Paper No. 94-GT-393. Associate Technical Editor: E. M. Greitzer.

As modern aircraft have developed, engine bleed temperatures have increased, demanding very high-speed ACM bearings. Bearings and lubricants have been improved over the years. The early bearings were 52100 steel, and the ball separators were phenolic. As bearing temperatures exceeded 150°C, the separators were changed to bronze. The bearing steel was improved to CEVM M-50, and the lubricant was changed from instrument oil to MIL-L-7808 or MIL-L-23699. Even with these improvements, the mean times between failures of ACMs in high-performance aircraft are running below 3000 hours. For comparison, in more benign commercial applications, ACM MTBFs are above 20,000 hours.

The next generation of bearing material appears to comprise ceramics. The engineers at AlliedSignal and Oklahoma City Air Logistics Center/Commodities Management Reliability and Engineering (ALC/LIIE) collaborated to define a R&D program to evaluate ceramic bearings in three high-performance ACMs now in service in the military fleet. This paper describes the progress on the ARPA-sponsored program. Included are the bearing design and analysis, the laboratory and flight testing, and the expected life-cycle cost improvements attributable to the incorporation of ceramics.

II Background

Silicon nitride, a polycrystalline material with an amorphous (glassy) intergranular binder phase, has become the most successful and widely applied ceramic in rolling element bearings. Silicon nitride is actually a family of materials whose specific compositions and processing, and therefore subsequent properties, may vary from manufacturer to manufacturer. Critical considerations include composition and amount of binder phase, powder preparation, and consolidation techniques. Most domestic bearing development in recent years has centered on NBD-200 or an equivalent.

Silicon nitride, with a typical hardness of KNH_{1000} 1600 (approximately equal to Rc 80) is twice as hard as conventional bearing steels, which are normally KNH_{1000} 700 to 800 (Rc 58 to 63). The Knoop scale is a better hardness scale for high-hardness materials. Hardness is one of the most critical properties of bearing materials and relates closely to bearing performance. The beneficial effect of high hardness on bearing performance is primarily attributable to improvement in wear resistance and increase in the compressive elastic limit, both of

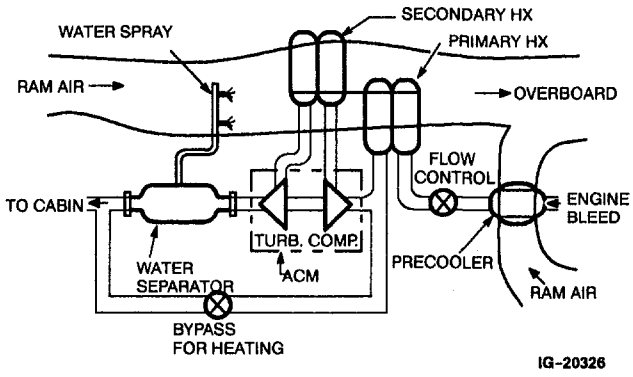

Fig. 1 Air-cycle environmental control unit

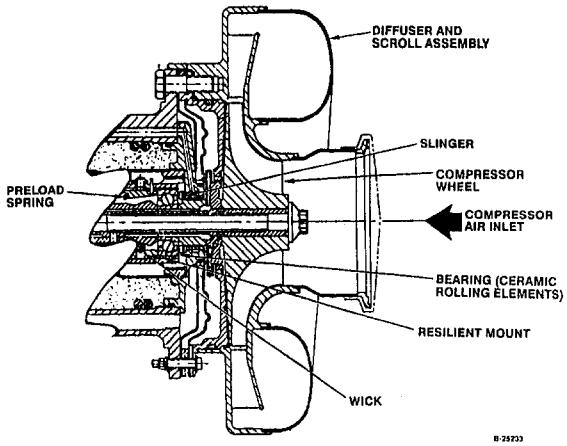

Fig. 3 F-111 compressor end components

which reduce the damaging effects of high stresses and surface rubbing at the contact point.

Silicon nitride has demonstrated a low coefficient of friction and excellent wear resistance. As reported by Bhushan and Sibley (1999), silicon nitride sliding against itself or steel has a low sliding friction coefficient similar to that of lubricated steel against steel. The friction coefficients for silicon nitride/silicon nitride, silicon nitride/M-50, or M-50/M-50 varied from 0.11 to 0.13 with MIL-L-23699 oil. The dramatic improvement occurs in unlubricated surfaces, where silicon nitride against itself shows a 0.17 coefficient and silicon nitride against M-50 shows a 0.15 coefficient, compared to a 0.54 coefficient of friction for M-50 steel against itself. Moreover, the silicon nitride against itself or M-50 steel has lower friction than silicon carbide or tungsten carbide. This may be the key to the ability of silicon nitride to run with momentary oil interruption or boundary lubrication.

The density of silicon nitride (3.2 gm/cc) is 40 percent of that of conventional bearing steel, reducing centrifugal ball loading at high rotational speeds. Since ball centrifugal loading is directly proportional to density, silicon nitride rolling elements offer the potential for significant improvement, in high-speed bearing applications where outer race loading is the limiting feature. This improvement can be achieved by using bearings with silicon nitride balls and M-50 races, known as ceramic hybrid bearings. Hybrid bearings with steel races and ceramic balls are substantially less expensive and are much simpler to install.

Rolling contact fatigue tests for silicon nitride balls with steel races have shown excellent results (Bhushan and Sibley, 1982; Hosang, 1987; Chiu, 1993). The thermal expansion coefficient of silicon nitride is 2.8×10^{-6} mm/mm/°C, approximately one third that of steel. Silicon nitride, although much tougher than other ceramics, has a toughness one third that of steel. The reduced toughness and the low coefficient of thermal expansion make installing ceramic rings onto steel shafts and into steel housings very risky. Hybrid bearings consisting of ceramic balls and steel rings look very attractive, especially considering that silicon nitride rubbing on M-50 steel offers friction and wear characteristics as good as those of silicon nitride rubbing on itself. For this reason and because this program is geared to retrofitting mature ACMs, hybrid bearings were selected.

Investigation of the manufacturing status of silicon nitride balls has shown that this material is already in limited production. Production manufacturing incorporates combined sintering and hot isostatic pressing (HIP) to ensure 100 percent dense balls. Nondestructive testing (NDT) includes 100 percent dimensional, density, and high-resolution contact X-ray testing.

III Program Technical Approach

Three mature ACMs were selected in order to evaluate potential improvements in MTBF attributable to incorporating ceramic hybrid bearings. These machines are the C-130, F-111, and F-15 ACMs. A photograph of the F-15 ACM is shown in Fig. 4. The other two machines are approximately the same size.

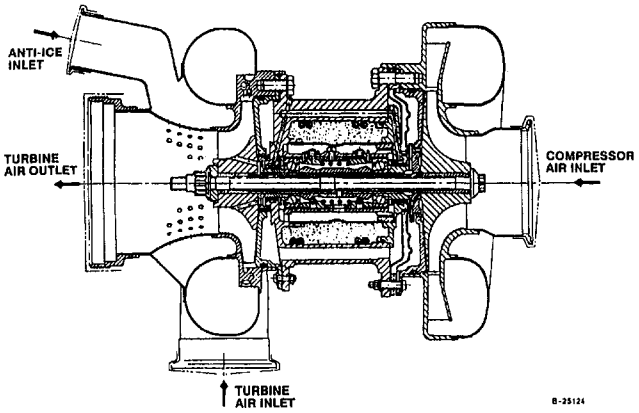

Fig. 2 Typical military air-cycle machine

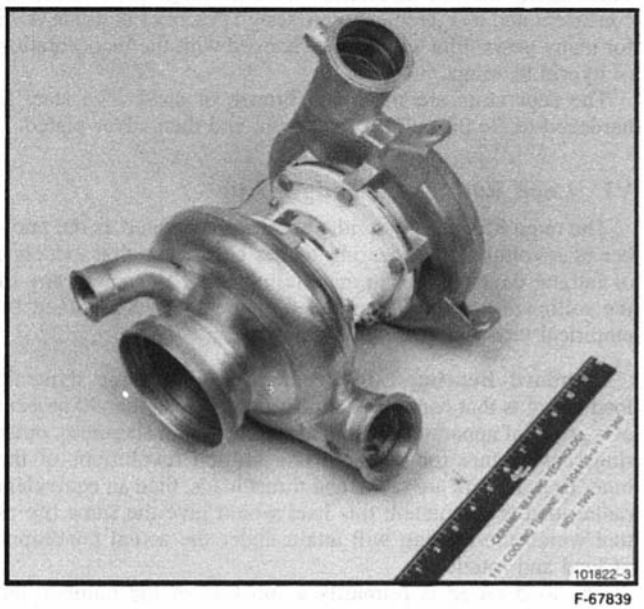

Fig. 4 F-15 air-cycle machine

The program technical approach was as follows:

(*a*) Conduct an analytical and design study to examine the impact of incorporating ceramic hybrid bearings into existing ACMs, and conduct discussions with ceramic ball and ball bearing manufacturers to ascertain the level of use of ceramic balls in service.

(*b*) Conduct baseline tests measuring bearing temperatures in the existing production bearings, and retest with ceramic hybrid bearings. Compare the measured temperatures and the microscopic conditions of the rolling surfaces. Although 50-hour hybrid bearing laboratory tests are relatively brief, at these operating speeds, the individual bearings would accumulate more than 180 million cycles.

(*c*) Analyze life-cycle costs to evaluate the impact of hybrid bearings on costs in an aircraft fleet.

(*d*) Conduct a field test to show whether MTBF improves with hybrid bearings.

IV Hybrid Bearing Selection Considerations: Ceramic Ball Material

The hybrid bearing, utilizing silicon nitride balls and steel rings, was selected for the near-term bearing insertion program for reasons of ease of retrofit, cost, and time.

In this program, the objective was to increase the mean time between bearing failures by changing only the bearings, without affecting the design of any other air-cycle machine components. Incorporating monolithic bearings (ceramic balls and rings) would require significant analysis, redesign, and requalification of the selected air-cycle machine due to differences in thermal expansion between the air-cycle machine shaft and inner ring, and between the resilient mount and outer ring.

V Hybrid Bearing Analysis

The bearings presently in use on the selected ACMs are manufactured from vacuum degassed 52100 and CEVM M-50 steel. Bore diameters are 10 and 15 mm, and the *DN* (diameter in mm × speed in rpm) varies from 0.9×10^6 to 1.125×10^6. Bearing design characteristics are summarized in Table 1.

All bearings are supported by resilient mounts, low-rate radial springs between the bearing and housing that reduce both rigid body natural frequency and radial loads caused by unbalance. The bearing fits and clearances were investigated, and all are consistent and in agreement with design practices in use at ASE for many years. Fits will not be changed with the incorporation of hybrid bearings.

The separators are machined bronze or steel. The steel is hardened to Rc 28 to 36 for strength, and then silver plated.

VI Load Rating and Fatigue Life

The rated life of an individual bearing is defined as the number of revolutions the bearing makes before the first evidence of fatigue develops in the material of either ring or of any of the rolling elements. The rated fatigue life is determined by empirical tests with actual bearings.

Standard Bearing Life Prediction. The basic dynamic load rating is that constant stationary radial load that 90 percent of a group of apparently identical bearings with stationary outer rings can endure for a life of one million revolutions of the inner ring. If there are radial and thrust loads, then an equivalent radial load is calculated; this load would give the same life as that which the bearing will attain under the actual conditions of load and rotation.

The load rating is primarily a function of the number and diameter of the balls, the pitch diameter, and the raceway curvature. Curvature is defined as the ratio of the radius of the ball groove divided by the ball diameter, and normally expressed as a percent. The ball bearing manufacturers publish load ratings for their products based on 51.5 to 52 percent curvature for the inner ring and 53 percent curvature for the outer ring. These life considerations apply to a majority of bearing applications.

Table 1 Bearing data for existing cooling turbines

Parameter	Airplane		
	C-130	F-111	F-15
Bearing grade, ABEC no.	7	7	7
Inner race:			
Material	52100	M-50	M-50
Bore, mm	10	15	15
Width, mm	8	11	9
Curvature, percent	53	54	53
Outer race:			
Material	52100	M-50	M-50
Diameter, mm.	26	35	32
Width, mm	8	11	9
Curvature, percent	55	52	54
Balls:			
Material	52100	M-50	M-50
Number	8	8	10
Diameter, in.	3/16	1/4	3/16
Diametral clearance, mm	0.022	0.045	0.045
Separator construction	Stamped	Machined	Machined

NOTES:
Dimensions are nominal values.
For tolerances and finishes, see AFBMA ABEC requirements.
Total tolerance on bore is 0.005 mm.
Total tolerance on OD is 0.005 mm.
Total tolerance on width is 0.076-0.127 mm.
Total tolerance on diametral clearance is 0.0011 mm.

Turbine Bearing Life Prediction. If the curvature is different from that described above, the rating is modified, using the appropriate equations. ASE has found that greater than standard curvatures work best in small high-speed bearings when the cooling and lubrication are minimal.

Exceptional applications such as turbomachinery require a more sophisticated approach to the calculation of fatigue life. This requires a retrogression to the Lundberg–Palmgren theory fundamentals. The probability of survival of a bearing raceway as a unit is then equivalent to the product of the probabilities of survival of the rolling contacts. The value of the Weibull slope is substituted in the equations, and the bearing life is derived after first calculating the life of the inner and outer ring separately.

Various computer programs have been developed and are now being perfected to predict the ball motion, load distribution, heat generation, stress on the surfaces, and fatigue life. The A. B. Jones bearing analysis program, which has gained widespread use in the industry, was used in this analysis. It includes the friction due to load but does not account for the viscous loss due to the lubricant. The EHL option of the program was not used because the lubrication system provides boundary lubrication only. Earlier wick lubrication tests measured bearing oil throughflow below the amount considered sufficient to produce the classic elastohydrodynamic film. Microscopic examination of posttest bearings verified that a lot of metal-to-metal contact occurred in the loaded zone.

The bearing analyses shown in Tables 2 and 3 were performed with the Jones program, which includes the higher modulus and lower density of the ceramic ball.

Table 2 Turbine bearing data summary ceramic bearing technology modified Jones computer program

	C-130		F-15		F-111	
	Std	Hybrid	Std	Hybrid	Std	Hybrid
Speed, rpm	75,000	75,000	54,500	54,500	50,200	50,200
Axial preload, N	178	178	133	133	133	133
Type (single or double)	S/ACT	S/ACT	D/ACT	D/ACT	D/ACT	D/ACT
Radial load, N	22	22	22	22	22	22
Bearing design						
Size	100	100	102	102	202	202
Curvature, percent (inner, outer)	53, 55	53, 55	53, 54	53, 54	54, 52	54, 52
Contact angle, deg	14.1	14.1	21.3	21.3	20.2	20.2
Ball no. -dia (in.)	8-3/16	8-3/16	10-3/16	10-3/16	8-1/4	8-1/4
Pitch dia, mm	18	18	23.5	23.5	25	25
Material						
I&O	52,100	52,100	M-50	M-50	M-50	M-50
Balls	52,100	Ceramic	M-50	Ceramic	M-50	Ceramic
Computed data						
Spring rate N/M x10^{-6}	37.6	69.7	12.6	31.8	23.4	36
Contact angle, deg						
Inner	23.9	19.4	32.4	27.9	26.3	24.5
Outer	12.2	15.0	11.6	17.6	8.3	13.7
Ball C.F., N	36	14.2	31	12	57	22.6
L10 life, hours	2289	1649	63,425	69,643	130,500	130,207
Life factor	3	3	10	10	10	10
Mean stress, MPa						
Inner	1020	1320	765	910	786	917
Outer	1040	1150	861	903	717	724
Torque, NxM	0.0039	0.0031	0.003	0.0021	0.0034	0.0023

Discussion of the Data Shown in Tables 2 and 3. Air-cycle machines with three bearing sizes were chosen for investigation, after consulting with Tinker Air Force Base regarding their usage and service history. The bearings, in ascending order of size, are the C-130 (100 size) bearing, F-15 (102 size) bearing, and F-111 (202 size) bearing. All bearings in these high-speed machines are axially preloaded to prevent ball skidding and or aerodynamics-caused bearing thrust reversals. The size of the preload was established in the design phase, and the machines have been successfully operating in service for 20 years. The traction characteristics of ceramic balls should be equal to or better than those of the steel balls. The axial preload is the largest (180 N) in the small C-130 turbine. This is because the preload spring is single acting in the C-130 unit and needs to have a higher value to ensure that the bearing at the other end, which is not spring loaded, does not become unloaded. The air-cycle machine is thrust balanced, but situations arise in some regions of the operating spectrum where an aerodynamic reverse thrust of approximately 130 N will be acting on the shaft.

As a result of the higher preload on the smaller bearing, the calculated L10 fatigue life, as shown in Table 2, is 2289 hours. A study on increasing bearing life was conducted and will be discussed later. The other two units have a double-acting preload design, which ensures that the minimum axial preload is acting on both bearings regardless of the aerodynamic thrust variations. This feature allows a lower preload to be used, which, in turn, leads to a higher theoretical fatigue life and less load-related heat generation.

The radial load in the air-cycle machine is that due to the weight of the rotating unit and any residual unbalance. It is normally less than 2.2 N.

The average ball contact angle in the bearing is a function of the ball diameter, bearing internal diametral clearance, raceway curvature, and thrust or axial preload. In Table 2, in the computed data section, the actual contact angles under load at the inner and outer race are given. The centrifugal force of the ball is taken into account, which makes the inner and outer contact angles different.

The mean contact stress at the inner and outer ring raceway is also given. The ceramic ball, because of its higher Young's modulus, produces a smaller contact ellipse on the raceway surface. This causes higher stress, and consequently, lower theoretical fatigue life than when the same material is used in the rings and balls, even though the ball centrifugal load is lower with ceramic balls. The smaller contact ellipse results in a smaller swept volume, which tends to improve the fatigue life slightly.

Fatigue Life. The calculated life identified in Tables 2 and 3 is the theoretical fatigue life calculated by the A. B. Jones computer programs using material fatigue improvement factors for the steels, but not for the silicon nitride. The basic fatigue life in the program is for air-melted 52100 steel. Material factors of 3 are introduced for ceramic and vacuum degassed 52100, and 10 for CEVM M-50. These factors are generally accepted throughout the industry.

Limited rolling fatigue data on ceramic balls on steel rings have been published by various investigators, and the Baharat and Sibley paper (1999) provides a good summary. Ceramic and hybrid bearing log average life at least five times longer than steel for all groups is quoted by Baharat and Sibley. Hosang (1987) also computed a fatigue life improvement factor of five times over an all M-50 steel bearing.

In the ASE ACM turbines, fatigue has not been identified as the mode of failure, and, therefore, ceramic fatigue improvement factors are not required and have not been used in Tables 2 and 3 or in any of these calculations. The improvements that are expected from using ceramic rolling elements are higher durability, and perhaps lower torque and lower bearing temperature, which would improve lubrication and wear life, rather than fatigue life. Fatigue life improvement would be a welcome bonus if the mode of failure progressed to fatigue.

VII Study Conclusions

F-111 and F-15 Units. Friction torque, which is the main source of heat generation in an air-cycle machine bearing, is reduced by 25 to 40 percent when ceramic balls are substituted for the steel balls in the three bearings. This should lead to

Table 3 Ceramic bearing technology modified Jones computer program alternative C-130 bearing study

Bearing Design								
Material I&O	M-50	M-50	M-50	M-50	M-50	M-50	M-50	M-50
Balls	Ceramic							
Curvature, %								
Inner	53.5	53.5	53.5	53	53	53	53	53
Outer	52	52	52	52	52	52	52	52
Cont. ang., deg	20	20	20	20	17.5	22.5	20	20
Axial load, N	178	133	89	178	178	178	133	89
Radial load, N	22	22	22	22	22	22	22	22
Computed data								
Spring rate, lb/in.	338K	264K	171K	338K	390K	285K	262K	170K
Cont. ang. inner	24.8	25.0	25.6	25.2	22.8	28.0	25.6	26.4
Cont. ang. outer	17.3	15.6	12.8	17.6	16.4	18.7	15.8	12.9
L10 life, hr	9169	21468	69614	11418	8735	14706	26804	86955
Mean stress, MPa								
Outer	908	841	779	896	917	882	841	772
Inner	1185	1089	972	1144	1179	1103	1048	937
Torque, NxM	.0029	.0021	.0013	.0030	.0032	.0030	.0022	.0013
The bearing in each case has eight 3/16-dia balls on an 18-mm pitch dia.								

Table 4 Test results matrix

Item	F-111	F-15	C-130
Maximum design speed, rpm	68K	75K	90K
Compressor outlet air temp., ° C	285-290	426-432	210-212
Hybrid bearing temperature, °C	96-108	137-150	131-138
Steel bearing temperature, °C	115-117	125-148	130-141
Hybrid bearing condition	Excellent	Excellent	Excellent
Steel bearing condition*	Excellent	Excellent	Excellent
*F-111 steel bearings tested for only 4 hours			

lower bearing operating temperature, lower lubricating oil temperature, and higher time intervals before the oil degrades to an extent where bearing performance becomes unsatisfactory. The reduced torque was not confirmed in the test program; however, some benefits from lower torque are expected.

The computer analysis further shows that the contact stress on the raceways increases by 15 to 20 percent when ceramic balls are used, because of the higher modulus and smaller contact area. The L10 life decreases consequently in the C130 bearing. Most of the service records kept by the agencies refer to the average life of the unit, and the average life is approximately five times the L10 life. In the case of the F-15 and F-111 air-cycle machines, the L10 bearing life with ceramic balls (69,643 and 130,207 hours, respectively) is significantly in excess of the MTBF life requirement of the units, and the primary concern reverts back to keeping the oil temperature low and prolonging the oil degradation period.

The L10 life calculations for the steel and hybrid bearings in Table 3 do not follow the expected stress relationship. For example, the inner race stress for the hybrid F-15 bearings is 19 percent larger than that of the steel bearings, and the predicted life is 10 percent greater, rather than less. This bearing is very lightly loaded, and there is a smaller spin-to-roll ratio and different ball modules in the hybrid bearing. For the C-130 bearings, the loads are higher, and the relationship between stress and life is closer to what was expected. The computer program does not simply compute the stress cycle relationship.

C-130 Unit. In the case of the C-130 cooling turbine, the L10 life of the existing bearing is relatively low, 2289 hours, because the bearing is made of 52100 steel, and the axial preload is 180 N versus 130 N for the F-15 and F-111. A separate C-130 bearing study was conducted (Table 3).

If ceramic balls are utilized in the C-130 bearings, the L10 fatigue life decreases to 1649 hours. In this case, additional bearing redesign is necessary. Table 3 shows the various options that would increase C-130 bearing life. The options are:

(*a*) Change the material of the inner and outer ring to M-50 steel. Do not change the raceway curvatures or the diametral clearance. B10 life increases to 5496 hours.

(*b*) Change the material to M-50 for both rings. Change the outer ring raceway curvature to 52 percent and the inner raceway curvature to 53.5 percent. Change the diametral clearance to give a 20-deg contact angle. L10 life increases to 9169 hours.

(*c*) In addition to changes as described in option (*b*), change the housing design for the preload to be the double-acting type and reduce the load to 130 N from 180 N. The life then goes to 26,804 hours. This change also reduces the friction due to load and could further extend the service life improvement expected from the changes in options (*a*) or (*b*). However, extensive redesign of the air-cycle machine would be required.

The C-130 bearings will be changed in accordance with option (*b*).

VIII Laboratory Test Program

Summary. A series of accelerated life screening tests were performed on the C-130, F-111, and F-15 air-cycle machines (ACMs) operating with steel bearings and steel/ceramic hybrid bearings.

In general, neither the steel nor the ceramic bearings showed any signs of distress from these tests. In particular, 50-hour tests on both sets of bearings in each machine showed the balls and raceways to be in excellent condition. Furthermore, detailed examination by the manufacturer of the tested ceramic balls found the balls to be in "as-new" condition.

A hybrid bearing oil interruption test was conducted using the F-111 ACM. An F-111 ACM was assembled without oil and run at the nominal design point until failure occurred at 117 min. The raceways showed severe damage. The ceramic balls were round and completely intact after failure. The oil interruption test was duplicated with the all-steel bearing, which failed in 94 min. The steel balls and raceways showed smearing.

Accelerated Life Test. Table 4 is a test results matrix, which shows the maximum operating conditions, measured compressor-end bearing temperatures, and the general condition of the bearings after the 50-hour tests. For these tests, 20 hours were at normal operating conditions and 30 hours were at maximum operating conditions. The bearing temperatures in the matrix were obtained using the temperature sensors installed during production assembly.

Discussion

F-111 ACM. The steel bearings after the 4-hour baseline tests (abbreviated for the F-111 steel bearing only) and hybrid bearings after 50-hour tests at different speed and power conditions were in excellent condition. Despite the longer operating time, the track made by the balls on the inner ring appeared less pronounced in the hybrid bearings than in the steel bearings, but neither track showed any signs at all of distress.

F-15 ACM. During this test program it was noted that the F-15 hybrid bearings did not have lower operating temperatures than the steel bearings, particularly in the case of the normally hotter running compressor bearing. In one test, the hybrid bearing at the compressor end measured 12°C above the temperature of the steel bearing at maximum design conditions. This result appeared contrary to theoretical predictions.

The confusing bearing temperature results led to further tests and a thermal analysis. In the F-15, bearing temperatures are measured by thermocouples tack-welded during production as-

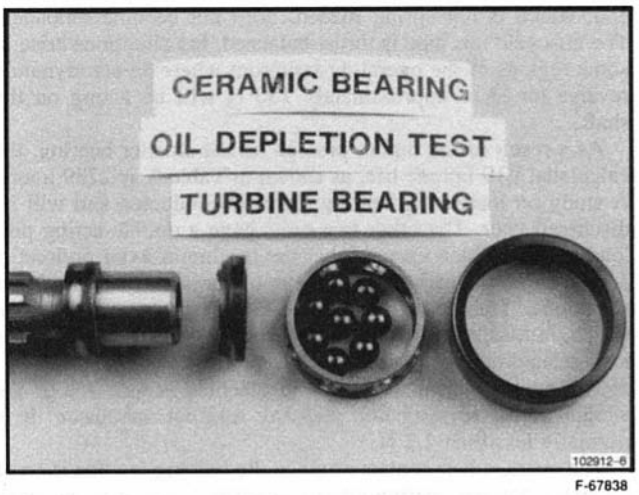

Fig. 5 Failed hybrid bearing

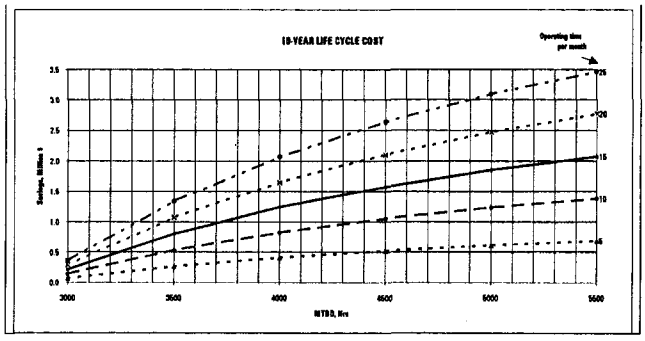

Fig. 6 C-130 10-year life-cycle cost analysis results

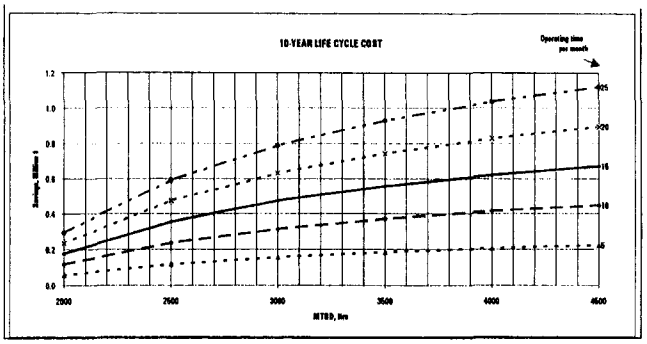

Fig. 8 F-111 10-year life-cycle cost analysis results

sembly to the bearing carrier in the proximity of each bearing. To obtain more direct compressor bearing temperatures, two tests were run, with two thermocouples installed on the outer race of a steel bearing and then a hybrid bearing. The results of these tests, coupled with the thermal analysis, indicated that the bulk bearing temperatures are, for all practical purposes, the same, whether steel or hybrid bearings are used.

The local heat generation difference at the ball-to-race contact is being masked by the complex air flow and heat exchange occurring in the ACM.

C-130 ACM. For this machine, bearing temperatures are measured by thermocouples placed in the air/oil mist discharging from the bearing slingers. Three 50-hour tests were run on the C-130 machine: one test with hybrid bearings with a bronze cage, a second test with steel bearings with a bronze cage, and a third test with hybrid bearings with a silver-plated steel cage. None of the tested bearings showed any signs of distress, and all were in excellent condition. The cages appeared to be in excellent condition, with no unusual contact or wear regions.

General Results. The ball manufacturer (CERBEC) was given test balls for examination. CERBEC reported that the balls were in "as new" condition. Two balls, one from the F-111 and the other from the F-15 bearing, had small hard particle dents from debris going through the bearing, but there is no indication of a crack or fatigue initiation at the dents or any condition that would affect the integrity of the ceramic ball.

Scanning electron microscope (SEM) examination of the raceways of the hybrid and steel bearing raceways showed no signs of distress.

Oil Interruption Test

Ceramic Bearing Test. An oil interruption test was conducted using an F-111 ACM. The bearings were dipped in MIL-L-23699 oil and drained. Five cc of oil was added to each wick contact. The machine was assembled with no additional oil. The ACM was run at the design point operating conditions.

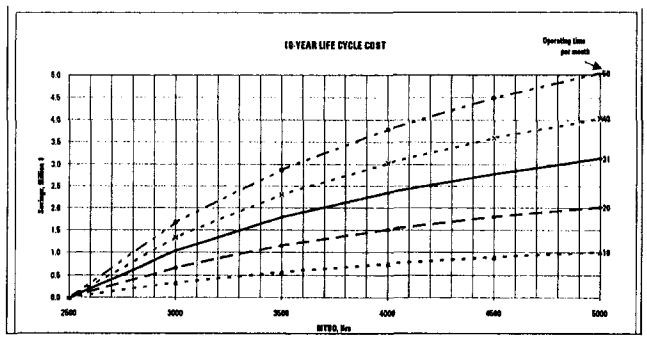

Fig. 7 F-15 10-year life-cycle cost analysis results

The test was conducted in the same setup as the accelerated life test. The failure indication was a sudden increase in measured bearing temperature, which occurred after 117 min of running. The compressor bearing stabilized at 59°C, and the turbine bearing stabilized at 46°C. At 117 min, the turbine bearing temperature suddenly increased to 54°C, and the machine was stopped and disassembled and the bearings inspected.

None of the balls showed any severe distress. There were no cracks or fractures. The surface finish of the balls showed mottling. The balls were in relatively good condition.

Both the inner and outer races showed severe heat and abrasion. The inner race had cracked through the middle of the ball track. Figure 5 is a photograph of the failed bearing.

Steel Bearing Test. This test was duplicated with the ball of an M-50 steel bearing. The compressor bearing stabilized at 69°C, and the turbine bearing stabilized at 55°C. At 94 min, the turbine bearing temperature suddenly increased to 72°C.

The machine was disassembled, and the bearings were inspected. The steel balls showed smearing on the surface, indicating softening and the onset of going out of round. The raceways also showed smearing.

Test Program Conclusions. The hybrid ball bearings have met the primary objectives of the ceramic bearing laboratory test program. The ceramic balls have not become worn or developed cracks during the 50-hour accelerated tests. Examination of the hybrid bearing raceways revealed no signs of wear or distress. The oil interruption test imposed severe distress on the ceramic balls with no detrimental effects. The same failure mode would have destroyed steel balls.

Wick-lubricated air-cycle machines present a significant challenge for ball bearings. At maximum operating conditions, bearing *DN*s are about 1 million, and bearing temperatures can go above 150°C (i.e., 165°C for the F-15). The lubrication/cooling provided by the self-contained wick lubrication system in an air-cycle machine is lean because of size and weight constraints and the limited amount of available cooling. Therefore, this test program has demonstrated that the hybrid bearings performed as well as or better than the steel bearings under the challenging conditions in a high-speed ACM. The success of the hybrid bearings in this laboratory test program validated the go-forward plan for flight tests.

IX Field Test Program

In service over extended operating times, wick lubrication decreases because of oil breakdown, oil loss, and wick glaze/wear at the shaft contact area. Ceramic balls are harder than steel balls and resist microwelding. Under reduced wick lubrication, these characteristics could greatly extend the life of hybrid bearings over steel bearings. The flight test program should provide sufficient bearing life data to demonstrate that hybrid bearings offer an advantage in reduced maintenance costs relative to steel bearings in air-cycle machines.

The field test program is now under way to field evaluate the hybrid bearings in the three different military aircraft fleets: the F-111, F-15, and C-130. Ten of each air-cycle machine have been assembled with hybrid bearings and are being run in service for 1 year. At the end of the year, the air-cycle machines will be disassembled and the bearings will be evaluated. If results are as expected, the hybrid bearings will then be incorporated into the fleet.

X Life-Cycle Cost Analysis

This life-cycle cost analysis provides parametric results because the actual life improvement will be established through a flight test program, which is not yet complete. The assumptions used in the analysis, the methodology, and the results of parametric analyses for the C-130, F-15, and F-111 cooling turbines are discussed. The cooling turbines from these aircraft were selected because the aircraft fleets are large, the mean time between demands (MTBD) is much lower than the predicted bearing life, and therefore, a near-term significant cost reduction should be realized if the program is successful. Mean time between demands is based on flight hours as follows:

$$\text{MTBD} = \frac{\text{Total flight hours}}{\text{Relevant failures}}$$

$$\text{MTBF} = \frac{\text{Total operating hours}}{\text{Relevant failures}}$$

$$\text{Total operating hours} = \frac{\text{Flight hours} + \text{Ground operating hours}}{}$$

Ground hours are not logged; however, the ground running time can be as much as 50 percent of the flight hours, and therefore the MTBF would be 1.5 times the MTBD. This factor would prevail with or without the ceramic bearing improvement, and, therefore, the life-cycle cost analysis will use MTBD.

Assumptions and Ground Rules. The life-cycle cost analysis employed an accounting model that used the following equations to generate the LCC for a given period:

$$\text{Number of failures per year} = \frac{\text{Fleet size} \times \text{Operating time}}{\text{Mean time between demands}}$$

$$\text{Annual cost to remove and replace} = \text{Number of failures per year} \times \text{Time to remove and replace a failed unit} \times \text{Hourly cost}$$

$$\text{Cost of packaging per year} = \text{Number of failures per year} \times \text{Cost of packaging a failed turbine}$$

$$\text{Cost of overhaul per year} = \text{Number of failures per year} \times \text{Cost of overhauling a failed unit}$$

To estimate the life-cycle cost for a given period, the different cost elements were summed to the end of the period. This procedure was applied to the current bearing and ceramic bearing for each type of aircraft. The savings, the difference between life-cycle costs estimated for both types of bearings, is plotted against the possible MTBDs of the ceramic bearings for each aircraft.

Results. The results of the parametric analyses for each aircraft type considered in this paper are given in Figures 6–8. If the hybrid bearings perform as expected in field testing, this program should lead to a substantial reduction in life-cycle costs in ACMs.

Acknowledgments

Portions of the research conducted at AlliedSignal and reported here were sponsored by the Advanced Research Projects Agency (ARPA) and monitored through Tinker Air Force Base. The authors thank Ray Bhikha, Seymour Lev, and John Stanko of AlliedSignal for their help during the preparation of this paper.

References

Bhushan, B., and Sibley, L. B., 1982, "Silicon Nitride Rolling Bearings for Extreme Operating Conditions," *ASLE Trans.*, Vol. 25.4, pp. 417–428.

Chiu, Y. P., 1993, "Rotating Beam Fatigue—Hybrid Bearings," *Meeting Notes, ACTIP 1993 Annual Review,* Annapolis, MD, Aug. 18–20.

Hosang, G. W., 1987, "Results and Design Techniques From the Application of Ceramic Ball Bearings to MERADCOM 10 kW Turbine," *Proc. AIAA 23rd Joint Propulsion Conference,* San Diego, CA, June 29–July 2.

Evaluation of Ceramic Rotor Strength by Cold and Hot Spin Tests

M. Watanabe
CGT Development Office,
Petroleum Energy Center,
Tokyo, Japan

H. Ogita
Ceramic Gas Turbine Research and
Development Division,
Japan Automobile Research Institute, Inc.,
Ibaraki, Japan

Presently in Japan 100 kW ceramic gas turbines (CGT) for automobiles are under development, parts of which include a turbine rotor, scrolls, a combustor, and other parts made of ceramics and ceramic matrix composites. The rotor is designed to rotate at 110,000 rpm, equal to the maximum stress of 300 MPa, and to be exposed to temperatures up to 1350°C. Initially, the strength of ceramic rotors was evaluated by a burst test using a cold spin tester. The burst picture was observed and compared with the 4pt bending strength of the ceramic test specimens. Next, the strength of the rotors was tested by a hot spin test and the burst result of the rotor was evaluated. A high-speed camera was used to observe the rotor at the instant of burst under a high-temperature condition. Applying the result of the cold and hot spin tests, ceramics for turbine rotor were selected and the shape of the rotor was designed.

Introduction

In Japan, 58 percent of all energy consumed is supplied by petroleum, more than 99 percent of which is imported from abroad. In the meantime, the energy consumed by the transportation industry accounts for more than 36 percent of the local demands for petroleum products, of which approximately 80 percent is consumed by automobiles. Such being the case, it is a very important issue in Japan's energy policy to work out strategies for conserving automotive fuels and providing compatibility with diverse types of fuels. In addition, to meet the growing world-wide concern for preservation of the environment, it is increasingly important to take significant steps for finding ways to ensure cleaner exhaust emissions from automobiles.

As a power source, the gas turbine is widely used in aircraft, power generation, and many other applications, because it offers better characteristics than other engines, such as higher efficiency, compatibility with diverse types of fuels, and less pollution. In Japan, national efforts for development of a gas turbine for future use as a practical automotive engine began in 1990 as a project of the Petroleum Energy Center with financial support from the Agency of Natural Resources and Energy, the Ministry of International Trade and Industry. In order to obtain a 40 percent or higher thermal efficiency, the automotive gas turbine requires the use of a turbine rotor, combustor, shroud, and other engine parts that can withstand temperatures of 1200°C to 1500°C. In addition, since their resistance to thermal stress and impact are primary considerations, it is necessary to develop high heat-resistant materials (ceramic-type materials). Figure 1 shows a sectional model of the automotive ceramic gas turbine now under development. Under this project, a monolithic ceramic rotor was first evaluated as a turbine rotor. Ceramic matrix composites were then studied.

Design of Turbine Rotor

Monolithic Ceramics. In view of its strength, heat- and impact-resistant abilities, silicon nitride was selected as a candidate material. Accordingly, SN252 and its improved version, SN253 (Kyocera Corporation products), SN90 and SN91 (NGK Insulator, Ltd. products) and EC152 (NGK Spark Plug Co., Ltd. product) were evaluated. When SN252 and SN253 were used as turbine rotor materials, the rotor was formed by slip casting. When SN90, SN91, and EC152 were used, the blades of a rotor were injection molded, the core of the rotor was CIP molded, and both were then joined together. Table 1 shows the major physical property values of the individual materials. Figure 2 shows a monolithic ceramic turbine rotor.

Matrix Composites. Monolithic ceramic materials have properties that cause a catastrophic fracture. To make up for this disadvantage, studies are presently under way for development of long fiber reinforced, short fiber reinforced, particle reinforced, and other types of ceramic matrix composites for gas turbines. In the short fiber and particle reinforced category, in-situ silicon nitride, SiC/silicon nitride, and SiC/Sialon, respectively, were selected. Table 2 shows the characteristics of the individual materials (Itoh and Kimura, 1993; Nakazawa et al., 1993).

Shape of Turbine Rotor. Turbine target performance conditions were set to ensure that the automotive ceramic gas turbine would be able to achieve a 40 percent thermal efficiency at the best fuel consumption point, while meeting its target performance requirements of 100 kW rated output and 1350°C turbine inlet highest gas temperature. Table 3 shows the turbine specifications at the rated output point. Under these conditions, an aerodynamic basic design and approximate strength studies were performed to determine the basic dimensions and rated speed.

In this case, a higher specific speed was selected to provide a stronger form against foreign object damage (FOD). In addition, three-dimensional analysis of gas flow between blades was performed to determine the number of blades, the blade surface shape, and blade thickness distribution. Figure 3 shows the overall dimensions of the turbine rotor for a 14-blade configuration.

Results of Stress Analysis. In performing turbine rotor stress analysis, three-dimensional analysis of gas flow between blades was first performed to calculate the heat transfer coefficient from the gas temperature, pressure, and flow rate distribution on the entire blade surface. Thermal conduction analysis was then performed to find the temperature distribution in all portions of the turbine rotor. Figure 4 shows the temperature

Contributed by the International Gas Turbine Institute and presented at the 39th International Gas Turbine and Aeroengine Congress and Exposition, The Hague, The Netherlands, June 13–16, 1994. Manuscript received by the International Gas Turbine Institute March 12, 1994. Paper No. 94-GT-460. Associate Technical Editor: E. M. Greitzer.

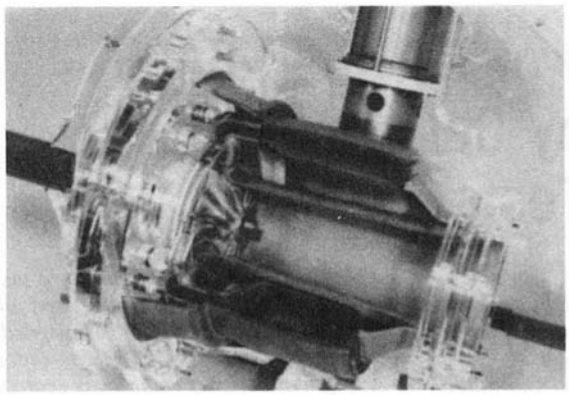

Fig. 1 Ceramic parts in assembled model of gas turbine

distribution in the SN90 rotor at the rated output point. The highest temperature of 1070°C occurs at the blade outside diameter tip. The combined stress of the thermal stress obtained from

Table 1 Properties of turbine rotor materials

	SN252	SN253	SN90	SN91	EC152
Density (g/cc)、RT	3.4	3.5	3.5	3.2	3.26
Young's Modulus (GPa)、RT	314	319	310	310	320
Poisson's Ratio RT	0.28	0.28	0.27	0.27	0.26
Thermal Expansion Coefficient (10^{-6}/K)、RT→1200℃	3.2*	3.8	3.5	3.8	3.3
Thermal Conductivity (W/m·K)、RT	67	79	70	40	24
1200℃	22	23	22	16	18
Specific Heat (J/g·K)、RT	0.65	0.64	0.7	0.7	0.72
1200℃	1.30	1.21	1.2	1.2	1.4

* : RT→800℃

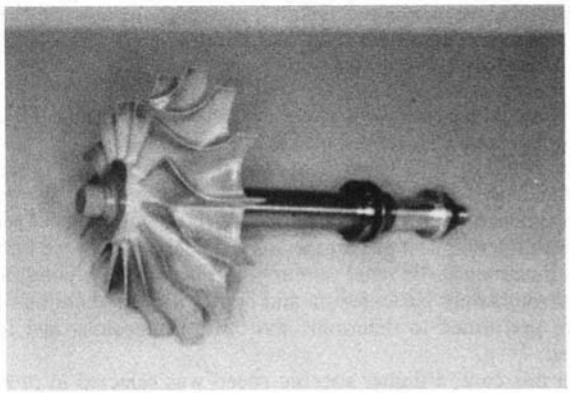

Fig. 2 Monolithic ceramic turbine rotor

Table 2 Properties of ceramic composites

	SiC/sialone	In-situ Si3N4	Whisker reinforced Si3N4
Flexural Strength (MPa)			
R.T	1100	1190	1100
1200℃	970	940	770
Fracture toughness (MPa/m)	6.4	7.6	7.3

Table 3 Turbine specifications (at rated output)

Gas Flow Rate	0.421 kg/s
Pressure Ratio	4.25
Inlet Gas Temperature	1,350℃
Inlet Total Pressure	478kPa (4.87kg/cm²A)
Outlet Gas Temperature	943℃
Outlet Gas Pressure	112kPa (1.145kg/cm²A)

the temperature distribution and the centrifugal stress caused by rotation is the stress at the rated output point. Figure 5 shows the stress distribution in the SN90. The maximum stress, which occurs at the center of the disk and the root of the blade, is 293 MPa. However, most of the stress is due to the centrifugal force. The temperature at the center of the disk where the maximum stress occurs is estimated to be 850°C, whereas the temperature at the root of blade is estimated to be 900°C. Stress analysis during cold start was also performed, but the maximum stress at the center of the disk was 284 MPa, and the maximum stress

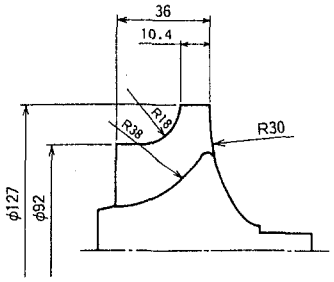

- Rated Speed 110,000rpm
- Number of Blades 14
- Blade Tip Diameter 127 mm
- Blade Outlet Dimeter 92 mm
- Rated Tip Speed 731 m/s

Fig. 3 Turbine rotor dimensions

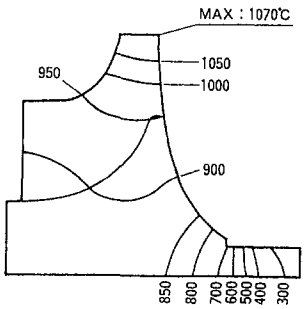

Fig. 4 Temperature distribution (at rated output)

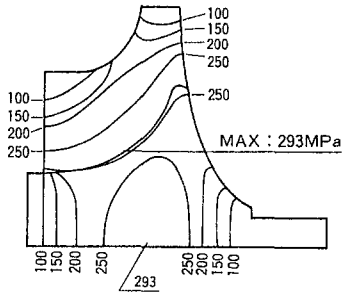

Fig. 5 Stress distribution (at rated output)

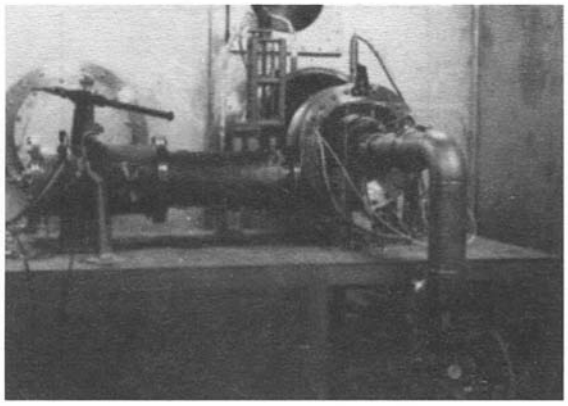

Fig. 6 Hot spin test rig

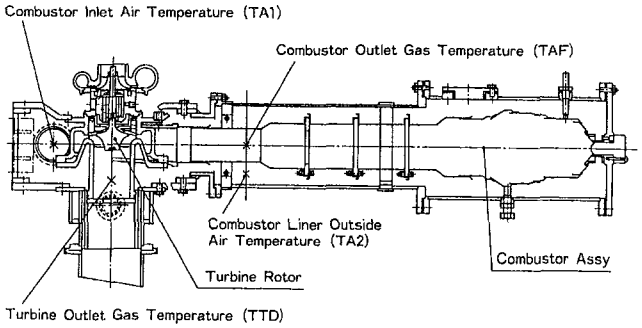

Fig. 7 Hot spin test rig configuration

at the root of blade was 291 MPa. Both values are smaller than those found at the rated output point.

Strength Evaluation Procedures

The following are probable causes for turbine rotor fracture that may occur while the engine is operating:

- Centrifugal stress and thermal stress: instantaneous fracture, fatigue fracture
- Thermal shock
- High-temperature oxidation
- Foreign object damage (FOD)
- Abnormal vibration

To locate the causes of fracture of a ceramic structural material and assure its strength, it is necessary that the component is fractured under similar conditions as in an actual engine. For evaluation of the strength of a turbine rotor and improvement of material strength, the following procedures were established.

Test piece strength evaluation

⇓

Cut rotor bar strength evaluation

⇓

Cold spin strength evaluation

⇓

Hot spin strength evaluation

Experimental Techniques

Hot Spin Test Equipment and Test Procedures. In order to evaluate the strength reliability of a turbine rotor under much the same conditions as in an actual engine, a hot spin test rig was manufactured for performing over-speed fracture tests through use of combustion gases. Figure 6 shows an exterior view of the rig. Figure 7 shows the internal construction of the rig (Ogita and Kimura, 1992).

Provisions were made to let a combustor generate high-temperature gases, and introduce the gases through a heat-resistant metal scroll into the turbine rotor assembly accommodated in a heat-resistant metal housing, and slowly increase the air flow rate and fuel flow rate to increase the rotation speed. Kerosene was used as the fuel. In the gas passage from the combustor outlet to the scroll, a straightening plate was installed to hold down the variance in turbine inlet gas temperature to ±50°C or less. As for the bearings, a floating bush-type slide bearing and taper land-type thrust bearing (their records proven in a turbocharger) were used to construct a shaft system that sustains stable vibration characteristics even at a 15 percent overspeed. A load compressor was provided for a rotor assembly to allow its operation under similar turbine inlet and outlet gas conditions as in an actual engine. For a rotor assembly without a load compressor, a sleeve was provided instead of the compressor. Figure 8 shows both turbine rotor assemblies.

The turbine rotors to be tested were limited to those that had been found defect-free by dimension, X-ray radiographic, and fluorescent penetrant tests. Also their rotational unbalance at the back plane and outlet hub areas were corrected to less than the specified limits and 90,000 rpm cold spin proof tests were performed to qualify the allowable minimum strength. A certified rotor was then joined to a metal shaft by the shrinkage fit or brazing method. After they were joined, their balance was recorrected to less than the specified limits. Figure 9 shows a photo of a rotating turbine rotor taken from behind the turbine outlet. Figure 10 shows an example of the progress in gas temperature and speed with the passage of time before fracture occurrence.

High-Speed Photographing Equipment. For observation of the fast fracture phenomena of a ceramic-type material at room temperature, instantaneous photography is performed by the wire cut or acoustic emission method. Photographs of the rotors are taken at burst by using the light, which the rotor emits during fracture, as a signal. It was verified that high-speed photography could be performed even at high temperatures. Successful instantaneous photography at high temperatures proved to be possible to analyze fracturing patterns. Figure 11 shows the equipment.

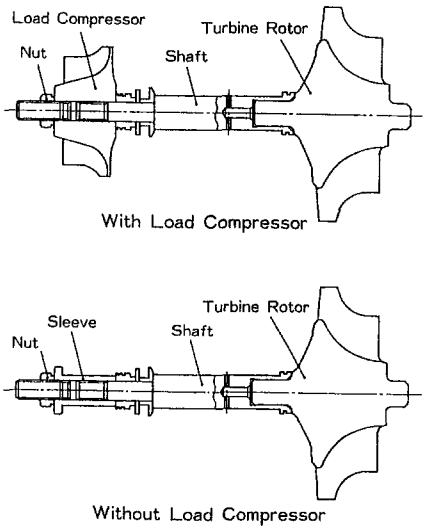

Fig. 8 Turbine rotor assembly

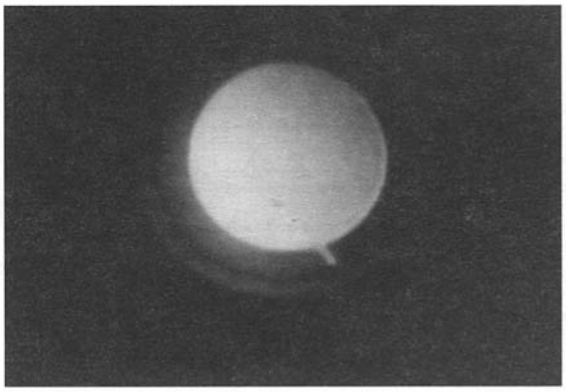

Fig. 9 Rotor in hot spin tester

Strength Evaluation Results

Strength Evaluation of Test Pieces and Bar Specimens Cut From Rotors. Figure 12 shows the relationships between mean flexural strength and temperature found by test piece flexural strength tests (JIS R 1601, test piece size 4 × 3 × 36 mm, surface roughness ≤0.8 μm). While SN252, SN253, and SN90 have characteristics that retain relatively constant strength up to high temperatures, SN91 and EC152 have characteristics that cause a drastic decline in strength at 1400°C, while retaining a very high strength at temperatures below 1200°C. SN253, compared with SN252, exhibits from 3 to 18 percent better mean strength at all temperatures, thereby revealing the improvement of the next generation material over the old. Figure

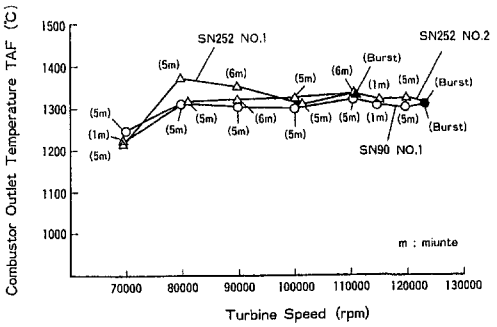

Fig. 10 Hot spin test time schedule

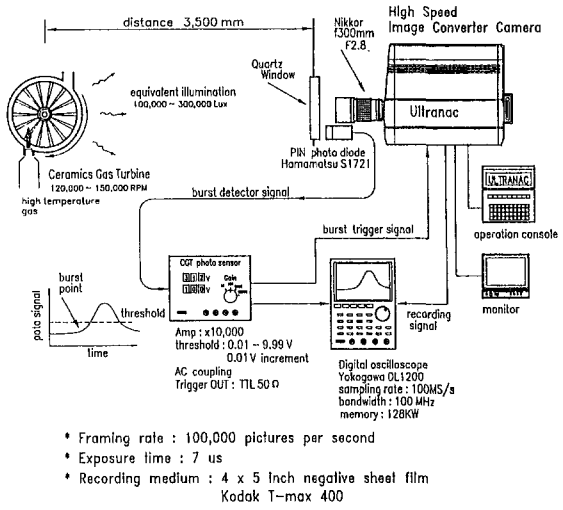

Fig. 11 High-speed camera system configuration

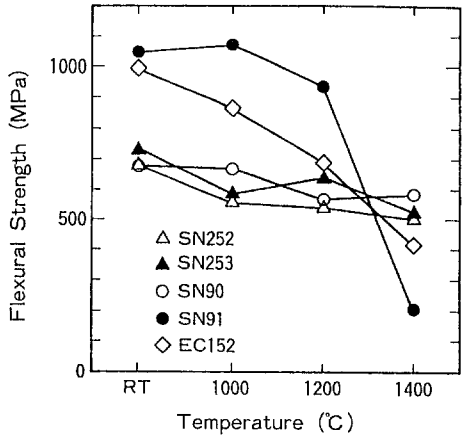

Fig. 12 Test piece flexural strength (JIS R 1601)

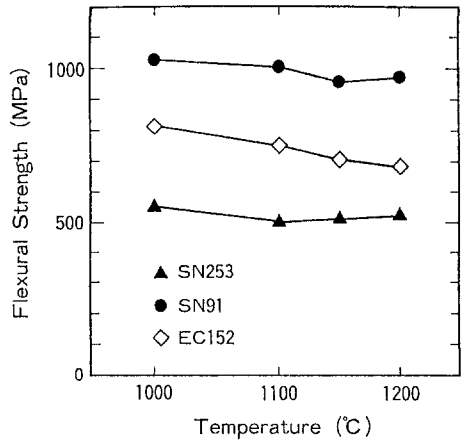

Fig. 13 Flexural strength of bar specimens cut from a rotor (JIS R 1601)

13 and Table 4 show the results of flexural strength tests (JIS R 1601, test piece size 4 × 3 × 36 mm, surface roughness ≤0.8 μm) on the bar specimens cut from SN253, SN91, and EC152 rotors. As shown in Fig. 14, the rotors were divided into three areas: edge of disk, core of disk, and disk/shaft boundary area, and as many bar specimens as possible were cut.

At all measuring temperatures, the variance in the mean flexural strength values of the edge of disk, core of disk, and disk/shaft boundary area was ±5 percent or less, and no appreciable differences in strength dependency on the cut positions were found. Figure 15 shows the results as compared with those of flexural strength tests on the test pieces. On all materials, the differences between the results were small, and the strength

Table 4 Flexural strength of bar specimens cut from a rotor (JIS R 1601)

Material	Temperature (℃)	No. of Test piece	Flexural Strength (mean) (MPa)	Scale Parameter (MPa)	Shape Parameter
SN253	1000℃	9	554	564	27
	1100℃	11	504	521	14
	1150℃	9	517	536	13
	1200℃	10	528	540	21
SN91	1000℃	10	1026	1052	19
	1100℃	10	1004	1029	20
	1150℃	9	957	975	26
	1200℃	10	974	1004	15
EC152	1000℃	11	810	826	25
	1100℃	12	745	761	25
	1150℃	10	703	726	15
	1200℃	11	681	688	50

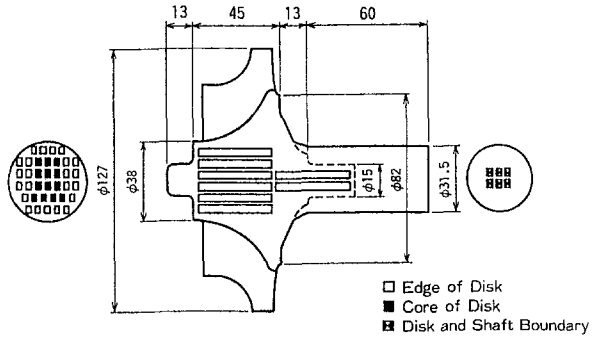

Fig. 14 Location of bar specimens cut from a rotor

values of the actual rotors were close to those of the test pieces. Since the strength dependency on the cut positions was small, the bar positions were disregarded when the strength data for each temperature value were analyzed. The data reveal that the Weibull modulus for all materials was 13 or more.

Cold Spin Tests. Figure 16 shows the results of cold spin tests of the turbine rotors previously subjected to 90,000 rpm proof tests. The first tests were performed on seven SN252, SN90, and EC152 rotors each, and the second tests performed on ten SN253, SN91, and EC152 rotors each. The time required before fracture varied between rotors because of differences in testing equipment. The variations in time were within the range from 15 to 60 seconds. If a fatigue index at room temperature is taken into consideration, the effects of the rate of rise in rotation speed on the fracture speed may be considered minimal.

While the SN252 rotors exhibited a mean fracture speed of 111,000 rpm (102,200 to 124,800 rpm) and a Weibull modulus of 6.1, the SN253 rotors exhibited a mean fracture speed of 125,500 rpm (114,100 to 136,000 rpm) and a Weibull modulus of 11.0, revealing a 30 percent improvement from 298 MPa to 387 MPa in terms of maximum stress, and consequently a higher Weibull modulus. The effects of the improvements were evident in the actual rotors as well.

While the SN90 rotors exhibited a mean fracture speed of 119,900 rpm (116,000 to 125,000 rpm) and a Weibull modulus of 21, the SN91 rotors exhibited a mean fracture speed of 137,400 rpm (109,900 to 149,000 rpm) and a Weibull modulus of 7.5, revealing a 20 percent improvement from 348 MPa to 418 MPa in terms of maximum stress, but the Weibull modulus decreased. One of the reasons for the reduced Weibull modulus is that one rotor, compared with the rest, exhibited an abnormally low fracture speed, which could be the result of a difference in the fracture pattern. If this rotor is excluded, the Weibull modulus is 13.8.

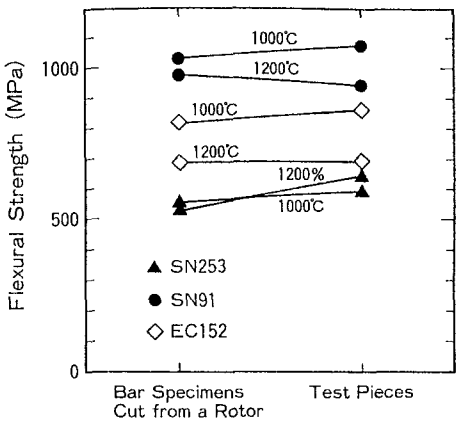

Fig. 15 Strength difference between test pieces and bar specimens cut from a rotor (JIS R 1601)

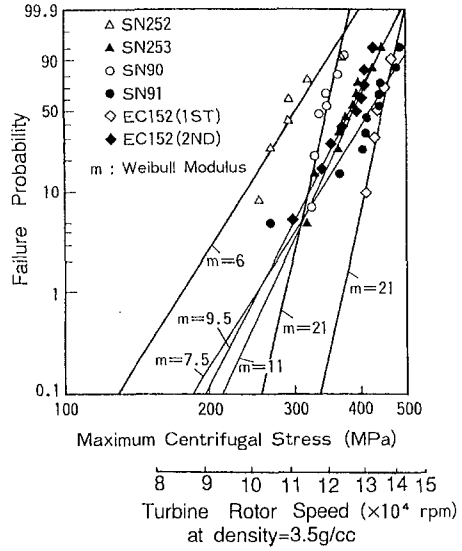

Fig. 16 Weibull plots for cold spin test

The EC152 rotors were divided into two groups by lot, and these two groups were separately tested. The first group revealed a mean fracture speed of 135,500 rpm (130,500 to 138,900 rpm) and a Weibull modulus of 21, whereas the second group revealed a mean fracture speed of 125,400 rpm (110,700 to 134,200 rpm) and a Weibull modulus of 9.5. The mean fracture speed decreased from 445 MPa to 381 MPa in terms of maximum stress, and the Weibull modulus also decreased. High-speed photos taken at the time of fracture show that most of the rotors in the second group fractured, beginning at the high stress center area, but some had only their blade portions fractured. Additionally, their fracture patterns were different. These irregularities seem to be due to lot-dependent manufacturing variances.

Since the mean flexural strength values of the SN253, SN91, and EC152 test pieces at room temperature are respectively 735 MPa, 1048 MPa, and 993 MPa, and considering the size effect between a flexure specimen (432 cc) and a rotor (18,700 cc), the fracture speed of the SN253 is relatively high. All cold spin test results show a lower Weibull modulus than obtained in the flexural strength tests on the bar specimens cut from rotors.

In the case of bar specimens cut from rotors, fractures caused by defects in the as-fired surface were not evaluated. Therefore, the real strength values obtained from the cold spin tests may not always coincide with the results of the flexural strength tests on the bar specimens cut from rotors. Additionally, it is considered to be possible that the strength of the as-fired surface has large effects on the real strength. Evaluation and improvement of the strength of the as-fired surface are one of the themes of future research in this area.

Hot Spin Tests. Although the turbine inlet gas temperature in the final specifications is 1350°C, hot spin tests are currently under way with the turbine inlet gas temperature at 1200°C level, as development work is at an interim stage. When the turbine inlet gas temperature in an actual engine is 1200°C, the turbine outlet gas temperature will be 850°C, because the temperature falls 350°C in the turbine due to the compressor drive power and shaft output power. Since the initial hot spin tests were performed at no load without power absorbing impellers, the temperature fall in the turbine was smaller, and the turbine outlet gas temperature was 1050°C to 1100°C.

As shown in Fig. 17, the temperature conditions were higher, as the turbine rotor temperature distribution at no load was

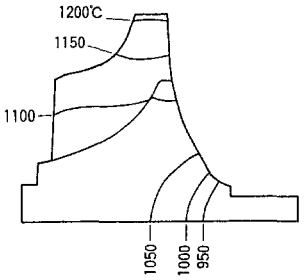

Fig. 17 Temperature distribution (turbine inlet gas temperature 1200°C, no load)

1050°C to 1100°C, compared with the temperature distribution at the rated output point, which was 850°C to 950°C at the center of the disk and the root of the blade. However, more recently, when hot spin tests were performed with the turbine inlet gas temperature at 1200°C, the load of power absorbing impellers was set to reduce the turbine gas outlet temperature from 960°C to 990°C to bring the turbine rotor temperature distribution closer to that of an actual engine (Petroleum Energy Center, 1992).

While the mean fracture speed of three SN252 rotors tested under no-load conditions was 115,300 rpm (110,000 to 124,000 rpm), the mean fracture speed of three SN253 rotors tested under no-load conditions was 127,400 rpm (120,900 to 130,700 rpm). Although the number of data was small, an improvement of about 10 percent in the fracture speed was revealed. The fracture speed was almost the same as that obtained during cold spin tests, which indicated a minimal decline in the material strength even at high temperatures. The SN253 rotors, when loaded, assured freedom from fracture up to 125,000 rpm.

One SN90 rotor was tested at no load, and its fracture speed was 124,700 rpm. Three rotors made of the SN91, a modified version of the SN90, were tested under no load, and their mean fracture speed was 117,800 rpm (111,200 to 123,200 rpm). Loaded tests were performed on two SN91 rotors. Their mean fracture speed was 125,700 rpm (125,300, 126,000 rpm). Although the number of data was insufficient, the results of the loaded tests on the SN91, compared with those of the no-load tests, revealed an improvement of about 7 percent in the fracture speed. However, the improvements revealed during the cold spin tests by changeover from the SN90 to the SN91 could not be verified in the hot spin tests. Judging from this, it would be safe to say that the strength of SN91 is highly dependent on temperature. Since a hot spin test is performed by increasing the rotating speed in stages and holding the speed at each stage for five minutes, it is necessary that a material, particularly a high-temperature-dependent one, has to have its static fatigue strength evaluated under high-temperature conditions.

Six EC152 rotors were tested at no load, and their mean fracture speed was 106,900 rpm (101,000 to 114,900 rpm). Loaded tests were performed on one EC152 rotor, and its fracture speed was 114,400 rpm. Improvement of its high-temperature strength is expected in the future.

Figure 18 shows photos at the moment of fracture. A photo diode, one of photo sensors, caught bursting radiation and triggered the high-speed camera. A high-speed camera was used to capture and record the event at a framing rate of 100,000 pictures per second with 7 μs of each exposures. In this case it is considered that fracture occurred from the center parts of the rotor.

Figure 19 shows the hot spin test results.

Ceramic Matrix Composites. Although ceramic matrix composites are still in the developmental stage, the short fiber reinforced type and whisker reinforced type allow application of the same evaluation procedures as for monolithic materials.

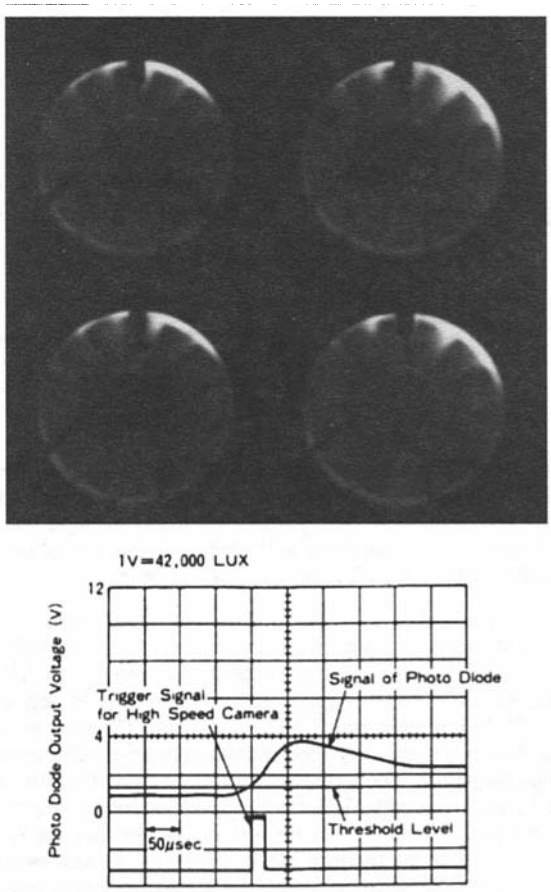

Fig. 18 Photo of hot spin test at the moment of fracture

For the candidate materials for a turbine rotor, therefore, the same strength evaluation procedures as for monolithic materials were used. The candidate materials include five in-situ type disks, five whisker-type disks, and one SiC/sialon disk (11 in total). These disks were subjected to spin fracture tests at atmospheric pressure (cold spin tests) performed by installing each disk on the end of a horizontal shaft of the turbine drive system. The disks are 120 mm in exterior diameter, 7.94 mm in interior diameter, and 15 mm in thickness. During the tests,

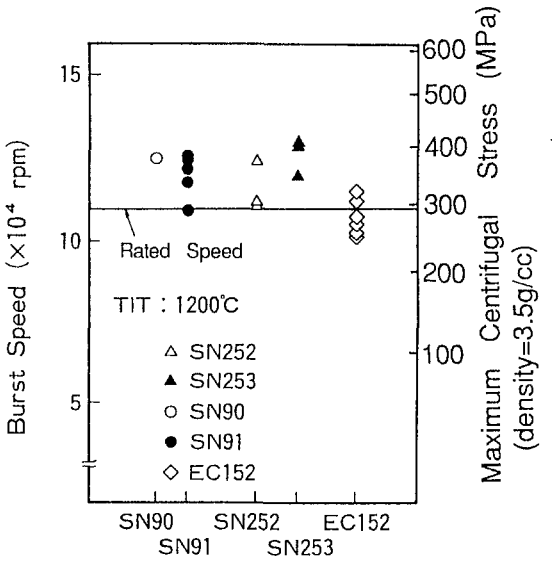

Fig. 19 Hot spin test results

the maximum fracture speed was 80,100 rpm, and the maximum peripheral velocity was 503 m/s.

High-speed photography triggered by light emitted when each disk fractured was also simultaneously performed by stroboillumination.

Achievements and Future Problems

The achievements and future problems are summarized below:

1 In regard to the target rotating speed at the rated output point, which is 110,000 rpm, a maximum fracture speed of 149,000 rpm was recorded during the cold spin tests and a maximum fracture speed of 130,700 rpm recorded during the hot spin tests. As a result, high expectations for successful development of a ceramic turbine rotor for CGT were obtained.

2 Individual materials were tested in the form of test pieces and bar specimens cut from the rotors, and their differences in fast fracture flexural strength were minimal. Differences in mean fast fracture strength dependence on the cut position in the rotor were also minimal.

3 The results of the cold spin tests, compared with the results of the flexural strength tests on the bar specimens cut from the rotors, exhibited a lower Weibull coefficient, revealing the possibility that the effects are caused by the strength of the as-fired surface, which cannot be evaluated by flexural strength tests on the bar specimens cut from the rotors.

4 High-temperature dependent materials cannot be fully evaluated by the fast fracture strength of materials. It is necessary that static fatigue strength at high temperatures also be evaluated.

5 The final objective of hot spin tests is to estimate the life of a turbine rotor in an actual engine. It is necessary not only to clarify the strength characteristics of the materials as described above but also to perform tests to clarify the static fatigue characteristics in an actual turbine rotor.

6 The high-temperature high-speed photography equipment was found to be useful to analyze the fracture pattern of a turbine rotor. The threshold level of the photo sensor is the most important. A lower threshold level can catch the earlier stage of the failure although it may often be triggered by noise.

7 In order to improve the high-temperature strength characteristics of materials, it is necessary that experiments for precise microscopic and fractographic analysis of the ceramic-type materials to be used at high temperatures be performed.

8 Since the final goal of turbine inlet gas temperature is 1350°C, hot spin tests at even higher temperatures must be performed.

9 Fracture of a turbine rotor involves problems like shaft joining strength, FOD, blade vibration, etc. These problems must be dealt with separately.

With these achievements and problems in mind, we are determined to continue the turbine rotor development research for achieving the final goal engine by further improving ceramic materials, estimating the turbine rotor life in an actual engine on the basis of various kinds of test data mentioned above, and performing engine tests under specific operating conditions to verify the strength reliability under actual engine conditions.

Acknowledgments

The authors are grateful to the Agency of Natural Resources and Energy of MITI for making this research possible, and would like to thank members of the 100 kW CGT project for technical support.

References

Itoh, T., and Kimura, H., 1993, "Status of the Automotive Ceramic Gas Turbine Development Program—Year 2 Progress," ASME Paper No. 93-GT-40.

Nakazawa, N., et al., 1993, "The Turbine Component Development for the 100 kW Automotive Ceramic Gas Turbine," ASME Paper No. 93-GT-64.

Ogita, H., and Kimura, H., 1992, "Strength Evaluation of Ceramic Rotor for Automotive 100 kW CGT," presented at the 70th National Conference of JSME, Paper No. 1992-10.

Petroleum Energy Center, 1992, "Technical Development of the Automotive Ceramic Gas Turbine," Report No. PEC-92C01.

E. Hansen

R. Godwin

University of Florida,
Mechanical Engineering Department,
237 MEB,
Gainesville, FL 32611

D. Wood

L. Turner

Florida Power Corporation,
3201 34th Street South,
St. Petersburg, FL 33711

Early Detection of Feedwater-Heater Leaks

This work describes a method of early detection of feedwater heater leaks. The method uses existing pressure, temperature, and flow measurements. The four leak indicators found were feedwater flow rate, drain temperature, drain cooler approach, and extraction line pressure drop. Deviations from normal operation were plotted for each of these indicators. Statistical process control was applied to these deviations. The progressive enlargement of leaks could be seen over a 10 hour period. The four indicators were shown to be good evidence of a tube leak. This method is an alternative to existing acoustic leak detection methods.

Introduction

Improvements in efficiency and the availability of power plant equipment decrease the cost of operation. If plant personnel have the information to detect abnormal operating conditions early, they can take quick corrective action. This prevents further damage to equipment, often avoiding forced outages. If the correction reverses performance deterioration, then heat rates improve immediately. This work will describe methods used by Godwin (1991) to detect feedwater heater tube leaks.

The two objectives of this work are:

1 Theoretically determine possible indicators of feedwater leaks. Predict the changes in various temperatures for some assumed leak conditions. Predict the mass flow rate out of a leaking tube assuming different size leak holes.

2 Analyze empirical data and define normal operating conditions for the heater system using regression analysis. Calculate deviations from normal operating conditions. Apply statistical analysis to resulting deviations to determine which variables deviate significantly during a leak.

Feedwater Heater Leaks

The arrangement of the vertical three-zone high-pressure feedwater heaters at CR Unit 2 is shown schematically in Fig. 1. These feedwater heaters have a design TTD of 5°F and a design DCA of 10°F. The full load (503 Mw) feedwater flow rate is 3,400,000 lb/hr (1,545,454 kg/h). Leakage of feedwater into the shell side of the heater is a maintenance problem that also affects heater performance. The most common source of this leakage is a failed feedwater tube.

Primary tube failure occurs because of design or manufacturing defects, operational thermal stresses, or aging. A summary of the typical primary failures described by Bell and Conley (1988), Strauss (1984), Andreone and Ross (1983, 1984), and Materials Technology (1990) are given as follows:

1 Improperly formed tube bends, which result in low yield strength (particularly for tight bends)
2 Stress corrosion
3 Mechanical wear between tubes and support brackets, which results in different expansion rates during thermal cycling
4 Bad welds at tube/tube-sheet interface
5 Improperly designed impingement plates at the extraction steam inlet, which exposes tubes to high-velocity steam

When the high-velocity steam from the primary leak damages adjacent tubes to the point of leaking, secondary tube failure occurs.

When operators suspect a heater tube leak, the general practice is to take the heater out of service and plug the failed tubes. As a precautionary step, directly adjacent tubes are often also plugged. Consequently, the heater loses an irretrievable level of performance as discussed by Linley (1987) and Singh and Maciunas (1989). The drop in plant and heater efficiency resulting from tube failures also translates into stiff financial penalties.

Theoretical Temperature and Flow Rate Indicators

Before analyzing empirical data, a theoretical model of the feedwater heater subsystem was developed to determine the effects of a leak. The model was designed to allow a leak of given flow rate at any of six predetermined locations along heater train. If the temperatures at these locations exhibited large enough changes, they would be considered possible leak indicators.

Model. Pressure, temperature, and flow rate were assumed constant at the following locations:

BFd: feedwater flow from low pressure feedwater heater train entering deaerator
Ed: extraction flow from low end of high-pressure turbine entering deaerator
E6: extraction flow from middle of high-pressure turbine entering Heater 6
E7: extraction flow from high end of high-pressure turbine entering Heater 7.

Variable temperatures were then calculated at the following locations:

BF6I: feedwater flow entering Heater 6
BF60: feedwater flow exiting Heater 6
BF70: feedwater flow exiting Heater 7
D6: condensate flow exiting Heater 6 drain
D7: condensate flow exiting Heater 7 drain.

A 10 percent feedwater flow leak was assumed to occur at one of six locations:

Contributed by the Power Division for publication in the JOURNAL OF ENGINEERING FOR GAS TURBINES AND POWER. Manuscript received by the Power Division March 1, 1992; revision received April 21, 1993. Associate Technical Editor: R. W. Porter.

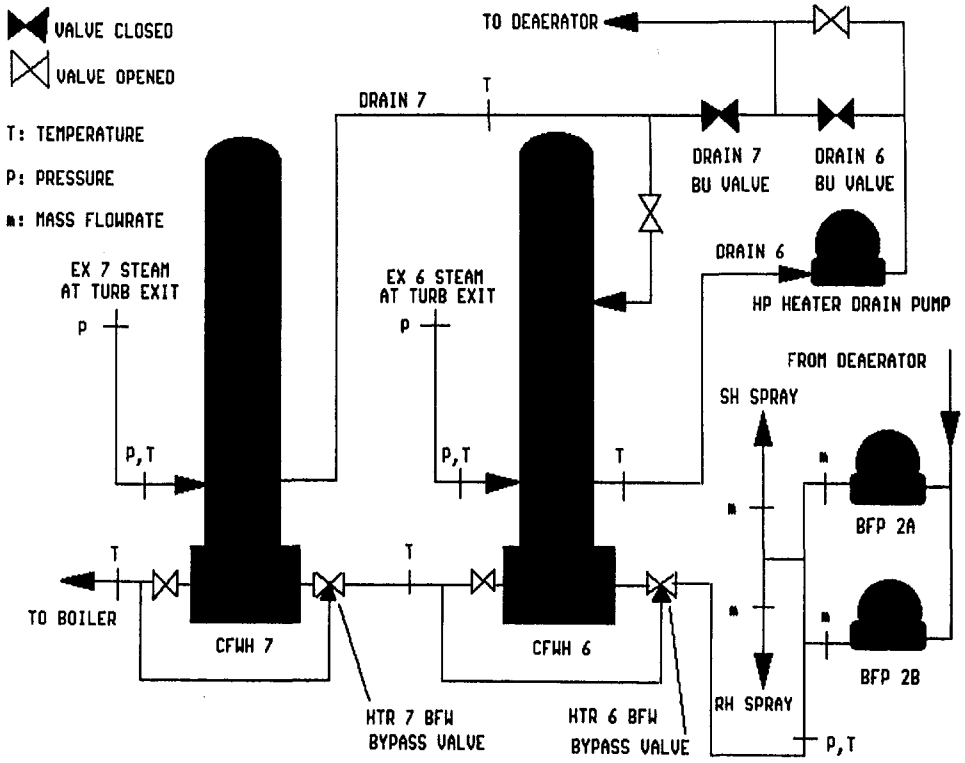

Fig. 1 Crystal River Unit 2 high-pressure closed feedwater heater subsystem

L1: tube/tubesheet junction at the inlet to Heater 6
L2: bend region of Heater 6
L3: shellside exit of Heater 6 desuperheating zone
L4: tube/tubesheet junction at the inlet to Heater 7
L5: bend region of Heater 7
L6: shellside exit of Heater 7 desuperheating zone.

Heaters 6 and 7 were each broken down into five zones. Each zone had its own overall heat transfer coefficient, U, and the effective heat transfer area, A. The interior leaks (L2, L3, L5, L6) were modeled as if the flow from each leak went directly to the surface of the drain cooler condensate of the respective heater. Further, the flow from the Heater 7 drain, D7, was modeled as if it separated into two parts upon entering heater 6. One part was saturated liquid that dropped to the drain cooler, and the other part was saturated steam that mixed with the steam. Design data were used for conditions entering and exiting each heater. Interior conditions had to be estimated. No pressure drops across the shell and tube side of each heater were assumed. The temperature differences between the leak and no-leak cases are shown in Table 1.

Indicators. Based on the results shown in Table 1, it was concluded that the following temperatures would be the best leak indicators:

Table 1 Temperature changes caused by a 10 percent feedwater flow leak in a feedwater heater

	Leak location					
Temperature, °F	L1	L2	L3	L4	L5	L6
BF6I	1	2.4	3.5	3.1	3.1	3.6
BF60	1	1	1	1	2.5	3.4
BF70	0.9	0.9	0.9	0.9	0.9	0.9
D6	−2.2	5.4	11.1	8.8	8.8	11.8
D7	0.9	0.9	0.9	−3.3	6	7

1: temperature at D6 for leaks L2, L3, L4, L5, and L6
2: temperature at D7 for leaks L5 and L6.

If drain valve position had been available, it would have also been used in this investigation.

Theoretical calculations were also performed to estimate the flow rate from a leaking tube assuming two leak hole areas. The larger area was the cross-sectional area of the tube. In this case feedwater would flow out of both ruptured ends of the U-tube. The smaller area was arbitrarily chosen to be the area of a circle $\frac{1}{10}$ the tube diameter.

The pressure drop along the nonruptured tubes was assumed negligible compared to the pressure drop between the tube tubesheet interface to the leak at the tube bend.

The $\frac{1}{10}$ tube diameter leak increased the feedwater flow rate by 0.64 percent. Such a small leak may not be detectable.

A completely ruptured tube increased the feedwater flow rate by 4.6 percent. Since many typical leak conditions involve more than one tube, it was concluded that in these situations the flow rate increase would be discernable and detectable.

Analysis Methods

The results of the theoretical calculations indicated that during a leak it should be possible to discern an increased feedwater flow rate and an increased drain temperature. Empirical data to test this conclusion became available during the course of this study when two separate leaks occurred in Heater 6.

The data were available as ten-minute moving averages obtained from 40 individual readings. Then normal operating conditions were defined by regression analysis of non-leak data. Deviations of leak data from expected values were calculated and plotted. Finally, deviation data were grouped into samples from which statistical process control charts were developed.

The data used for this study were restricted to data available from normal plant instrumentation. The data for 17 of the 22 variables analyzed in this study were obtained from direct measurements. The locations at which these variables were mea-

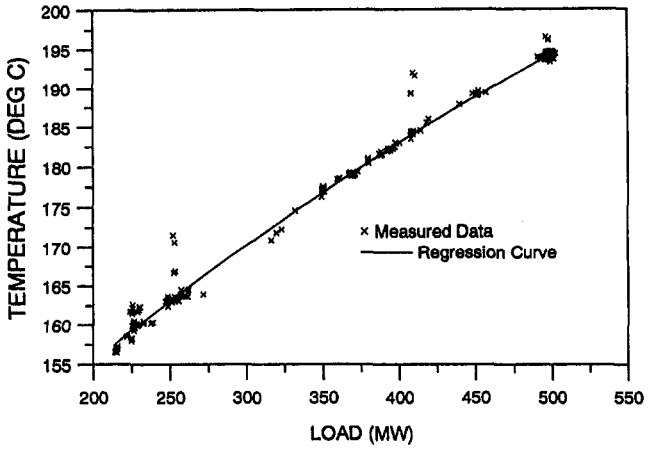

Fig. 2 Variation of feedwater heater drain 6 temperature with generator load

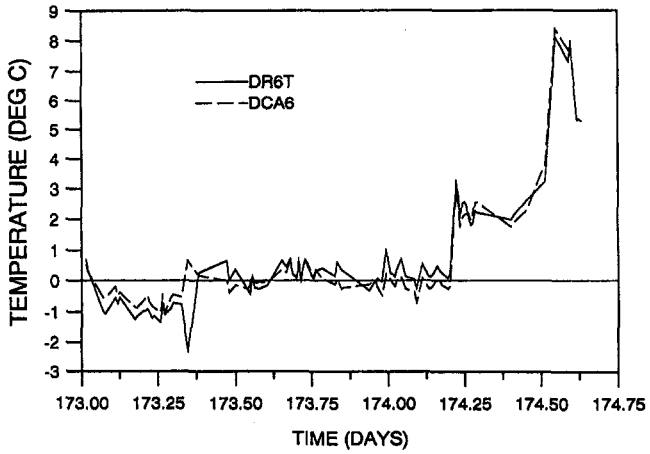

Fig. 4 Deviation from normal operation of heater 6 drain cooler approach and drain temperature plotted against time

sured are shown in Fig. 1. Generator load is also a variable but is not shown in Fig. 1. A heater level control signal was not available.

Values for five additional variables (total feedwater mass flow rate, two DCA's, and two extraction steam pressure drops) were calculated from directly measured variables. The extraction pressure drops were felt to be indirect measures of the extraction steam mass flow rates.

The leaks occurred on April 25, 1991, and June 24, 1991. The April leak occurred during the ramping of a cold startup. Because of ramping, consistent deviations were not found from the April data. They will not be shown. The June leak began during a steady low load. The authors' findings indicate that the leak began at 174.22 days when the unit was producing 225 MW. The size of the initial leak was 75,000 lb/hr (34,091 kg/h). This is only 2 percent of the rated feedwater flow. At 174.38 days the unit was ramped up to 500 MW. Eight hours after the initiation of the leak, it had grown to over 7 percent of the rated feedwater flow. This initiated emergency dumps. The heater was taken out of service at 174.6319 days.

Data Refinement. Plant ramping increased the scatter in the data. By trial and error, it was determined that the "steady" data used in this analysis would have an absolute ramping value of less than 120 klb/hr (4.4 percent of full-load flow).

Regression Analysis. Regression analysis was used to estimate an expected value of the measured pressures, temperatures, and flows. The first step of the regression analysis was to determine the best independent variable (or variables) to use for each dependent variable. The second step was to select the most appropriate time frame from which to calculate the regression curves.

The variables considered as inputs and outputs of the heater train were the 22 variables already described. The Heater 6 drain temperature was viewed as an output that was influenced by all the variables at the Heater 6 inlets.

It was quickly determined that these inputs appeared to be very interdependent and all were not required in the analysis. After trying different combinations of independent variables, it was found that a regression curve could best be calculated for each dependent variable using only one independent variable, load. Except for the DCA6 and the extraction steam temperatures, a correlation factor of at least 0.95 was obtained for every variable using only one dependent variable.

The regression curve calculations of heater 6 drain temperature for the June data base illustrate the basic process. Employing the load as the single independent variable, the polynomial curve fit and the data used to produce it are shown in Fig. 2.

The deviation of the measured value from the expected value was then plotted in Fig. 3. The sudden increase in measured drain temperature is a result of a tube leak.

Statistical Process Control. The control limits for all the control charts were based on the first twenty samples, each with a sample size of five discrete data points. The methods are outlined by Godwin (1991) and Ross (1987).

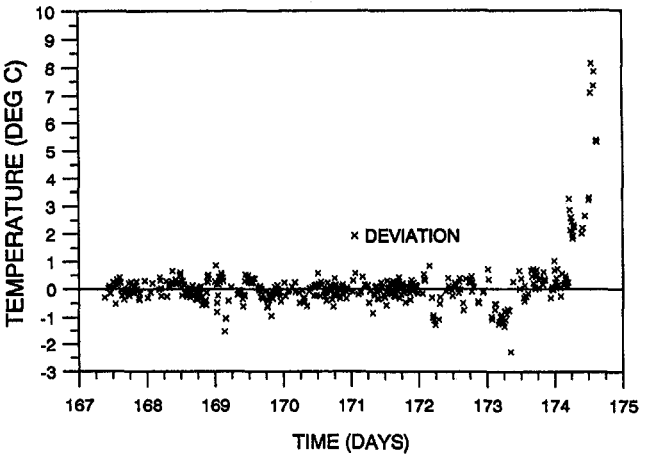

Fig. 3 Deviation of measured heater 6 drain temperature from expected regression curve plotted against time

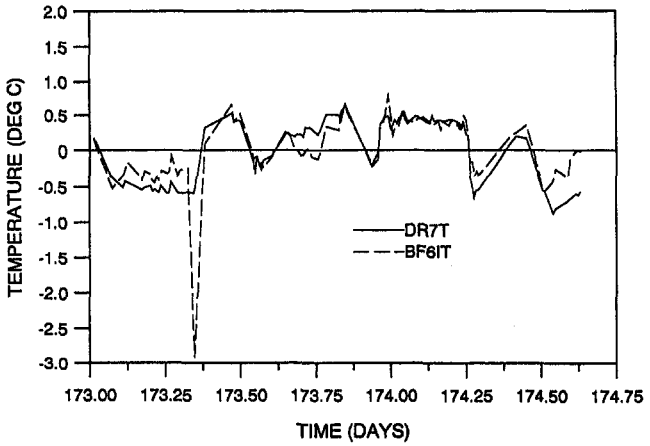

Fig. 5 Deviation from normal operation of heater 7 drain temperature and heater 6 inlet temperature plotted against time

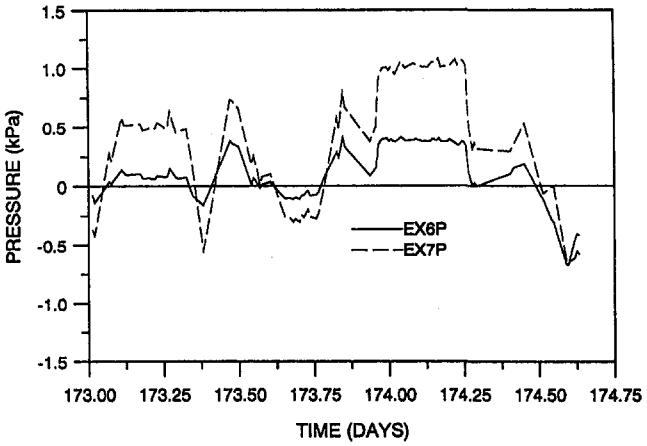

Fig. 6 Deviation from normal operation of heaters 6 and 7 extraction pressures plotted against time

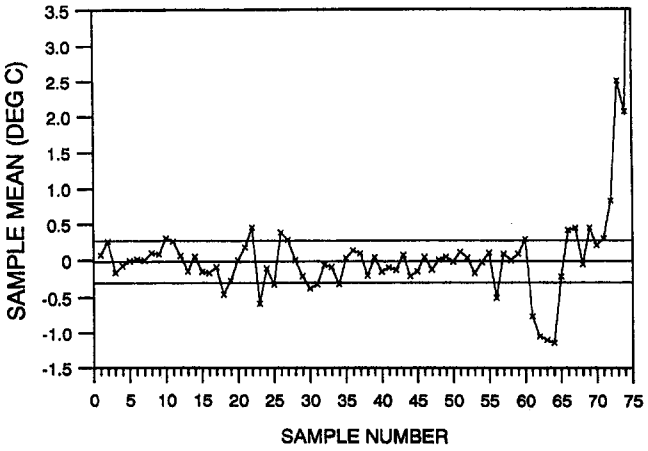

Fig. 8 Deviation from normal operation of measured heater 6 drain temperature plotted on a sample mean process control chart

The data refinement process discussed earlier resulted in many data points being dropped out, so the remaining points were no longer necessarily consecutive. Five data points making up each sample were chosen so that each point was no more than 50 minutes later than the preceding point. This method produced only about 12 percent of the samples, which spanned more than 1.3 hours. The control charts for the June data contained 75 samples between times 167.3611 and 174.6319 days.

Early Detection of Leaks

Deviation Monitoring. The deviation monitoring stage of the analysis focused attention on the deviation of each variable from its expected value, Fig. 3.

Time plots of the regression curve deviations are presented in Figs. 4–7. Each figure shows a variable over about a two-day period leading up to the shutdown of Heater 6. As indicated in the theoretical model, drain 6 temperature, DCA 6, and the flow rate are expected to increase when a tube leak occurs at the bend. The other variables (drain 7 temperature, heater 6 inlet temperature, and extraction 6 and 7 pressures) were expected to show small or negligible changes.

Drain 6 temperature and DCA 6 showed two step increases (Fig. 4). These steps correspond to two sets of tube leaks. The first leak is a primary leak and the next is assumed to be a secondary leak. The time of the primary leak was 174.2153 days with the secondary leak occurring at 174.5347 days. The primary leak was observed 10 hours before the heater was taken out of service.

The increase in measured DCA is close to the theoretical DCA, which assumed a 10 percent feedwater heater leak. Heater 6 inlet temperature and heater 7 drain temperature, Fig. 5, show insignificant changes during the period of the leak.

Extraction pressures 6 and 7 show no significant indications of a leak, Fig. 6. However, the pressure difference along heater 6 extraction line does show an increase, Fig. 7. This trend suggests that when leaking, the feedwater condenses additional extraction steam. The greater extraction steam flow is indicated by a higher pressure drop as the leak grows. As would be expected, the leak is also observed as a feedwater flow rate deviation increase (Fig. 7). The size of the indicated leak flow is 7 percent of the feedwater flow.

The advantage of plotting deviations of each variable is immediately clear from these graphs. Each variable can be analyzed separately without having to look for changes relative to other variables. The evidence of the first leak occurs at 174.2153 days using indicators in Figs. 4 and 7. A second leak, a secondary tube failure, appears at 174.5347 days.

The deviation scatter about zero is not completely random. Clearly, other variables besides the load have an influence on the indicators analyzed in this study.

Statistical Process Control. Control charts for the sample mean and sample standard deviation were constructed for each variable. All 75 samples for heater 6 drain temperature are shown in Figs. 8 and 9. Problems were seen in the first 20 samples used to establish the control limits for this mean control

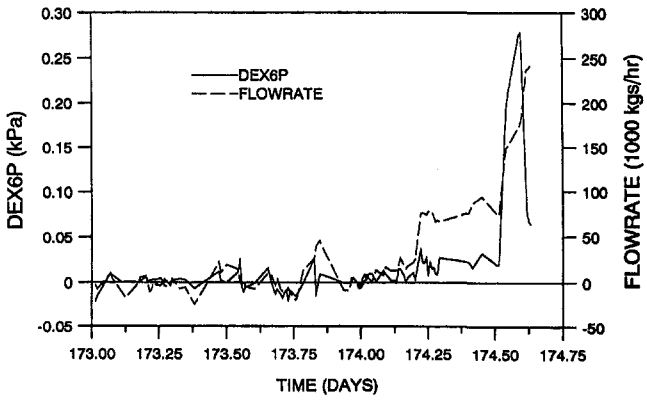

Fig. 7 Deviation from normal operation of feedwater flow rate and heater 6 extraction pressure drop plotted against time

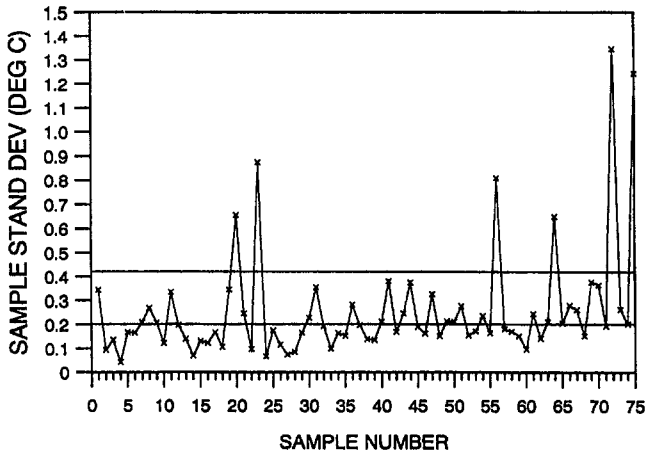

Fig. 9 Deviation from normal operation of measured heater 6 drain temperature plotted on a sample standard deviation process control chart

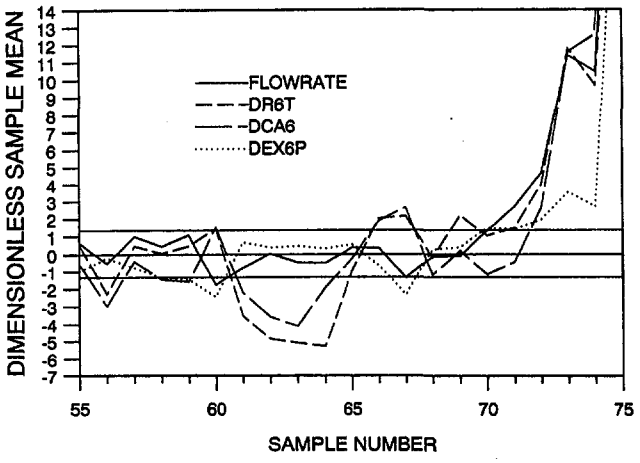

Fig. 10 Deviation from normal operation of measured flow rate, heater 6 drain temperature, heater 6 drain cooler approach, and extraction pressure drop plotted on a sample mean process control chart. The sample mean has been shifted to zero and nondimensionalized by the control limits.

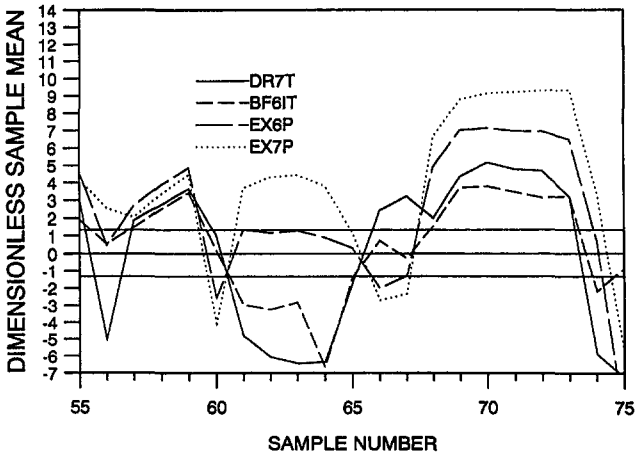

Fig. 12 Deviation from normal operation of measured heater 7 drain temperature, heater 6 inlet temperature, and heaters 6 and 7 extraction pressures plotted on a sample mean process control chart. The sample mean has been shifted to zero and nondimensionalized by the control limits.

chart and for the other variables. Several samples of the mean control chart are outside the control limits (Fig. 8). The standard practice in SPC would be to eliminate a sample that is outside of the limits and to recompute those limits. This was not done because some of the variables had too many samples outside the limits.

Another problem with the first 20 samples was the lack of randomness in the pattern of the data. The process was not random from sample point 3 to sample 9.

The standard deviation control chart had only one point outside its control limits for the first 20 samples. For all of the variables, the first 20 samples of the samples standard deviation control charts tended to have fewer points out of control than the sample mean control charts. Additionally, the patterns of the plots were more random than in the mean control charts.

The control limits for each variable in Figs. 8–13 were not accurate as the authors had hoped they might be. Despite this, control charts can help one better judge a trend when control limits are defined. The control limits of Figs. 10–13 are presented in a nondimensional form so that several plots can be presented in one figure.

A rising trend of DR6T, DCA6, flow rate, and DEX6P (Fig. 10) was in effect by sample 72 (the flow rate was low). The last discrete deviation value in sample 72 corresponded to time 174.2222. This was one ten-minute increment after the time at which the leak was first noticed in the regression stage of the analysis (174.2153). The data at 174.2153 dropped out in the process of grouping discrete data into samples. This rising trend appears to have begun at sample 71 (fifth data point was at time 174.1597) for each of these four variables.

This is significant, since it suggests that the effects of the leak may have been manifested in the control charts about 80 minutes earlier than was seen in the regression analysis. Sample 71 in the flow rate mean control chart is far above the UCL and illustrates this best.

The sample standard deviation charts (Fig. 11) showed sharp increases above the UCL at samples 72 and 75. This suggests

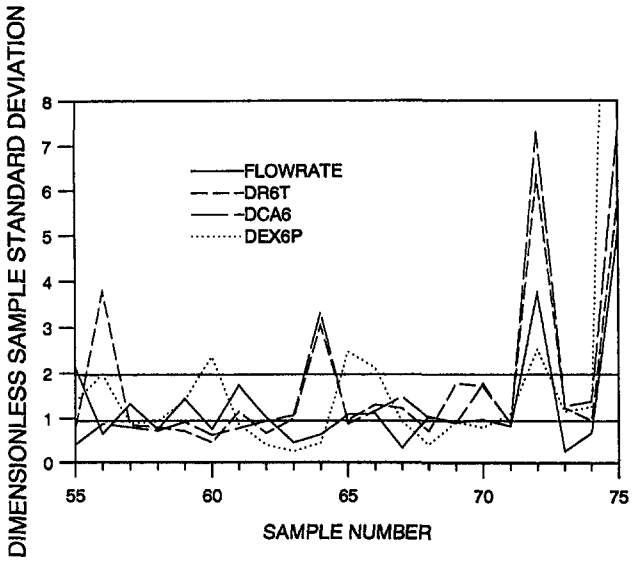

Fig. 11 Deviation from normal operation of measured flow rate, heater 6 drain temperature, heater 6 drain cooler approach, and extraction pressure drop plotted on a sample standard deviation process control chart. The standard deviation has been nondimensionalized by the control limits.

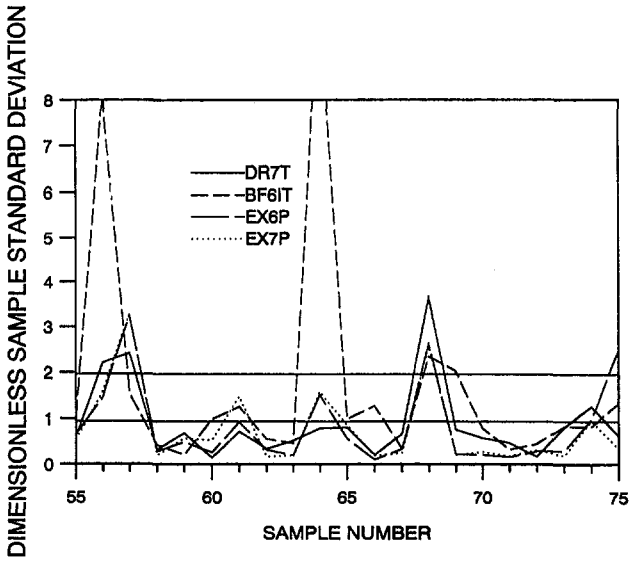

Fig. 13 Deviation from normal operation of heater 7 drain temperature, heater 6 inlet temperature, and heaters 6 and 7 extraction pressures plotted on a sample standard deviation process control chart. The standard deviation has been nondimensionalized by the control limits.

that the sample standard deviation may be an additional indicator of leaks.

The variables that were not considered to be indicators are shown in Figs. 12 and 13. The variation about the mean shows no significant difference between before or after the leak, Fig. 12. No increase in the sample standard deviation was seen during the leak (Fig. 13).

Conclusions

This investigation was carried out with the full realization that acoustic leak detection equipment is available. The purpose of this work was to demonstrate a general method of detecting early equipment failure, which could be programmed into the plant computer. The work's philosophy is to extract more information from existing measurements rather than adding new sensors.

1 Four measurements were found to be indicators of feedwater heater leaks: drain outlet temperature, drain cooler approach temperature, feedwater mass flow rate, and extraction steam pressure drop.
2 Using deviations from normal operating conditions furnished the ability to discern when a leak is beginning.
3 Regression analysis was limited in its ability to detect other important independent variables that define normal operation.
4 When statistical process control is applied to deviations, control charts can be helpful in detecting leaks.
5 Quality of the control charts is dependent upon correctly determining the normal operating conditions of each variable.
6 Sample mean and sample standard deviations can both be used as indicators of a leak.

Acknowledgments

The authors wish to express their gratitude to Florida Power Corporation, which financially and logistically supported this work. Thanks are also given to God for the providence and understanding He granted during this work.

References

Andreone, C. F., and Rose, D. M., 1983, "Closed-Feedwater Heaters: New Emphasis on Efficiency, Reliability, and Maintainability," *Power Engineering,* Nov., pp. 62–64.

Andreone, C. F., and Rose, D. M., 1984, "Highly Reliable Feedwater Heaters: Specification, Design, and Operation Guidelines," *Power Engineering,* Jan., pp. 36–39.

Bell, R. J., and Conley, E. P., 1988, *High Reliability Feedwater Heater Study,* Electric Power Research Institute, EPRI cs-5856, Project 1887-2.

Godwin, R. E., 1991, "Leak Detection in Closed-Feedwater Heaters Using Statistical Analysis," Thesis, University of Florida.

Linley, F. H., 1987, "The Impact of Tube Plugging on Closed-Feedwater Heater Operation and Maintenance," ASME *Journal of Pressure Vessel Technology,* Vol. 109, pp. 212–218.

Materials Technology, 1990, "Failure Analysis of Bartow #5 and #6 Feedwater Heaters," Report MTSR, Oct., pp. 1, 7–9.

Ross, S. M., 1987, *Introduction to Probability and Statistics for Engineers and Scientists,* Wiley, New York.

Singh, K. P., and Maciunas, V., 1989, "Feedwater Heater Performance Prediction Code 'Heater'," *Heat Transfer Equipment Fundamentals, Design, Application, and Operating Procedures,* ASME HTD-Vol. 108, p. 134.

Strauss, S. D., 1984, "Industry Strives for Improved Feedwater-Heater Reliability," *Power,* Sept., pp. 51–54.

S. J. Koffman
School of Mechanical Engineering,
Purdue University,
West Lafayette, IN 47907

R. C. Brown
Department of Mechanical Engineering,
Iowa State University,
Ames, IA 50011

R. R. Fullmer
Department of Mechanical and Aerospace Engineering,
Utah State University,
Logan, UT 84322

Control of a Fluidized Bed Combustor Using Fuzzy Logic

Application of fuzzy logic control to a fluidized bed combustor (FBC) is examined. Major aspects of fuzzy control are reviewed, and design of a fuzzy controller for the FBC is described. Selected experimental results are presented, and performance of the fuzzy controller is evaluated through comparisons to results from classical PI control of the combustor.

Introduction

Recently, fluidized bed combustors (FBC) have attracted interest for generating industrial power and steam because of their ability to burn low-grade fuels while maintaining strict emission standards. However, FBCs have coupled dynamics and severe nonlinearities that have frustrated attempts to automate their operation using conventional control techniques effectively [1], especially during start-up. In the past, combustor operation has depended on frequent human intervention. For coal-fired FBCs to be an economical energy system for small industries, their operation must have a high degree of automation and reliability—the expense of human labor devoted to combustor operation and maintenance would otherwise make FBCs prohibitive. Furthermore, because small industries tend to use power intermittently, FBCs in such industries are expected to have frequent restarts after periods of nonuse. Therefore, efficient start-up operation will be required of these combustors. Aside from coupled dynamics and severe nonlinearities, conventional control algorithms may not be suitable for this task since parameters of the process, upon which classical design methods are based, change rapidly during combustor start-up. To automate these combustors for start-up and normal operation adequately, new approaches need to be examined.

Fuzzy logic—an artificial intelligence technique—can be employed to exploit the wealth of information human experts have learned about complex systems while attempting to control them. This information is usually of a qualitative nature that is unusable by rigid conventional control techniques. Fuzzy logic, used as a control method, manipulates linguistically expressed, heuristic knowledge from a human expert to derive control actions for a described system. As an alternative approach to classical controls, fuzzy logic is examined for start-up control and normal regulation of a bubbling fluidized bed combustor. To validate the fuzzy logic approach, the fuzzy controller is compared to a classical proportional and integral (PI) controller, commonly used in industrial applications, designed by Ziegler–Nichols tuning [2].

Fuzzy Logic Theory

Fuzzy logic, developed by L. A. Zadeh [3, 4], is an artificial intelligence technique that manipulates expert human knowledge to make decisions in ill-defined systems. Fuzzy logic systems are a subset of expert systems using approximate reasoning techniques based on qualitative, imprecise information. The idea in many expert systems is to extract precise expert knowledge from a person who is often unable to quantify his actions exactly. Fuzzy logic was developed to utilize this valuable (though inexact) information that would normally be difficult or impossible to exploit otherwise.

Fuzzy logic is composed of two main components—an information base and an inference engine. The information base is a set of linguistic rules that qualitatively describe the system or actions to be performed on the system, and associated fuzzy sets. These rules are gleaned from an expert. Because humans communicate and think in imprecise terms, the rules are expressed in qualitative (fuzzy) terms. Numerical meaning is given to the qualitative terms of the rules via fuzzy sets. The rule and fuzzy sets are operated on by an inference engine to infer actions or decisions. As in the case of process control, the rules give qualitative control action for qualitative operating points of a system whereas the inference mechanism gives quantitative actions for quantitative operating points.

The first step in implementing a fuzzy controller is to quiz the human operator about his actions for varying system states. Knowledge extracted from the expert is stated in rule form. Rules have the following structure:

$$\text{If } X = \{\text{antecedents}\}, \text{ then } Y = \{\text{consequents}\}$$

where, in general, X and Y are vectors. The rules are interpreted as: If the antecedents of the rule are met, then apply the consequents to the system. Here X represents process outputs of the system and/or system states; Y represents process inputs. Antecedents and consequents, being expressed linguistically, are descriptions of system state and inputs, respectively. After obtaining a suitable set of rules for a particular system, the qualitative terms of the antecedents and consequents of each rule must be defined using fuzzy sets.

A fuzzy set is a collection of elements having a common feature, but the elements have this feature to varying degrees. Each element x_i of a fuzzy set X has graded membership $\mu_x(x_i)$ ranging between 0.0 (no membership) and 1.0 (full membership) to the set. "Fuzzy" refers to the fact that these sets do no have sharp boundaries between nonmembers and members. A relation giving grades of membership for each element of a fuzzy set is known as a membership function, and all membership functions describing a fuzzy variable are defined on the universe of discourse for that variable. Rules with corresponding fuzzy sets comprise the information base that is manipulated by an inference engine to produce control actions. When this

Contributed by the Fuels and Combustion Technologies Division for publication in the JOURNAL OF ENGINEERING FOR GAS TURBINES AND POWER. Manuscript received by the Fuels and Combustion Technologies Division January 13, 1992. Associate Technical Editor: D. W. Pacer.

work was initiated, the approach[1] to fuzzy inferencing as described by Zadeh [3, 4] was standard. Since this work, new and preferred methods of fuzzy inferencing have evolved. Kosko [5] gives an excellent overview of the various approaches. In the following, only Zadeh's classical approach will be described in detail.

Each rule of the rule set forms a fuzzy relation that is mathematically defined as the product of the membership functions of the antecedents and the consequents. This product is formed by a minimum operation between membership functions. For a controller with one input and one output, the equation to generate a fuzzy relation is

$$\mu_{R^m}(x_i, y_j) = \min [\mu_{X^m}(x_i), \mu_{y^m}(y_j)]$$

where the superscript m refers to the rule number. This equation is used to formulate fuzzy relations separately for each rule.

After all relations are formed, they are combined to give a complete (overall) relation for the system. This is done by taking the union of the individual relations:

$$\mu_R(x_i, y_j) = \max [\mu_{R^1}(x_i, y_j), \mu_{R^2}(x_i, y_j), \ldots, \mu_{R^M}(x_i, y_j)]$$

After the overall relation is generated, control actions are inferred from a two-step process. First, Zadeh's compositional rule of inference, an approximate extension of modus ponens [4], is used to find fuzzy output sets for fuzzy input sets. Second, because each output set has many elements, it is defuzzified to obtain a unique control action.

In general, Zadeh's rule generates fuzzy output sets for fuzzy input sets. However, if precise inputs are known, then fuzzy singleton inputs [6] are used to infer control actions. Fuzzy singletons are sets having one element with full membership, and all other elements have zero membership. This single element is a precisely measured process variable. If process variables can not be exactly quantified, then fuzzy input sets can be used. Note that the output from the inference process will be fuzzy regardless if the input is fuzzy or not.

Again for a controller with one input, a fuzzy output set $\mu_{Y'}(y_j)$ is inferred from a fuzzy input set $\mu_{X'}(x_i)$ by applying Zadeh's rule:

$$\mu_{Y'}(y_j) = \max_{x_i \in X} [\min [\mu_{X'}(x_i), \mu_R(x_i, y_j)]]$$

In words, the grade of membership of the inferred fuzzy set is the largest value over the universe of discourse for the controller input of the intersection of membership functions for an input set and the overall fuzzy relation. For all inputs being fuzzy singletons, the rule reduces to:

$$\mu_{Y'}(y_j) = \mu_R(x, y_j)|_{x=x_{\text{measured}}}$$

[1] Herein, this approach will be referred to as the "classical" approach.

where x specifies a precisely measured process quantity.

Since the controlled system only accepts nonfuzzy inputs, the inferred controller output set is defuzzified to obtain one control action. Mean-of-maximum and center-of-area are the two main defuzzification techniques most frequently employed. The mean-of-maximum method selects the control action having the largest grade of membership. For instances where more than one maximum occurs, an average is taken of the multiple maximums. This method only takes into account the strongest elements of the output set. The center-of-area technique chooses the element having half the area enclosed by the output membership function on one side of the element and half on the other side. All elements of the output set are taken into account by this method. As indicated by Larkin [7], the center-of-area technique is preferred because it yields better results with smaller control effort than the mean-of-maximum technique.

Several methods are used to implement the fuzzy logic algorithm as described above. If controller rules and parameters are static, control actions for selected fuzzy singletons can be calculated off-line prior to controller usage. These actions are placed in look-up tables for referencing during on-line control. Actions can also be calculated on-line using a computationally efficient algorithm.

Apparently, Larkin [7] was the first to describe such an algorithm. Pedrycz [8] later proposed the same algorithm. For each rule, the algorithm calculates a measure of how similar the inputs match the antecedents of that rule. This measure is used to "scale" the output set for the rule. The scaled output sets for all rules are combined through a union (max) operation to get the overall fuzzy output set. Thus, only rules that have antecedents similar to the inputs contribute to the overall output set. Defuzzification is now done on this set. Kosko ([5], Chap. 8) uses graphic arguments to describe modern variants of the algorithm. One of the more interesting variants uses simple addition of the grades of membership to combine the scaled output sets from each rule rather than using the max operation. The reader is referred to [5] for details.

As with any control system, questions of stability and tuning must be addressed. Although advances have been made [9], fuzzy stability theory is largely undeveloped. However, stable system behavior can be achieved through tuning. King and Mamdani [10] state that tuning can be accomplished in three different ways:

1 modify control rules,
2 change discretization levels of discretized membership functions, and
3 change definitions of the linguistic variables—modify the membership functions.

Concerning the second method, membership functions, while continuous in theory, are generally discretized to be manipulated

Nomenclature

$\mu_{R^m}(x_i, y_j)$ = grade of membership over relation space for mth rule
$\mu_R(x_i, y_j)$ = grade of membership for overall fuzzy relation
$\mu_{X^m}(x_i)$ = grade of membership for x_i element of fuzzy antecedent for mth rule
$\mu_{X'}(x_i)$ = grade of membership for fuzzy input set to compositional rule
$\mu_{y^m}(y_j)$ = grade of membership for y_j element of fuzzy consequent for mth rule
$\mu_{y'}(y_j)$ = grade of membership for inferred fuzzy output set of compositional rule

Conversion factors

°C = 5/9(°F-32)

1 kg/h = 2.21 lb/hr
1 m^3/min = 35.29 scfm

in digital computations. However, if membership functions consist of simple geometric shapes such as triangles, they do not need to be discretized to calculate defuzzified control actions. For example, when addition[2] is used to combine the scaled output sets and center-of-area defuzzification is used, the control action can be calculated as the average of the easily obtained centroids of the scaled output sets of individual rules.

King and Mamdani found the second method to be the most effective for tuning. However, Tong [11] argues via a relation matrix analysis that the best way to tune a fuzzy controller is to modify the control rules. He states that items 2 and 3 should be chosen to match qualitative assumptions made about the process and should not be changed unless the assumptions prove incorrect.

Experimental Apparatus and Procedures

A fluidized bed consists of a chamber filled with particles, such as sand and/or limestone, through which a stream of air is passed vertically upward [12]. If the air stream is at sufficiently high velocity, the drag force acting on the particles balances the weight of the particles; in this state the bed is said to be fluidized. A schematic of the computer-controlled FBC used in this research is depicted in Fig 1. The cylindrical combustor is of a novel two-bed design [13]. The inner bed is for the combustion of coal while the annular bed provides a mechanism for temperature control of the combustion bed.

The combustion bed is provided with air through a circular distributor plate from an air plenum. Coal is fed by auger into the combustion bed at a rate determined by the desired heat generation rate. If fluidization requirements are satisfied, air flow into this bed (known as primary air) is typically set at a level 20 percent greater than stoichiometric requirements to ensure good combustion. The annular heat transfer bed is supplied with air (known as secondary air) from another plenum. The annular bed is surrounded by a water jacket that removes heat from the combustor in the form of hot water. The annular bed acts as a thermal transistor. A variable secondary air flow rate controls the amount of heat released across the annular bed width to the water jacket, thereby providing a means for controlling combustion bed temperature independent of fuel feed rate.

[2] The addition method is in reference to a modern approach to fuzzy inferencing and not Zadeh's classical approach.

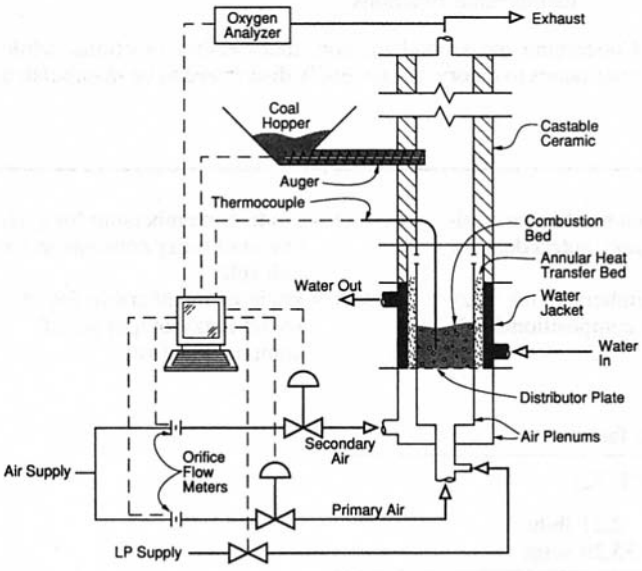

Fig. 1 Schematic of computer-controlled FBC

Control inputs for this system are fuel feed rate, primary air flow rate, and secondary air flow rate. System outputs are combustion bed temperature and oxygen percentage in flue gas indicating combustor efficiency.

The task of the controller is to mimic the following manual operating procedures. The combustor is brought up to a nominal operating point from ambient conditions by burning liquid-petroleum (LP) gas in the combustion bed. When a temperature of 1200°F is reached, coal feeding commences. LP gas flow is terminated at 1450°F—a point where coal combustion is self-sustaining.

When coal feeding begins at 1200°F, coal feed rate is not immediately set to its desired value. Instead, it is increased in small steps to avoid degraded combustor efficiency associated with incomplete combustion caused by large step changes in fuel feed rate. Flue gas oxygen, an indication of combustor efficiency, is maintained at 3.5 percent since this value implies complete combustion of the test coal with 20 percent excess air. When flue gas oxygen is below 3.5 percent, increments to feed rate are smaller.

Although not addressed in this study, sulfur dioxide can be captured from the waste gases by admitting limestone sorbent to the combustion bed. The rate of SO_2 absorption is maximized near 1600°F [14]. Therefore, to reduce SO_2 emissions in future studies, combustion bed temperature will be maintained at 1600°F.

Fuzzy Logic Controller Design

Implementation of a fuzzy controller for the FBC is outlined in this section; further details can be found in [15]. First, control rules were acquired by observing FBC operation and interviewing the human operator. Three different sets of control rules were obtained for this combustor—one set for controlling each of temperature, flue gas oxygen, and coal feed rate. Because temperature and flue gas oxygen have constant setpoints, 1600°F and 3.5 percent, respectively, an error signal for each of these variables is not necessary to drive the controller. Instead, control actions prescribed for these variables are based upon their current values. However, fuel feed rate is expected to have many different setpoints. Therefore, an error signal is generated for this variable. The form of each rule set is depicted below:

- If temperature = _____ and temperature change = _____, then secondary air flow rate adjustment = _____.
- If oxygen = _____ and oxygen change = _____, then primary air flow rate adjustment = _____.
- If oxygen = _____ and coal feed rate error = _____, then coal feed rate adjustment = _____.

In the last rule structure, fuel feed rate is present in both the input and output of the controller. This is done to implement the incremental firing rate approach. After the desired fuel feed rate is obtained, no more control actions occur for this loop. From this point on, the only adjustments are made to combustion bed and annular bed air flow rates to effect changes in flue gas oxygen concentration and combustion bed temperature, respectively.

Output of the control rules represents changes to be made to control settings of the combustor. This type of output implements an incremental control scheme. An incremental approach is used because the human operator of the FBC was only able to state approximately how much he would change combustor inputs for given combustor states. An added benefit of incremental control is that control actions are summed to force process outputs to their respective setpoints at steady state.

Before the operator could be quizzed about his actions, the questions had to be formulated by asking the operator to describe input conditions to the above rule structure. Using these descriptions as fuzzy set names of the antecedents, questions

Table 1 Truth table of temperature control rules

T_{BED}	ΔT_{BED}	ΔSec. air flow
LOW	POSITIVE LARGE	NONE
LOW	NEAR ZERO	LESS
LOW	NEGATIVE LARGE	LESS
OK	POSITIVE LARGE	MORE
OK	NEAR ZERO	NONE
OK	NEGATIVE LARGE	LESS
HIGH	POSITIVE LARGE	MORE
HIGH	NEAR ZERO	MORE
HIGH	NEGATIVE LARGE	NONE

for a particular rule set were generated by using all possible combinations of these descriptions. The operator characterized combustion bed temperature and flue gas oxygen as either "low," "ok," or "high." Temperature change, oxygen change and coal feed rate error were identified as "positive large," "near zero," or "negative large."

The operator was then asked to list his actions for each question. The actions were given as "more," "none," or "less" for increments in control settings. These labels are used to describe changes in all controller outputs, but "more," for example, has a different meaning for changes in primary air than it does for secondary air.

As an example of the rules, the rule set for temperature control is examined here. These rules are given in "truth table" format in Table 1. Some rules have the same response for similar antecedents. Take, for example, the second and third entries in Table 1. They can be combined into one rule by defining the new fuzzy set NOT POSITIVE LARGE, which is simply the complement of POSITIVE LARGE. The new rule reads as:

> If temperature = LOW and temperature change = NOT POSITIVE LARGE, *then* secondary air flow rate adjustment = LESS.

Thus, this rule set can be reduced. The process is analogous to Karnaugh mapping [16] used in digital circuit design. Rule reduction is not always possible; it depends upon the operator's responses. Whenever one antecedent changes between two rules and no corresponding change occurs in the consequents between the rules, reduction is possible.

The operator now needs to explain what he considers "low," "ok," "high," etc. which is the formation of membership functions for all fuzzy sets. To generate membership functions for a particular variable, the operator was asked what was 100 percent "low," 100 percent "ok," and 100 percent "high" as well as what was 0 percent "low," 0 percent "ok," and 0 percent "high" for the variable. Because the operator tended to think linearly when comparing magnitudes, fuzzy sets were generated by drawing straight lines through 100 percent points to 0 percent points for each fuzzy state of the variable. Figure 2 illustrates this point for temperature fuzzy sets. The desired temperature is 1600°F, which is 100 percent "ok" temperature. Temperature could drop to 1525°F and could rise to 1675°F before being completely intolerable. The 1525°F and 1675°F are the 0 percent end points for OK. LOW and HIGH were similarly obtained.

After all fuzzy sets are established, their discretization levels are selected. The levels need to be judiciously chosen to balance between fineness of control and extensive computational load caused by using small discretization levels. Discretization levels for input sets were chosen as twice the values that the controlled variables were desired to be within their setpoints at steady state. Note that the controller will take no action when controlled variables fall within half a discretization level away from their setpoints because each input is rounded to the nearest element of its universe of discourse before calculating control actions. Thus, when inputs fall within less than half the interval of their respective discretization levels from their desired values, the inputs are rounded to their desired values causing no controller action. The discretization levels of the output sets are chosen slightly larger than the largest increments in the manipulated variables that still allow controlling the controlled variables to within half a discretization level from their setpoints. The slightly larger levels are chosen because the defuzzification process will produce finer control actions than the discrete elements of the fuzzy output sets.

For example, consider temperature fuzzy sets and corresponding fuzzy sets for adjustments to secondary air flow. For the temperature sets, a discretization level of 10°F was chosen because temperature was desired to be within 5°F of its setpoint at steady state. Fuzzy sets describing adjustments to secondary air have discretization intervals of 0.5 scfm. This level will produce control actions that still allow tuning of temperature to within 5°F of its setpoint.

The last consideration in controller implementation is sampling time. As in any sampled-data system, sampling time affects the system's dynamic response. Also, sampling time, as well as membership functions, affects effective gains of the fuzzy controller using incremental output. The human operator said he would enact new control actions approximately every 30 seconds. Desiring to obtain more "accurate" sampling time, the combustor was operated under fuzzy control with a human observer deciding when new control actions were to be applied. Determining the sampling time is best described as a cognitive process. When the human observer perceived sufficient system response to previous actions, new actions were given. This type of behavior is reminiscent of a "wait-and-see" controller [17]. A sampling time of 20 seconds produced the best result and was selected as the final sampling period.

In this investigation, the FBC is controlled by referencing control actions in look-up tables. With all implementation decisions made, control actions were calculated using fuzzy logic inferencing and then placed in look-up tables.

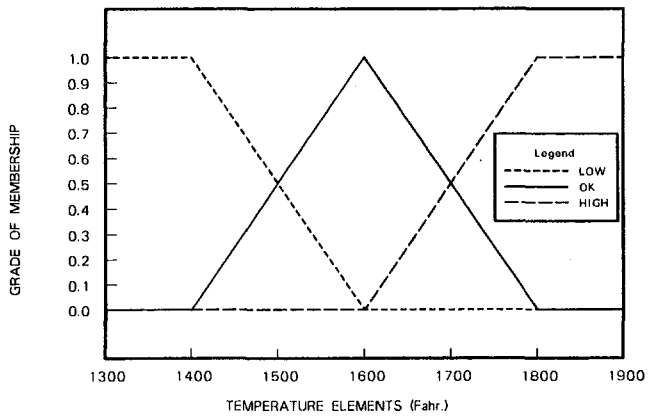

Fig. 2 Relation between membership functions for LOW, OK, and HIGH combustor temperature

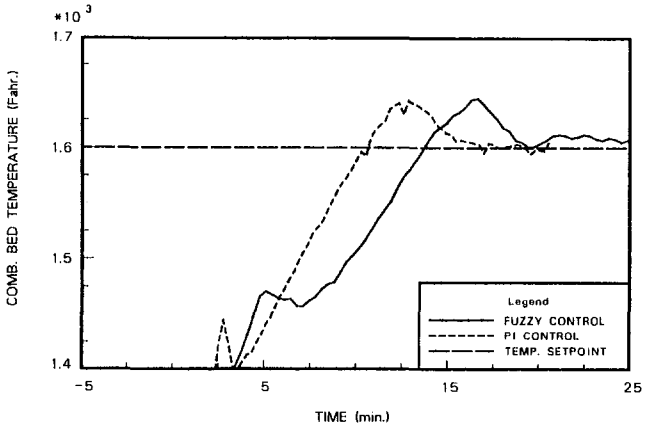

Fig. 3 Temperature responses for fuzzy and PI control during start-up

Table 2 Comparison of fuzzy and PI control using settling time and IAE criteria

	Variable affected	$T_{settling}$[a]		IAE[b]	
		Fuzzy	PI	Fuzzy	PI
Startup	Temp.	18.36	15.44	2177.6	1768.0
Response	Oxygen	9.84	5.36	9.5	10.3
Disturbance	Temp.	7.49	6.36	86.4	52.7
Response[c]	Oxygen	3.40	1.27	2.4	1.4

[a] For temperature responses, this is the time to enter a ±10°F band about 1600°F. For oxygen responses, this is the time to enter a ±0.75 percent band about 3.5 percent oxygen. In both cases, units are in minutes.
[b] Units are in °F · min. for temperature responses and percent min. for oxygen responses.
[c] The disturbance is a 5 lb/hr reduction in coal feed rate.

Results and Discussion

The following results are typical of fuzzy control and classical PI control of the FBC. Classical control is presented to evaluate the fuzzy controller's performance. For the PI controller, gains were designed by the Ziegler–Nichol method. Gain scheduling is employed for oxygen control as constant gains will not satisfactorily control oxygen for both operating régimes of LP gas preheating and coal feeding. The PI control actions are enacted as fast as possible (approximately every 0.6 seconds on a PC/XT) since gains from the Ziegler–Nichols method are determined for continuously operated systems. Comparisons between the controllers are based upon settling time and Integral of Absolute Error (IAE); these values are listed Table 2.

Figure 3 shows combustion bed temperature for both controllers. Although not shown, these temperatures rise from an ambient 70°F to 1200°F from solely burning LP gas in the combustor. When temperature reaches 1450°F, LP gas flow is terminated, causing a slight temperature drop. The PI controller shows a larger drop in temperature than does the fuzzy controller.

As temperature surpasses its setpoint, the controllers increase secondary air to increase cooling of the combustion bed. Each controller roughly gives the same overshoot, but temperature for the PI controller reaches a ±10°F band about the setpoint 2.9 minutes faster than the fuzzy controller. Also, the IAE criterion for PI control is 18.8 percent smaller than for fuzzy control.

Here, the PI controller's faster response is expected since a greater bed loading (amount of fuel present in the combustor) is initially present due to immediately setting coal feed rate to the desired value. In this instance, the performance criteria are deceptive because high heating rate can cause thermal stresses to crack the combustor's ceramic lining. Most industrial operations require low heating rates to reduce thermal stressing of their systems. Although not considered in this investigation, control loops for heating rate could have been added to both controllers.

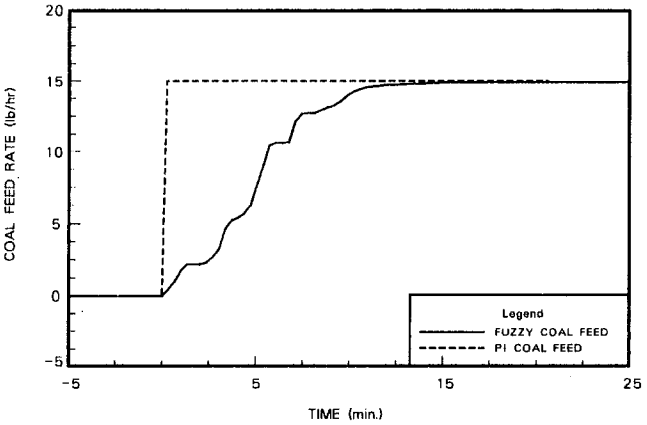

Fig. 5 Coal feed rates for fuzzy and PI control during start-up

Figure 4 shows flue gas oxygen responses. Oxygen percentage starts at an ambient 21 percent and rapidly decreases when LP gas is ignited. The controllers adjust primary air to maintain flue gas oxygen at its setpoint of 3.5 percent. For both controllers, the large downward swing in oxygen about the setpoint results from introduction of coal into the combustor, and the single large upward spike results from LP gas shut-off.

The PI controller exhibits a large, lengthy decrease in oxygen as coal feed rate is immediately set to the desired value of 15 lb/hr. Oxygen response for fuzzy control has similar characteristics but not nearly as severe as those for PI control. After LP gas is turned off, the fuzzy controller has a smaller oxygen peak but also has a greater oxygen valley than does the PI controller. The PI controller causes oxygen to settle within a ± 0.75 percent band about the setpoint 4.5 minutes faster but has 8.4 percent more IAE than the fuzzy controller.

Figure 5 depicts coal feed rates. The fuzzy controller increases feed rate in a stepwise fashion, so as not to decrement combustor efficiency severely. When flue gas oxygen is low, increments in feed rate for fuzzy control are also low (see Figs. 4 and 5). Feed rate for PI control is immediately set to the desired value because it was believed that a *logical* stepping up of coal feed rate based on flue gas oxygen was not consistent with a classical framework. However, for future studies, the authors will incorporate ramping up feed rate for PI control with the ramping rate determined by flue gas oxygen content.

During the start-up test, the PI controller used 17.5 scfm more primary air flow than did the fuzzy controller, as shown in Fig. 6. High air flow rates can blow small bed and fuel

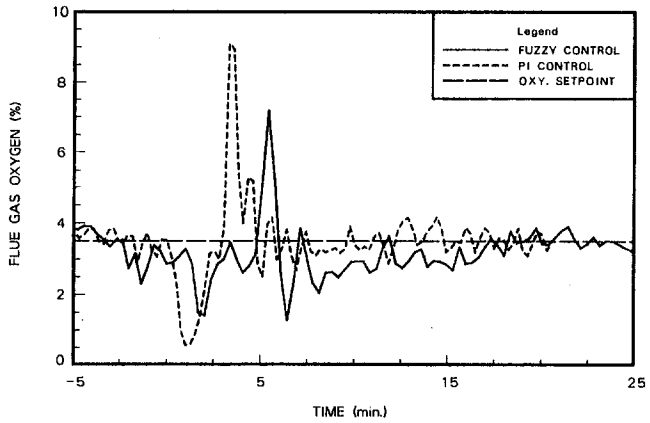

Fig. 4 Oxygen responses for fuzzy and PI control during start-up

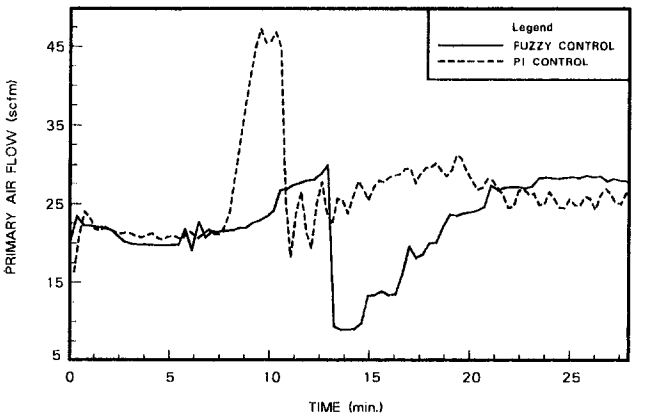

Fig. 6 Primary air flows for fuzzy and PI control during start-up

particles from the combustor. For this investigation, an oxygen criterion is used as a measure of combustor efficiency, but true efficiency can only be determined by evaluating the amount of unburned carbon in the fly ash. At the time these tests were conducted, no method existed to measure the amount of elutriated carbon on-line. If this carbon could have been measured, the fuzzy controller would have appeared even more preferable to the PI controller than that indicated in Fig. 6. These observations validate the "stepwise" approach taken to increment feed rate under fuzzy control. Also, another difference between controllers is that the transition from LP gas preheating to coal feeding is handled by the fuzzy controller in a robust manner in terms of oxygen control. The same fuzzy control law is used for both operating régimes whereas the PI controller needs to use gain scheduling to manage the transition.

The next test shows the controllers' responses for a 5 lb/hr reduction in coal feed rate. Figure 7 depicts temperature responses for the two controllers. Both controllers demonstrate similar temperature drop. However, the PI controller exhibits settling time 1.1 minutes faster than the fuzzy controller, also, IAE for the PI controller is 39 percent less than that for the fuzzy controller. Figure 8 shows flue gas oxygen responses for the feed rate reduction. Although the PI controller has larger peak oxygen, it also has a settling time 2.1 minutes faster and 41.7 percent less IAE.

As a final word, the PI controller's faster responses, other than heating rate are attributed mainly to its faster sampling time of 0.6 seconds as opposed the 20 seconds for the fuzzy controller. The combustor under fuzzy control has 19.4 seconds more than the combustor under PI control to wander off course before control adjustments are made. Recall that the fuzzy controller's sampling time was selected/limited by human cognition of combustor responses. A scheme could be devised to project fuzzy controller actions designed with a "cognitive" time of 20 seconds back to quicker times by normalizing controller increments. That is, control actions could be divided by 20 and multiplied by a new sampling time to get projected incremental control actions. Such a controller should exhibit better performance than the nominal fuzzy controller.

Conclusions

The fuzzy controller satisfactorily achieved the desired objectives. The PI controller, used for evaluating the fuzzy controller's performance, also gave desirable responses, usually faster than the fuzzy controller. The PI controller's faster response times are mainly attributed to the controller's faster sampling rate. Although the fuzzy controller's performance was good, it could be improved by projecting control actions to quicker sampling rates by normalizing nominal control actions.

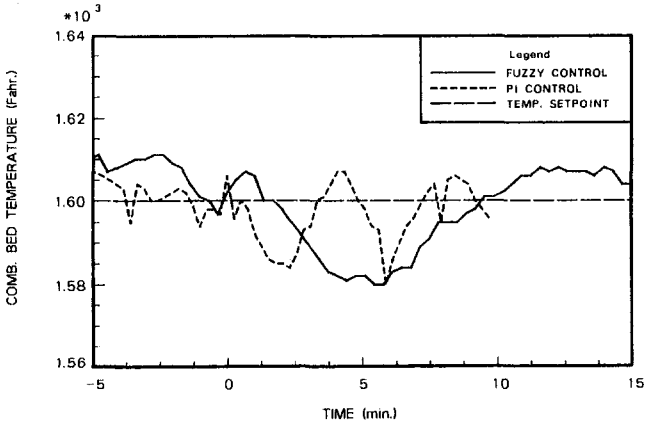

Fig. 7 Temperature responses for fuzzy and PI control for feed rate reduction

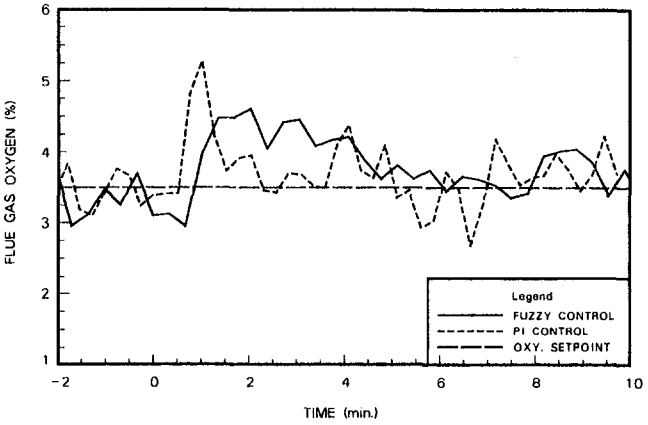

Fig. 8 Oxygen responses for fuzzy and PI control for feed rate reduction

Even with the lengthy 20-second sampling time, the fuzzy controller is preferred during start-up because of its much lower primary air flow requirement for good oxygen control. The fuzzy controller also exhibits a robust nature not seen in the PI controller for the transition between LP gas preheating and coal feeding. As for normal operation, the PI controller is preferred because of its quicker rejection of disturbances.

The possibility of using a hybrid controller for FBCs is suggested—fuzzy control during start-up and PI control during normal operation. However, further tests with the fuzzy controller using a faster sampling time need to be conducted before trying this approach. A faster fuzzy controller may perform better than the PI controller, in which case fuzzy control could be used exclusively.

References

1 McFarlane, R. C., Hoffman, T. W., Taylor, P. A., and MacGregor, J. F., "Control of Fluidized Bed Reactors. 1. Modeling, Simulation, and Single-Loop Control Studies," *Industrial Engineering: Chemical Process Design and Development,* Vol. 22, 1983, pp. 22–31.

2 Åström, K. J., and Wittenmark, B., *Computer-Controlled Systems: Theory and Design,* Prentice-Hall, Inc., Englewood Cliffs, NJ, 1984, pp. 186–187.

3 Zadeh, L. A., "Fuzzy Sets," *Information and Control,* Vol. 8, 1965, pp. 338–353.

4 Zadeh, L. A., "Outline of a New Approach to Analysis of Complex Systems and Decision Processes," *IEEE Transactions on Systems, Man, and Cybernetics,* Vol. SMC-3, 1973, pp. 28–44.

5 Kosko, B., *Neural Networks and Fuzzy Systems: A Dynamical Systems Approach to Machine Intelligence,* Prentice-Hall, Inc., Englewood Cliffs, NJ, 1992.

6 Tong, R. M., "A Control Engineering Review of Fuzzy Systems," *Automatica,* Vol. 13, 1977, pp. 559–569.

7 Larkin, L. I., "A Fuzzy Logic Controller for Aircraft Flight Control," in: *Industrial Applications of Fuzzy Control,* M. Sugeno, ed., North-Holland, Amsterdam, 1985, pp. 87–103.

8 Pedrycz, W., *Fuzzy Control and Fuzzy Systems,* Research Studies Press Ltd., Taunton, Somerset, United Kingdom, 1989, pp. 73–74.

9 Kiszka, J. B., Gupta, M. M., and Nikiforuk, P. N., "Energetistic Stability of Fuzzy Dynamic Systems," *IEEE Transactions on Systems, Man, and Cybernetics,* Vol. SMC-15, 1985, pp. 783–792.

10 King, P. J., and Mamdani, E. H., "The Application of Fuzzy Control Systems to Industrial Processes," *Automatica,* Vol. 13, 1977, pp. 235–242.

11 Tong, R. M., "Analysis of Fuzzy Control Algorithms Using the Relation Matrix," *International Journal of Man-Machine Studies,* Vol. 8, 1976, pp. 679–686.

12 Kunii, D., and Levenspiel, O., *Fluidization Engineering,* Wiley, New York, 1969.

13 Brown, R. C., and Foley, J. E., "A Method for Improving Load Turndown in Fluidized Bed Combustors," *Industrial and Engineering Chemistry Research,* Vol. 27, 1987, pp. 24–30.

14 Gibbs, B. M., and Hampartsoumian, E., "Limiting Air Pollution From Atmospheric Fluidised Bed Combustors," in: *Fluidized Bed Boilers: Design and Application,* P. Basu, ed., Pergamon Press, Toronto, 1984, pp. 131–154.

15 Koffman, S. J., "Fuzzy Logic Control of a Fluidized Bed Combustor," M. S. Thesis, Iowa State University, Ames, IA, Spring, 1990.

16 Mano, M. M., *Digital Design,* Prentice-Hall, Inc., Englewood Cliffs, NJ, 1984, pp. 72–83.

17 Doebelin, E. O., *Control System Principles and Design,* Wiley, New York, 1985, pp. 485–486.

Functional Forms to Describe Thermodynamic Properties of Gases for Fast Calculations

J. Pátek
Institute of Thermomechanics,
Czechoslovak Academy of Sciences,
Dolejškova 5,
18200 Prague 8, Czech Republic

A simple way to derive physically based functional forms for approximate description of thermodynamic properties of gases is presented. The polynomials in transformed variables obtained are intended for fast industrial calculations. The approach is applied on eleven thermodynamic dependencies with pairs of independent variables most frequently encountered in turbine calculations. These functional forms were originally derived for the description of steam properties, but they are equally applicable to any gas in adequate region of state parameters. Approximation function for the dependence T(h, s) of steam is presented as an example including the values of 18 fitted parameters.

Introduction

The design of processes and apparatus in the field of energy technology and chemical engineering requires a sufficiently accurate, effectively computerized, and time-efficient description of the thermophysical properties of the working fluids. This description must be valid over a wide range of state parameters.

It appears difficult to meet all these demands simultaneously within a framework of a single thermodynamically consistent formulation. These formulations commonly use temperature and pressure or density as input parameters. As the industrial calculations require different pairs of independent variables, time-consuming iterations or approximation techniques have to be executed. Iterative evaluations can be avoided by using simplified approximation equations in required variables (called reversal functions) valid with adequate accuracy within a restricted range sufficient for solution of a particular type of problem.

Reversal functions can be constructed as correlation functions for a suitably chosen set of data points calculated by means of a thermodynamically consistent and sufficiently accurate formulation of properties of the gas.

Background

Water is one of the fluids widely used in modern technological applications and it is therefore well investigated and analyzed. Two thermodynamic property formulations have been given international recognition in release form by the International Association for Properties of Steam (IFC, 1967; Sytchev and White, 1984). In both cases the input parameters are v, T or p, T.

In addition to these internationally recognized formulations, a number of particular functions or their subsystems have been constructed by various authors for diverse thermodynamic relationships and couples of independent variables (Campbell and Jener, 1980; Dohrendorf and Schwindt, 1970; Magerfleisch, 1979; McClintock and Silvestri, 1979; Meyer-Pittrof and Vesper, 1969; Meyer-Pittrof and Grigull, 1969; Schwindt, 1978; Tratz, 1962; Young, 1988; Ziskuhr, 1974). These functions differ from one another in range of validity, accuracy, functional form, and intended application. Polynomials and rational functions in the original (untransformed) variables are most frequently employed as the fitting functions.

Contributed by the Power Division for publication in the JOURNAL OF ENGINEERING FOR GAS TURBINES AND POWER. Manuscript received by the Power Division March 18, 1992. Associate Technical Editor: R. W. Porter.

Derivation of the fitting functions structure presented here has been motivated by the effort to get a simple approximation of the superheated steam properties, which depend on the couples of independent variables most frequently used in power engineering. The state parameter region sufficient for common turbine calculations extends from the saturation line up to 600°C and between isobars 0.001 MPa and 30 MPa. The following functions were identified as those most frequently used in these calculations (Kretzschmar et al., 1987; Meyer-Pittrof, 1986)

$$\begin{array}{lll} v(p,T) & h(p,T) & s(p,T) \\ v(p,h) & T(p,h) & s(p,h) \\ v(T,s) & T(p,s) & h(p,s) \\ p(h,s) & T(h,s) & \end{array} \tag{1}$$

Starting from demands declared by various users (Rukes, 1990) the following limits for maximum relative (δx) or absolute (Δx) deviations from the accurate formulation might be considered reasonable for many industrial calculations:

$$|\delta v| \le 0.05 \text{ percent}, \quad |\delta p| \le 0.05 \text{ percent}, \quad |\Delta T| \le 0.1 \text{ K},$$

$$|\Delta h| \le 1 \text{ kJ/kg} \quad (0.43 \text{ Btu/lb})$$

$$|\Delta s| \le 0.0005 \text{ kJ/(kg·K)} \quad (0.00012 \text{ Btu/lb·R}) \tag{2}$$

Depending on the nature of the calculations, thermodynamic consistency of a formulation may be required to an accuracy better then might otherwise be apparent, in order to ensure convergence of iterative engineering calculations. Tighter tolerances than those of (2) are then required (Rukes, 1991). Thus the use of the simplified approximation equations presented below is limited to suitable applications.

Fitting Functions Structure Development

The demands (2) can be satisfied using the following relatively simple approach. The fitting function of thermodynamic property $z(x, y)$ is sought in the form of a polynomial in transformed variables ξ, ν, ζ:

$$\zeta = \sum_{i}^{N} a_i \xi^{m_i} \nu^{n_i} \tag{3}$$

Table 1 Selected thermodynamic functions of the ideal gas with constant specific heat c_P and c_V

$v(p,T)$	RT/p
$h(p,T)$	$c_pT + h_0$
$s(p,T)$	$s_0 + c_p\ln(T/T_0) - R\ln(p/p_0)$
$v(p,h)$	$(R/c_p).(h-h_0)/p$
$T(p,h)$	$(h-h_0)/c_p$
$s(p,h)$	$s_0 + c_p\ln[(h-h_0)/(c_pT_0)] - R\ln(p/p_0)$
$T(p,s)$	$T_0\exp[(s-s_0)/c_p].(p/p_0)^{R/c_p}$
$h(p,s)$	$c_pT_0\exp[(s-s_0)/c_p].(p/p_0)^{R/c_p} + h_0$
$v(p,s)$	$(v_0p_0/p).\exp[(s-s_0)/c_p)].(p/p_0)^{R/c_p}$
$T(h,s)$	$(h-h_0)/c_p$
$p(h,s)$	$\left\{[(h-h_0)/(c_pT_0)].\exp[(s_0-s)/c_p]\right\}^{c_p/R}$

Table 2 Transformed variables derived from the ideal gas functions

$z(x,y)$	$\zeta(x,y,z)$	$\xi(x,y)$	$\upsilon(x,y)$
$v(p,T)$	$(vp/T).(T_c/v_cp_c)$	T_c/T	p/p_c
$h(p,T)$	$(h-h_c)/c_p$	T_c/T	p/p_c
$s(p,T)$	$s-s_c-c_p\ln(T/T_c)+R\ln(p/p_c)$	T_c/T	p/p_c
$v(p,h)$	$(vp)/(v_cp_c)$	$(h-h_c)/c_p$	$(p/p_c)^{1/2}$
$T(p,h)$	T/T_c	$(h-h_c)/c_p$	$(p/p_c)^{1/4}$
$s(p,h)$	$\exp[(s-s_c)/c_p]$	$[(h-h_c)/c_p]^{1/2}$	$(p/p_c)^{R/c_p}$
$v(p,s)$	$(vp)/(v_cp_c)$	$\exp[(s-s_c)/c_p]-1$	$(p/p_c)^{R/c_p}$
$T(p,s)$	T/T_c	$\exp[(s-s_c)/c_p]$	$(p/p_c)^{R/c_p}$
$h(p,s)$	$(h-h_c)/c_p$	$\exp[(s-s_c)/c_p]-1$	$(p/p_c)^{R/c_p}$
$T(h,s)$	T/T_c	$[(h-h_c)/c_p]^{1/2}$	$\exp[(s_c-s)/3R]$
$p(h,s)$	$(p/p_c)^{R/c_p}$	$(h-h_c)/c_p$	$\exp[(s_c-s)/c_p]$

where

$$\zeta = Z(x, y, z); \quad \xi = X(x, y); \quad \nu = Y(x, y) \tag{4}$$

are variables transformed by means of suitable functions. The explicit general form of the fitting function is then

$$z = F\{x, y, Q[\xi(x, y), \nu(x, y)]\}, \tag{5}$$

where F denotes the inverse transformation of the dependent variable ζ defined by the identical relation

$$z = F[x, y, \zeta(x, y, z)]. \tag{6}$$

Q is the polynomial (3) optimum in the sense of minimum sum of square deviations. Its terms can be determined by any regression method developed for this purpose (e.g., de Reuck and Armstrong, 1979; Setzman and Wagner, 1989). In this way the transformed relation is fitted by a polynomial in the transformed variables suitably selected for this purpose and only then it is transformed back to the original variables.

The suitable form of the variables ξ, ν, ζ for description of thermodynamic properties of gases can be derived using the model of ideal gas or van der Waals gas if necessary. In Table 1 a survey of thermodynamic functions (1) of the ideal gas with constant specific heat c_P and c_V is given. It is evident from these expressions that for most functions under consideration, the transformed variables can be selected in such a way that in the case of an ideal gas the transformed dependence is linear. For example if new variables for $v(p, s)$ are defined as

$$\xi(p, s) = (p/p_0)^{R/c_P},$$
$$\nu(p, s) = \exp[(s - s_0)/c_P],$$
$$\zeta(p, s, v) = (vp)/(v_0p_0), \tag{7}$$

the transformed relation $\zeta(\xi, \nu)$ takes the following form:

$$\zeta = \xi\nu. \tag{8}$$

The same function of real gas, expressed in such transformed variables, can be then approximated with a polynomial composed of a relatively low number of terms.

In Table 2, the functions $X(x, y)$, $Y(x, y)$, $Z(x, y, z)$, derived from the ideal gas functions (Table 1) are presented, after some modifications as mentioned below. A critical point is selected here as the reference state, so that it holds $v_O = v_C$, $T_0 = T_C$, $p_0 = p_C$, etc., and the variable $(h - h_0)/(c_PT_0)$ is replaced by $(h/h_C - 1)$, equivalent as regards the general form of the fitting function. The transformed variables for the dependence $T(p, s)$ derived from ideal gas relations are used without additional modifications. Concerning the other functions, fractional exponents or the origin of the independent variable shifted to the critical point are used in cases when such modification results in fewer deviations or a lower number of fitting polynomial terms. The terms with fractional exponents are suitable for relations with negative second derivatives minimal in one of the border points of the interval of interest.

So the origin of transformed entropy is shifted into the critical point in the case of $v(p, s)$ and $h(p, s)$ and fractional exponents in transformed pressure are introduced for $v(p, h)$ and $T(p, h)$ as well as in transformed enthalpy for $s(p, h)$ and $T(h, s)$.

Ideal gas relationships naturally provide no basis concerning the dependence of $T(p, h)$ on pressure and $T(h, s)$ on entropy. To derive it, it is necessary to make use of a state equation implying nontrivial dependence on the required variables, for example, the van der Waals equation

$$p = RT/(v - b) - a/v^2, \quad b = v_C/3,$$
$$a = (9/8)\cdot RT_Cv_C \tag{9}$$

which gives for enthalpy and entropy

$$h = c_pT + RT\cdot b/(v - b) - 2a/v + h_0, \tag{10}$$

$$\exp[(s - s_0)/c_V] = T/T_0\cdot[(v - b)/v_0]^{R/c_V}. \tag{11}$$

The required form of dependence of $T(h, s)$ on entropy follows from these expressions by eliminating the variable v and expressing T explicitly as a function of h and s. We suppose for this purpose that the terms containing the constants a and b introduce the dependence of T on entropy as a small deviation compared to the ideal gas relation. Consequently temperature can be substituted here by the approximate expression $T =$

Nomenclature

a_i = fitted coefficient
c_P = specific heat at constant pressure
c_V = specific heat at constant volume
h = specific enthalpy
p = pressure
R = gas constant
s = specific entropy
T = temperature, K
v = specific volume

Subscripts

0 = reference state
c = critical point

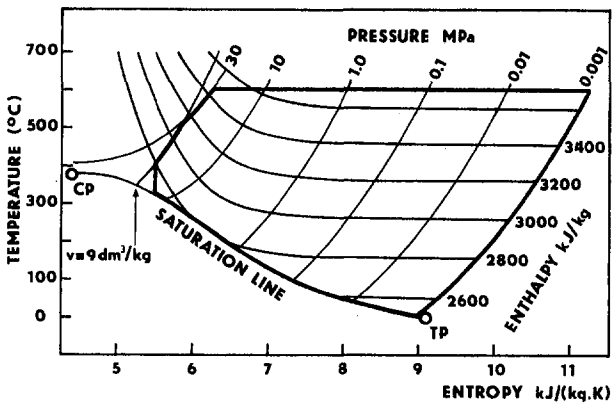

Fig. 1 Entropy dependence of steam temperature along isenthalpic lines

$(h - h_0)/c_P$. Retaining only the term linear on v_C/v, we obtain the expression

$$T/T_0 = \xi + (R/c_V)\cdot\xi^{c_V/R}\cdot\exp[(s_0 - s)/R]\cdot \quad (9/4 - \xi/3) \tag{12}$$

with

$$\xi = (h - h_0)/(c_P T_0),$$

implying as a suitable transformed variable for entropy

$$\nu = \exp[(s_0 - s)/R]. \tag{13}$$

The graphs of the original and transformed isenthalpic lines of $T(h, s)$ are compared in Figs. 1 and 2. The temperature is close to a constant along the particular lines of constant enthalpy in the subregion corresponding to low pressures. Consequently the dependence cannot be fitted well using any polynomial here. The transformation (13) solves this difficulty by transforming the whole low-pressure region close to the origin of the new independent variable. The variable $\exp[(s_0 - s)/3R]$, corresponding to the application of fractional exponent with denominator equal to 3, provides best results.

An analogous procedure based on the van der Waals equation results in the variable p/p_0 for $T(p, h)$, but $\xi(p, h) = (p/p_0)^{1/4}$ provided much better results and was therefore selected. Similarly for the relations $v(p, T)$, $h(p, T)$, $s(p, T)$, it follows that terms with negative exponents for temperature and positive exponents for pressure are to be preferred. The resulting recommended forms of the fitting functions are given

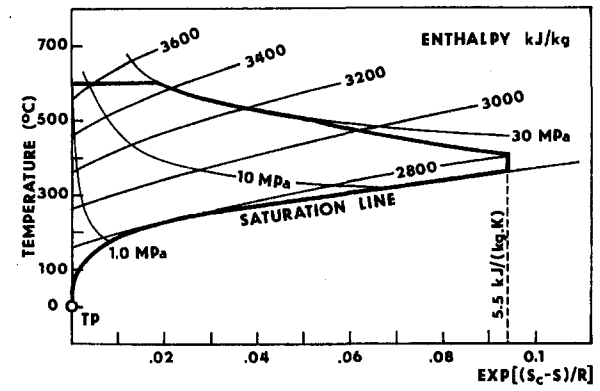

Fig. 2 Dependence of steam temperature versus transformed entropy variable at constant enthalpy

Table 3 Resultant functional expressions

$$v(p,T) = RT/p + v_c \sum_1^N a_i (T_c/T)^{m_i} (p/p_c)^{n_i}$$

$$h(p,T) = h_c \sum_1^N a_i (T_c/T)^{m_i} (p/p_c)^{n_i}$$

$$s(p,T) = s_c + c_p \ln(T/T_c) - R\ln(p/p_c) + \sum_1^N a_i (T_c/T)^{m_i} (p/p_c)^{n_i}$$

$$v(p,h) = v_c (p_c/p) \sum_1^N a_i (h/h_c - 1)^{m_i} (p/p_c)^{n_i/2}$$

$$T(p,h) = T_c \sum_1^N a_i (h/h_c - 1)^{m_i} (p/p_c)^{n_i/4}$$

$$s(p,h) = s_c + c_p \ln\left[\sum_1^N a_i (h/h_c - 1)^{m_i/2} (p/p_c)^{n_i R/c_p} \right]$$

$$v(p,s) = v_c (p_c/p) \sum_1^N a_i \{\exp[(s - s_c)/c_p] - 1\}^{m_i/2} (p/p_c)^{n_i R/c_p}$$

$$T(p,s) = T_c \sum_1^N a_i \exp[m_i (s - s_c)/c_p] \cdot (p/p_c)^{n_i R/c_p}$$

$$h(p,s) = h_c \sum_1^N a_i \{\exp[(s - s_c)/c_p] - 1\}^{m_i/2} (p/p_c)^{n_i R/c_p}$$

$$T(h,s) = T_c \sum_1^N a_i (h/h_c - 1)^{m_i/2} \exp[n_i (s_c - s)/3R]$$

$$p(h,s) = p_c \left\{ \sum_1^N a_i (h/h_c - 1)^{m_i} \exp[n_i (s_c - s)/c_p] \right\}^{c_p/R}$$

in Table 3. They are not fundamentally thermodynamically consistent; their numerical consistency depends on the accuracy achieved in a particular application.

The functional forms presented above were used by Pátek and Šifner (1991) to approximate thermodynamic properties of superheated water in the region of state parameters marked in Fig. 1 by bold line. The fitted data used were calculated from the 1984 IAPS Formulation. The fitting polynomials obtained have no more than 20 terms, except for the polynomials for $T(p, s)$, which has 27 terms, and $T(p, h)$ which has 25 terms. Approximating the respective thermodynamic relationships with maximum deviations within the limits (2) they suit the needs of many industrial calculations.

In Table 4 the exponents m_i, n_i of polynomial terms $\xi^{m_i}\nu^{n_i}$ and associated coefficients a_i for dependence $T(h, s)$ approximated by means of the functional form given in Table 3 are presented as an example. The deviations of the fitting function from the fitted data are shown in Fig. 3.

Conclusion

The general structure of the fitting functions presented here is by no means bound up with steam and can be employed for description of thermodynamic properties of any other gas in an analogous region of state parameters.

Table 4 Exponents and coefficients of the approximation function $T(h, s)$

i	m_i	n_i	a_i	i	m_i	n_i	a_i
1	2	0	0.519279E+01	10	6	3	-0.132842E+02
2	3	0	-0.157931E+02	11	0	4	-0.945244E+01
3	4	0	0.294422E+02	12	2	4	0.254967E+02
4	5	0	-0.224513E+02	13	6	4	-0.119913E+02
5	7	0	0.625539E+01	14	3	5	-0.191337E+01
6	10	0	-0.995044E+00	15	0	6	-0.290979E+02
7	0	3	0.106939E+02	16	8	6	-0.323930E+03
8	2	3	-0.295281E+02	17	2	9	0.729229E+03
9	4	3	0.532225E+02	18	6	13	-0.405753E+05

T_c = 647.126 K, R = 0.461513 kJ/(kg.K)

h_c = 2086 kJ/kg, s_c = 4.409 kJ/(kg.K)

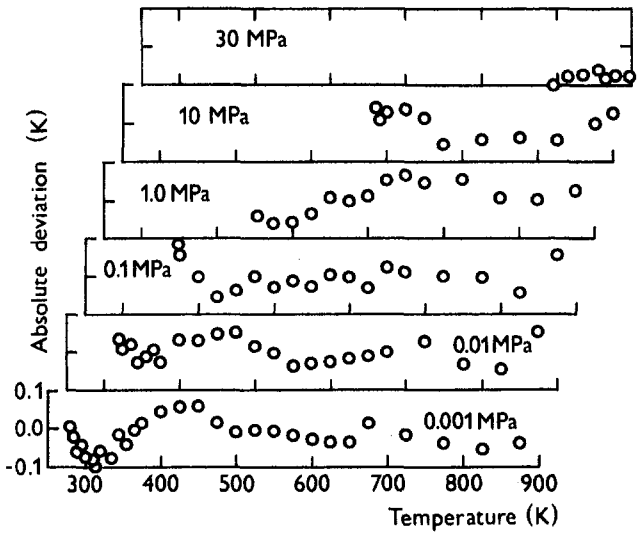

Fig. 3 Deviations of the approximation equation for $T(h, s)$ from 1984 IAPS Formulation data along selected isobars

The same approach gives suitable transformed variables for further thermodynamic relationships in the single-phase region employed in other types of problems surveyed by Kretzshmar et al. (1987), e.g., $p(T, s)$, $p(v, s)$, $T(v, s)$, $p(v, h)$. The following equations are recommended for them:

$$p(T, s) = p_C \{ \sum_i^N a_i (T/T_C)^{m_i} \exp[n_i (s_C - s)/c_P] \}^{c_P/R}$$

$$p(v, s) = p_C \{ \sum_i^N a_i (v/v_C)^{m_i} \exp[n_i (s_C - s)/c_P] \}^{-c_P/c_V}$$

$$T(v, s) = T_C \sum_i^N a_i (v_C/v)^{m_i R/c_V} \cdot \exp[n_i (s - s_C)/c_V]$$

$$p(h, v) = p_C \sum_i^N a_i (h/h_C - 1)^{m_i} (v_C/v)^{n_i}.$$

All equations obtained in this way can be employed in preliminary industrial calculations and evaluation of starting values for iterative procedures in more complex thermodynamically consistent formulations of properties of gases.

References

Campbell, J. W., and Jener, R. W., 1980, "Computational Steam/Water Property Routines for Industrial Use," *Proceedings, 9th International Conference on the Properties of Steam,* J. Straub and K. Scheffler, eds., Pergamon Press, Oxford, pp. 142–149.

Dohrendorf, E., and Schwindt, H., 1970, "Näherungsformeln für die Zustandsgrössen des Wasserdampfes Abhängigkeit von Enthalpie und Entropie," *Brennstoff-Warme-Kraft,* Vol. 22, pp. 578–583.

IFC, 1967, *The 1967 IFC Formulation for Industrial Use,* International Formulation Committee of the 6th International Conference on the Properties of Steam, ASME, New York.

Kretzshmar, H. J., Klinger, J., Schneider, St., and Dittmann, A., 1987, "Zur Bereitstellung thermophysikalischer Stoffdaten für die Modellierung energiewandelnder Prozesse auf Personalcomputer," *Wissenshaftliche Berichte IH Zittau,* Vol. 709, No. VI/5, pp. 16–22.

Magerfleisch, J., 1979, "Umkehrbare Gleichungen zur Berechnung von Entspannungsvorgängen im Wasserdampf," *Brennstoff-Warme-Kraft,* Vol. 31, pp. 403–407.

McClintock, R. B., and Silvestri, G. J., 1979, "Some Improved Steam Property Calculation Procedures," ASME JOURNAL OF ENGINEERING FOR GAS TURBINES AND POWER, Vol. 92, pp. 123–134.

Meyer-Pittrof, R., and Vesper, H., 1969, "Einige Umkehrfunktionen und Näherungsgleichungen zur '1967 IFC Formulation for Industrial Use' für Wasser und Wasserdampf," *Brennstoff-Warme-Kraft,* Vol. 21, pp. 139–142.

Meyer-Pittrof, R., and Grigull, U., 1969, "Eine Umkehrfunktion zu der '1967 IFC Formulation for Industrial Use' für die Berechnung der Temperatur von überhitzen Wasserdampf, abhangig von Druck und Enthalpie," *Brennstoff-Warme-Kraft,* Vol. 21, pp. 636–638.

Meyer-Pittrof, R., 1986, "What Power Industry Expects of Steam Research," *Proceedings, 10th International Conference on the Properties of Steam,* V. V. Sytchev and A. A. Aleksandrov, eds., Mir Publishers, Moscow, Vol. 1, pp. 57–70.

Pátek, J., and Sifner, O., 1991, "Fast Property Calculations of Wet and Superheated Steam up to 30 MPa and 600°C," *Proceedings of Symposium on Chemistry of Water and Steam in Power Plants,* Japan National Committee of IAPWS, Tokyo.

Reuck, K. M. de, and Armstrong, B., 1979, "A Method of Correlation Using a Search Procedure Based on a Step-wise Least-Square Technique and Its Applications to an Equation of State for Propylene," *Cryogenics,* Vol. 19, pp. 505.

Rukes, B., 1990, *Summary of Survey Results. Requirements of Power-Related-Industries on a New Industrial Formulation,* Siemens/KWT T 121, Erlangen.

Rukes, B., 1991, "Final Set of Specifications for the New Industrial Formulation," *Minutes of the Meetings of the Executive Committee of the IAPWS,* B. Dooley, ed., Tokyo, attach. 19, pp. 78–82.

Schwindt, H., 1978, "Neue Näherungsformeln für die Zustandsgrössen des Wasserdampfes in Abhängigkeit von Enthalpie und Entropie," *Brennstoff-Warme-Kraft,* Vol. 30, pp. 30–32.

Setzman, U., and Wagner, W., 1989, "A New Method for Optimizing the Structure of Thermodynamic Correlation Equations," *International Journal of Thermophysics,* Vol. 10, pp. 1103–1126.

Sytchev, V. V., and White, J. H., 1984, *The IAPS Formulation 1984 for the Thermodynamic Properties of Ordinary Water Substance for Scientific and General Use,* 10th ICPS Moscow, USSR.

Tratz, H., 1962, "Neue Zustandgleichungen für flüssiges Wasser und eine verbeserte Gleichung der Dampfdruckkurve," *Brennstoff-Warme-Kraft,* Vol. 14, pp. 379–383.

Young, J. B., 1988, "An Equation of State for Steam for Turbomachinery and Other Flow Calculations," ASME JOURNAL OF ENGINEERING FOR GAS TURBINES AND POWER, Vol. 110, pp. 1–7.

Ziskuhr, W., 1974, "Calculation of Thermodynamic Properties of Steam With Small Computers," *Proceedings, 8th International Conference on the Properties of Steam,* Vol. 2, pp. 852–867.

R. H. Tindell

T. M. Alston

Northrop-Grumman Corporation,
Advanced Technology &
Development Center,
Bethpage, NY 11714

C. A. Sarro

G. C. Stegmann

Consolidated Edison Company
of New York, Inc.,
New York, NY 10003

L. Gray

J. Davids

Westinghouse Electric Corporation,
Orlando, FL 39826

Computational Fluid Dynamics Analysis of a Steam Power Plant Low-Pressure Turbine Downward Exhaust Hood

Computational fluid dynamics (CFD) methods are applied to the analysis of a low-pressure turbine exhaust hood at a typical steam power generating station. A Navier–Stokes solver, capable of modeling all the viscous terms, in a Reynolds-averaged formulation, was used. The work had two major goals. The first was to develop a comprehensive understanding of the complex three-dimensional flow fields that exist in the exhaust hood at representative operating conditions. The second was to evaluate the relative benefits of a flow guide modification to optimize performance at a selected operating condition. Also, the influence of simulated turbine discharge characteristics, relative to uniform hood entrance conditions, was evaluated. The calculations show several interesting and possibly unique results. They support use of an integrated approach to the design of turbine exhaust stage blading and hood geometry for optimum efficiency.

Introduction

Traditional approaches to the fluid dynamic design and analysis of exhaust hoods for low-pressure steam turbines have relied largely on information obtained from small-scale laboratory models using air as the test fluid and having no rotating blade elements. This has been supplemented in a limited number of instances by confirmational testing on actual steam turbine elements involving both field units as well as large-scale laboratory models. This approach has generally been satisfactory during a period when the principal focus was to assure performance near a selected thermodynamic design point where blade exit flow conditions are close to ideal.

More recently, advancements in the methodology to analyze and optimize turbine blade path designs have led to an improved understanding of the complexity of blade exit flow field conditions and their interaction with exhaust hood loss characteristics. Concurrently, it became apparent that there was a need to optimize exhaust hood losses over a relatively wide range of variation in normal operating conditions and that the design of the exhaust hood and last stage of blading be developed as an integrated system.

A recent study (Gray et al., 1989) describes an approach to improving exhaust hood losses for an existing turbine design that operates over a substantial variation in exhaust pressure conditions during the normal annual cycle. In this approach, small-scale air model tests simulating some complex flow conditions existing at the blade path exit plane formed the primary quantitative technique for evaluating and selecting an improved flow guide design. Predictions based on air model measurements were subsequently verified by field test measurements.

The present work described herein was initiated to provide an independent analytical basis for support of such exhaust system flow guide modifications. Specifically, the goals of this work were to evaluate the complex exhaust system flow fields and to determine the fluid mechanical benefits to the system resulting from modification to the exhaust system flow guides. The evaluations were made using CFD methods. This approach can provide a cost-effective way of studying configurations in a diagnostic manner not readily available in experimental subscale model testing. For example, CFD analysis can permit the representation of nonuniform turbine discharge conditions, i.e., velocity, pressure, and temperature distributions, that are difficult to provide for in small-scale model tests. It is realized that the best use of CFD involves an integrated approach with an experimental program. Such an approach would yield synergistic and technical cost benefits. Although this investigation is basically analytical, the work described herein does provide some worthwhile results.

In a typical low-pressure steam turbine, the exhaust hood region is normally considered to be bounded at its entrance by the turbine blade path exit plane, and, at its exit, by the condenser neck flange. Figure 1 shows the general arrangement. The flow guide forms the outer boundary of the annular turbine discharge flow; the bearing cone forms the inner boundary. The turbine outer cylinder envelope generally consists of straight side walls with a cover half of oval cross section. The annular flow divides in some fashion after it leaves the flow guide, some of it flowing down around the bearing cone. In a full-scale plant, the operating back pressure is controlled by the cooling water temperature in the condenser tube bundle. A well-designed turbine exhaust system that allows the flow leaving the blade path to diffuse more efficiently to the condenser results in reduced exhaust losses, a lower blade path exit pressure, and increased turbine work.

The complexity of the low-pressure turbine exhaust flow field primarily results from the superposition of an axial-to-radial diffusing flow and a 90 deg turn of the whole flow field. The 90 deg turn leads to radial and circumferential static pressure gradients and a highly vortical secondary flow pattern at the exit

Contributed by the Power Division for publication in the JOURNAL OF ENGINEERING FOR GAS TURBINES AND POWER. Manuscript received by the Power Division March 8, 1992; revision received September 17, 1992. Associate Technical Editor: R. W. Porter.

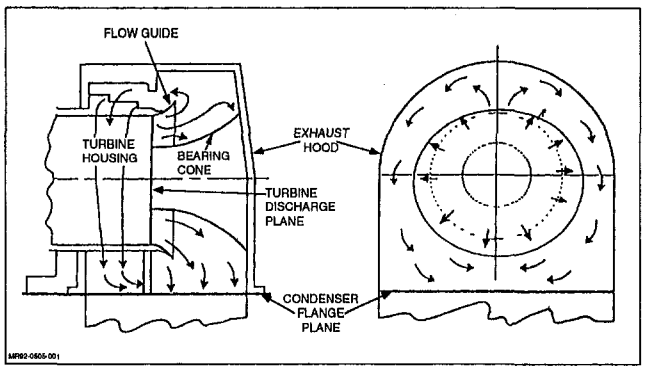

Fig. 1 Turbine exhaust system: general arrangement

of the turn. The combination of these two effects is considered to be the fundamental driving fluid dynamic force at work in this type of turbine exhaust system. The vortical flow pattern may lead to large total pressure losses that would result in increased back-pressure at the blade path exit plane, and reduced power generation. The exhaust flow characteristics are further complicated by the normal presence of nonuniform velocity and pressure distributions at the blade path exit plane. A proper simulation of the exhaust flow field should consider these nonuniform conditions.

In addition to developing a general understanding of turbine exhaust system flow characteristics, this work was directed toward evaluating the benefits of a certain type of modification to the exhaust hood flow guide under study. The modification was aimed at improving performance for the high back pressure operating condition. The improved design investigated here is a shortened version, denoted S-2, of the basic flow guide, denoted L-1, which allows a larger opening between the flow guide exit edge and the outer cylinder end wall. This occurs at the expense of a reduced area ratio for the annular diffuser region between the flow guide and bearing cone surfaces.

General Approach

The ability to predict losses in total pressure and to describe the fluid mechanical basis for them is of prime importance to this study. Therefore, the analytical method must be capable of describing rotational, three-dimensional flow fields. A computerized solution to the Navier–Stokes (N–S) equations (PARC) has been selected to do this. The PARC code is a three-dimensional flow field simulation program developed by the Air Force Arnold Engineering Development Center, and is an extension of the three-dimensional Navier–Stokes algorithm developed by the NASA Ames Research Center (Pulliam, 1984). Program options allow calculation of inviscid, laminar, or turbulent flow fields. The calculation of turbulent flow utilizes an algebraic turbulence model derived from the Baldwin–Lomax model (Baldwin and Lomax, 1978). Generalized boundary conditions are specified through code inputs. The fluid may be modeled as a "real" gas by inputting the appropriate equations (or tables) of state, or as an ideal gas. We have elected to describe the flows in air models and full-scale steam systems as ideal gases having specific heat ratios of $\gamma = 1.40$ and $\gamma = 1.10$, respectively. The similarity parameters of geometry, Mach number, and Reynolds number were maintained between both cases and their computational counterparts.

It is recognized that exhaust hood fluid in a steam turbine is usually wet steam, i.e., a two-phase fluid. Typical operation is in a pressure–temperature region where γ does not vary significantly from exhaust hood inlet to exit. In fact, the maximum temperature difference between total and static conditions within the exhaust hood is 10°C. Because a constant value of $\gamma = 1.10$ provides a good representation of the flow of wet steam in this region, this value was used for the PARC calculations. Any effects of the two-phase flow or changes in the steam quality, i.e., condensation, were not modeled.

In addition to describing the flow fields throughout the system in terms of velocity components, total pressure, static pressures and temperatures, mass-weighted average values of these parameters are determined by integrating them across stations of interest. The averaging process is described as follows, using total pressure as a typical example:

$$\bar{P}_T = \frac{\int P_{T_i} \rho_i V_i \, dA}{\int \rho_i V_i \, dA}$$

where dA is the local incremental area and V_i the local velocity at the station of interest, i.e., inlet station, flange plane station, etc.

Computational Models

A general representation of the computational model is shown in Fig. 2. The system exit plane for the analysis is the condenser flange plane, which is 10 full-scale feet upstream of the computational exit boundary. This is necessary to assure reasonably uniform flow at the computational exit boundary, where the exit static pressure boundary condition is prescribed.

The geometries of the S-1 and L-1 flow guide designs, Fig. 3, have been modeled into the grid configurations shown in Fig. 4. A total of 118,080 grid points were used, with extremely dense gridding near the surfaces to reconcile the boundary layer properties in the diffuser region. The grid configurations consist of 45 grid points in the circumferential direction, 32 in the axial direction, and 82 in the radial direction. Figure 4 shows an isometric view of the complete grid arrangement and also compares the lower central vertical planes for the two primary flow guide configurations. The grid model was run both in a full scale, and also as a $\frac{1}{36}$th scale model simulation, to evaluate effects of size, i.e., Reynolds number, and to compare with experimental results.

This analytical model embodies several simplifications relative to actual turbine exhaust geometries. First, no attempt is made to model features of the turbine casing such as internal

Nomenclature

A = area
$C_{P_S} = (P_S - P_{S_{REF}})/(P_{T_{REF}} - P_{S_{REF}})$
$C_{P_T} = (P_T - P_{T_{REF}})/(P_{T_{REF}} - P_{S_{REF}})$
H = annulus height/maximum annulus height
HL/CL = hood loss coefficient
$K = (P_T - P_{T_{REF}})/(\frac{1}{2} PV^2)_{REF}$
L = length
M = Mach number
P = density
P_S = static pressure
P_T = total pressure
T = temperative
U = axial velocity
V = velocity

Subscripts

ABS = absolute
ANN = mass flow averaged condition at plane of turnfire exit annulus
F = mass flow averaged conditions at flange plane
r = radial
S = static
t = tangential
T = total

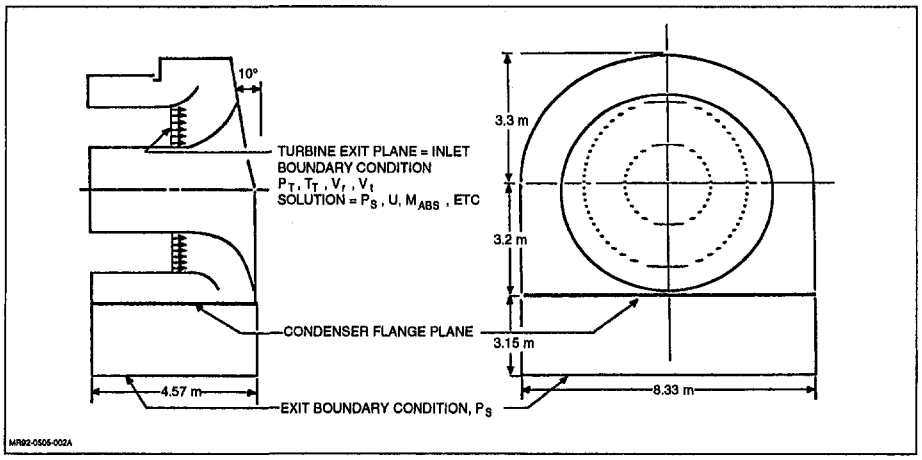

Fig. 2 Representation of the computational model

structural ribs and struts that can constrain the flow and lead to additional losses. Secondly, there is no representation of any condenser blockage downstream of the flange plane; therefore, the flange plane static pressure and velocity characteristics are probably different than for the case with condenser simulation. Nevertheless, the present computational model is considered adequate to define the relative benefits of the two flow guide designs, and to provide insight into essential three-dimensional flow phenomena.

Computational Procedure

In this application of the PARC code, development of a flow field solution commences with a partial specification of the flow properties existing at the turbine blade exit plane (inlet boundary to the analytical model) and an initial guess for the static pressure at the computational exit boundary. Parameters specified at the inlet boundary include the total pressure and tangential/radial velocity components. The resulting flow field solution is then obtained by relaxing on the axial velocity component and static pressure conditions on the inlet boundary until a satisfactory degree of convergence is established.

A subsequent comparison of the computational solution for the inlet boundary flow properties with those expected on the basis of the specified conditions in terms of a weighted mean Mach number is used to determine acceptance of the solution. In general, several iterations of the assumed static pressure value on the exit boundary are required in order to obtain a satisfactory match between calculated and prescribed inlet boundary conditions.

In the present work, an acceptable level of convergence in the final solution is determined by obtaining approximately a three to four order of magnitude reduction in the norm of the residuals for all the governing equations at each grid point in the computational model. This generally requires some 2.50 to 2.75 hours of CPU time on a CRAY XMP2 for the model size represented here.

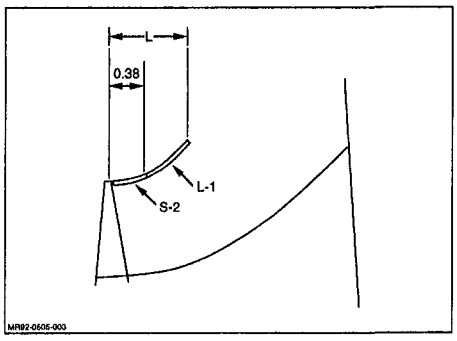

Fig. 3 Turbine exhaust system flow guide geometry

Analytical Validation

While validity of the PARC code in applications to various types of internal flows has been established (Tindell, 1988, 1991; Phares et al., 1986), no comparisons against measurements for a low-pressure steam turbine exhaust hood are known to have been published. Unfortunately, in the present analytical study, a reliable quantitative comparison with measurements on the actual steam turbine could not be obtained; however, it was possible to make direct comparisons with the results of recent air model exhaust hood tests conducted by Lehigh University (Owczarek et al., 1989; Owczarek and Warnock, 1989). The test model was a $\frac{1}{36}$th scale version of the basic configuration investigated in the present analytical study, having a short guide vane denoted IP No. 3.

Figure 5 shows a comparison of the computational and test-derived assessments of the hood loss coefficient. This parameter is the ratio of the isentropic static enthalpy change, between the turbine exit annulus and the condenser flange plane, to the turbine exit annulus flow kinetic energy (see the equation in Fig. 5). Both the computational and the test-derived approach for assessing the hood loss coefficients employ the mass flow parameter method of Owczarek and Warnock (1989) for determining annulus Mach number and static pressure.

In both cases the area-weighted average annulus total pressure was used in conjunction with the mass flow parameter method. The ratio of annulus static-to-total pressure corresponds to the mass flow parameter-derived Mach number. The flange plane static pressures used in the test cases were measured values, and were area-weighted averages of the calculated results across the plane in the computational case.

Although both sets of results compare well relative to an overall trend, each set has a somewhat different characteristic. The computational results show no variation in hood loss below $M_{ANN} = 0.53$, while the test results show a continuous variation. The two highest Mach number test points are assumed to be within a reasonable scatter of the measurement-calculation process. The general result of the comparison of Fig. 5 suggests that the PARC code may be a reasonable tool for analytical investigations of hood exhaust systems.

It is not clear whether the Baldwin and Lomax (algebraic) turbulence model in PARC models relatively dominating exhaust hood turbulence phenomena well, or whether other than turbulence phenomena dominate the exhaust hood performance.

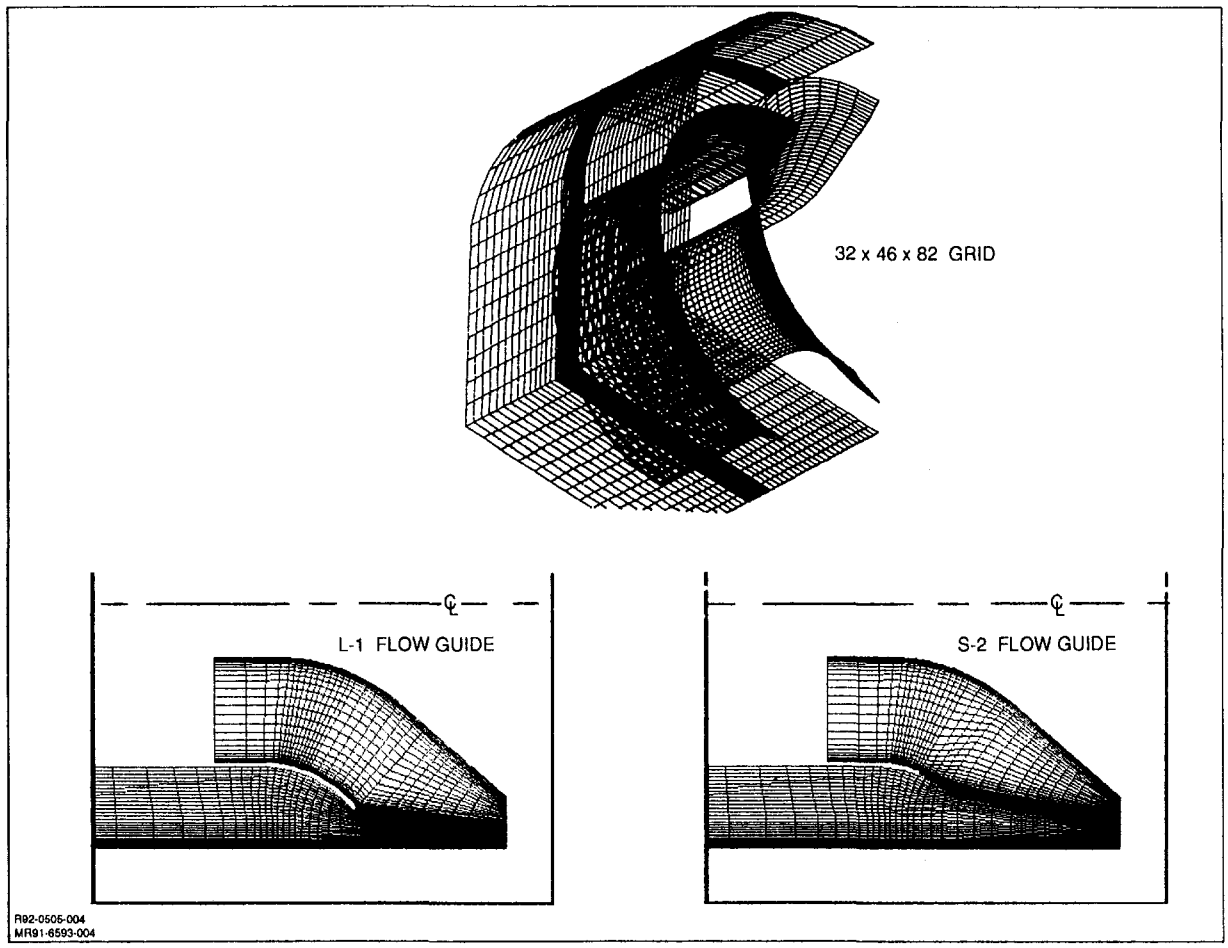

Fig. 4 Complete grid arrangement and comparison of lower central vertical planes

Nevertheless, we will use PARC to examine some interesting aspects of exhaust hood fluid mechanics. More work, however, should be done to understand the capability of this and other computational methods to accurately simulate exhaust hood flows. The impact of various turbulence models, i.e., algebraic and two-equation models, would be of particular importance.

Inlet Boundary Flow Conditions

An assumption that uniform total pressure conditions exist at the location of the blade exit boundary over the entire annulus area is generally appropriate for baseline calculations of hood flow properties and for comparison with air model test measurements. Previous work (Gray et al., 1989), however, has shown that the nonuniform distributions in total pressure, swirl angle, etc., existing in an actual turbine can lead to substantially different results on the relative benefits of alternative flow guide geometries. Accordingly, a principal objective of the present analytical study is to attempt calculations representing actual turbine operating behavior.

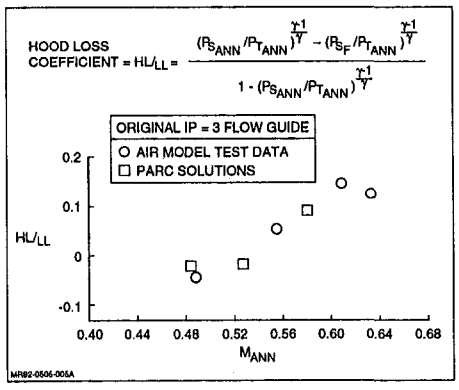

Fig. 5 Comparison of PARC solution and exhaust hood air model test results of Owczarek and Warnock (1989)

In general, information available to permit a description of the three-dimensional variation in flow conditions existing over an entire turbine blade path exit plane annulus is limited to that obtainable from measurements with traverse probes and wall static pressure taps. In the present case, combined traverse measurements at a single radial alignment and a series of wall pressure measurements on the bearing cone and flow guide surfaces were available over a range of operating conditions. The traverse measurements are interpreted to obtain the localized radial variation in flow conditions with changes in average static pressure while the static tap measurements are used to determine the circumferential wall static pressure distribution.

In the presence of substantial choking of the last row blade passage, assumptions that the circumferential distribution in blade exit mass flow is uniform and that the radial distribution properties are dependent only on a local averaged static pressure, allow for an approximate representation of the three-dimensional blade exit plane flow conditions. Figures 6 and 7 present a comparison summary of such nonuniform distributional flow properties at two selected conditions representative of low back-pressure (winter time) and high back-pressure (summer time) operating conditions. Applicable annulus aver-

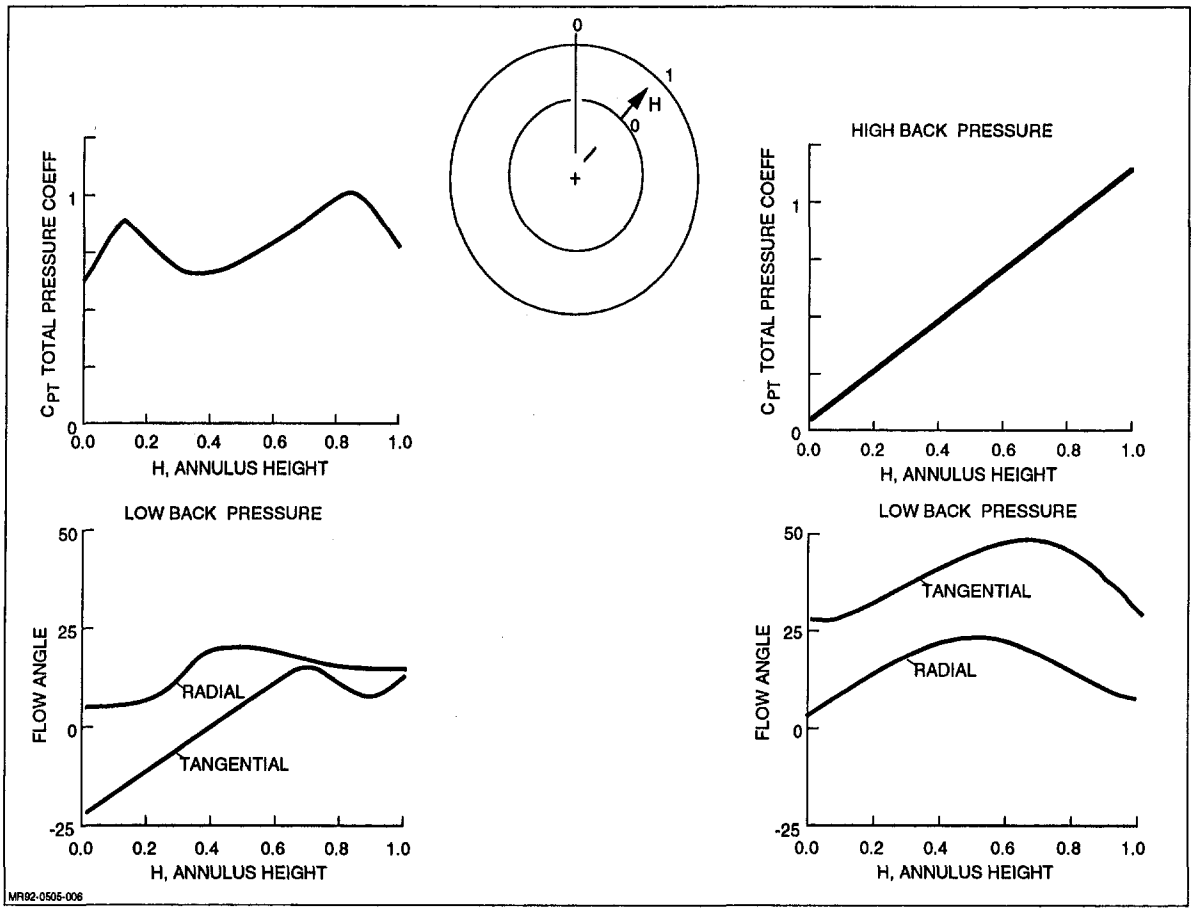

Fig. 6 Representative variation in blade exit flow conditions with annulus height

age Mach numbers are approximately 0.88 and 0.60, respectively.

It should be noted that Fig. 6 and 7 evidence the changing distributional properties that are a normal response to variations in exhaust volumetric flow. The precise nature of these properties is, however, also dependent on the physical blading design geometry. Thus, substantial variations can exist between different turbine designs and even differing units of the same design operating at the same back-pressure conditions.

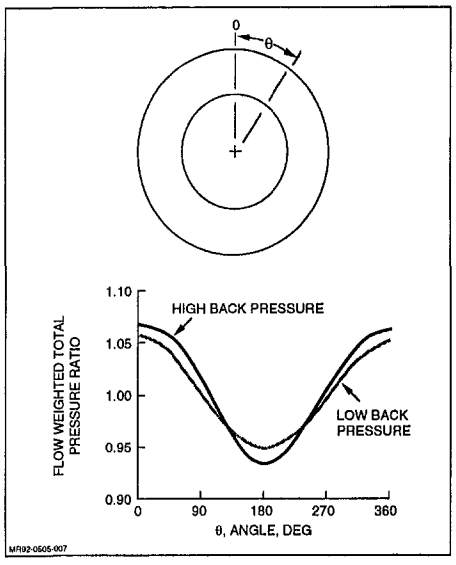

Fig. 7 Representative variation in blade exit flow conditions with circumferential location

Scope of Analytical Study

A total of six analytical configurations are considered in this study, as identified in Table 1. This group includes variations in exhaust hood geometry, geometric scale, and inlet boundary flow conditions. As previously described, the two geometric variations are represented by different lengths of the flow guide element, L-1 versus S-2. Calculations for the small-scale model (Owczarek, et al., 1989) were run with fluid properties for air and simulated both uniform inlet boundary flow conditions (as tested) as well as the nonuniform conditions selected to represent two actual turbine operating points, as discussed earlier. Calculations for the full-scale geometries were run with idealized properties for steam (γ = 1.10) and with the applicable nonuniform flow conditions on the inlet boundary. Table 1 also summarizes the principal study comparisons discussed in this paper.

Study Results

Performance. Comparisons of the total pressure recovery performances of Configurations 1 through 6 are shown in Fig. 8. These curves, which plot total pressure ratio between the condenser flange and turbine discharge planes, $P_{T_F}/P_{T_{ANN}}$, against turbine discharge Mach number, were faired through the calculated points, showing several interesting results. At a Mach number of M_{ANN} = 0.60, for example, the full-scale hood system loses approximately 18–20 percent in total pressure between the annulus and flange plane stations. Improvement of

Table 1 Summary of study configurations

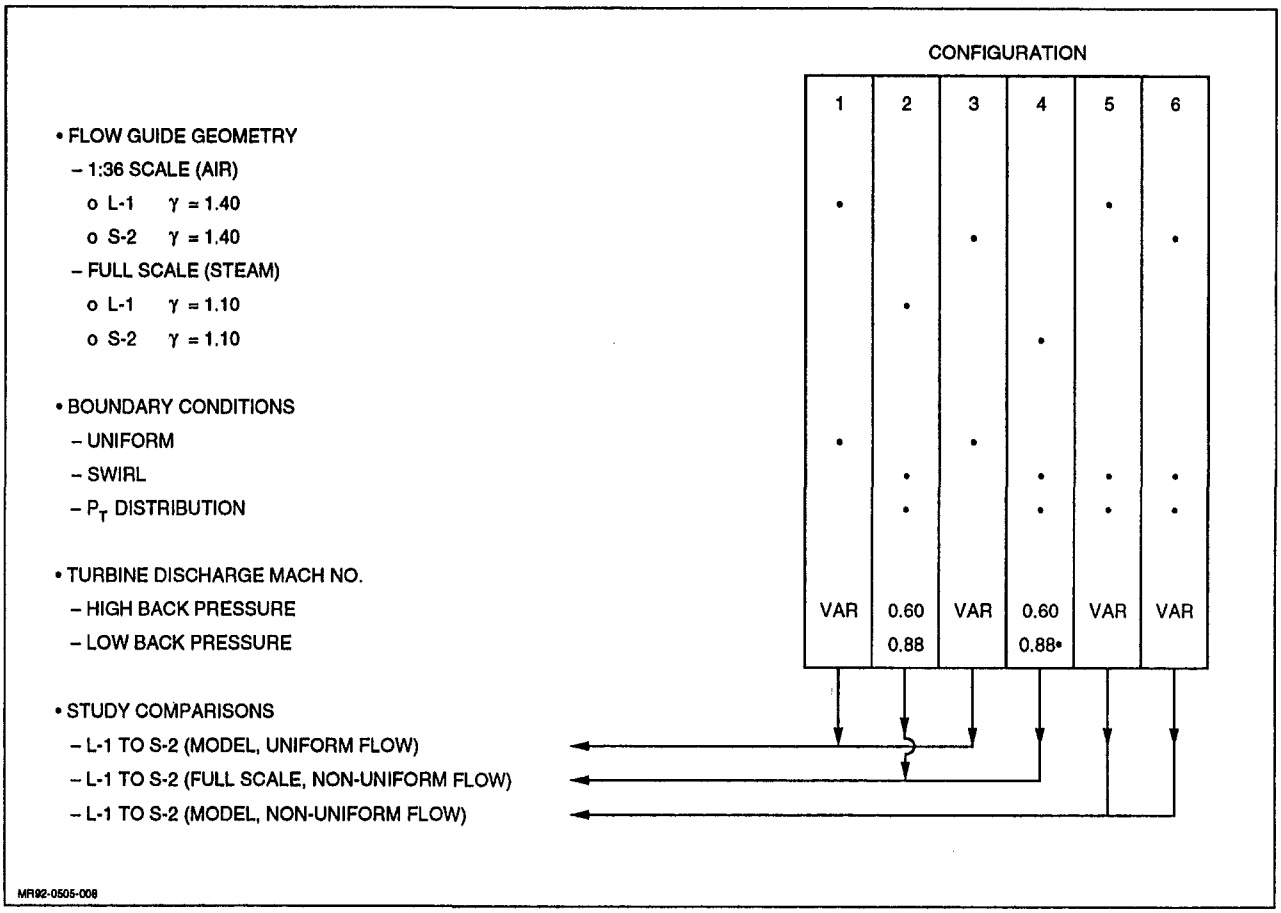

this relatively high loss could result in significant increases in power plant output. We will employ the flow field analysis (discussed below) to determine primary mechanisms for this loss. Another significant effect is the result of varying the turbine discharge boundary conditions for the small scale air model from a uniform flow to the simulated swirl and total pressure distributions, i.e., Configurations $\frac{1}{3}$ and $\frac{5}{6}$. At $M_{ANN} = 0.60$, the addition of swirl and pressure distribution at the turbine discharge causes a 5 and 9 percent reduction in total pressure ratio across the exhaust system for the S-2 and L-1 flow guides, respectively. An important aspect of this result is that the indicated superiority of the L-1 flow guide (relative to the S-2 guide) under uniform flow conditions is inverted with the addition of a nonuniform swirl and total pressure distribution. The S-2 flow guide is evidently better attuned to the nonuniform turbine discharge characteristics than is the L-1 design. This suggests that model tests that simulate turbine swirl and total pressure distributions may produce more meaningful results.

The effects of enlarging configurations $\frac{5}{6}$ to full scale and simulating steam ($\gamma = 1.10$) instead of air ($\gamma = 1.40$) are defined by Configurations $\frac{2}{4}$. Performance is improved by about 1 to 2 percent. This improvement is attributed largely to increased Reynolds number (a factor of 2.7). Also, the effects of operation at higher M_{ANN} (low back pressure) are less severe, i.e., the slope of total pressure ratio versus M_{ANN} is reduced. This slope is reduced more for the L-1 design than for the S-2

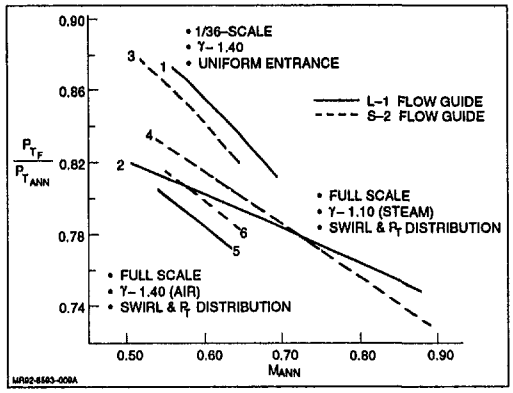

Fig. 8 Calculated total pressure ratio characteristics

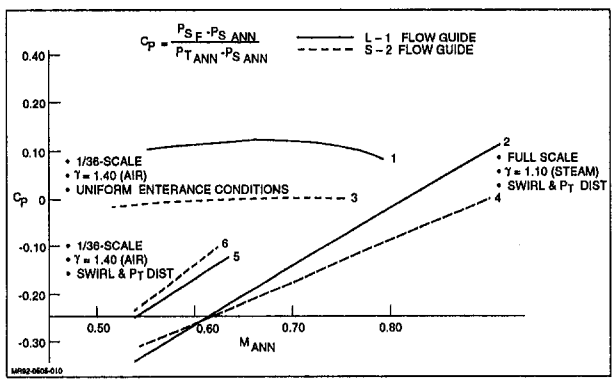

Fig. 9 Calculated static pressure coefficient characteristics

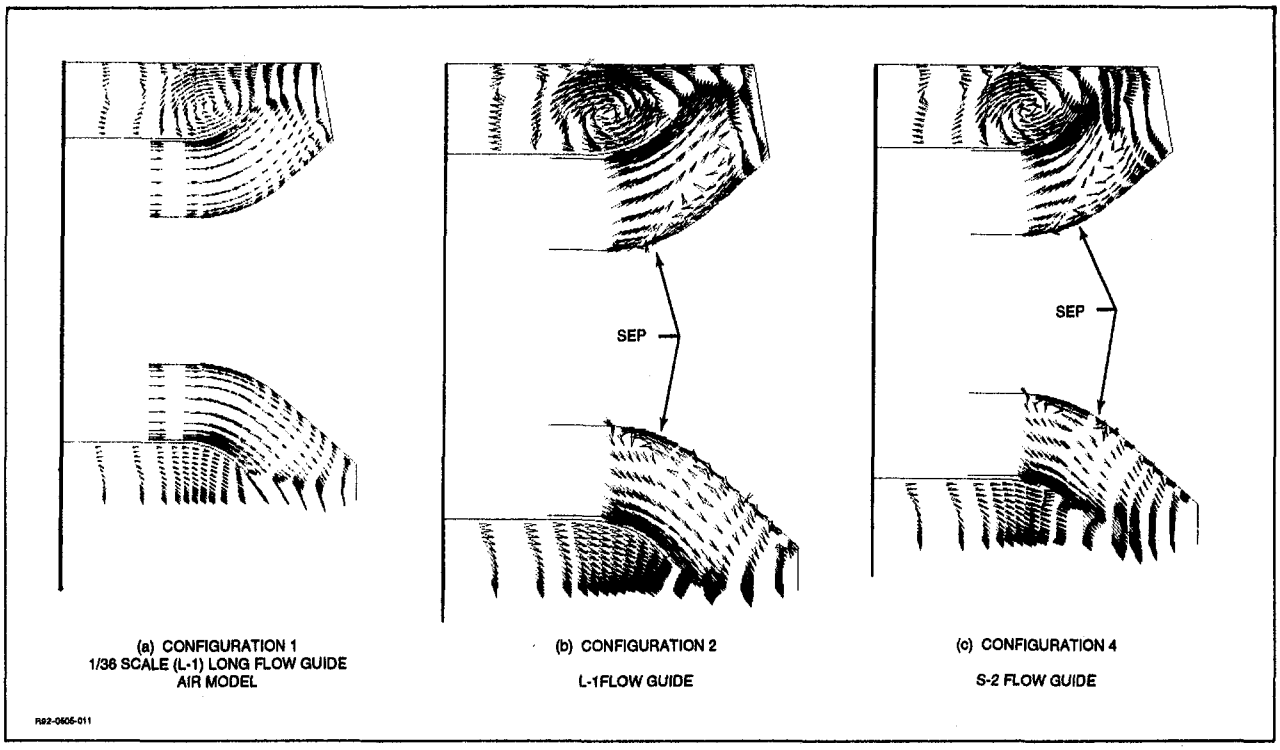

Fig. 10 Velocity distribution in vertical center plane; high back-pressure

design, with the result that they have the same performance at $M_{ANN} = 0.73$. Because, in actuality, total pressure ratio curves may not be linear, the crossover point may not be located accurately.

All total pressure ratio comparisons of Fig. 8 are cast in terms of the condenser flange plane static pressure recovery coefficient in Fig. 9. Here the small-scale, uniform flow configurations are clearly better diffusers at Mach numbers in the low back-pressure operating range. This is consistent with the total pressure performance comparison. The addition of swirl and total pressure distribution causes considerable loss in performance and inverts the relative superiority of the two flow guides, also similar to the total pressure ratio picture. However, enlarging the system to full scale does not improve static pressure performance, in contrast to the improvement seen in total pressure ratio. Notice that the S-2 design will be superior in static pressure recovery at $M_{ANN} = 0.62$ and lower. This also is true of total pressure ratio, but only above $M_{ANN} = 0.7$.

These comparisons lead to three major conclusions. First, significant differences can be expected between models that do not simulate both velocity and total pressure turbine discharge characteristics, and those that do. Not only can the basic performance level differ, but also the relative merit of candidate improvement devices may be inverted. Second, the S-2 flow guide design is better attuned to the turbine discharge characteristics at the high back-pressure (low M_{ANN}) operating condition. On the basis of the better performance calculated for the S-2 flow guide configuration, we would expect it to provide better performance during high back pressure operation. The third conclusion is that there is a significant sensitivity in the exhaust system performance to variations in turbine discharge conditions. This suggests that exhaust system and turbine blade design should be an interactive process. It may be possible for synergistic benefits to be achieved with this approach.

Flow Field Analysis—High Back-Pressure Operation. In order to understand the physical basis for the foregoing performance results, it is helpful to consider the flow fields as characterized by velocity and pressure distributions. This discussion examines the flow fields in selected planes throughout the exhaust systems, with an eye toward determining the general three-dimensional nature of the fields, and how the flow losses vary among the several configurations investigated.

We begin by comparing the velocity vectors in the vertical center plane of the L-1 small scale air model having uniform flow, the L-1 full-scale configuration, and the S-2 full-scale configuration, the latter two having simulated turbine flows (Fig. 10). Flow over the flow guide surfaces of all three configurations is unseparated. The air model flow, with the exception of the small bearing cone separation at the corner, is relatively well behaved. The large horseshoe-shaped vortex at the top of the air model causes severe separation and reverse flow between the inner and outer cylinders. Flow along the lower surface of the inner cylinder and the adjacent condenser flange plane is generally in a rearward direction over the initial $\frac{2}{3}$ of the plane. This rearward flow represents the approximate dividing streamline that separates both branches of the horseshoe vortex. It splits into the two counterrotating patterns seen in Fig. 11. The energy consumed by the vortical flow may be a large contributor to the overall system losses.

The portion of the flange plane field having the largest vertical velocity component, i.e., having the greatest mass flow rate, flows from the lower section of the flow guide-bearing cone annulus, and covers $\frac{1}{3}$ of the flange plane nearest the rear turbine wall. Because this analytical model does not simulate condenser neck blockage effects, flange plane flow characteristics in systems with condenser neck sections probably will be somewhat different.

The effect of increasing the size of the L-1 system to full scale, already shown to be relatively small, and the more substantial effect of simulating the turbine discharge characteristics are shown by comparing Fig. 10(*a*) to 10(*b*) (Configuration 1 compared to Configuration 2). The flow over the upper and lower bearing cone surfaces of Configuration 2 is separated. Notice that the root velocities on the lower cone surface (which

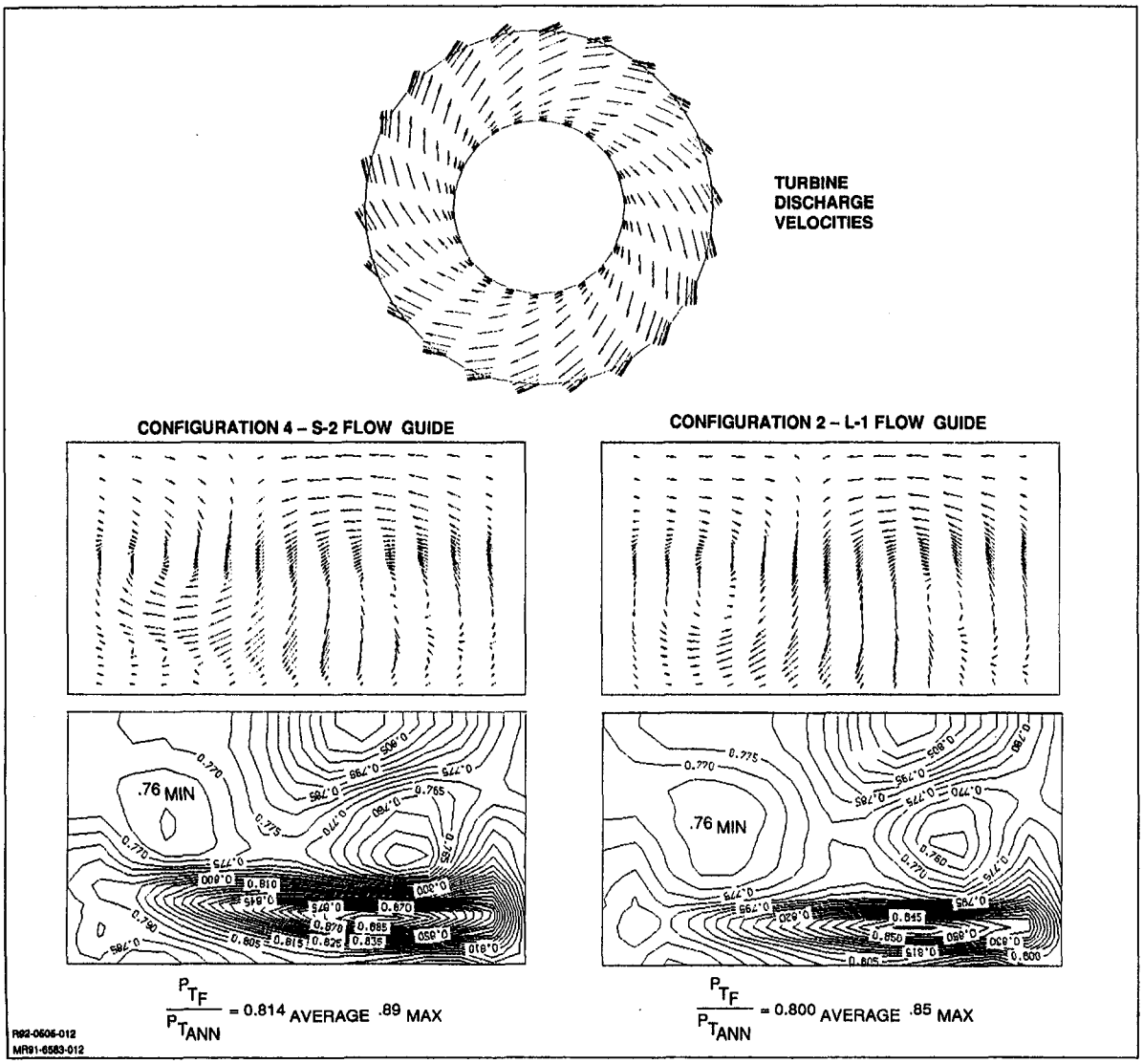

Fig. 11 Comparison of plane velocities and total pressure ratio contours: high back-pressure

reflect specified turbine discharge conditions) are virtually tangential to the discharge plane. This is not the case on the upper bearing cone surface. The velocity patterns on the short S-2 flow guide of Configuration 4 (Fig. 10*c*) appear similar to those of the long L-1 flow guide. There is no apparent basis for the improved performance of the S-2 configuration in the velocity fields shown.

Focusing on the flange plane characteristics, Fig. 11 compares the velocity patterns and total pressure ratio contours, $P_{T_F}/P_{T_{ANN}}$, of the L-1 and S-2 designs. The velocity patterns clearly describe two vortices, which reflect the strength of the large horseshoe vortex developed around the base of the flow guide trailing edge. The centers of these vortices correspond to the lowest total pressures in the plane. The higher total pressures act over the rearward section of the flange plane. We estimate that an increase of approximately 24 percent flange plane area of the S-2 over the L-1 configuration, over which the higher pressures act, is responsible for the 1.40 percent improvement in average total pressure. Also, the highest recoveries of the S-2 configuration are 3.5 percent higher than for the L-1 design.

Figure 12 shows the flange plane velocities and total pressures for the small scale air model, which has uniform entrance conditions. Comparison of Fig. 12 with Configuration 2 on Fig. 11 shows the effects of the simulated turbine discharge conditions, albeit for a small-scale air model versus a large scale steam simulation. As mentioned previously, the effects of differences in size and specific heat ratios for these configurations are outweighed by the effects of turbine discharge characteristics. The symmetry of flange plane flow fields allowed by the uniform entrance conditions (Fig. 12) is striking. The minimum total pressure located at the center of the vortex patterns is 5.5 percent lower for the simulated turbine discharge case. The high-pressure zone at the rear section of the simulated turbine case also is significantly lower than for the uniform flow case. An overall net of 7 percent lower total pressure ratio is assessed for the turbine simulation effects.

Flow Field Analysis—Low Back-Pressure Operation. It is important to evaluate the relative performance of the L-1 and S-2 flow guide configurations under low back-pressure operating conditions, during which transonic flow generally occurs. The following comparisons highlight the fundamentally important aspects of the flow fields for the two configurations at this high-M_{ANN} condition.

Figure 13 compares the velocity fields in the vertical centerplane of the S-2 and L-1 flow guide configurations. At the top

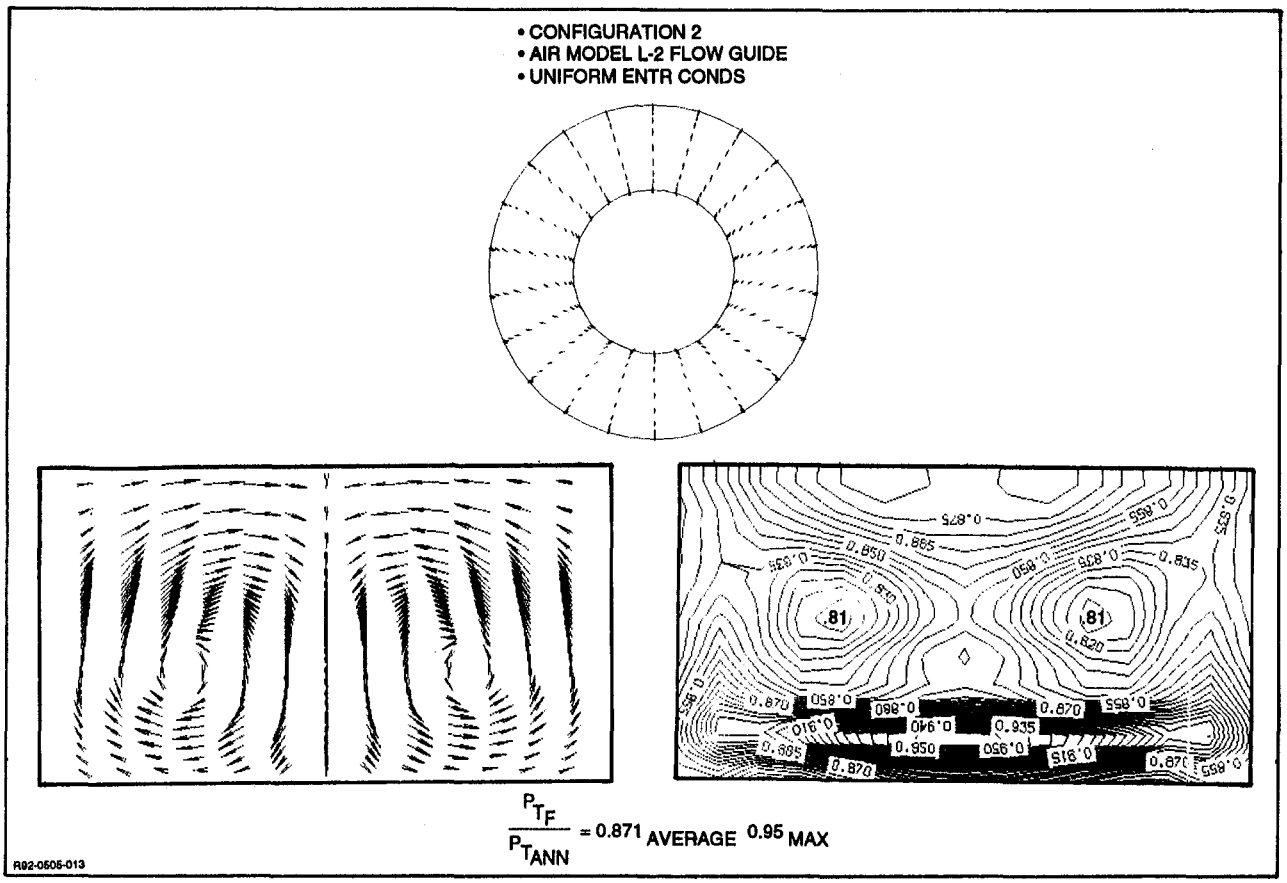

Fig. 12 Comparison of flange plane velocities and total pressure ratio contours: L-1 flow guide high back-pressure

of the figure is the turbine discharge plane velocity field. Notice the positive and negative tangential (swirl) velocity components, reflecting the turbine blade work distribution at this operating condition. This more "balanced" swirl distribution should reduce the asymmetry caused by the single-direction swirl distribution of the high back-pressure condition.

The S-2 configuration has a much larger separated upper bearing cone flow than the L-1. Under the higher back pressure condition of Fig. 10(c), the lower bearing cone of S-2 also was separated. This was not seen at the low back-pressure condition, although not shown in Fig. 13. These results are evidently favorable effects of the low back-pressure turbine discharge characteristics.

It is interesting to compare the center-plane velocities for the L-1 configuration at both back-pressure operating conditions (see Configuration 2 in Figs. 10 and 13). The severely separated flow in the flow guide-bearing cone annulus of the high back-pressure condition is almost eliminated at the low back-pressure condition. Thus, we conclude that at the low back-pressure operating condition, the L-1 configuration has a more efficient hood flow than at the high back-pressure condition. This conclusion is borne out by correlating the calculated averaged total pressure recovery characteristic with lines of constant hood inlet dynamic head loss (see Fig. 14). The high back-pressure condition correlates with a head loss factor of 1.00 compared with 0.80 for the low back-pressure condition. There is a 20 percent improvement in the efficiency of the hood flow during low back-pressure operation, based upon total pressure loss factors. Notice that if the high back-pressure condition were to operate at the same loss factor as the low back-pressure condition, there would be a 4 percent increase in total pressure ratio.

An underlying reason for this significant improvement in the low back-pressure aerodynamics may be the relative compatibility of the turbine discharge velocity and total pressure distributions with the hood geometry, i.e., with the annular diffuser. This relatively balanced swirl distribution may reduce shearing losses that are present in the high swirling velocity patterns of the high back-pressure condition.

Conclusions

This investigation was aimed at evaluating three-dimensional flow fields in the low-pressure steam turbine exhaust hood of a typical power generating station, and establishing the relative merits of two flow guide designs installation. Both objectives were accomplished by application of a Navier–Stokes flow field simulation program, PARC.

PARC simulation results, for a small-scale laboratory model of an exhaust hood having uniform entrance flow conditions, compare reasonably well with experimental measurements of hood loss coefficient. This comparison does not fully validate PARC as an accurate simulator of exhaust hood flows, but provides a significant step in that direction. The validation of Navier–Stokes codes, such as PARC, as accurate simulators of exhaust hood flow systems for low-pressure steam turbines clearly remains as an essential objective in developing an analytical design methodology.

Calculation results for both the full-scale and model exhaust hoods indicated that hood performance was highly dependent upon inlet flow condition. Consequently, the inlet conditions played an important role in evaluating the two flow guide designs. Inlet conditions for two operating points (a high and

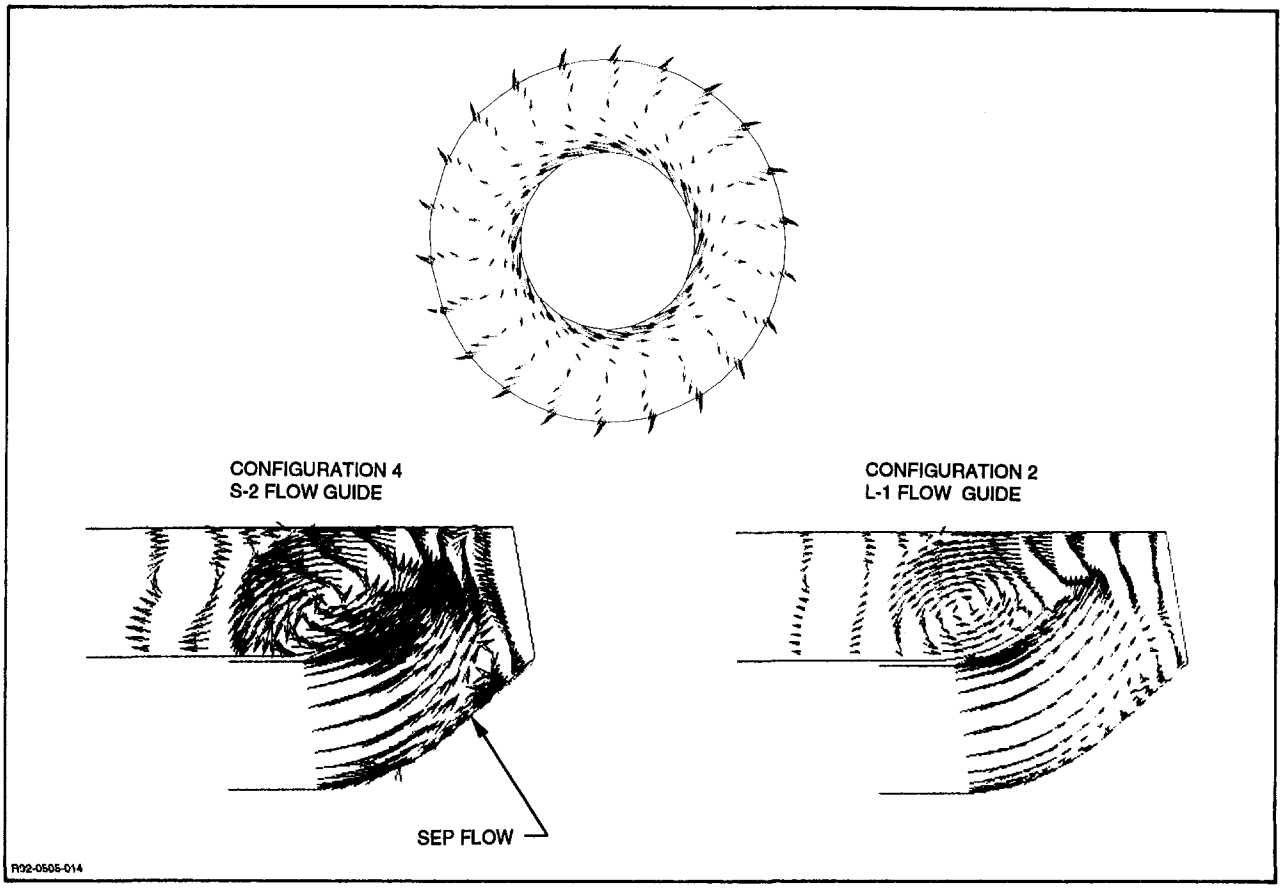

Fig. 13 Comparison of L-1 and L-2 flow guide configurations: upper vertical center-plane velocities, low back-pressure

a low back-pressure condition) were derived from field test measurements on the subject turbine exhaust hood.

At the simulated high back-pressure condition, substantial regions of flow separation from the bearing cone surface are indicated for both flow guide configurations. In this environment, a performance improvement is achieved by cutting back the long L-1 flow guide to obtain the shorter S-2 version. The improved performance is attributed to an increased flow area between the flow guide and outer cylinder endwall, which outweighs the loss in diffusion caused by the cut back and allows better flow mixing from the annular diffuser exit to the condenser, resulting in a reduced total pressure loss.

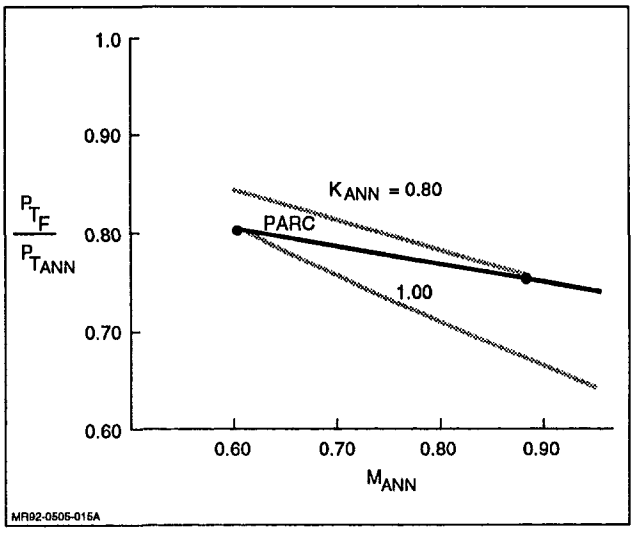

Fig. 14 Correlation of L-1 configuration results with theoretical dump loss characteristics

At low back-pressure conditions, the flow field for both flow guide designs is much cleaner and the static pressure recovery is significantly higher than for the high back-pressure condition. The low back-pressure inlet flow conditions are more compatible with the overall exhaust system configuration. In this environment no performance improvement is gained by cutting back the L-1 flow guide. In fact, the L-1 flow guide, with its larger area ratio, provides more flow diffusion in the annular diffuser than the S-2 flow guide and results in somewhat better static pressure recovery.

A fundamentally significant result of the total pressure recovery calculations is the fact that the system loses approximately 15–20 percent in the flow path between the annulus and flange plane stations. A large horseshoe vortex system is seen as a possible primary contributor to this loss.

The small-scale model simulation, run with uniform entrance conditions and simulating an air model, showed that the longer flow guide configuration was superior to the shorter flow guide configuration. This result is inverted when simulation of turbine swirl and total pressure distribution is introduced. This suggests that model tests that simulate turbine discharge characteristics may produce more useful results.

Most significant is the fact that a reasonably detailed picture of the complex three-dimensional exhaust hood flow has been demonstrated using the Navier–Stokes code PARC. This offers the possibility of enhanced productivity for the development of advanced

power systems, by integrating computational methods such as PARC into the analytical-experimental cycle. More CFD development work is required to tailor PARC and other, possibly more appropriate methods, to accommodate the specific needs of power plant systems. Better turbulence models and more accurate simulation of steam, for example, are areas that should be developed.

References

Baldwin, B. S., and Lomax, H., 1978, "Thin Layer Approximation and Algebraic Model for Separated Turbulent Flows," AIAA Paper No. 78–257.

Gray, L., et al., 1989, "Technical Considerations in Optimizing Blade-Exhaust Hood Performance for Low Pressure Steam Turbines," in: *Latest Advances in Steam Turbine Design, Blading, Repairs, Condition, Assessment, and Condenser Interaction,* D. M. Rasmussen, ed., ASME PWR-Vol. 7.

Owczarek, J. A., and Warnock, A. S., 1989, "Improvement of a Low Pressure Turbine Exhaust Flow," EP 86–36, Empire State Electric Energy Research Corporation, Dec.

Owczarek, J. A., Warnock, A. S., and Malik, P., 1989, "A Low Pressure Turbine Exhaust End Flow Model Study," in: *Latest Advances in Steam Turbine Design, Blading, Repairs, Condition, Assessment, and Condenser Interaction,* D. M. Rasmussen, ed., ASME PWR-Vol. 7, pp. 77–88.

Phares, W. J., et al., 1986, "Application of Computational Fluid Dynamics to Test Facility and Experiment Design," AIAA Paper 86–1733.

Pulliam, T. H., 1984, "Euler and Thin Layer Navier–Stokes Codes: ARC2D, ARC3D." Notes for Computational Fluid Dynamics User's Workshop, University of Tennessee Space Institute, Tullahoma, TN, Mar. 12–16 (UTSI Publication E02-4005-023-84).

Tindell, R. H., 1988, "Highly Compact Inlet Diffuser Technology," *AIAA Journal of Propulsion and Power,* Vol. 4, pp. 557–563.

Tindell, R. H., 1991, "Computational Fluid Dynamic Applications for Jet Propulsion System Integration," ASME JOURNAL OF ENGINEERING FOR GAS TURBINES AND POWER, Vol. 113, pp. 40–50.

Journal of Engineering for Gas Turbines and Power

Technical Brief

Magnetism and Stray Currents in Rotating Machinery

P. I. Nippes[1]

The case for elimination of stray currents and magnetism in turbomachinery is being recognized as an issue to be dealt with in industries that design and operate rotating machinery. Of main concern are bearings, seals, gears, couplings, etc. Resulting problems extend from surface damage to unit crashes. It is important to recognize the symptoms, to heed the warnings, and to enact preventive and corrective measures. Recommendations are to eliminate or minimize the source, and to bond the machinery to ground, especially the shaft, with a reliable shaft brush and a qualified current monitor. Information and guidance are provided from MPS job files covering some of the 200 installations visited in the past 15 years.

Introduction

Catastrophic bearing failures in rotating electrical machinery in the early 1900s were found to be caused by an imbalance in magnetism and electric circuits causing stray currents. Clear problem identification, adequate explanations, and problem correction were presented by engineers at that time. Periodic reappearance over the years of identical bearing damage and failures in rotating electrical machinery has been attributed to advances in technology, design, and materials, as well as the lack of application of preventive measures.

In recent years, however, electric current damage has appeared in new and unexpected situations. A prime example is that problems are not limited to shaft systems with electrical machines but also to trains made up of purely mechanical units. The majority of new cases are produced either electrically by harmonics of rectifier or inverter-supplied windings, electromagnetically by residual magnetism or electrostatically by electric charge separation in the steam, oil, process fluid, etc. Some occurrences are attributed to advances in technology as units are larger (up to 1500 megawatts) and turn at considerably higher speeds (15,000 rpm and higher). Other important factors are advances made in areas such as materials (high-alloy steels for shafts and casings), unit components (unconventional seals, bearings, gears, couplings, oils), testing (magnetic particle inspection), and welding.

[1] Magnetic Products and Services, Inc., Holmdel, NJ 07733.

Contributed by the Power Division of THE AMERICAN SOCIETY OF MECHANICAL ENGINEERS. Manuscript received at ASME Headquarters March 1995. Associate Technical Editor: D. Lou.

The problem of stray currents from electrostatic charge buildup is addressed by both controlling the source of generation and by diverting possible remaining current around sensitive items such as bearings and seals. The problem with respect to magnetically generated stray currents is sometimes illusive as there is no certainty that the presence of high magnetism will produce damage from shaft currents. It is an indisputable fact, however, that when high magnetism or uncontrolled shaft voltages exist, there is the potential for electric current damage. Electrostatic currents, if not drained away, can build shaft voltages to the point of discharge, usually across the bearings or seals. Electromagnetic-generated voltages require a closed electric circuit for current to flow. In either case, initiating factors can be oil film breakdown due to excessive shaft voltage, high vibration, rotor-to-stator rubs, thrusting, surge, overtemperature, lubricating oil insufficiency, dirt, etc.

It is important to conduct a thorough inspection and magnetic survey of the components and assemblies at shutdown. Even when damage is determined to be from electrostatic causes, careful attention should be paid to the presence of possible magnetism.

Experience and references are useful in identifying tracks, frosting, or pitting when they are found. A guide for identifying shaft current damage and making corrections is provided in the following sections. It has been found that the corrective measures recommended are effective in controlling shaft current damage and in improving rotating machinery operation.

Stray Current Generation

Common configurations of magnets, electromagnets, and electrostatics capable of voltage generation are the Faraday disk or homopolar generator (Fig. 1), the AC generator (Fig. 2), and the electrostatic generator (Fig. 3). That these exist in rotating machinery, either singly or in combinations, can be ascertained from damage patterns and accompanying circumstances encountered on the machinery. Where and when these may occur and what effects they may produce are not always clear. How they can be detected, quantized and controlled, and their effects minimized, is often the job of the engineer, who may find that they present a challenge.

Electrical Machinery

The presence of stray currents in electrical machinery can be easily understood, since by design there are very intense magnetic fields in the core section that serve as primary energy transfer between electrical and rotational means. It is to be expected that a certain amount of magnetism may stray from the main core, unless preventive measures are taken. The results can range from disastrous failure to mild pitting and/or blackening of the lubricating oil. There are limits to the amount of leakage fields that may be tolerated. This requires that certain rules be observed in the design, construction and installation of

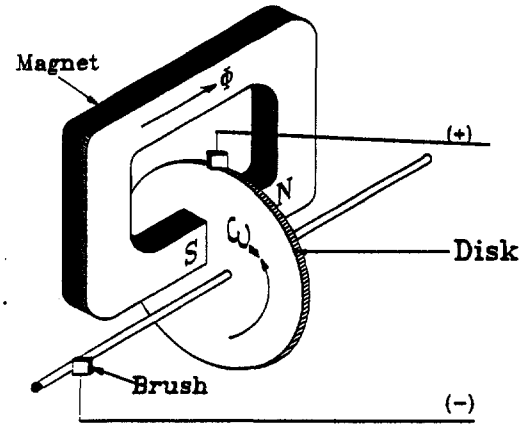

Fig. 1 Homopolar or Faraday disk

the unit. These include the following three important considerations:

1 Insulate electrically and ensure installed integrity of the bearing and seal insulation. *This places a positive barrier, preventing bearing through-current flow on:*

   (*a*) The outboard bearing on single drive-shaft units.
   (*b*) Multiple bearings on dual drive-shaft units.
   (*c*) Hydrogen or other close-running seals.
   (*d*) Couplings, when insulation need is determined.

2 Avoid encircling the shaft with electrical windings to limit currents to less than 1000 ampere-turns. (True for DC machines as well.) *Controls the level of magnetism passing through the bearing, seals, etc.*

3 Design AC machine stator cores that avoid the following: *Limits the amount of axially generated shaft magnetism and/or voltage that may produce currents in bearings.*

   (*a*) When the stator is split into equal sections, $A = 2 \times$ sections/poles; if A is odd.
   (*b*) When symmetric, segmental laminations are half-lapped, A = segments/circle/poles; if A is odd. (True for DC machine armatures as well.)
   (*c*) When the slots/(pole pair) is an odd integer.

These considerations apply to well-built symmetric magnetic cores and electrical circuits. Clearly, any unbalance or asymmetry in the construction, or as may develop in assembly, service, or repair, may also generate stray magnetism and/or stray currents. Shaft voltage traces from these causes are invariably sinusoidal in nature at the rotational or power frequency plus harmonics, and this usually distinguishes them from electrostatic or residual magnetic-generated voltages (Fig. 4).

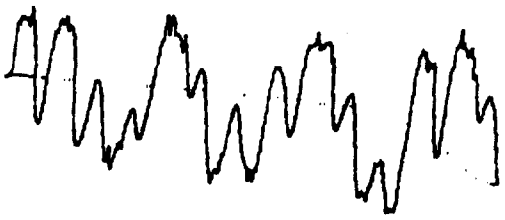

Fig. 4 Electrical machine shaft voltage

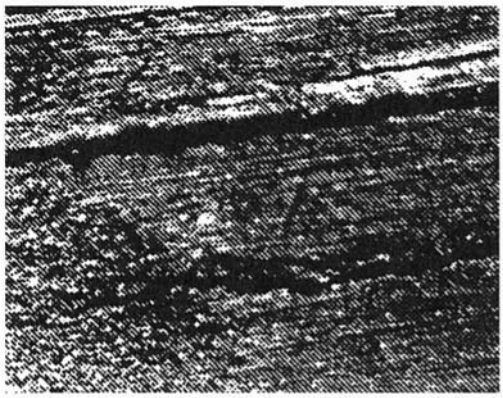

Fig. 5 60× magnification of bearing current pitting and spark tracks

Residual Magnetic

There are many possible residual magnetic sources for electromagnetic current generation. These are in the rotating machinery or in the structure or piping, or from another machine on the line, any of which act as permanent magnets. Usually involved are alloy steels that are magnetically hard and have been subjected to induced magnetic fields from actions such as magnetic particle inspection, magnetic chucks, welding, etc. Magnetic-generated currents are persistent. Pits they cause can become continuous in a wandering pattern, producing "spark tracks" on babbitted surfaces as (Fig. 5) with pitting on journal or thrust collars (Fig. 6). A "fluting" pattern or frosting is created by electric current and magnetism in anti-friction bearings, both ball and roller types.

Spark frosting and tracks due to through-currents are spread generally over the width of the affected surface, being concentrated in the zone of minimum oil film. Its powerful effect often eats completely through the babbitt layer and attacks the shell material with equal ease. The measured shaft voltage waveshape is highly irregular, appearing as if it were high-level noise. Peaks can reach hundreds of volts (Fig. 7).

Spark frosting and tracks occur at the extremities of the affected surface from through flux. Here the current crosses the

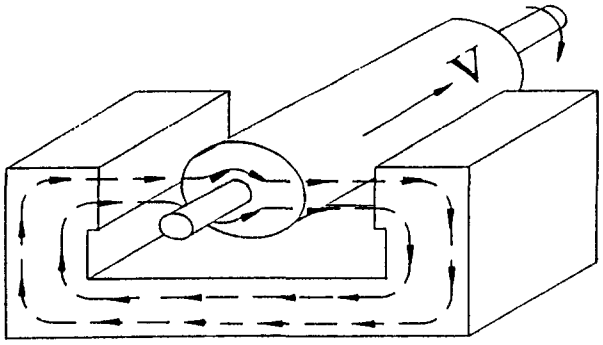

Fig. 2 AC generator action

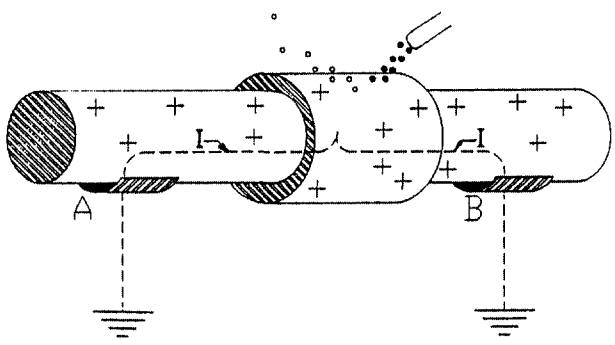

Fig. 3 Electrostatic generator action

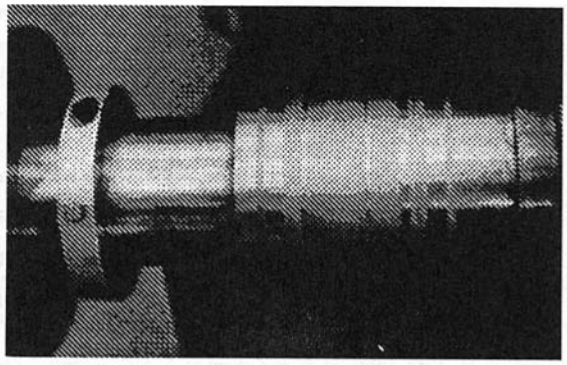

Fig. 6 Shaft journal current frosting

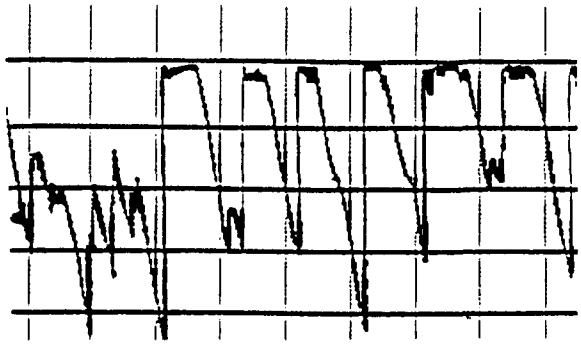

Fig. 8 Electrostatic shaft voltage

oil film at one bearing edge, traverses to the opposite bearing edge, where it recrosses the oil film and returns along the surface, closing the current loop, producing current pitting at the edges of the contact surfaces. Current sometimes passes over the outside surfaces of the bearing, indicating that it is of very high frequency.

Electrostatic

Stray currents from electrostatic sources are the same as static electricity, which one experiences from a comb rubbed on a sweater or the charge picked up when a person walks across a carpet on an especially dry day. Common to steam turbines is charge separation in the steam itself. There are many other sources for static electricity, including high-velocity lubricating oil in pipes and filters, charge separation in the process products, friction-excited currents from rubs of certain materials, etc. Static electricity shows up as frosting due to current discharges at either close gaps or contact points of oil film surfaces. The shaft voltage has but one polarity and measured traces exhibit a saw-tooth pattern (Fig. 8). This can be described as a gradual charge build-up to voltages reaching as high as several hundred volts with discharges in a variably discontinuous, repeating pattern. Static current searches out a means to equalize the charge. In doing so, it will follow a return path to a region of charge neutralization or equalization, which could be the piping, the condenser, a cooler, the oil reservoir, etc. Solid ground bonding of all units and their components minimizes errant and possibly destructive current return paths.

Recommendations

At the time of unit shutdown, perform inspection, identification, correction of shaft current damage, and removal of residual magnetism. In checking for residual magnetism, it is important to employ a versatile and reliable gaussmeter. It will be found that an analog, auto-ranging type provides the best accuracy and efficiency in making measurements. Record readings in gauss for comparison with readings before and after degaussing and at a later shut-down. Based upon field experience, and to ensure safe levels of magnetism, maximum permissible gauss levels are shown in Table 1.

Higher levels may be encountered at corners and edges up to 1.5 to 2.5 times. Magnetism will increase by factors of hundreds to thousands in an assembled unit, which is akin to placing a keeper onto a horseshoe magnet. At speeds exceeding 3000 rpm, thousands of gauss will generate troublesome voltages. It has been found that damaging shaft currents can occur if open-air magnetism exceeds the limiting values of Table 1 materially.

To remove magnetism, degaussing of shafts and steel sections thicker than $\frac{1}{2}$ inch requires programmed down-cycling or magnetic massaging, as is available with the Auto Degauss.

A reliable shaft condition indicator, such as the VCM, will monitor electrical current in the cable of the shaft grounding brush and the shaft voltage at a selected location. Local display, as well as transmitted readings to the control room, provides a means for trending shaft conditions that relate to shaft electrical conditions, and also supply valuable predictive/preventative maintenance information.

The process described above deals only with damage aspects of shaft currents and magnetism. There are other important items, such as continuous power loss due to circulating eddy currents (especially in thick frames and casings), and the affinity of magnetized parts for attracting metallic particles and chips, known to cause problems in the bearings, seals, etc.

Conclusion

It is recommended that diligence be employed in locating and assessing possible shaft current damage. By following corrective and preventive measures with respect to electrical machine design, construction, and maintenance, reduction of residual magnetism and the prevention of electrostatic charging of the shaft, resulting damage and forced outages can be averted.

An effective way to shunt shaft current harmlessly from the unit is to conduct it from the rotor to ground and to be certain

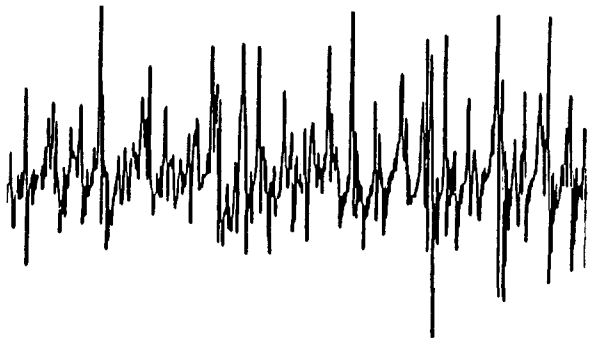

Fig. 7 Residual shaft voltage

Table 1 Maximum allowable residual magnetic field levels as measured in open air

2 gauss:	Bearing components, including pads and retainers, journals, thrust disc, seals, gears and coupling teeth.
4 gauss:	Bearing housings.
6 gauss:	Mid-shaft and wheel areas, diaphragms, etc.
10 gauss:	Components remote from minimum clearance areas, such as casings, pipings, etc.

that plant equipment and machinery are all electrically bonded to ground. An effective brush properly applied eliminates or averts shaft current damage, and with the brush current monitored accurately and regularly, valuable operational and preventive predictive information is obtained.

References

Alger, P. L., and Samson, W., 1924, "Shaft Currents in Electric Machines," *AIEE Trans.,* Vol. 43, pp. 235–245.

Ammann, C., Reichert, K., et al., "Shaft Voltages in Generators With Static Excitation Systems—Problems and Solutions," Swiss Federal Institute of Technology, Zurich, Switzerland; Brown Boveri Company, Baden, Switzerland.

Nippes, P. I., and Sohre, J. S., 1978, "Electromagnetic Shaft Currents and Demagnetization of Rotors of Turbines and Compressors," presented at the 7th Turbomachinery Symposium, Texas A&M University, Houston, TX.

Nippes, P. I., and Sohre, J. S., et al., 1981, "Panel on Electromagnetic Shaft Current Control," presented at 10th Turbomachinery Symposium, Texas A&M University, Houston, TX.

Nippes, P. I., 1992, "Detecting and Identifying Vibration Problems in Rotating Electrical Machinery," presented at the 16th Annual Meeting of the Vibration Institute, Williamburg, VA.

Rosenberg, L. T., 1955, "Eccentricity, Vibration, and Shaft Currents in Turbine Generators," *AIEE Transactions,* Apr., pp. 38–41.

Salomon, T., 1959, "Harmful Effects of Electrostatic Charges on Machinery and Lubricating Oils," *J. Inst. Pet.,* Vol. 45, Mar., No. 423.

Schier, V., 1965, "Selbsterregte Unipolare Gleichstrome in Maschinenwallen," *Elektrotechnische Zeitschrift,* Nov. 12 [in German], Translation #3925, "Self-Excited Homopolar Direct Currents in the Shafts of Machines," Associated Electrical Industries, Ltd., Power Group, Research Laboratory, Trafford Park, Manchester 17, United Kingdom.

Wilcock, D. F., 1949, "Bearing Wear Caused by Electric Current," *Electric Manufacturing,* Feb., pp. 108, 111.